Centrifugal Casting of an Aluminium Alloy

By

Eduardo Trejo

A thesis submitted to the
University of Birmingham
for the degree of
DOCTOR OF PHILOSOPHY

Metallurgy and Materials
School of Engineering
University of Birmingham
Edgbaston
Birmingham
B15 2TT
United Kingdom

October 2011

ABSTRACT

In centrifugal casting, molten metal is introduced into a mould which is rotated at high speed. The centrifugal force helps to fill thin sections but this benefit may be offset by the effect of the turbulent flow on the casting quality. In this research, the effect of direct and indirect gated mould designs on the quality and reliability of aluminium alloy investment castings made by centrifugal casting was investigated. The scatter in the ultimate bend strength and the modulus of elasticity was analyzed using the Weibull statistical technique, which showed that the Weibull modulus of both properties was significantly improved for the indirect gated cast test bars compared to the direct gated bars.

A detailed microstructural characterization was carried out on the cast test bars, which included grain size, dendrite cell size and porosity. Scanning electron microscopy was used to examine and analyze the presence of defects on the fracture surfaces such as shrinkage pores, entrapped bubbles and oxide films resulting from surface turbulence during mould filling. The results indicated a clear correlation between the mechanical properties and the presence of casting defects.

Water modelling experiments were carried out using purpose-built experimental centrifugal casting equipment and filling sequences recorded using a high speed video camera. The water modelling results showed that the general tendency for the direct and indirect gated mould designs was that the higher the rotational velocity, the lower the filling length and consequently the lower the filling rate. Subsequently, this information was used to validate the computer software ANSYS CFX. An excellent correlation was obtained between the experimental water modelling and simulation results for both direct and indirect gated moulds.

ANSYS CFX and the Oxide Film Entrainment Model (OFEM) technique implemented in Flow-3D were used to model centrifugal casting experiments and to understand and assess quantitatively how the mould design damages the molten metal through the generation of surface turbulence and consequently the generation of bubbles and oxide films. These results were compared with the water modelling, radiography and mechanical properties obtained from the direct and indirect gated cast moulds. This confirmed that the less turbulent metal flow resulting from indirect gating significantly increased the reliability of the castings.

ACKNOWLEDGMENTS

I am grateful to my supervisors Dr. Richard Harding and Professor Nick Green for their excellent support, advice, guidance and patience throughout my PhD. Working under their supervision has been a great experience and a huge learning curve.

Special thanks to research fellow Dmytro Shevchenko for his guidance using CFX, help doing casting experiments and constructive criticism. Thanks to Jean Christophe Gebelin and colleague Yang Yue for their help and support on computer modelling, and Nick Humphreys for his invaluable advice.

I would like to express my gratitude to the technicians Adrian Caden, Peter Cranmer, Grant Holt and David Price for their help, assistance and experience provided throughout my PhD; and especially to Mick Wickins for all those conversations and good humour, which made an enjoyable atmosphere while working in the foundry. Also thanks to Hu-Tian Li at Brunel University for his advice on anodizing. My appreciation to research colleagues in the PRISM 2 office for their friendship during my stay in the Department of Metallurgy and Materials.

I would like to thank the National Council on Science and Technology of Mexico (CONACYT) for financial support and the School of Metallurgy and Materials in the University of Birmingham for provision of research facilities.

Additional thanks to my great friends Manuel, Florian, Markus, Esteban, Ola, Roman, Adolfo, and ‘Grace House’ friends Thanh, Arezoo, Masoud and Cezania, for all our celebrations and gatherings which made my experience in Birmingham enjoyable.

I want to thank to my best friend and wife Jane for her support through the gloomy days and loving company in the most memorable moments of my PhD.

Finally, I want to express my love and gratitude to my parents Fernando and Rosa Maria for their encouragement and support throughout my studies in the UK.

Eduardo Trejo

October 2011

TABLE OF CONTENTS

LIST OF TABLES

CHAPTER 2

CHAPTER 4

CHAPTER 5

CHAPTER 6

CHAPTER 7

LIST OF FIGURES

CHAPTER 2

CHAPTER 4

CHAPTER 5

CHAPTER 6

CHAPTER 7

1. INTRODUCTION

The ultimate goal of the centrifugal casting research carried out in the Department of Metallurgy and Materials at the University of Birmingham is to develop techniques for centrifugally casting complex thin wall engineering components in γ-TiAl alloys. However, the aim of this work as a first stage was to carry out centrifugal casting experiments using a medium strength aluminium alloy. The intention of this first stage was to compare the quality and reliability of centrifugally cast test bars using direct and indirect gated mould designs with those obtained by conventional casting processes such as gravity and tilt casting (under turbulent and controlled conditions), whose extensive data has been reported in the literature. The reasons of using the centrifugal casting process to produce complex thin wall engineering components in γ-TiAl alloys are given in the following paragraphs.

TiAl alloys have density-corrected tensile, fatigue and creep properties which make them competitive with nickel-base superalloys. Based largely on these properties, TiAl alloys can find use in a wide range of components in the aerospace and automotive industry. The intention of these applications is to substitute the heavier nickel or iron-based alloys in certain ranges of stress and temperature (Leyens and Peters, 2003).

The application of TiAl alloys in the aerospace industry has been aimed at the production of turbine blades. Extrusion and forging have been used to produce compressor blades for engine testing, but the processing costs are very high (Wu, 2006). Investment casting, which is a well established process, is the most cost-effective route (Bidwell, 1997). However, TiAl alloys are very reactive in the molten condition and it is difficult to melt them in a conventional refractory crucible. Instead, it is common practice to melt them in a water-cooled copper

crucible using energy supplied by an induction coil (Induction Skull Melting or ISM). Although this melting process prevents contamination of the molten metal by oxygen and refractory inclusions, it provides only limited superheat ~ 40 - 60°C (Harding and Wickins, 2003), which therefore makes it difficult to fill thin section castings.

Centrifugal casting has been used to produce a variety of components made of ferrous and non-ferrous alloys including conventional Ti alloys, which are commonly used to produce golf clubs (Polmear, 2006). However, engineering components have more stringent mechanical property requirements, which has led to worldwide research on centrifugal casting of TiAl alloys to produce particularly automotive valves and turbo-charger rotors (Choudhury and Blum, 1996), (Blum et al., 2002), (Liu et al., 2005), (Sung and Kim, 2007), (Fu et al., 2008). Furthermore, little research has been done to apply this process to produce thin wall engineering components of gamma titanium aluminide alloys (Wu, 2006).

The main benefit is that the high g-force resulting from high speed rotation of the mould not only assists in mould filling, but may also help to feed the shrinkage during the solidification of the casting. However, this may be partly offset by the very turbulent nature of the mould filling process which may entrain various defects such as bubbles and oxide films (Campbell, 2003).

However, there are various possibilities for improving the casting quality either by optimizing the design of the mould (e.g. the running, gating and vent system) or the process parameters such as rotation speed, inlet condition and temperature of the molten metal and mould.

The detailed objectives of this investigation are presented in Chapter 3 and a summary is given as follows:

- To carry out centrifugal casting experiments for an aluminium alloy and to investigate the effect of direct and indirect mould designs on the formation of casting defects such as entrapped bubbles and double oxide films and inter-relate these results with the mechanical properties.

- To validate the computer modelling software (ANSYS CFX) based on water modelling for simple direct and indirect gated mould designs.

- To use computer modelling to study the metal flow during the centrifugal casting process and quantitatively assess the damage provoked by surface turbulence-related phenomena during the metal flow in direct and indirect gated moulds.

2. LITERATURE REVIEW

2.1 Introduction

End-users of castings are always interested in the best possible performance (a sufficiently high and reproducible set of properties such as strength, ductility, toughness, etc., depending on the application) at the minimum cost. The required performance can only be achieved by producing the required microstructure and an acceptably low number of defects. For a given material, this can be achieved by understanding the selected manufacturing process so that it can be optimised.

In this Chapter, an introduction will be given to the centrifugal casting process. As in any casting process, the two most important stages which determine the structure and defects are mould filling and solidification and these two stages will be considered separately. The techniques for assessing the microstructure and presence of defects will then be reviewed, and finally the factors affecting the mechanical properties and reliability of castings will be considered. Finally, computational techniques for predicting the flow of molten metal inside moulds will be reviewed.

2.2 Centrifugal Casting

2.2.1 General Principles

A particle is in uniform circular motion if it travels around a circle at constant uniform speed. Although the speed does not vary, the particle is accelerating. That fact may be surprising because acceleration is often thought of as an increase or decrease in speed. However,

actually velocity is a vector, not a scalar (Halliday et al., 2001). Figure 2 - 1 shows the relation between the velocity and the acceleration vector at various stages during uniform circular motion. The velocity is always directed at a tangent to the circle in the direction of motion and the acceleration is always directed radially inwards. As a result of this, the acceleration associated with uniform circular motion is called centripetal ('centre seeking') acceleration. The magnitude of this acceleration is:

$$a = \frac{s^2}{r} \qquad \text{Equation 2 - 1}$$

where r is the radius of the circle and s is the tangential velocity of the particle.

Subsequently, from Newton's second law and Equation 2 - 1, the magnitude F of the centripetal force is:

$$F = m\frac{v^2}{r} \qquad \text{Equation 2 - 2}$$

where m is the mass of the particle.

Since the speed v is constant, so are also the magnitudes of the acceleration and force. However, the directions of the centripetal acceleration and force are not constant; they vary continuously so as to always point toward the centre of the circle.

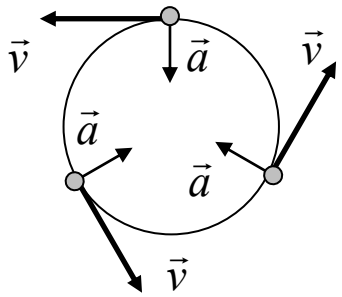

Figure 2 - 1. Velocity and acceleration vectors for a particle in anticlockwise uniform circular motion.

2.2.2 Essential feature of Centrifugal Casting

The essential feature of centrifugal casting is the introduction of molten metal into a mould which is rotated during filling and solidification of the casting. Centrifugal casting is widely used to produce a variety of components made of both ferrous and non-ferrous alloys. One of its main benefits is that the centrifugal force enables thinner wall castings to be produced than is possible by conventional static casting, partly because of the higher pressure exerted on the molten metal during mould filling and partly because the reduced filling time results in less heat loss from the molten metal to the mould. The pressure exerted on the molten metal may reduce the solidification time (due to better contact with the mould) and may also help to feed the shrinkage during solidification compared to castings made by static casting processes (Zhang et al., 2004).

Centrifugal casting can be carried out with the axis of rotation either vertical or horizontal. Horizontal centrifugal casting is generally used to produce tubes, pipes, etc. Vertical centrifugal casting can be used to make shaped individual (large) components or numerous components in one mould. A typical arrangement is illustrated in Figure 2 - 2. Vertical centrifugal casting is the specific process that is treated in this investigation and for simplicity purposes it will be just named 'centrifugal casting'.

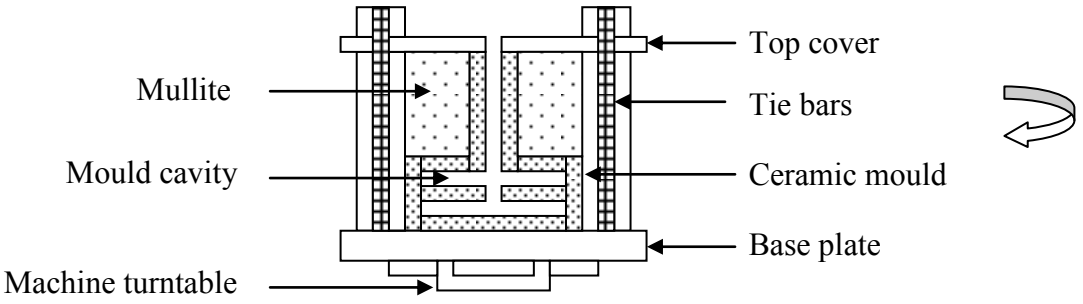

Figure 2 - 2. Mould assembly for vertical centrifugal casting process.

2.2.3 Engineering Components and Gating Design in Centrifugal Casting

Considerable interest has been focused on centrifugal casting for producing engineering components made of TiAl alloys particularly automotive valves and turbocharger rotors (Liu et al., 2005), (Fu et al., 2008), (Sung and Kim, 2007). In these processes, the component cavities have been connected directly to the central sprue, which is commonly known as a direct gated mould, Figure 2 - 3. Although direct gating is widely used in the industry, the filling process is difficult to control and leads to extensive surface turbulence. The principal advantage of this system is the simplicity for moulding and its low consumption of additional metal. An indirect gating system, Figure 2 - 4, has a lower yield since more metal is used to fill the running system. However, it improves the control over the metal stream which enables the mould cavity to be back-filled in a less turbulent manner.

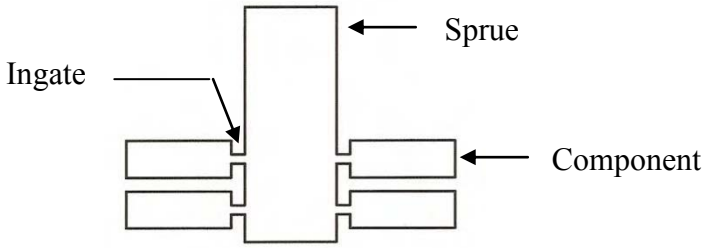

Figure 2 - 3. Schematic view of direct gated mould design.

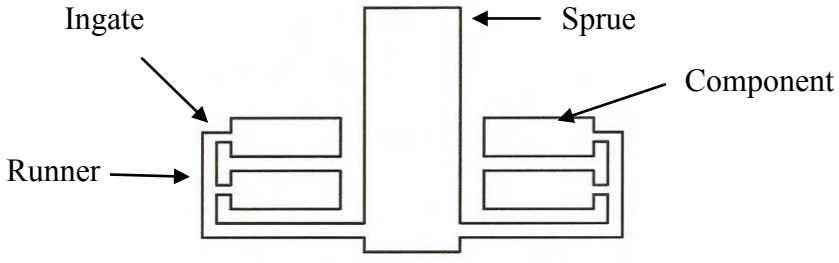

Figure 2 - 4. Schematic view of indirect gated mould design.

Wu et al (2006), Li et al. (2006) and Jakumeit et al (2007) suggested that it is better to use an indirect gating than direct gating system since it could reduce the turbulence generated during the filling process. However, experimental evidence on cast components has not been reported to validate their modelling results.

2.3 Mould Filling

2.3.1 General Principles of Metal Flow

At low velocities, the flow of a liquid is laminar and the liquid can be considered as numerous particles all moving smoothly and parallel to the direction of flow. There are no particles moving perpendicular to the direction of the flow. On the other hand, at high velocities, the flow becomes turbulent, which is characterised by irregular movements of the particles across the stream, in addition to their movement in the direction to the flow (Sutton, 2007).

The criterion which determines whether the flow of a liquid in a pipe is laminar or turbulent is given according to the following formula (Reynolds, 1883):

$$\mathrm{Re} = \frac{\rho V L}{\mu} = \frac{VL}{\nu} \qquad \text{Equation 2 - 3}$$

where Re is the Reynolds number, V is the velocity of the liquid, ρ is the density of the liquid, L is the diameter of the tube, μ is the dynamic viscosity of the liquid and ν is the kinematic viscosity ($\nu = \mu / \rho$).

Experiments carried out with a number of different fluids in straight pipes of different diameters have established that if the Reynolds number is calculated by making L equal to the pipe diameter and using the mean velocity $\overline{V}$, then, below a critical value of Re = 2000, flow

will normally be laminar. This value of the Reynolds number applies only to flow in pipes, but critical values of the Reynolds number can be established for other types of flow (Douglas et al., 2005).

It is important to mention that this flow behaviour takes place in the bulk of the liquid, underneath the surface. During such turbulence in the bulk liquid, therefore, the surface of the melt may remain relatively tranquil. Turbulence as predicted and measured by Re does not apply to the problem of assessing whether the surface will be incorporated into the melt (Campbell, 2003). Surface turbulence is more dangerous and creates additional free surface, which can lead to the generation of oxide films and entrapment of bubbles. These can have a profound influence on the presence of defects and subsequently the mechanical properties.

The generation of oxide films and entrapment of bubbles will be explained in more detail in Section 2.3.3.1.

2.3.2 Examples of Flow Involving Surface Turbulence

2.3.2.1 Returning Waves, Fluid Front Collisions and Rising Jets

Returning waves can be formed during the filling of component cavities, oversized runners, etc. The returning wave rolls over the underlying fast jet, rolling in oxides at the interface between the two (Campbell, 2004), Figure 2 - 5. In general, the higher the velocity of the returning wave, the greater the possibility of oxide film entrainment and generation of bubbles (refer to Section 2.3.3.1), which are formed by the vortices in the shear zone.

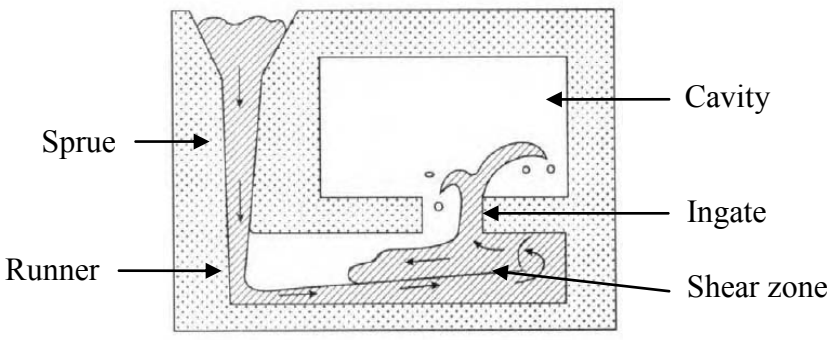

Figure 2 - 5. Schematic diagram of a returning wave (Campbell, 2004).

Fluid front collisions or confluence welds (Campbell, 2003) are formed when the free surfaces of two liquid metal fronts are brought together. One of the main causes of this phenomenon is when the geometry of the casting causes the metal stream to separate. This involves the formation of films on the advancing fronts of both streams, which subsequently join together again at some location, Figure 2 - 6 (a). In extreme cases, this can entrap air resulting in the formation of bubbles.

Rising jets are usually formed when liquid emerges from vertical ingates to enter the mould at high velocity. At high velocities, the liquid can enfold its surface during its subsequent fall, Figure 2 - 6 (b).

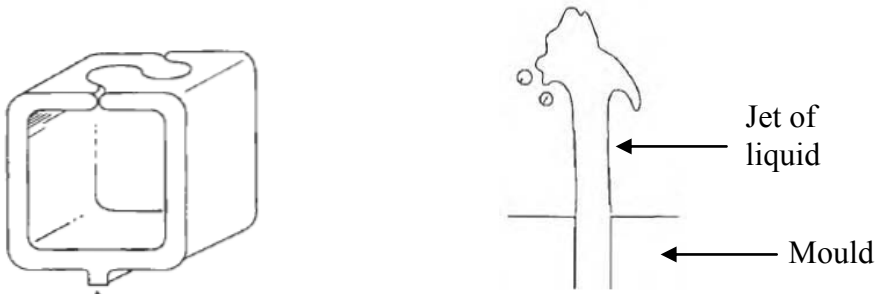

(a) (b)

Figure 2 - 6. Schematic diagram of (a) fluid front collision and (b) rising jet (Campbell, 2003).

2.3.2.2 Plunging Jets

Plunging jets are usually formed when transferring molten metal from either the crucible or ladle into the pouring basin. The dross is carried under the surface of the liquid and in extreme cases, air can also be entrained (Campbell, 2003), Figure 2 - 7.

McKeogh and Ervine (1981) defined three typical scenarios of the air entrapment process at the impinging point in a liquid pool. In the first scenario, a laminar jet penetrates deeply into the pool and provokes an air cavity beneath the free surface. Any interfacial disturbance on the jet makes the cohesion of the air cavity unstable, provoking its puncture at one or several locations, Figure 2 - 7 (a). The second scenario is the transition of the jet from a laminar flow to turbulence. An intermittent vortex is formed at the impinging point and the free surface of the pool deepens around the jet. The dip is explained by the increasingly axial momentum driven by the jet and also by the axial flow of the air boundary layer which surrounds the jet, Figure 2 - 7 (b). The third scenario is related to an established turbulent plunging jet. Both the surface of the jet and the surface of the pool undulate at the vicinity of the impact point so that many bubbles are generated, Figure 2 - 7 (c).

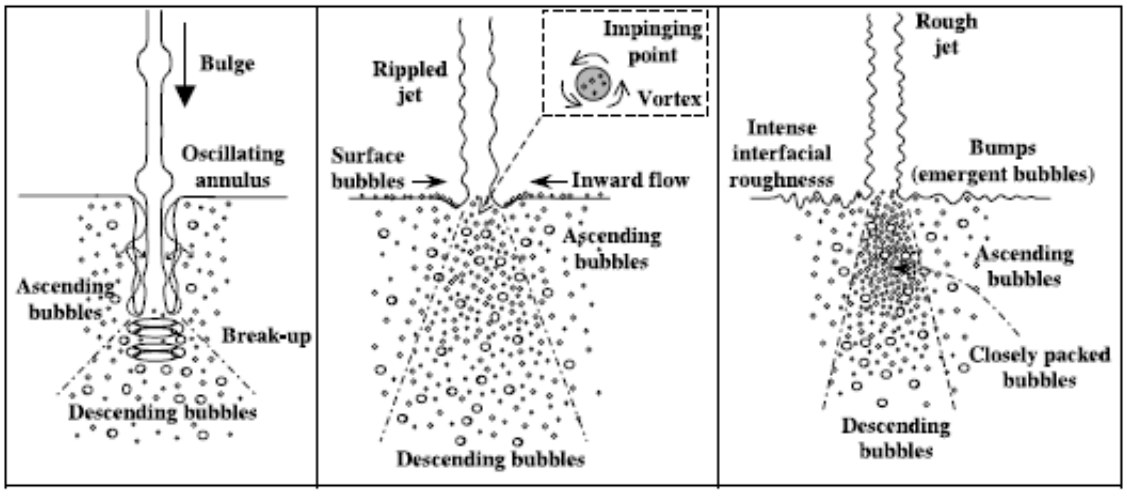

(a) (b) (c)

Figure 2 - 7. Schematic diagram of the plunging jet scenarios (Davoust et al., 2002).

2.3.2.3 Circular Hydraulic Jump

The circular hydraulic jump can be formed as a consequence of normal impingement of a cylindrical liquid jet on a smooth horizontal surface. The liquid spreads out radially along the surface forming a thin film and at some radial distance from the impingement point (or stagnation point), the film thickness abruptly increases, Figure 2 - 8. Close to the jet, the fluid layer is thin and the motion is rapid. However, somewhat away from the impingement zone the flow velocities are slower, with a consequent increase in the film thickness. (Kate et al., 2008). This kind of hydraulic jump involves a strongly distorted free surface, a boundary layer region and a subsequent separation of the flow (Kenuke and Feng, 2002).

Figure 2 - 8. Circular hydraulic jump due to a normal impinging circular liquid jet (Kate et al., 2008).

2.3.2.4 Hydraulic Jumps

In open channel flow, the transition from a rapid (supercritical) to a tranquil (subcritical) flow is called a hydraulic jump. It is characterized by the development of large-scale turbulence (strong turbulent mixing), surface waves and spray, energy dissipation and air bubble entrainment (Chanson, 1995) (Chanson, 2007). The large-scale turbulence region is usually called the 'roller'.

In a horizontal rectangular channel, Chanson (1995) defined the characteristics of a hydraulic jump and the three types of inflow conditions: (i) partially developed supercritical flow, (ii) a fully developed boundary layer flow and (iii) a pre-entrained jump. A partially developed jump exhibits a developing boundary layer. For a fully-developed jump, the boundary layer has expanded over the entire flow depth. Figure 2 - 9. A pre-entrained jump is a fully-developed jump with free-surface aeration. The air-water mixture next to the free-surface modifies the jet impingement and hence the roller characteristics. "With any inflow configuration, large quantities of air are entrained at the toe of a jump. Air bubbles are entrapped by vortices with axes perpendicular to the flow direction. The entrained bubbles are advected downstream into a free shear layer characterized by intensive turbulence production before reaching the free-surface and escaping to the atmosphere" (Chanson, 1995).

Likewise, Chanson (1995) described the structure of the bubbly flow as follows: "Air entrainment occurs in the form of air bubbles and air pockets entrapped at the impingement of the upstream jet flow with the roller. The air pockets are broken up into very thin air bubbles as they are entrained. When the bubbles are diffused into regions of lower shear stresses, the coalescence of bubbles yields to larger bubble sizes and these bubbles are driven by buoyancy

to the boiling region. Near the free-surface, the liquid is reduced to thin films separating the air bubbles".

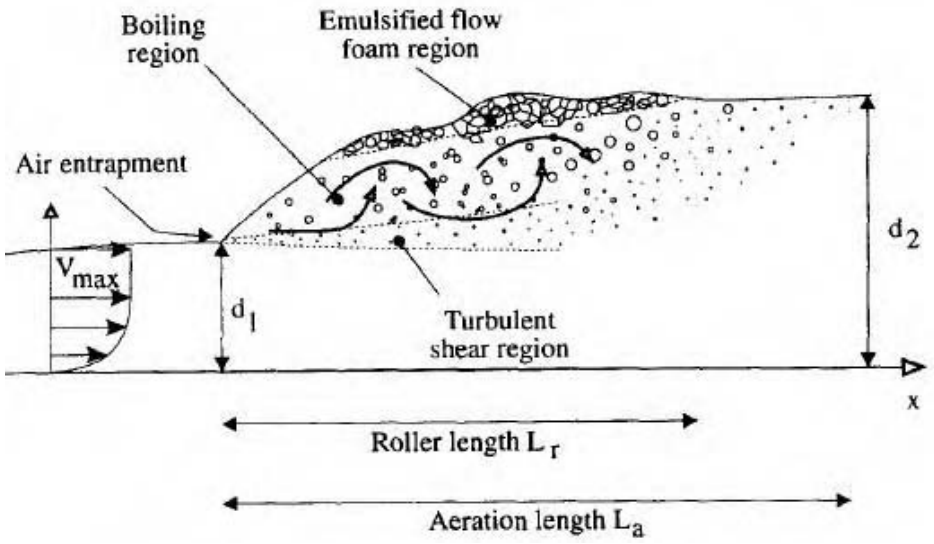

Figure 2 - 9. Air -water flow region of a hydraulic jump (Chanson, 1995)

2.3.3 Defects Caused by Surface Turbulence

2.3.3.1 Entrainment Mechanisms, Oxide Films and Entrapped Bubbles

Centrifugal casting is naturally a very turbulent filling process and can lead to the generation of entrainment mechanisms such as hydraulic jumps, returning waves, plunging jets, fluid front collisions and rising jets, which can be formed in the sprue, runner system and component cavities.

In aluminium alloys, the reaction between the free surface and oxygen in the atmosphere creates oxide films. Therefore, when splashing at the surface occurs it can lead to the formation of double oxide film defects (or bi-films), which become entrained in the bulk

liquid, Figure 2 - 10. Since the surface entrains as a double oxide film folded dry side to dry side, it forms two non-wetting surface films (Campbell, 2003), which act as cracks in the solidified castings, Figure 2 - 11. Additionally, if the surface turbulence is severe, it can lead to entrapment of bubbles, Figure 2 - 10. The characteristics of bubble trails will be described in more detail in Section 2.3.3.2.

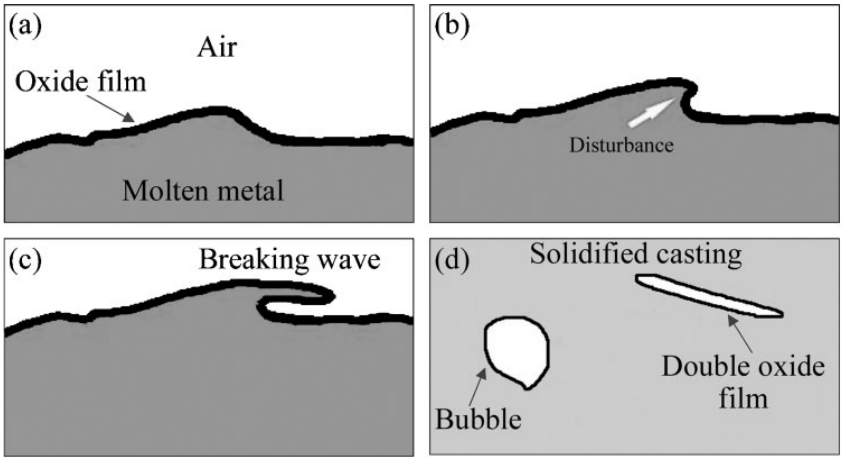

Figure 2 - 10. Surface turbulence leading to the entrainment of gas bubbles and the formation of double oxide film defects (Harding, 2006).

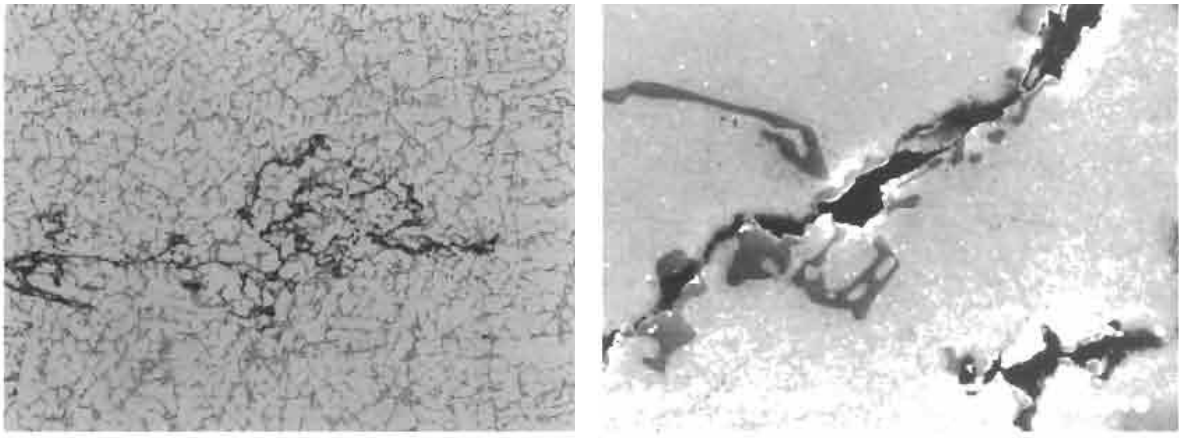

(a) (b)

Figure 2 - 11. (a) Convoluted bifilm in Al-7Si-0.4Mg alloy and (b) high magnification of the double film revealing its canyon-like appearance (Green and Campbell, 1994)

Campbell (2003) categorized oxide films as old thick oxide films and young thinner oxide films. The old oxide films are thought to come from remelted ingots or castings or from the melting crucible where oxidation of the surface occurs and young oxide films are formed during the filling process due to high surface turbulence as shown in Figure 2 - 10. Usually, in EDX analysis these old thick films show a much higher oxygen peak compared to young oxide films (Nyahumwa et al., 1998).

Oxide films are well-known to be detrimental to the mechanical properties of aluminium alloys such as tensile strength (Green and Campbell, 1993), (Green and Campbell, 1994) and fatigue life (Nyahumwa et al., 1998). They have also been shown to affect the reliability of steels (Griffiths et al., 2007) and, to a lesser extent, vacuum cast nickel alloys (Cox et al., 2000).

The effect of oxide films and porosity on casting quality and reliability will be covered in Section 2.6.1.

2.3.3.2 Bubble Trails

When a bubble of gas is entrained in the molten metal (Figure 2 - 10) it can move upwards due to a buoyancy effect or in any direction due to bulk turbulence generated during the filling process. Since the gas contained in the bubble is highly oxidizing (if the casting process is carried out under normal air conditions), it will react with the liquid metal as it moves, leaving a collapsed tube in its wake. Since the inner walls of the trail are non-wetting, this will again form a double oxide film (Campbell, 2003). Figure 2 - 12 shows the common shapes of rising bubbles, associated trails and their progressive collapse.

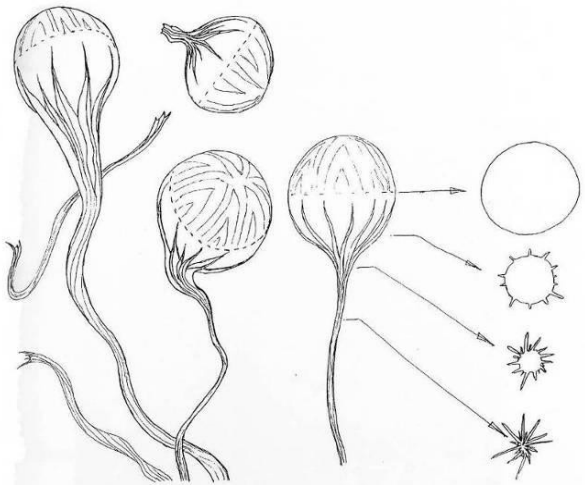

Figure 2 - 12. Schematic illustration of rising bubbles, associated trails and cross-sections showing the progressive collapse of the bubble trail (Campbell, 2003).

Likewise, Divandari and Campbell (2001) reported that three possible forms of bubble trail may exist: (i) a continuous bubble trail in open tube form, Figure 2 - 13; (ii) a continuous bubble trail in collapsed tube form, Figure 2 - 14, which is often mistaken in transverse section as a shrinkage pore; and (iii) dispersed fragments of collapsed tube, Figure 2 - 15. This kind of bubble trail is fragmented and settled at random locations in the casting as tangled oxide films during solidification.

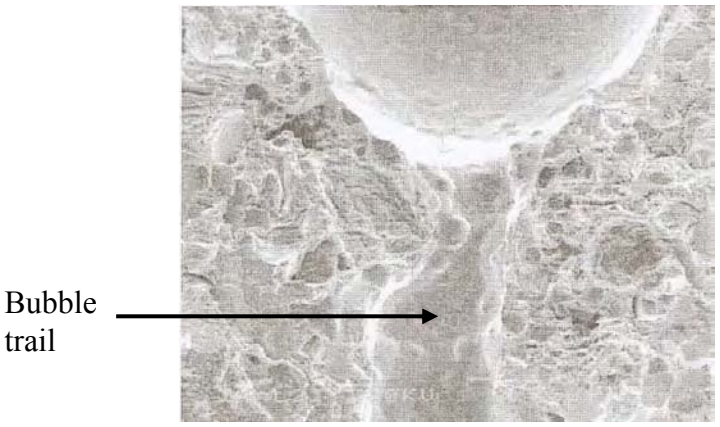

Figure 2 - 13. SEM micrograph showing a bubble and its associated bubble trial (Divandari and Campbell, 2001).

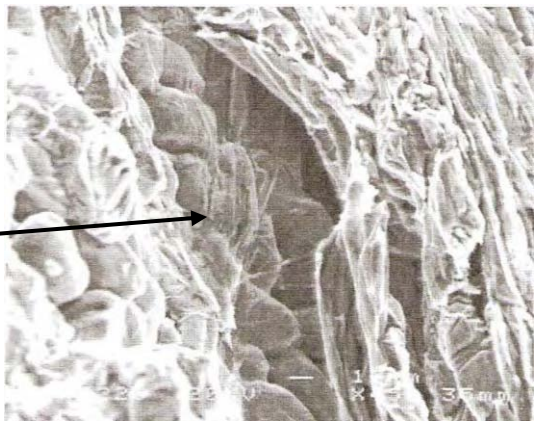

Figure 2 - 14. SEM micrograph showing details underneath the collapsed tube (Divandari and Campbell, 2001).

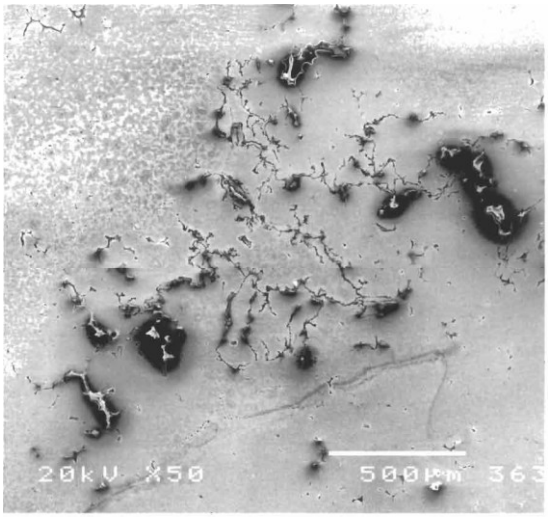

Figure 2 - 15. SEM metallographic section of a number of bubble trails (Campbell, 2003)

2.3.3.3 Oxide films in Ti and Al alloys

Molten titanium has a high affinity for oxygen, nitrogen and hydrogen. This is the reason why melting and pouring are carried out under vacuum or inert atmosphere. After casting titanium alloys, it is standard practice to hot isostatically press (HIP) high-quality castings in order to remove porosity (Polmear, 2006). In TiAl alloys Hu and Loretto (Campbell, 2003) showed

that thick oxide films can go into solution during hot isostatic pressing, which suggests that these oxide films are soluble under appropriate time and temperature.

Mi et al. (2003) reported that during the tilt casting process of a TiAl alloy surface turbulence may lead to the generation of oxide films. The authors reported that detailed SEM examinations revealed that about 10-20% of the dendrites within the porosity were draped with films, which are believed to be oxide films because their similar appearance to those reported in aluminium alloys (Divandari and Campbell, 2001) (Divandari and Campbell, 2004). Likewise, Figure 2 - 16 illustrates the results of a pore, where the higher magnification showed that a film was draped over the inner surface of the pore and the EDX analysis results showed the characteristic oxygen peak of oxide films (Mi et al., 2003). The presence of these oxide films in TiAl has only been reported so far by Mi et al. (2003).

The oxidation of pure aluminium melt starts by the fast formation of an amorphous alumina layer. Then, it changes to crystalline γ-alumina slowing the rate of oxidation and after a further incubation period, the oxide structure converts to α-alumina (Thiele, 1962). In the presence of alloying elements in the metal, the rate of this oxidation is modified, *e.g.* Mg, Na and Ca increase the rate of oxidation, whereas Si, Fe, Cu and Zn have a minimum effect on the oxidation (Cochran et al., 1977) (Divandari and Campbell, 2005). As described in Section 2.3.3.1, surface turbulence in molten aluminium alloys results in the formation of oxide films. These defects have been widely studied in the last two decades (Campbell, 2003).

Nyahumwa et al, (2001) demonstrated that the HIP process can improve the fatigue-life performance in an alloy Al-7Si-Mg, which was attributed to a possible deactivation of entrained oxide film defects. In contrast, Wakefield and Sharp (1992) demonstrated that oxide films in hipped Al-10Mg are impossible to deactivate, which is attributed to the different

oxide film of magnesia (MgO) entrained during casting. This magnesia film is thicker and has a stable structure, which does not transform during hipping.

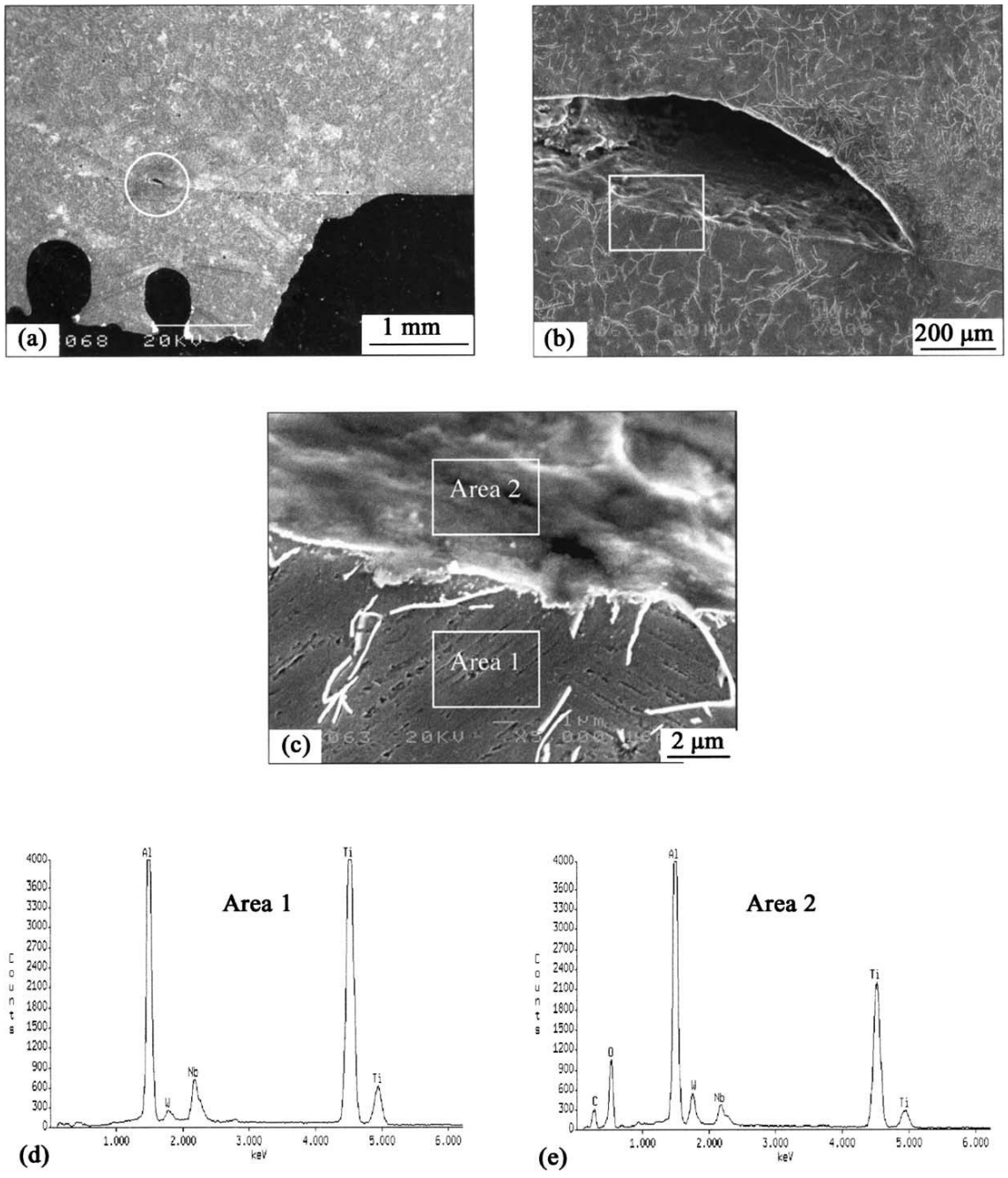

Figure 2 - 16. SEM secondary electron micrographs and EDX spectra of a cold lap, showing (a) a cold lap with a pore (circled area), (b) a close-up of the pore, (c) the inner surface of the pore in the framed area in (b) showing the areas analysed, (d) and (e) the EDX spectra of areas 1 and 2 (Mi et al., 2003).

It seems that the deactivation of oxide films with the HIP process depends on the processed aluminium alloy, although is not as effective as that in TiAl alloys, Hu and Loretto (Campbell, 2003). Therefore, the importance of having oxide films depends on the alloy cast, and hence the importance of controlling the filling process during centrifugal casting.

2.3.4 Visualization of Mould Filling

Understanding and controlling the flow of metal during mould filling is of critical importance in the production of high quality castings. There are techniques to visualize the mould filling such as moulds with a glass window and real-time radiography. However, these are difficult to implement with a mould rotating at high speed.

Alternatively, a water analogue has been used as an effective technique to visualize the mould filling in different casting processes (Nguyen and Carrig, 1986), (Cleary et al., 2002), (Cleary et al., 2006). Among the main disadvantages of this method is that the experiments commonly are carried out using Perspex moulds, which do not have the permeability of sand and ceramic moulds (Brown, 1999). However, it is considered a very useful technique for validating CFD modelling (Cleary et al., 2006).

Li et al. (2006) modelled the filling process of simple moulds during centrifugal rotation using water as a fluid. The authors named these moulds as top and bottom gating systems. In order to avoid confusion and to be consistent with terminology in this investigation, the name of ‘direct’ and ‘indirect’ gating systems instead of top and bottom gating systems will be used throughout this work. A detailed explanation of the experimental conditions chosen by Li et al. (2006) was not given and just the following information was reported:

- The plan view and dimensions of the direct and indirect gating mould designs are illustrated in Figure 2 - 17.

- Three rotational velocities were used in these experiments: 163, 245 and 375 rpm in the anti-clockwise direction.

- The liquid was poured at the same height of 50 mm and the experiments were carried out in air.

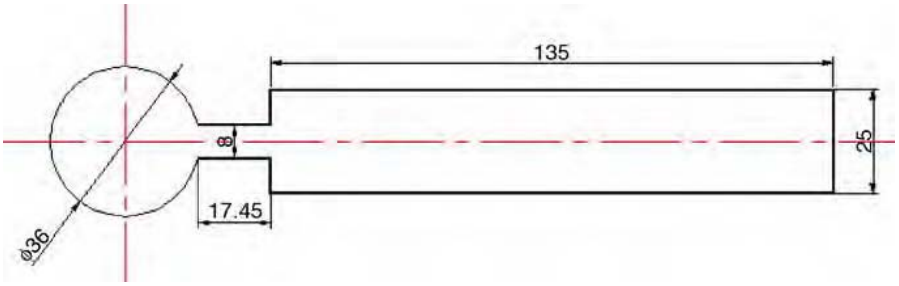

(a)

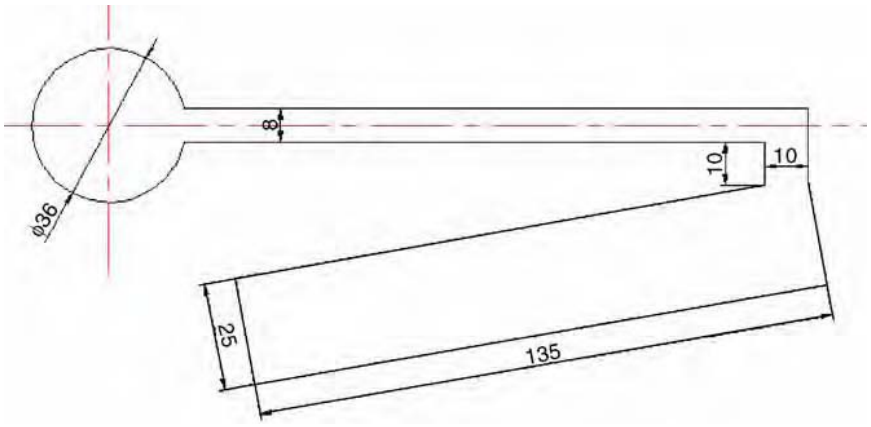

(b)

Figure 2 - 17. Plan view of (a) direct and (b) indirect gating mould designs (Li et al., 2006); all dimensions in mm.

A representative example of the filling sequence for both direct and indirect gated moulds is illustrated in Figure 2 - 18. Since the flat test bars of the two mould designs had the same dimensions (Figure 2 - 17), the measurement of the filled lengths of the test bars was carried out according to the following formula:

$$FL = \frac{L_1 + L_2}{2} \qquad \text{Equation 2 - 4}$$

where FL is the filled length, and L_1 and L_2 are described in Figure 2 - 19.

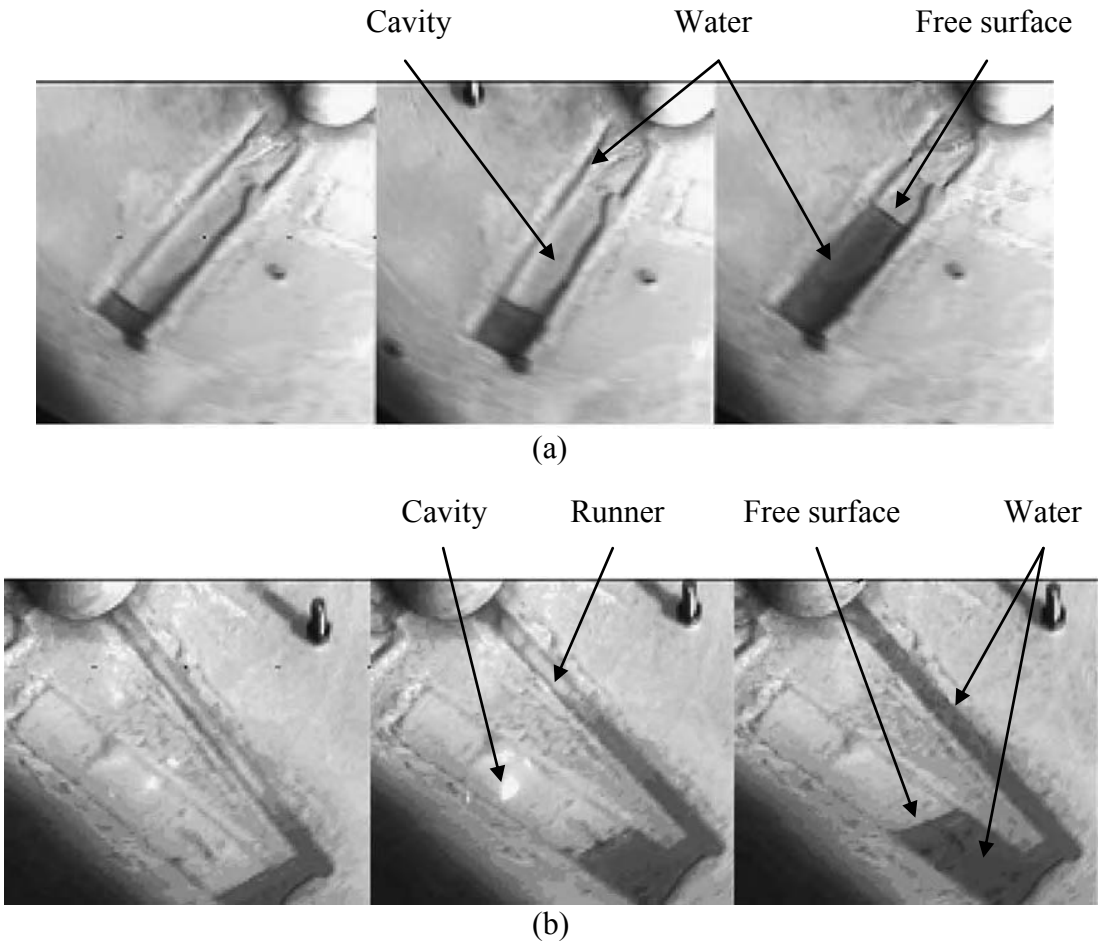

Figure 2 - 18. Filling sequence of (a) direct and (b) indirect gated moulds at rotational velocity of 245 rpm in anticlockwise direction (Li et al., 2006)

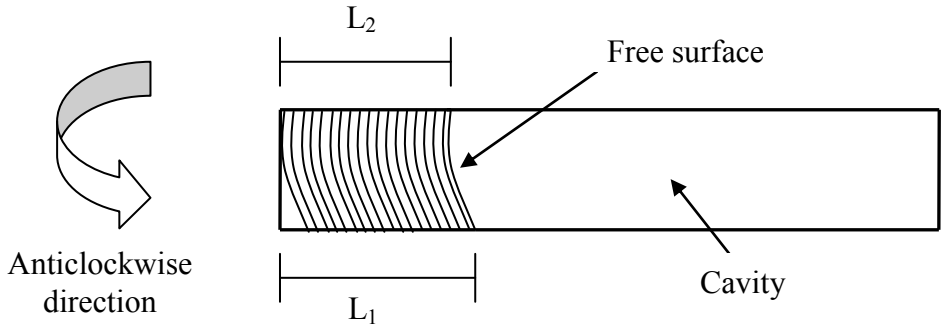

Figure 2 - 19. Schematic plan view of filling length definition on flat test bars. For simplicity, the water is represented by curved lines.

The results of filled length as a function of rotational velocity for the direct and indirect gating mould designs are shown in Figure 2 - 20. In general, for both gating mould designs, the filling rate increased with increasing rotational velocity. Likewise, the filling rate was lower for the indirect gated mould compared to the direct gated mould.

Li et al. (2006) attributed their results due to two factors: the length of the runner and a backpressure effect. Since the runner of the indirect gated mould had a length of 165 mm the water needed more time to reach the cavity. However, the second factor seemed more important since a proper venting system was not used and the air was trapped in the cavities leading to a backpressure generated during the filling process. This backpressure did not have an effect on the direct gated mould since the entrapped gas was exhausted quickly through the ingate. However, for the indirect gated mould, the liquid overflowed the bottom of the runner and it was difficult for the entrapped gas in the cavity to escape through the gas vent. Then, when the volume of liquid in the cavity increased, the backpressure increased too, which decreased the filling rate. Although the authors mentioned the use of a gas vent, which was smaller than the runner inlet, its position was not specified.

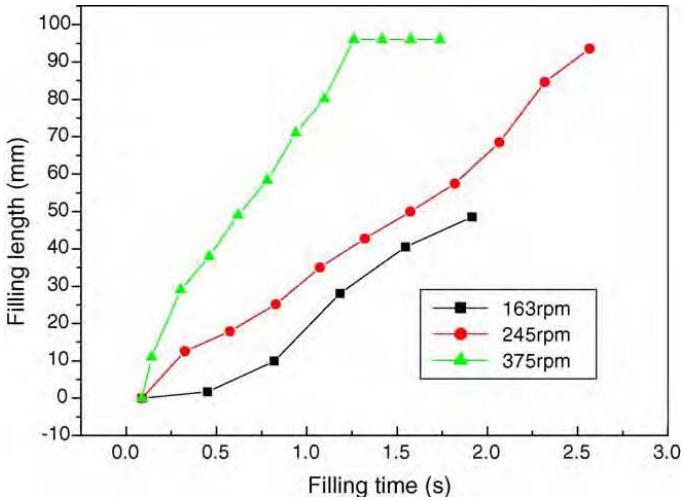

(a)

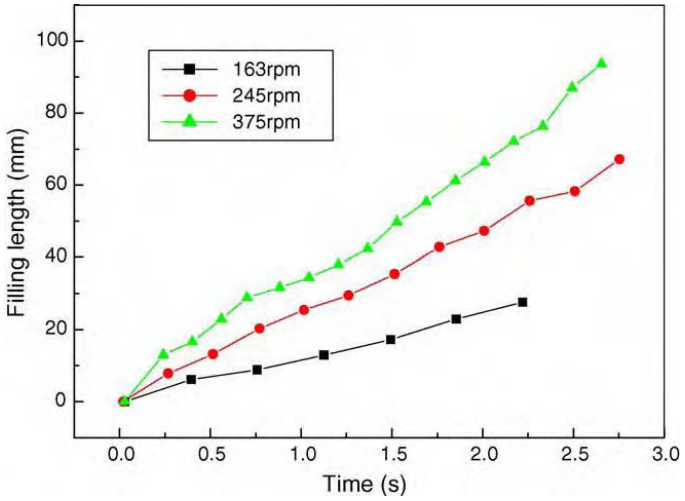

(b)

Figure 2 - 20. Experimental results of filling length as a function of time and different rotational velocities for (a) direct and (b) indirect gated moulds (Li et al., 2006).

Additionally, Wu et al. (2006) using a self-developed casting simulation software, carried out the numerical modelling of the same direct and indirect gated moulds used by Li et al. (2006). The results of the experimental results reported by Li et al. (2006) previously illustrated in

Figure 2 - 20 and the computer modelling results were reported jointly in Figure 2 - 21. It can be seen that for both mould designs, the calculated filling rate also increased with increasing rotational velocity.

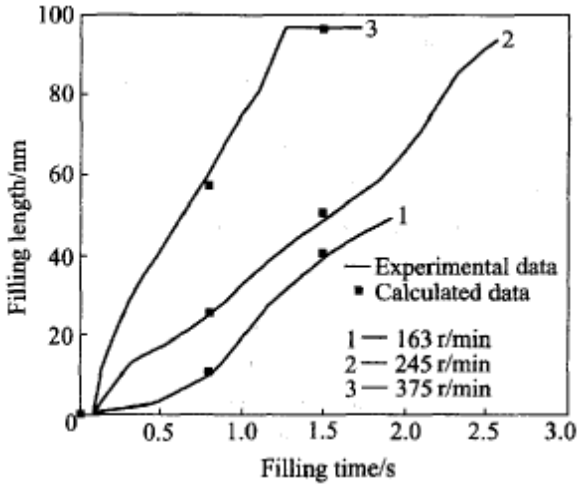

(a)

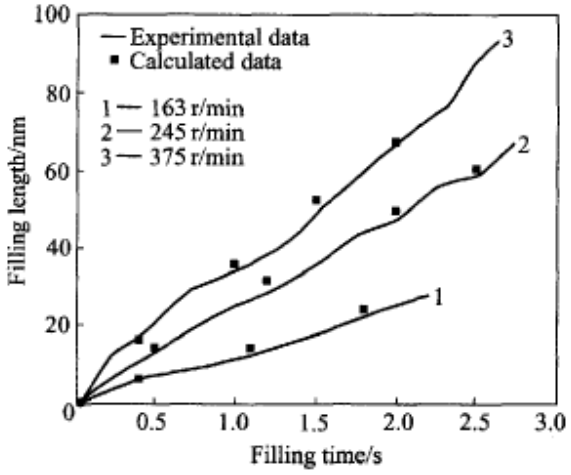

(b)

Figure 2 - 21. Experimental and numerical results of filling length as a function of time and different rotational velocities for (a) direct and (b) indirect gated moulds (Wu et al., 2006).

Changyun et al. (2006) investigated the effect of two kinds of gating systems and varied rotational velocity on the mould filling using a water analogue. The mould designs or gating systems were named bottom (indirect) and stepped gating systems. The bottom gating system had the same characteristics and dimensions as those reported by Li et al. (2006) and the stepped gating system is illustrated in Figure 2 - 22. The rotational velocities studied for the bottom gating system were 163, 245 and 375 rpm and for the stepped gating system were 211, 366 and 428 rpm in the anticlockwise direction. The measurement of the filled length of the test bars was carried out according to Equation 2 - 4. Since the results for the bottom gating system are the same as those reported by Li et al. (2006), it is assumed that the experimental conditions for both gating systems, which are not described in this paper, were the same as those reported by Li et al. (2006).

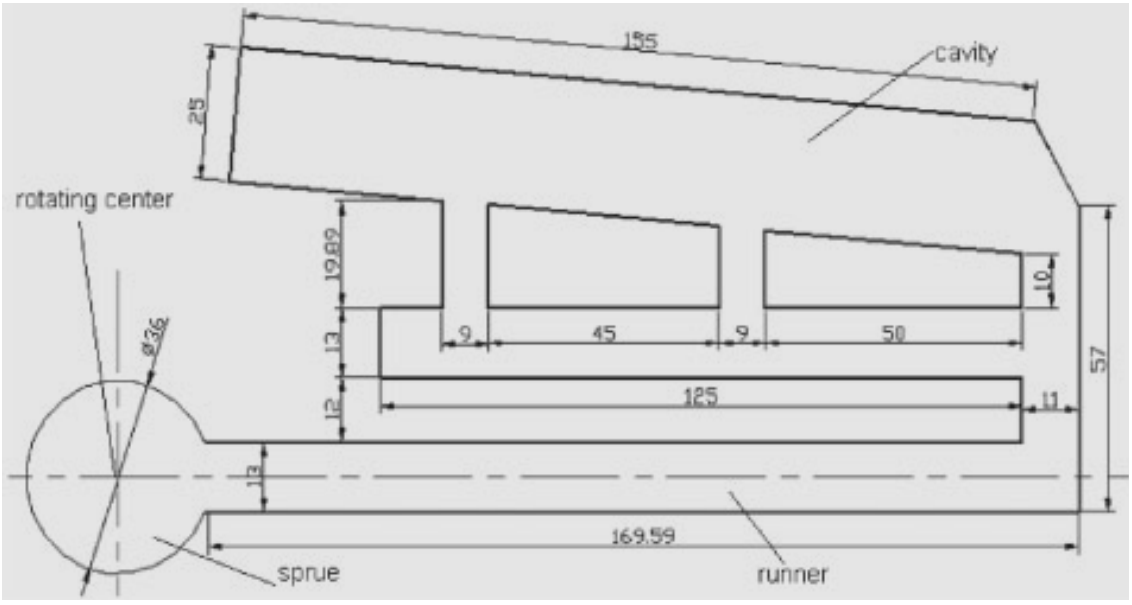

Figure 2 - 22. Schematic diagram of stepped gating system; all dimensions in mm (Changyun et al., 2006).

The results of filling length as a function of rotational velocity for the stepped gating system are illustrated in Figure 2 - 23. It can be seen that for the rotational velocities of 211 and 366 rpm, the general tendency is the same as that seen for the bottom gating design, Figure 2 - 20(b). However, when the rotational velocity was increased to 428 rpm, the filing rate was reduced. This tendency differs completely to that reported by Li et al. (2006) and Wu et al. (2006). Therefore, there is an inconsistency of results reported by these authors.

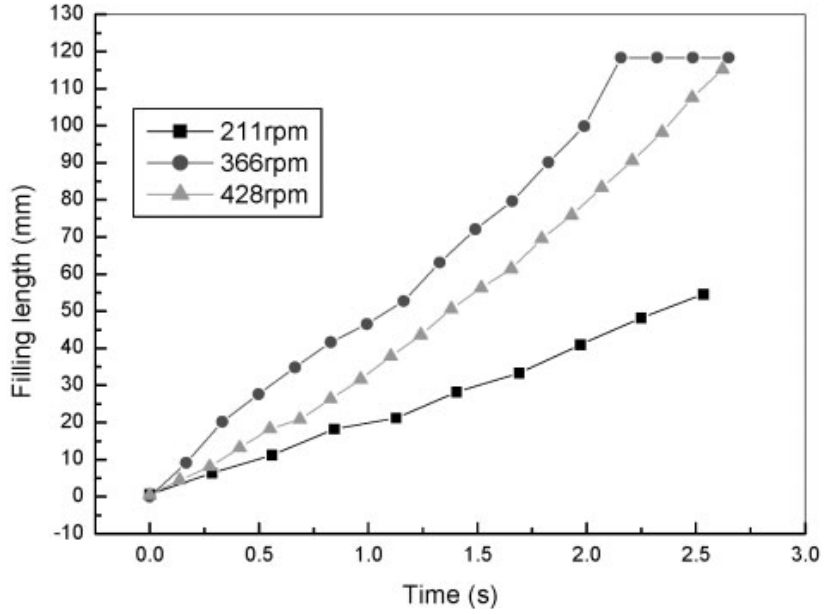

Figure 2 - 23. Experimental results of filling length as a function of time and different rotational velocities for stepped gating system (Changyun et al., 2006).

It should be pointed out that full details of the geometry and experimental conditions used by Li et al. (2006), Wu et al. (2006) and Changyun et al. (2006) were not reported. Therefore, water modelling and computer simulations of geometries with similar characteristics were planned as part of the current investigation, which are presented in Section 4.3 and Section 5.3 respectively. The experimental and computer modelling results are presented in Section 6.2.

2.3.5 Computational Modelling

Computational modelling of fluid flow and solidification has been developed by the research community and applied by the industry in order to produce engineering components of high integrity. The reason for the challenge in computational modelling of casting arises from a range of diverse issues: (i) capturing the interactions involving complex fluid flow and heat transfer with solidification; (ii) the representation of complex, fully three-dimensional (3-D) geometries; (iii) the solution of computer simulations within a practical timescale, (iv) the prediction of defects and structure (Cross et al., 2006) and (v) free surface treatment.

There are a diverse number of computer packages for mould filling and solidification in casting process. However, only those used in this investigation will be covered in the following paragraphs.

2.3.6 Governing Equations

The set of equations which describe the processes of momentum, heat and mass transfer are known as the Navier-Stokes equations for an incompressible flow (Welty et al., 2008). These partial differential equations can be discretized and solved numerically.

$$\rho \frac{D\upsilon_x}{D_t} = \rho g_x - \frac{\partial P}{\partial x} + \mu\left(\frac{\partial^2 \upsilon_x}{\partial x^2} + \frac{\partial^2 \upsilon_x}{\partial y^2} + \frac{\partial^2 \upsilon_x}{\partial z^2}\right) \qquad \text{Equation 2 - 5}$$

$$\rho \frac{D\upsilon_y}{D_t} = \rho g_y - \frac{\partial P}{\partial y} + \mu\left(\frac{\partial^2 \upsilon_y}{\partial x^2} + \frac{\partial^2 \upsilon_y}{\partial y^2} + \frac{\partial^2 \upsilon_y}{\partial z^2}\right) \qquad \text{Equation 2 - 6}$$

$$\rho \frac{D\upsilon_z}{D_t} = \rho g_z - \frac{\partial P}{\partial z} + \mu\left(\frac{\partial^2 \upsilon_z}{\partial x^2} + \frac{\partial^2 \upsilon_z}{\partial y^2} + \frac{\partial^2 \upsilon_z}{\partial z^2}\right) \qquad \text{Equation 2 - 7}$$

where: υ_x, υ_y and υ_z are the velocities in each of the axial directions, ρ is the density, μ is the dynamic viscosity and g is the gravitational acceleration.

These equations may be expressed in a more compact form in the single vector equation.

$$\rho \frac{Dv}{D_t} = \rho g - \Delta P + \mu \Delta^2 v \qquad \text{Equation 2 - 8}$$

Likewise, equations describing other processes can also be solved in conjunction with the Navier-Stokes equations. Often, an approximating model is used to derive these additional equations, *e.g.* turbulence models.

2.3.7 Modelling Entrainment of Oxide Films

There have been a few attempts to model and quantify the entrainment of oxide films in gravity castings in aluminium alloys. However, due to the complexity that these casting phenomena represent, these models have had some limitations.

Dai et al. (2004) and Yang et al. (2004) developed a numerical algorithm in 2D called Oxide Film Entrainment Tracking (OFET) for predicting the entrainment of oxide films and distribution during the filling of two different runner system designs: a vortex-flow runner (VR) and a rectangular runner (RR), Figure 2 - 24. These runner systems provided quite different flow conditions in the runner and different velocities through the cavity ingate.

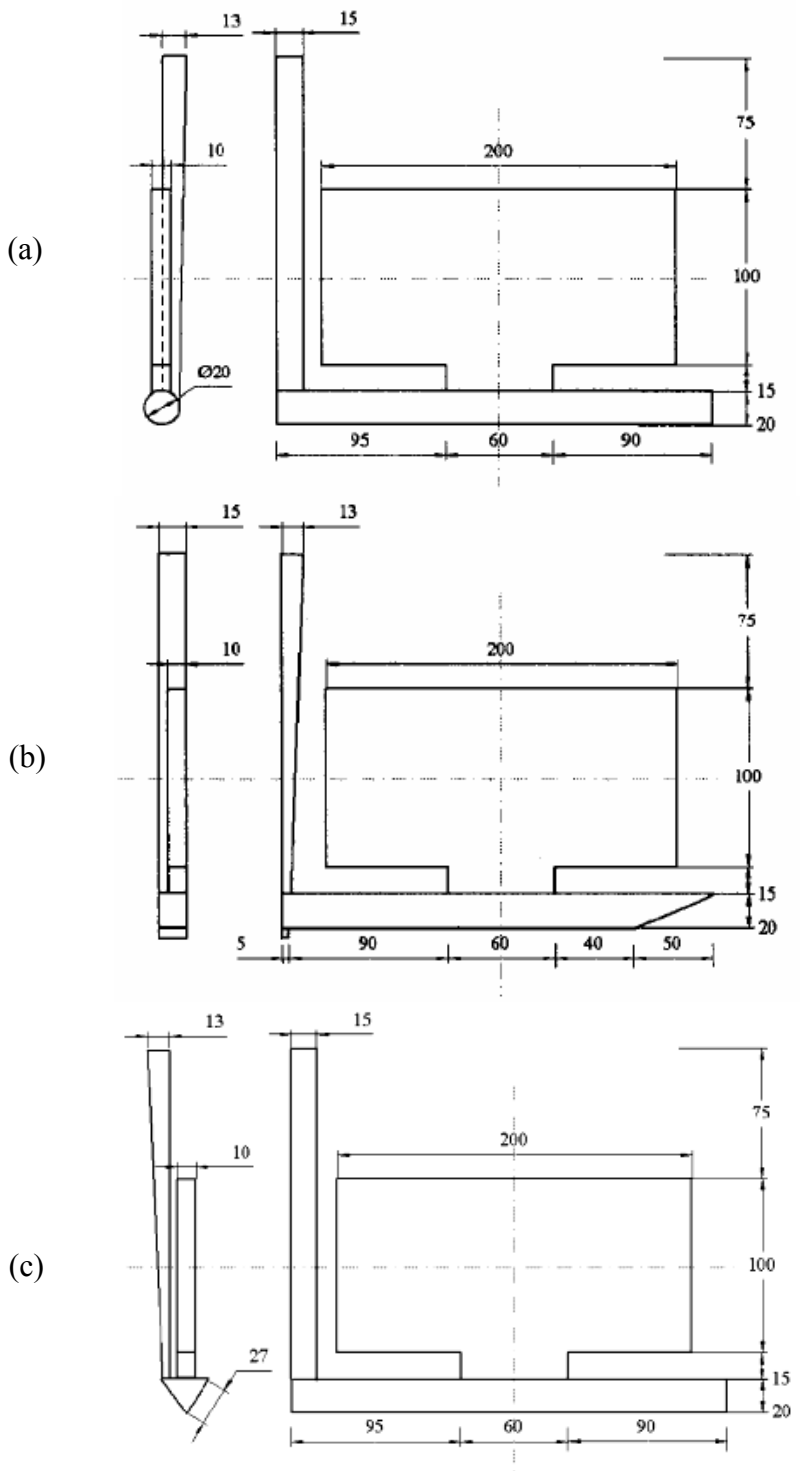

Figure 2 - 24. Schematic diagram of (a) vortex-flow runner (VR), (b) rectangular runner (RR) and (c) triangular runner (TR); all dimensions in mm (Dai et al., 2003) (Dai et al., 2004).

The modelled fluid flow and predicted distribution of entrained oxide films using the 'OFET' model are shown in Figure 2 - 25. They showed that for the VR system, the liquid entered cavity ingate at an approximate velocity of 0.4 m/s and did not provoke surface turbulence. Most of the generated oxide films were distributed around the edge of the bulk liquid. On the other hand, for the RR system the liquid entered the cavity ingate at an approximate velocity of 0.7 m/s, provoking a rising jet and enfolding itself after the fall. The entrained oxide films were distributed in the bulk liquid.

These results were compared with experimental data and it was concluded that a consistent correlation with the modelled results was found. However, in the author's opinion, these conclusions are unlikely due to the following reasons: the OFET numerical model was only developed in 2D; this technique was only applicable to hydraulic structures such as returning waves and folding surfaces; the model did not take into account the possible formation of oxide films in the sprue and runner system, which could have been entrained in the casting cavity. Likewise, the OFET model was validated with bend testing samples that were firstly tested in four-point bend testing and subsequently the broken samples were tested in three-point testing. In the final results, the possible effect of the four-point bend testing in the samples used for the subsequent three-point bend testing was not considered (refer to Section 2.6.1).

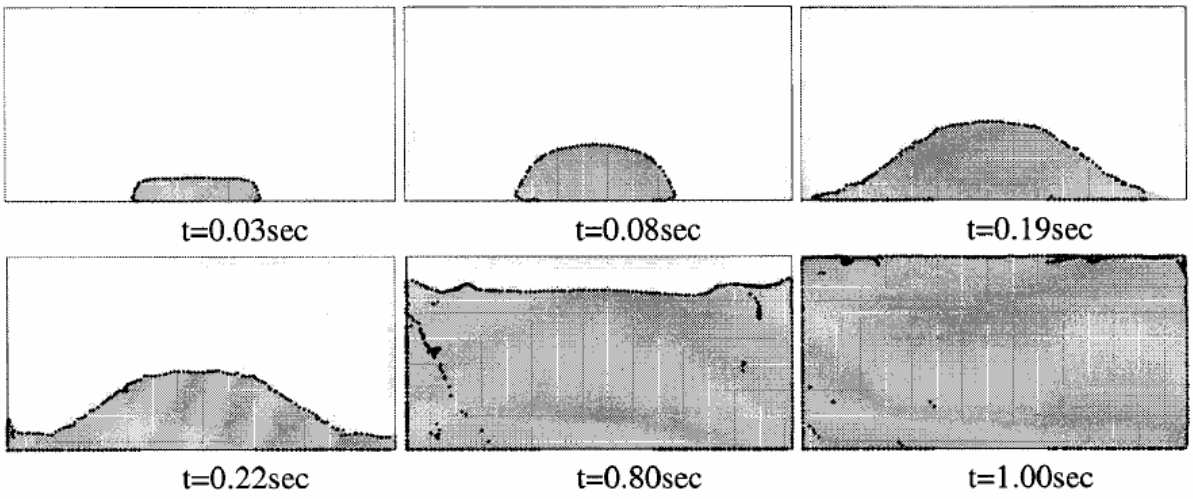

(a)

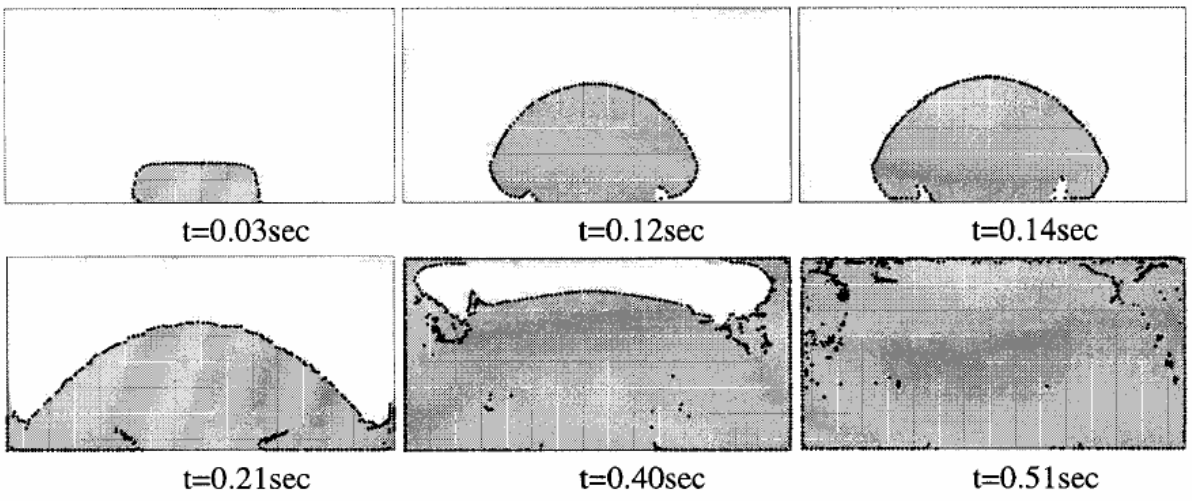

(b)

Figure 2 - 25. OFET numerical results of oxide film distribution for (a) vortex-flow runner (VR) and (b) rectangular runner (RR) (Dai et al., 2004).

2.3.8 Free Surface and Multiphase Flow

Free surface flow refers to a multiphase flow situation where the phases are separated by a distinct interface. Examples of free surface flows include open channel flow, flow around ship hulls and, in the present investigation, the filling of centrifugal casting moulds.

Multiphase flow refers to the situation where more than one fluid is present. In general, the fluids consist of different chemical species *e.g.* as air-water. The difference between multiphase flow and multicomponent is that in a multiphase flow the fluids are assumed to be mixed on a macroscopic scale, with a discernible interface between the fluids *e.g.* gas bubbles in liquid, liquid droplets in gas or in another immiscible liquid, etc. In this case, it is necessary to solve for different velocity, temperature fields, etc., for each fluid. The fluids may interact with each other by means of interfacial forces and heat and mass transfer across the phase interfaces. On the other hand, a multicomponent fluid consists of a mixture of chemical species which are mixed at the molecular level *e.g.* gaseous mixtures and solutes in liquids. In this case, single mean velocity and temperature fields, etc., are solved for the fluid.

In general, there are three main approaches for modelling multiphase flows: (i) Volume of fluid (VOF) approach (Eulerian framework for both the phases with reformulation of interface forces on volumetric basis), (ii) Eulerian framework for the continuous phase and Lagrangian framework for all the dispersed phases and (Eulerian-Lagrangian) (iii) Eulerian framework for all phases, without explicitly accounting for the interface between phases (Eulerian-Eulerian) (Ranade, 2002).

The volume of fluid (VOF) approach is conceptually the simplest. The motion of all phases is modelled by formulating local, instantaneous conservation equations for mass, momentum and energy, which can be solved using appropriate jump boundary conditions at the interface.

However, the interface between different phases may not remain stationary and imposing boundary conditions at the interface becomes a very complicated moving boundary problem. The VOF approach tracks motion of all the phases, from which motion of the interface is inferred indirectly and consequently all the interfacial forces have to be replaced by smoothly varying volumetric forces. The disadvantage of this method is that it is limited to modelling the motion of only a few dispersed phase particles, Figure 2 - 26. Therefore, this approach is not suitable for simulations of dispersed multiphase flows, as it requires huge computational resources to resolve flow processes around each dispersed phase particle (Ranade, 2002).

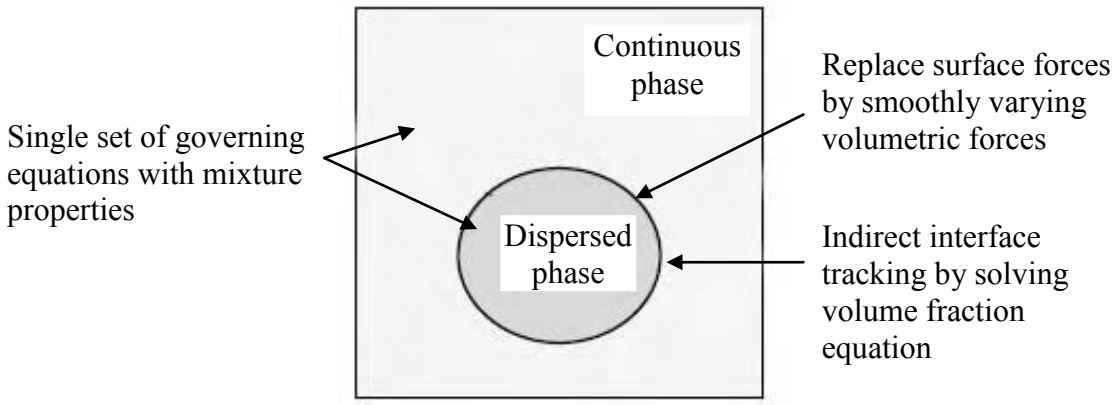

Figure 2 - 26. Volume of fluid approach for multiphase flows (Ranade, 2002).

In the Eulerian–Lagrangian approach, explicit motion of the interface is not modelled, which means that small-scale fluid motions around individual dispersed phase particles are not considered and their influence is modelled indirectly. The motion of the continuous phase is modelled using an Eulerian framework and the motions of dispersed phase particles (trajectories) are explicitly simulated in a Lagrangian framework. Averaging over a large number of trajectories is then carried out to derive the required information for the modelling

of the continuous phase (Ranade, 2002). This approach can simulate in adequate detail particle-level processes *e.g.* reactions. Likewise, it is suitable for simulating dispersed multiphase flows containing a low (<10%) volume fraction of the dispersed phases, Figure 2 - 27. For denser dispersed phase flows, it may be necessary to use an Eulerian–Eulerian approach.

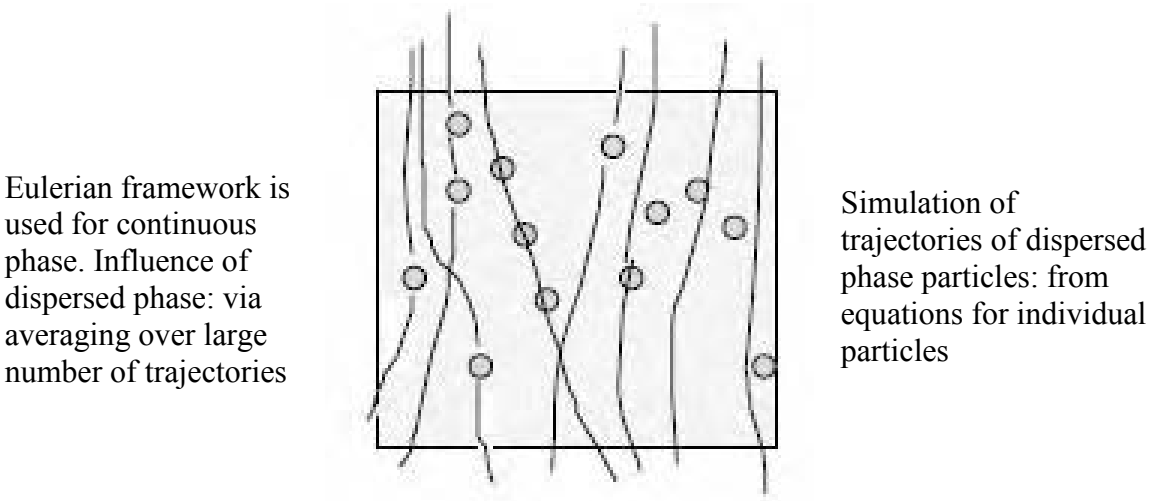

Figure 2 - 27. Eulerian-Lagrangian approach for multiphase flows (Ranade, 2002).

The Eulerian–Eulerian approach models the flow of all phases in an Eulerian framework. In this approach, trajectory simulations and averaging are not carried out at a computational level but are implicitly achieved at a conceptual level. Likewise, this approach is the most difficult one to understand conceptually and requires extensive modelling efforts. However, if it is modelled successfully, it can be applied to multiphase flow processes containing large volume fractions of dispersed phase *e.g.* industrial multiphase reactors consisting of a large number of dispersed particles, Figure 2 - 28 (Ranade, 2002).

Phase volume fractions and velocities are defined over a suitable control volume

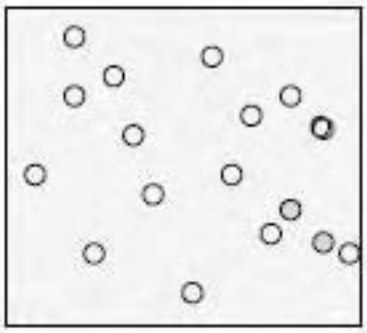

Averaging methods to derive time and/or volume averaged equations for all phases

Figure 2 - 28. Eulerian-Eulerian approach for multiphase flows (Ranade, 2002).

2.3.9 Computational Modelling with ANSYS CFX

ANSYS CFX (2011) software is a general purpose computational fluid dynamics (CFD) program. The solution method, on which this software is based, is known as the finite volume (FV) technique. In this technique, the region of interest is divided into small sub-regions called control volumes. The equations are discretized and solved iteratively for each control volume. As a result, an approximation of the value of each variable at specific points throughout the domain can be obtained. Further details about this method can be found in (Versteeg and Malalasekera, 2007) (ANSYS-CFX, 2011).

In ANSYS CFX, two distinct flow models are available, the Eulerian-Eulerian multiphase model and the Lagrangian Particle Tracking multiphase model. However, due to the limited relevance to the present investigation, further reviewing of literature was not undertaken on the Lagrangian Particle Tracking multiphase model.

2.3.10 Computational Modelling with Flow-3D

FLOW-3D (2011) is a general purpose computational fluid dynamics (CFD) package. The approach of this software is to subdivide the flow domain into a mesh of rectangular cells, sometimes called brick elements. The oldest numerical algorithms based on the finite difference and finite volume (FV) methods have been originally developed on this kind of mesh, which form the core of the numerical approach in FLOW-3D. The finite difference method is based on the properties of the Taylor expansion and on the straightforward application of the definition of derivatives. The finite volume method derives directly from the integral form of the conservation laws for fluid motion. When modelling a free surface, the Volume of Fluid (VOF) method is employed for this purpose, which consists of three main components: the definition of the volume of fluid function, a method to solve the VOF transport equation and setting the boundary conditions at the free surface. A discussion of these developments has been given by Barkhudarov (2004).

2.3.10.1 Oxide Film Entrainment Model (OFEM) Code

Initially the OFEM code was developed in 2D and was applied in the gravity casting of a vertical top filled plate with an extended horizontal runner (Reilly et al., 2009). Subsequently, its application was extended to a more robust 3D version and applied to the unfiltered and filtered gravity casting of tensile test bars (Reilly, 2010), which was validated with data reported by Green and Campbell (1994). The essential function of this code is that when an entraining event has occurred in a given cell, a particle is placed to represent an entrained oxide film. This particle is then tracked and its final location identified. A brief description about this technique will be given in the following paragraphs.

The customisation of the Oxide Film Entrainment Model (OFEM) code allows the placing of particles when a flow structure is likely to entrain an oxide film. Among the main entrainment mechanisms are the returning wave, colliding fronts, rising jet, plunging jet, circular hydraulic jump and hydraulic jump (refer to Section 2.3.2.1 to 2.3.2.4). An example of this code for a plunging jet is illustrated in Figure 2 - 29.

In the mesh domain, each cell has a unique value for each physical property e.g. velocity (in each coordinate direction), fraction of liquid, temperature, density, fraction solid, etc. To determine when an entraining event occurs, the values of these unique physical properties are used by a series of logic criterion functions. Details about these criterion functions can be found in Reilly's work (2010).

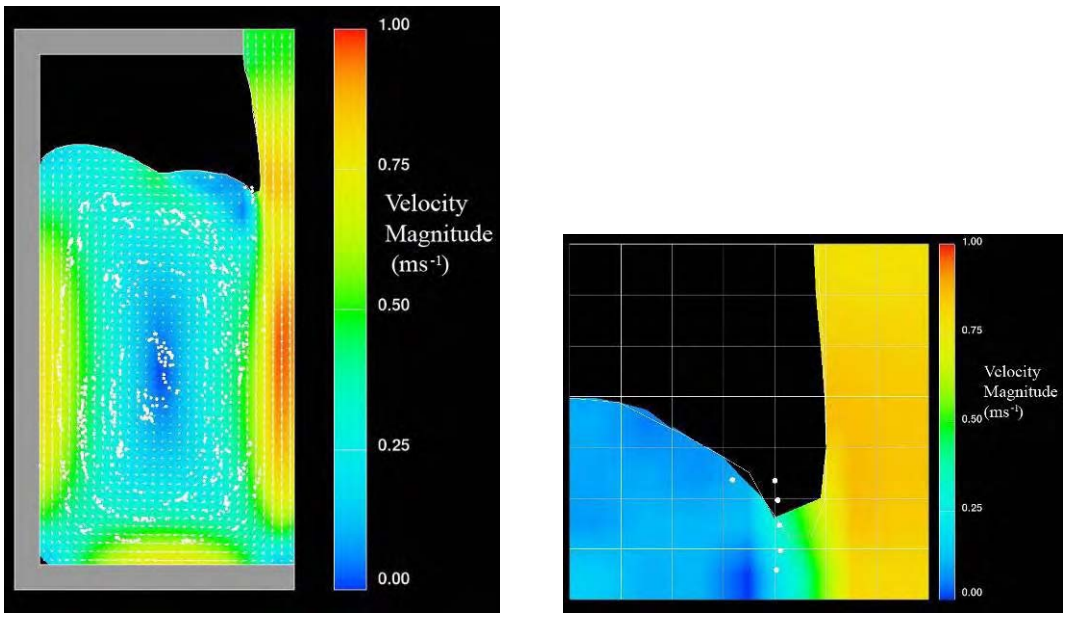

a) Velocity magnitude plot of plunging jet example

b) Close up of velocity magnitude plot of plunging jet example (dashed square marks assessed cell)

Figure 2 - 29. Example of entrainment from a plunging jet (Reilly, 2010).

As noted above, the essential function of the Oxide Film Entrainment Model (OFEM) code is to mark an entraining event by placing a particle within the assessed cell to represent an entrained oxide film. In the current version of this code, all particles must have either the same density but varying size or the same size but varying density. However, in real aluminium alloy castings, the generated oxide films vary in size and density (Campbell, 2003). Another important limitation of this code is that the coefficient of restitution can only be either activated or deactivated for all the generated particles. This coefficient of restitution dictates whether the particles stick to the mould wall indefinitely upon impact (factor 0) or reflected from the mould wall with a fractional energy loss (factor 1).

In order to regulate the particle placement frequency within a given cell or, in other words, to stop over-population of particles, when a particle is placed to mark an entrainment event, the time period of placement is recorded as a scalar for that particular cell. In every time period, this scalar is assessed and once the scalar was less than the current time period minus a user defined value, the cell was once again assessed for entraining events (Reilly, 2010). This is particularly important when modelling centrifugal casting, since the surface turbulence generated during the mould filling is expected to be far higher than in gravity casting. Likewise, setting the correctly this parameter reduces the computational intensity.

The Oxide Film Entrainment Model (OFEM) technique initiated by Reilly (2010) is currently under further development by Yue (2011b). In the present investigation, this technique was applied to the centrifugal casting of an aluminium alloy. However, the results obtained should not be considered as definitive and further validation would need to be undertaken.

2.3.10.2 Fluid - Particle Drag Force

A drag force is imposed on a particle when it moves in the liquid. This force is only applied to mass particles but not the liquid. The particle motion is governed by the following equation (Barkhudarov, 1995):

$$\frac{\partial u_p}{\partial t} = g - \frac{1}{\rho_p}\nabla P + \alpha \cdot (u - u') + \beta \cdot (u - u') \cdot |u - u'| \qquad \text{Equation 2 - 9}$$

Where u_p and ρ_p are the particle mean velocity and density, respectively, g is the gravity, u and P are the fluid velocity and pressure, respectively, u' is the full particle velocity, which is the sum of u_p and the diffusion velocity (Barkhudarov and Ditter, 1994), and α and β are the drag coefficients. The model does not describe accurately the variation of the drag force with particle size since the drag coefficients are constant and specified by the user.

An additional drag force, F_D, was added to take into account the variation in particle size. This additional drag force model is based on an empirically derived function that ties the value of the drag coefficient, Equation 2 - 10, to the Reynolds number in the flow around the particle (Barkhudarov, 1995).

$$C_D - \frac{8|\ F_D\ |}{\rho U^2 \pi a^2} \qquad \text{Equation 2 - 10}$$

For a steady flow around a sphere this coefficient is given by the following equation:

$$C_D = \frac{24}{\mathrm{Re}} + \frac{6}{1 + \sqrt{\mathrm{Re}}} + 0.4 \qquad \text{Equation 2 - 11}$$

where:

$$F_D = C_D \cdot \frac{\rho U \pi d^2}{8} \cdot (u - u') \qquad \text{Equation 2 - 12}$$

is the drag force, $U=|u - u'|$, d is the particle diameter and μ is the fluid dynamic viscosity coefficient. Equation 2 - 11 is a good approximation for the drag force in a range of Re between 0 and 10^5. For small Reynolds numbers the drag force approaches the Stokes analytical solution for a viscous laminar flow around a sphere without separation. According to Barkhudarov (1995) this expression for the drag force takes into account the particle size and mass.

2.4 Solidification

2.4.1 Solidification Mode

Alloys can be classified into three types based on their freezing ranges (Rooy, 1988):

- Short: liquidus-to-solidus interval < 50 °C
- Intermediate: interval of 50 to 110 °C
- Long: interval > 110 °C

This classification is not precise and the general solidification mode of each type is explained in the following paragraphs.

Short freezing range alloys show a strong tendency toward skin formation, and the fronts of the crystals solidifying inward (start of freezing) will not advance much faster than their bases

(end of freezing). Such relatively short crystalline growth helps keep liquid feed metal in contact with all the solidifying surfaces. Strong progressive solidification in these short freezing range alloys promotes the development of directional solidification along any temperature gradients in the solidifying casting, Figure 2 - 30 (a).

For long freezing range alloys, the development of directional solidification is difficult. Although a thin skin may initially form on the mould walls, solidification does not proceed progressively inwards. Rather, it develops throughout the solidifying casting at scattered locations. This mushy mode of solidification results in the development of numerous small channels of liquid metal late in solidification. Feeding through these channels is restricted, and dispersed shrinkage porosity occurs throughout the casting, Figure 2 - 30 (b).

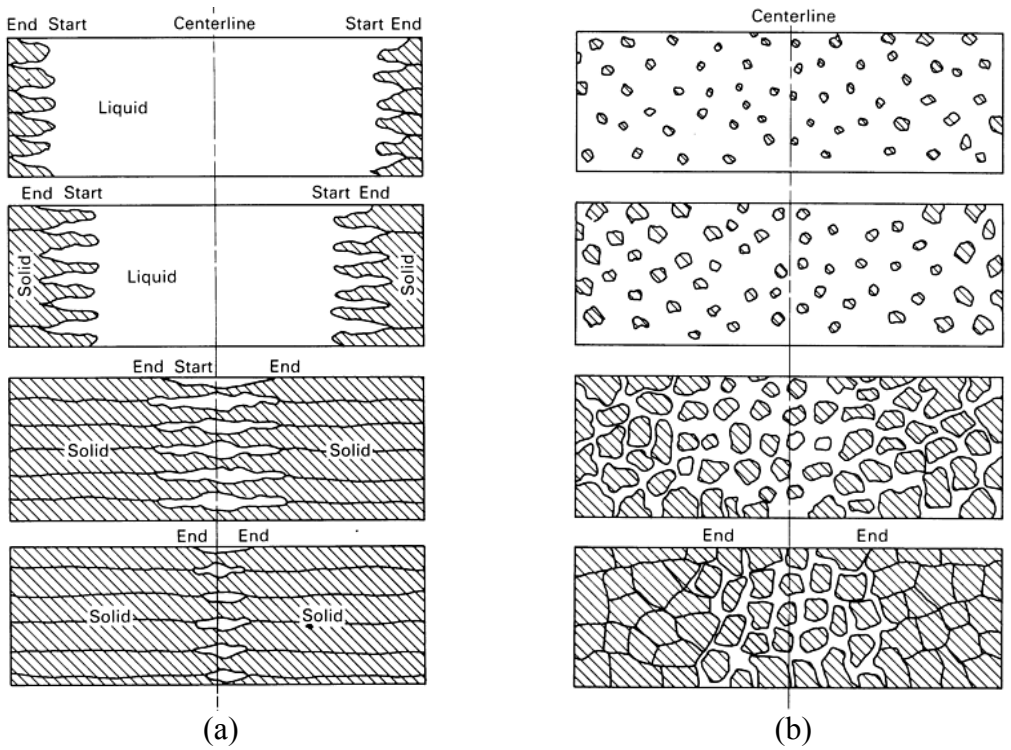

Figure 2 - 30. Schematic diagram of freezing mode in alloys having (a) short and (b) long freezing range (Rooy, 1988).

For alloys with an intermediate freezing range, the mode of solidification will combine elements of both the skin forming and mushy solidification modes. Short freezing range alloys may shift to a more intermediate mode of solidification in heavy casting sections, in which heat loss from the casting surface will be slowed. As temperature gradients from the centre of the solidifying section to the casting edge are reduced, crystal growth will change from the columnar pattern growing in from the mould walls to an equiaxial pattern dispersed throughout the still-liquid centre, Figure 2 - 31.

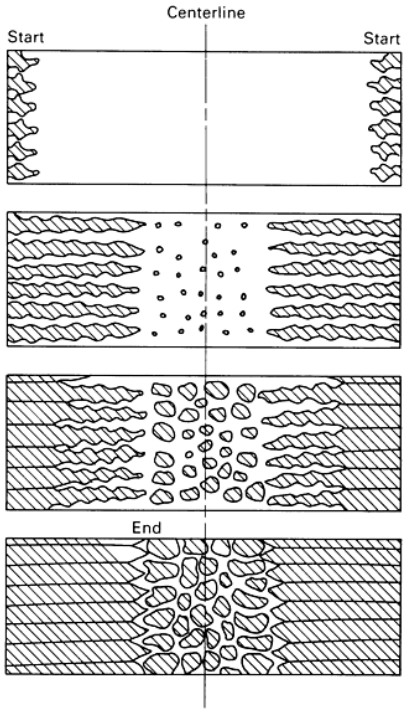

Figure 2 - 31. Schematic diagram of intermediate freezing mode in alloys having a moderate freezing range (Rooy, 1988).

The various solidification modes result in very different typical shrinkage configurations in the casting and feeder, Figure 2 - 32 and Figure 2 - 33. Selection of appropriate methods will depend largely on the possibility of promoting directional solidification (Rooy, 1988).

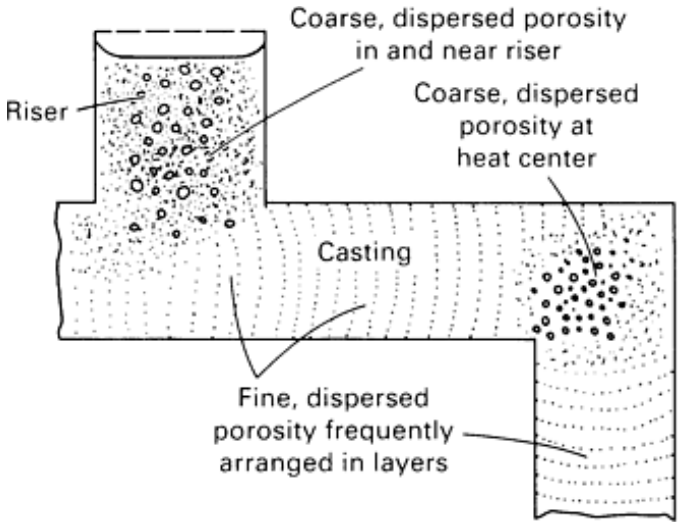

Figure 2 - 32. Forms of shrinkage porosity in the sand castings of alloys that freeze in a pasty manner (Rooy, 1988).

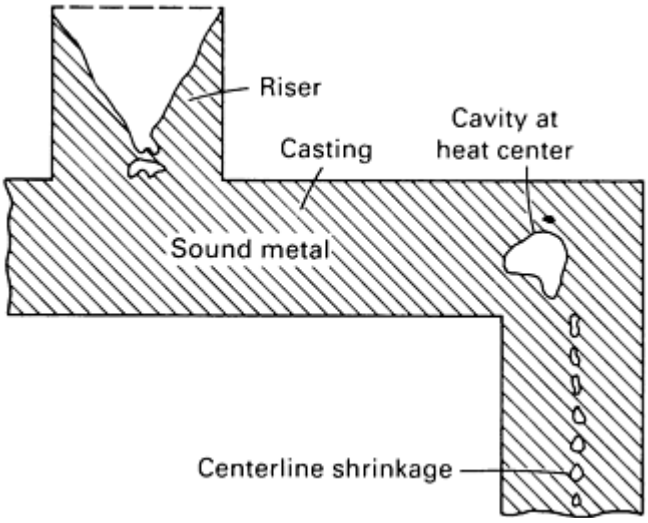

Figure 2 - 33. Shrinkage cavities produced by skin formation (Rooy, 1988).

2.4.2 Solidification Defects

2.4.2.1 Shrinkage Porosity

For most metals, the transformation from the liquid to the solid state is accompanied by a decrease in volume. More specifically, there are three quite different contractions, Figure 2 - 34.

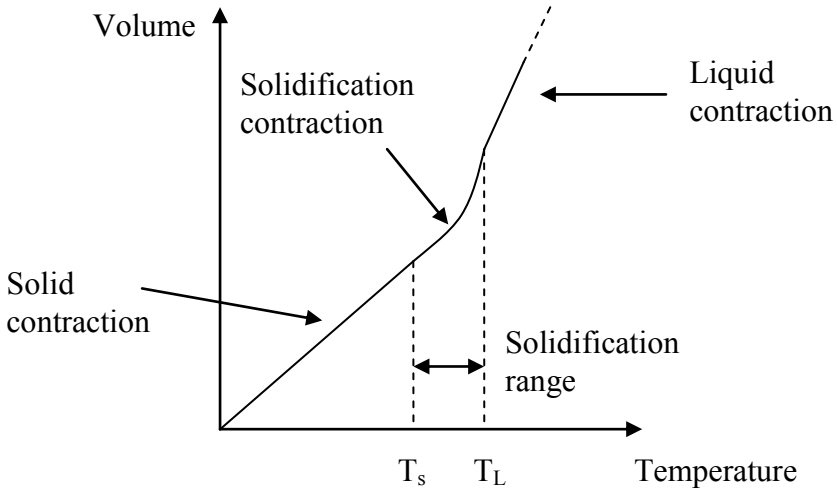

Figure 2 - 34. Schematic illustration of the three shrinkage regimes: during liquid, freezing and solid stages (Campbell, 2003).

The first contraction occurs during the liquid state. The extra liquid metal required to compensate for this reduction in volume can be provided by the feeder. The second contraction occurs during solidification. This causes a couple of problems: the requirements for feeding, which is defined as any process that will allow for the compensation of solidification contraction by the movement of either liquid or solid, and 'shrinkage porosity', which is the result of failure to feed effectively. The final stage of shrinkage is in the solid state, which can cause a few other problems. As cooling progresses, the casting is constrained

to some extent either by the mould, or often by other parts of the casting that have already solidified and cooled. This leads to difficulties in predicting the size of the pattern (patternmaker's allowance), which is not easy to quantify. The mould constraint during the solid-state contraction can also lead to more localized problems such as hot tearing or cracking of the casting (Campbell, 2003).

For static casting processes, an approach to describe the shrinkage formation has been reported by Kaufman and Rooy (2004). It is a common practice to maintain a path of fluid flow from the feeder to the solidifying casting. Shrinkage formation takes place in three modes: (i) Mass feeding of liquid. In this case, the pressure at the solidification interface and pressure in the feeder system are essentially similar; (ii) Interdendritic feeding. It takes place up to the point where sufficient resistance is developed and the liquid cannot flow through the solidifying dendrite network; (iii) Solid feeding occurs when the surrounding solidified metal collapses to fill the shrinkage void.

Shrinkage porosity may be present as distributed voids or micro shrinkage, which can be found between dendrite arms as a result of failure during the last stages of interdendritic feeding. Centreline or piping voids result from gross directional effects. However, discrimination between porosity caused by shrinkage and porosity caused by hydrogen is difficult and is often subject to misinterpretation (Rooy, 1988).

2.4.2.2 Hydrogen Gas Porosity

Aluminium and its alloys are very susceptible to hydrogen absorption in the molten state due to its high temperature solubility. Figure 2 - 35 shows that the liquid and solid solubilities in pure aluminium just above and below the solidus are 0.65 and 0.034 mL/100 g, respectively.

There are different sources of hydrogen in aluminium. The principal source comes from humidity of the atmosphere in contact with the liquid metal, which reacts with aluminium offering a concentration of atomic hydrogen capable of diffusing into the melt (Totten and MacKenzie, 2003):

$$3H_2O_{(v)} + 2Al \rightarrow 3H_{Al} + Al_2O_3 \qquad \text{Equation 2 - 13}$$

The barrier of aluminium oxide resists hydrogen solution by this mechanism, but disturbances on the melt surface that break the oxide barrier result in rapid hydrogen dissolution. An additional source of hydrogen can be from a reaction involving the molten metal and water in the mould, *e.g.* in sand casting.

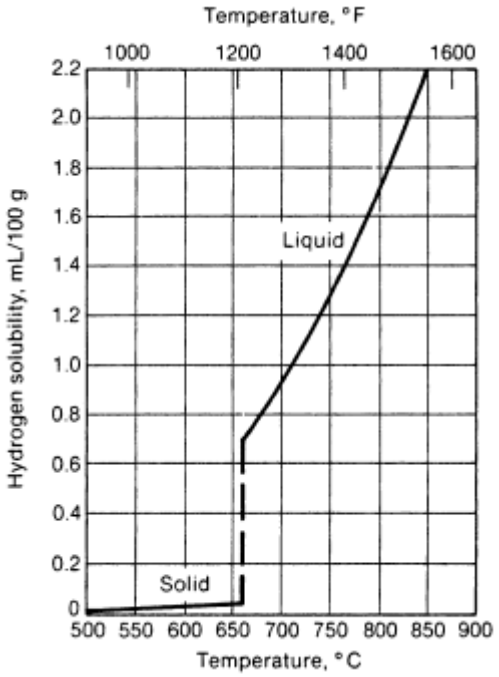

Figure 2 - 35. Solubility of hydrogen in aluminium at 1 atm Hydrogen pressure (Rooy, 1988).

Various aluminium alloys have different sensitivities to hydrogen absorption, Table 2 - 1. Since the solubility of hydrogen is significantly higher in the liquid state compared with the solid, there will be enrichment in the liquid during solidification. If it is assumed that there is no solid diffusion and complete liquid diffusion occurs during casting, at the end of the solidification there will be a large increase in hydrogen concentration in the casting. Therefore, even when the hydrogen content is below the solubility for the bulk liquid during solidification, concentration in the liquid will increase, and the solubility limit might be exceeded, resulting in porosity in the casting (Totten and MacKenzie, 2003).

Table 2 - 1. Solubility of Hydrogen in aluminium and its alloys at 750 °C (Totten and MacKenzie, 2003).

Alloy	Hydrogen solubility (ppm)
Pure aluminium	1.20
Al-7Si-0.3Mg	0.81
Al-4.5Cu	0.88
Al-6Si-3.5Cu	0.67
Al-4Mg-2Si	1.15

Hydrogen porosity occurs mainly as interdendritic porosity and is encountered when hydrogen contents are sufficiently high that hydrogen rejected at the solidification front results in solution pressures above atmospheric. Secondary porosity, the size of which is of the order of microns, occurs when dissolved hydrogen contents are low leading to void formation (Rooy, 1988).

2.5 Quantitative Assessment of Microstructure and Casting Defects

The development of various methods of microstructural quantification is known as quantitative metallography or more generally, stereology.

Stereological measurements of microstructure parameters and porosity can be carried out either manually *i.e.* by point counting and intercept methods or digitally *i.e.* by using image analysis software. Likewise, such measurements can be made either on individual micrographs or digitally processed images, which are better known as seamless montages (Balasundaram and Gokhale, 2001). These and the stereological measurements are explained in the following sections.

2.5.1 Quantitative Assessment of Dendrite Cell Size

Solidification takes place through the formation of dendrites from the liquid, which is mainly controlled by the solidification rate, Figure 2 - 36 and Table 2 - 2.

There are three measurements used to describe dendrite refinement (Spear and Gardner, 1963):

- Dendrite arm spacing: The distance between developed secondary dendrite arms
- Dendrite cell interval: The distance between centrelines of adjacent dendrite cells
- Dendrite cell size: The width of individual dendrite cells

Subsequently, the cooling rate can be calculated using Equation 2 - 14, which was reported by Flemings et al. (1991). This equation was obtained from the data reported jointly by Spear and Gardner (1963), and Bardes and Flemings (1966) for different aluminium alloys. These

authors concluded that the chemical composition of the alloy had an effect on the dendrite arm spacing and dendrite cell size, although this effect was small compared with that of the local solidification time.

$$d = 45\varepsilon^{-0.39} \qquad \text{Equation 2 - 14}$$

where d is the dendrite cell size (μm) and ε is the cooling rate (°C/s).

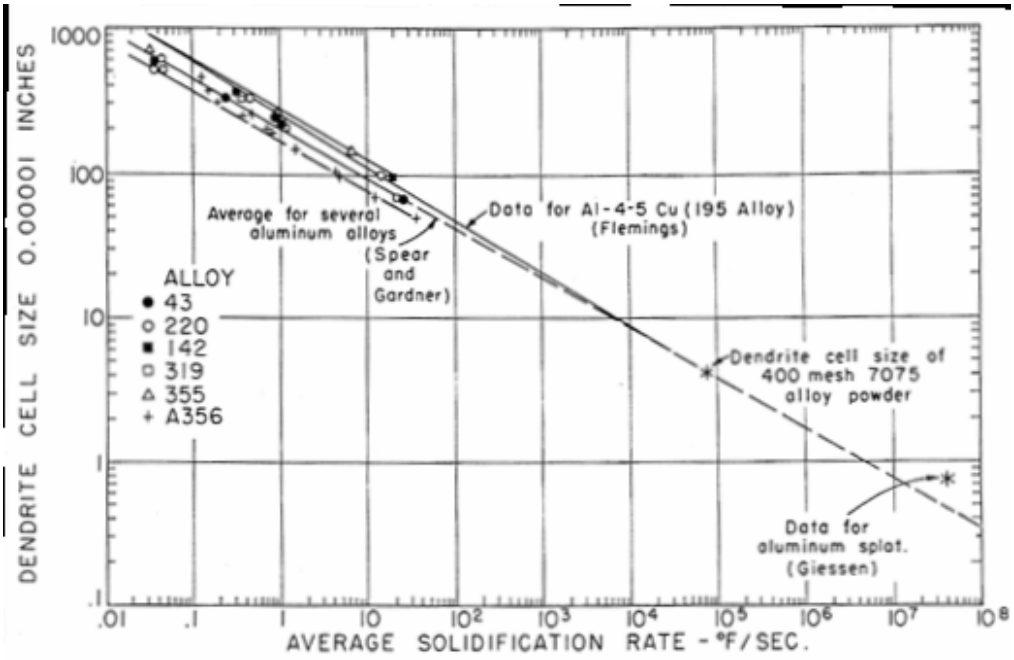

Figure 2 - 36. Relationship between dendrite cell size and local solidification rate for aluminium alloys (Flemings et al., 1991).

Table 2 - 2. Relationship between cooling rate and dendrite arm spacing for different casting processes (Kaufman and Rooy, 2004).

Casting processes	Cooling rate		Dendrite arm spacing	
	°F/s	°C/s	mils	μm
Plaster, investment	1.80	1	3.94–39.4	100–1000
Green sand, shell	18.0	10	1.97–19.7	50–500
Permanent mold	180.0	100	1.18–2.76	30–70
Die	1800	1000	0.20–0.59	5–15

2.5.2 Quantitative Assessment of Grain Size

Among some other methods (ASTM, 2004), the grain size can be measured by using circular test lines rather than straight test lines. This has been advocated by Underwood (1965), Hilliard (1964) and Abrams (1971). Circular test arrays automatically compensate for departures from equiaxed grain shapes, without overweighting any local portion of the field and ambiguous intersections at ends of test lines are eliminated. Circular intercept procedures are most suitable for use as fixed routine manual procedures for grain size estimation in quality control (ASTM, 2004).

The characteristics of the Abrams three-circle procedure are described in detail in the ASTM E112-96 Standard test methods for determining average grain size (2004). A brief description of the procedure and calculations is as follows.

Once the number of intersections for each circle is obtained, the ASTM grain size '*G*' and mean intercept value are calculated using the following equations:

$$P_L = \frac{P}{(L_T / M)} \qquad \text{Equation 2 - 15}$$

where P_L is the number of grain boundary intersections per unit length of test line, P is the number of grain boundary intersections with a test line, L_T is the length of the test line (500 mm) and M is the magnification.

$$G = (6.643856 \times \log_{10} P_L) - 3.288 \qquad \text{Equation 2 - 16}$$

where G is the ASTM grain size

Finally, the average grain diameter (μm), average grain area (mm^2) and mean intercept (mm) can be obtained from the grain size relationship presented in Table 2 - 3 (ASTM, 2004).

Table 2 - 3. Grain size relationships for uniform, randomly oriented and equiaxed grains (ASTM, 2004)

Grain Size No. G	N_A Grains/Unit Area		A Average Grain Area		$\bar{d}$ Average Diameter		$\bar{\ell}$ Mean Intercept		N_L
	No./in.^{2} at 100X	No./mm^2 at 1X	mm^2	μm^2	mm	μm	mm	μm	No./mm
00	0.25	3.88	0.2581	258064	0.5080	508.0	0.4525	452.5	2.21
0	0.50	7.75	0.1290	129032	0.3592	359.2	0.3200	320.0	3.12
0.5	0.71	10.96	0.0912	91239	0.3021	302.1	0.2691	269.1	3.72
1.0	1.00	15.50	0.0645	64516	0.2540	254.0	0.2263	226.3	4.42
1.5	1.41	21.92	0.0456	45620	0.2136	213.6	0.1903	190.3	5.26
2.0	2.00	31.00	0.0323	32258	0.1796	179.6	0.1600	160.0	6.25
2.5	2.83	43.84	0.0228	22810	0.1510	151.0	0.1345	134.5	7.43
3.0	4.00	62.00	0.0161	16129	0.1270	127.0	0.1131	113.1	8.84
3.5	5.66	87.68	0.0114	11405	0.1068	106.8	0.0951	95.1	10.51
4.0	8.00	124.00	0.00806	8065	0.0898	89.8	0.0800	80.0	12.50
4.5	11.31	175.36	0.00570	5703	0.0755	75.5	0.0673	67.3	14.87
5.0	16.00	248.00	0.00403	4032	0.0635	63.5	0.0566	56.6	17.68
5.5	22.63	350.73	0.00285	2851	0.0534	53.4	0.0476	47.6	21.02
6.0	32.00	496.00	0.00202	2016	0.0449	44.9	0.0400	40.0	25.00
6.5	45.25	701.45	0.00143	1426	0.0378	37.8	0.0336	33.6	29.73
7.0	64.00	992.00	0.00101	1008	0.0318	31.8	0.0283	28.3	35.36
7.5	90.51	1402.9	0.00071	713	0.0267	26.7	0.0238	23.8	42.04
8.0	128.00	1984.0	0.00050	504	0.0225	22.5	0.0200	20.0	50.00
8.5	181.02	2805.8	0.00036	356	0.0189	18.9	0.0168	16.8	59.46
9.0	256.00	3968.0	0.00025	252	0.0159	15.9	0.0141	14.1	70.71
9.5	362.04	5611.6	0.00018	178	0.0133	13.3	0.0119	11.9	84.09
10.0	512.00	7936.0	0.00013	126	0.0112	11.2	0.0100	10.0	100.0
10.5	724.08	11223.2	0.000089	89.1	0.0094	9.4	0.0084	8.4	118.9
11.0	1024.00	15872.0	0.000063	63.0	0.0079	7.9	0.0071	7.1	141.4
11.5	1448.15	22446.4	0.000045	44.6	0.0067	6.7	0.0060	5.9	168.2
12.0	2048.00	31744.1	0.000032	31.5	0.0056	5.6	0.0050	5.0	200.0
12.5	2896.31	44892.9	0.000022	22.3	0.0047	4.7	0.0042	4.2	237.8
13.0	4096.00	63488.1	0.000016	15.8	0.0040	4.0	0.0035	3.5	282.8
13.5	5792.62	89785.8	0.000011	11.1	0.0033	3.3	0.0030	3.0	336.4
14.0	8192.00	126976.3	0.000008	7.9	0.0028	2.8	0.0025	2.5	400.0

2.5.3 Quantitative Assessment of Casting Defects

2.5.3.1 Detection of Pores

In most cases, pores are the darkest regions of the image due to the physical properties of microscopes and can be easily detected by simple binarization or thresholding. This will be described in more detail in Section 2.5.3.4.

In the most convenient case, a polished section without any etching can be used for this purpose and the better prepared the specimen is, the less image treatment is necessary and the more precise the results of the whole analysis (Wojnar, 1999).

2.5.3.2 Parameters to Measure and Report Porosity

Once the correct threshold level has been selected on the analyzed image or seamless montage (Section 2.5.3.4), the regions in the binary image can be used as a mask to measure porosity due to shrinkage pores, entrapped and fragmented bubbles and oxide films in the gray scale.

There is a basic distinction between field features and region features. Field features refer to the image as a whole. Parameters such as total object count, total area, total perimeter, area fraction, and number of intercepts, commonly used in traditional metallographic analysis, are field features. Region features refer to each object in the image. Parameters such as object area, perimeter, major axes, shape, average intensity, and so forth are region features. Evidently, all field features can be derived from region features, but most programs provide this separation to facilitate basic measurements (Paciornik and Henrique de Pinho Mauricio, 2004).

In region features, the simplest measurement of size is the area (A). The measurement of area is obtained by digitally counting the number of pixels in the object, Figure 2 - 37. Another important parameter to measure porosity is the maximum Feret diameter (Wojnar and Kurzydlowski, 2000), which is also known as the maximum calliper. This is a linear measurement that corresponds to the longest dimension of the particle, Figure 2 - 37. In order to avoid confusion and to be consistent with terminology in this investigation, the name of 'maximum Feret diameter' instead of 'maximum calliper' will be used throughout this work.

To report the porosity measurements, two parameters can be calculated: area fraction of porosity (A_p) and density of porosity (ρ_p) using Equation 2 - 17 and Equation 2 - 18 respectively:

$$A_p = \frac{A_i}{A_T}$$ Equation 2 - 17

where A_i is the detected area of porosity and A_T is the total area in the image.

$$\rho_p = \frac{\sum N_i}{A_T}$$ Equation 2 - 18

where N_i is the detected number of pores and A_T is the total area in the image.

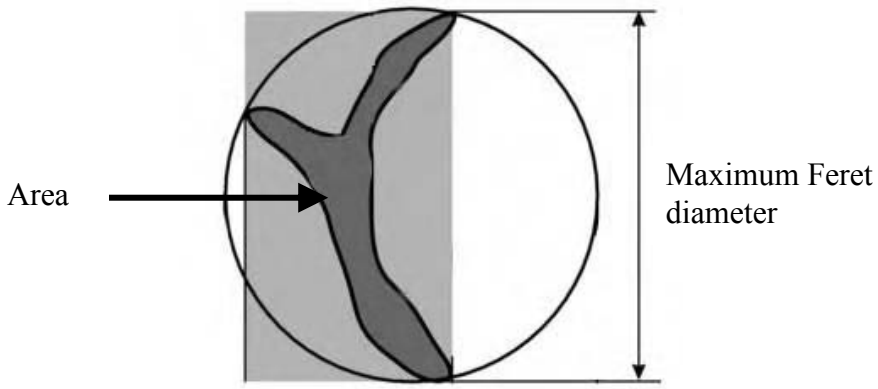

Figure 2 - 37. Schematic representation of area and maximum Feret diameter (Wojnar and Kurzydlowski, 2000)

2.5.3.3 Seamless Digital Montages

Balasundaram and Gokhale (2001) firstly developed an image analysis procedure for automatic segmentation and measurement of shrinkage pores and gas (air) pores present in the cast microstructure of a high pressure die-cast alloy.

Subsequently, Lee et al. (2006) studied the effect of processing parameters on the total porosity and shrinkage and gas porosity in a high pressure die cast Mg-alloy. This porosity was experimentally measured using seamless montages, which permitted the quantification of

both gas and shrinkage pores. Porosity distribution maps and the dependence of these distributions on the individual process parameters were reported. Likewise, pore volume fractions, average size, size distribution and other attributes of the pore geometry were also measured. Figure 2 - 38 shows an example of the seamless montage technique that Lee et al. (2006) used to measure porosity in high pressure die cast Mg-alloy.

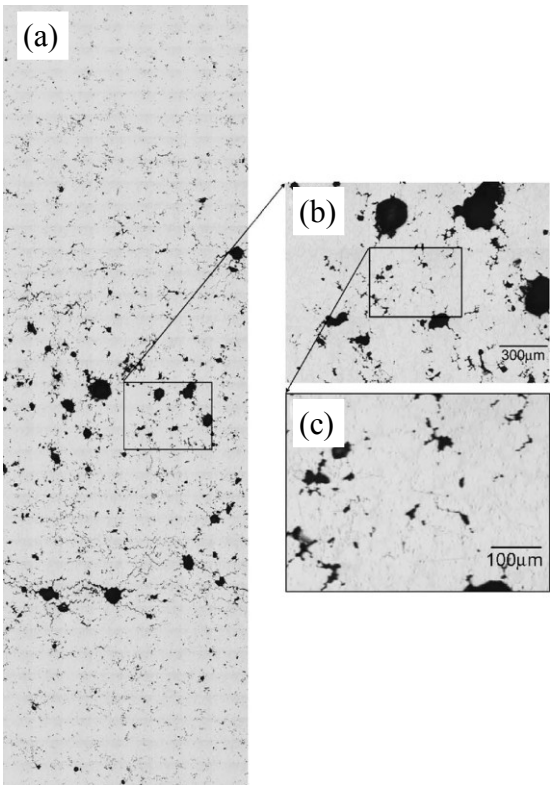

Figure 2 - 38. (a) Digitally compressed seamless montage of 280 contiguous microstructural fields covering the complete thickness of the plate (14.3 mm). (b) Enlarged view of the small window in (a). (c) Enlarged view of the small window in (b), (Lee et al., 2006).

2.5.3.4 Binarization or Thresholding

The process of transformation of gray-scale images into binary ones is called binarization or thresholding. The proper choice of threshold level is decisive for the results of analysis.

Manual adjustment of thresholds to produce a result that is considered to be correct based on visual inspection by a human operator is common, but in most cases this should be avoided if possible. In addition to taking time and being incompatible with automatic processing, different results are likely to be obtained at different times or by different people. Manual thresholding errors are probably responsible for more problems in subsequent image analysis than any other cause (Russ, 2007).

A number of algorithms have been developed for automating the thresholding procedure. Most of the automatic methods utilize the histogram in their calculations, but some also involve the image itself to make use of the location information for the pixels (and their neighbours). All automatic methods make some assumptions about the nature of the image, and if one is to choose the proper algorithm it is important to know as much as possible about the nature of the image and what kinds of scenes or subjects are dealt with (Russ, 2007).

Changes in the illumination, the camera or the positioning of the parts being examined make it necessary to have a method that adapts to the actual images. The accuracy and precision of automatic thresholding depends on choosing the appropriate method. This will be described in more detail in Section 4.2.3.

2.5.3.5 Characterization of Error in Digital Measurements

Digital measurements are based on analysis of the spatial distribution of pixels within an image, which usually are very precise, especially compared with manual measurements, and appropriate measuring procedures are built into the image analysis software (ImageJ, 2011).

Some theoretical formulae for error quantification of a given method have been developed in classical stereology. These formulae also can be used to predict the required number of measurements (number of fields of view, total intercept length, or number of test points). Unfortunately, all these considerations provide estimates of the error for a particular test method based on abstract, ideal conditions of their application. This allows prediction of how the error will change if, for example, the number of test points is doubled. However, these methods usually are not helpful for predicting error quantification under real experimental conditions. Consequently, errors estimated by means of statistical analysis of results (generally based on evaluation of the standard deviation) are usually greater than estimates based on theoretical stereological considerations (Wojnar and Kurzydlowski, 2000).

In the case of image analysis, it is not necessary to evaluate an error of the measurement strategy used because all of the information stored in the analyzed image is taken into consideration. Digital measurements introduce some error, but it is relatively easily estimated, (see Table 2 - 4).

Digital measurements also are both accurate and inaccurate. They are accurate (or precise) with respect to the applied algorithms, which are expected to give identical measurement results for the same image regardless of which software and computer are used. However, measurement results can be far from the correct value, as demonstrated in Figure 2 - 39. The error of the data in Figure 2 - 39 is surprisingly high for circles smaller than ten pixels in

diameter. Note, however, that every single pixel accounts for 5% of the area in the case of a circle having a diameter of five pixels (Wojnar and Kurzydlowski, 2000).

Table 2 - 4. Characterization of the error in digital measurements (Wojnar and Kurzydlowski, 2000).

Type of measurement	Characteristics	Most probable source of the bias	Suggested action
Counting objects	Provides exact results only if the particles crossed by the image edge are correctly analyzed	Incorrect detection or erroneous counting of particles crossed by the image edge	Apply proper correction procedures
Distances	Accuracy to a single pixel	Incorrect detection of very small objects	Avoid measurement of objects having length smaller than 10 pixels
Length (including curved lines)	Can be inaccurate, especially in the case of lines having small radius of curvature	Incorrect detection of objects having edges of very small radius of curvature	Avoid these measurements, especially if the radius of curvature is smaller than 5 pixels
Area	Can be measured precisely; improper binarization can introduce large errors, especially in the case of small precipitates	Incorrect detection	If possible, avoid particles smaller than 10 pixels in diameter and test how variation in threshold level affects the results

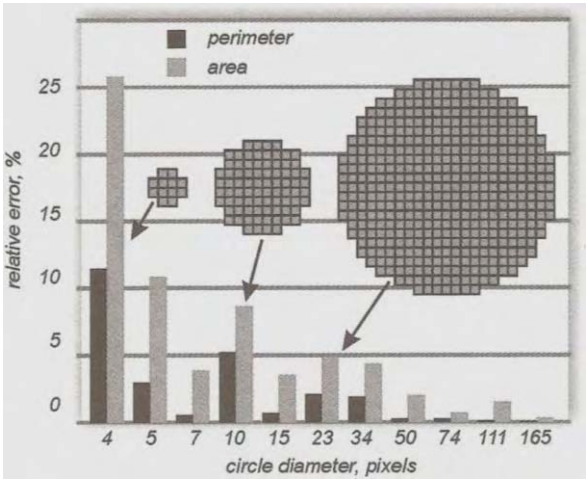

Figure 2 - 39. Relative error of digital measurements of the area and perimeter of circles of different diameters (Wojnar and Kurzydlowski, 2000).

Table 2 - 4 and Figure 2 - 39 show that there are two main sources of error in digital measurements: incorrect detection and, in the case of length measurements, analysis of very small objects. Changing the magnification can minimize error for the latter source. Also, correction procedures can be applied to the results of measurements carried out on small objects. As a result, the main source of error in digital measurements remains incorrect detection. This reinforces the necessity of the highest possible quality at all the stages of the metallographic procedure (specimen preparation and image processing), as each stage can introduce large errors to the final results of analysis.

In practice, it is relatively difficult to quantify measurement errors. One possible solution is to determine the errors experimentally using model materials or images with dimensions that are known. Comparing apparent and predicted results allows an approximation of the measure of accuracy of applied methods. It is also possible to use computer models of the experimental procedure in question. The problem of error in image analysis might have less importance in practical applications than in the context of deriving correct values for every object measured. The main requirement of using digital methods is to obtain the highest repeatability and reproducibility of results, which is almost always achieved at a satisfactory level (Wojnar and Kurzydlowski, 2000).

2.6 Properties of Castings

2.6.1 Effect of Porosity and Oxide Films in Mechanical Properties

Besides the oxide films, surface turbulence can lead to entrapment of gas resulting in porosity with a characteristic size, morphology, density and distribution which adversely affect the mechanical properties of any cast material.

Boileau et al. (2001) studied the effect of porosity size on the tensile properties of a cast Al alloy. The results showed that tripling the average pore size decreased the average ultimate tensile strength by around 19%, the average ductility was decreased by a factor of three and no significant difference was observed for the yield strength.

Tiryakioglu (2008a) reviewed the use of defect size distributions of porosity for fatigue life in Al and Mg alloys. In this review it was mentioned that there seem to be two approaches taken by researchers in the literature: (i) taking the entire pore size distribution into account or (ii) taking only the distribution of the largest defects/inclusions. Regarding the first consideration, Yi et al. (2006) established a physical relationship between the casting-related microstructural features and the resultant fatigue life of cast A356-T6. Likewise, it was demonstrated by statistical modelling that when a large pore or oxide film is present at or close to the specimen surface it can act as a favourable crack initiating site. However, in the absence of large pores or oxide films near the specimen surface, the scale of the micro-cells, comprised of eutectic surrounding the primary phase, determined the fatigue performance. Regarding the second approach, Casellas et al. (2005) demonstrated that the variability of pore size produced a noticeable scatter in fatigue life results, which was associated with differences in the size of the fracture-controlling pores. Thus, pore size distribution accounted for the fatigue variability in Al-Si cast alloys.

The effect of oxide films and porosity on the quality and reliability of aluminium alloy castings has been assessed successfully using the Weibull distribution (Green and Campbell, 1993) (Green and Campbell, 1994) (Nyahumwa et al., 1998), which is an indicator of the variability of mechanical properties. This is described in more detail in Section 2.6.2.

Yang et al. (2006) reported the ultimate bend strength (UBS) of flat test bars cast from an Al-7Si-Mg alloy. Firstly, casting plates were made using three different runner systems: vortex flow runner (VR), rectangular runner (RR) and triangular runner (TR). The full description and dimensions of these designs were reported by Dai et al. (2003) (2004), Figure 2 - 24. The resulting plates were cut into small specimens as described in Figure 2 - 40. After being subjected to four point bend test, the broken specimens had a length ranging from 40 to 60 mm. Subsequently, these specimens subjected to a three point bend testing and the quantitative characterization of the casting defects was performed by using image analysis software.

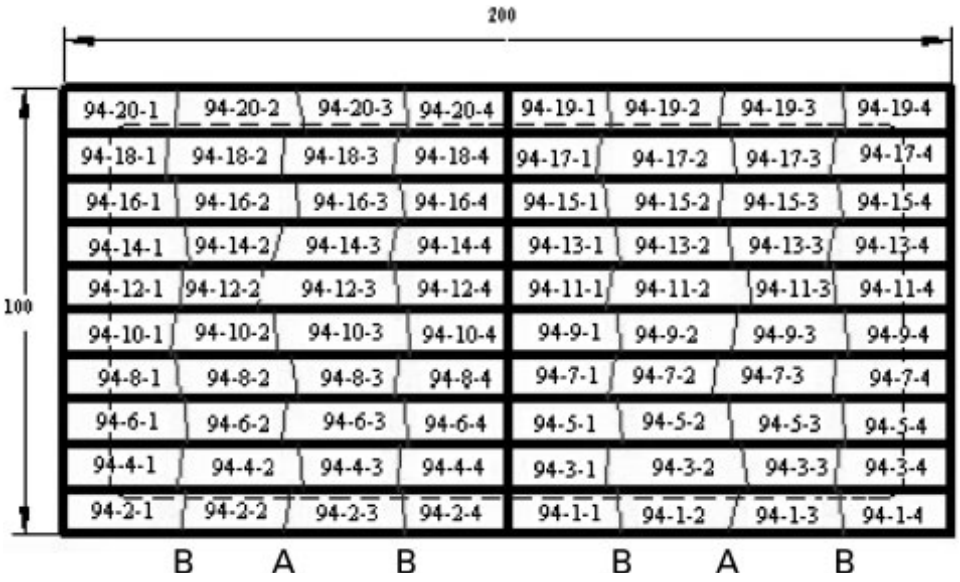

Figure 2 - 40. Schematic plan view of the cast plate obtained from the vortex flow runner (VR). The plate is marked with test sequence number: lines A represent fracture positions after specimens were subjected to four point bend testing and lines B represent fracture positions after specimens were subjected to three point bend testing; dimension in millimetres (Yang et al., 2006).

The authors defined the Casting defect area fraction (α_F) as the detected area of the casting defects divided by the measurement field area; and the Casting defect density (ρ_F) as the total number of casting defects divided by the measurement field area. The results are illustrated in Figure 2 - 41 and Figure 2 - 42 respectively.

In Figure 2 - 41, it can be seen that the UBS was decreased as the Casting defect density increased. The test bars obtained from the vortex flow runner (VR) had the fewest defects, which resulted in the most of the values clustered together with high UBS. The plots obtained for the rectangular runner (RR) and triangular runner (TR) showed a higher dispersion of results and in some cases the casting defect density reached values of nearly 120. Similarly, the UBS was also reduced when the Casting defect area (%) increased, Figure 2 - 42. Again, the test bars obtained from the vortex flow runner (VR) had the lowest casting defect area, which resulted in the most of the values clustered together with high UBS. On the other hand, the results for the rectangular runner (RR) and triangular runner (TR) showed higher porosity area fractions.

Based on the microstructure analysis, Yang et al. (2006) confirmed that a better and more balanced casting defect distribution existed in the casting plate made by using the VR runner while a harmful and unbalanced casting defect distribution occurred in the casting plates made by using the RR and TR runners. Likewise, the microstructure analysis results were consistent with the Weibull distributions of three point bend strength (UBS) on the specimens from the casting plates. The Weibull analysis indicated that the Weibull moduli were in the following order: VR (16.9), RR (12.4) and TR (5.6).

However, the possible effect of the four-point bend testing in the samples used for the subsequent three-point bend testing was not considered, which may have affected the UBS.

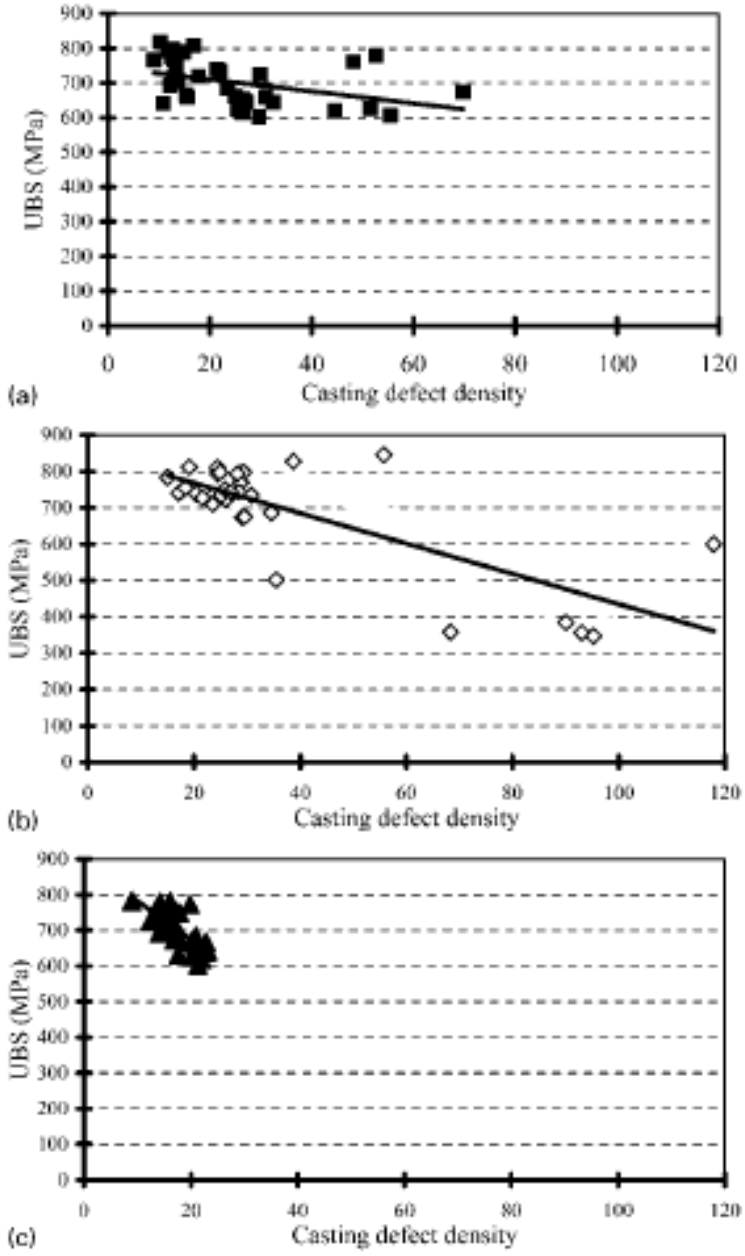

Figure 2 - 41. UBS as a function of casting defect density of (a) rectangular runner (RR), (b) triangular runner (TR) and (c) vortex flow runner (VR) (Yang et al., 2006).

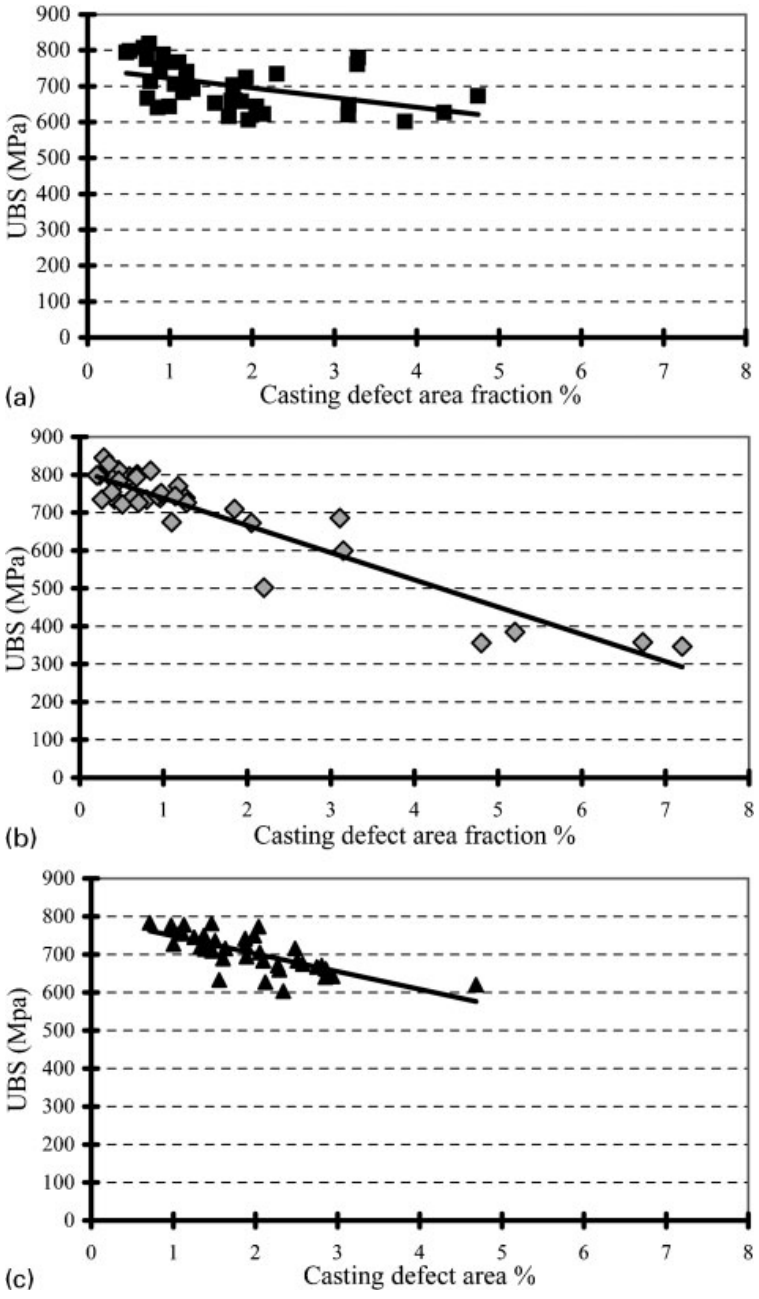

Figure 2 - 42. UBS as a function of casting defect area (%) of (a) rectangular runner (RR), (b) triangular runner (TR) and (c) vortex flow runner (VR) (Yang et al., 2006).

2.6.2 Weibull Statistical Technique

The Weibull distribution can be expressed in the cumulative three-parameter form as:

$$F_w = 1 - exp\left\{-\left(\frac{x - \mu}{\sigma - \mu}\right)^{\lambda}\right\} \qquad \text{Equation 2 - 19}$$

where F_w is the cumulative fraction of failures for a given value of x, σ is the characteristic value of x at which 63% of specimens have failed, x is the variable of interest (e.g. bend strength), μ is a boundary value (below which no failures can occur) and λ is the width parameter, commonly known as the Weibull modulus.

It has been demonstrated that distributions of mechanical properties such as tensile strength can be satisfactorily characterized using the Weibull distribution in the two-parameter form with μ set to zero, Equation 2 - 20, compared with other distributions (Green and Campbell, 1993).

$$F_w = 1 - exp\left\{-\left(\frac{x}{\sigma}\right)^{\lambda}\right\} \qquad \text{Equation 2 - 20}$$

Equation 2 - 20 can be rearranged to plot ln(x) against ln[ln[1/(1 – F_w)]]. Subsequently, a straight line fitted to the data will have a slope equal to the Weibull modulus (λ), where the greater the value of λ, the narrower the spread of x.

The cumulative fraction of failures F_w for each specimen is calculated using the following relation (Khalili and Kromp, 1991):

$$F_w = \frac{j - 0.5}{N} \qquad \text{Equation 2 - 21}$$

where j is the ranked position of the specimen bend strength in the set of castings and N is the total number of specimens tested.

The Weibull distribution is an indicator of the variability of the strength of the material, which is attributed to flaws of critical size resulting from its manufacture. The Weibull distribution has been proved to be a convenient tool for quality and reliability analysis of different casting processes. The correlation between the Weibull modulus λ and different casting processes is summarized in the following section.

2.6.3 Weibull Modulus and Conventional Casting Processes

Weibull modulus values have been reported for conventional casting processes such as gravity and tilt casting, where bend testing was used to evaluate the mechanical properties of flat test bars.

Cox et al. (2003) obtained the Weibull modulus of 2L99 (Al-7Si-Mg) castings made using different gravity-filled mould designs and related them to the surface turbulence created during mould filling. Four different running systems were designed to provide different amounts of surface turbulence: top filled, uncontrolled bottom filled, and controlled bottom filled with and without a filter. Figure 2 - 43 shows the schematic view of the three running systems. The top filled and uncontrolled bottom filled systems produced significant turbulence resulting in the least reliable castings with Weibull modulus values of 26 and 27, respectively. The results obtained for the controlled bottom filled system without and with the addition of a ceramic filter were 38 and 54 respectively. The last number represents more than double the value obtained with top filled systems. These values were confirmed in later work

by Cox and Harding (2007) in which Weibull modulus values of 23 and 49 respectively were obtained for identical top and filtered controlled bottom filled systems (Figure 2 - 43) using an aluminium alloy 2L99 (Al-7Si-0.4Mg), which were included in the casting programme to provide a benchmark with which to compare results for tilt filled moulds.

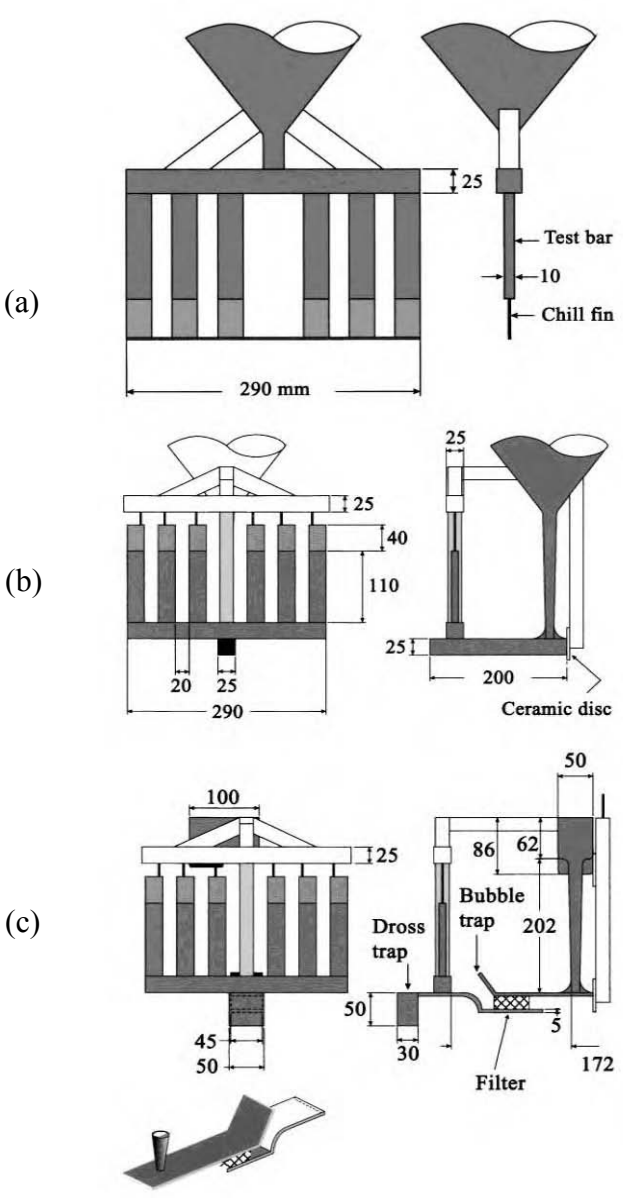

Figure 2 - 43. Schematic view of (a) top filled, (b) bottom filled, and (c) controlled bottom filled mould designs; all dimensions in mm (Cox et al., 2003).

Cox and Harding (2007) also studied the effect of different conditions in the tilt casting process and their relation to oxide film entrainment and reliability of castings. Rotation was controlled by computer and allowed controlled pauses and changes of speed in the rotation cycle, Figure 2 - 44. Firstly, a batch of experiments was carried out using single stage cycles, which consisted of uniform speed rotation throughout the cycle, except for the initial acceleration up to speed from rest and the final deceleration to rest. These conditions produced Weibull modulus values of 30 and 45. Secondly, another batch of experiments was obtained from multi stage cycles, which consisted of a number of uniform velocity stages separated by pauses to allow the metal level to stabilise. These conditions improved the Weibull modulus to values between 42 and 55.

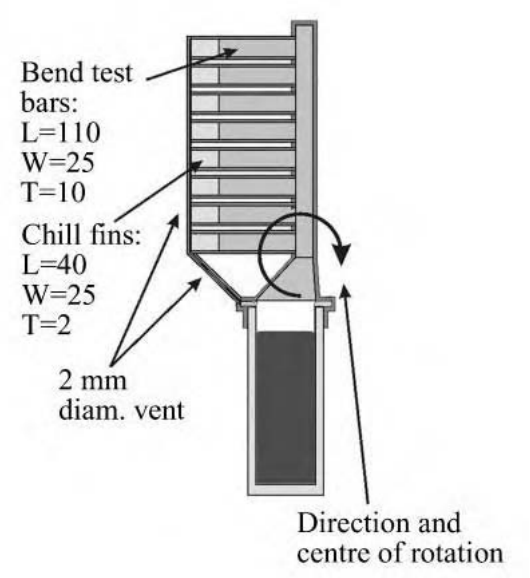

Figure 2 - 44. Schematic view of tilt casting mould and direction of rotation; all dimensions in mm (Cox and Harding, 2007).

3. OBJECTIVES

The objectives of the present research are as follows:

- To carry out centrifugal casting experiments for an aluminium alloy and to investigate the effect of direct and indirect mould designs on the formation of casting defects such as entrapped bubbles and double oxide films and inter-relate these results with the mechanical properties.

- To analyze the quality and reliability of castings produced by direct and indirect gated mould designs.

- To investigate the effect of rotational velocity in the filling rate of direct and indirect gated test bars using water modelling.

- To validate the computer modelling software (ANSYS CFX) based on water modelling for simple direct and indirect gated mould designs.

- To use ANSYS CFX to identify the active entrainment mechanisms during the filling process of direct and indirect gated moulds in centrifugal casting.

- To use the oxide film entrainment model (OFEM) implemented in Flow-3D to quantitatively assess the damage provoked by surface turbulence-related phenomena during the filling process of direct and indirect gated moulds in centrifugal casting.

4. EXPERIMENTAL METHODS

4.1 Centrifugal Casting of Direct and Indirect Gated Moulds

4.1.1 Mould Designs

The different designs of gating systems in centrifugal casting may be expected to result in different qualities of castings. In this investigation, direct and indirect gating designs were chosen to investigate the effect of surface turbulence on the quality and reliability of test bars. The dimensions of the mould designs and flat test bars were chosen according to the limitations imposed by the characteristics of the experimental equipment. The test bar dimensions were 120 x 25 x 4 mm for direct gated moulds and 80 x 25 x 4 mm for indirect gated moulds and were oriented horizontally, Figure 4 - 1.

4.1.2 Mould Making

The ceramic shell moulds were made using the lost wax process. This process began by injecting wax into metal dies to produce flat bars of dimensions 150 x 25 x 4 mm, 150 x 25 x 10 mm and 150 x 25 x 25 mm. Then, the test bars and gates (Figure 4 - 2) for both gating systems were cut off according to the dimensions shown in Figure 4 - 1.

The down-sprue was made using a metal mould with inner diameter of 100 mm and height of 355 mm. Molten wax was poured into the mould and the sprue removed when it had solidified. Subsequently, the runner system was made for the indirect gated mould by assembling and moulding a combination of flat bars of 150 x 25 x 10 mm and 150 x 25 x 25 mm, according to the dimensions specified in Figure 4 - 1.

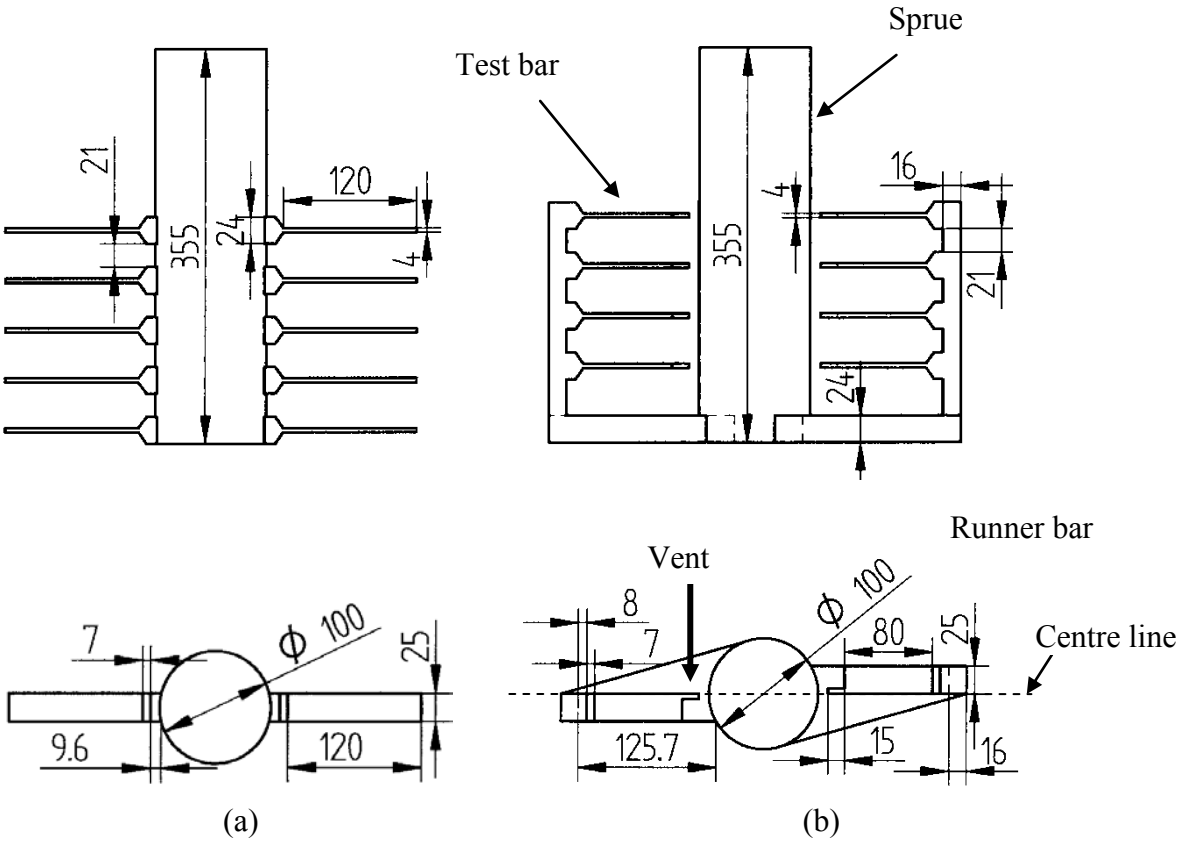

Figure 4 - 1. Side and plan views of (a) direct and (b) indirect gating mould designs used for producing centrifugally cast aluminium test bars; all dimensions in mm.

The test bars, gates, runner system (indirect gating mould) and sprue were assembled together as illustrated in Figure 4 - 2 and then used to make the ceramic shell moulds suitable for centrifugal casting. The process to produce the ceramic moulds was as follows:

- The primary coat slurry was based on a Remet LP-BV binder and 200 mesh Zircosil 200M filler, which was applied manually. The stucco was 80 mesh zircon sand with an average grain size of 230 μm, which was also applied manually. The mould was dried for 12 to 14 hours at an air speed of 0.1 m/s, Figure 4 - 3.

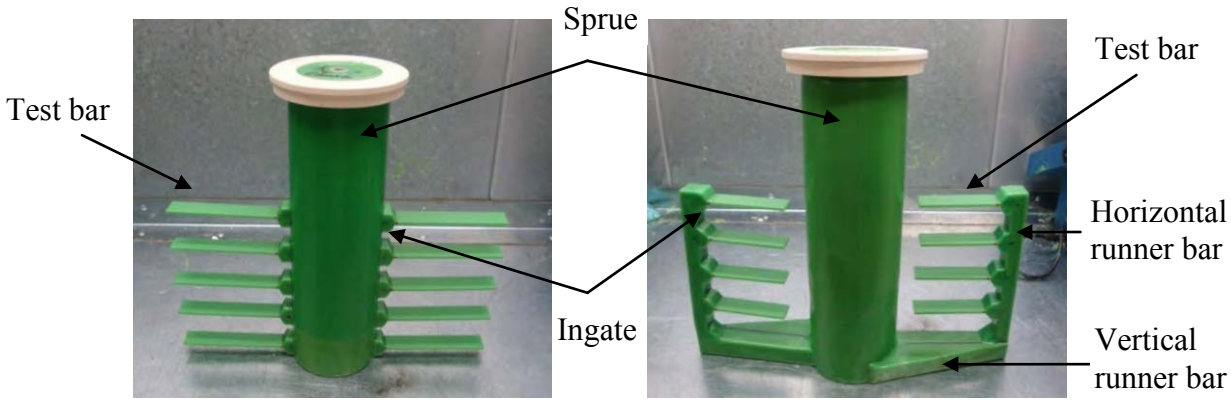

Figure 4 - 2. Wax patterns of (a) direct and (b) indirect gating mould designs used for making ceramic shell moulds.

Figure 4 - 3. Drying of ceramic shell moulds.

- For the second and third coats, the mould was dipped in a slurry container, Figure 4 - 4 (a) (b), which contained a slurry made from a Remet LP binder and a blend of 200 mesh fused silica and 200 mesh (0-0.75 μm) Molochite fillers. The stucco was 30-80 mesh Molochite (230-500 μm) and was applied using a raining cabinet by holding and rotating the mould inside, Figure 4 - 4 (c). The mould was dried for 1½ to 2 hours at an air speed of 3 m/s, Figure 4 - 3.

- To apply the subsequent coats the same previous slurry was used and the stucco was 16-30 Molochite (0.5 – 1.0 mm). The mould was dried for 1½ to 2 hours at an air speed of 3 m/s, Figure 4 - 3.

- A total of 9 coats were applied and finally the moulds were dewaxed using high pressure steam in a Boilerclave and fired for 2 hours at 1000°C in an electrically heated furnace, Figure 4 - 5, and then cooled down to room temperature.

- Finally, the ceramic moulds were patched and repaired with fire cement, Figure 4 - 6.

(a) (b) (c)

Figure 4 - 4. (a) and (b) Dipping process and (c) applying stucco.

(a) (b)

Figure 4 - 5. (a) Boilerclave and (b) Firing furnace for ceramic shell moulds.

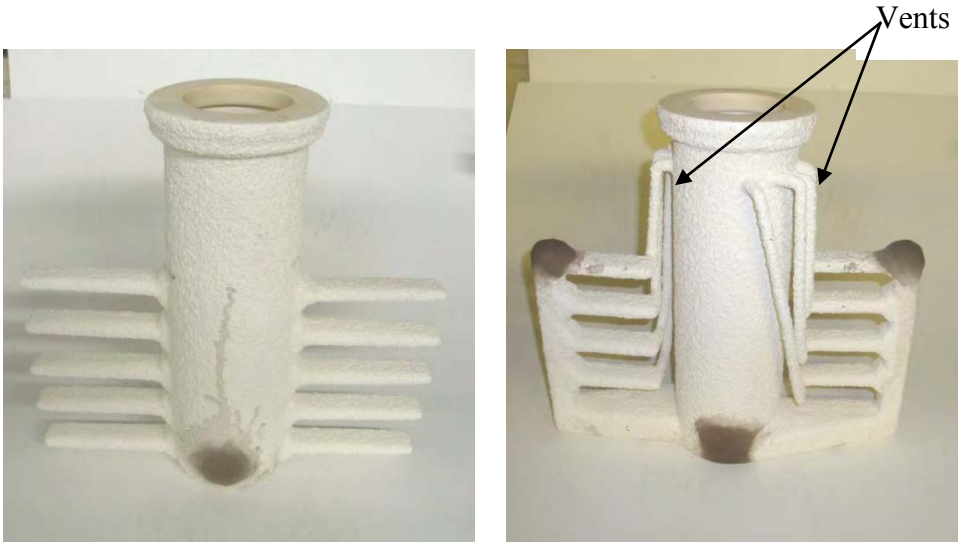

Figure 4 - 6. Ceramic shell moulds suitable for centrifugal casting of (a) direct and (b) indirect gating mould designs.

4.1.3 Experimental Alloy, Equipment and Casting procedure

The chemical analysis of the aluminium alloy 6082 used in this research was carried out by Inco Test Laboratory (a sub-contract company) using the Optical Emission Inductively Coupled Plasma (ICP) method.

A Consarc induction skull melting (ISM) furnace equipped with a water-cooled copper crucible was used in this investigation, Figure 4 - 7. This is normally used when melting and casting TiAl alloys, but in this research, it was used to air melt the 3 kg charges of aluminium alloy 6082.

Before each casting, the ceramic shell mould was put inside an Inconel 718 box and carefully centred. Then, it was packed in place with coarse mullite and covered with insulating fibre and the Inconel 718 lid, which helped to insulate the mould and reduced the temperature loss before casting, was placed. The dimensions of the box were 44 x 30 x 20 cm.

Figure 4 - 7. The vacuum chamber containing the Induction Skull Melting (ISM) furnace.

The box containing the ceramic mould was preheated in an electric resistance furnace to 550°C for 5 hours (2 hrs preheating and 3 hrs to homogenise the temperature), transferred and mounted on a rotary turntable within the vacuum chamber housing the ISM furnace, Figure 4 - 7. Horizontal bars were then fixed and nuts screwed on to hold the box during rotation, Figure 4 - 8.

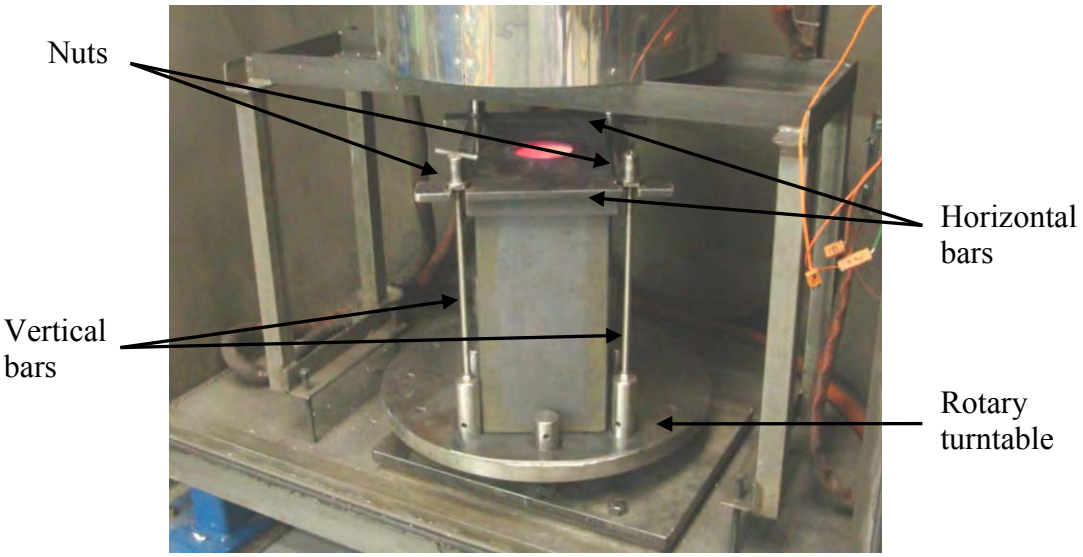

Figure 4 - 8. Clamping system to attach Inconel box to centrifugal casting table.

The power applied to the induction coil was increased by steps of 30 kW according to Table 4 - 1 until the maximum power of 182 kW was reached. The maximum power was maintained for almost 2 minutes to achieve the maximum superheat of the aluminium alloy. The mould temperature at the time of pouring was 450 ± 10°C (Shevchenko, 2011) and the metal temperature was 695 ± 10°C (Shevchenko, 2011). The liquidus and solidus temperature are 642 and 600, respectively (Mills, 2002).

Table 4 - 1.Power steps to melt aluminium alloy in a Consarc ISM furnace

Time (min)	**Power (kW)**
0:00 – 0:59	30
1:00 – 1:59	60
2:00 – 2:59	90
3:00 – 5:49	120
5:50 – 6:59	150
7:00 – 8:55	182

The molten metal was poured from the crucible into the ceramic mould through a funnel at a rate of ~2 kg/s. The funnel was made of commercial purity titanium CP and was preheated in an electric resistance furnace to 500°C for 30 minutes to minimise heat loss from the molten metal, Figure 4 - 9 and Figure 4 - 10. The centrifugal casting was carried out at a rotational velocity of 400 r.p.m. clockwise direction for all the experiments. Three moulds were cast for each gating system.

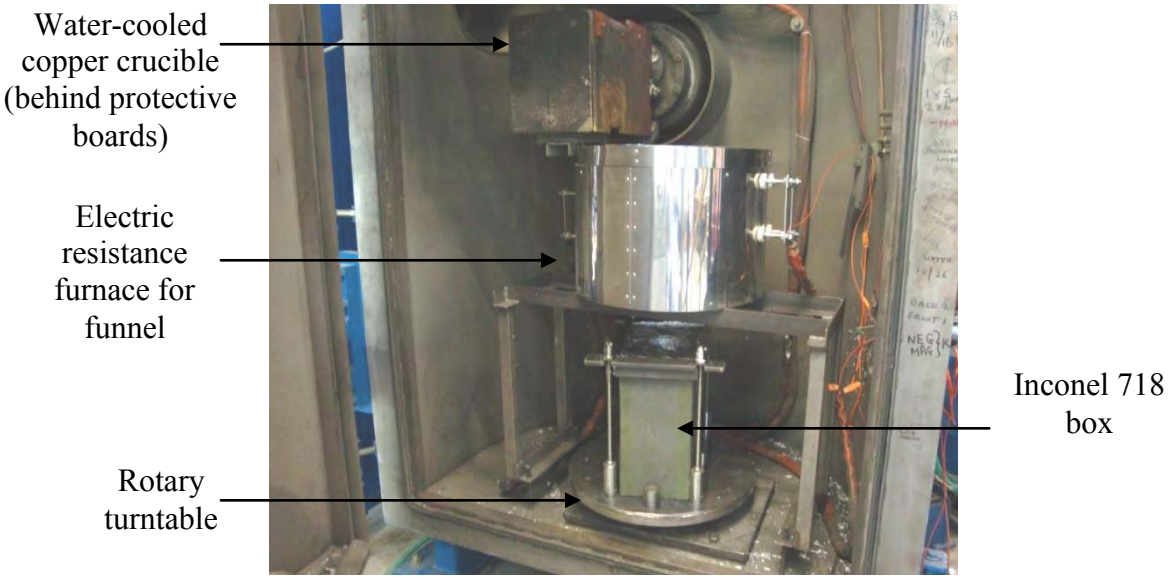

Figure 4 - 9. Centrifugal casting equipment within the vacuum chamber of the induction skull melting (ISM) furnace.

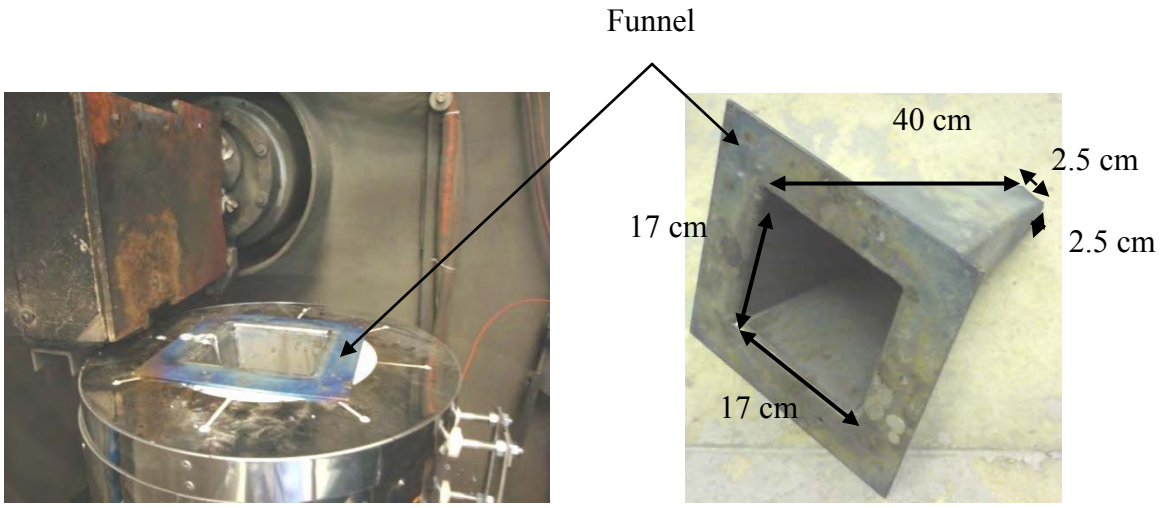

Figure 4 - 10. (a) Close-up of the funnel inserted in the electric resistance furnace and (b) dimensions of funnel.

4.1.4 X-ray radiography

The test bars were removed from the castings and X-ray radiographed by Exova (a sub-contract radiography company). The test bars were grouped by casting batch. This allowed an easy identification and correlation with subsequent individual characteristics. Subsequently, the radiographs were converted into digital files by scanning them at a resolution of 300 pixels/in.

4.1.5 Heat Treatment

In order to achieve maximum strength, the test bars were heat treated to the T6 condition by solution treating at 540°C for 6 hours, quenching in room temperature water and ageing in an air circulating furnace at 160°C for 18 h.

4.1.6 Bend Testing

Three-point bend testing was performed using a Zwick/Roell servohydraulic machine, Figure 4 - 11. The 4 mm thick cast bars were tested to failure in the non-machined condition as close as possible to the standards BS EN ISO 7438:2005 (BRITISH-STANDARD, 2005), ASTM E290-09 (ASTM, 2009) and ASTM E855 – 08 (ASTM, 2008).

The test rig consisted of two supports and a 6 mm radius load roller. The distance between the supports was 35.6 mm and the crosshead speed was 0.5 mm/min, Figure 4 - 11 and Figure 4 - 12. Data of Force vs. Displacement were automatically recorded and exported to Microsoft Excel for analysis.

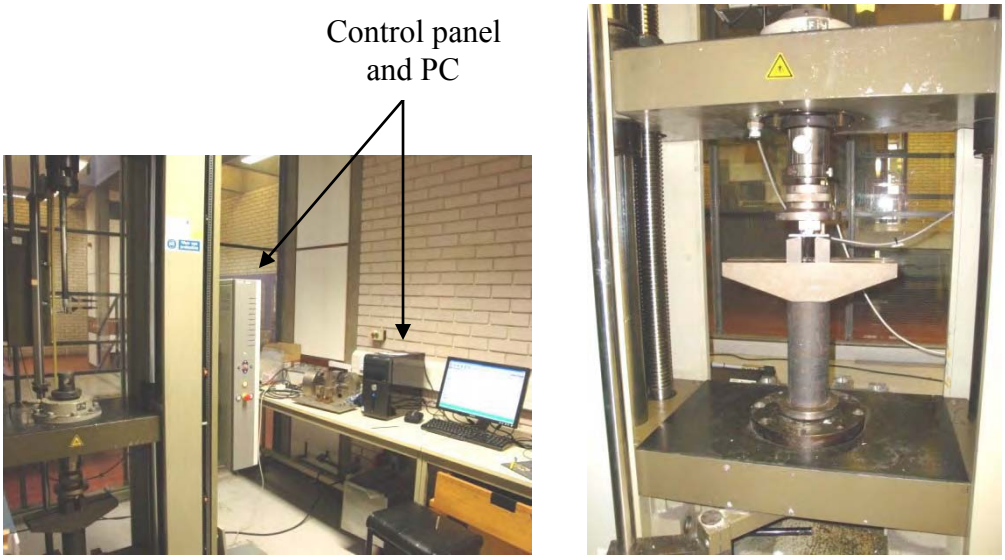

Figure 4 - 11. (a) Zwick/Roell servohydraulic machine and (b) close-up of three-point bend testing set-up.

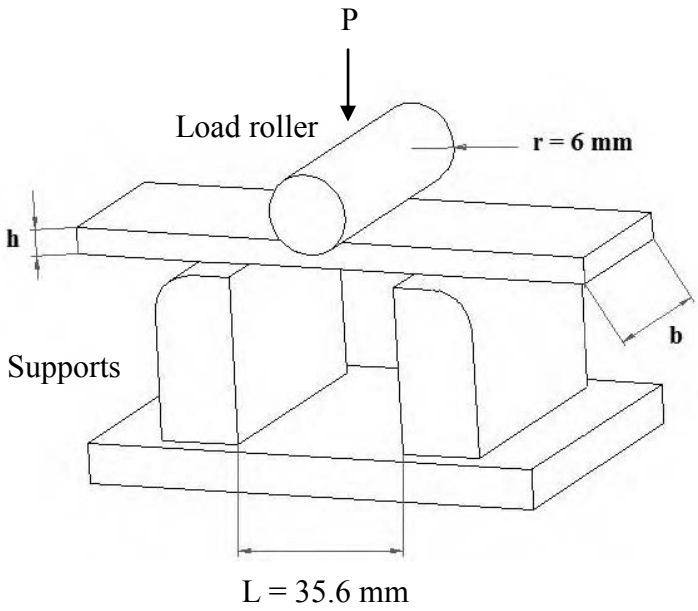

Figure 4 - 12. Schematic 3D geometry of the three-point bend testing set-up.

The ultimate bend strength was calculated using the following equation (Dowling, 1999) and (Shapiro, 2000):

$$\sigma_B = \frac{3PL}{2bh^2} \qquad \text{Equation 4 - 1}$$

where σ_B is the bend strength (MPa), P is the applied load (N), L is the distance between the two supports or span length (mm), b is the specimen width (mm) and h is the specimen thickness (mm).

The modulus of elasticity in bending was calculated from the load increment and the corresponding deflection increment between the two points on the straight line as far apart as possible by using the following equation (Shapiro, 2000):

$$E = \frac{L^3 \Delta P}{4bh^3 \Delta \delta} \qquad \text{Equation 4 - 2}$$

where E is the modulus of elasticity in bending (MPa), ΔP is the load increment as measured from the preload (N) and $\Delta\delta$ is the deflection increment at midspan as measured from the preload (mm).

The scatter in the ultimate bend strength and modulus of elasticity was analyzed using the two-parameter Weibull statistical technique which was reviewed in Section 2.6.2.

4.2 Characterization of Microstructure and Casting Defects

As reported later, it was found that the indirectly gated castings had improved properties and therefore quantitative characterization of the bend test samples was carried out to determine whether this improvement could be attributed to (i) a reduction of porosity due to shrinkage,

entrapped bubbles and oxide films generated during mould filling or (ii) differences in microstructure resulting from different solidification conditions.

This characterization involved dendrite cell size, grain size, stereological measurements of porosity such as size distribution, area fraction and density, and qualitative characterization of fracture surfaces.

4.2.1 Metallographic Preparation

During bend testing of the cast bars, the strains and stresses on the tensile surface are maximum at a position in line with the load roller and decrease away from this position towards the centre line (neutral axis) of the samples, Figure 4 - 13. Failure was expected to be initiated at casting defects such as oxide films and porosity defects generated during mould filling. Therefore, the metallographic section selected for detailed quantitative characterization of dendrite cell size, grain size and porosity was located near to the fracture on the test bar tensile face. As presented in Section 6.1.2 and 6.1.6, the variability in ultimate bend strength (UBS) and modulus of elasticity (E) was related to the presence of large porosity and oxide films. These defects are rarely observed on metallographic planes close to the surface. However, the probability of intersecting these defects on internal metallographic planes is higher. Therefore, material was removed from the surface so that the section examined was approximately 0.7 mm below the tensile surface, Figure 4 - 14.

The samples were prepared metallographically as follows: they were ground using 240 to 4000 grit SiC abrasive papers and then polished using 6 and 1 μm oil-based diamond compounds on a MD-Nap. For characterizing the microstructure, the specimens were anodized with Barker's reagent. The composition of the Barker's reagent was 40 ml HBF_4 per

litre of water. The anode was the specimen and the cathode was the stainless steel vessel, which contained the chemical solution. The current density varied from sample to sample since the surface area was slightly different, although it was in the range of 1.4 - 1.8 A/cm^2 and the D.C. voltage was 2 V. The time of etching was around 3 minutes depending on the sample (Warmuzek, 2004).

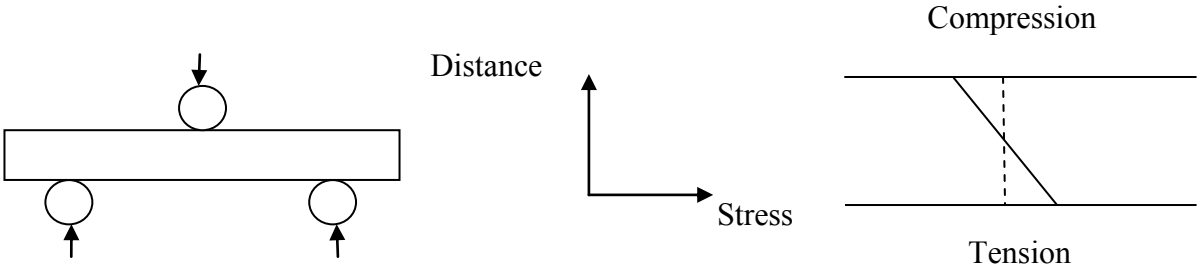

Figure 4 - 13. Schematic 2D view of three-point bend test showing distribution of stresses across section.

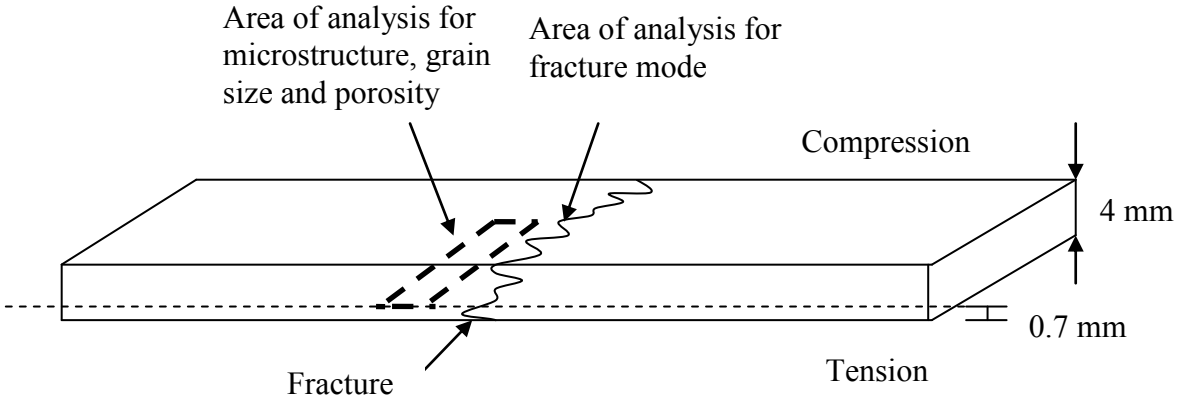

Figure 4 - 14. Schematic 3D view of area selected for characterization of microstructure, grain size, porosity and fracture mode on cast test bars.

Microstructures were observed under polarized and normal light and photographs obtained using a Zeiss optical microscope (Axioskop 2 MAT mot), CCD Sony digital camera (XC-77CE) and software KS 400 v3.0.

4.2.2 Characterization of Dendrite Cell Size and Grain size

Since the heat treated microstructure had a rosette-like morphology for both gating designs as illustrated in Figure 4 - 15, the dendrite cell size *d* was measured instead of the dendrite arm spacing (Section 2.5.1). Digital image analysis software (ImageJ, 2011) was used to carry out the measurements on 8-bit gray scale images, which were obtained with a resolution of 0.47 pixel/µm. Subsequently, the cooling rate was calculated as described in Section 2.5.1.

The grain size measurements were made on 8-bit gray scale images, which were also obtained with a resolution of 0.47 pixel/µm. The measurement technique was the Abrams three-circle procedure as described in Section 2.5.2.

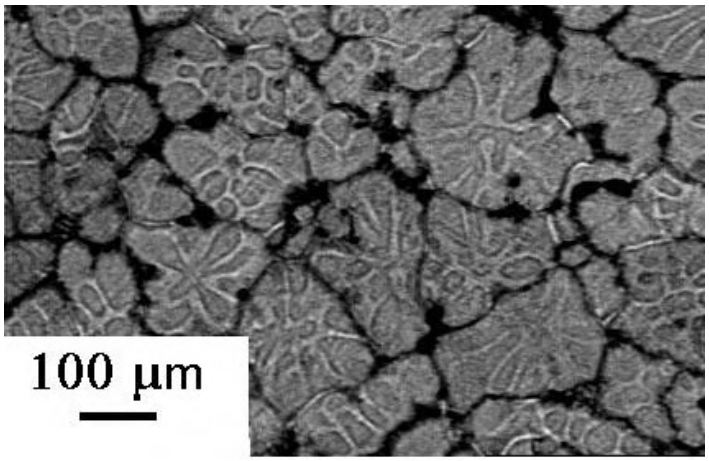

Figure 4 - 15. Rosette-like morphology in cast aluminium alloy 6082.

4.2.3 Stereological Measurements

In order to understand the effect of centrifugal pressure on the formation of porosity, a detailed quantitative characterization of this was carried out on selected bars. For the estimation of the microporosity, seamless montages of at least 60 contiguous micrographs were created using digital imaging software (Axiovision, 2011). It has been reported (Lee et al., 2006) that the use of the seamless montage technique minimizes the error due to edge effects since pores lying across an observation micrograph are counted only once which allows measurement of porosity that is not in the same field of view.

Great care was taken during the acquisition of the images to ensure that the lamp intensity was kept constant for all the samples. 8-bit gray scale images were obtained from specimens in the as-polished condition with a resolution of 0.47 pixel/μm. This resolution was sufficient to resolve the porosity and convoluted oxide films. In the case of oxide films, it has been reported by Nyahumwa et al. (1998) in their detailed study of oxide films in an aluminium alloy that these defects observed on metallographic sections constitute cracks showing no bound developed across the oxide-oxide interface. The width between the two dry surfaces of folded oxide films varies from 1 to 10 μm. However, the overall size of these defects is far larger than 10 μm. Likewise, the largest defects (upper tail of the defect size distribution) are responsible for initiating cracks in metals (Murakami and Endo, 1994). Therefore, defects smaller than 2 μm have a minimum detrimental effect on the mechanical properties compared to that of larger defects, which result from tangled networks of oxide films or entrapped bubbles with two or more larger orders of magnitude.

In order to have comparable results, 4 selected broken samples with different ultimate bend strengths (UBS) were selected for each gating system and a total area of at least 119 mm^2 was covered for each specimen.

The area of analysis was located close to the fracture caused by the three-point bend test along the longitudinal dimension of the cast test bars, Figure 4 - 14. The porosity due to shrinkage, fragmented and entrapped bubbles and convoluted oxide films appeared darker on the images than the surrounding matrix and intermetallic phases.

Digital image analysis software (ImageJ, 2011) was used to carry out the porosity measurements of the seamless montages representing two-dimensional metallographic planes. This software allows 16 different automatic thresholding methods to be selected. These methods are described on Fiji's Auto Threshold website (2011). Since the accuracy and precision of automatic thresholding depends on choosing the appropriate method, it was required to carry out a series of preliminary experiments to choose the proper algorithm, which was selected carefully since it affected the amount and morphology of the porosity.

Firstly, the inaccurate algorithms were ruled out by comparing the threshold limits covering roughly the true porosity. Subsequently, the correct algorithm was chosen, where the threshold limits covered only the true porosity and more precisely the porosity boundaries. It was found out that for the most cases, the default method (IsoData) was the most accurate to threshold the porosity. However, in some cases it was necessary to slightly adjust manually the threshold limits in order to improve the precision of the method.

The stereological measurements of porosity were characterized in terms of area and maximum Feret diameter, Figure 2 - 37. Likewise, area fraction and density of total porosity were calculated (Wojnar and Kurzydlowski, 2000) as defined in Section 2.5.3.2.

As presented in Section 6.1.5, the quantitatively characterized porosity was a combination of shrinkage pores, fragmented and entrapped bubbles, trails and oxide films. Due to the high surface turbulence generated during the whole filling process, some of the entrapped bubbles were fragmented and dispersed randomly resulting in small and large scale porosity. Therefore, no attempt was made to distinguish between shrinkage porosity and small scale gas porosity.

4.2.4 Fractography

A digital single lens reflex camera with automatic focus and automatic exposure control was used to obtain macrophotographs of the test bar fracture surfaces. Five samples with different UBS were selected for each gating system and digital images with a resolution of 43 pixels/mm were produced.

A Philips XL-30 scanning electron microscope (SEM) equipped with an energy dispersive X-ray analyzer was used in this investigation. Three of the five samples previously used for obtaining macrofractographs from each gating system were used for this analysis. Energy dispersive X-ray analysis was used to analyze the chemical composition of the casting defects on the fracture surfaces. The conditions were the following: beam voltage of 15.0 kV, working distance of 10 mm (WD), spot size 6.4 – 7.0 nm (Spot).

Additionally, a fracture mode analysis on metallographic sections was made in order to identify the propagation paths of fracture through the tested bars, Figure 4 - 14. The samples were prepared metallographically as described previously in Section 4.2.1.

4.3 Water Modelling

Water modelling was used to obtain data to validate the computer modelling presented in Section 5.3, so that the software could then be used with confidence to model the centrifugal casting process.

4.3.1 Experimental Equipment

Experimental centrifugal casting equipment was built in order to carry out water modelling. This consisted of a motor-driven rotating table to which Perspex moulds could be attached, a control panel to set the desired rotating velocity which was in the range of 200 - 400 rpm and a system to deliver water under controlled conditions. Subsequently, a high speed video camera system was fixed to the experimental equipment, Figure 4 - 16 and Figure 4 - 17.

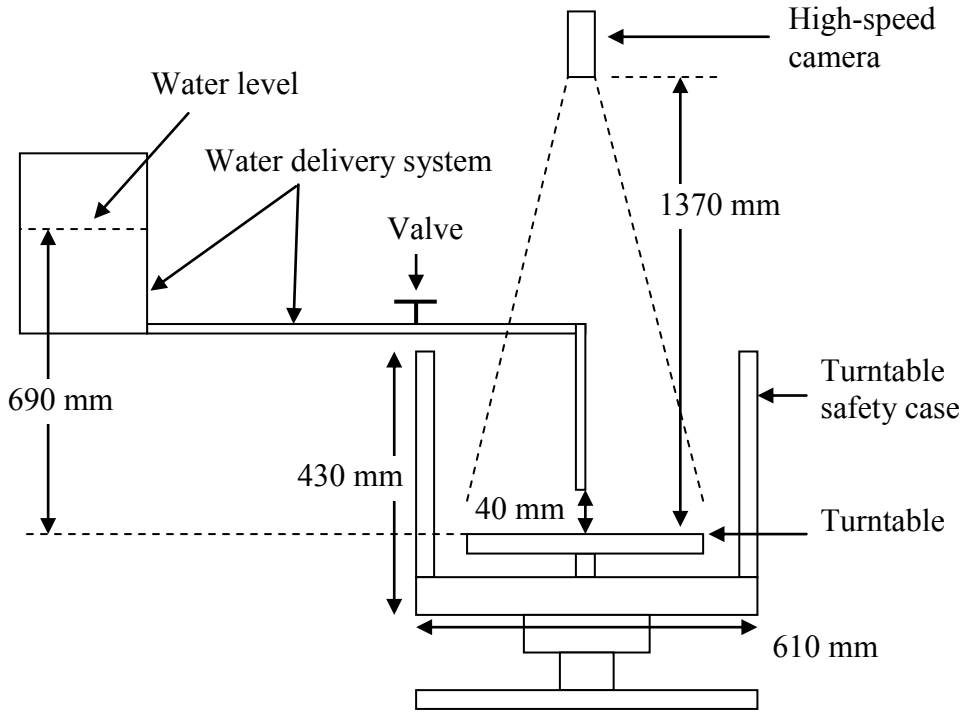

Figure 4 - 16. Schematic diagram showing the main features and dimensions of the equipment for water modelling.

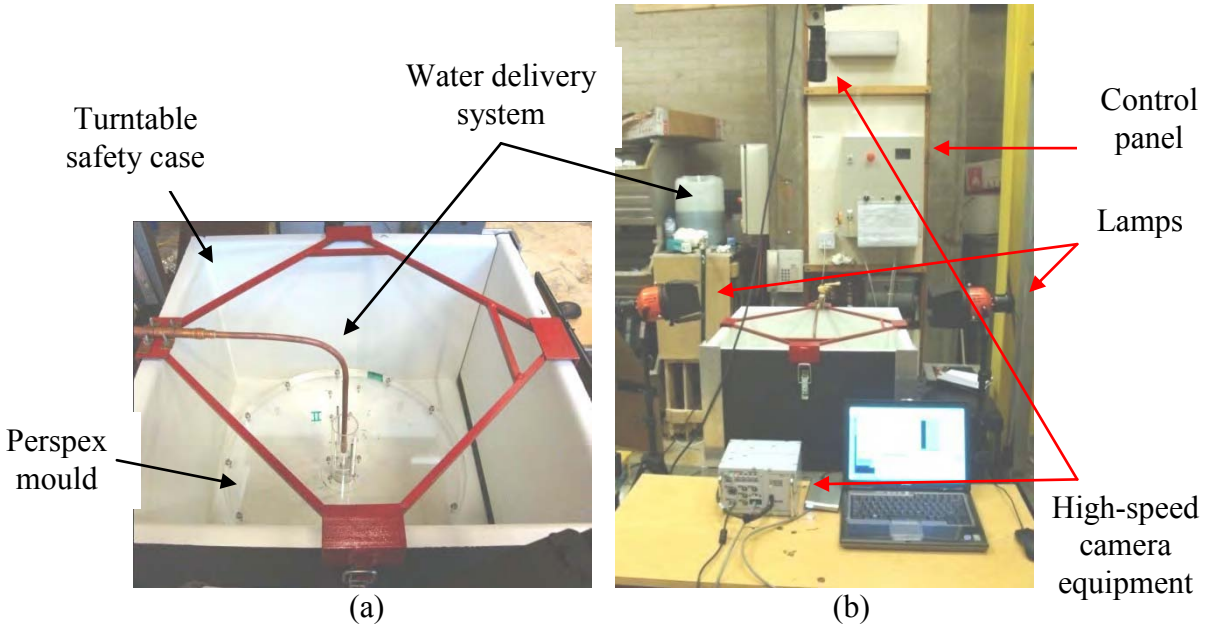

Figure 4 - 17. Experimental centrifugal equipment for water modelling.

The high speed camera was a Photron Model FASTCAM MC1, Model 2K. It was able to take up to 2000 frames per second at maximum resolution of 1.5 pixels/mm (512 x 512 pixels) with a recording duration of 4 sec and a memory of 2GB.

Initially, preliminary experiments were carried out with an electro-magnetic valve to control the water flow, which was operated with an electrical switch. However, the water pressure resulted in an inconsistent flow rate. Therefore, this was substituted by a full bore lever handle ball valve, which was operated manually and calibrated to deliver a constant flow rate of 38 ml/s. This manual valve provided a much more consistent flow rate.

For the water modelling experiments, the high speed camera was positioned at the top of the water modelling equipment, Figure 4 - 16 and Figure 4 - 17, and it was only possible to record the filling evolution after the water reached the bottom of the sprue but not the initial stage

(water coming out of the nozzle). Therefore, in order to have accurate measurements, the high speed camera was used to record the time for the water to reach the sprue base from the nozzle, immediately after the valve was turned on. The exact distance was 40 mm (Figure 4 - 18) and the schematic diagram showing the main features of the equipment is illustrated in Figure 4 - 19. The experimental procedure is explained in Section 4.3.2.

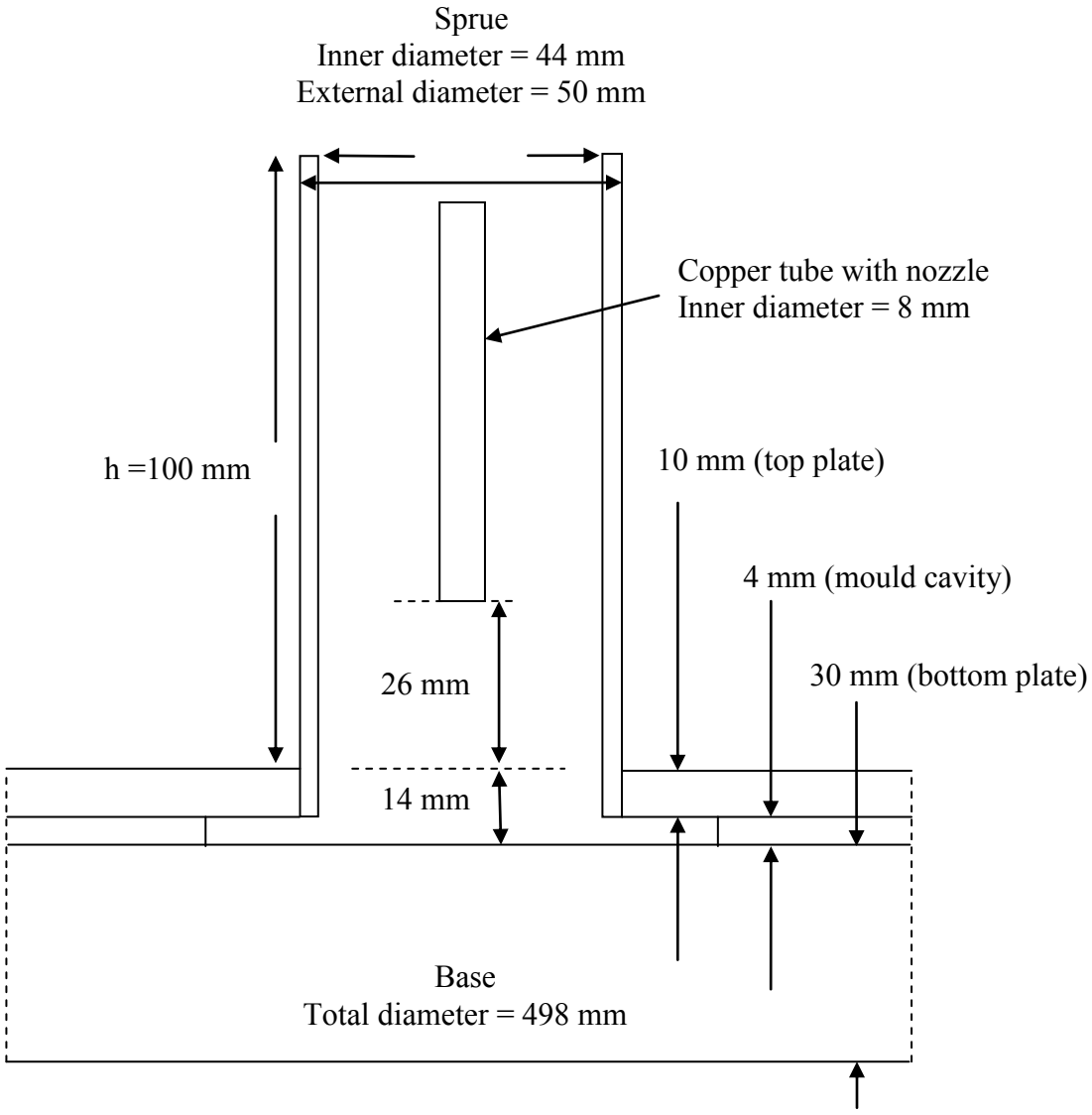

Figure 4 - 18. Perspex mould assembly for water modelling experiments.

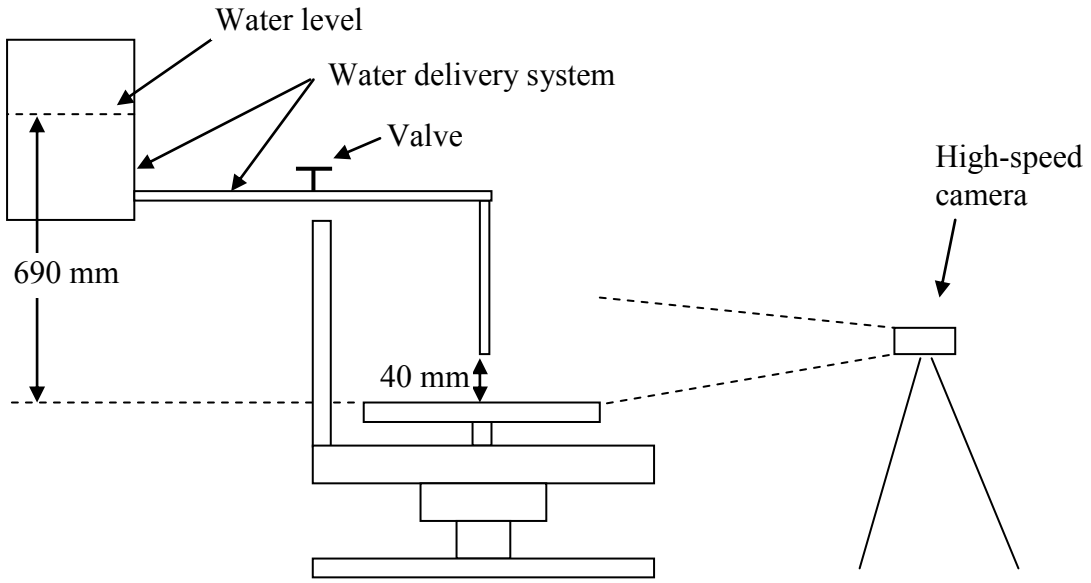

Figure 4 - 19. Schematic diagram showing the arrangement of the water modelling equipment for measuring time for the water to reach the bottom of the downsprue.

The velocity of the rotating table was measured and calibrated with an optical tachometer. A relation between frequency, which was displayed by the digital control panel, and rotating velocity was established for 200, 300 and 400 rpm, Table 4 - 2.

Table 4 - 2. Relation between drive motor frequency and rotational speed of the turntable of the water modelling equipment.

Frequency (Hz)	**Rotational velocity (rpm)**
13.44	200
20.16	300
26.88	400

4.3.2 Experimental Procedure

To record the water fall and the filling of the mould, all the sequences were recorded at 1000 frames/s and 8-bit gray scale images were obtained with a resolution of 1.5 pixels/mm. Water modelling experiments were carried out using the direct, indirect and modified indirect gated mould designs described in Section 4.3.3 with rotational speeds of 200, 300 and 400 rpm in the anti-clockwise direction. The Perspex moulds were fixed individually to a Perspex centrifugal platform, Figure 4 - 17 and Figure 4 - 18. After every experiment, the Perspex moulds were unscrewed, disassembled, dried, cleaned and assembled back again. Meticulous care was taken to ensure no water or residual cleaning paper was left in the Perspex moulds since this could have affected the filling process of the following experiment. This operation was repeated for all the experiments.

Additionally, water modelling experiments were carried out using only the indirect gated mould design described in Figure 4 - 21(b) and Figure 4 - 23. However, for these particular experiments, the vents in the runners were removed. The rotational speeds were also 200, 300 and 400 rpm in the anti-clockwise direction. The preliminary experiments showed that the filling time was far longer compared to the experiments carried out for the Perspex mould with vents in the runners (Figure 6 - 98, page 236); consequently it was necessary to reduce the acquisition rate to 500 frames/s (resolution of 1.5 pixels/mm). Since the memory of the high speed camera was 2 GB, it was not possible to record at 1000 frames/s for a duration longer than 8.188 s. Therefore, it was necessary to reduce the acquisition rate to 500 frames/s to record a maximum of 16.376 s.

Water modelling experiments were carried out using similar direct and indirect gated moulds as those described in Section 4.3.3 but with a cavity thickness of 2 mm and only with a

rotational speed of 400 rpm in the anti-clockwise direction. The high speed camera was used in the position described in Figure 4 - 20 and the field of view covered only one side of the turntable. This allowed the filling evolution of the mould design to be recorded in more detail. All the sequences were recorded at 2000 frames/s and 8-bit gray scale images were obtained with a resolution of 1.5 pixels/mm.

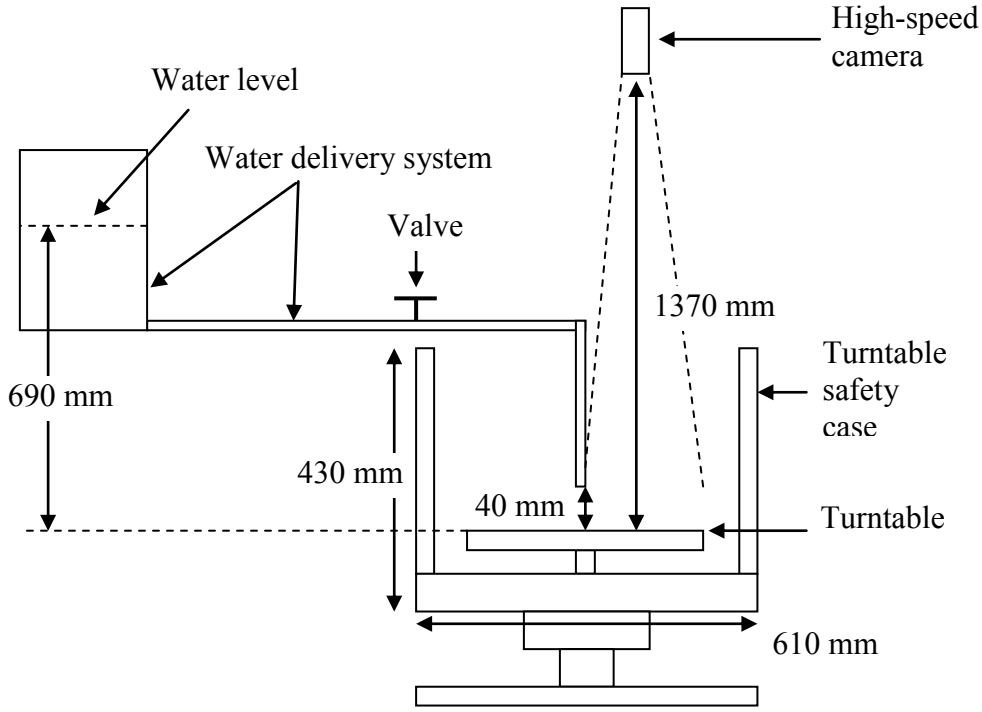

Figure 4 - 20. Schematic diagram showing the main features and dimensions of the equipment for water modelling and close-up experiments.

4.3.3 Mould Designs

Direct, indirect and modified indirect gating mould designs were chosen to investigate the effect of mould design on the filling process and surface turbulence. The dimensions of the flat test bars are illustrated in Figure 4 - 21. The only difference between the indirect and modified indirect gating moulds it that the second one had a curved ingate, Figure 4 - 21 (b)

and Figure 4 - 21 (c). These dimensions were chosen according to the limitations imposed by the characteristics of the water modelling equipment (Section 4.3.1) and to compare the results obtained to those reported in the literature (refer to section 2.3.4).

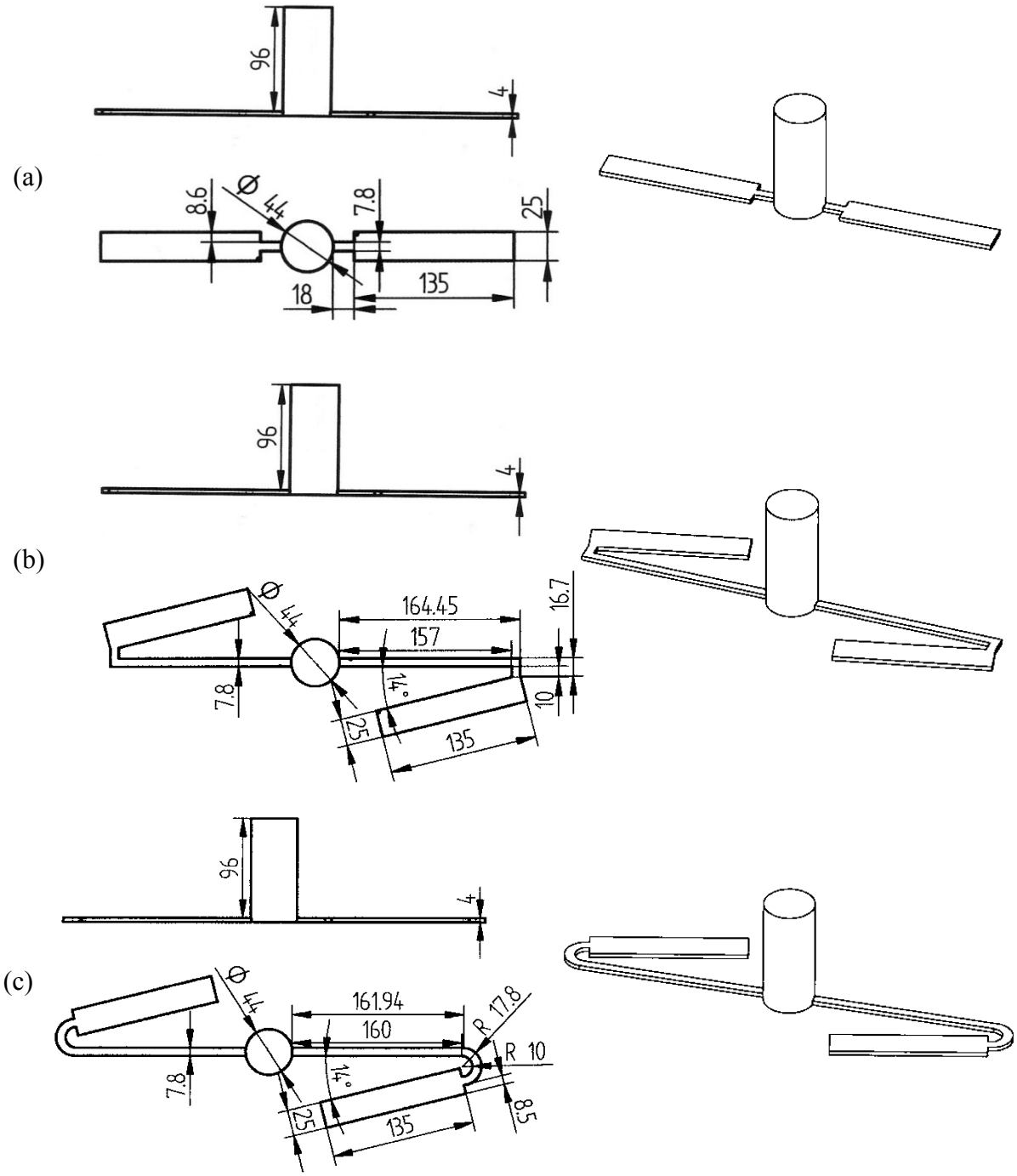

Figure 4 - 21. Side, plan and 3D views of (a) direct, (b) indirect and (c) modified indirect gating mould designs used for the water modelling experiments; all dimensions in mm.

4.3.4 Mould Making

The moulds and components for the rotary turntable were machined from Perspex. The three mould designs were manufactured according to Figure 4 - 21. For the three mould designs, 2 mm diameter vents were attached to the top surface of the mould to avoid any backpressure effect on the filling process, Figure 4 - 22 to Figure 4 - 24. Additionally, to improve the contrast when recording the filling, the water used in the experiments was coloured green with natural food colouring, Figure 4 - 22 to Figure 4 - 24.

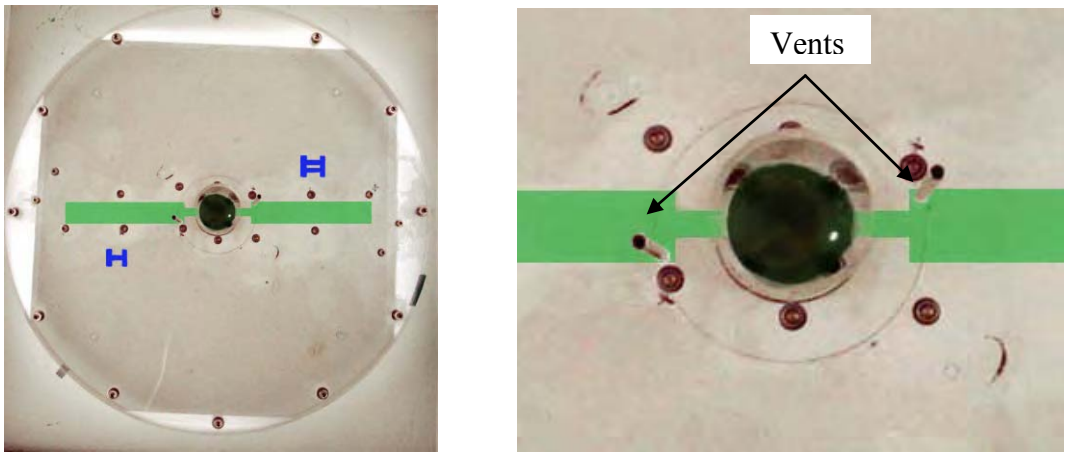

(a) (b)

Figure 4 - 22 Assembly for (a) direct gated mould and (b) close-up showing position of vents.

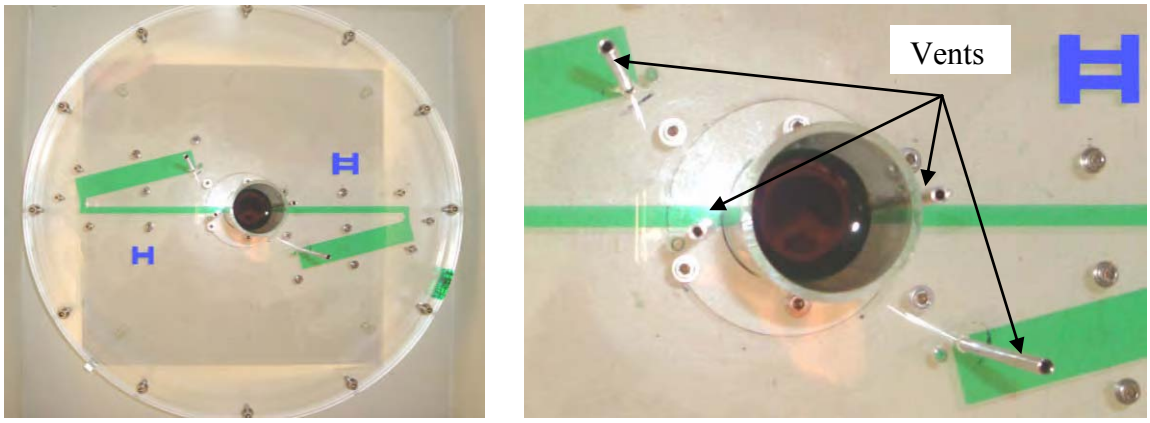

(a) (b)

Figure 4 - 23. Assembly for (a) indirect gated mould and (b) close-up showing position of vents.

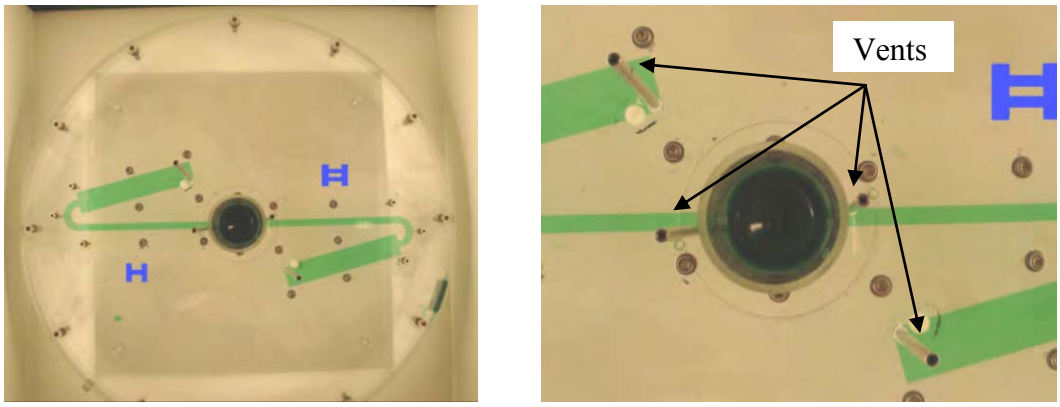

(a) (b)

Figure 4 - 24. Assembly for (a) modified indirect gated mould and (b) close-up showing position of vents.

4.3.5 Evaluation and Measurement of the Filling Process

Since the flat test bars of three mould designs had the same dimensions (Figure 4 - 21), the measurement of the filled length of the test bars was carried out according to Equation 2 - 4, which was defined by Li et al. (2006).

The filling process measurements were carried out on selected images (approximately 8-10 frames per experiment) using image analysis software (ImageJ, 2011). These were selected from the recorded filling evolution of only the test bars and not the gating or runner systems, Figure 4 - 25.

The direct gating mould was used to carry out preliminary experiments for rotational velocities of 200, 300 and 400 rpm. These showed evidence that the two cavities filled in a similar way. Therefore, it was decided to carry out only one experiment per condition for the three mould designs. Further evidence is given in Section 6.2.1.

Additionally, measurements of the water jet thickness as a function of the rotational velocity were carried out, Figure 6 - 86 (page 226). The measurements for the direct and indirect gated mould were made at a radial distance of 95 mm.

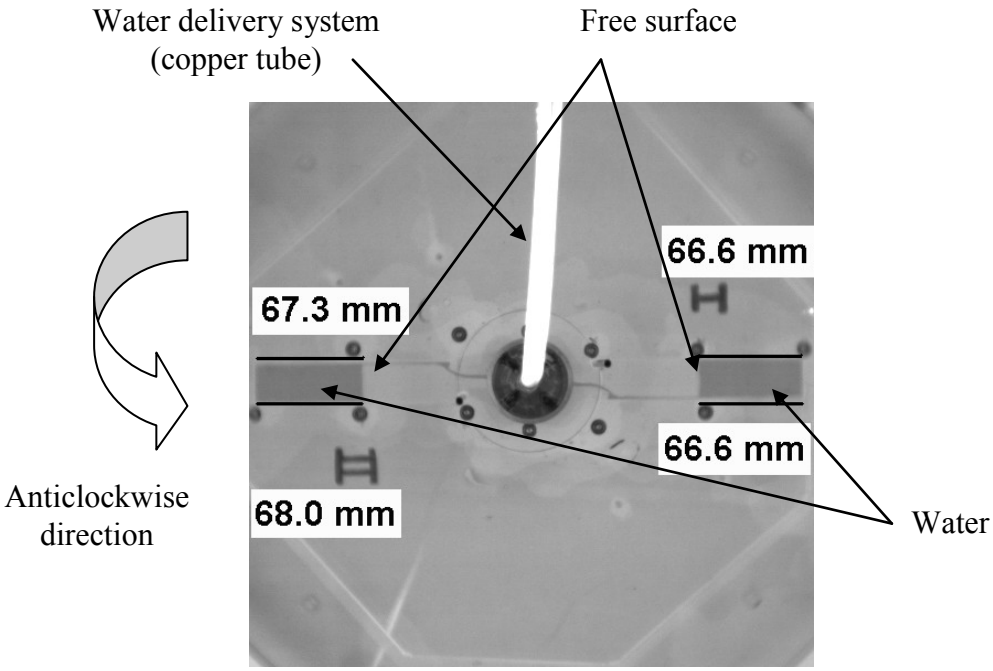

Figure 4 - 25. Example of individual measurements of filling length for the direct gated mould.

5. COMPUTATIONAL MODELLING

In the first phase of this investigation, the software package ANSYS CFX (2011) was used to simulate the water modelling experiments described previously in Section 4.3.

In the second stage, ANSYS CFX (2011) and Flow-3D (2011) were used to model the centrifugal casting of an aluminium alloy. Flow-3D (2011) and the recently developed Oxide Film Entrainment Model 'OFEM' (Reilly, 2010) were used to predict the severity of entrainment events during the filling process of direct and indirect gated moulds in centrifugal casting.

5.1 Hardware

Computer simulations using ANSYS CFX were run on the Birmingham Environment for Academic Research 'BlueBEAR' cluster (2011). The characteristics of the cluster were: 384 dual-processor dual-core (4 cores/node) 64-bit 2.6 GHz AMD Opteron 2218 worker nodes giving a total of 1536 cores. Most of these nodes have 8 GB of memory with 16 of them having 16 GB and 4 quad-processor dual-core (8 cores/node) 64-bit 2.6 GHz AMD Opteron 8218 nodes with 32 GB of memory.

Computer simulations using Flow-3D were run on the PRISM2 cluster with the following characteristics: from nodes 1 to 8, dual core (4 cores/node) 64-bit 2.6 GHz AMD Opteron 2218 and from nodes 9 to 16, 2 quad core (8 cores/node) 64-bit 2.2 GHz AMD Opteron 2352. These nodes have 2 GB of memory per core.

5.2 Software

The operating system of the BlueBEAR cluster was Scientific Linux 5.2 with the ability to run Scientific Linux 4.7 for applications that require this. The operating system of PRISM2 cluster was RHEL4.

The versions of the computer software were ANSYS CFX v12.1 and Flow-3D v9.4. Further information about this software can be found on ANSYS CFX (2011) and Flow-3D (2011).

5.3 Simulations of Water Modelling

Computer modelling of direct and indirect gated moulds was carried out with ANSYS CFX. These modelling results were validated against experimental data which are presented in Section 6.2.1 and Section 6.2.3.

Due to time limitations it was not possible to simulate the modified indirect gated mould. However, the information obtained by the indirect gated mould was considered satisfactory, which will be presented in Section 6.2.4.

5.3.1 Computational Modelling with ANSYS CFX

To allow comparison between experimental and computer modelling results obtained by ANSYS CFX, the direct and indirect gating mould designs had the same characteristics as the moulds used for experimental water modelling presented in Figure 4 - 21. Likewise, these dimensions were chosen in order to compare the experimental and computer modelling results with those reported by Li et al. (2006), Wu et al. (2006) and (Changyun et al., 2006).

Since ANSYS CFX is capable of modelling both the liquid and gas phases, the CAD geometries generated for both mould designs included a venting system as illustrated in Figure 5 - 1. These were placed in the same position as those described for the Perspex moulds used for the water modelling (Section 4.3.4). This allowed the air, which was initially in the cavities, to be exhausted.

The meshes for both mould designs were generated with ANSYS Workbench. A combination of tetrahedral cells and inflation layers near the wall was created which provided more accurate prediction of the flow velocities in this region. A mesh sensitivity study for the direct gated mould was carried out by performing simulations with an initial coarse mesh, which was then refined until the mesh size did not have an effect on the filling length results. The total number of elements for each mesh and the corresponding results are summarized in Appendix 1. It can be seen that the filling length increased when the mesh was refined and the results between Mesh 3 and 4 were rather similar. Therefore, Mesh 3 was chosen to carry out the subsequent modelling simulations for the direct gated mould. A mesh with similar characteristics was created for the indirect gated mould. The characteristics of the final mesh for both direct and indirect gating moulds were the following: for the flat test bars and runner system a cell size between 0.5 and 1.0 mm with 5 inflated layers (expansion factor of 1.2); for the inlet region of the sprue a cell size of 0.8 mm with radius of influence of 5 mm (expansion factor of 1.2); for the sprue body a maximum cell size of 3 mm with 5 inflated layers (expansion factor of 1.2), Figure 5 - 2 and Figure 5 - 3. The total number of elements for the direct and indirect gated moulds was around 510,000 and 516, 900, respectively.

The simulation conditions were specified to be as close as possible to the experimental conditions for the water modelling with rotational velocities of 200, 300 and 400 rpm, which

were described in Section 4.3. Since water modelling only involved the filling process, the computer simulations did not include heat transfer. The detailed input parameters of the model are described in Table 5 - 1. These simulations typically required 3 - 4 days of runtime using 8 cores as described in Section 5.1.

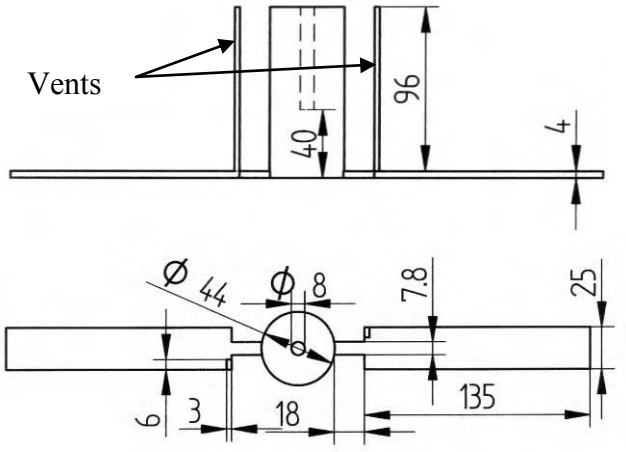

(a)

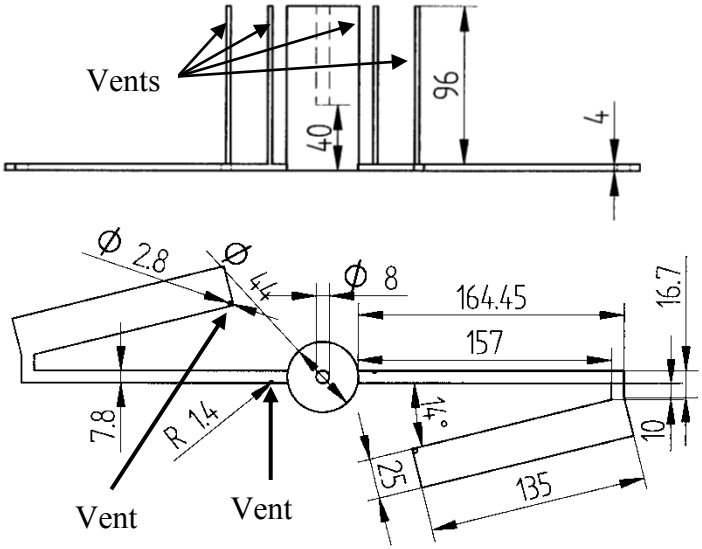

(b)

Figure 5 - 1. Side and plan views of (a) direct and (b) indirect gating mould designs used for the computer simulations of water modelling; all dimensions in mm.

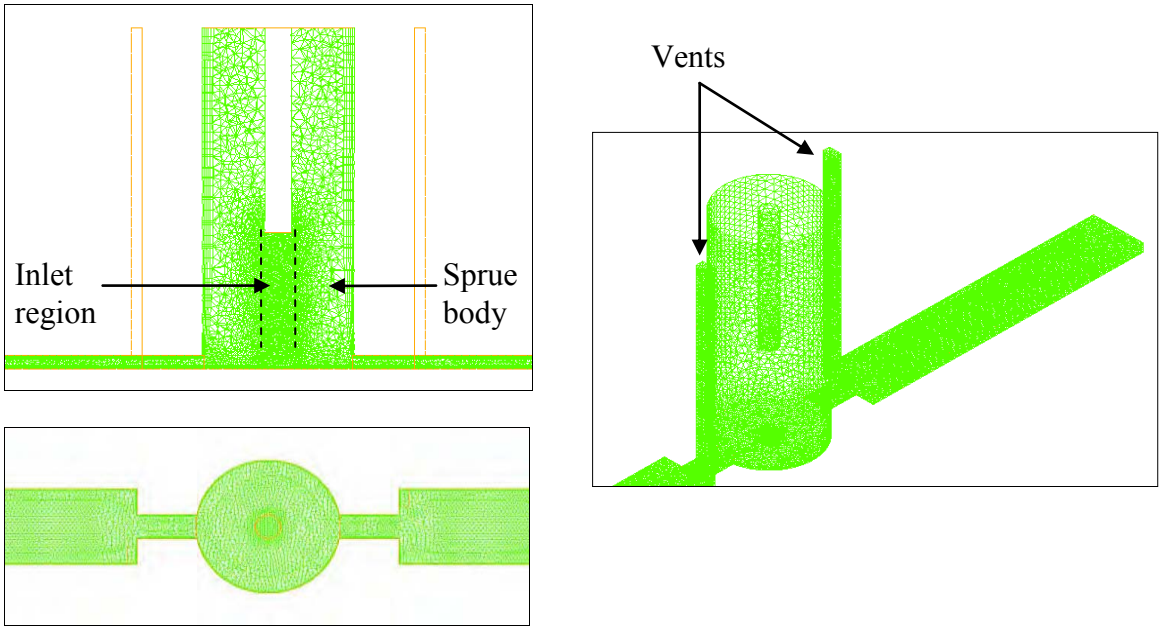

Figure 5 - 2. Mesh of direct gated mould for computer simulations of water modelling with ANSYS CFX

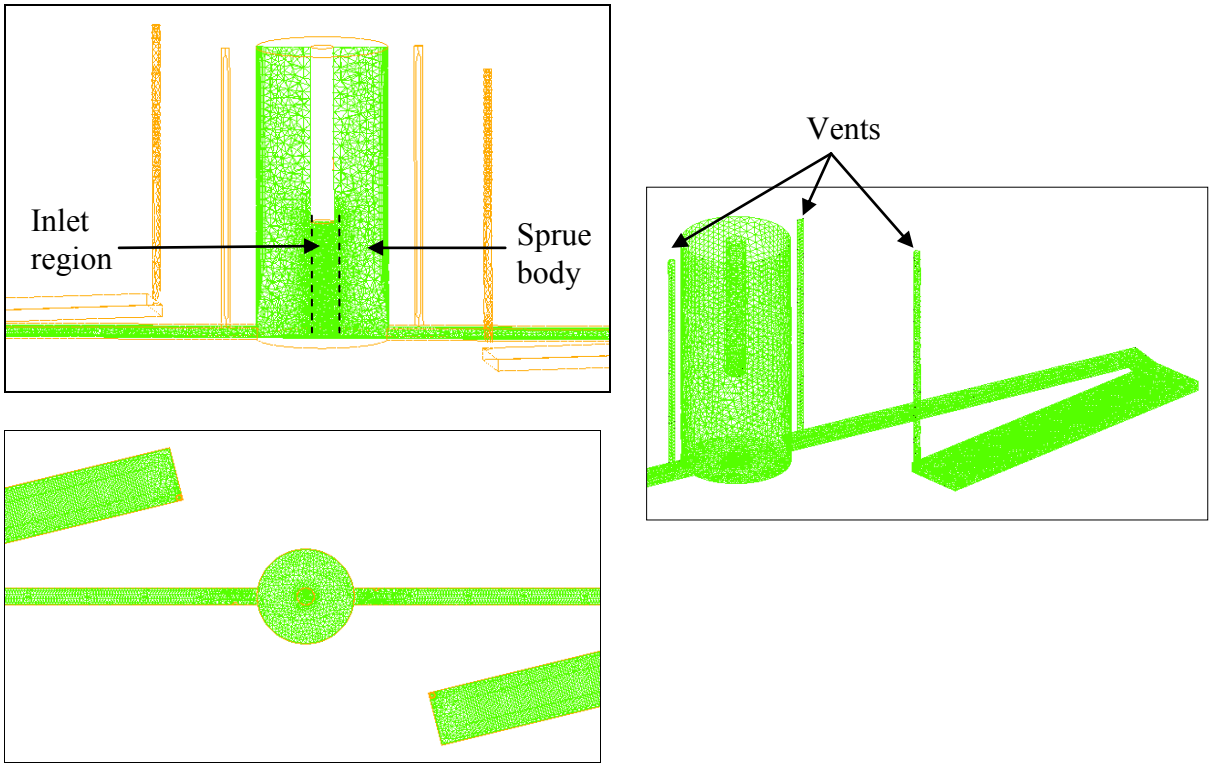

Figure 5 - 3. Mesh of indirect gated mould for computer simulations of water modelling with ANSYS CFX

Table 5 - 1. ANSYS CFX input parameters of water modelling simulations for direct and indirect gated moulds.

Description	Value
Analysis type	Transient
Time duration	2 s
Time step	0.001 s
Default Domain Modified	
Basic Settings	
Fluid 1	Air
Fluid 2	Water
Reference pressure	1 atm
Gravity X dirn.	0 m/s^2
Gravity Y dirn.	0 m/s^2
Gravity Z dirn.	-9.8 m/s^2
Bouyancy reference density	1.185 kg/m^3
Domain motion	Rotating
Angular velocity - anticlockwise	200, 300 and 400 rpm *
Rotation axis	Global Z
Fluid Models	
Free surface model	Standard
Heat transfer	Isothermal
Turbulence	Fluid dependent
Fluid Specific Models	
Turbulence model for fluid 1	k-Epsilon
Turbulence model for fluid 2	k-Epsilon
Fluid buoyancy model	Density difference
Fluid Pair Models	
Surface tension coefficient (20 °C)	0.0728 N/m (White, 1999)
Interphase transfer	Free surface
Initialization	
Frame type	Stationary
Relative pressure	Automatic with value = 1 Pa
Turbulence kinetic energy	Automatic
Turbulence eddy dissipation	Automatic
Volume fraction of fluid 1	Automatic with value = 1
Volume fraction of fluid 2	Automatic with value = 0
Default Domain Modified Default	
Basic Settings	
Boundary type	Wall
Frame type	Rotating
Boundary Details	
Mass and momentum	Fluid dependent
Wall roughness	Smooth wall
Wall contact model	Use volume fraction

Fluid Values	
Fluid 1	No slip wall
Fluid 2	No slip wall
Boundary: In	
Basic Settings	
Boundary type	Inlet
Frame type	Stationary
Boundary Details	
Mass and momentum	Bulk mass flow rate = 38g/s
Flow direction	Normal to boundary condition
Fluid Values	
Volume fraction of fluid 1	0
Volume fraction of fluid 2	1
Boundary: Top and Vents	
Basic Settings	
Boundary type	Opening
Frame type	Stationary
Boundary Details	
Mass and momentum	Opening pres. and dirn
Relative pressure	0 Pa
Flow direction	Normal to boundary condition
Fluid Values	
Volume fraction of fluid 1	1
Volume fraction of fluid 2	0
Solver Control	
Advection scheme	High resolution **
Transient scheme	Second order backward Euler
Timestep initialization	Previous timestep
Turbulence numerics	First order
Convergence criteria	RMS = 1E-4
Materials	
Fluid 1 - Air at 25 °C	
Thermodynamic state	Gas
Density	1.185 kg/m^3 (White, 1999)
Dynamic viscosity	1.8 E -05 kg/m s (White, 1999)
Component contact angle	160 °
Fluid 2 - Water at 20 °C	
Thermodynamic state	Liquid
Density	998 kg/m^3 (White, 1999)
Dynamic viscosity	0.001 kg/m s (White, 1999)

* Rotational velocity for three independent simulations as described in Section 5.3.1.

** The high resolution option in ANSYS CFX means that the blend factor values vary throughout the domain based on the local solution field. A value of 0.0 is equivalent to using the first order advection scheme and is the most robust option. A value of 1.0 uses second order differencing for the advection terms. This setting is more accurate but less robust.

5.4 Computational Modelling of Centrifugal Castings

Computer modelling of centrifugal casting of the direct and indirect gated moulds presented in Section 4.1 was carried out with commercial computer software packages ANSYS CFX and Flow-3D. The mesh characteristics and input parameters for each software package are described in the following sections.

5.4.1 Computational Modelling with ANSYS CFX

To allow comparison between experimental and computer modelling results obtained by ANSYS CFX, the same mould geometries for direct and indirect gating mould designs were used. The characteristics and dimensions for the experimental moulds were described in Section 4.1.1. Since ANSYS CFX is capable of modelling both the liquid and gas phases, the CAD geometry generated for the indirect gated mould included a venting system as illustrated in Figure 4 - 1. This allowed the air, which was initially in the cavity, to be removed.

The meshes for both mould designs were generated with ANSYS Workbench and a combination of tetrahedral cells and inflation layers near the wall was created which provided more accurate prediction of the flow velocities in this region. Likewise, the meshes for both mould designs had similar characteristics to those created for the water modelling simulations, which modelled accurately the flow velocities involved in the filling process of direct and indirect gated moulds as described in Section 6.2.4 and Section 6.2.4.1. Therefore, a mesh sensitivity study was not carried out.

The characteristics of the mesh for both the direct and indirect gated moulds were the following: for the flat test bars and the runner system a cell size between 0.5 and 1.0 mm with 5 inflated layers (expansion factor of 1.2); for the inlet region of the sprue, a cell size of 3.0

mm with radius of influence of 10 mm (expansion factor of 1.2); for the sprue body, a maximum cell size of 5 mm with 4 inflated layers (expansion factor of 1.2), Figure 5 - 4 and Figure 5 - 5. The total number of elements for the direct and indirect gated moulds was around 817, 000 and 918,800, respectively.

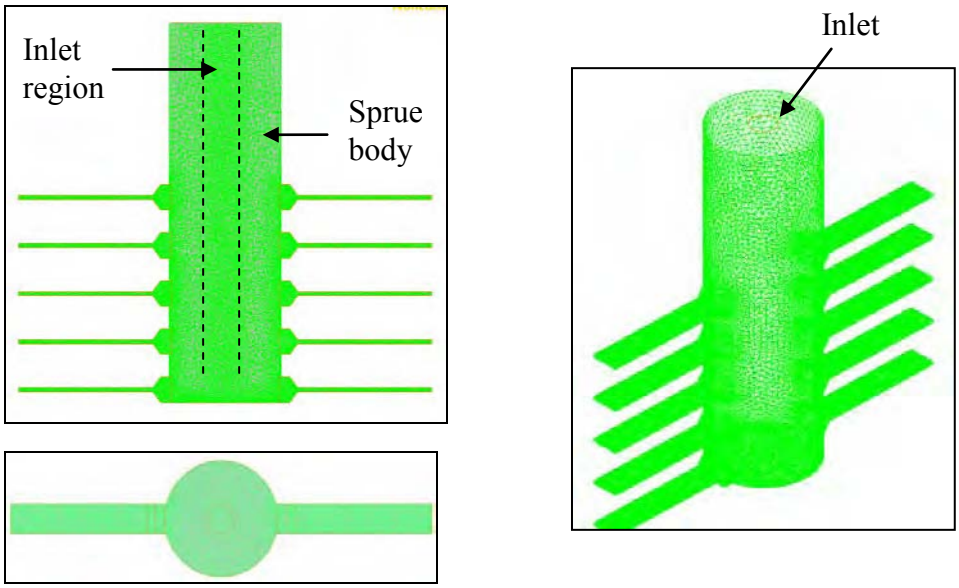

Figure 5 - 4. Mesh of direct gated mould used for computer simulations of centrifugal casting with ANSYS CFX.

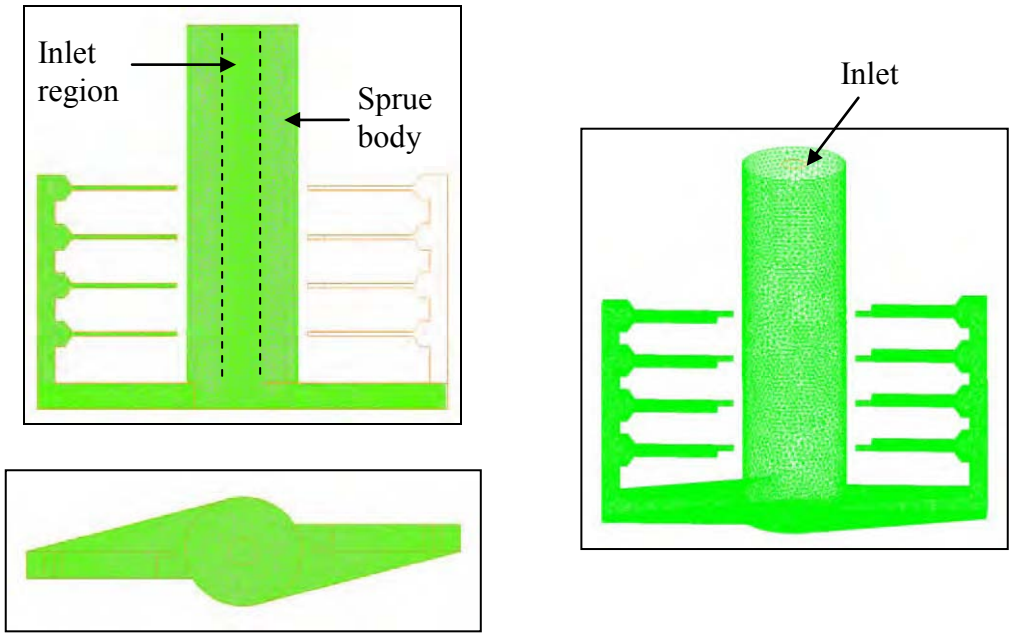

Figure 5 - 5. Mesh of indirect gated mould used for computer simulations of centrifugal casting with ANSYS CFX.

The simulation conditions were specified to be as close as possible to the experimental conditions for the centrifugal castings, which were described in Section 4.1.3. Regarding the inlet condition, Figure 4 - 10 shows that the funnel had a 25 x 25 mm exit. However, when generating the mesh for the sprue (inlet region), the inlet was considered to be circular with diameter of 25 mm and positioned at the top centre of the sprue, Figure 5 - 4 and Figure 5 - 5. It is considered this change would have had a negligible effect on the filling process. The detailed input parameters of the model are described in Table 5 - 2. The computer simulations did not include heat transfer and consequently solidification.

Table 5 - 2. ANSYS CFX input parameters of centrifugal casting simulations for direct and indirect gated moulds

Description	Value
Analysis type	**Transient**
Time duration	2.5 s
Time step	0.001 s
Default Domain Modified	
Basic Settings	
Fluid 1	Air
Fluid 2	Aluminium 6082
Reference pressure	1 atm
Gravity X dirn.	0 m/s^2
Gravity Y dirn.	0 m/s^2
Gravity Z dirn.	-9.8 m/s^2
Bouyancy reference density	1.185 kg/m^3
Domain motion	Rotating
Angular velocity - anticlockwise	- 400 rpm
Rotation axis	Global Z
Fluid Models	
Free surface model	Standard
Heat transfer	Isothermal
Turbulence	Fluid dependent
Fluid Specific Models	
Turbulence model for fluid 1	k-Epsilon
Turbulence model for fluid 2	k-Epsilon
Fluid buoyancy model	Density difference
Fluid Pair Models	
Surface tension coefficient (Reference temperature = 700 °C)	0.864 N/m (Mills, 2002)
Interphase transfer	Free surface
Initialization	
Frame type	Stationary
Relative pressure	Automatic with value = 1 Pa
Turbulence kinetic energy	Automatic
Turbulence eddy dissipation	Automatic
Volume fraction of fluid 1	Automatic with value = 1
Volume fraction of fluid 2	Automatic with value = 0
Default Domain Modified Default	
Basic Settings	
Boundary type	Wall
Frame type	Rotating
Boundary Details	
Mass and momentum	Fluid dependent
Wall roughness	Smooth wall

Wall contact model	Use volume fraction
Fluid Values	
Fluid 1	No slip wall
Fluid 2	No slip wall
Boundary: In	
Basic Settings	
Boundary type	Inlet
Frame type	Stationary
Boundary Details	
Mass and momentum	Bulk mass flow rate = 2 kg/s
Flow direction	Normal to boundary condition
Fluid Values	
Volume fraction of fluid 1	0
Volume fraction of fluid 2	1
Boundary: Top and Vents	
Basic Settings	
Boundary type	Opening
Frame type	Stationary
Boundary Details	
Mass and momentum	Opening pres. and dirn
Relative pressure	0 Pa
Flow direction	Normal to boundary condition
Fluid Values	
Volume fraction of fluid 1	1
Volume fraction of fluid 2	0
Solver Control	
Advection scheme	High resolution
Transient scheme	Second order backward Euler
Timestep initialization	Previous timestep
Turbulence numerics	First order
Convergence criteria	RMS = 1E-4
Materials	
Fluid 1 - Air at 25 °C	
Thermodynamic state	Gas
Density	1.185 kg/m^3 (White, 1999)
Dynamic viscosity	1.8 E -05 kg/m s (White, 1999)
Component contact angle	
Fluid 2 – Aluminium alloy 6082 at 700 °C	
Thermodynamic state	Liquid
Density	2400 kg/m^3 (Mills, 2002)
Dynamic viscosity	0.00105 Pa s (N s/m^2 or kg/ m s) (Mills, 2002)
Reference temperature	700 °C (Mills, 2002)

The thermophysical properties selected for the aluminium alloy 6082 used in ANSYS CFX and Flow-3D were obtained from the published data by Mills (2002). Although the properties for the specific aluminium alloy 6082 are not reported, there are data available for the aluminium alloy 6061 which has very similar chemical composition and therefore was suitable for practical purposes in this investigation. These simulations typically required 4 - 5 days of runtime using 8 cores as described in Section 5.1.

5.4.2 Computational Modelling with Flow-3D

Flow-3D and the recently developed Oxide Film Entrainment Model 'OFEM' (Reilly, 2010) were used to study and understand quantitatively how the mould design damages the molten metal through its effect on the generation of surface turbulence and the generation of double oxide films.

As explained in Section 4.1.4, the experimentally obtained cast test bars for both gating mould designs were radiographed after being removed from the individual castings. Likewise, as will be shown in Section 6.1.4, different distributions of defects were found in the direct and indirect gated bars. Therefore, it was decided to model and predict the final location of the mentioned defects generated using the oxide film entrainment model (OFEM) in Flow-3D.

It has been reported (Reilly, 2010) that there is no trend between mesh size and number of particles placed in the domain under study. Only the plunging jet model has a direct relationship between the number of particles placed and mesh size, in which the smaller the mesh size, the larger the number of particles placed. However, due to the time limitations in the present investigation, meshes with similar characteristics to those used by Reilly (2010) in his study of entrainment in the gravity casting process were used.

The regular Cartesian meshes for both mould designs were created with the Flow-3D Mesh Generator and in order to reduce the computational intensity, the mesh generated had five mesh blocks with different specifications. An individual extra block was created for the inlet condition and was positioned at the top centre of the down-sprue for both gating systems, Figure 5 - 6 and Figure 5 - 7. The mesh size of each block was the following: block # 1 = 2 mm, block # 2 and # 3 = 2 mm, block # 4 and # 5 = 1 mm. This meshing work was undertaken by research colleague Yue (2011b) and the author provided the CAD geometries generated for both mould designs.

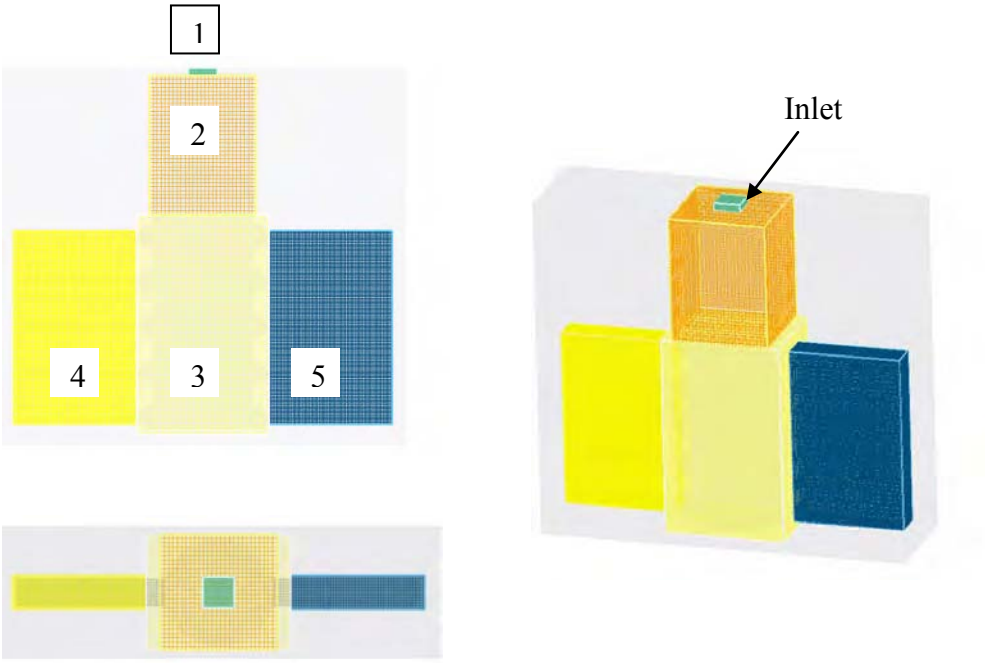

Figure 5 - 6. Mesh of direct gated mould used for computer simulations of centrifugal casting with Flow-3D. The mesh blocks are numbered from 1 to 5.

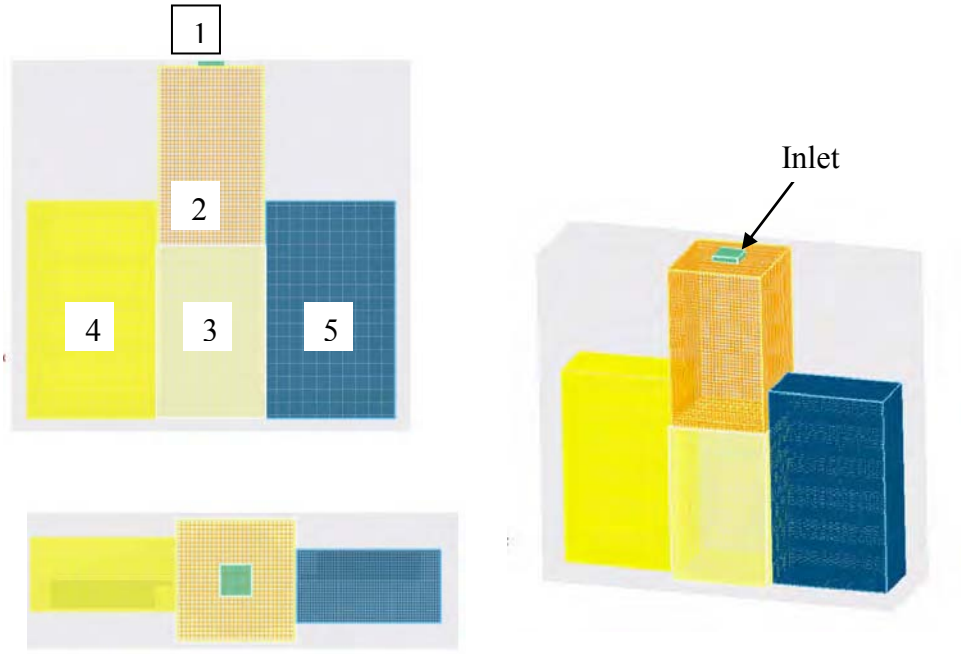

Figure 5 - 7. Mesh of indirect gated mould used for computer simulations of centrifugal casting with Flow-3D. The mesh blocks are numbered from 1 to 5.

Important limitations of the oxide film entrainment model are that the shape of the generated particles is limited to spheres and it is only possible to give each entrained particle either a unique size and varying density or unique density and varying size. In this investigation, it was decided to give each entrained particle a unique density and varying size. The density was 2250 kg/m^3 and the size in terms of diameter was in the range of 25 and 60 µm. However, the casting defects formed during the filling process can have different density and size, which can range from a few tens of microns to millimetres (Campbell, 2003). Likewise, it is important to mention that a detailed study of the physical properties of the casting defects such as oxide films, fragmented and entrapped bubbles was not carried out in the present investigation and the density and range size were chosen according to the limitations of the oxide film entrainment model and the values used by Reilly (2010) in his study of gravity casting.

As mentioned in Section 2.3.10.1, another important limitation is that the coefficient of restitution can only be either activated or deactivated for all the generated particles. This coefficient of restitution dictates whether the particles stick to the mould wall indefinitely upon impact (factor 0) or detach from the mould wall with a fractional energy loss (factor 1). It has been mentioned (Campbell, 2003) that oxide films may stick to the mould during the turbulent filling process in static casting processes. However, no information has been reported about the possible sticking of generated oxide films to ceramic moulds in centrifugal casting process, where the radial pressure gradient undoubtedly affects the movement of these defects in the liquid metal. Therefore, it was assumed that the oxide films could be detached from the ceramic wall and the coefficient of restitution was set to factor 1, Table 5 - 3.

The detailed input parameters and thermophysical properties for the aluminium alloy 6082 and the ceramic mould are defined in Table 5 - 3. Due to time restrictions, the heat transfer and solidification models were not activated.

A sub-routine was written to count the number of entraining events in different parts of the mould designs. This work was undertaken by research colleague Yue (2011b).

For the direct gated mould, the sub-routine was applied to the sprue, ingates, complete test bars and test length (or test volume), Figure 4 - 12 and Figure 5 - 8 (a). For the indirect gated mould, the sub-routine was applied to the sprue, runners, ingates, complete test bars and the test length (or test volume), Figure 4 - 12 and Figure 5 - 8 (b). The volume contained in the test length for both direct and indirect gated test bars was 3560 mm^3, which resulted from the dimensions of 35.6 x 25 x 4 mm, Figure 5 - 8.

Table 5 - 3. Flow-3D input parameters of centrifugal casting simulations for direct and indirect gated moulds

Description	Value
Analysis type	Transient
Time duration	6.2 s
Initial time step	1e-3
Minimum time step	1e-10 s
Time step controlled by	Stability and convergence
Basic Settings	
Fluid	Aluminium 6082
Flow mode	Incompresible
Gravity Z dirn.	-9.8 m/s^2
Boundary type	Domain
Frame type	Rotating
Angular velocity - anticlockwise	400 rpm
Rotation axis	Global Z
Bulk mass flow rate	2 kg/s
Interface tracking	Free surface
Viscosity and turbulence model	Activated
Viscosity type	Newtonian
Turbulence	Activated
Turbulence type	Renormalized group model (RNG)
Friction coefficient	-1
Surface tension	Activated
Wall boundary condition	No slip
Surface tension coefficient (Reference temperature = 700 °C)	0.864 N/m (Mills, 2002)
Contact angle	160 °
Numerical approximation for surface tension pressure	Implicit
Particles	Activated
Particle type	Variable size
Initialization	Random
Maximum number of particles	10000000
Particle specific gravity (density)	2250 kg/m^3
Drag coefficient	1
Diffusion coefficient	0
Coefficient of restitution	1
Free surface interaction	Particles move only in fluid
Maximum frequency to place particle in a given cell (Dum 7)	0.05
Minimum particle diameter	0.000025 m
Maximum particle diameter	0.000060 m

Heat transfer and solidification	Activated
Pouring temperature	695 °C (968 K)
Numerical approximation	Explicit
Fluid to solid heat transfer	Full energy equation
Heat transfer coefficient	840 W/m^2 K (Gunewardane, 2009)
Solver Control	
Pressure solver option	Implicit
Implicit solver options	GMRES
Viscous stress	Explicit
Heat transfer	Explicit
Surface tension pressure	Implicit
Advection	Explicit
Moving object	Explicit
Coriolis acceleration implicit weight factor	1
Volume of fluid advection	Split Lagrangian method
Materials	
Fluid	Aluminium alloy 6082
Thermodynamic state	Liquid
Reference temperature	700 °C (Mills, 2002)
Specific gravity (density)	2400 kg/m^3 (Mills, 2002)
Dynamic viscosity	0.00105 Pa s (Mills, 2002)
Heat capacity	1170 J/kg K (Mills, 2002)
Solidus temperature	600 °C (873 K) (Mills, 2002)
Liquidus temperature	642 °C (915 K) (Mills, 2002)
Solidified alloy	
Reference temperature	25 °C (Mills, 2002)
Specific gravity (density)	2705 kg/m^3 25 °C (Mills, 2002)
Heat capacity	870 J/kg K (Mills, 2002)
Ceramic mould	
Initial temperature	450 °C (723 K)
Specific gravity (density)	2390.8 kg/m^3 (Browne and Sayers, 1995)
Component contact angle	160 °
Heat transfer coefficient	840 W/m^2 K (Gunewardane, 2009)
Heat transfer to void	34 W/m^2 K
Specific heat capacity	0.75 kJ/kg (Browne and Sayers, 1995)
Thermal conductivity	0.81 W/mK
Density*Specific heat capacity	1793100 J/m^{3}K
Coefficient of linear expansion	4.4 x10^{-6}/°C (Browne and Sayers, 1995)

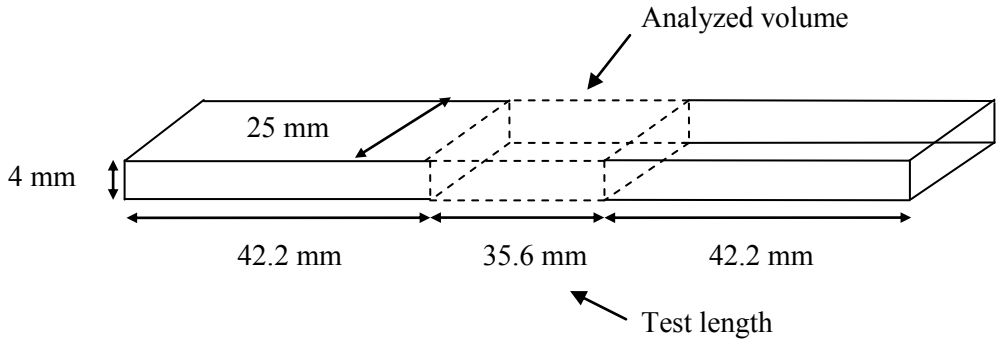

(a)

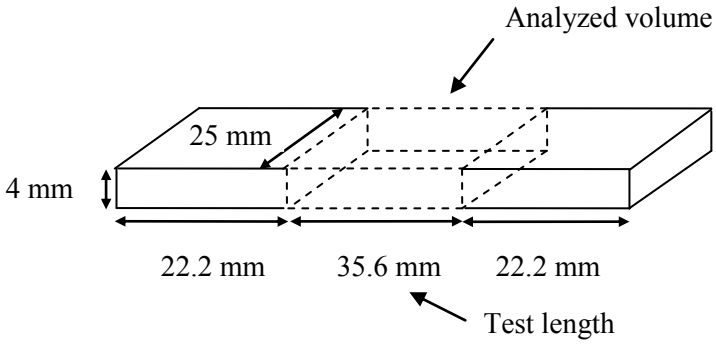

(b)

Figure 5 - 8. Schematic view of (a) direct and (b) indirect gated test bars showing the test length and volume analyzed to count the number of entraining events

6. RESULTS

6.1 Experimental Centrifugal Castings

6.1.1 Alloy Composition and Cast Moulds

The composition of the aluminium alloy 6082 used in this research is reported in Table 6 - 1. It can be seen that all the elements were within the specification, including silicon which was on the lower limit.

Three moulds were cast for each direct and indirect gating system. A representative example of each cast is shown in Figure 6 - 1 and Figure 6 - 2, which also show the code that was used to identify the position of the test bars and the mould design. Subsequently it was used to relate the test bars to individual characteristics such as X-ray plates, mechanical properties and computer modelling results.

The code used was as follows:

- C = the number of the casting (C1, C2 or C3)
- L = the left position in the casting (e.g. L1, L2, L3...)
- R = the right position in the casting (e.g. R1, R2, R3...)
- DG = test bars obtained from direct gated mould design
- IG = test bars obtained from indirect gated mould design
- (Number) is the position which is also related to the computer modelling results

6.1.2 Bend Testing Properties and Weibull Modulus

For the alloy 6082 used in this investigation, no data was found in the literature on the ultimate bend strength (UBS) or modulus of elasticity (E) obtained with a bend testing method. E values obtained with tensile test are commonly reported for this alloy, Table 6 - 2, and they can be compared with the experimental results obtained in this investigation (Mujika et al., 2006).

It is important to mention that for all the experimental values of the direct and indirect gated test bars presented in this and the subsequent sections, it was found out that the UBS values have to be multiplied by a factor of 1.371. This change did not affect the calculated values of the Weibull modulus, which will be also presented in this section.

Table 6 - 3 and Figure 6 - 3 show the results of UBS for the direct gated samples, which are organized by casting and position. It can be seen that in the Casting 3, the test bars # 6, # 8 and # 9 had the lowest values of UBS.

Table 6 - 4 and Figure 6 - 4 show the results of ultimate bend strength UBS for the indirect gated samples, which are also organized by casting and position. It can be seen that there was no systematic variation in the UBS with position in the mould or from one casting to another.

For the direct gating mould design, Table 6 - 5 shows the same results of UBS presented in Table 6 - 3 but the data are organized in five levels in descending order from L5-R5 to L1-R1 (Figure 6 - 1). Similarly, for the indirect gating mould design, Table 6 - 6 shows the same results of UBS presented in Table 6 - 4 but the data are organized in four levels in descending order from L4-R4 to L1-R1 (Figure 6 - 2). It can be seen that UBS was more affected by the

particular level of the direct gated test bars, Figure 6 - 5. The test bar levels L4-R4 and L3-R3 had the lowest values and L5-R5 had the highest value.

Table 6 - 7 and Figure 6 - 6 show the results of E for direct gated samples organized by casting and position (see Figure 6 - 1). It can be seen that most of the test bars in casting 3 had a consistently lower modulus of elasticity.

Table 6 - 8 and Figure 6 - 7 show the results of modulus of elasticity (E) for indirect gated samples (see Figure 6 - 2). It can be seen that there was no systematic variation in the E with position in the mould or from one casting to another.

For the direct gating mould design, Table 6 - 9 shows the same results of E presented in Table 6 - 7 but the data are organized in five levels in descending order from L5-R5 to L1-R1 (Figure 6 - 1). Similarly, for the indirect gating mould design, Table 6 - 10 shows the same results of E presented in Table 6 - 8 but the data are organized in four levels in descending order from L4-R4 to L1-R1 (Figure 6 - 2). For both mould designs, it can be seen that there was no significant effect on E with the level in the mould, Figure 6 - 8.

The summary of UBS, E and Weibull modulus results for both gating systems is presented in Table 6 - 11. It can be seen that the average ultimate bend strength (UBS) was improved from a value of 323 MPa for the direct gating system to 346 MPa for the indirect gating system. Furthermore, the Weibull modulus of the UBS was significantly improved from a value of 23 for the direct gating system to 45 for the indirect gated mould design, Table 6 - 11 and Figure 6 - 9. It is important to remember that this average UBS values have to be multiplied by a factor of 1.371 and this change did not affect significantly the calculated values of the Weibull modulus, Figure 6 - 10.

The average modulus of elasticity (E) was improved from 53.35 GPa for the direct gated bars to 55.83 GPa for the indirect gated test bars. The Weibull modulus of E was also clearly improved from 19 for the direct gated mould to 32 for the indirect gated mould, Table 6 - 11 and Figure 6 - 11. In both cases, the standard deviation was also considerably lower for the indirect gated bars.

6.1.3 Microstructure

As described in Section 4.2.1, the measurement area selected for quantitative characterization of dendrite cell size, grain size and porosity was located near to the fracture, which was situated at approximately mid-length of the test bar, Figure 4 - 14. Since the direct and indirect gated moulds had different designs and the test bars had different lengths of 120 and 80 mm respectively (Figure 4 - 1), the measurement areas were situated in different radial locations, so they solidified under different pressures. The approximate radial locations of the fracture and measurement area were 125 and 114 mm for the direct and indirect gated test bars respectively, Figure 6 - 12. The pressure predicted by the computer software ANSYS CFX and Flow-3D will be presented in Section 6.3.1 and 6.3.2., respectively.

The heat treated microstructure obtained from both gating designs had a rosette-like morphology as illustrated in Figure 6 - 13 and Figure 6 - 14. The measurement results of dendrite cell size obtained from three individual micrographs for both gating designs are presented in Table 6 - 12 and Table 6 - 13 respectively. Table 6 - 14 shows that for direct gating design, the average dendrite cell size was 25 μm with standard deviation of 5 μm and for indirect gating design was 31 μm with standard deviation of 6 μm.

The calculated solidification rates (Equation 2 - 14) for the specimens of both gating systems are also presented in Table 6 - 14. It can be seen that the solidification rate for the direct gated test bars was 73% higher than for the indirect gated test bars.

As presented in Section 2.5.2, the grain size measurements were made manually using the Abrams three-circle procedure (ASTM, 2004). Representative examples showing the three circles required for this procedure are presented in Figure 6 - 15 and Figure 6 - 16. The number of intersections for each micrograph is presented in Table 6 - 15 and the results of ASTM grain size '*G'*, average grain diameter and mean intercept for each gating design are presented in Table 6 - 16.

Samples from bars made using both gating systems presented similar microstructures which consisted mainly of α-Al matrix, Chinese-script and fine intermetallic particles of α-$Al_{15}(FeMn)_3Si$ type (Mrowka-Nowotnik et al., 2006) (Mrowka-Nowotnik et al., 2007) which were distributed along the grain and interdendritic boundaries, Figure 6 - 17 and Figure 6 - 18.

6.1.4 X-ray Radiography

Figure 6 - 19 shows the X-ray images of cast test bars obtained from the three direct gated moulds. The test bars are organized from L1 to L5 (left side from left to right) and from R1 to R5 (right side from left to right). The position of each cast test bar on the mould can be identified according to the code shown in Figure 6 - 1. It can be seen that especially the samples from casting 3 showed big pores (dark spots) scattered randomly over the samples.

Figure 6 - 20 shows the equivalent X-ray images of cast test bars obtained from the three indirect gated moulds, which are organized in a similar way. It can be seen that, except for the test bars 'C3L4' and 'C3R4', the porosity appeared on the end opposite to the ingate. The

position of each cast test bar on the mould can be identified according to the code shown in Figure 6 - 2.

Figure 6 - 21 and Figure 6 - 23 show the individual X-ray results of two direct and indirect gated test bars scanned at high resolution. These show that careful adjustment of the contrast can reveal defects which are not visible on the standard scans. Figure 6 - 22 and Figure 6 - 24 show the same bars in the as-polished condition. For both direct and indirect gated samples, it can be seen that the small scale porosity (small black spots), which was randomly distributed over the whole sample, was only visible in the radiographs which were scanned under optimized conditions, Figure 6 - 21 (b) and Figure 6 - 23 (b). However, for the indirect gated samples, the large scale porosity, which consisted of large fragmented and entrapped bubbles, was concentrated in the far end, Figure 6 - 23 and Figure 6 - 24.

6.1.5 Casting Defects and Digital Montages

Figure 6 - 25 shows a digital montage of contiguous micrographs obtained for a direct gated test bar with a UBS of 338 MPa. It can be seen that the porosity was distributed randomly at different locations on the metallographic section. This porosity was a combination of small shrinkage pores, fragmented bubbles and large entrained bubbles. The small pore indicated in the single optical micrograph (Figure 6 - 25) was assumed to be a shrinkage pore. However, due to the high surface turbulence generated during the filling process, this defect could have been a small fragmented bubble.

Likewise, due to the constant centrifugal pressure on the solidifying metal, the entrained bubbles did not always have a circular appearance, although their size was much greater than shrinkage pores, Figure 6 - 25. Shrinkage pores and bubbles are frequently related to the

presence of oxide films (Campbell, 2003), so no attempt was made to distinguish between them.

Similarly, Figure 6 - 26 shows a representative digital montage of contiguous micrographs obtained for a direct gated test bar with a UBS of 265 MPa and SEM micrographs. Based on the work by Divandari and Campbell (2001) these are considered to show a fragmented bubble trail and oxide films.

Additionally, to facilitate the qualitative comparison of Figure 6 - 25 and Figure 6 - 26 with the rest of the samples prepared metallographically, Figure 6 - 27 and Figure 6 - 28 show the digital montages of samples with different UBS values for direct and indirect gated test bars respectively. Comparing both groups, it can be seen that the amount of porosity in the direct gated test bars is clearly higher than those of indirect gated test bars. This is more noticeable for the direct gated test bars with UBS values of 265 and 302 MPa, Figure 6 - 27 (a) and (b). Likewise, comparing the direct and indirect gated bars with equal UBS values of 338 MPa, Figure 6 - 27 (d) and Figure 6 - 28 (a) respectively, it can be seen that the amount of porosity seems rather similar. The quantitative comparison of all these samples will be presented in more detail in Sections 6.1.6.1 and 6.1.6.2.

6.1.6 Casting Defects and Stereological Measurements

In order to explain the results clearly and carry out a detailed analysis of the stereological measurements, the results were divided into two groups, and separate frequency histograms and cumulative probability plots were obtained. The first purpose was to analyze the effect of porosity on UBS for only four test bars. The first two bars had the same UBS of 338 MPa but were cast using different mould designs, the third test bar was the weakest with a UBS of 265

MPa, obtained with the direct gating design, and the fourth test bar was obtained from the indirect gating design with a UBS of 347 MPa. The second purpose was to explain the overall effect of porosity on the UBS for four test bars produced in direct gated mould (including two test bars used in the previous analysis) and to compare them to four test bars produced in indirect gated moulds (including two test bars used in the previous analysis). Each group is explained in the following two sections.

6.1.6.1 Stereological Measurements (Group 1)

In the first group, Table 6 - 17, Table 6 - 20, Table 6 - 21, Table 6 - 22, Table 6 - 25 and Figure 6 - 29 to Figure 6 - 35 show the results of stereological measurements obtained from 4 cast test bars.

The direct gated sample with the lowest UBS (265 MPa) contained the highest number of pores for all the size categories and had a pore area fraction of 6.9% and a density of 49 pores/mm^2, Table 6 - 17, Table 6 - 25 and Figure 6 - 29. In contrast, the indirect gated sample with the higher UBS of 347 MPa showed a frequency histogram with the lowest number of pores for almost all the size categories, Table 6 - 22 and Figure 6 - 29. In this particular group, this sample also presented the lowest pore area fraction and density, Table 6 - 25.

The frequency histograms from the direct and indirect gated test bars with equal UBS (338 MPa) showed small differences for pore sizes bigger than 50 μm, Table 6 - 20, Table 6 - 21 and Figure 6 - 29. However, when all pores were taken into account, there was a significantly higher density of 30 pores/mm^2 for the direct gated bar compared with 22 pores/mm^2 for the indirect gated sample, Table 6 - 25.

Figure 6 - 30 to Figure 6 - 35 illustrate the cumulative probability curves of the 4 cast test bars. The cumulative probability '*P*' was assigned to each data point using the modified Kaplan-Meier probability estimator (Tiryakioglu, 2008b). For pore sizes below 100 μm, the differences in the slope are better described by the frequency histograms in Figure 6 - 29. For direct gated cast bars, the weakest sample had large pores with a maximum Feret diameter of approximately 3600 μm, Figure 6 - 30 and Figure 6 - 31. These large defects were a combination of fragmented bubbles trapped between the oxide films, large entrapped bubbles and a bubble trail, Figure 6 - 26.

Figure 6 - 32 and Figure 6 - 33 compare two indirect gated cast bars. It can be seen that the sample with a UBS of 338 MPa had larger pores which reached a Feret diameter of approximately 560 μm compared to the stronger sample (347 MPa) with a maximum size of 390 μm. Although there was a small difference in maximum pore size, this had an effect on the UBS.

For direct and indirect gated cast bars with equal UBS (338 MPa), Figure 6 - 34 and Figure 6 - 35, it is not surprising that both curves are also similar in shape and trend. Both samples had a maximum pore size of approximately 560 μm.

6.1.6.2 Stereological Measurements (Group 2)

In the second group, Table 6 - 17 to Table 6 - 25 and Figure 6 - 36 to Figure 6 - 38 show the results of stereological measurements obtained from four selected cast test bars produced by direct and indirect gating design, including two test bars used in the previous section for each gating design.

Table 6 - 17 and Figure 6 - 36 show that the weakest test bar with a UBS of 265 MPa did not have the greatest number of pores in all size categories. Surprisingly, the test bar with a UBS of 302 MPa had the highest number of pores for almost all the size categories, and when all pores were taken into account, this sample also had the highest density of porosity (57 pores/mm^2) but almost half the area fraction of porosity compared to the weakest test bar, Table 6 - 18 and Table 6 - 25. In contrast, the test bar with a UBS of 338 MPa showed a frequency histogram with the lowest number of pores for almost all the size categories, including pores bigger than 100 μm, Table 6 - 20 and Figure 6 - 36. The area fraction and density of porosity were the lowest from the four direct gated test bars, 1.7 % and 30 pores/mm^2 respectively, Table 6 - 25. In general, the frequency histograms of the direct gated cast bars were shifted to the left and the number of pores was reduced when the strength increased, Figure 6 - 36.

Comparing the frequency histograms of the four indirect gated test bars, Table 6 - 21 to Table 6 - 24 and Figure 6 - 37, it can be seen that the strongest bar with a UBS of 357 MPa did not have the lowest number of pores for all the size categories as would be expected. Furthermore, the area fraction and density of porosity of this test bar were not the lowest values in the group, Table 6 - 25. On the other hand, the test bar with a UBS of 347 MPa, with a slightly lower number of pores for the size categories lower than 60 μm, had the lowest area fraction and density of porosity, 1.4% and 15 pores/mm^2 respectively, Table 6 - 25.

In general, the frequency histograms of indirect gated cast bars were also shifted to the left but unlike the direct gated test bars, the bars had similar number of pores in each size category, especially for pores bigger than 40 μm, Figure 6 - 37. When comparing the frequency histograms for the two size categories ≤ 40 μm, it can be seen that all the columns are lower

than 9 pores/mm^2 and were almost half the number of pores obtained for the direct gating design in the same size range, Figure 6 - 36 to Figure 6 - 38.

Figure 6 - 39 and Figure 6 - 40 illustrate the cumulative probability curves of the same four direct gated cast test bars. For pore sizes below 100 μm, the differences in the slope are better described by the frequency histograms in Figure 6 - 36 and Figure 6 - 38. In this group, the weakest sample with a UBS of 265 MPa also had the largest pores with a maximum Feret diameter of approximately 3600 μm. As mentioned in Section 6.1.5, this was the only one of the four selected direct gated test bars that contained large defects, which were a combination of fragmented bubbles trapped between the oxide films, large entrapped bubbles and a bubble trail, Figure 6 - 26.

Figure 6 - 40 shows a zoom of the cumulative probability axis and helps to distinguish between the four curves representing the largest pores contained in the selected test bars. The largest pores with maximum Feret diameters of approximately 880 and 640 μm were found for the test bars with UBS values of 302 and 327 MPa respectively. The strongest bar in this group with a UBS of 338 MPa had smaller pores with a maximum Feret diameter of approximately 560 μm.

Figure 6 - 41 and Figure 6 - 42 are the cumulative probability curves of the four indirect gated cast test bars analyzed in Figure 6 - 37 and Figure 6 - 38. For pores sizes below 100 μm, the differences are better described by the frequency histograms in Figure 6 - 37 and Figure 6 - 38. The zoom of the cumulative probability axis in Figure 6 - 42 helps to distinguish between the four curves. Similar to the results obtained in Figure 6 - 37, the strongest bar with a UBS of 357 MPa did not have the smallest pores in the large scale porosity (bigger than 100 μm) as would be expected. On the contrary, the approximate maximum Feret diameter was 800 μm.

Regarding the rest of the test bars, the approximate Feret diameters of the largest pores were as follows: sample with 349 MPa: 530 μm; sample with 347 MPa: 390 μm; sample with 338 MPa: 560 μm.

Table 6 - 25, Figure 6 - 43 and Figure 6 - 44 illustrate the effect of the porosity area fraction on the UBS of test bars from both gating systems. It can be seen that when the data are combined there is a clear relation between these two parameters: the higher the area fraction of porosity, the lower the UBS.

Table 6 - 25, Figure 6 - 45 and Figure 6 - 46 illustrate the UBS as a function of the porosity density. It is evident that when the data of direct and indirect gated test bars are combined there is also a clear relation between these two parameters: the UBS increases as the density of porosity decreased.

6.1.7 Fractography

6.1.7.1 Macrofractographs

The enlarged macrofractographs of five selected direct gated test bars with different values of UBS are shown in Figure 6 - 47 to Figure 6 - 51. The individual UBS of each test bar selected were: 265, 302, 324, 338 and 353 MPa. Similarly, macrofractographs of five selected indirect gated test bars with UBS values of 331, 348, 356, 357 and 370 MPa are shown in Figure 6 - 52 to Figure 6 - 56 respectively.

The macrofractographs of the direct gated test bars show that specimens with high amount of porosity failed at much lower stresses. This porosity, which appeared as darker areas on the fracture surface, was a combination of shrinkage, fragmented bubbles and large entrapped

bubbles, which were frequently linked to oxide films. A detailed description of these defects is presented in Section 6.1.7.2. In the test bars with UBS values of 265, 302 and 324 MPa, large pores were distributed randomly through the fracture surface and dark areas which were related to clusters of pores, Figure 6 - 47 to Figure 6 - 49.

The zone bounded by a superimposed rectangle presented in the test bar with a UBS of 265 MPa (Figure 6 - 47) is a representative example of the dark areas selected for detailed examination with a scanning electron microscope (SEM) and Energy Dispersive X-ray (EDX) analysis. The results for this and some other specimens are presented in Section 6.1.7.2.

In the macrofractographs of the indirect gated test bars, it can be seen that the amount and size of pores were significantly reduced for almost all the samples (Figure 6 - 52 to Figure 6 - 56) compared to direct gated test bars. Moreover, dark areas related to clusters and large pores were not present on the fracture surfaces, which complicated the search for oxide films. However, the presence of these oxide films in these samples was also confirmed by EDX (Section 6.1.7.2).

6.1.7.2 SEM and Energy Dispersive X-ray analysis

Figure 6 - 57 and Figure 6 - 58 show typical fractographs exhibiting porosity. Shrinkage porosity could be identified from the tortuously-shaped spaces between unfractured dendrites, Figure 6 - 57, whilst the entrapped bubbles had more rounded or semi-rounded shapes, Figure 6 - 58.

A representative example of some of the largest pores, which were generated by high surface turbulence, found within the dark areas of a direct gated test bar (UBS of 302 MPa) is shown in Figure 6 - 59. The size range of large pores was between approximately 400 and 900 μm.

Furthermore, it can be seen that the combination of fragmented and entrapped bubbles formed sharp and tortuously-shaped spaces.

Energy Dispersive X-ray (EDX) analysis was carried out on direct gated test bars with UBS values of 265 and 324 MPa, and the results are presented in Figure 6 - 60 and Figure 6 - 61. The characteristics of the oxide films found on the fracture surfaces such as size, shape and oxygen peak, correlate well with the results reported by Green and Campbell (1994) and Campbell (2003).

EDX analysis of indirect gated test bars with UBS values of 331 and 356 MPa also showed oxide films with a characteristic oxygen peak, Figure 6 - 62 and Figure 6 - 63. In general, oxide films were found more frequently through the whole fracture surface in direct gated samples than in indirect gated samples.

Figure 6 - 64 and Figure 6 - 65 illustrate the general appearance of the brittle fracture of the α-Al matrix in direct and indirect gated test bars with UBS values of 324 and 356 MPa respectively. Figure 6 - 66 and Figure 6 - 67 illustrate areas in the same test bars, which were free from oxide films. The results of the EDX analysis show the absence of oxygen.

6.1.7.3 Fracture Mode

Metallographic sections of the propagation paths through the direct and indirect gated test bars can be seen in Figure 6 - 68 and Figure 6 - 69, respectively. It seems that the propagation of the fracture was facilitated by the porosity present.

6.2 Water Modelling

6.2.1 Experimental Data - High Speed Camera

Firstly, the high speed camera was used to record the time for the water to reach the sprue base from the nozzle, immediately after the valve was opened (a distance of 40 mm). The results obtained from five experiments are given in Table 6 - 26. The summary of a representative sequence obtained from the first experiment is shown in Figure 6 - 70 and Figure 6 - 71. The average value obtained from five experiments was 0.110 s, and this was considered to be constant in all the water modelling experiments. The analytical solution is also presented in Table 6 - 26 and it can be seen that the experimental value was higher compared to the analytical solution.

A typical snapshot obtained with the high speed camera for the direct gated mould at 200 rpm is illustrated in Figure 6 - 72. It shows the test bar cavities, water stream, vents and water delivery tube. Snapshots of the filling process for the direct gated mould obtained for 200, 300 and 400 rpm are shown in Figure 6 - 73 to Figure 6 - 75. Summaries of the sequences are illustrated in Appendix 2 to Appendix 4 and the video sequences can be seen in Appendix 32 to Appendix 34, respectively.

It can be seen that for the three rotational velocities, the filling process was bidirectional and was divided into two stages: radially outwards and radially inwards. In the radially outwards stage, the water flowed on the cavity wall (opposite to the rotation direction) and was accelerated until it reached the far end. Then, the direction of the liquid changed, which started the radially inwards filling stage. Eventually, the water filled completely the cavities of the test bars.

Figure 6 - 76 shows a comparison of the high speed camera snapshots of the direct gated mould at rotational velocities of 200, 300 and 400 rpm. The water jet thickness measurement results as a function of the rotational velocity are presented in Table 6 - 27 and Figure 6 - 86 (pages 161 and 226). It can be seen that the water jet flowing on the wall of the cavities was thinner when the rotational velocity increased. Next, the experimental water jet velocity was calculated using the water jet thickness measurements (at a radial distance of 95 mm) and the filling velocity in the test bar cavities, Table 6 - 28 and Figure 6 - 87. The higher rotational velocity resulted in a higher water jet velocity flowing radially outwards.

For the indirect and modified indirect gated moulds, typical snapshots obtained with the high speed camera at 200 rpm are illustrated in Figure 6 - 77 and Figure 6 - 82. They show the test bar cavities and runners, water stream, vents and water delivery tube. Snapshots of the sequences of the filling process for the indirect and modified indirect gated moulds obtained for 200, 300 and 400 rpm are shown in Figure 6 - 78 to Figure 6 - 80 and Figure 6 - 83 and Figure 6 - 85. The corresponding summaries of the sequences are illustrated in Appendix 5 to Appendix 7 and Appendix 8 to Appendix 10, and the video sequences can be seen in Appendix 35 to Appendix 37 and Appendix 38 to Appendix 40 respectively.

Figure 6 - 81 shows a comparison of the high speed camera snapshots of the indirect gated mould at rotational velocities of 200, 300 and 400 rpm. The measurement results of the jet thickness as a function of the rotational velocity are presented in Table 6 - 27 and Figure 6 - 86 (pages 161 and 226). The water jet flowing on the wall of the runners was also thinner when the rotational velocity increased.

For both the indirect and modified indirect gated moulds and for the three rotational velocities, the filling process was also bidirectional. In the radially outwards stage, the water

flowed on the runner wall (opposite to the rotation direction) and was accelerated until it reached the runner end. Subsequently, the water was forced to flow through the ingate and started the radially inwards stage, which continued until it completely filled the test bar cavities.

For the indirect gated mould, which did not include the vents in the runners, a typical snapshot obtained with the high speed camera at 200 rpm is illustrated in Figure 6 - 88 (page 227). It shows the test bar cavities and runners, water stream, vents and water delivery tube. Snapshots of the sequences of the filling process for 200, 300 and 400 rpm are shown in Figure 6 - 89 to Figure 6 - 91 (page 228). The corresponding summaries of the sequences are illustrated in Appendix 11 and Appendix 13.

Similar to the indirect gated mould illustrated in Figure 6 - 78 to Figure 6 - 80 (page 222), for the three rotational velocities, the filling process was also bidirectional. Likewise, since the filling time was far longer compared to the experiments carried out for the Perspex mould with vents in the runners, Figure 6 - 98 (page 236), it was necessary to reduce the acquisition rate to 500 frames/s to record a maximum of 16.376 s (Section 4.3.2). As a result of this change, the obtained snapshots were not as sharp as those obtained using an acquisition rate of 1000 frames/s. Therefore, it was not possible to measure the water jet thickness flowing on the wall of the runner bars.

6.2.2 Experimental Data - High Speed Camera (2)

Figure 6 - 93 and Figure 6 - 94 show the direct gated mould filling process with a cavity thickness of 2 mm. The video sequence can be seen in Appendix 41. Since the filling process involved liquid flowing radially outwards and inwards (Section 6.2.1), it created a constant

formation of bubbles in the shear zone during the whole filling process. Subsequently, due to the specific gravity difference between the air bubbles and the water, and the continuous centrifugal force, the bubbles were pushed into the test bar ingate, and eventually escaped through it.

Figure 6 - 95 and Figure 6 - 96 show the indirect gated mould filling process with a cavity thickness of 2 mm. The video sequence can be seen in Appendix 42. The formation of small bubbles in the runner bar can be seen. Subsequently, the bubbles were forced to flow through the ingate and were pushed into the far end of the test bars, and eventually escaped through the vent.

6.2.3 Filling Length Measurements

The precision of the measuring technique, which involved individual measurements between the ends of the test bar cavities and the free surface (Figure 6 - 72, Figure 6 - 77, Figure 6 - 82, Figure 6 - 88) ranged from 1 to 3 pixels. Since the 8-bit grey scale images were obtained with a resolution of 1.5 pixels/mm (Section 4.3.5), it represented a maximum error of ± 2 mm. Therefore, it is considered that this would have had a negligible effect on the general trend of filling length as a function of the rotational velocity.

For the direct gated mould, the filling length measurements are shown in Table 6 - 29 and Figure 6 - 97. It can be seen that from approximately 0.54 to 0.80 s, the filling length was rather similar for the three rotational velocities. Subsequently, the curves showed a different slope. The general tendency was that the higher the rotational velocity, the lower the filling length.

For the indirect gated mould, the filling length measurements are shown in Table 6 - 30 and Figure 6 - 98. It can be seen in Figure 6 - 98 (a) that the results obtained at a rotational velocity of 200 rpm did not follow the same tendency as that shown for the direct gated mould (Figure 6 - 97). Unlike all the experimental water modelling results, where the filling rate for both test bars was rather similar, in this particular experiment, the filling rate of test bar # 1 was lower than test bar # 2, Figure 6 - 78 and Table 6 - 30. However, when only the filling length results of test bar # 2 were considered, the results showed a clear trend, Figure 6 - 98 (b), where the higher the rotational velocity, the lower the filling length.

The filling length results for the modified indirect gated mould are shown in Table 6 - 31 and Figure 6 - 99. It can be seen that from approximately 0.71 to 0.97 s, the filling length was similar for the three velocities. Subsequently, the curves developed different slopes. The general tendency confirmed the results obtained for direct and indirect gated moulds, *i.e.* the higher the rotational velocity, the lower the filling length.

Figure 6 - 100 shows the comparison of the filling length as a function of the rotational velocity for the three mould designs. It can be seen that it took longer to fill the cavities of the indirect and modified indirect gated moulds compared to the direct gated mould.

The filling length results for the indirect gated mould without vents in the runners are shown in Table 6 - 32 and Figure 6 - 101 (pages 165 and 238). It can be seen that for 200 rpm the filling time was far longer than expected and the water did not completely fill the test bar cavities within the maximum acquisition time (16.376 s). For 300 and 400 rpm the filling time was also much longer compared to the results obtained for the indirect gated mould, which included the vents in the runners. The general tendency was that the higher the rotational velocity, the higher the filling length.

6.2.4 Computational Modelling with ANSYS CFX

Typical 2D snapshots obtained with ANSYS CFX for the direct and indirect gated moulds are illustrated in Figure 6 - 102 and Figure 6 - 103 respectively. These show the radial outwards flow of the water along the walls of the test bars (direct gated moulds) or runner bars (indirect gated moulds), followed by the backfilling of the test bars in both mould designs.

Snapshots of the direct gated mould obtained for 200, 300 and 400 rpm Figure 6 - 104 to Figure 6 - 106. Summaries of the sequences of the filling process for the direct gated mould obtained for 200, 300 and 400 rpm showing a plan view are illustrated in Appendix 14 to Appendix 16. The video sequences can be seen in Appendix 43 to Appendix 45.

Figure 6 - 107 illustrates a 3D view of the right hand test bar showing the comparison at the three rotational velocities at the same time (1.05 s). The function calculator implemented in ANSYS CFX was used to calculate the mass flow rates of the liquid flowing radially outwards on the test bar cavity. This mass flow rate was calculated on the cross-section cut plane, which was perpendicular to the flow direction, Figure 6 - 107. Additionally, a summary of the filling process at 400 rpm showing a close-up plan view of the right test bar with velocity vectors and isosurface (0.5 volume fraction) with velocity gradients in X and Y are illustrated in Figure 6 - 108, and Figure 6 - 109 and Figure 6 - 110 (Appendix 17 and Appendix 18).

Comparing the effect of the rotational velocity in the water stream flowing on the cavity wall, Figure 6 - 107, it can be seen that the water stream thickness was reduced as the rotational velocity increased. Likewise, the mass flow rate calculated on the cross-section plane showed that it was reduced from 10.31 g/s at 200 rpm to 9.11 g/s at 400 rpm.

In the filling process at 400 rpm (Figure 6 - 108) it can be seen that the maximum velocity of the liquid initially filling the test bar cavity ranged between 3.2 and 3.6 m/s, which gradually reduced as the free surface approached the test bar ingate. This resulted in rotational flow within the liquid during the whole filling process. Figure 6 - 109 and Figure 6 - 110 show that, as a consequence of liquid flowing in opposite directions (radially outwards and inwards), continuous velocity gradients were developed, which ranged approximately between 0 and -900 s^{-1} in the X direction and between 1800 and -1800 s^{-1} in the Y direction. This resulted in a continuous entrainment of air in the shear zone, as shown by the isolated areas. It is also noticeable that there are some high values at the start of filling (0.30 s) but these did not result in the immediate entrainment of air, Figure 6 - 110. This figure also shows high velocity gradients in the Y direction near the ingate; however, these did not lead to air entrainment.

Snapshots of the indirect gated mould for 200, 300 and 400 rpm are illustrated in Figure 6 - 111 to Figure 6 - 113. Sequences of the filling process are summarised in Appendix 19 to Appendix 21. The video sequences can be seen in Appendix 46 to Appendix 48. Additionally, a summary of the filling process at 400 rpm showing a close-up plan view of the left hand test bar with velocity vectors and isosurface (0.5 volume fraction) with velocity gradients in X and Y are illustrated from Figure 6 - 114 to Figure 6 - 116 (Appendix 22 to Appendix 24). As seen in the water model for the three rotational velocities, the water flowed radially outwards on the runner wall (opposite to the rotation direction) and was accelerated until it reached the runner end. Subsequently, the water flowed through the ingate and flowed radially inwards to fill the test bar cavities, Figure 6 - 111 to Figure 6 - 113.

In the filling process obtained for 400 rpm (Figure 6 - 114) it can be seen that the velocity of the liquid initially filling the runner bar cavity reached 4 m/s, and this reduced gradually as

the free surface approached the sprue. Figure 6 - 115 and Figure 6 - 116 show that the counter-flow of liquid resulted in continuous velocity gradients in the runner, which ranged approximately between 0 and -600 s^{-1} in the X direction and between 0 and -1200 s^{-1} in the Y direction. This also provoked a continuous entrainment of air in the runner.

Figure 6 - 117 shows a 2D side view of the direct and indirect gated moulds for rotational velocities of 200, 300 and 400 rpm. The cut plane was along the sprue diameter. It is important to mention that the complete moulds were modelled, but the images were cropped to show the flow only in the sprue. For both mould designs, it seems that the rotational velocity affected the formation of the vortex *i.e.* the faster the rotational velocity, the higher the vortex angle. This was more obvious at filling times of 0.54 s and 0.90 s.

6.2.4.1 Filling Length Measurements

The filling length measurements from the simulations of the direct gating mould design are shown in Table 6 - 33 and Figure 6 - 118. It can be seen that from approximately 0.54 to 0.78 s, the filling length for the rotational velocity of 200 rpm was the lowest. Subsequently, the curves showed different slopes and the higher the rotational velocity, the lower the filling length. The results for the indirect gating mould design are shown in Table 6 - 34 and Figure 6 - 119. Again, in the initial stages, the filling length for the rotational velocity of 200 rpm was the lowest but the curves later developed different slopes and the higher the rotational velocity, the lower the filling length. Figure 6 - 120 and Figure 6 - 121 show that the computer modelling results correlated well with the experimental water modelling results for both mould designs. However, the simulation and water model results agreed better for the direct gated mould than for the indirect gated mould.

6.3 Computational Modelling of Centrifugal Castings

Since ANSYS CFX is capable of modelling both the liquid and gas phases, the simulation results differed from those obtained with Flow-3D, which models only the liquid phase. Therefore, in the results obtained with ANSYS CFX it was possible to identify the air entrainment and in severe cases the formation of big bubbles. The differences between ANSYS CFX and Flow-3D are more evident during the formation of the plunging jet in the sprue of both direct and indirect gated moulds and the filling process of the direct gated test bars. The description of these entrainment mechanisms will be described in the following sections.

6.3.1 Computational Modelling with ANSYS CFX

Summaries of the filling sequences of the direct gated mould showing side view and isosurface (0.5 volume fraction) are illustrated in Figure 6 - 122 and Figure 6 - 123. The video sequences can be seen in Appendix 49 and Appendix 50. A summary of the sequence of the filling process showing plan view of the test bar pair C1L2DG (4) - C1R2DG (7) is shown in Figure 6 - 124 and the video sequence can be seen in Appendix 51. Additionally, summaries of the filling process showing a plan view close-up of the left test bar with velocity vectors and isosurface (0.5 volume fraction) with velocity gradients in X and Y are illustrated in Figure 6 - 125 (Appendix 52), Figure 6 - 126 and Figure 6 - 127, respectively.

It can be seen that the falling stream of liquid impacted the sprue bottom and spread across the whole bottom surface area. The liquid then splashed onto the sprue wall, sending a fraction of the liquid straight to the first two levels of test bar cavities. The remaining liquid entrained its surface after the fall, Figure 6 - 122 and Figure 6 - 123. Once the sprue had partially filled, a

plunging jet was generated leading to high surface turbulence. The latter provoked a continuous surface entrainment and formation of bubbles in the sprue during the whole filling process. Eventually, the test bars were completely filled after approximately 2.22 s, Figure 6 - 122 and Figure 6 - 123.

As seen previously, filling of the individual direct gated test bars consisted of two stages. The liquid flowed radially outwards on the cavity wall (opposite to the rotation direction) where it was accelerated until it reached the far end. The direction of the liquid then changed by following the cavity shape resulting in a backward wave (0.39 s), Figure 6 - 124. The maximum velocity of the liquid was approximately 6.0 m/s, which reduced gradually as the free surface approached the ingate. This resulted in a recirculating flow in the liquid during the whole filling process, Figure 6 - 125. Likewise, Figure 6 - 126 and Figure 6 - 127 show that as a consequence of the liquid flowing in opposite directions, continuous velocity gradients were developed in the shear zone, which led to the continuous formation of bubbles. These ranged between -600 and 0 s^{-1} in the X direction and between 0 and 600 s^{-1} in the Y direction. Eventually, the test bars were completely filled and the generated bubbles disappeared after approximately 0.69 s, Figure 6 - 124.

Figure 6 - 128 illustrates a plan view of the same test bar pair showing the pressure contours developed during the filling process. It can be seen that the pressure reached a maximum of approximately 68.75 kPa at the far end, and gradually decreased away from this position towards the sprue.

Similar summaries of the sequences of the filling process for the indirect gated mould showing left and right side views, and the isosurface (0.5 volume fraction) are illustrated in Figure 6 - 129 to Figure 6 - 131. The video sequences can be seen in Appendix 53 to

Appendix 55. Additionally, summaries of the filling process showing a close-up of the left horizontal and vertical runners and isosurface (0.5 volume fraction) with velocity gradients in X and Y are illustrated in Figure 6 - 132 and Figure 6 - 133 (Appendix 56) respectively.

The filling process of the test bar pair C1L1IG (4) - C1R1IG (5) is summarized in Figure 6 - 134 and the video sequence is given Appendix 57. Additionally, summaries of the filling process showing a plan view close-up of the left test bar with velocity vectors and isosurface (0.5 volume fraction) with velocity gradients in X and Y are illustrated in Figure 6 - 135 (Appendix 58) and Figure 6 - 136 and Figure 6 - 137, respectively (see Figure 6 - 2).

Since the test bars were positioned either side of the plane through the sprue diameter (see Figure 4 - 1 (b)), it was necessary to show both left and right vertical cut views individually. It was not possible to show both sides using a single side view. This was not foreseen when designing the indirect gated mould.

Figure 6 - 129 to Figure 6 - 131 show that the falling stream of liquid impacted and spread across the sprue base and then splashed on the sprue wall and entrained its surface after the fall, although this was with less intensity compared to that of the direct gated mould (Figure 6 - 122 and Figure 6 - 123). In addition to the vertical plunging jet generated by the falling stream of liquid metal, a horizontal plunging jet was formed when the liquid flowed radially outwards in the horizontal runner bars and reached the vertical runner bars, Figure 6 - 132 and Figure 6 - 133. The liquid then flowed upwards and started the radially inwards filling process through the ingates. Likewise, as a consequence of the liquid flowing in opposite directions, continuous velocity gradients were developed, which ranged between -600 and 0 s^{-1} in the X direction and between -600 and 600 s^{-1} in the Y direction. However, the formation of bubbles was only evident in a few frames during the whole filling process (0.63 and 0.72 s), Figure 6 -

132 and Figure 6 - 133. All the test bar cavities and vents were filled after approximately 0.99 s, Figure 6 - 129 to Figure 6 - 131.

The filling of the individual indirect gated test bars started at approximately 0.66 s when the vertical runner was full, Figure 6 - 134. This liquid reached a maximum velocity of approximately 2.3 m/s, which gradually reduced as the free surface approached the test bar far end, Figure 6 - 135. Eventually, the test bar cavities and vents were filled after approximately 0.96 s, Figure 6 - 134 and Figure 6 - 135. Since the filling process of the individual indirect gated test bars was only unidirectional (radially inwards), shear gradients were not developed like those in the direct gated test bars. Figure 6 - 136 and Figure 6 - 137 show that velocity gradients were generated only in the vertical runner bar and ingate reaching a maximum of approximately -300 and 300 s^{-1} in the X direction and between -300 and 0 s^{-1} in the Y direction. It is important to notice that during the filling of the individual test bars, no bubbles were found.

Figure 6 - 138 illustrates a plan view of the same test bar pair showing pressure contours developed during filling. It can be seen that the pressure reached a maximum of approximately 50 kPa at the point of entry into the test bars and decreased towards the sprue.

6.3.2 Computational Modelling with Flow-3D

Snapshots of the sequences of the filling process for the direct gated mould showing the side view and the plan view of the test bar pair C1L2DG (4) - C1R2DG (7) are illustrated in Figure 6 - 139 and Figure 6 - 140 (Appendix 25) respectively. The video sequences can be seen in Appendix 59 and Appendix 60. Additionally, a summary of the filling process showing a close-up plan view of the left test bar with vectors is illustrated in Figure 6 - 141.

It can be seen that the falling stream of liquid impacted the sprue bottom and splashed on the sprue wall. Some of this liquid then entered four levels of test bar cavities, which were from L1-R1 to L4-R4 (see Figure 6 - 1). Once the sprue contained enough liquid, a plunging jet was generated leading to a persistent large-scale entrainment during the whole filling process. Eventually, the test bars were completely filled after approximately 1.90 s, Figure 6 - 139.

The code incorrectly placed some particles in the hollow sprue, but the number was insignificant compared to the total number of particles generated by the surface entrainment of the liquid.

Figure 6 - 140 shows that Flow-3D confirmed that liquid initially flowed radially outwards on the cavity wall and was accelerated until it reached the far end. The direction of the liquid then changed, resulting in a backward wave (0.48 s), which started the radially inwards back-filling. It is important to notice that the liquid initially filling the test bar cavity was already damaged, as shown by the presence of entrained particles before the onset of the mentioned backward wave.

The particles dispersed randomly in the hollow cavities were incorrectly placed by the code. However, their number was insignificant compared to the total number of particles generated by the surface entrainment of the liquid.

Likewise, as a consequence of the counter-current flow of the liquid, a further continuous large-scale entrainment occurred in the already damaged liquid leading to the generation of particles during the whole filling process. The maximum velocity of the liquid was approximately 4.5 m/s (0.48 s), which reduced gradually as the free surface approached the ingate. This resulted in circulating flow in the liquid during the filling, Figure 6 - 140 and Figure 6 - 141 (Appendix 26), which can be confirmed by the higher concentration of

particles at mid-width of the test bars. The test bars were completely filled after approximately 0.60 s, Figure 6 - 140.

Figure 6 - 142 shows the pressure contours developed during the filling of the test bar pair C1L2DG (4) - C1R2DG (7). The pressure gradually increased and reached a maximum of almost 68.75 kPa at the far end, which was similar to that predicted by ANSYS CFX, Figure 6 - 128.

Additional plan views were obtained in order to compare the filling process of the test bar pair # 4 and # 7 with the other four levels. In ascending order, the test bar pair # 5 and # 6 is illustrated in Appendix 27 (video sequence in Appendix 61); test bar pair # 4 and # 7 was already illustrated in Figure 6 - 140 (Appendix 25 and video sequence in Appendix 60); test bar pair # 3 and # 8 in Appendix 28 (video sequence in Appendix 62); test bar pair # 2 and # 9 in Appendix 29 (video sequence in Appendix 63); and test bar pair # 1 and # 10 in Appendix 30 (video sequence in Appendix 64).

It can be seen that the filling time varied with the test bar position. For example, for the test bars # 2 and # 9, (Appendix 29 and video sequence Appendix 63) the liquid metal reached the end of the test bars at approximately 0.48 and 0.44 s, whereas the filling was completed at 1.38 and 1.26 s, respectively. Similarly, the filling time for the rest of the test bar pairs is presented in Table 6 - 35 and Figure 6 - 143. The shortest filling time was obtained for the test bar pair # 5 and # 6 and the longest filling time was obtained for the test bar pair # 2 and # 9.

Similar filling sequences for the indirect gated mould showing the left side are illustrated in Figure 6 - 144 and the video sequence in Appendix 65. The plan view of the test bar pair C1L1IG (4) - C1R1IG (5) are illustrated in Figure 6 - 145 (Appendix 31). The video

sequences can be seen in Appendix 66. Additional snapshots showing a plan view close-up of the left test bar with vectors is illustrated in Figure 6 - 146.

As noted earlier, the mould design (Figure 4 - 1(b)) prevented side views of the left and right bars being shown simultaneously. Since the filling process of the left and right bars was similar, only the left hand side view is presented in the results.

Figure 6 - 144 shows that the liquid did not form a clear plunging jet compared to that of the direct gated mould (Figure 6 - 139). However, a persistent large-scale entrainment was also generated due to the liquid splashing on the sprue wall and enfolding itself after the fall. The liquid then flowed radially outwards in the horizontal runner bars and upwards in the vertical runners. The already damaged liquid started filling the ingates at approximately 0.80 s and the test bar cavities and vents were filled after approximately 1.20 s.

The filling process of the individual indirect gated test bars was only unidirectional. The liquid flowing from the vertical runner reached a maximum velocity of approximately 1.5 m/s and gradually reduced as the free surface approached the test bar far end, Figure 6 - 146. The simulation was continued after the mould was filled and the entrained particles, which had been generated in the horizontal and vertical runners, started moving radially inwards. This effect was clearly seen between 2.20 and 6.20 s, Figure 6 - 145 (Appendix 31 and video sequence in Appendix 66).

Figure 6 - 147 is a plan view of the same test bar pair showing pressure contours developed during the filling. It can be seen that the pressure reached a maximum of approximately 50 kPa at the ingate and decreased towards the sprue, again confirming the value predicted by ANSYS CFX, Figure 6 - 138.

6.3.2.1 Oxide Film Entrainment Model (OFEM) Results

Table 6 - 36, Table 6 - 37 and Figure 6 - 148 compare the total number of particles placed in the sprue, ingates, runner bars and test bars of the direct and indirect gated moulds (see Figure 6 - 1 and Figure 6 - 2). The total number of particles placed in the ten direct gated test bars is more than double than those placed in eight indirect gated bars. A similar amount of particles was placed in the sprue and ingates of the direct gated mould compared to the sprue of the indirect gated mould.

Comparing the total amount of particles placed in both mould designs, it can be seen that the indirect gated mould had 284522 entrainment events compared to the direct gated mould with 207796 entrainment events. This was mainly attributed to the high number of particles generated in the horizontal and vertical runner bars.

Table 6 - 38, Table 6 - 39, Figure 6 - 149 and Figure 6 - 150 show the number of particles placed in the complete test bars and test lengths (Figure 5 - 8), which are organized by position in the direct and indirect gated moulds. It can be seen that the number of particles placed in the test length of both direct and indirect gated bars followed the same trend to the total number of particles placed in the complete test bars.

Since the purpose of this investigation was to compare the number of particles placed in the test length with the mechanical properties obtained in the experimental test bars of both mould designs, the explanation of the subsequent results and discussion will only be focused on the number of particles placed in the test length. For the direct gated test bars, Figure 6 - 151 shows that except for the test bar pair # 1 and # 10, there was an increased variation in the number of particles placed in the test length in comparison with the indirect gated test bars. The positions # 2 and # 9 had the maximum, whilst the positions # 5 and # 6 had the

minimum number of particles. The minimum and maximum number of particles ranged between 987 (# 5) and 10014 (# 9), with a standard deviation of 3007.4, Table 6 - 38. As noted above, the test bar pair # 1 and 10 did not follow the same trend. This was related to the filling time of the test bar cavities and will be discussed in more detail in Section 7.3.2. For the indirect gated test bars, Figure 6 - 152 shows that the number of particles were similar in each bar and the minimum and maximum values were 1132 (# 4) and 2151 (# 2) respectively, with a lower standard deviation of 328.9, Table 6 - 39.

Table 6 - 40, Table 6 - 41 and Figure 6 - 153 show the number of particles in the test length as a function of test bar pair and position for both mould designs, where each point is the average of two test bars. For the direct gated mould, the test bar pairs L4-R4 and L1-R1 had the maximum and minimum average number of particles (9484.5 and 1130 respectively). For the indirect gated mould, the difference between the test bar pairs was relatively small compared to the direct gated bars; the minimum and maximum values were 1258 and 2046.5 particles.

Table 6 - 40, Table 6 - 41 and Figure 6 - 154 show the relation between average UBS and the average number of particles as a function of test bar pair and position for direct and indirect gated moulds. It can be seen that the results for the four indirect gated test bar pairs were clustered together and that there was no discernible effect of the number of particles. The results for the direct gated bar were lower and more dispersed.

Figure 6 - 155 shows the combined data from both gating systems with a fitted straight line and its equation and correlation coefficient. It can be seen that there was a correlation showing that the average UBS decreased as the average number of particles increased.

6.4 Tables

Table 6 - 1. Composition of the aluminium alloy 6082

	Composition, weight %	
Element	**Actual**	**Specification**
Silicon	0.70	0.70 – 1.3
Magnesium	0.76	0.6 – 1.2
Manganese	0.66	0.4 – 1.0
Iron	0.47	0.50 max.
Chromium	0.04	0.25 max.
Zinc	0.11	0.20 max.
Copper	0.05	0.10 max.
Titanium	0.05	0.10 max.
Aluminium	Balance	Balance

Table 6 - 2. Modulus of elasticity (E) of aluminium alloy 6082.

E (GPa)	**Reference**
69	(Brandes and Brook, 1998)
70	(Alcan, 2011)

Table 6 - 3. Ultimate bend strength 'UBS' data of direct gated samples organized by casting and position (see Figure 6 - 1). Note: These values have to be multiplied by a factor of 1.371.

* This sample was used for porosity examination
** This sample was not filled completely

	Direct gated mould					
	1st Casting		**2nd Casting**		**3rd Casting**	
#	**Code**	**UBS (MPa)**	**Code**	**UBS (MPa)**	**Code**	**UBS (MPa)**
1	C1L5DG	327	C2L5DG	353	C3L5DG	317
2	C1L4DG	315	C2L4DG	319	C3L4DG	324
3	C1L3DG	331	C2L3DG	335	C3L3DG	324
4	C1L2DG	321	C2L2DG	338	C3L2DG	316
5	C1L1DG	316	C2L1DG	330	C3L1DG	332
6	C1R1DG	340	C2R1DG	337	C3R1DG	297
7	C1R2DG	327	C2R2DG	338	C3R2DG	319
8	C1R3DG	330	C2R3DG	331	C3R3DG	265
9	C1R4DG	324	C2R4DG	317	C3R4DG	302
10	C1R5DG	*	C2R5DG	329	C3R5DG	**

Table 6 - 4. Ultimate bend strength 'UBS' data of indirect gated samples organized by casting and position (see Figure 6 - 2). Note: These values have to be multiplied by a factor of 1.371.

* These samples were used for porosity examination.

	Indirect gated mould					
	1st Casting		**2nd Casting**		**3rd Casting**	
#	**Code**	**UBS (MPa)**	**Code**	**UBS (MPa)**	**Code**	**UBS (MPa)**
1	C1L4IG	343	C2L4IG	349	C3L4IG	327
2	C1L3IG	347	C2L3IG	349	C3L3IG	347
3	C1L2IG	339	C2L2IG	331	C3L2IG	357
4	C1L1IG	349	C2L1IG	*	C3L1IG	347
5	C1R1IG	338	C2R1IG	*	C3R1IG	344
6	C1R2IG	348	C2R2IG	336	C3R2IG	348
7	C1R3IG	352	C2R3IG	348	C3R3IG	370
8	C1R4IG	356	C2R4IG	338	C3R4IG	346

Table 6 - 5. Ultimate bend strength 'UBS' data of direct gated cast samples organized by test bar position and pair. (see Figure 6 - 1). Note: These values have to be multiplied by a factor of 1.371.

Test bar pair	Test bar with minimum 'UBS' (MPa)	Test bar with maximum 'UBS' (MPa)	Average 'UBS' (MPa)
L5 and R5	317	353	332
L4 and R4	302	324	317
L3 and R3	265	335	319
L2 and R2	316	338	327
L1 and R1	297	340	325

Table 6 - 6. Ultimate bend strength 'UBS' data of indirect gated cast samples organized by test bar position and pair. (see Figure 6 - 2). Note: These values have to be multiplied by a factor of 1.371.

Test bar pair	Test bar with minimum 'UBS' (MPa)	Test bar with maximum 'UBS' (MPa)	Average 'UBS' (MPa)
L4 and R4	327	356	343
L3 and R3	347	370	352
L2 and R2	331	357	343
L1 and R1	338	349	345

Table 6 - 7. Modulus of elasticity ‘E’ data of direct gated samples organized by casting and position (see Figure 6 - 1).

* This sample was used for porosity examination
** This sample was not filled completely

	Direct gated mould					
	1st Casting		**2nd Casting**		**3rd Casting**	
#	**Code**	**E (GPa)**	**Code**	**E (GPa)**	**Code**	**E (GPa)**
1	C1L5DG	51.93	C2L5DG	60.48	C3L5DG	50.34
2	C1L4DG	54.91	C2L4DG	54.84	C3L4DG	48.70
3	C1L3DG	53.87	C2L3DG	55.50	C3L3DG	50.05
4	C1L2DG	54.47	C2L2DG	58.34	C3L2DG	49.91
5	C1L1DG	52.49	C2L1DG	55.09	C3L1DG	50.14
6	C1R1DG	54.24	C2R1DG	52.88	C3R1DG	46.90
7	C1R2DG	57.20	C2R2DG	55.27	C3R2DG	54.98
8	C1R3DG	54.42	C2R3DG	53.11	C3R3DG	45.20
9	C1R4DG	55.88	C2R4DG	57.06	C3R4DG	52.00
10	C1R5DG	*	C2R5DG	53.68	C3R5DG	**

Table 6 - 8. Modulus of elasticity ‘E’ data of indirect gated samples organized by casting and position (see Figure 6 - 2).

* These samples were used for porosity examination.

	Indirect gated mould					
	1st Casting		**2nd Casting**		**3rd Casting**	
#	**Code**	**E (GPa)**	**Code**	**E (GPa)**	**Code**	**E (GPa)**
1	C1L4	56.29	C2L4	58.81	C3L4	50.20
2	C1L3	55.18	C2L3	57.34	C3L3	57.03
3	C1L2	53.19	C2L2	53.91	C3L2	57.68
4	C1L1	54.30	C2L1	*	C3L1	57.73
5	C1R1	53.42	C2R1	*	C3R1	56.79
6	C1R2	55.17	C2R2	54.44	C3R2	57.88
7	C1R3	54.93	C2R3	56.73	C3R3	59.76
8	C1R4	55.56	C2R4	55.59	C3R4	56.35

Table 6 - 9. Modulus of elasticity ‘E’ data of direct gated cast samples organized by test bar position and pair. (see Figure 6 - 1).

Test bar pair	Test bar with minimum ‘E’ (GPa)	Test bar with maximum ‘E’ (GPa)	Average ‘E’ (GPa)
L5 and R5	50.34	60.48	54.11
L4 and R4	48.70	57.06	53.90
L3 and R3	45.20	55.50	52.03
L2 and R2	49.91	58.34	55.03
L1 and R1	46.90	55.09	51.96

Table 6 - 10. Modulus of elasticity ‘E’ data of indirect gated cast samples organized by test bar position and pair. (see Figure 6 - 2).

Test bar pair	Test bar with minimum ‘E’ (GPa)	Test bar with maximum ‘E’ (GPa)	Average ‘E’ (GPa)
L4 and R4	50.20	58.81	55.47
L3 and R3	54.93	59.76	56.83
L2 and R2	53.19	57.88	55.38
L1 and R1	53.42	57.73	55.56

Table 6 - 11. Summary of UBS, E and Weibull modulus results for both gating systems. Note: Note: The UBS values have to be multiplied by a factor of 1.371, except the Weibull modulus.

	Ultimate Bend Strength 'UBS'				
Gating system	**Average (MPa)**	**St. Dev. (MPa)**	**σ (MPa)**	**Weibull modulus**	**R^2**
Direct	323	15.9	330	23	0.90
Indirect	346	8.9	350	45	0.90
	Modulus of Elasticity 'E'				
Gating system	**Average (GPa)**	**St. Dev. (GPa)**	**σ (GPa)**	**Weibull modulus**	**R^2**
Direct	53.35	3.3	54.91	19	0.98
Indirect	55.83	2.1	56.80	32	0.98

Table 6 - 12. Results of dendrite cell size measurements for a direct gated test bar (C1L2DG).

	Micrograph 1	**Micrograph 2**	**Micrograph 3**
# Measurement	**Dendrite cell size (µm)**	**Dendrite cell size (µm)**	**Dendrite cell size (µm)**
1	21.8	26.7	30.1
2	25.5	18.2	20.2
3	19.2	43.2	29.6
4	31.9	19.6	26.6
5	26.6	29.1	21.9
6	17.2	26.3	30.2
7	27.9	17.0	20.3
8	20.2	28.1	20.5
9	26.3	21.9	25.2
10	18.6	28.3	26.3
11	24.3	20.5	21.0
12	30.9	20.3	24.8
13	19.2	30.2	23.8
14	18.1	24.5	25.1
15	28.1	27.7	22.6
Average	**23.7**	**25.4**	**24.6**
St. Dev.	**4.7**	**6.3**	**3.4**

Table 6 - 13. Results of dendrite cell size measurements for an indirect gated test bar (C1L1IG)

	Micrograph 1	**Micrograph 2**	**Micrograph 3**
# Measurement	**Dendrite cell size (μm)**	**Dendrite cell size (μm)**	**Dendrite cell size (μm)**
1	26.3	32.3	30.7
2	39.5	24.3	20.9
3	27.9	33.3	30.9
4	32.4	35.7	24.3
5	40.5	38.2	39.4
6	33.0	23.4	38.5
7	35.4	27.3	27.8
8	36.1	24.5	23.3
9	38.7	34.3	25.7
10	34.3	39.2	27.1
11	37.2	22.4	35.7
12	24.3	28.6	20.5
13	26.7	33.8	28.5
14	36.6	25.2	40.0
15	27.1	30.1	34.5
Average	**33.1**	**30.2**	**29.9**
St. Dev.	**5.2**	**5.4**	**6.3**

Table 6 - 14. Summary of dendrite cell size measurements and calculated solidification rates for both gating systems.

Gating system	**Average dendrite cell size (μm)**	**Standard deviation (μm)**	**Calculated solidification rate using average dendrite cell size (°C/s)**
Direct	25	5	4.5
Indirect	31	6	2.6

Table 6 - 15. Results of number of interceptions using Abraham three circles (ASTM, 2004) for both gating systems.

Direct		**Indirect**	
# **Micrograph**	# **Intersections**	# **Micrograph**	# **Intersections**
1 (C1L2DG)	55	1 (C1L1IG)	40.5
2 (C1L2DG)	57.5	2 (C1L1IG)	38
3 (C1R2DG)	49.5	3 (C1R2IG)	36
4 (C1R2DG)	53	4 (C1R2IG)	35
Average	**53.8**	**Average**	**37.4**
St. Dev.	**2.9**	**St. Dev.**	**2.1**

Table 6 - 16. Results of calculated grain size for both gating systems (ASTM, 2004)

Gating system	**Total test line length (mm)**	**Magnifi-cation**	**ASTM Grain size 'G'**	**Average grain diameter (μm)**	**Mean Intercept (μm)**
Direct	500	50x	1.5	213.6	190.3
Indirect	500	50x	0.5	302.1	269.1

Table 6 - 17. Numerical results of stereological measurements of porosity obtained from direct gating test bar with UBS of 265 MPa (C3R3DG).

Size category (µm)	**Frequency**	**Pores/mm^2**
20	1331	18.66
30	1134	15.90
40	423	5.93
50	221	3.10
60	125	1.75
70	82	1.15
80	37	0.52
90	26	0.36
100	17	0.24
More	128	1.79
Total	**3524**	

Table 6 - 18. Numerical results of stereological measurements of porosity obtained from direct gating test bar with UBS of 302 MPa (C3R4DG).

Size category (µm)	**Frequency**	**Pores/mm^2**
20	2001	16.03
30	2548	20.42
40	1020	8.17
50	549	4.40
60	292	2.34
70	210	1.68
80	124	0.99
90	86	0.69
100	55	0.44
More	221	1.77
Total	**7106**	

Table 6 - 19. Numerical results of stereological measurements of porosity obtained from direct gating test bar with UBS of 327 MPa (C1R2DG).

Size category (µm)	**Frequency**	**Pores/mm^2**
20	1826	17.74
30	911	8.85
40	473	4.59
50	250	2.43
60	156	1.52
70	107	1.04
80	75	0.73
90	48	0.47
100	42	0.41
More	152	1.48
Total	**4040**	

Table 6 - 20. Numerical results of stereological measurements of porosity obtained from direct gating test bar with UBS of 338 MPa (C2R2DG).

Size category (µm)	**Frequency**	**Pores/mm^2**
20	1540	12.94
30	1206	10.13
40	413	3.47
50	165	1.39
60	70	0.59
70	46	0.39
80	23	0.19
90	17	0.14
100	8	0.07
More	70	0.59
Total	**3558**	

Table 6 - 21. Numerical results of stereological measurements of porosity obtained from indirect gating test bar with UBS of 338 MPa (C1R1IG).

Size category (µm)	**Frequency**	**Pores/mm^2**
20	996	8.36
30	880	7.39
40	319	2.68
50	139	1.17
60	75	0.63
70	64	0.54
80	22	0.18
90	14	0.12
100	14	0.12
More	56	0.47
Total	**2579**	

Table 6 - 22. Numerical results of stereological measurements of porosity obtained from indirect gating test bar with UBS of 347 MPa (C1L3IG).

Size category (µm)	**Frequency**	**Pores/mm^2**
20	691	5.80
30	520	4.36
40	203	1.70
50	110	0.92
60	41	0.34
70	35	0.29
80	35	0.29
90	18	0.15
100	19	0.16
More	68	0.57
Total	**1740**	

Table 6 - 23. Numerical results of stereological measurements of porosity obtained from indirect gating test bar with UBS of 349 MPa (C1LIIG).

Size category (µm)	**Frequency**	**Pores/mm^2**
20	759	6.69
30	808	7.12
40	280	2.47
50	168	1.48
60	89	0.78
70	57	0.50
80	39	0.34
90	25	0.22
100	17	0.15
More	61	0.54
Total	**2303**	

Table 6 - 24. Numerical results of stereological measurements of porosity obtained from indirect gating test bar with UBS of 357 MPa (C1R3IG).

Size category (µm)	**Frequency**	**Pores/mm^2**
20	759	7.04
30	875	8.12
40	328	3.04
50	159	1.48
60	74	0.69
70	58	0.54
80	29	0.27
90	20	0.19
100	12	0.11
More	62	0.58
Total	**2376**	

Table 6 - 25. Stereological measurements of total porosity in cast test bars from both gating systems

Gating system	Code	UBS (MPa)	Area fraction of Porosity (%)	Pores/mm^2
Direct	C3R3DG	265	6.9	49
	C3R4DG	302	3.6	57
	C1R2DG	327	3.3	39
	C2R2DG	338	1.7	30
Indirect	C1R1IG	338	1.8	22
	C1L3IG	347	1.4	15
	C1L1IG	349	1.5	20
	C3L2IG	357	1.6	22

Table 6 - 26. Analytical solution and results of five water modelling experiments showing the time for the water to reach the sprue base from the nozzle (a distance of 40 mm) immediately after the valve was opened.

Analytical solution	Time (s)
	0.090
# Experiment	**Time (s)**
1	0.107
2	0.115
3	0.121
4	0.101
5	0.106
Average	0.110
St. Dev.	0.007

Table 6 - 27. Experimental measurements of the water jet thickness at a radial distance of 95 mm for the direct and indirect gated mould designs at 200, 300 and 400 rpm.

Dir Gat	**Water jet thickness**		
Rotational velocity (RPM)	**Test bar 1 (mm)**	**Test bar 2 (mm)**	**Average (mm)**
200	2.60	2.70	2.65
300	2.30	2.20	2.25
400	1.60	1.50	1.55
Ind Gat	**Water jet thickness**		
Rotational velocity (RPM)	**Test bar 1 (mm)**	**Test bar 2 (mm)**	**Average (mm)**
200	2.80	2.70	2.75
300	2.10	2.20	2.15
400	1.60	1.70	1.65

Table 6 - 28. Calculated water jet velocity obtained from experimental water jet thickness and filled length measurements at 1.05 s. The water jet thickness was assumed to be rectangular.

Rotational velocity (RPM)	**Water jet thickness (mm)**	**A_J (mm^2)**	**V_M (mm/s)**	**A_M (mm^2)**	**V_J (m/s)**
200	2.65	10.6	62.49	100	0.59
300	2.25	9.0	61.38	100	0.68
400	1.55	6.2	59.24	100	0.96

Table 6 - 29. Experimental water model results of filling length measurements for the direct gated mould design for three rotational velocities.

200 RPM								
		Test bar 1			Test bar 2			Overall Average (mm)
#	Time (s)	L_1 (mm)	L_2 (mm)	Average (mm)	L_1 (mm)	L_2 (mm)	Average (mm)	
1	0.57	13.2	18.5	15.8	14.5	18.2	16.4	16.1
2	0.63	18.0	23.3	20.6	18.3	23.6	21.0	20.8
3	0.78	33.5	37.4	35.4	34.2	39.1	36.7	36.0
4	0.93	52.2	54.6	53.4	48.6	52.5	50.6	52.0
5	1.08	67.7	71.2	69.4	70.1	73.3	71.7	70.6
6	1.21	83.5	87.8	85.7	86.4	90.2	88.3	87.0
7	1.34	100.3	105.8	103.0	104.2	107.1	105.6	104.3
8	1.44	114.4	119.2	116.8	117.1	121.5	119.3	118.1

300 RPM								
		Test bar 1			Test bar 2			Overall Average (mm)
#	Time (s)	L_1 (mm)	L_2 (mm)	Average (mm)	L_1 (mm)	L_2 (mm)	Average (mm)	
1	0.54	13.3	16.9	15.1	13.6	18.7	16.2	15.6
2	0.64	20.5	23.7	22.1	22.6	25.5	24.1	23.1
3	0.74	30.2	32.3	31.2	32.3	35.2	33.8	32.5
4	0.84	40.2	42.0	41.1	42.7	44.5	43.6	42.4
5	0.94	51.0	52.4	51.7	53.9	55.3	54.6	53.1
6	1.04	62.1	63.2	62.7	64.3	66.4	65.3	64.0
7	1.14	73.2	74.3	73.8	76.5	77.6	77.0	75.4
8	1.24	84.0	86.5	85.3	87.2	89.0	88.1	86.7
9	1.34	96.2	98.4	97.3	99.5	102.3	100.9	99.1
10	1.44	108.4	110.6	109.5	112.7	114.5	113.6	111.6
11	1.50	116.3	119.6	117.9	120.6	123.5	122.1	120.0

400 RPM								
		Test bar 1			Test bar 2			Overall Average (mm)
#	Time (s)	L_1 (mm)	L_2 (mm)	Average (mm)	L_1 (mm)	L_2 (mm)	Average (mm)	
1	0.54	14.5	15.9	15.2	13.5	15.9	14.7	15.0
2	0.66	23.4	25.2	24.3	24.8	25.5	25.2	24.7
3	0.81	36.1	36.5	36.3	37.9	39.0	38.4	37.4
4	0.96	51.7	51.7	51.7	52.4	52.8	52.6	52.2
5	1.11	65.6	65.6	65.6	67.7	67.7	67.7	66.6
6	1.26	80.8	81.9	81.3	82.9	84.0	83.4	82.4
7	1.40	97.1	98.2	97.6	99.9	101.3	100.6	99.1
8	1.57	117.3	119.1	118.2	119.8	122.2	121.0	119.6

Table 6 - 30. Experimental water model results of filling length measurements for the indirect gated mould design for three rotational velocities.

200 RPM								
		Test bar 1			Test bar 2			Overall Average (mm)
#	Time (s)	L_1 (mm)	L_2 (mm)	Average (mm)	L_1 (mm)	L_2 (mm)	Average (mm)	
1	0.71	8.9	17.9	13.4	15.8	25.6	20.7	17.1
2	0.76	9.3	18.6	14.0	19.5	29.2	24.3	19.2
3	0.91	22.3	30.8	26.6	32.8	41.8	37.3	31.9
4	1.06	36.1	44.2	40.1	49.9	56.8	53.3	46.7
5	1.21	50.3	60.0	55.1	65.3	77.0	71.1	63.1
6	1.36	66.1	77.4	71.8	81.9	96.1	89.0	80.4
7	1.51	81.9	95.3	88.6	98.5	112.3	105.4	97.0
8	1.66	97.3	112.7	105.0	113.5	135.0	124.3	114.6

300 RPM								
		Test bar 1			Test bar 2			Overall Average (mm)
#	Time (s)	L_1 (mm)	L_2 (mm)	Average (mm)	L_1 (mm)	L_2 (mm)	Average (mm)	
1	0.62	13.5	22.2	17.8	11.5	23.0	17.2	17.5
2	0.73	23.4	30.9	27.1	21.4	29.7	25.5	26.3
3	0.83	30.9	38.8	34.8	29.3	38.0	33.7	34.2
4	0.93	39.2	48.7	43.9	36.8	45.5	41.2	42.6
5	1.03	45.1	56.2	50.7	46.7	57.4	52.1	51.4
6	1.13	55.0	68.1	61.6	53.8	65.7	59.8	60.7
7	1.23	64.5	76.8	70.7	62.6	74.4	68.5	69.6
8	1.33	72.1	85.9	79.0	71.7	85.1	78.4	78.7
9	1.43	81.6	95.4	88.5	80.4	94.6	87.5	88.0
10	1.53	89.5	107.3	98.4	88.7	106.5	97.6	98.0
11	1.63	99.2	117.4	108.3	100.2	114.8	107.5	107.9
12	1.73	109.3	131.0	120.2	109.3	130.2	119.8	120.0

400 RPM								
		Test bar 1			Test bar 2			Overall Average (mm)
#	Time (s)	L_1 (mm)	L_2 (mm)	Average (mm)	L_1 (mm)	L_2 (mm)	Average (mm)	
1	0.61	11.4	21.6	16.5	11.0	19.7	15.3	15.9
2	0.68	17.3	24.8	21.1	16.5	23.6	20.1	20.6
3	0.83	26.8	37.4	32.1	26.8	35.0	30.9	31.5
4	0.98	39.0	48.8	43.9	36.6	47.6	42.1	43.0
5	1.13	49.2	60.6	54.9	49.2	57.9	53.5	54.2
6	1.28	61.0	73.6	67.3	58.6	72.8	65.7	66.5
7	1.43	72.8	87.4	80.1	70.5	83.4	76.9	78.5
8	1.58	84.6	102.7	93.7	83.0	99.2	91.1	92.4
9	1.73	98.0	116.9	107.4	97.2	115.3	106.3	106.9
10	1.86	109.0	134.6	121.8	106.7	131.5	119.1	120.4

Table 6 - 31. Experimental water model results of filling length measurements for the modified indirect gated mould design for three rotational velocities.

200 RPM								
		Test bar 1			Test bar 2			Overall Average (mm)
#	Time (s)	L_1 (mm)	L_2 (mm)	Average (mm)	L_1 (mm)	L_2 (mm)	Average (mm)	
1	0.76	14.8	24.0	19.4	9.2	16.4	12.8	16.1
2	0.84	20.4	30.0	25.2	15.6	24.8	20.2	22.7
3	0.99	34.7	44.7	39.7	26.4	35.9	31.2	35.4
4	1.14	49.1	60.7	54.9	39.9	51.1	45.5	50.2
5	1.29	65.1	78.3	71.7	55.1	66.7	60.9	66.3
6	1.44	81.1	95.9	88.5	71.1	83.9	77.5	83.0
7	1.59	96.3	115.4	105.8	84.3	102.2	93.3	99.6
8	1.68	105.0	127.4	116.2	93.5	112.2	102.8	109.5
9	1.76	115.0	135.0	125.0	104.6	126.2	115.4	120.2

300 RPM								
		Test bar 1			Test bar 2			Overall Average (mm)
#	Time (s)	L_1 (mm)	L_2 (mm)	Average (mm)	L_1 (mm)	L_2 (mm)	Average (mm)	
1	0.74	13.3	22.6	17.9	10.9	19.3	15.1	16.5
2	0.85	21.8	31.8	26.8	18.9	28.6	23.8	25.3
3	0.97	30.2	40.7	35.5	28.2	38.3	33.2	34.4
4	1.07	38.7	48.4	43.5	35.9	46.3	41.1	42.3
5	1.17	46.7	58.0	52.4	45.1	56.0	50.6	51.5
6	1.27	54.8	68.1	61.5	53.2	65.7	59.4	60.4
7	1.37	62.3	76.3	69.3	62.3	74.6	68.4	68.8
8	1.47	71.3	87.9	79.6	68.9	83.8	76.4	78.0
9	1.57	80.9	97.2	89.1	77.9	95.2	86.5	87.8
10	1.67	90.3	110.4	100.3	88.7	106.0	97.3	98.8
11	1.77	99.5	122.1	110.8	97.6	119.7	108.6	109.7
12	1.87	108.0	135.0	121.5	107.2	133.4	120.3	120.9

400 RPM								
		Test bar 1			Test bar 2			Overall Average (mm)
#	Time (s)	L_1 (mm)	L_2 (mm)	Average (mm)	L_1 (mm)	L_2 (mm)	Average (mm)	
1	0.71	12.1	21.4	16.8	8.5	18.6	13.5	15.2
2	0.82	19.4	29.9	24.7	16.2	25.5	20.8	22.7
3	0.93	27.5	37.6	32.5	22.2	33.5	27.9	30.2
4	1.08	38.0	50.1	44.1	32.3	44.1	38.2	41.1
5	1.23	49.3	62.2	55.8	43.7	56.2	49.9	52.8
6	1.38	61.0	77.2	69.1	55.0	69.9	62.4	65.8
7	1.53	72.4	90.5	81.4	67.5	84.1	75.8	78.6
8	1.68	85.7	106.7	96.2	82.1	101.5	91.8	94.0
9	1.83	99.8	125.7	112.8	94.6	116.8	105.7	109.2
10	1.92	107.9	137.0	122.5	104.7	130.2	117.4	119.9

Table 6 - 32. Experimental water model results of filling length measurements for the indirect gated mould design for three rotational velocities. The Perspex mould did not include the vents in the runners.

200 RPM								
		Test bar 1			Test bar 2			Overall Average (mm)
#	Time (s)	L_1 (mm)	L_2 (mm)	Average (mm)	L_1 (mm)	L_2 (mm)	Average (mm)	
1	0.81	15.2	25.5	20.3	18.9	27.0	23.0	21.7
2	2.60	47.0	59.1	53.0	40.7	51.8	46.2	49.6
3	4.40	55.6	68.7	62.1	47.7	60.1	53.9	58.0
4	6.20	59.3	72.5	65.9	51.3	64.6	58.0	61.9
5	7.99	63.9	78.0	71.0	56.6	69.4	63.0	67.0
6	9.79	68.7	83.3	76.0	61.9	74.5	68.2	72.1
7	11.59	72.0	88.1	80.1	65.7	80.3	73.0	76.5
8	13.39	78.8	94.2	86.5	69.2	84.3	76.8	81.6
9	15.19	82.6	101.0	91.8	83.3	100.8	92.0	91.9

300 RPM								
		Test bar 1			Test bar 2			Overall Average (mm)
#	Time (s)	L_1 (mm)	L_2 (mm)	Average (mm)	L_1 (mm)	L_2 (mm)	Average (mm)	
1	1.10	22.4	33.3	27.9	22.1	32.3	27.2	27.5
2	1.90	33.6	45.1	39.3	28.4	38.3	33.3	36.3
3	2.70	43.4	55.5	49.4	31.6	41.8	36.7	43.1
4	3.30	49.2	62.5	55.9	34.0	45.3	39.6	47.8
5	4.10	58.6	73.4	66.0	47.3	58.2	52.7	59.4
6	4.90	72.3	87.9	80.1	63.7	77.3	70.5	75.3
7	5.70	84.0	103.9	93.9	74.2	90.6	82.4	88.2
8	6.50	96.9	119.1	108.0	86.3	104.7	95.5	101.8
9	7.18	107.8	133.6	120.7	94.5	118.0	106.3	113.5

400 RPM								
		Test bar 1			Test bar 2			Overall Average (mm)
#	Time (s)	L_1 (mm)	L_2 (mm)	Average (mm)	L_1 (mm)	L_2 (mm)	Average (mm)	
1	1.28	21.3	30.5	25.9	17.6	25.4	21.5	23.7
2	1.87	30.5	40.1	35.3	22.1	30.5	26.3	30.8
3	2.47	46.0	58.5	52.2	31.3	42.3	36.8	44.5
4	3.07	56.6	69.9	63.2	47.4	57.4	52.4	57.8
5	3.67	63.6	78.3	71.0	57.0	69.9	63.4	67.2
6	4.27	71.3	86.8	79.0	64.3	78.7	71.5	75.3
7	4.79	76.8	94.1	85.5	72.4	87.5	80.0	82.7
8	5.39	85.7	104.8	95.2	79.8	96.3	88.1	91.6
9	6.07	93.8	115.4	104.6	88.2	109.6	98.9	101.7
10	6.59	100.4	125.0	112.7	96.7	119.1	107.9	110.3

Table 6 - 33. Filling lengths predicted by ANSYS CFX for the direct gated mould design for three rotational velocities.

200 RPM								
		Test bar 1			Test bar 2			Overall Average (mm)
#	Time (s)	L_1 (mm)	L_2 (mm)	Average (mm)	L_1 (mm)	L_2 (mm)	Average (mm)	
1	0.54	14.8	21.6	18.2	14.9	21.7	18.3	18.2
2	0.66	24.9	30.5	27.7	24.5	30.6	27.6	27.6
3	0.78	36.7	41.7	39.2	36.5	41.3	38.9	39.1
4	0.90	49.3	53.1	51.2	50.3	53.7	52.0	51.6
5	1.02	63.3	65.7	64.5	63.5	65.9	64.7	64.6
6	1.14	76.7	78.7	77.7	76.7	79.1	77.9	77.8
7	1.26	90.5	92.1	91.3	91.7	93.1	92.4	91.8
8	1.38	104.6	108.6	106.6	105.4	109.0	107.2	106.9
9	1.47	116.7	120.8	118.7	117.1	121.0	119.0	118.9

300 RPM								
		Test bar 1			Test bar 2			Overall Average (mm)
#	Time (s)	L_1 (mm)	L_2 (mm)	Average (mm)	L_1 (mm)	L_2 (mm)	Average (mm)	
1	0.54	19.1	22.5	20.8	17.5	22.3	19.9	20.3
2	0.66	27.8	30.6	29.2	27.4	30.8	29.1	29.2
3	0.78	38.0	40.8	39.4	38.0	41.0	39.5	39.4
4	0.90	49.3	51.7	50.5	49.7	51.7	50.7	50.6
5	1.02	62.2	62.8	62.5	62.4	63.6	63.0	62.8
6	1.14	75.0	76.0	75.5	73.2	76.3	74.8	75.1
7	1.26	87.9	89.3	88.6	87.7	89.1	88.4	88.5
8	1.38	101.0	102.8	101.9	100.6	102.8	101.7	101.8
9	1.53	118.5	121.7	120.1	118.1	120.9	119.5	119.8

400 RPM								
		Test bar 1			Test bar 2			Overall Average (mm)
#	Time (s)	L_1 (mm)	L_2 (mm)	Average (mm)	L_1 (mm)	L_2 (mm)	Average (mm)	
1	0.54	18.5	22.0	20.3	19.9	22.6	21.2	20.8
2	0.66	26.6	30.1	28.3	28.0	30.5	29.3	28.8
3	0.78	37.5	38.0	37.8	38.2	40.1	39.2	38.5
4	0.90	47.6	49.7	48.6	49.0	50.1	49.5	49.1
5	1.02	58.8	60.3	59.5	59.5	61.2	60.3	59.9
6	1.14	71.0	72.4	71.7	71.2	72.9	72.0	71.9
7	1.26	83.2	84.6	83.9	84.5	85.0	84.7	84.3
8	1.38	96.2	98.1	97.1	96.9	97.8	97.3	97.2
9	1.50	110.1	111.5	110.8	109.8	111.5	110.6	110.7
10	1.59	118.7	121.7	120.2	118.9	121.4	120.1	120.2

Table 6 - 34. Filling lengths predicted by ANSYS CFX for the indirect gated mould design for three rotational velocities.

200 RPM								
		Test bar 1			Test bar 2			Overall Average (mm)
#	Time (s)	L_1 (mm)	L_2 (mm)	Average (mm)	L_1 (mm)	L_2 (mm)	Average (mm)	
1	0.60	12.9	23.7	18.3	14.2	25.0	19.6	18.9
2	0.75	22.5	33.7	28.1	24.6	34.4	29.5	28.8
3	0.90	35.4	46.9	41.2	36.5	47.9	42.2	41.7
4	1.05	48.7	60.6	54.6	49.6	62.1	55.9	55.2
5	1.20	62.1	75.4	68.8	64.0	77.5	70.8	69.8
6	1.35	76.0	92.3	84.1	78.3	94.6	86.4	85.3
7	1.50	90.2	110.2	100.2	93.5	111.9	102.7	101.4
8	1.65	105.0	131.2	118.1	107.1	132.7	119.9	119.0

300 RPM								
		Test bar 1			Test bar 2			Overall Average (mm)
#	Time (s)	L_1 (mm)	L_2 (mm)	Average (mm)	L_1 (mm)	L_2 (mm)	Average (mm)	
1	0.60	15.2	25.5	20.3	15.4	25.9	20.7	20.5
2	0.75	25.1	35.8	30.4	24.9	36.8	30.8	30.6
3	0.90	36.6	48.3	42.4	37.4	47.9	42.6	42.5
4	1.05	48.3	61.2	54.8	48.9	62.5	55.7	55.2
5	1.20	60.6	75.6	68.1	61.8	75.4	68.6	68.4
6	1.35	73.2	90.0	81.6	74.2	91.0	82.6	82.1
7	1.50	86.9	107.7	97.3	87.9	108.1	98.0	97.7
8	1.65	100.3	123.7	112.0	102.3	127.8	115.1	113.5
9	1.71	106.0	134.0	120.0	107.9	135.0	121.4	120.7

400 RPM								
		Test bar 1			Test bar 2			Overall Average (mm)
#	Time (s)	L_1 (mm)	L_2 (mm)	Average (mm)	L_1 (mm)	L_2 (mm)	Average (mm)	
1	0.60	16.6	27.4	22.0	16.8	26.8	21.8	21.9
2	0.75	26.0	38.0	32.0	25.2	36.5	30.8	31.4
3	0.90	35.3	48.7	42.0	36.1	48.7	42.4	42.2
4	1.05	47.3	60.3	53.8	47.1	60.1	53.6	53.7
5	1.20	58.7	73.3	66.0	58.9	73.1	66.0	66.0
6	1.35	70.9	87.3	79.1	70.9	86.7	78.8	79.0
7	1.50	83.6	103.7	93.6	84.0	102.9	93.4	93.5
8	1.65	97.2	120.8	109.0	96.4	120.0	108.2	108.6
9	1.77	106.8	135.0	120.9	107.6	135.0	121.3	121.1

Table 6 - 35. Flow-3D results showing the approximate time to fill the test bar cavities as a function of test bar position in the direct gated mould.

# Test Bar	Initial time (s)	Final time (s)	Total (s)	# Test Bar	Initial time (s)	Final time (s)	Total (s)
1	1.64	1.78	0.14	10	1.70	1.88	0.18
2	0.48	1.38	0.90	9	0.44	1.26	0.82
3	0.28	0.98	0.70	8	0.24	0.86	0.62
4	0.28	0.60	0.32	7	0.42	0.58	0.16
5	0.24	0.36	0.12	6	0.24	0.32	0.08

Table 6 - 36. Number of particles placed in the direct gated mould (see Figure 6 - 1).

Number of entrained particles		
Sprue and ingates	**Test bars**	**Total**
104146	103650	207796

Table 6 - 37. Number of particles placed in the indirect gated mould (see Figure 6 - 2).

Number of entrained particles				
Sprue	**Horizontal runners**	**Vertical runners and ingates**	**Test bars**	**Total**
103760	60630	77885	42247	284522

Table 6 - 38. Number of particles in the complete direct gated test bars and test length (see Figure 6 - 1).

Direct gated mould			
		Number of particles	
#	**Code**	**Complete test bar**	**Test length**
1	C1L5DG	5887	1661
2	C1L4DG	20421	8955
3	C1L3DG	13280	5639
4	C1L2DG	7321	2894
5	C1L1DG	2395	987
6	C1R1DG	3194	1273
7	C1R2DG	7424	3048
8	C1R3DG	13613	4740
9	C1R4DG	21558	10014
10	C1R5DG	8557	2379
Total		**103650**	**41590**
Average		**10365**	**4159**
St. Dev.		**6337.5**	**3007.4**

Table 6 - 39. Number of particles in the complete indirect gated test bars and test length (see Figure 6 - 2).

Indirect gated mould			
		Number of particles	
#	**Code**	**Complete test bar**	**Test length**
1	C1L4IG	5479	1659
2	C1L3IG	6213	2151
3	C1L2IG	4602	1485
4	C1L1IG	3813	1132
5	C1R1IG	4571	1384
6	C1R2IG	5990	1812
7	C1R3IG	5608	1942
8	C1R4IG	5971	2047
Total		**42247**	**13612**
Average		**5280.9**	**1701.5**
St. Dev.		**799.5**	**328.9**

Table 6 - 40. Average number of particles in the test length and average UBS as a function of test bar pair and position for the direct gated test bars (see Figure 6 - 1). Note: The UBS values have to be multiplied by a factor of 1.371.

Test bar pair	Average number of particles in the test length	Test bar with minimum 'UBS' (MPa)	Test bar with maximum 'UBS' (MPa)	Average 'UBS' (MPa)
L5 and R5	2020	317	353	332
L4 and R4	9484.5	302	324	317
L3 and R3	5189.5	265	335	319
L2 and R2	2971	316	338	327
L1 and R1	1130	297	340	325

Table 6 - 41. Average number of particles in the test length and average UBS as a function of test bar pair and position for the indirect gated test bars (see Figure 6 - 2). Note: The UBS values have to be multiplied by a factor of 1.371.

Test bar pair	Average number of particles in the test length	Test bar with minimum 'UBS' (MPa)	Test bar with maximum 'UBS' (MPa)	Average 'UBS' (MPa)
L4 and R4	1853	327	356	343
L3 and R3	2046.5	347	370	352
L2 and R2	1648.5	331	357	343
L1 and R1	1258	338	349	345

6.5 Figures

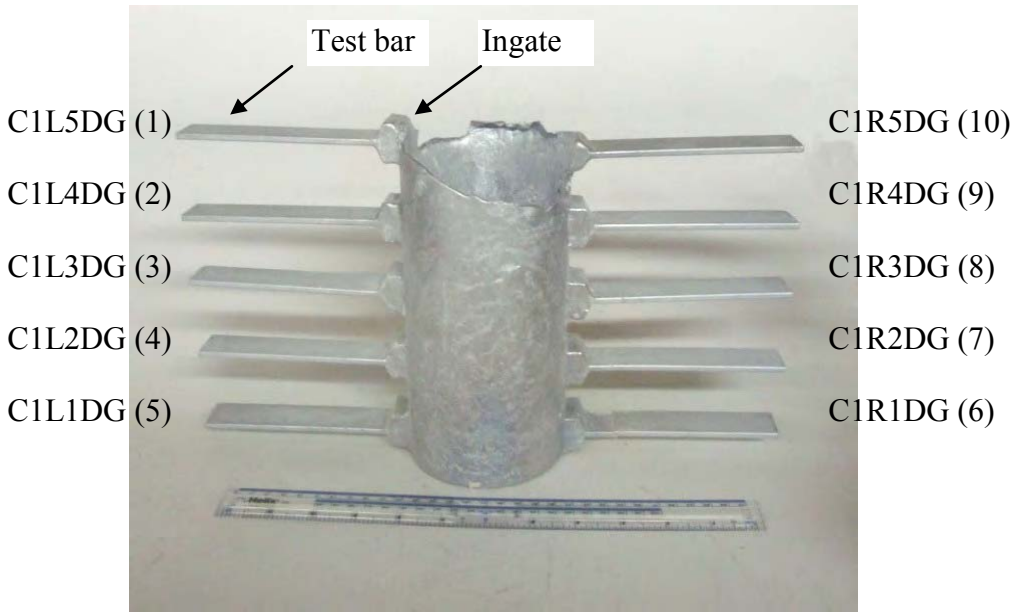

Figure 6 - 1. Experimental casting of direct gating mould design. The test bars were identified according to the code shown.

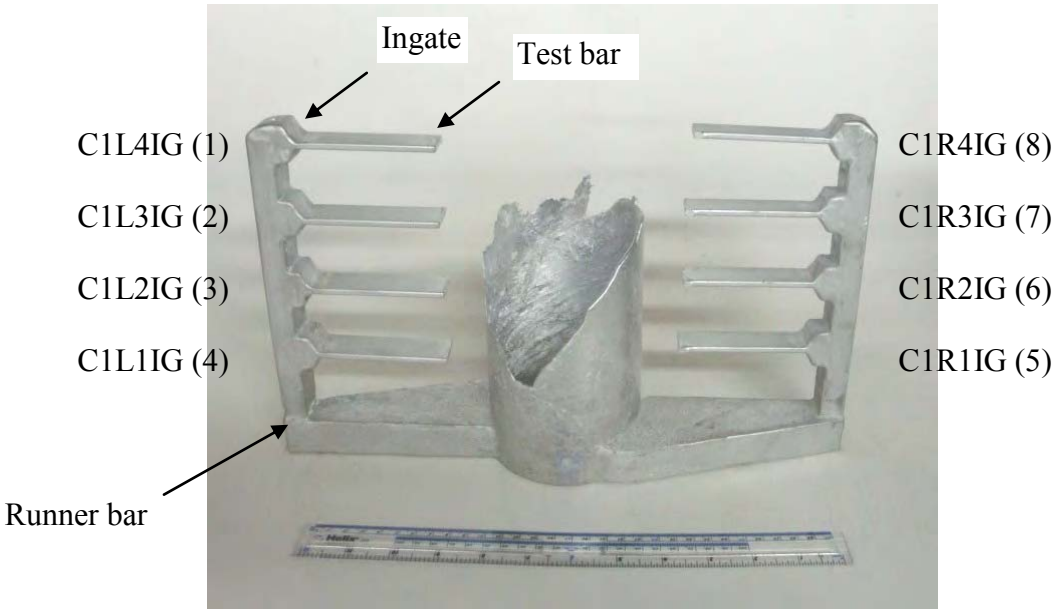

Figure 6 - 2. Experimental casting of indirect gating mould design. The test bars were identified according to the code shown.

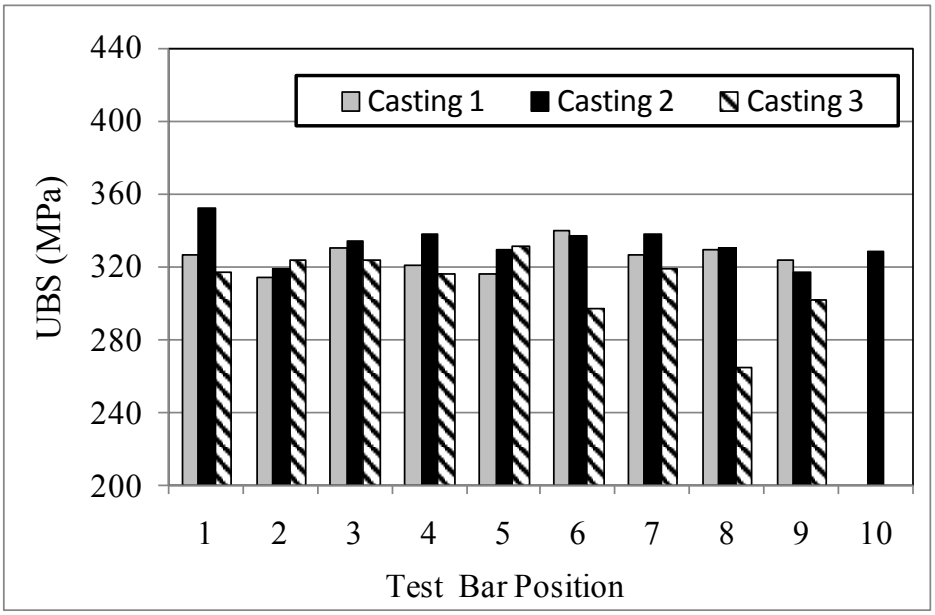

Figure 6 - 3. Ultimate bend strength 'UBS' data organized by casting and individual test bar position for the direct gated mould design (see Figure 6 - 1). Note: These values have to be multiplied by a factor of 1.371.

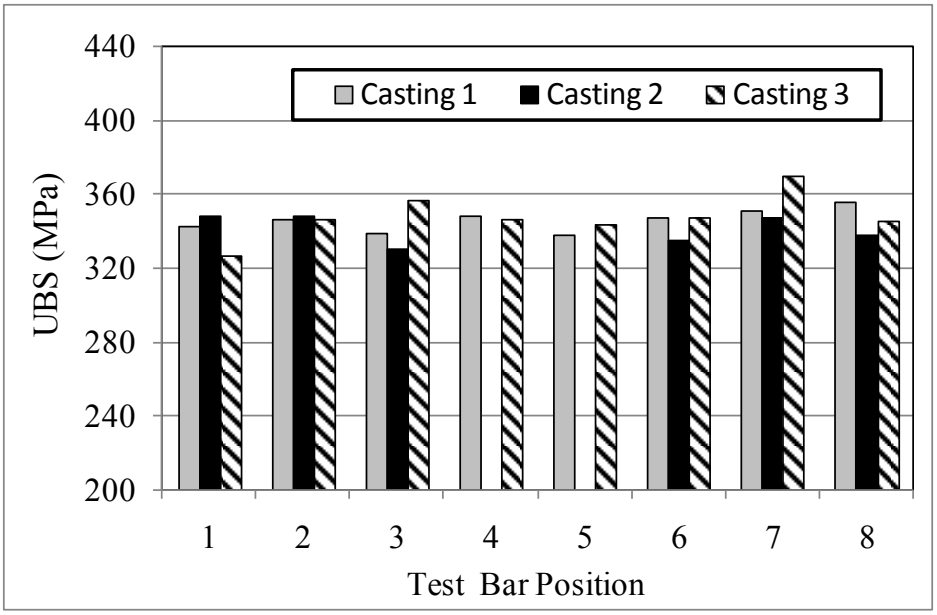

Figure 6 - 4. Ultimate bend strength 'UBS' data organized by casting and individual test bar position for the indirect gated mould design (see Figure 6 - 2). Note: These values have to be multiplied by a factor of 1.371.

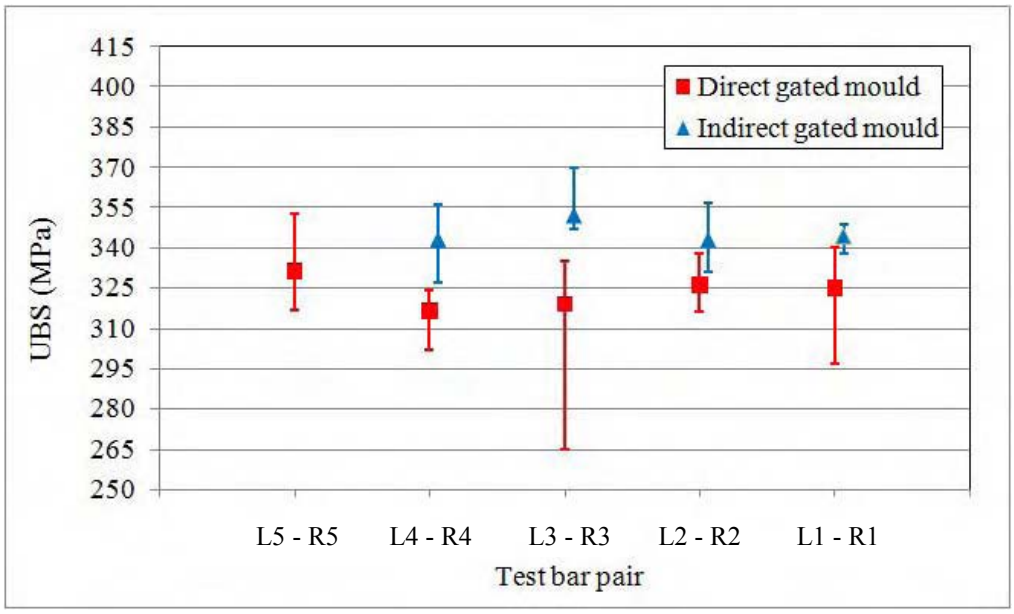

Figure 6 - 5. Ultimate bend strength 'UBS' data of both gating systems as a function of position. Each point is the average of up to 6 bars (see Figure 6 - 1 and Figure 6 - 2). Note: These values have to be multiplied by a factor of 1.371.

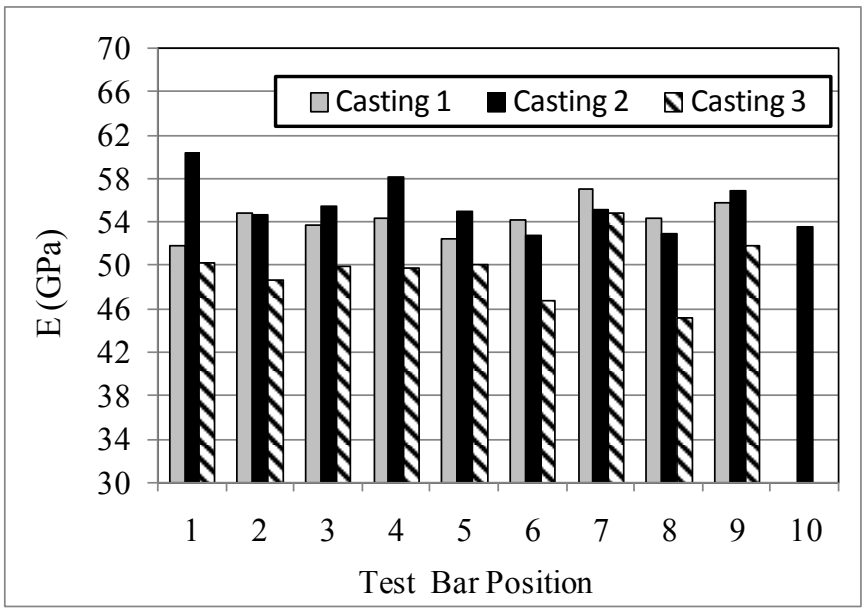

Figure 6 - 6. Modulus of elasticity 'E' data organized by casting and individual test bar position for the direct gated mould design (see Figure 6 - 1).

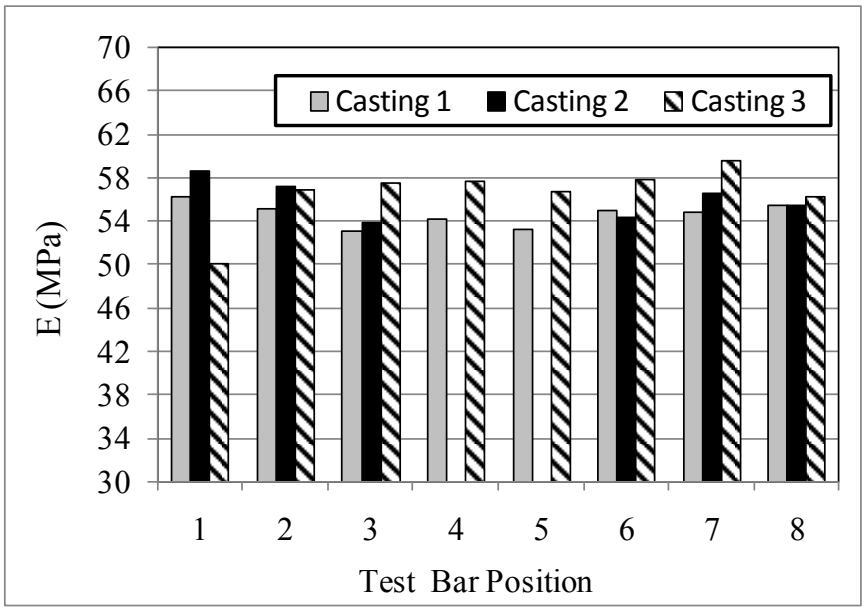

Figure 6 - 7. Modulus of elasticity 'E' data organized by casting and individual test bar position for the indirect gated mould design (see Figure 6 - 2).

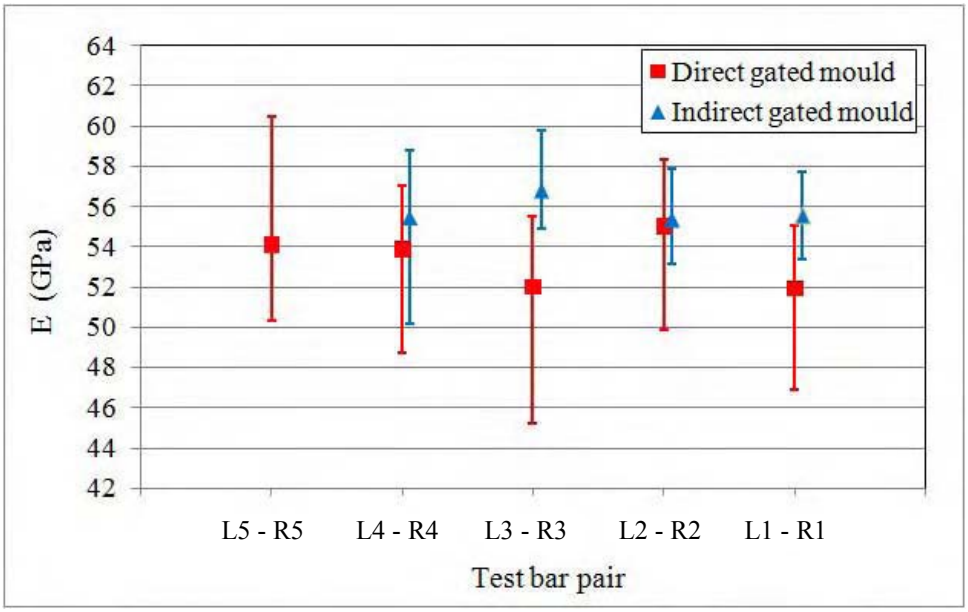

Figure 6 - 8. Modulus of elasticity 'E' data of both gating systems as a function of position. Each point is the average of up to 6 bars (see Figure 6 - 1 and Figure 6 - 2.

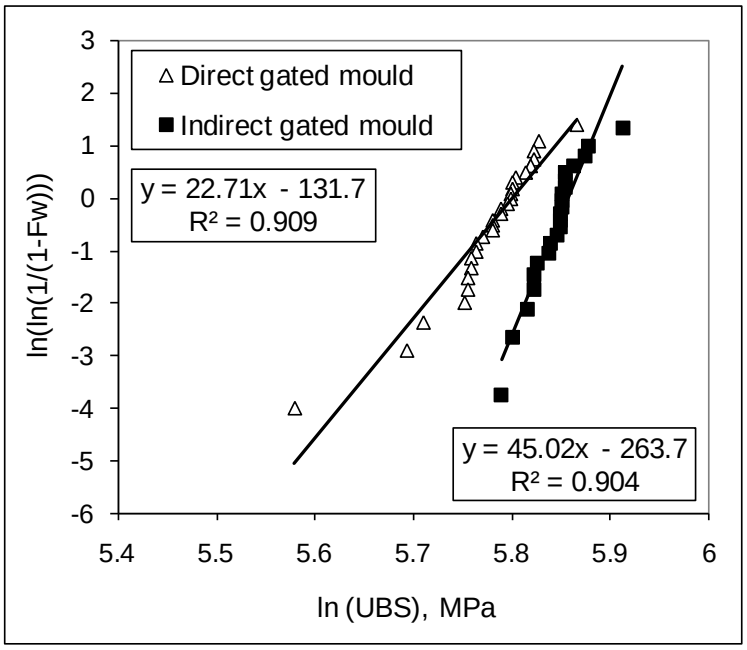

Figure 6 - 9. Weibull plot of ultimate bend strength 'UBS' for both gating systems.

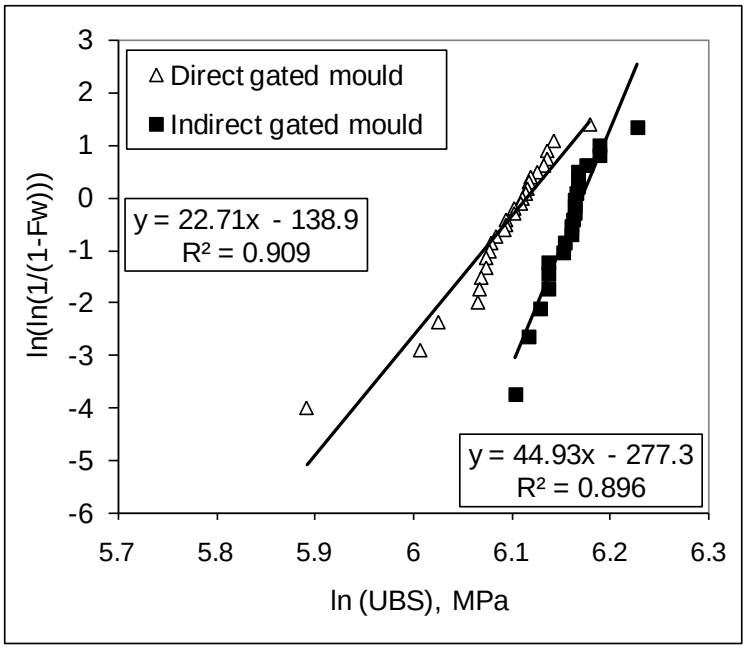

Figure 6 - 10. Weibull plot of ultimate bend strength 'UBS' for both gating systems, which was obtained using the correction factor of 1.371.

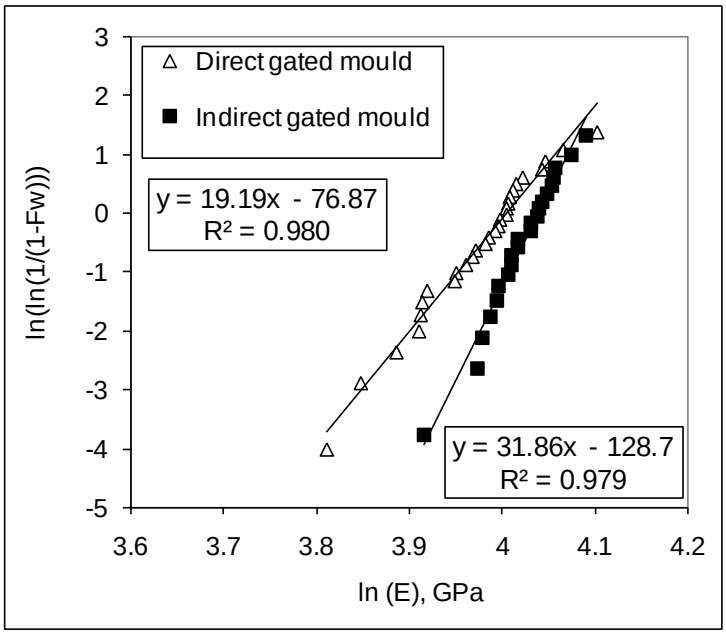

Figure 6 - 11.Weibull plot of modulus of elasticity 'E' for both gating systems.

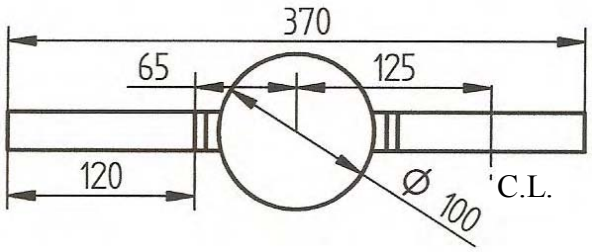

(a)

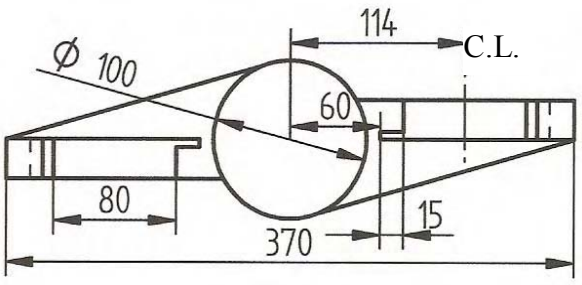

(b)

Figure 6 - 12. Plan views of (a) direct and (b) indirect gating mould designs used for producing centrifugally cast aluminium test bars; all dimensions in mm (see Figure 4 - 1)

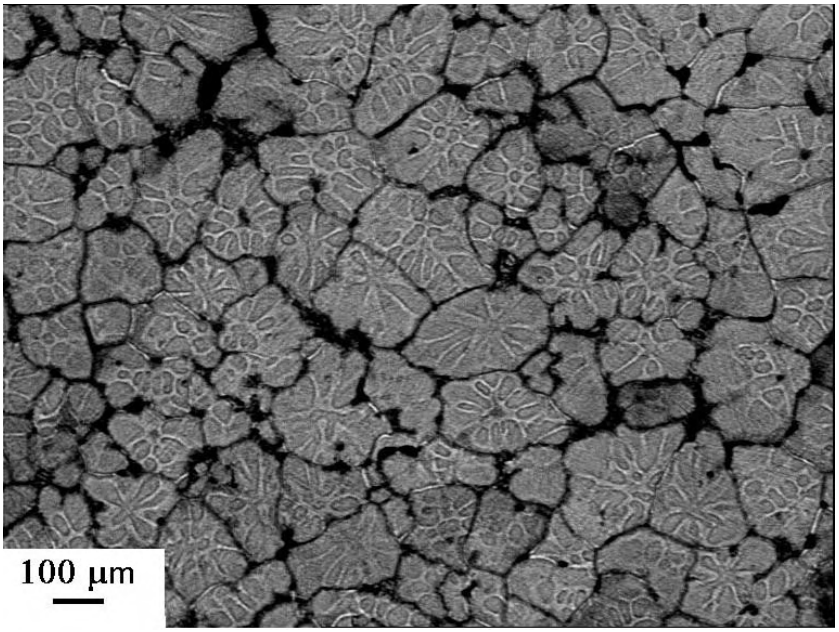

Figure 6 - 13. Microstructure after heat treatment (T6) showing dendrite morphology and grain boundaries of direct gated cast sample (C1L2DG).

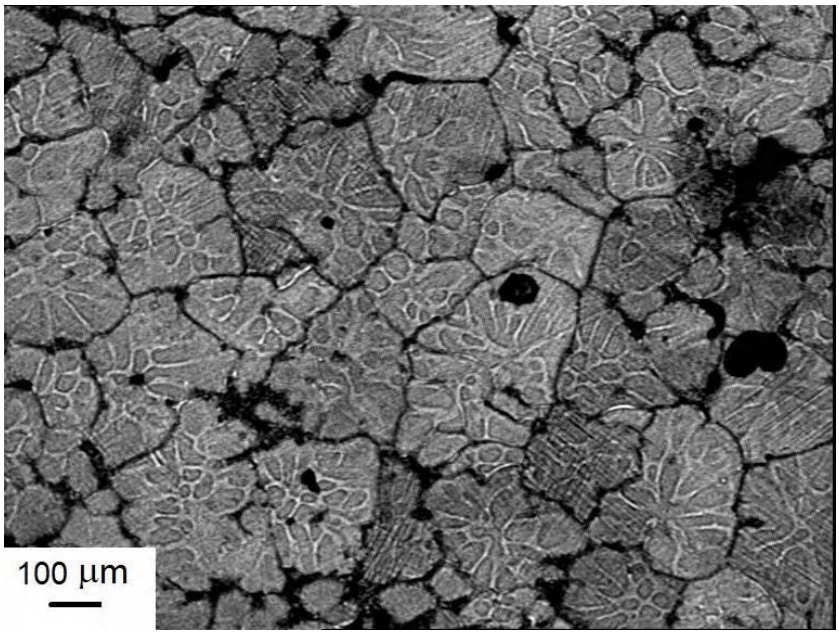

Figure 6 - 14. Microstructure after heat treatment (T6) showing dendrite morphology and grain boundaries of indirect gated cast samples (C1L1IG).

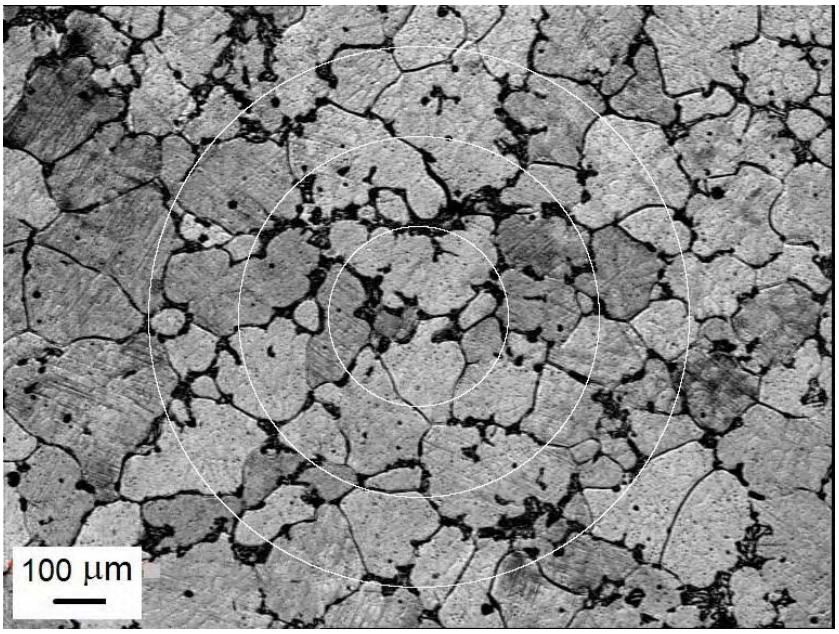

Figure 6 - 15. Microstructure after heat treatment (T6) showing grain boundaries and the Abrams three circles (ASTM, 2004) of direct gated cast sample (C1L2DG).

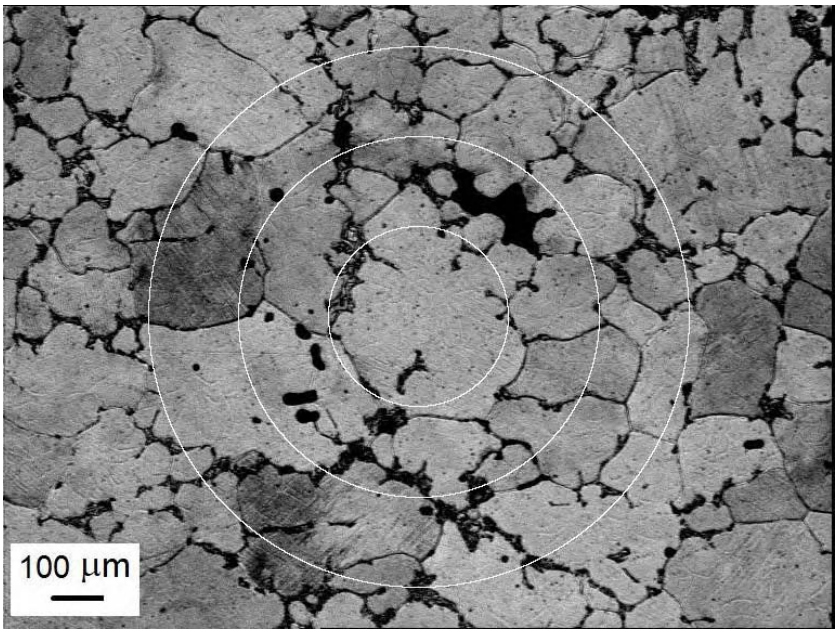

Figure 6 - 16. Microstructure after heat treatment (T6) showing grain boundaries and the Abrams three circles (ASTM, 2004) of indirect gated cast sample (C1L1IG).

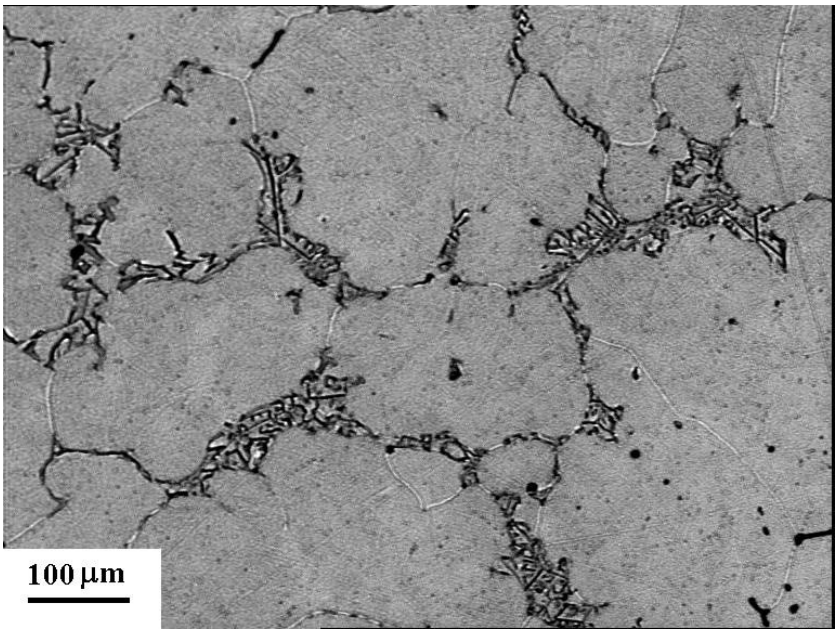

Figure 6 - 17. Microstructure after heat treatment (T6) showing α-Al matrix and $Al_{15}(FeMn)_3Si$ intermetallic particles (direct gated sample, C1R2DG).

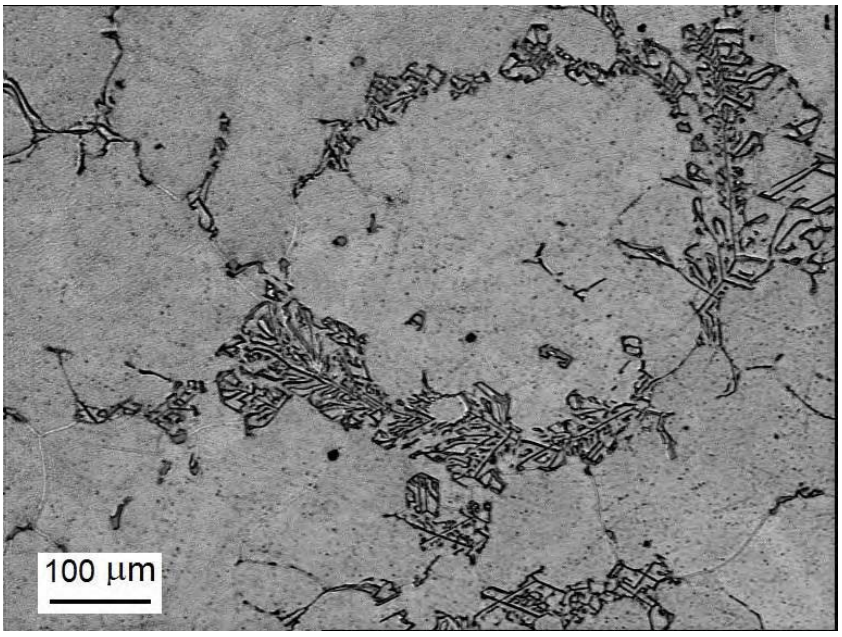

Figure 6 - 18. Microstructure after heat treatment (T6) showing α-Al matrix and $Al_{15}(FeMn)_3Si$ intermetallic particles (indirect gated sample, C1L1IG).

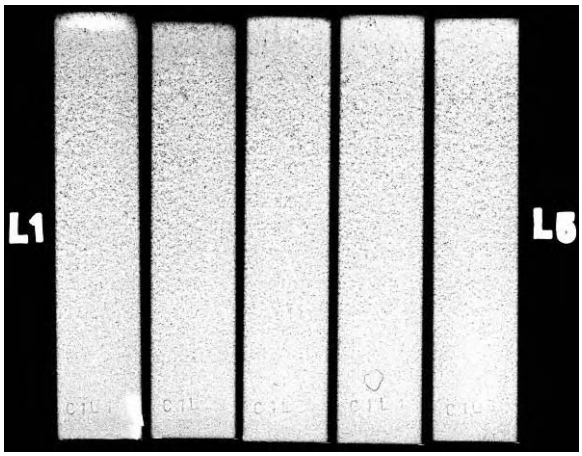

(a) Casting 1. Left test bars

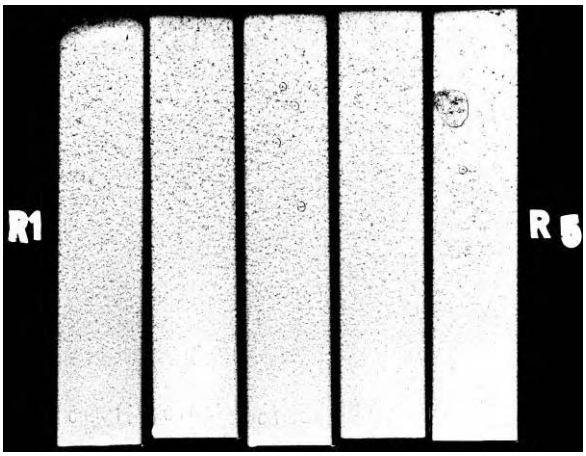

(b) Casting 1. Right test bars

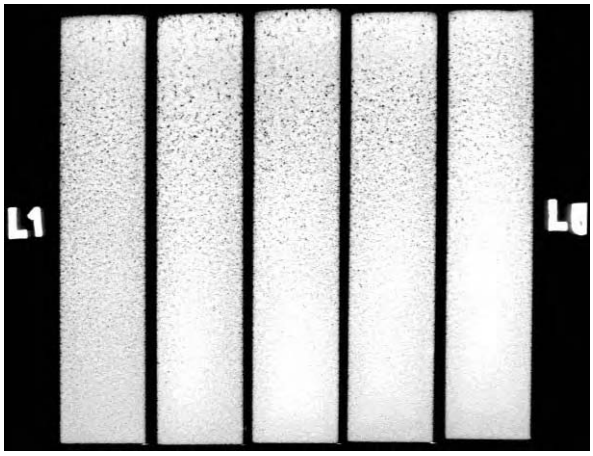

(c) Casting 2. Left test bars

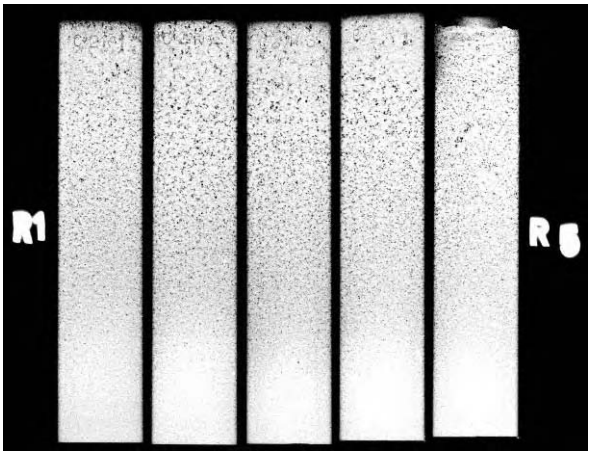

(d) Casting 2. Right test bars

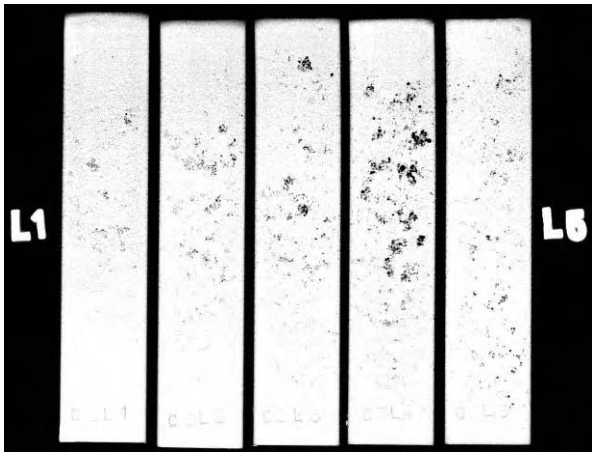

(e) Casting 3. Left test bars

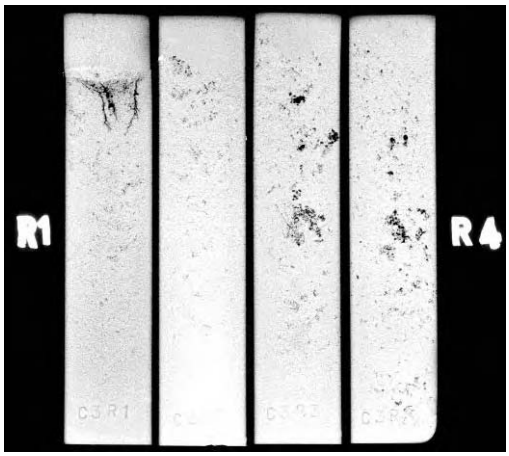

(f) Casting 3. Right test bars

Figure 6 - 19. X-Ray images of the direct gated test bars obtained from three cast moulds with a resolution of 300 pixels/in. The ingate was located at the top of each test bar.

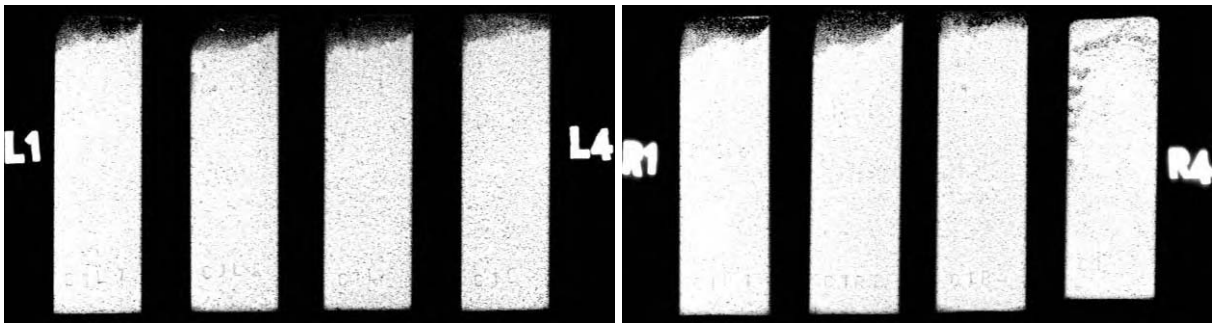

(a) Casting 1. Left test bars (b) Casting 1. Right test bars

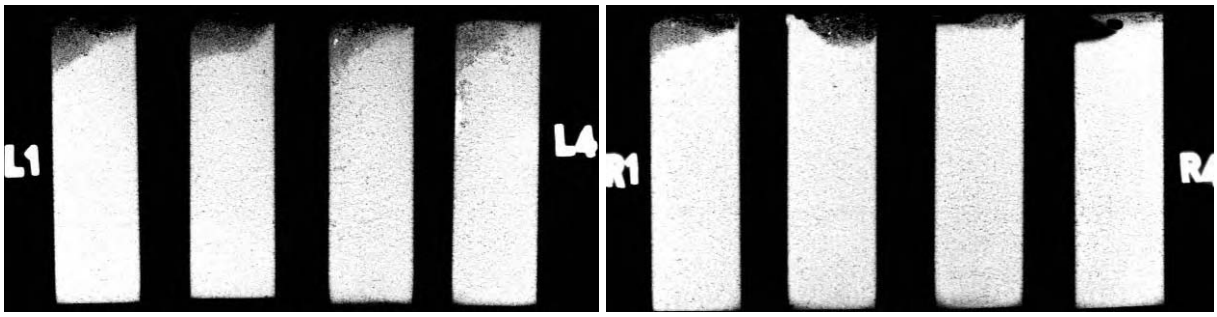

(c) Casting 2. Left test bars (d) Casting 2. Right test bars

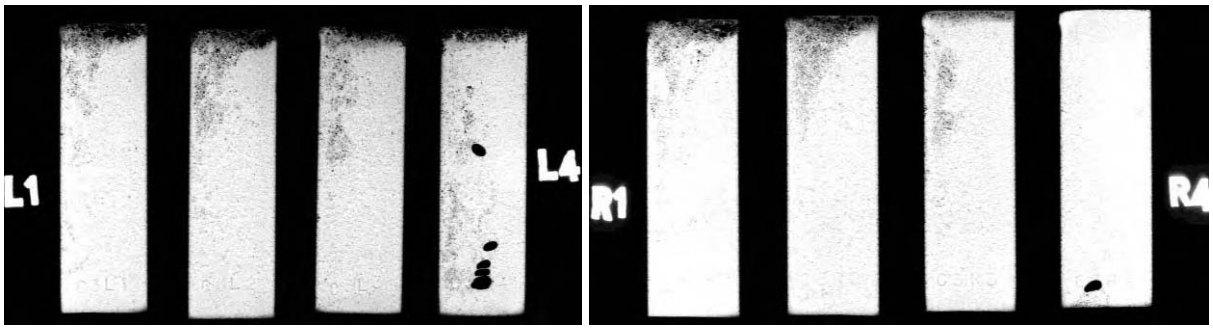

(e) Casting 3. Left test bars (f) Casting 3. Right test bars

Figure 6 - 20. X-Ray images of the indirect gated test bars obtained from three cast moulds with a resolution of 300 pixels/in. The ingate was located at the bottom of each test bar.

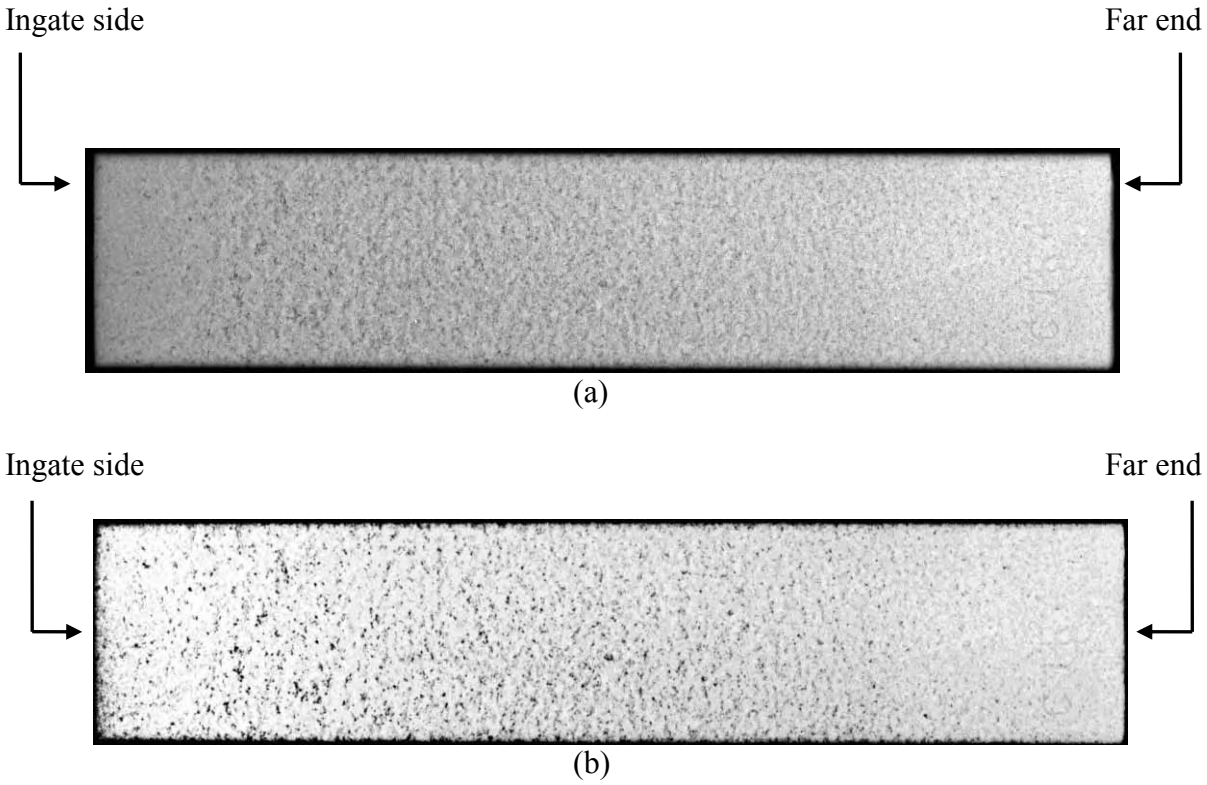

Figure 6 - 21. X-ray images of direct gated test bar with resolution of 600 pixels/in (a) standard scan and (b) optimized image, which clearly reveals more details (C1R4DG).

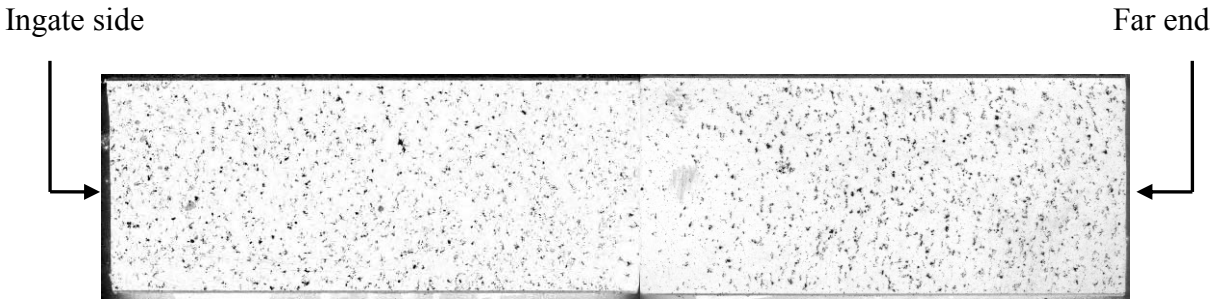

Figure 6 - 22. Direct gated cast bar in the as-polished condition showing microporosity (C1R4DG). This sample was split into two to facilitate the metallographic preparation.

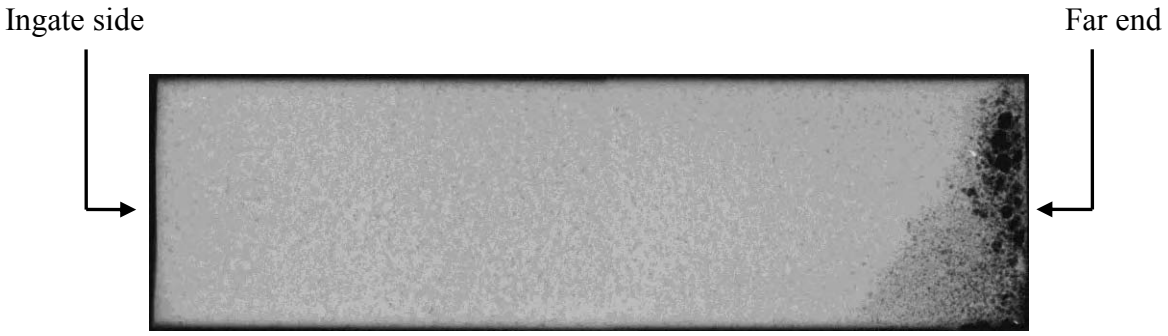

(a)

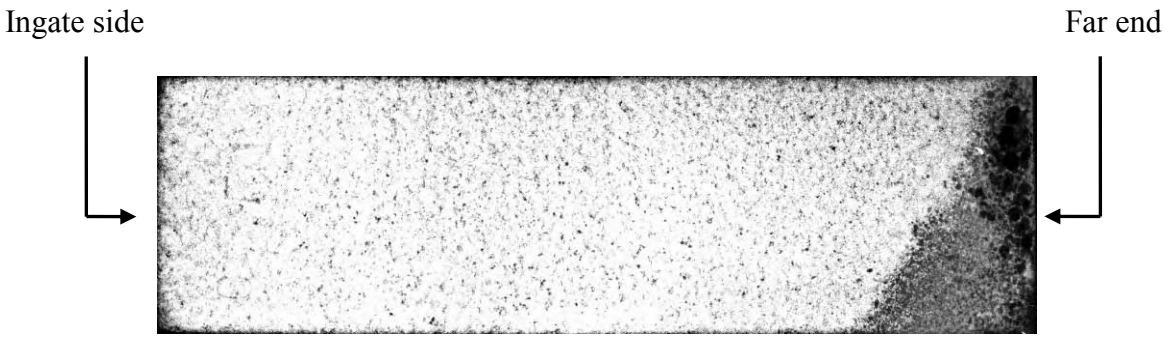

(b)

Figure 6 - 23.X-ray image of indirect gated test bar with resolution of 600 pixels/in (a) standard scan and (b) optimized image, which clearly reveals more details (C2L1IG).

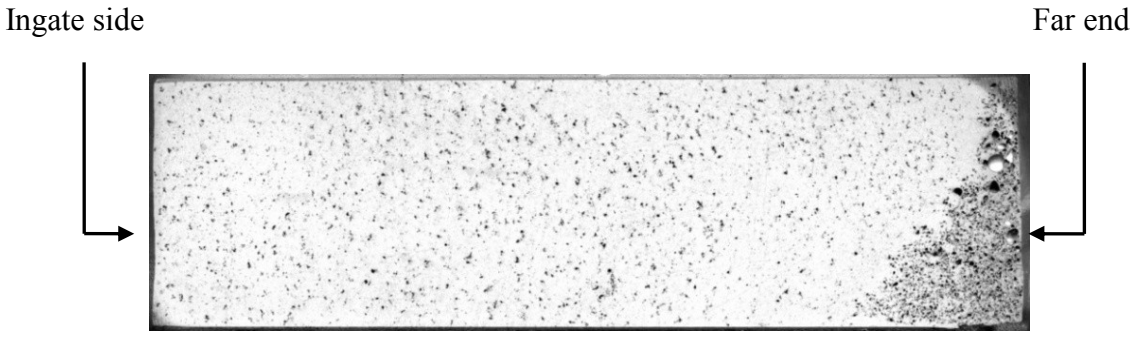

Figure 6 - 24. Indirect gated cast bar in the as-polished condition showing microporosity (C2L1IG).

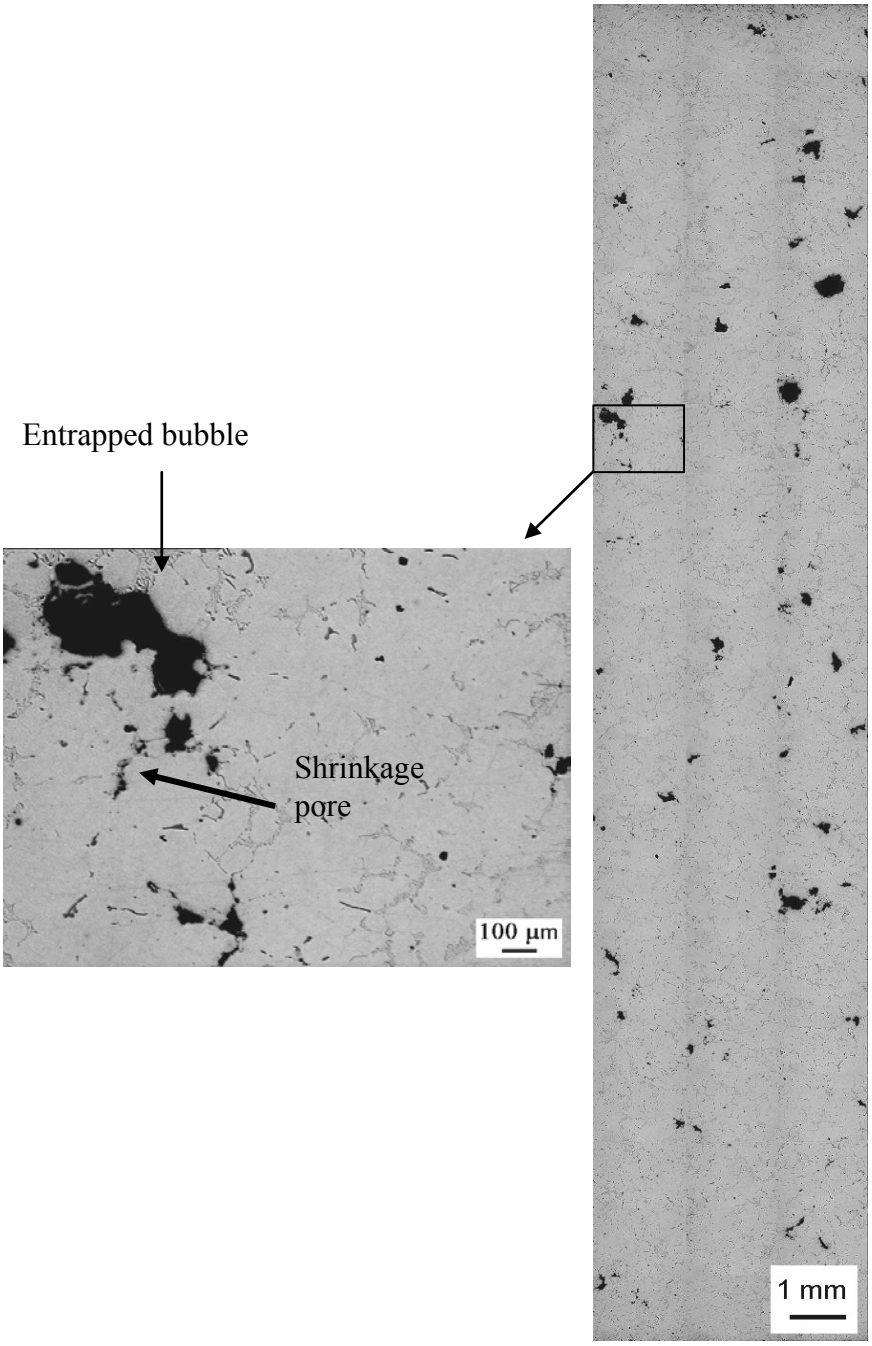

Figure 6 - 25. Digital montage of 60 contiguous micrographs obtained for a direct gated test bar with 'UBS' of 338 MPa and optical micrograph in the as-polished condition with a resolution of 0.47 pixel/µm (C2R2DG).

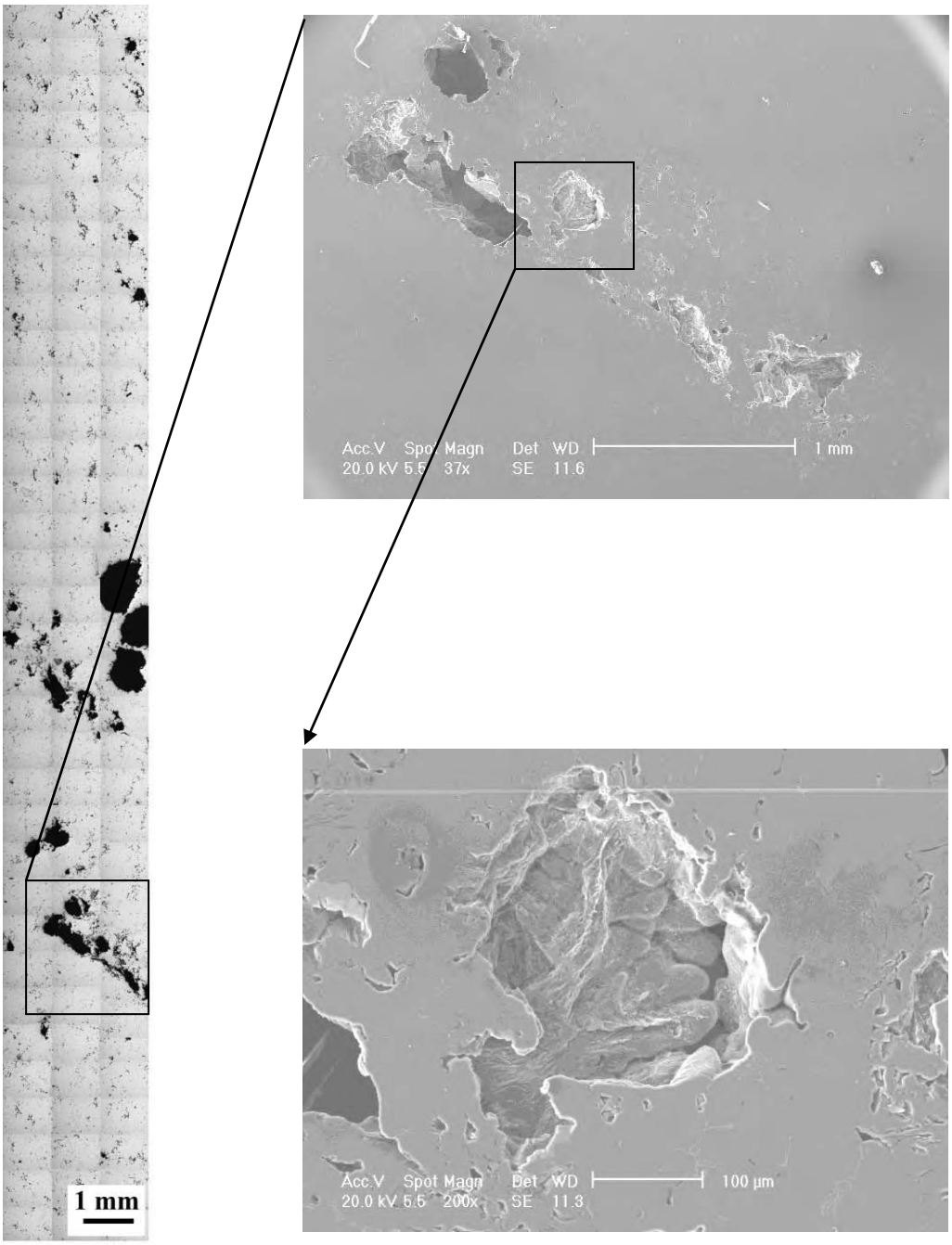

Figure 6 - 26. Digital montage of 102 contiguous micrographs obtained for a direct gated test bar with 'UBS' of 265 MPa and SEM micrographs showing close-up of defects (C3R3DG).

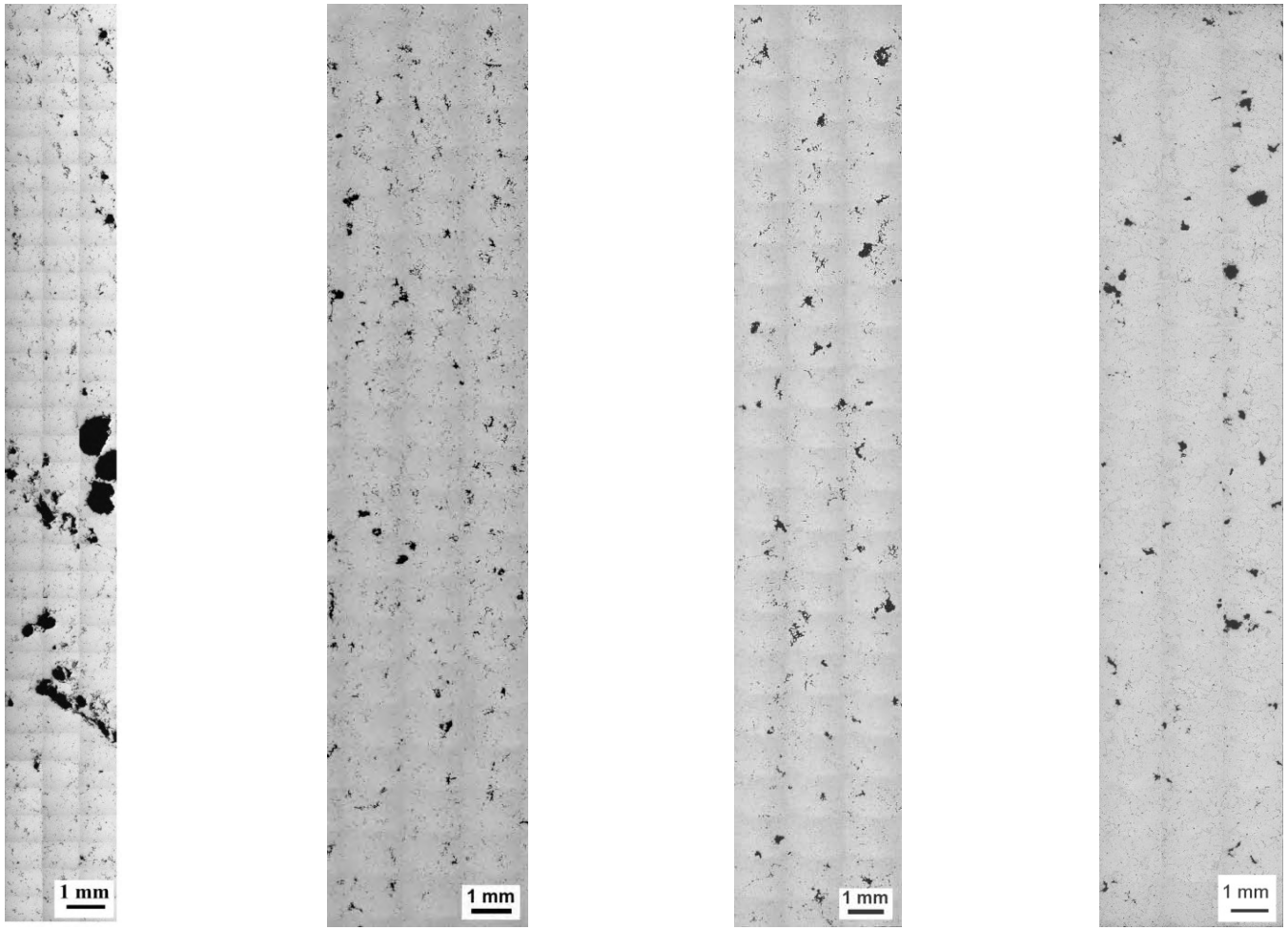

(a) (b) (c) (d)

Figure 6 - 27. Digital montages of contiguous micrographs obtained for direct gated cast specimens with different UBS (a) 265 MPa ‘C3R3DG’, (b) 302 MPa ‘C3R4DG’ (c) 327 MPa ‘C1R2DG’and (d) 338 MPa ‘C2R2DG’.

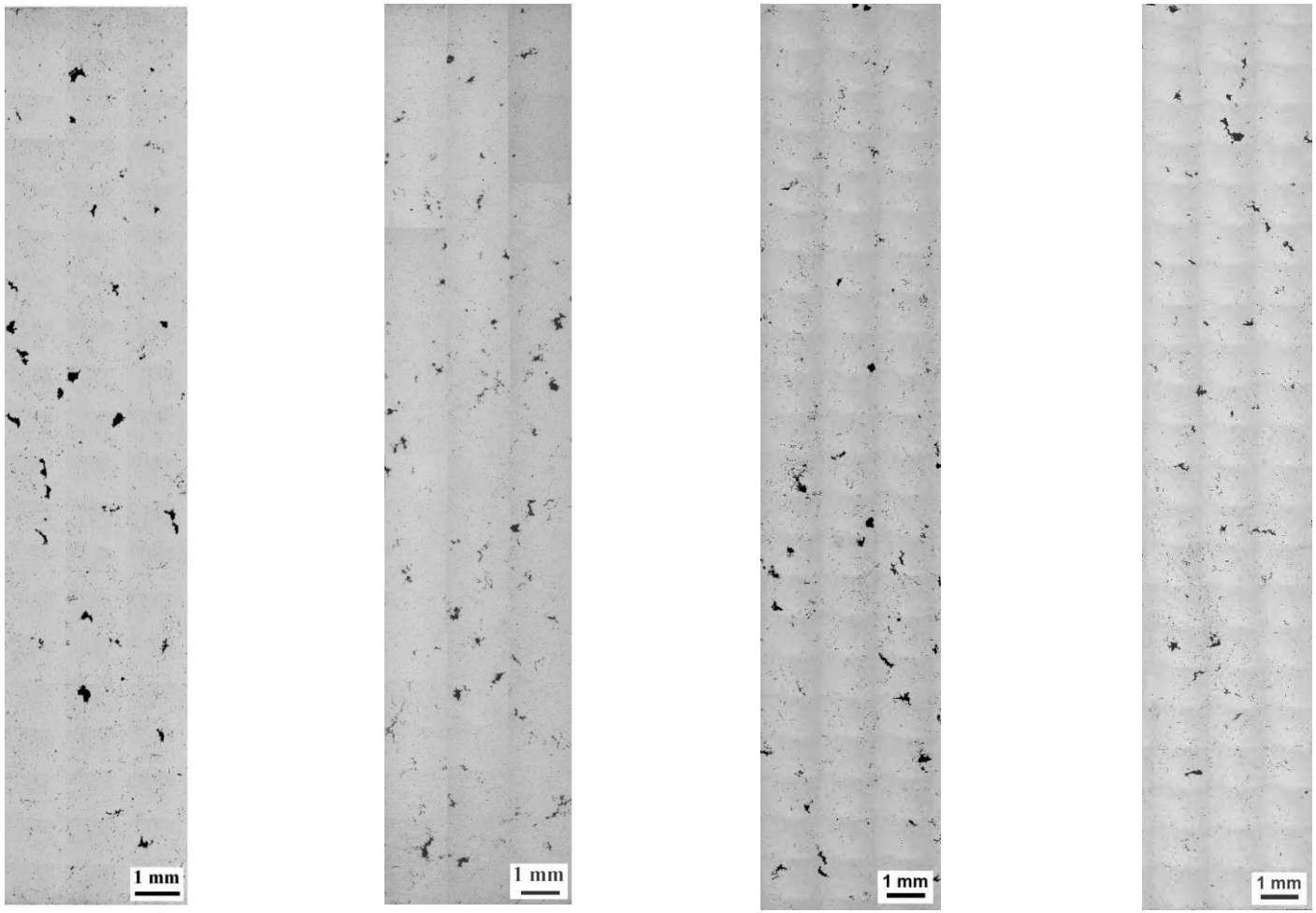

(a) (b) (c) (d)

Figure 6 - 28. Digital montages of contiguous micrographs obtained for indirect gated cast specimens with different UBS (a) 338 MPa 'C1R1IG', (b) 347 MPa 'C1L3IG' (c) 349 MPa 'C1L1IG'and (d) 357 MPa 'C3L2IG'.

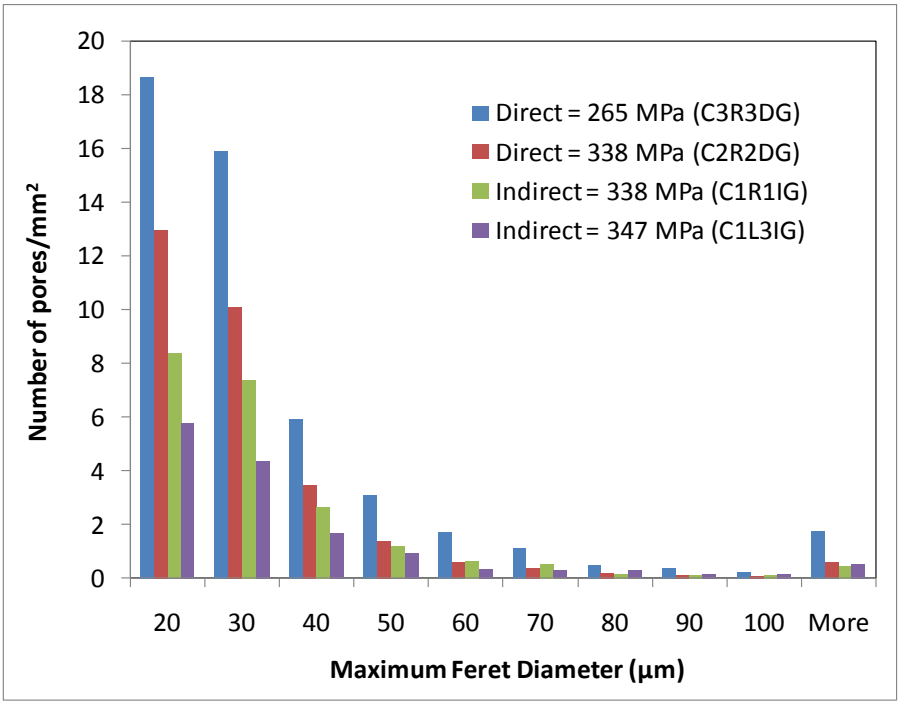

Figure 6 - 29. Frequency histograms of pore size distributions for four selected cast bars from both gating systems. The UBS values and bar codes are shown in the legend.

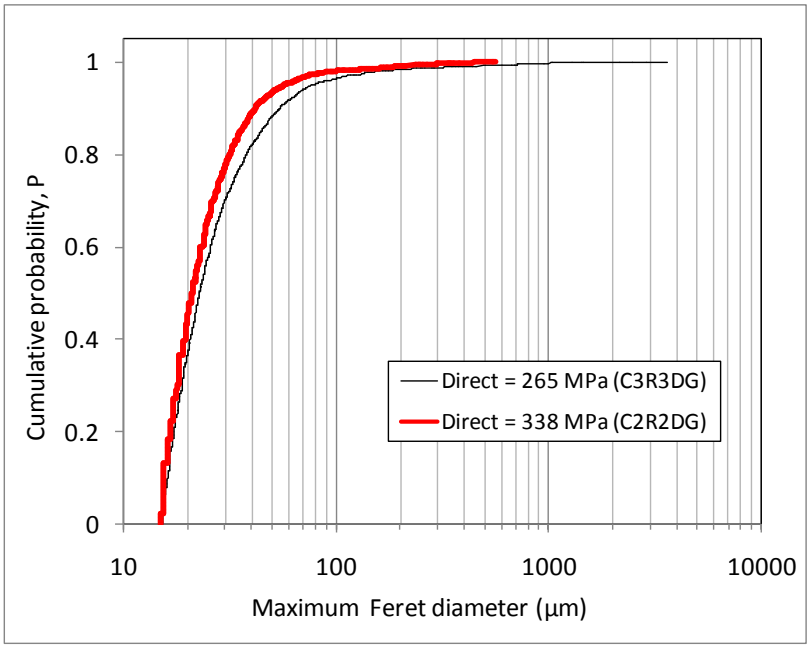

Figure 6 - 30. Cumulative probability plots for the porosity data of direct gated cast bars. The UBS values and bar codes are shown in the legend.

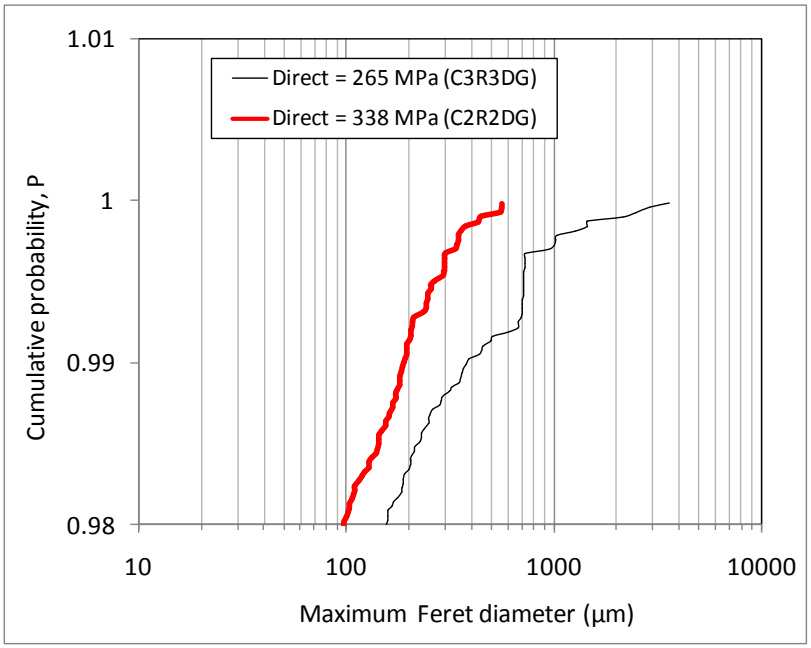

Figure 6 - 31. Zoom of cumulative probability plots for the porosity data of direct gated cast bars. The UBS values and bar codes are shown in the legend.

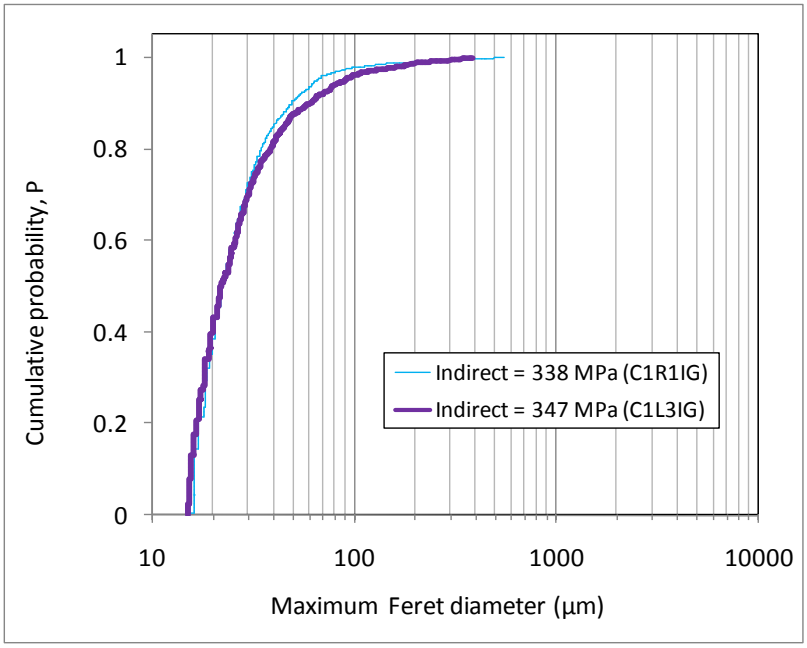

Figure 6 - 32. Cumulative probability plots for the porosity data of indirect gated cast bars. The UBS values and bar codes are shown in the legend.

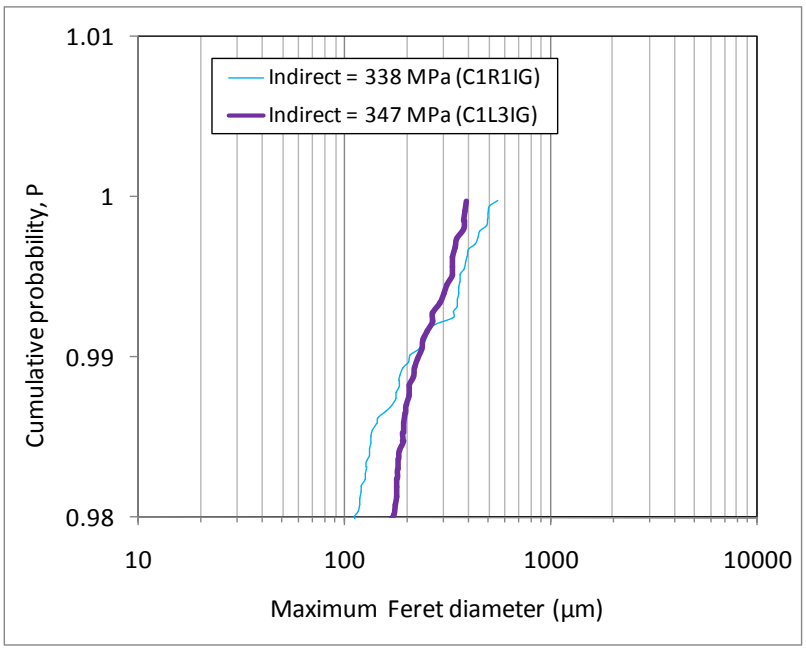

Figure 6 - 33. Zoom of cumulative probability plots for the porosity data of indirect gated cast bars. The UBS values and bar codes are shown in the legend.

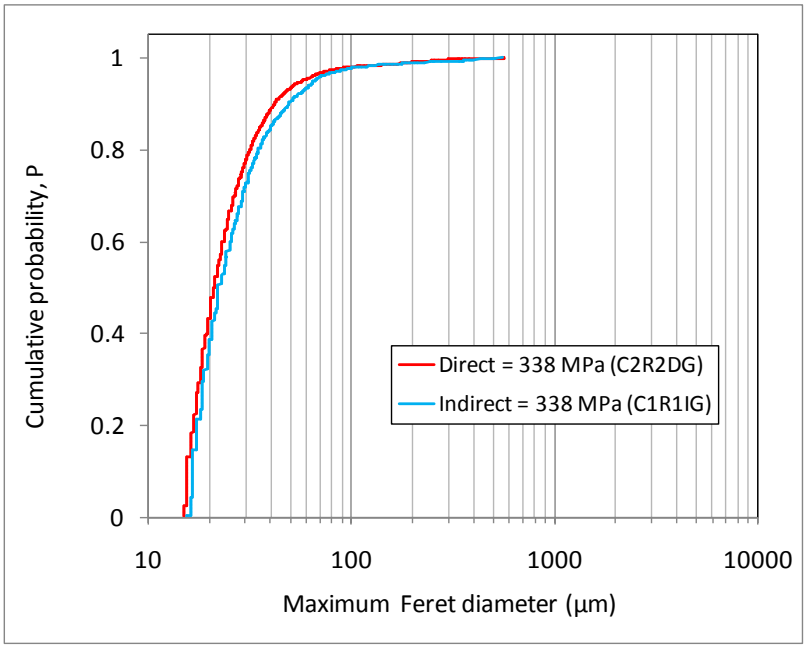

Figure 6 - 34. Cumulative probability plots for the porosity data of direct and indirect gated cast bars with equal UBS. The UBS values and bar codes are shown in the legend.

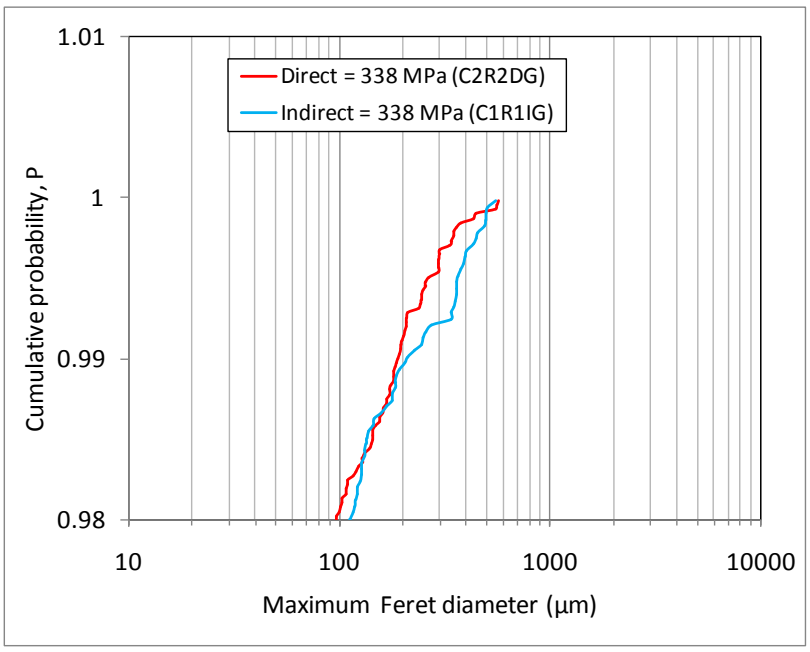

Figure 6 - 35. Zoom of cumulative probability plots for the porosity data of direct and indirect gated cast bars. The UBS values and bar codes are shown in the legend.

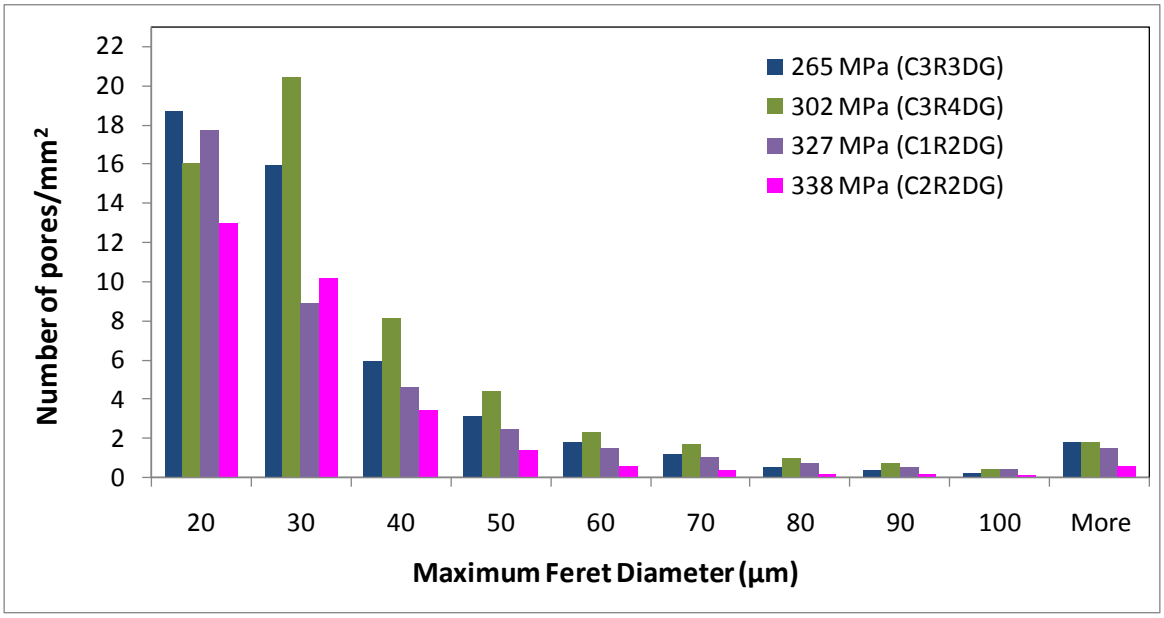

Figure 6 - 36. Frequency histograms of pore size distribution for direct gated cast bars. The UBS values and bar codes are shown in the legend.

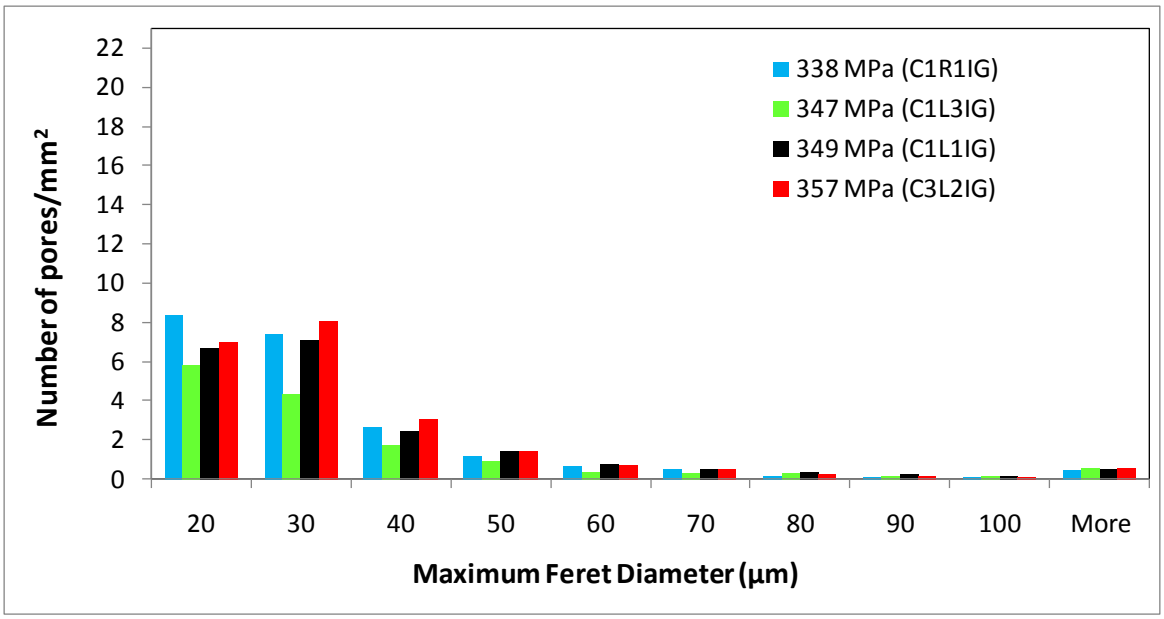

Figure 6 - 37. Frequency histograms of pore size distribution for indirect gated cast bars. The UBS values and bar codes are shown in the legend.

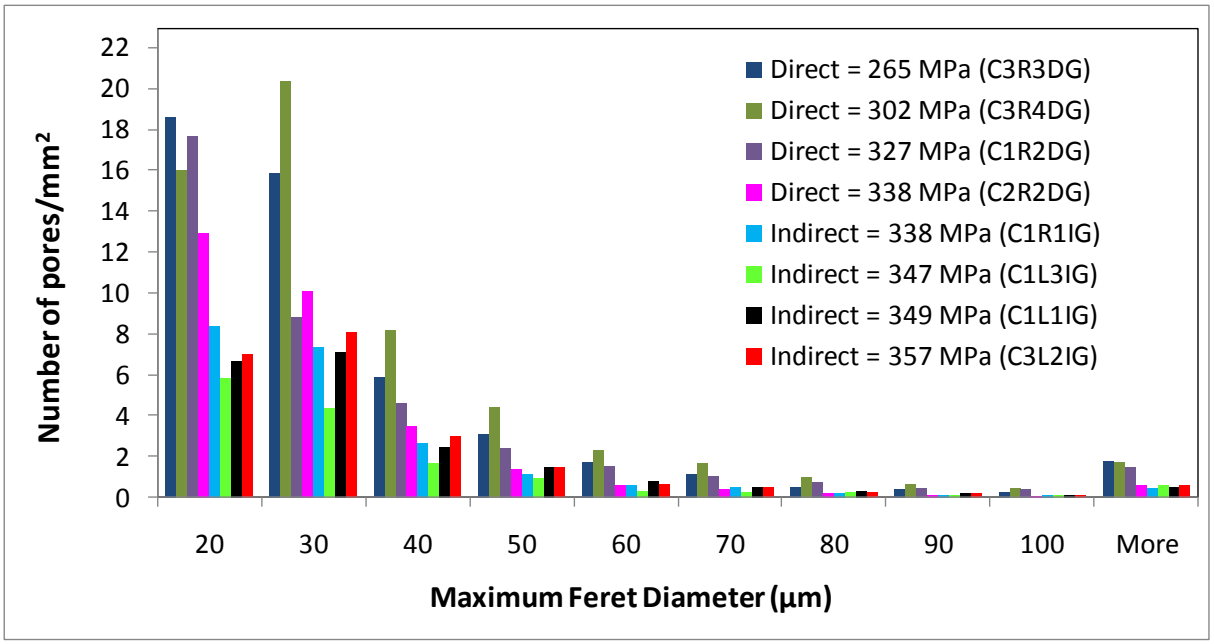

Figure 6 - 38. Frequency histograms of pore size distribution for direct and indirect gated cast bars. The UBS values and bar codes are shown in the legend.

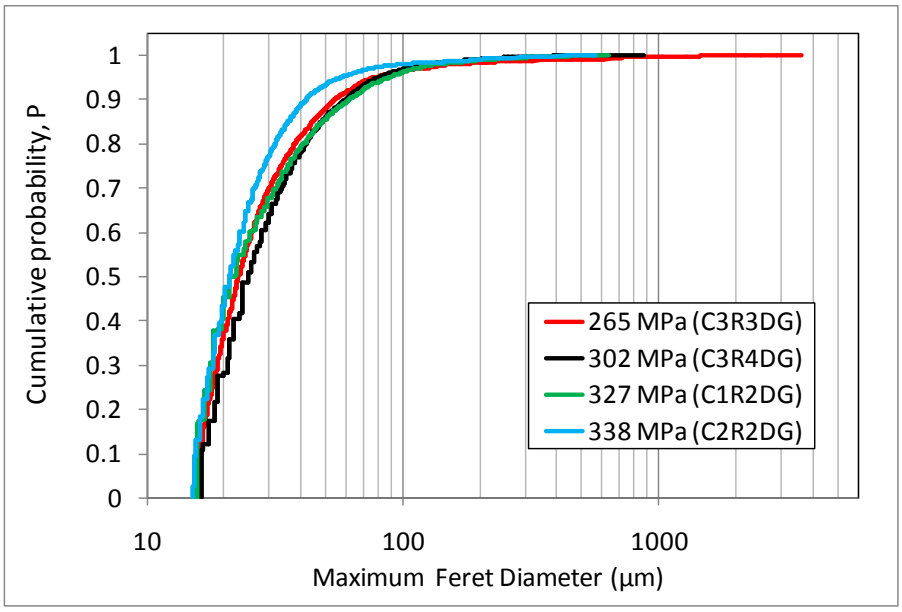

Figure 6 - 39. Cumulative probability plots for the porosity data of direct gated cast bars. The UBS values and bar codes are shown in the legend.

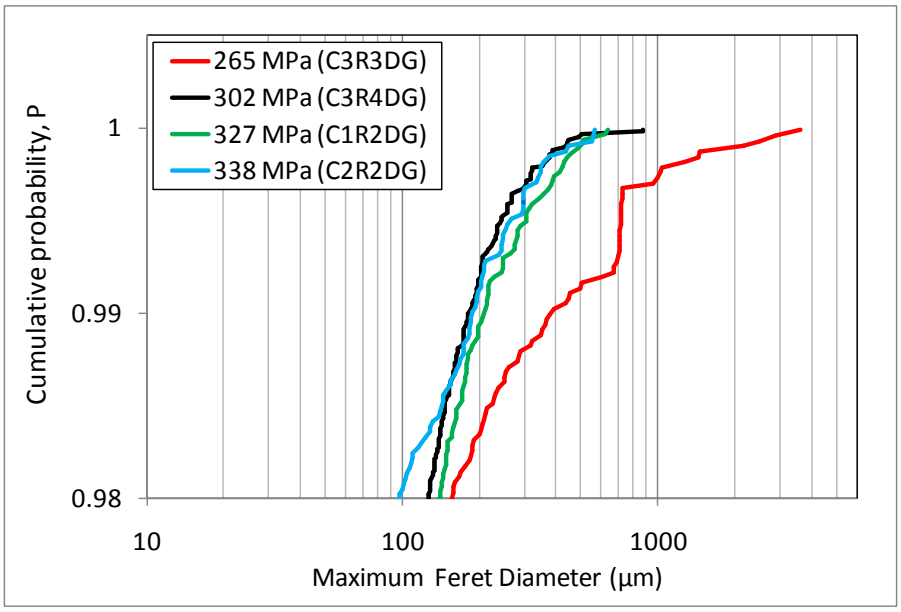

Figure 6 - 40. Zoom of cumulative probability plots for the porosity data of direct gated cast bars. The UBS values and bar codes are shown in the legend.

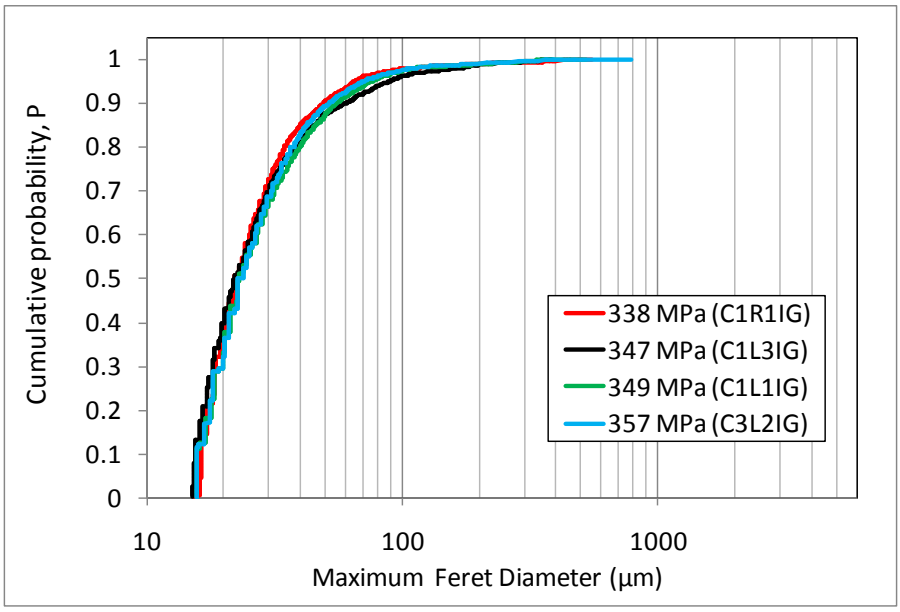

Figure 6 - 41. Cumulative probability plots for the porosity data of indirect gated cast bars. The UBS values and bar codes are shown in the legend.

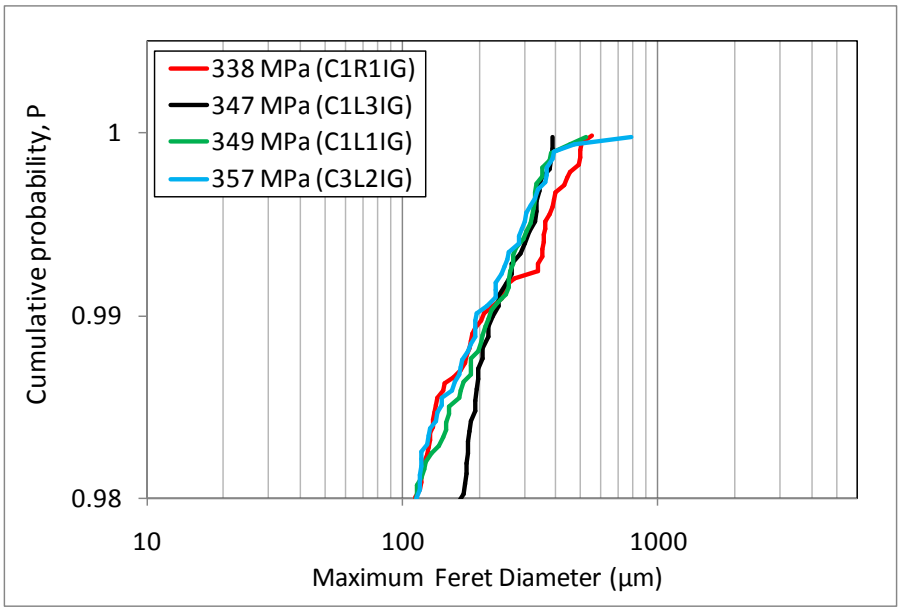

Figure 6 - 42. Zoom of cumulative probability plots for the porosity data of indirect gated cast bars. The UBS values and bar codes are shown in the legend.

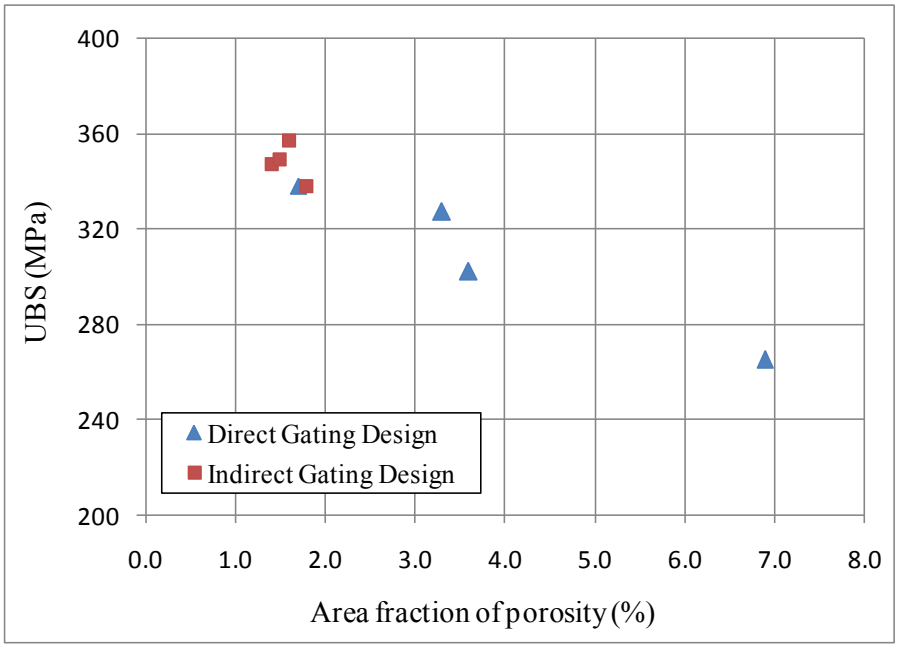

Figure 6 - 43. Ultimate bend strength 'UBS' as a function of area fraction of porosity (%) for direct and indirect gating designs.

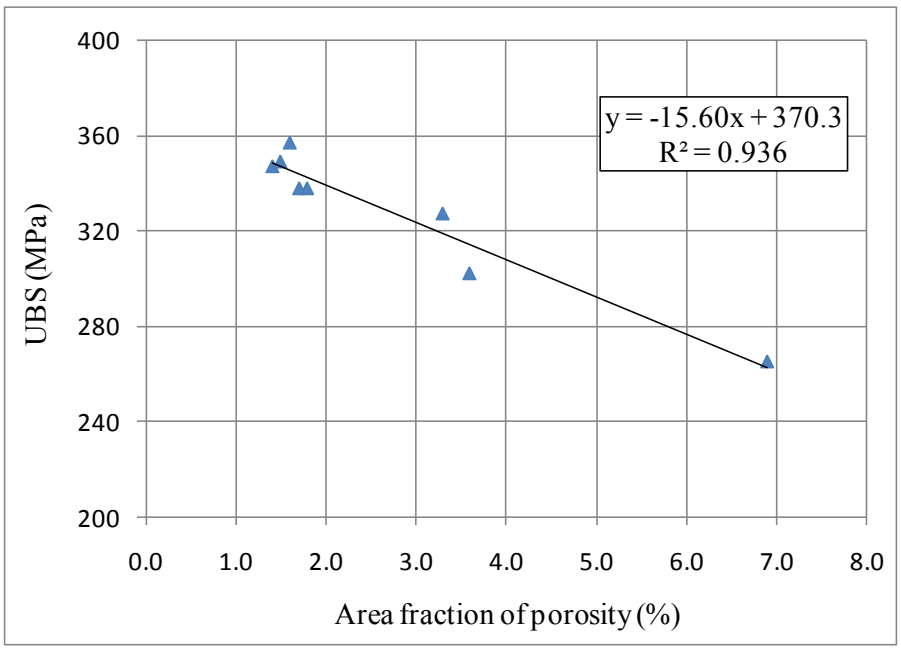

Figure 6 - 44. Ultimate bend strength 'UBS' as a function of area fraction of porosity (%) for the combined data obtained from direct and indirect gating designs.

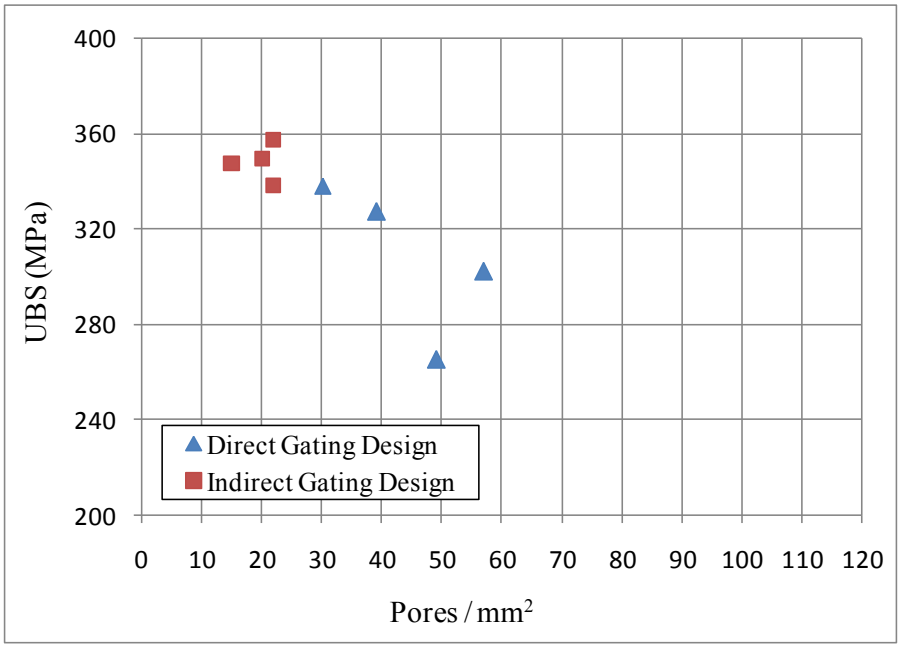

Figure 6 - 45. Ultimate bend strength 'UBS' as a function of porosity density for direct and indirect gating designs.

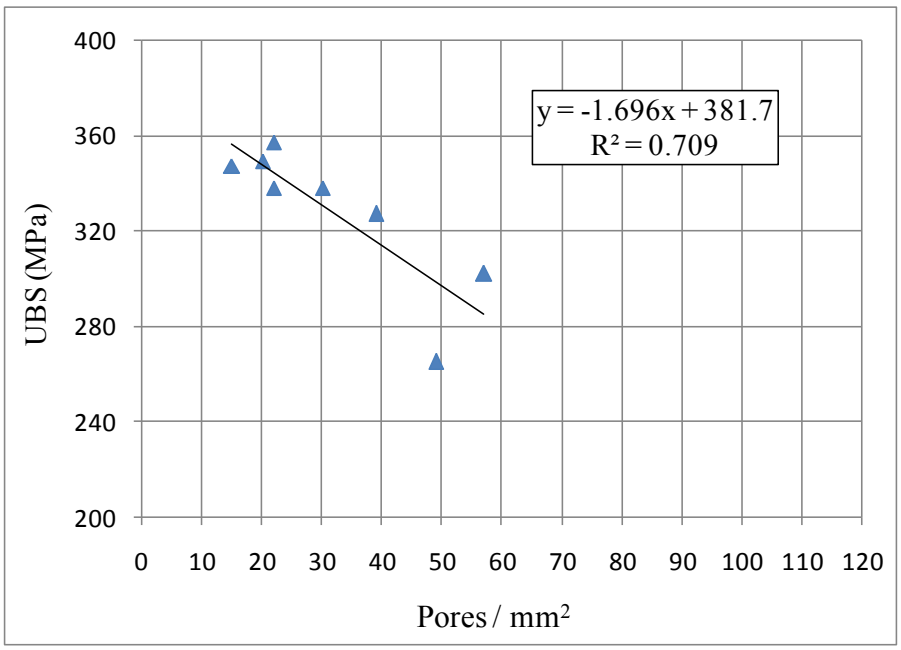

Figure 6 - 46. Ultimate bend strength 'UBS' as a function of porosity density for the combined data obtained from direct and indirect gating designs.

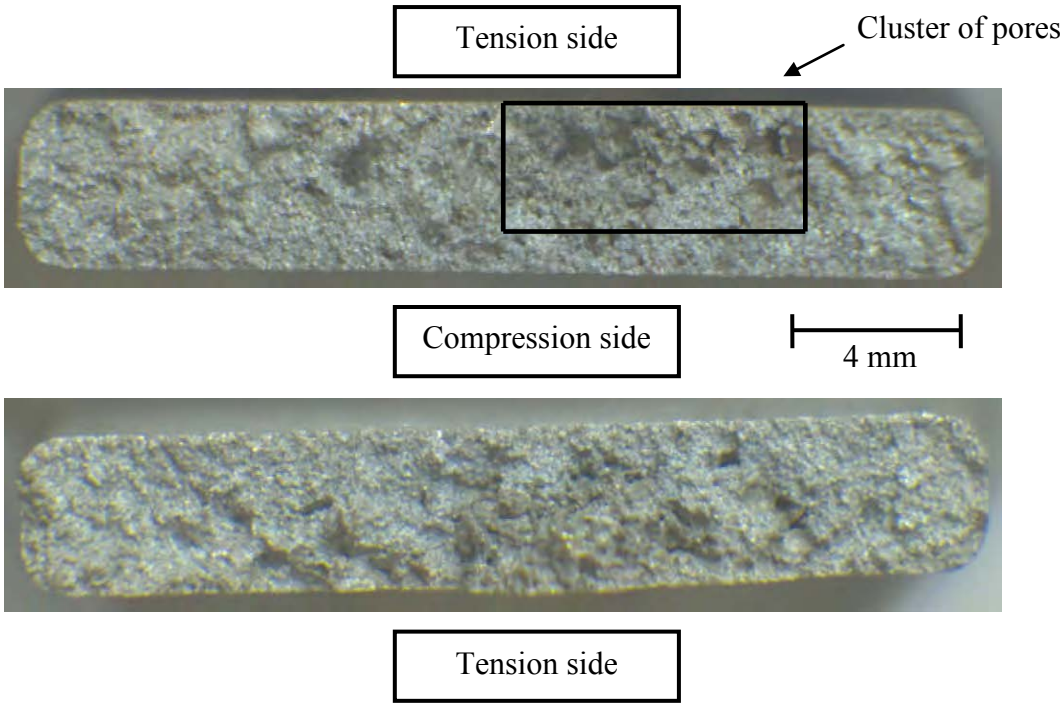

Figure 6 - 47. Macrophotographs of direct gated test bar, C3R3DG (UBS = 265 MPa).

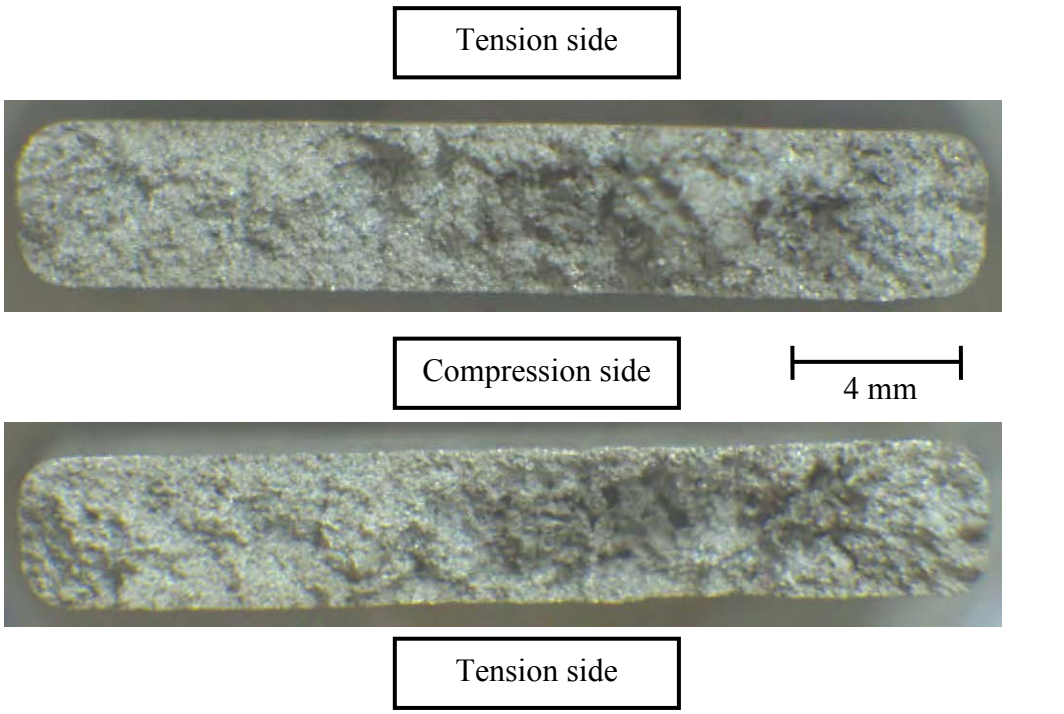

Figure 6 - 48. Macrophotographs of direct gated test bar, C3R4DG (UBS = 302 MPa).

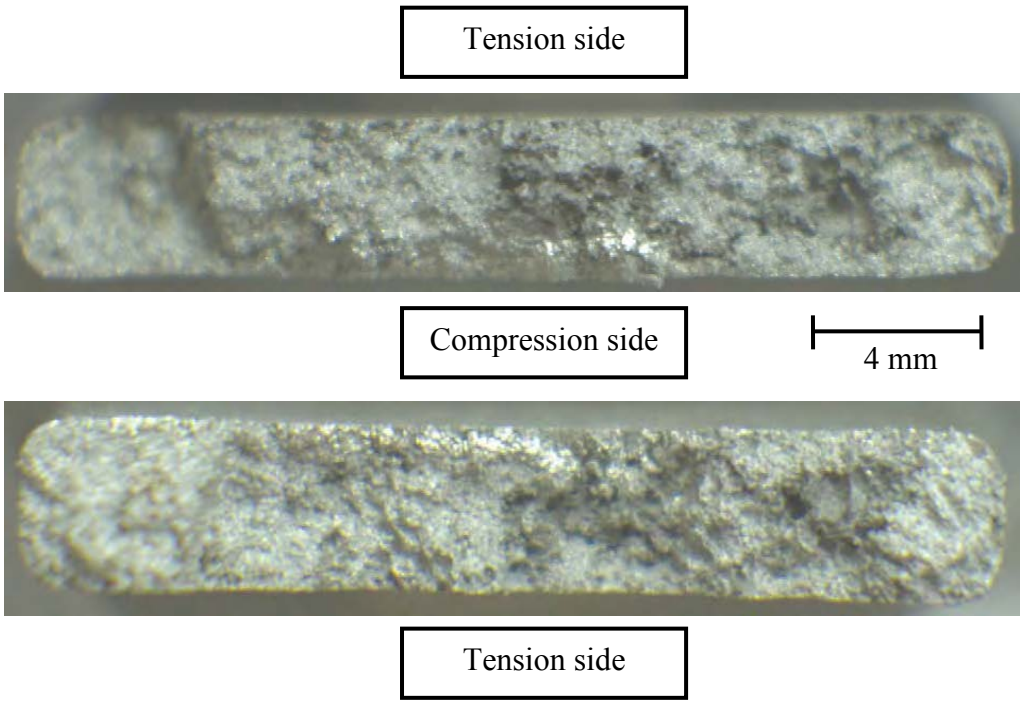

Figure 6 - 49. Macrophotographs of direct gated test bar, C3L4DG (UBS = 324 MPa).

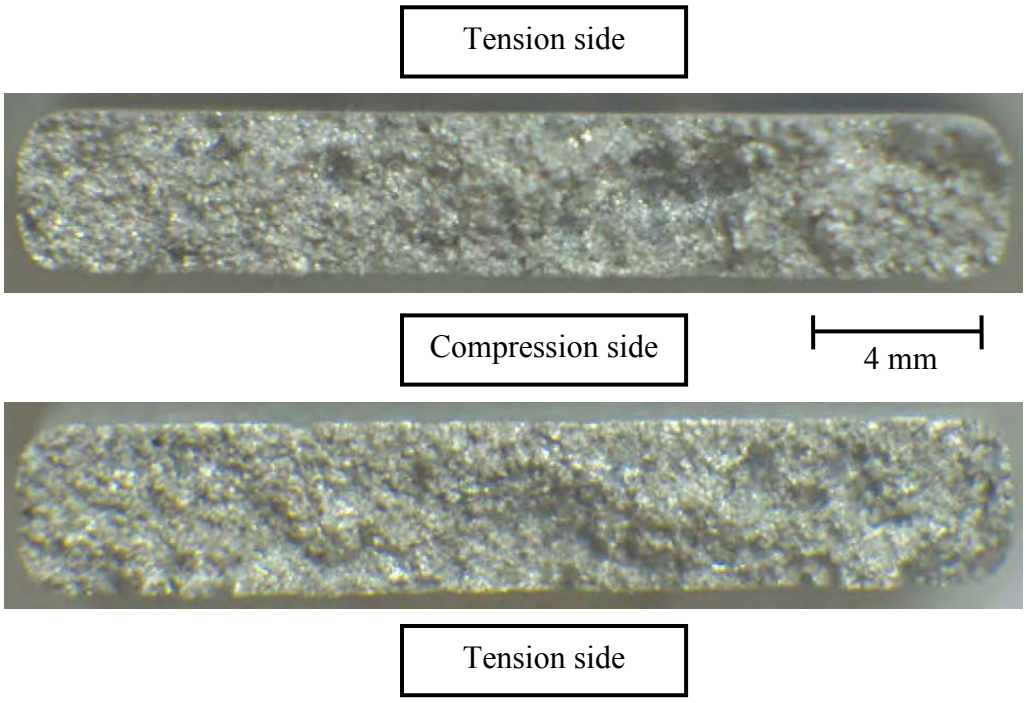

Figure 6 - 50. Macrophotographs of direct gated test bar, C2R2DG (UBS = 338 MPa).

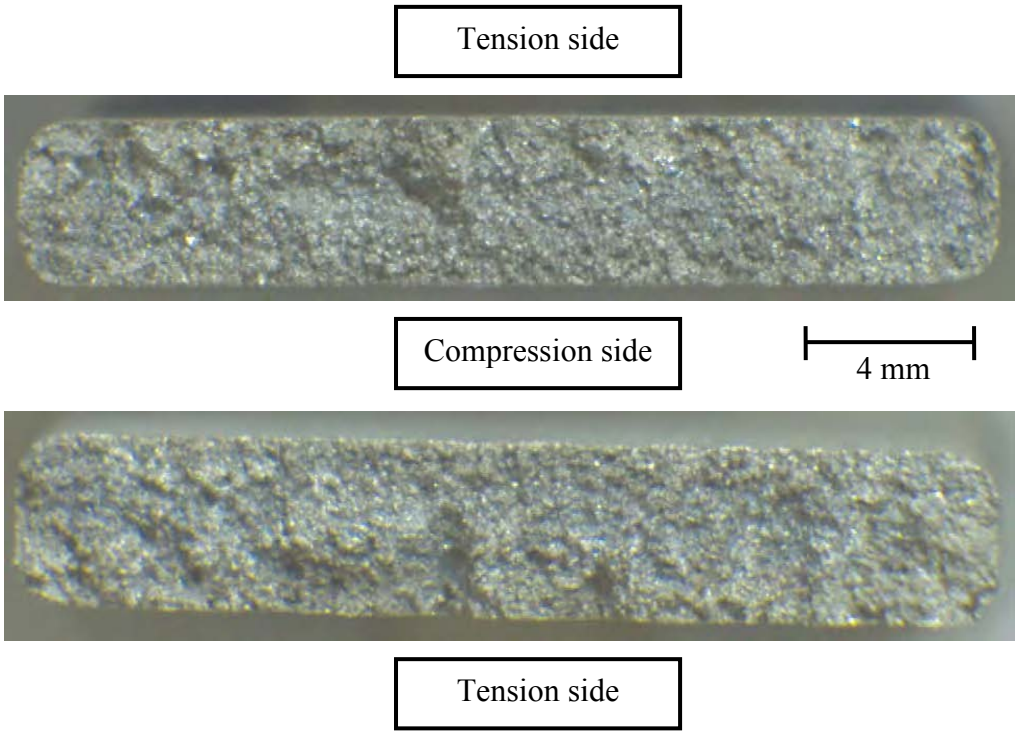

Figure 6 - 51. Macrophotographs of direct gated test bar, C2L5DG (UBS = 353 MPa).

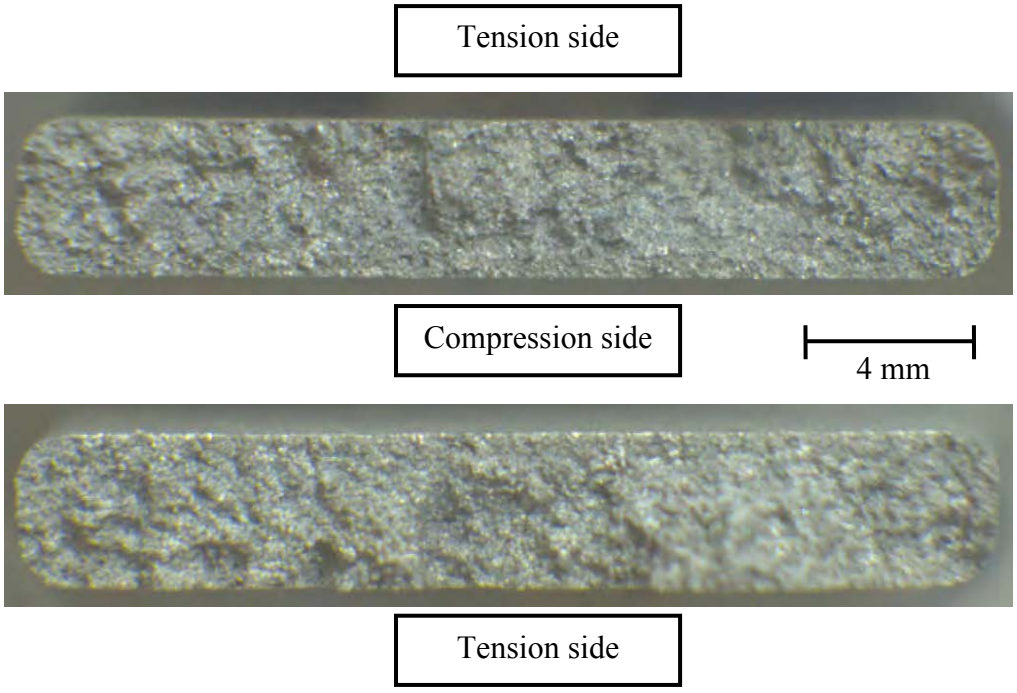

Figure 6 - 52. Macrophotographs of indirect gated test bar, C2L2IG (UBS = 331 MPa).

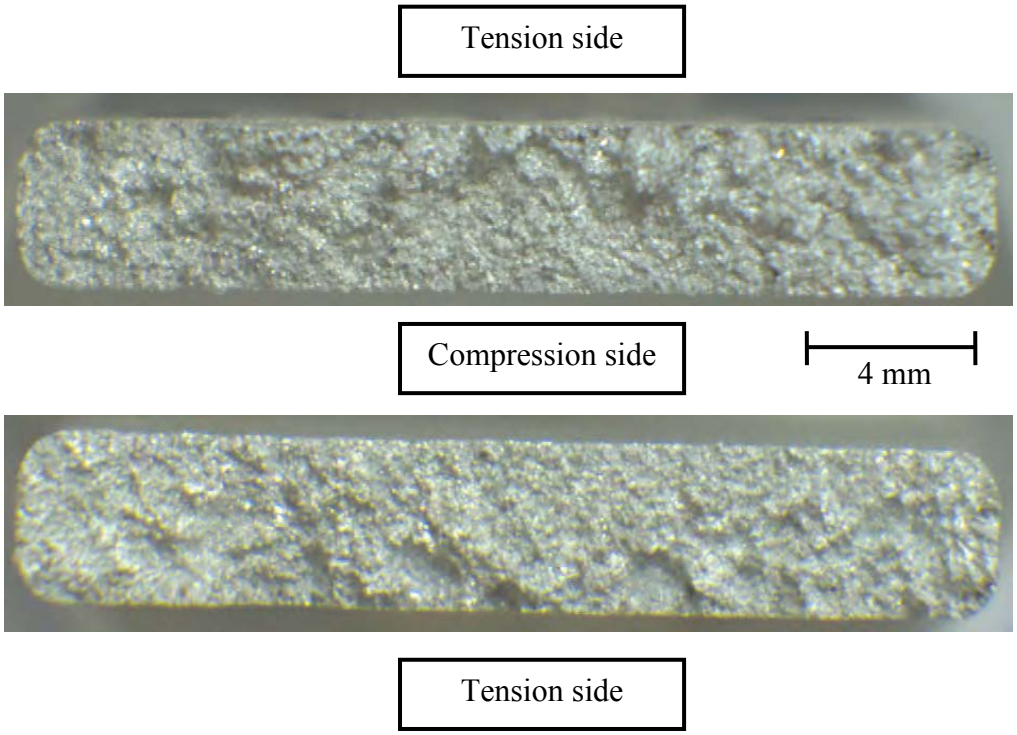

Figure 6 - 53. Macrophotographs of indirect gated test bar, C2R3IG (UBS = 348 MPa).

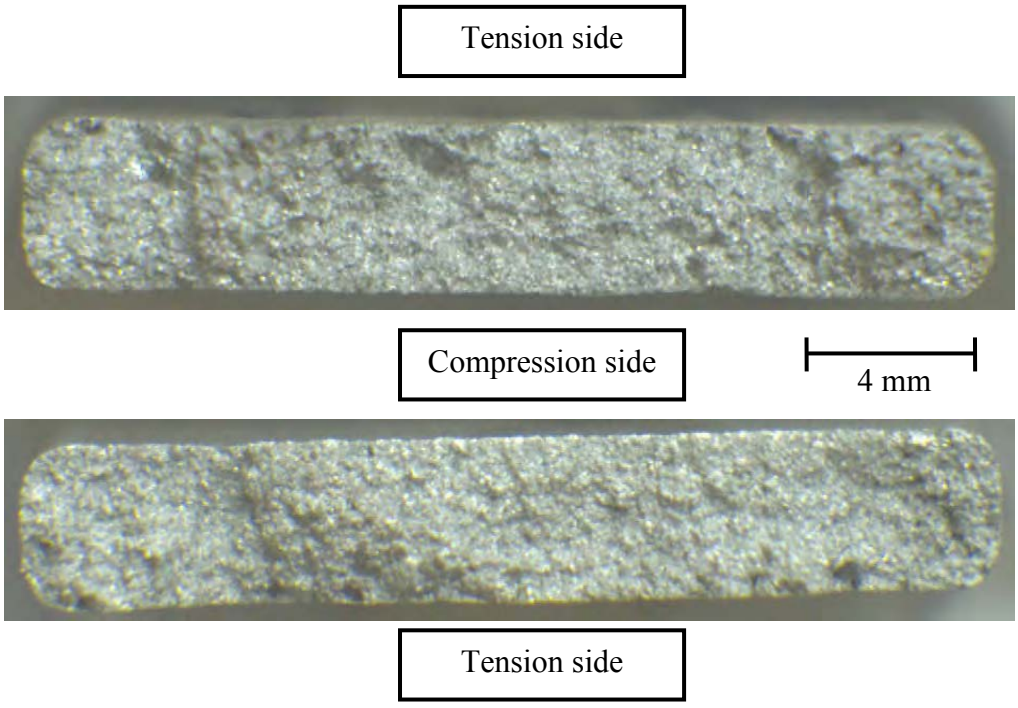

Figure 6 - 54. Macrophotographs of indirect gated test bar, C1R4IG (UBS = 356 MPa).

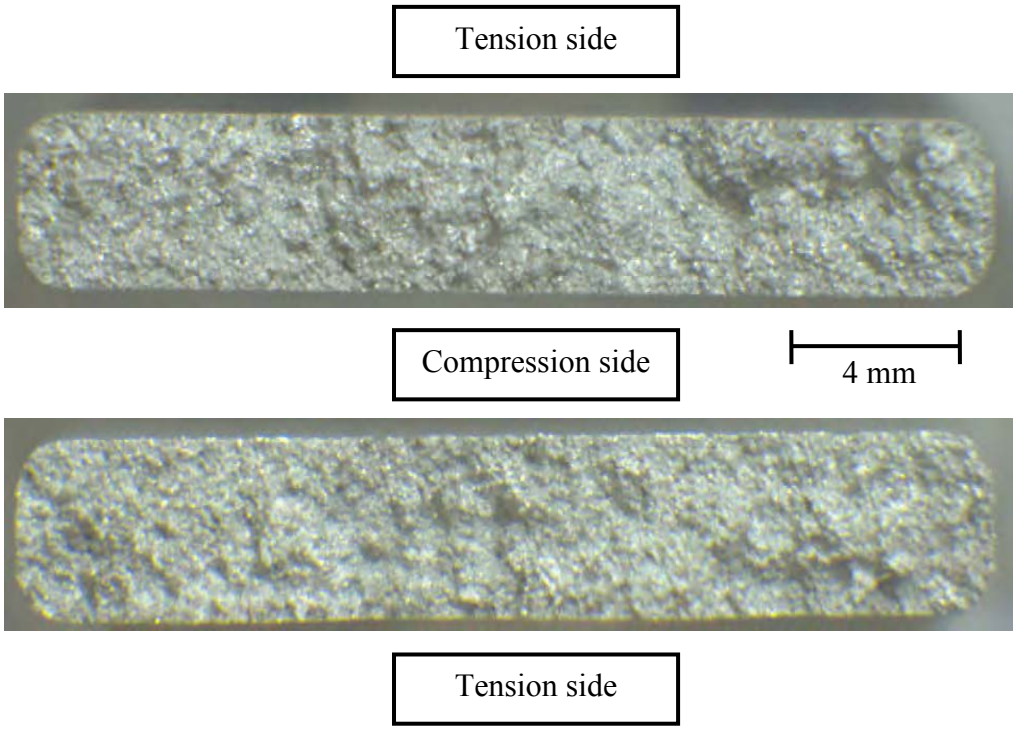

Figure 6 - 55. Macrophotographs of indirect gated test bar, C3L2IG (UBS = 357 MPa).

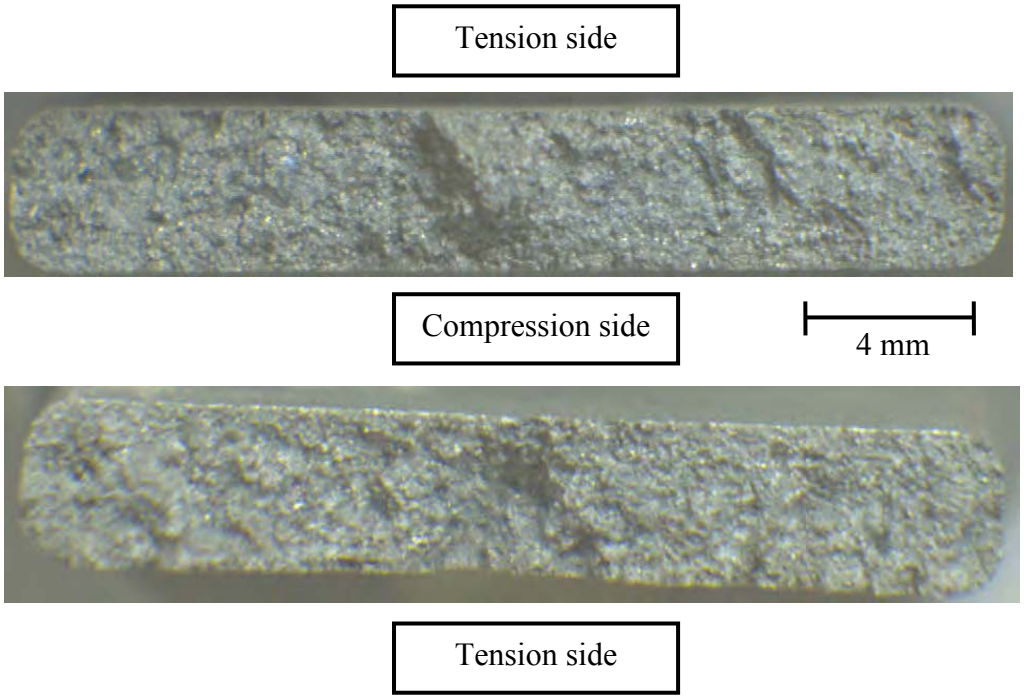

Figure 6 - 56. Macrophotographs of indirect gated test bar, C3R3IG (UBS = 370 MPa).

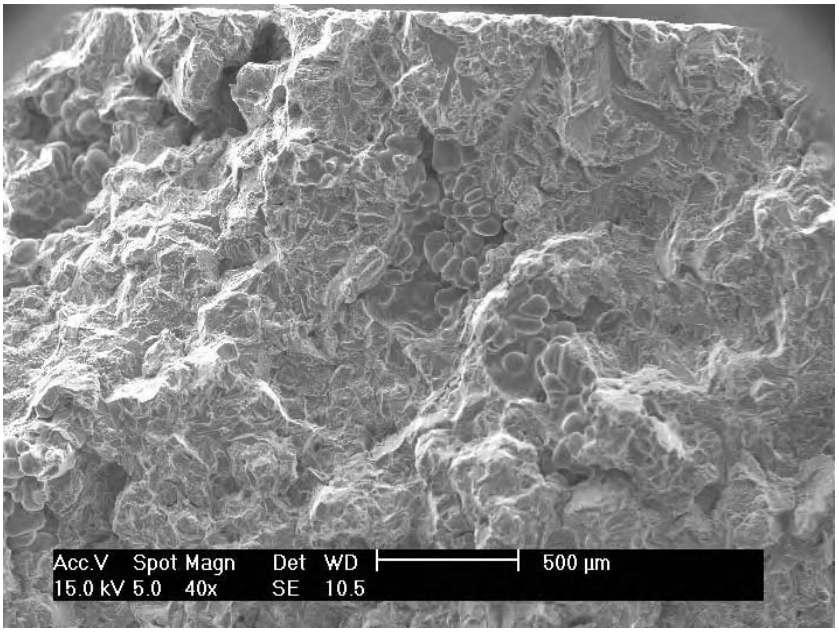

(a)

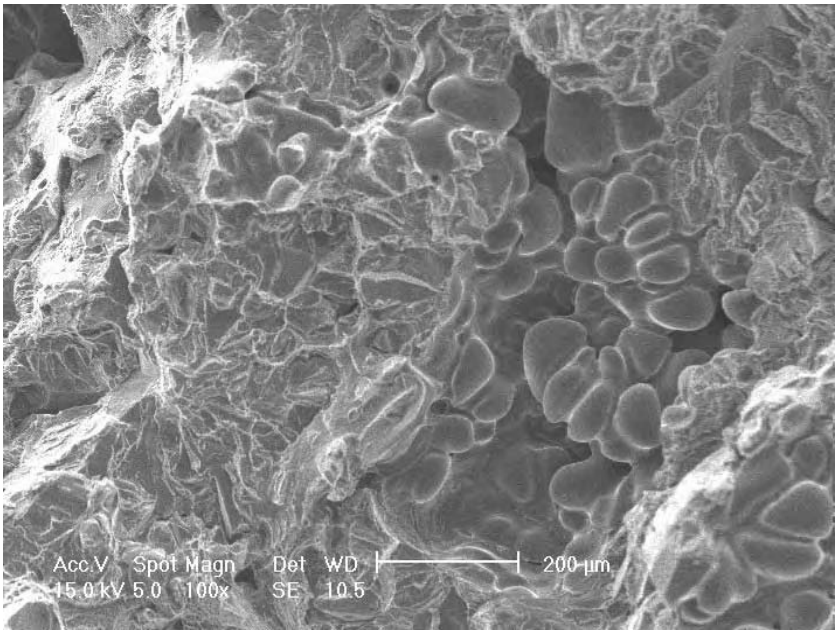

(b)

Figure 6 - 57. Secondary electron micrographs showing (a) bend testing fracture surface, and (b) higher magnification of the shrinkage pore. Direct gated test bar with a UBS of 265 MPa (C3R3DG).

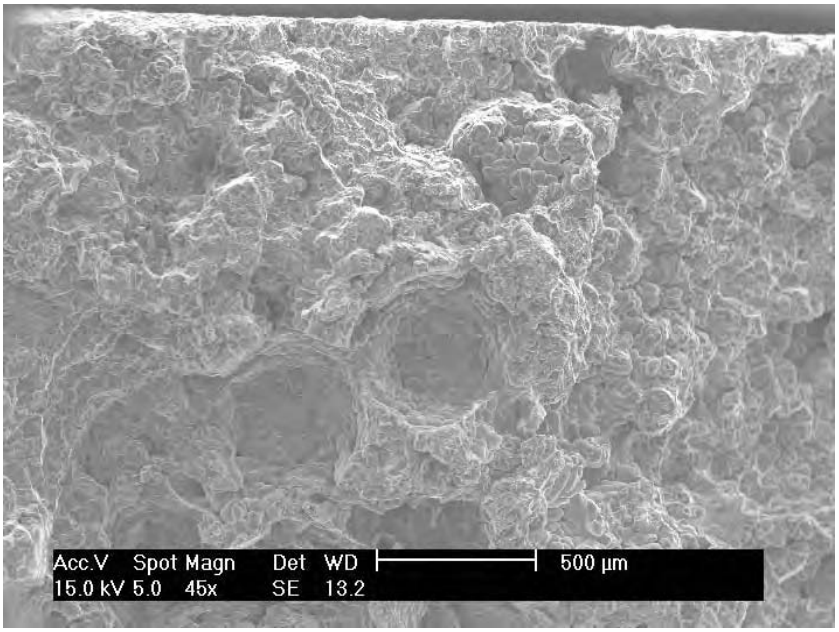

(a)

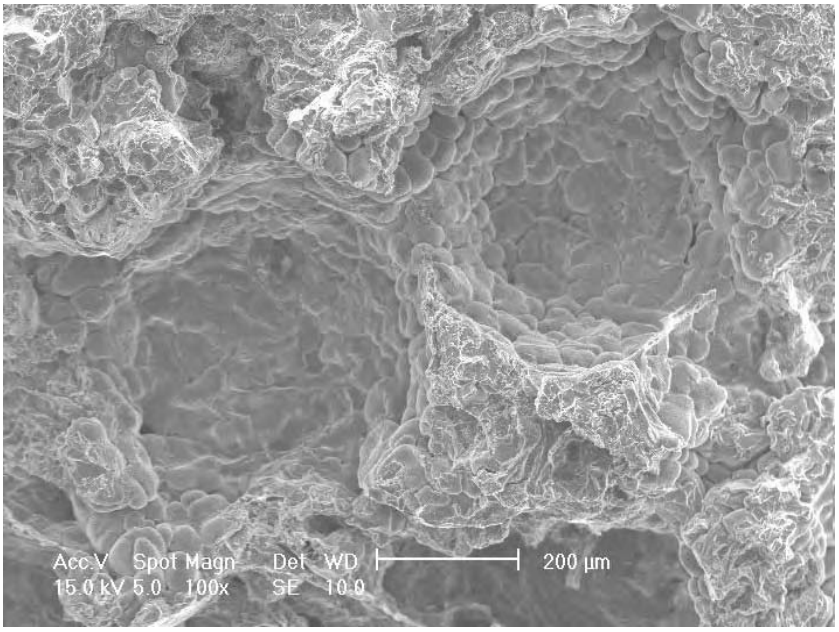

(b)

Figure 6 - 58. Secondary electron micrographs showing (a) bend testing fracture surface, and (b) higher magnification of the entrapped bubbles. Direct gated test bar with a UBS of 324 MPa (C3L4DG).

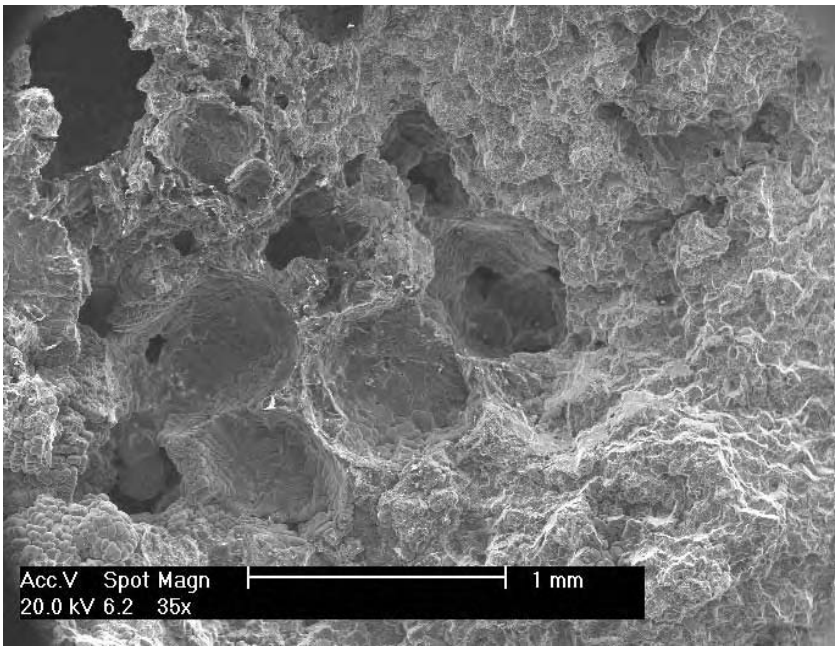

(a)

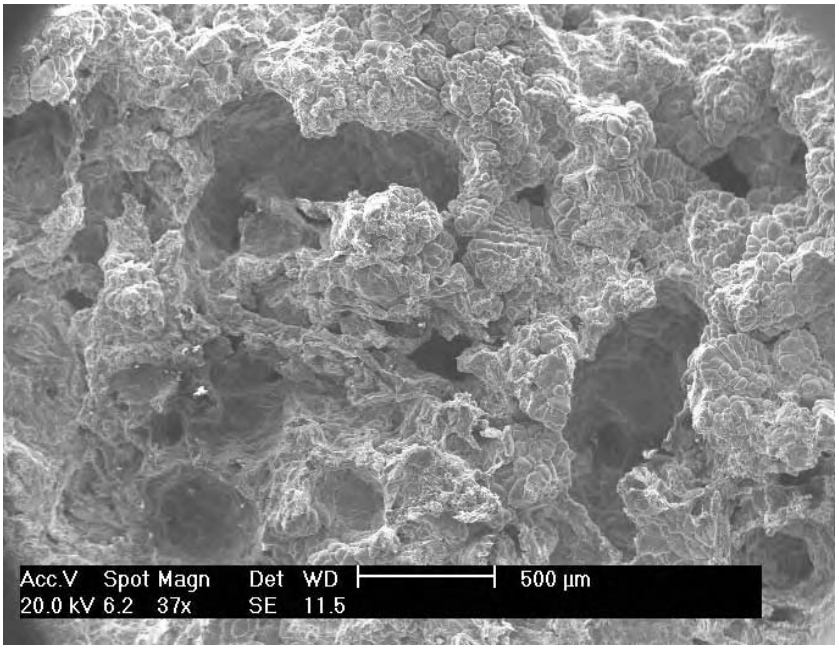

(b)

Figure 6 - 59. (a) and (b) Secondary electron micrographs of direct gated test bar (C3R4DG), showing clusters of porosity formed by shrinkage, fragmented and entrapped bubbles present in dark areas.

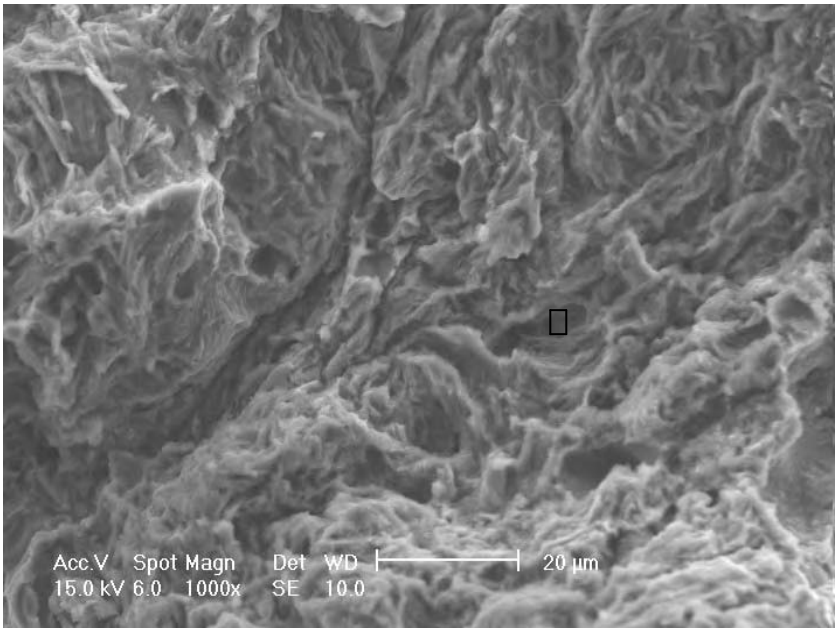

(a)

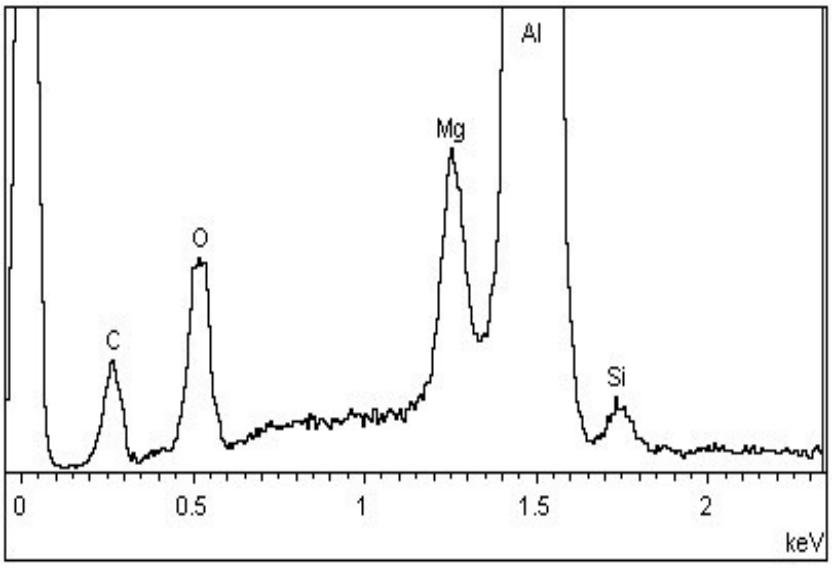

(b)

Figure 6 - 60. Secondary electron micrograph showing (a) oxide film defect, and (b) energy dispersive X-ray (EDX) analysis results of marked area. Direct gated test bar with a UBS of 265 MPa (C3R3DG).

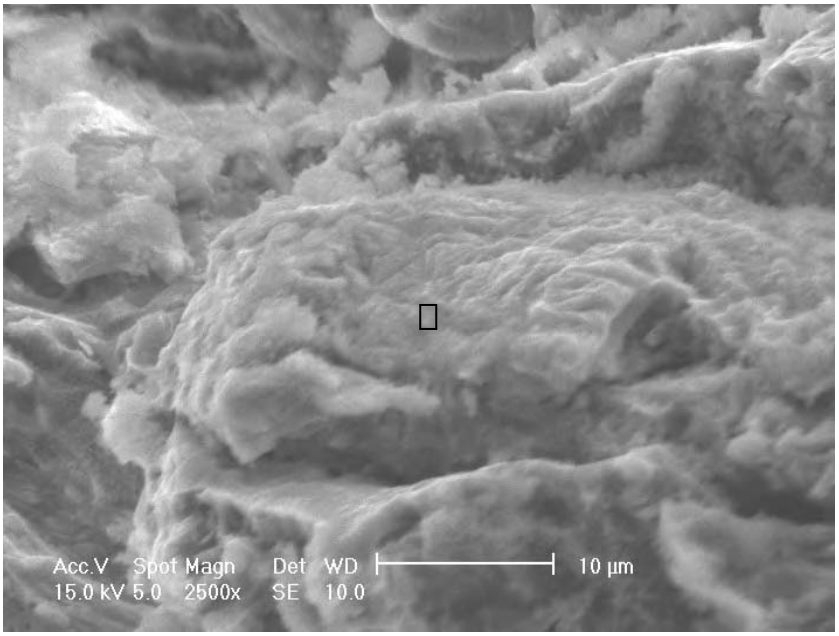

(a)

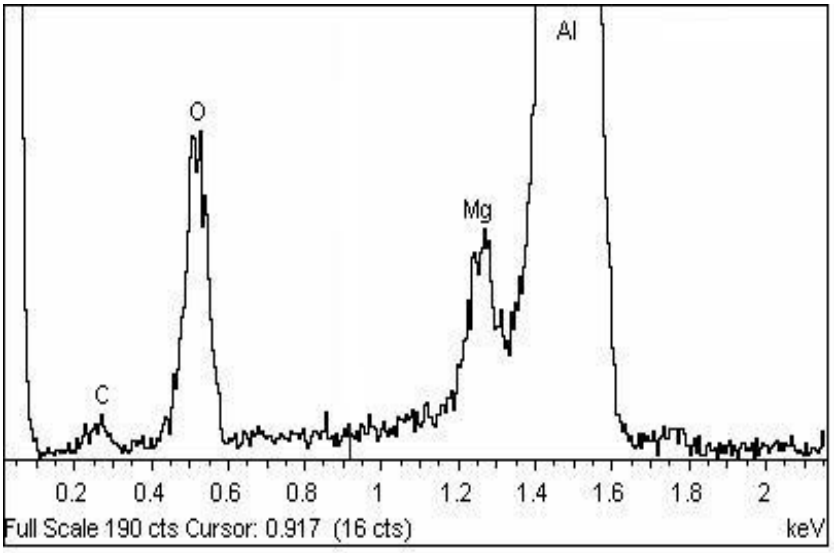

(b)

Figure 6 - 61. Secondary electron micrograph showing (a) oxide film defect, and (b) energy dispersive X-ray (EDX) analysis results of marked area. Direct gated test bar with a UBS of 324 MPa (C3L4DG).

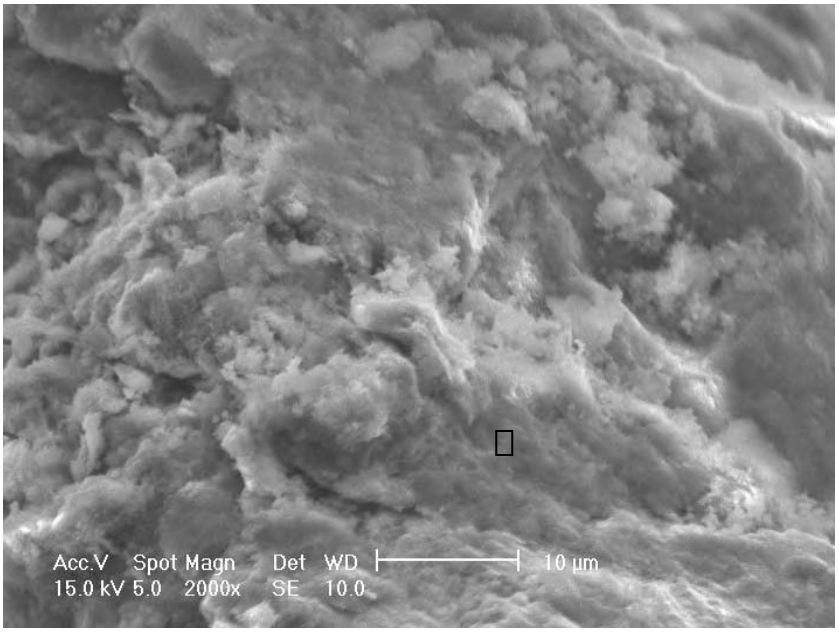

(a)

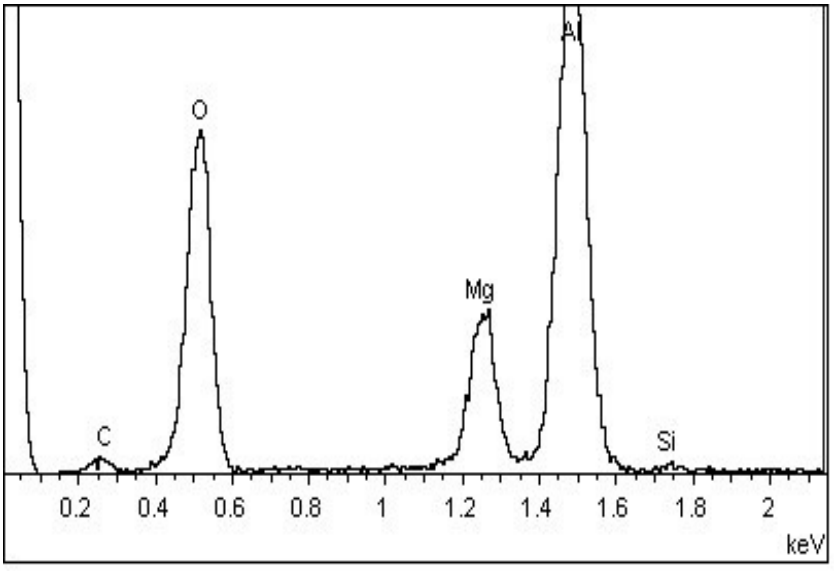

(b)

Figure 6 - 62. Secondary electron micrograph showing (a) oxide film defect, and (b) energy dispersive X-ray (EDX) analysis results of marked area. Indirect gated test bar with a UBS of 331 MPa (C2L2IG).

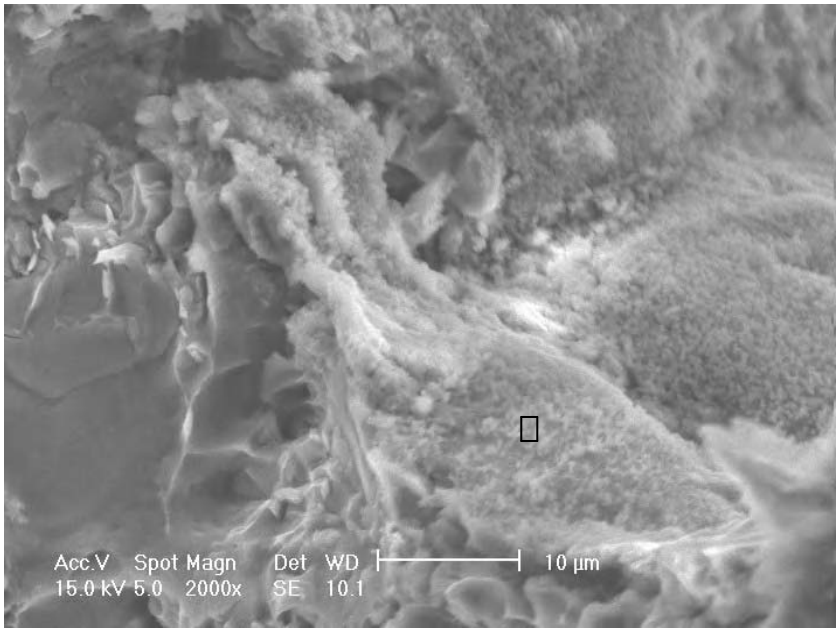

(a)

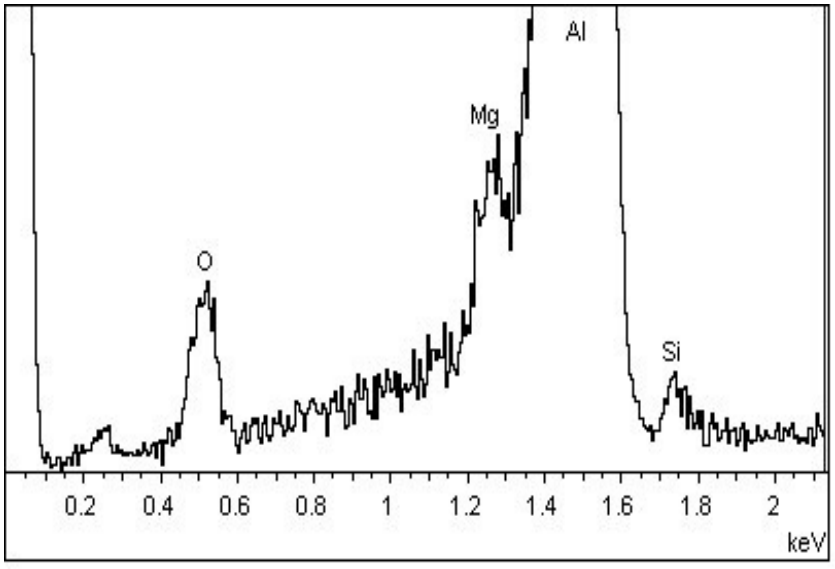

(b)

Figure 6 - 63. Secondary electron micrograph showing (a) oxide film defect, and (b) energy dispersive X-ray (EDX) analysis results of marked area. Indirect gated test bar with a UBS of 356 MPa (C1R4IG).

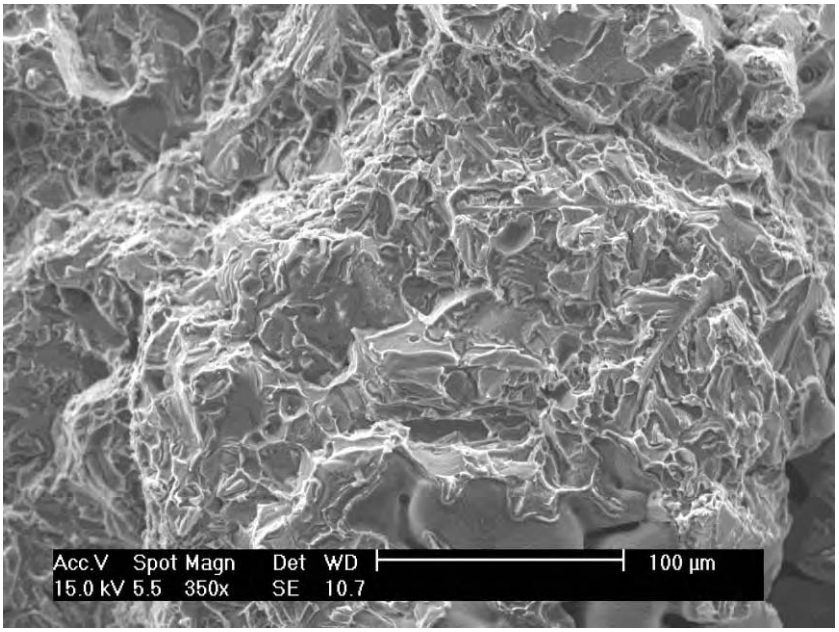

(a)

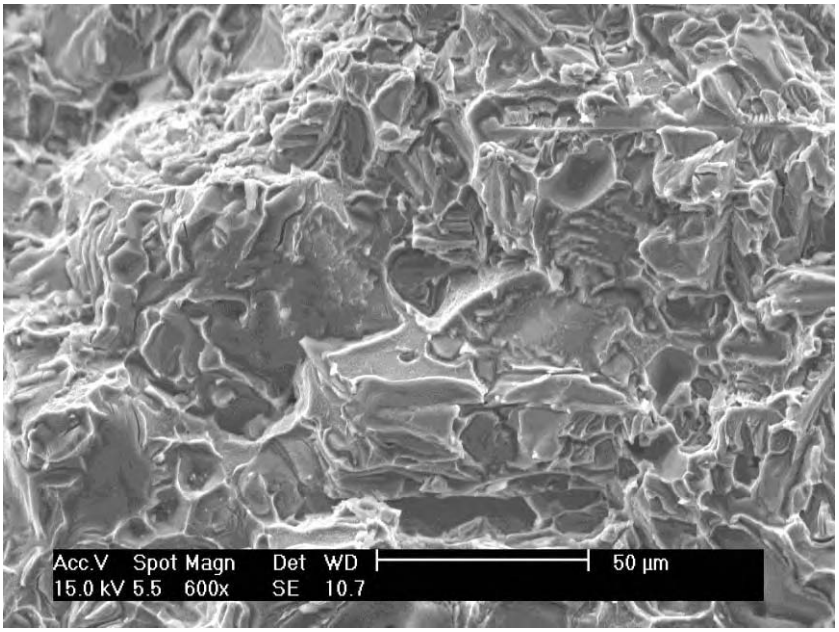

(b)

Figure 6 - 64. Secondary electron micrographs showing (a) bend testing fracture surface, and (b) higher magnification of the brittle fracture. Direct gated test bar with a UBS of 324 MPa (C3L4DG).

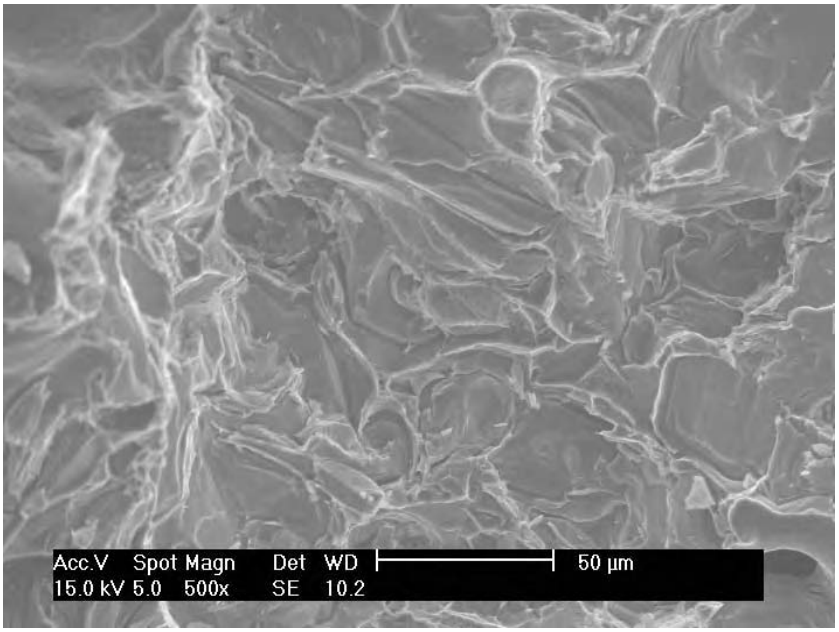

(a)

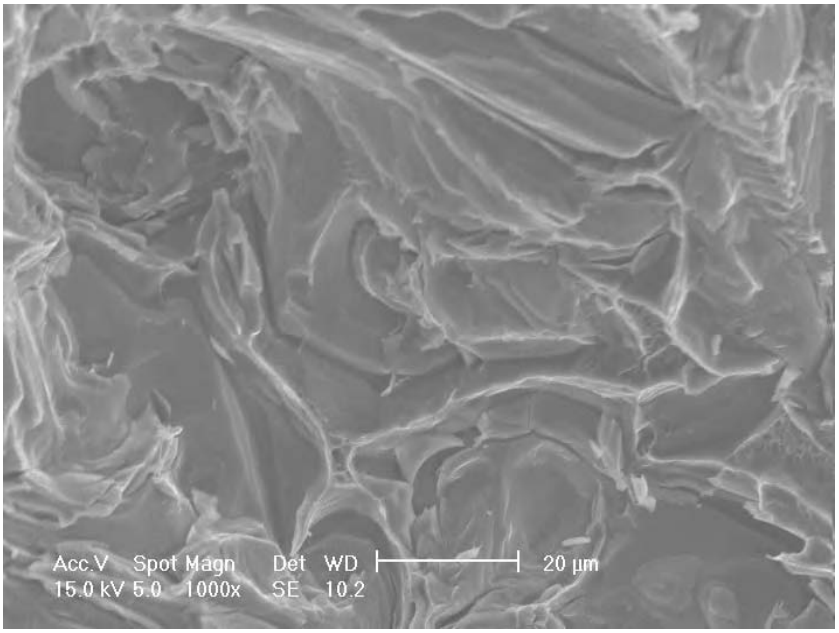

(b)

Figure 6 - 65. Secondary electron micrographs showing (a) bend testing fracture surface, and (b) higher magnification of the brittle fracture. Indirect gated test bar with a UBS of 356 MPa (C1R4IG).

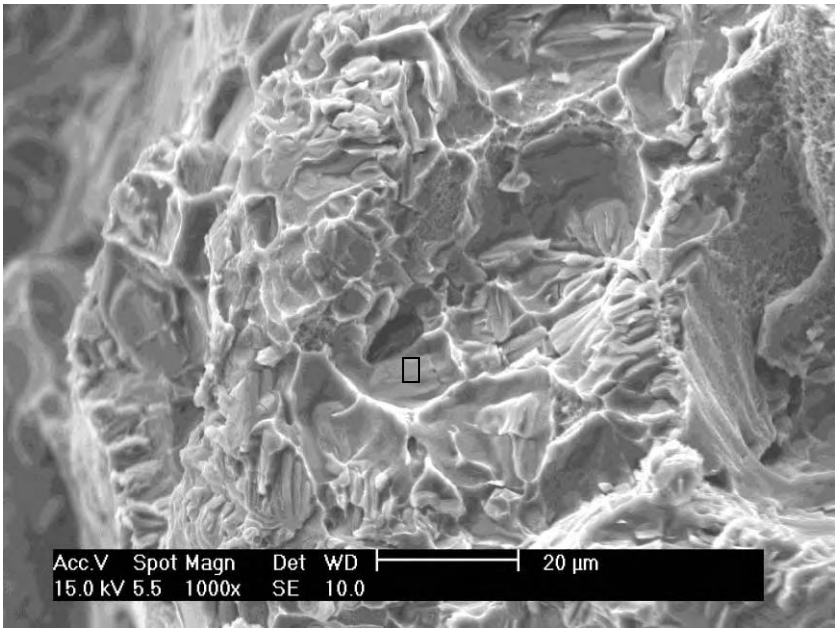

(a)

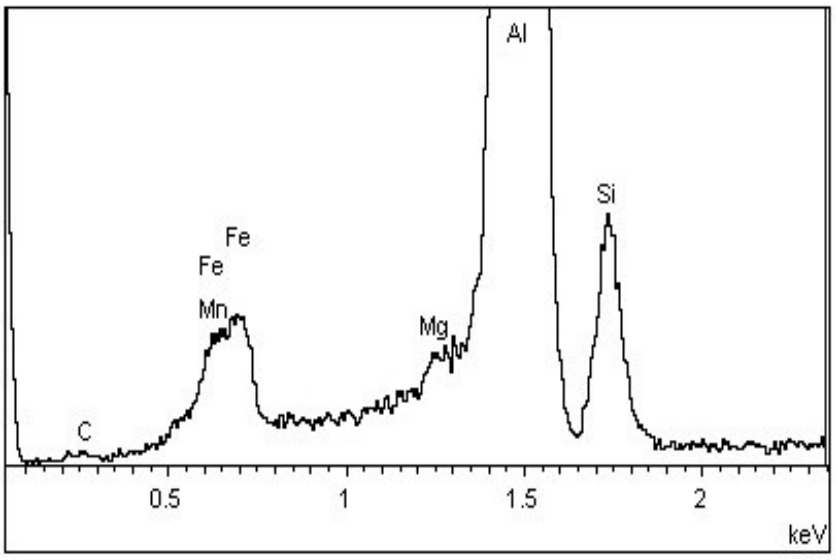

(b)

Figure 6 - 66. Secondary electron micrograph showing (a) bend testing fracture surface, and (b) energy dispersive X-ray (EDX) analysis results. Direct gated test bar with a UBS of 324 MPa (C3L4DG).

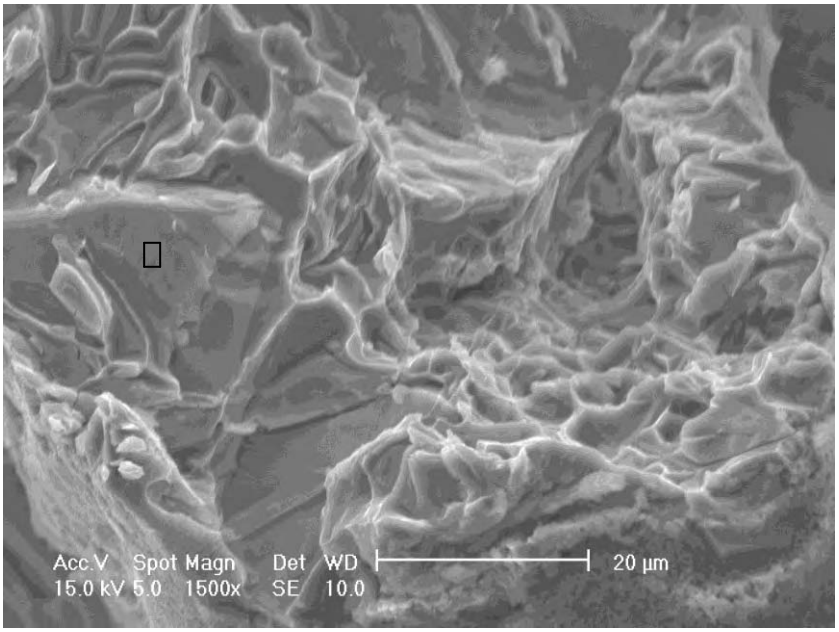

(a)

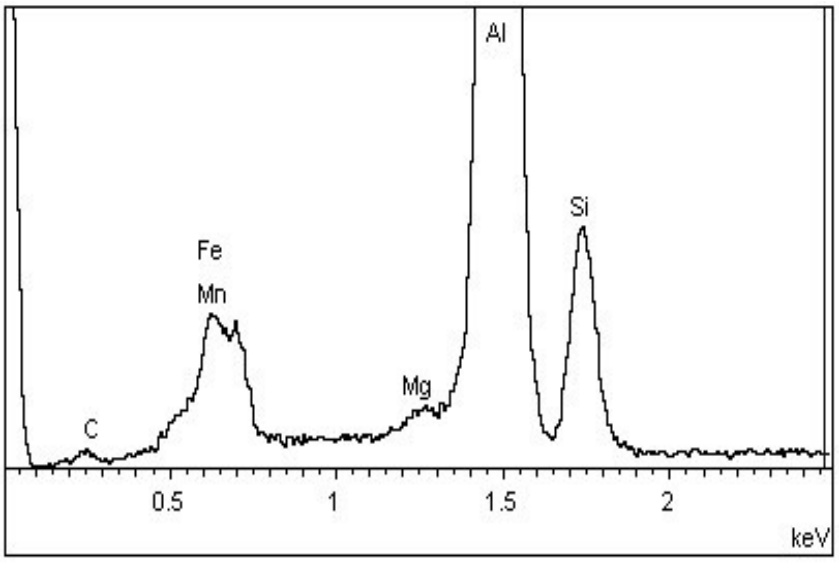

(b)

Figure 6 - 67. Secondary electron micrograph showing (a) bend testing fracture surface, and (b) energy dispersive X-ray (EDX) analysis results. Indirect gated test bar with a UBS of 356 MPa (C1R4IG).

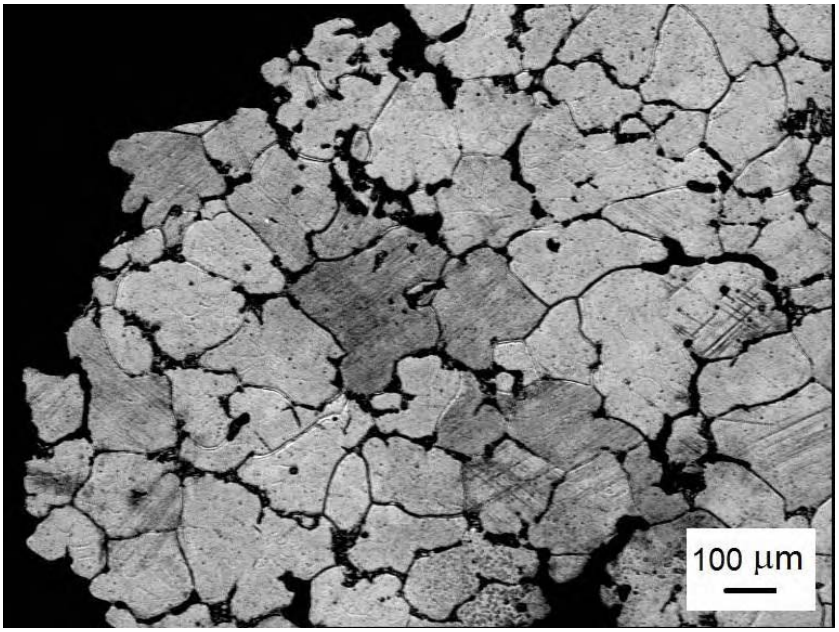

(a)

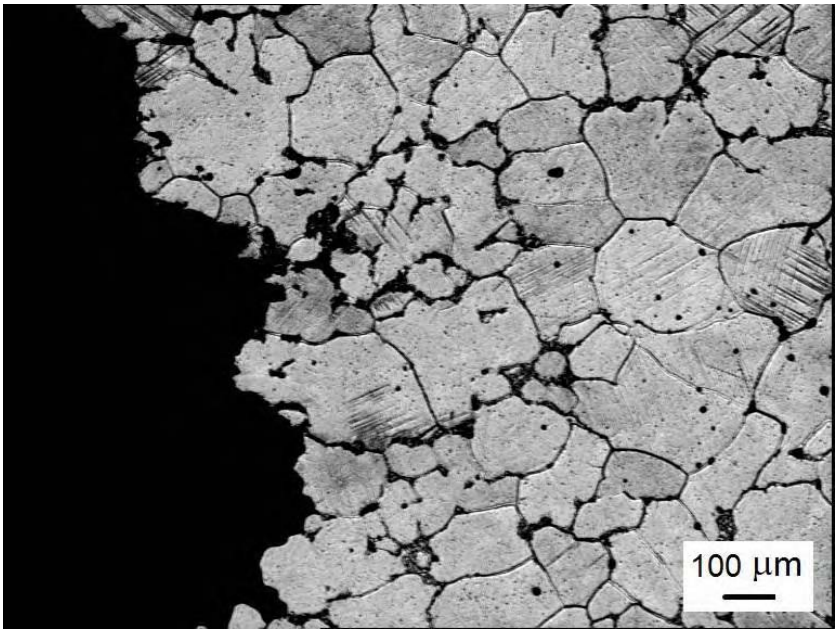

(b)

Figure 6 - 68. Microstructure of fractured direct gated specimen showing grain boundaries. Direct gated test bar with a UBS of 321 MPa (C1L2DG).

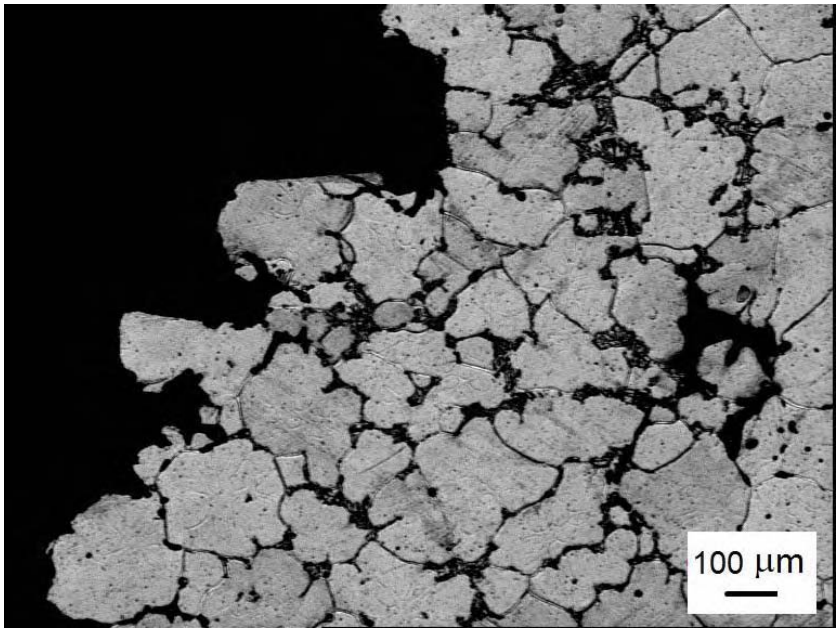

(a)

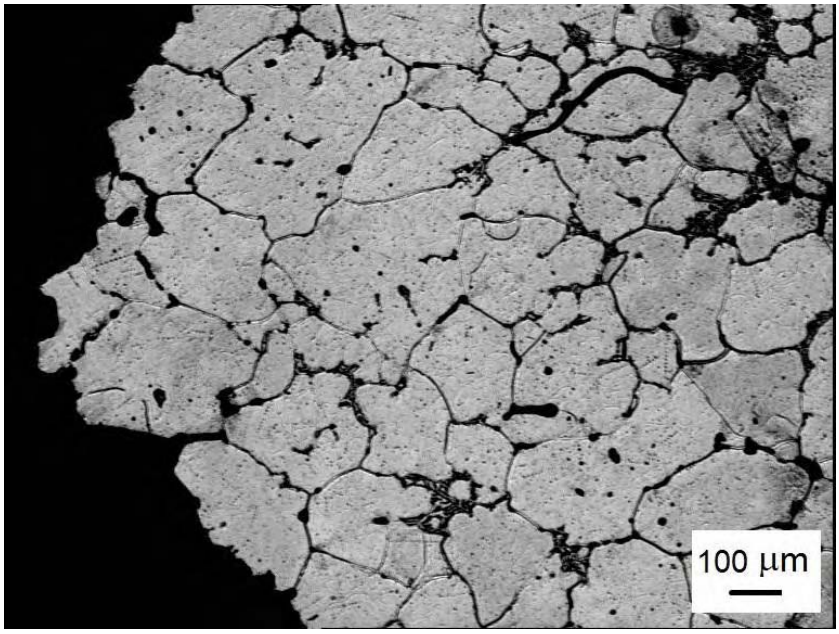

(b)

Figure 6 - 69. Microstructure of fractured indirect gated specimen showing grain boundaries. Indirect gated test bar with a UBS of 349 MPa (C1L1IG).

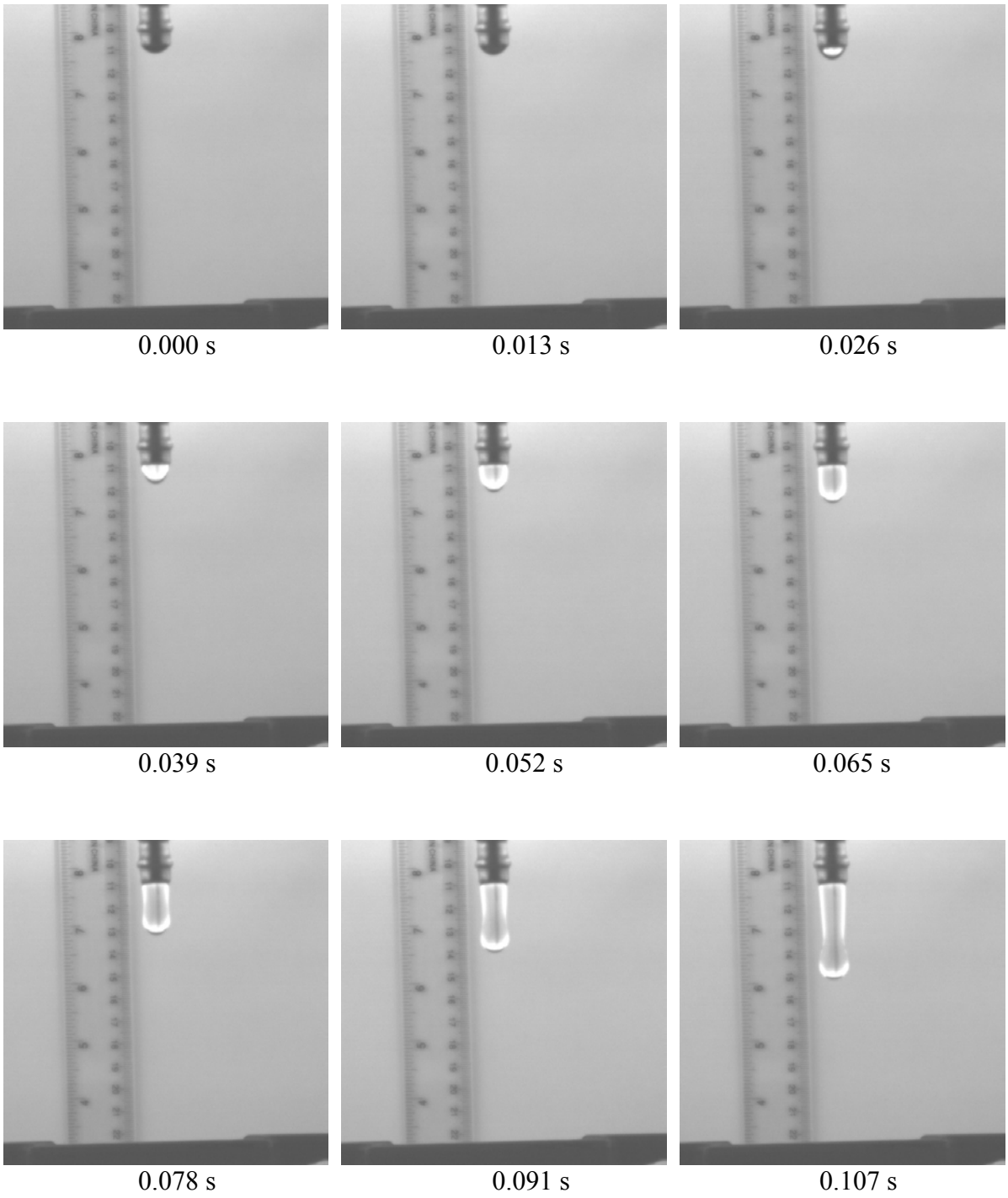

Figure 6 - 70. Summary of high speed camera results of water modelling inlet condition obtained from experiment # 1 (see Table 6 - 26).

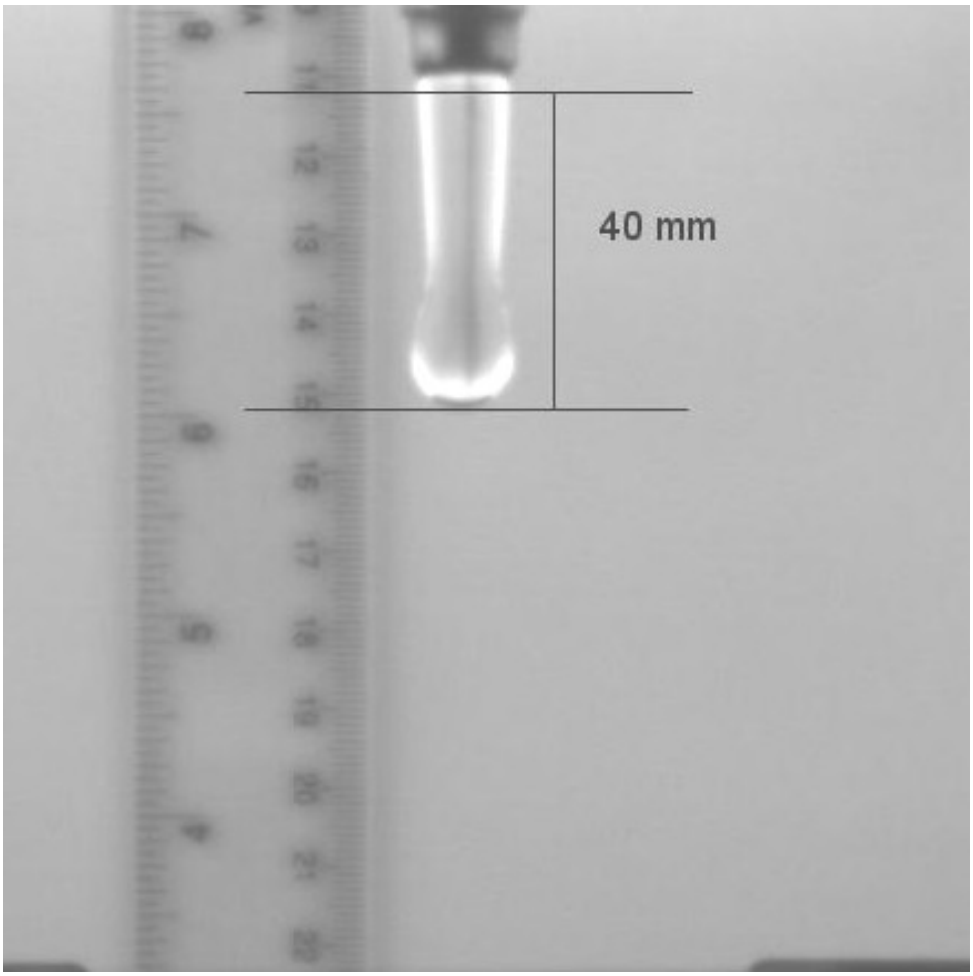

Figure 6 - 71. Snapshot of water inlet condition at 0.107 s obtained from experiment # 1 (see Table 6 - 26)

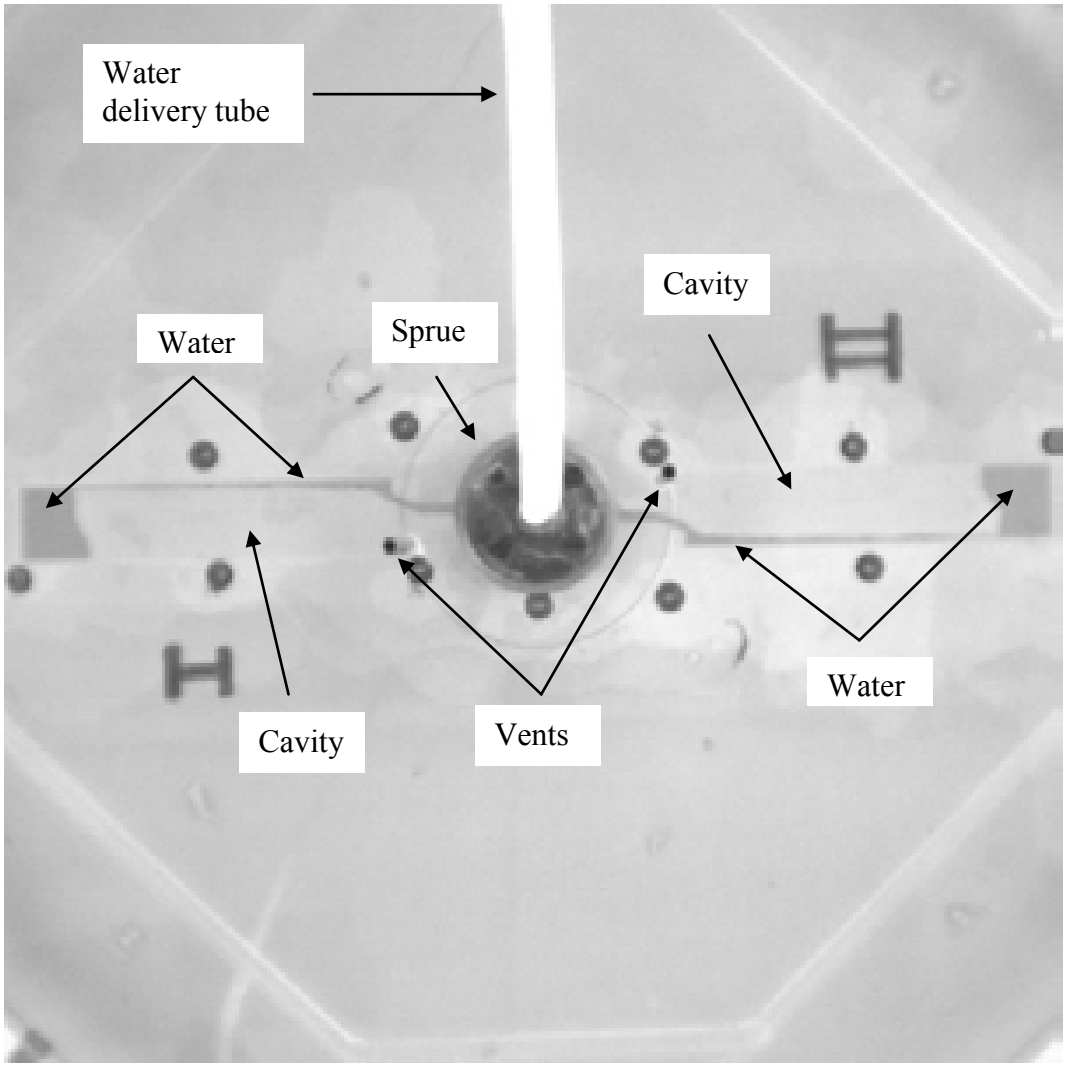

Figure 6 - 72. Snapshot obtained with the high speed camera for the direct gated mould at 0.63 s. The rotational velocity was 200 rpm in the anti-clockwise direction.

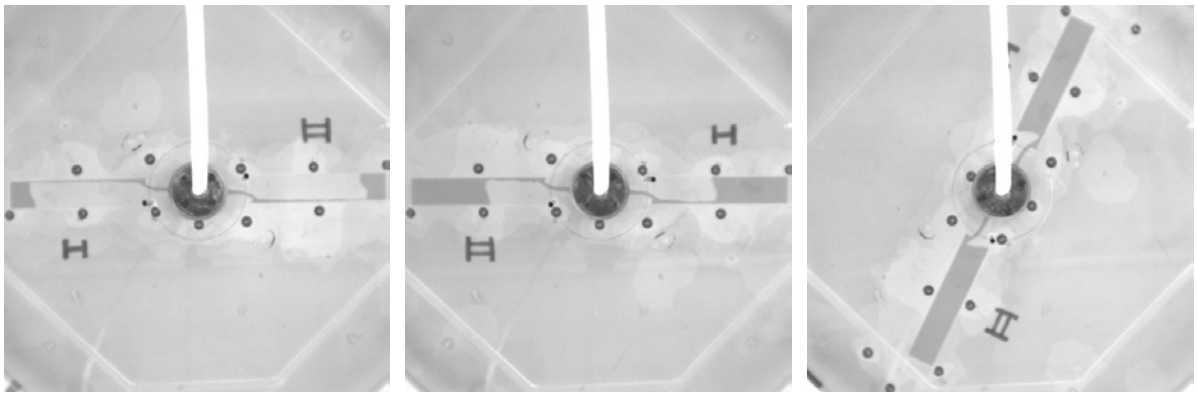

0.63 s 1.08 s 1.44 s

Figure 6 - 73. Summary of the high speed camera results of the direct gated mould filling process. The rotational velocity was 200 rpm in the anti-clockwise direction. Note: Full summary and video sequence can be seen in Appendix 2 and Appendix 32.

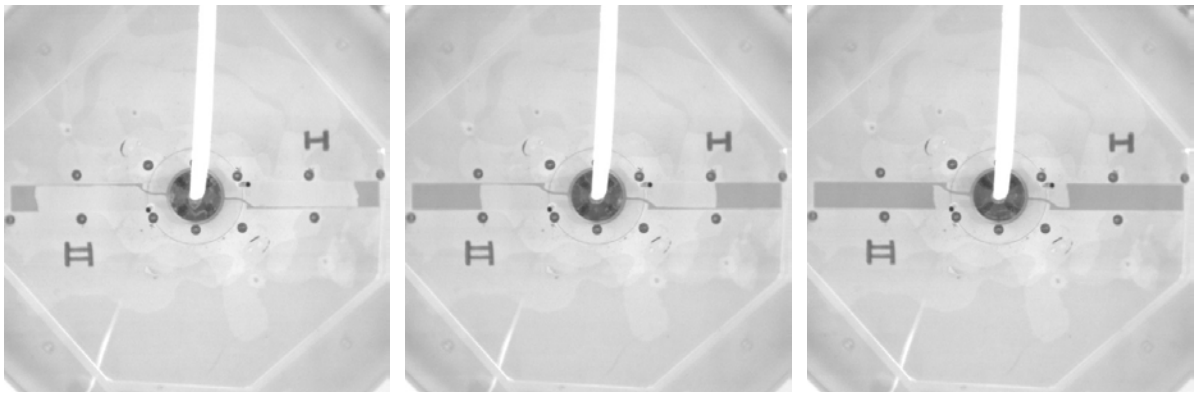

0.64 s 1.04 s 1.44 s

Figure 6 - 74. Summary of the high speed camera results of the direct gated mould filling process. The rotational velocity was 300 rpm in the anti-clockwise direction. Note: Full summary and video sequence can be seen in Appendix 3 and Appendix 33.

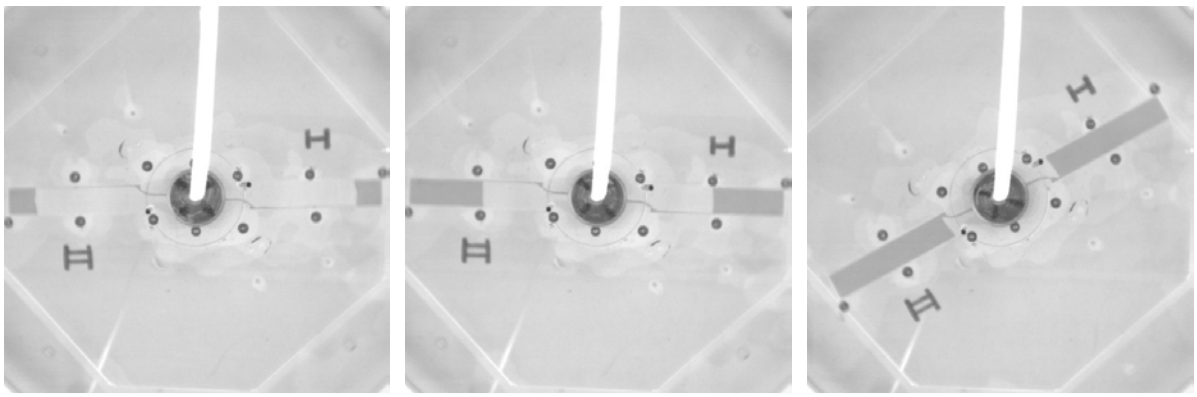

0.66 s 1.11 s 1.57 s

Figure 6 - 75. Summary of the high speed camera results of the direct gated mould filling process. The rotational velocity was 400 rpm in the anti-clockwise direction. Note: Full summary and video sequence can be seen in Appendix 4 and Appendix 34.

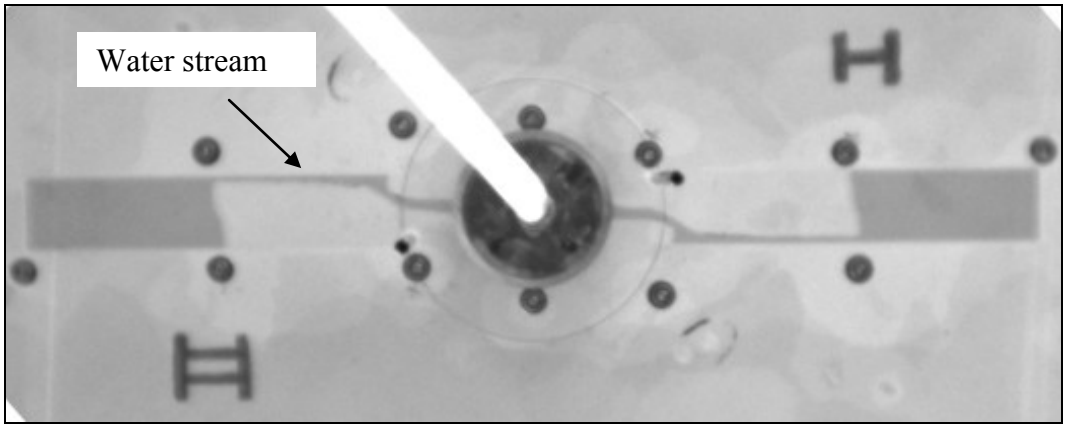

(a) 200 rpm (t = 1.05 s)

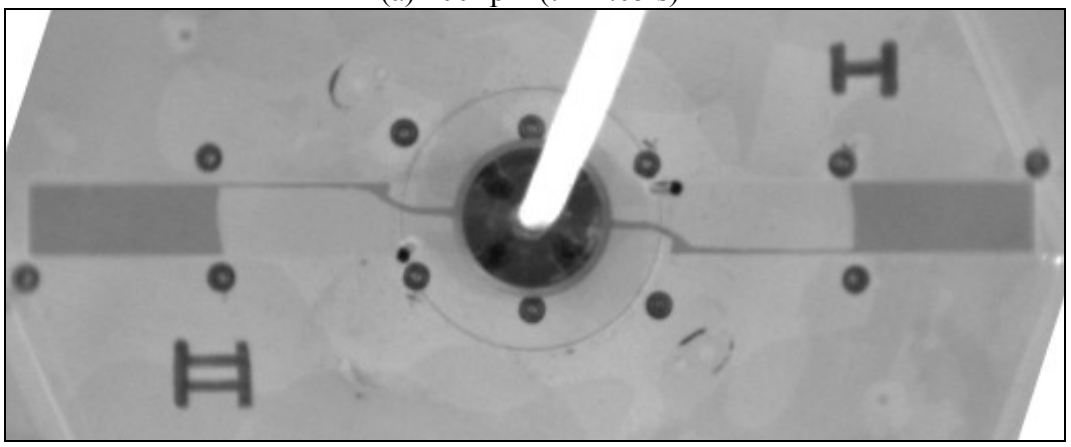

(b) 300 rpm (t = 1.05 s)

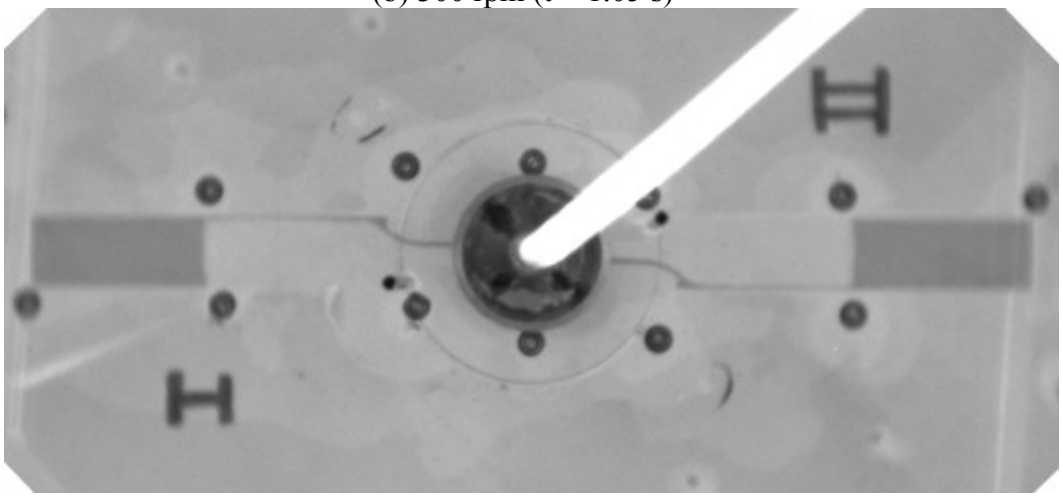

(c) 400 rpm (t = 1.05 s)

Figure 6 - 76. Comparison of the high speed camera snapshots of the direct gated mould at 200, 300 and 400 rpm in the anti-clockwise direction.

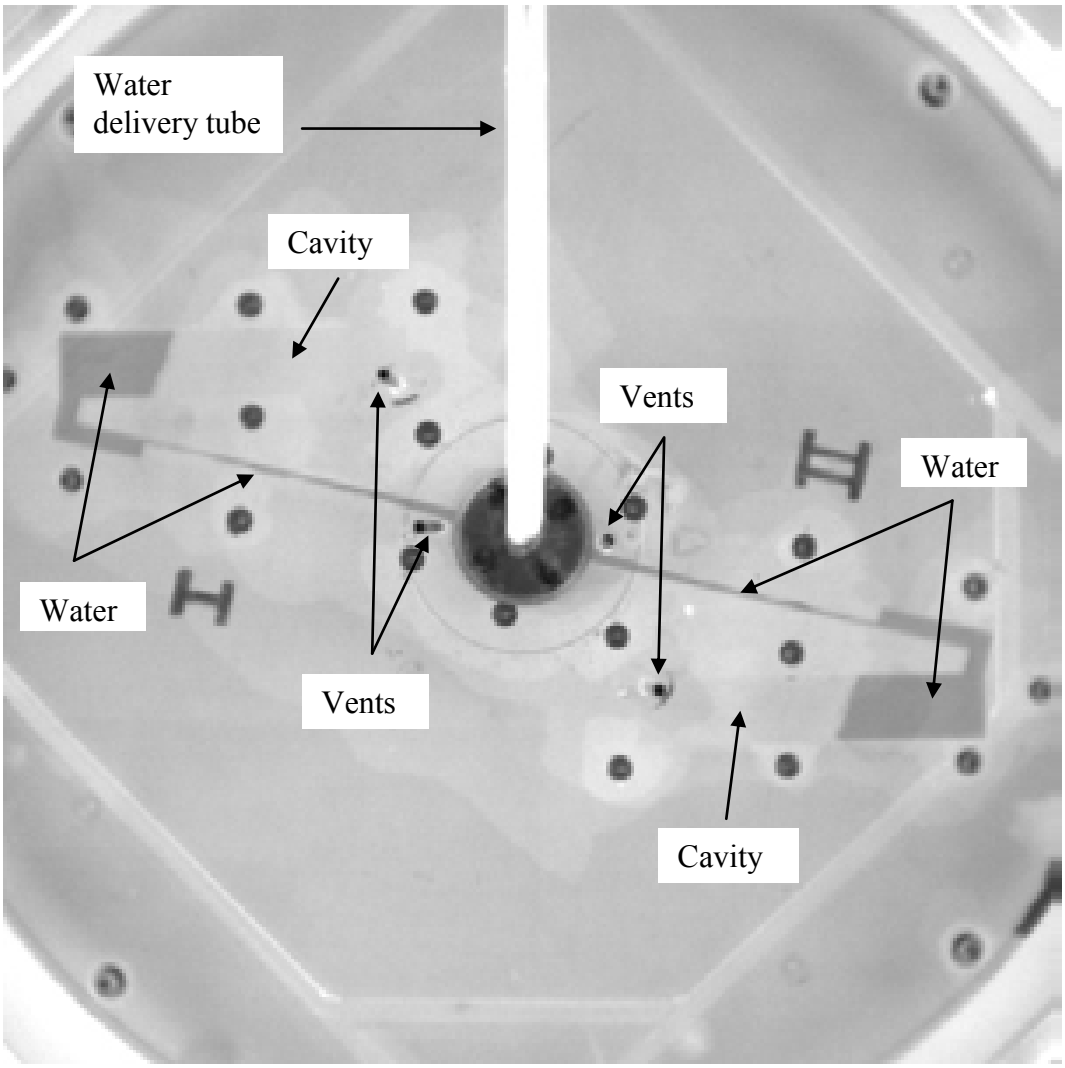

Figure 6 - 77. Snapshot obtained with the high speed camera for the indirect gated mould at 1.06 s. The rotational velocity was 200 rpm in the anti-clockwise direction.

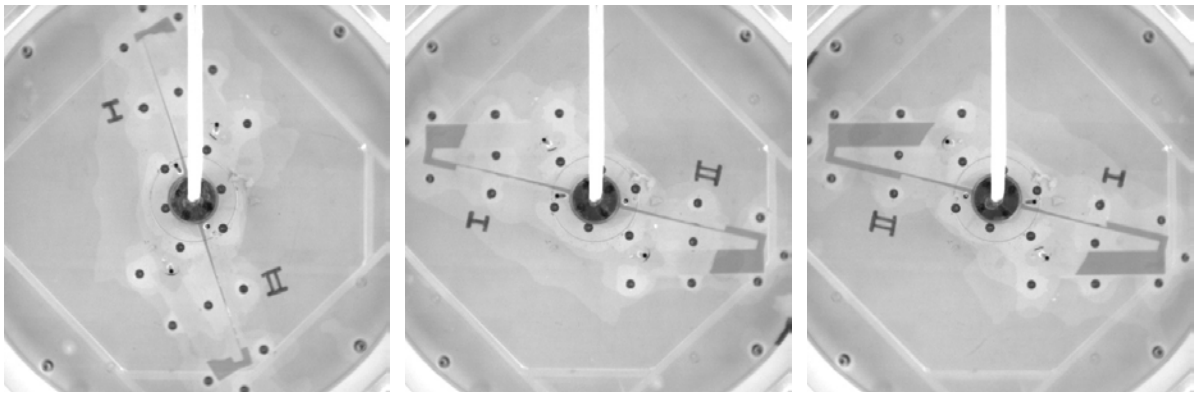

0.71 s 1.06 s 1.51 s

Figure 6 - 78. Summary of the high speed camera results of the indirect gated mould filling process. The rotational velocity was 200 rpm in the anti-clockwise direction. Note: Full summary and video sequence can be seen in Appendix 5 and Appendix 35.

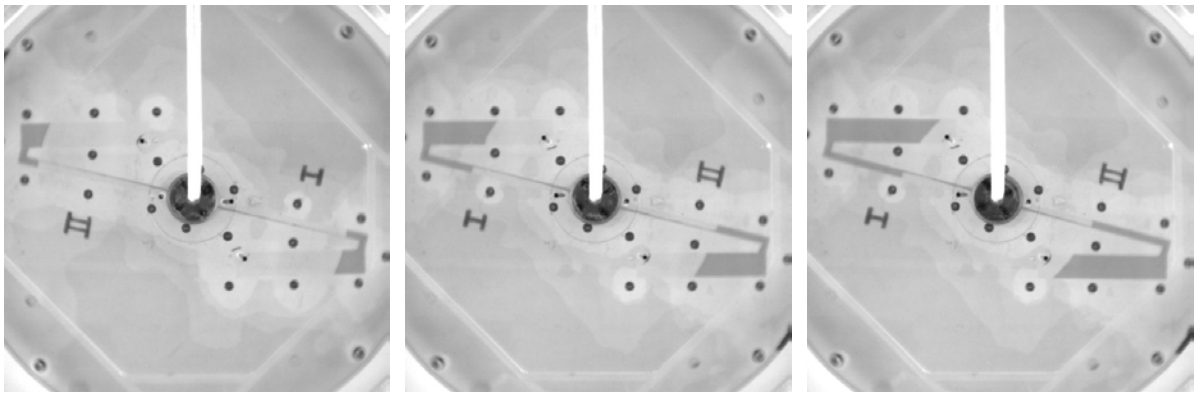

0.73 s 1.23 s 1.63 s

Figure 6 - 79. Summary of the high speed camera results of the indirect gated mould filling process. The rotational velocity was 300 rpm in the anti-clockwise direction. Note: Full summary and video sequence can be seen in Appendix 6 and Appendix 36.

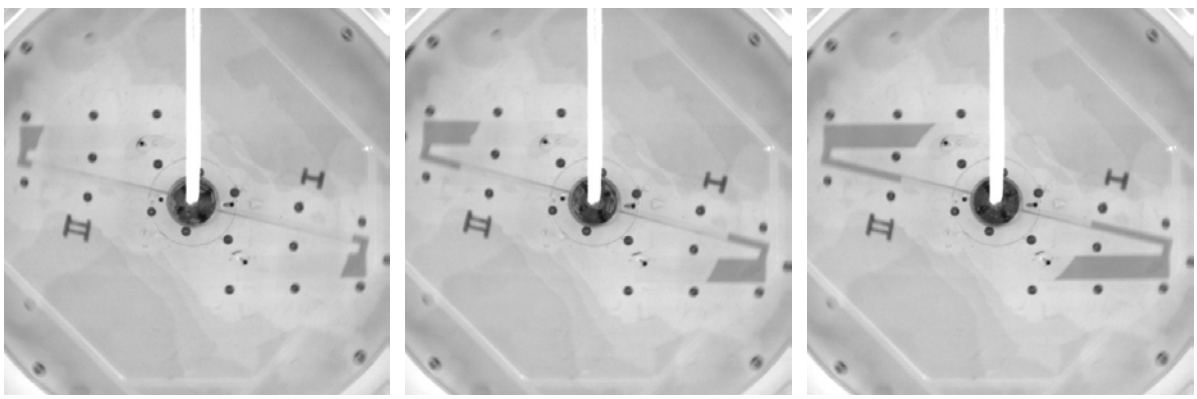

0.68 s 1.13 s 1.73 s

Figure 6 - 80. Summary of the high speed camera results of the indirect gated mould filling process. The rotational velocity was 400 rpm in the anti-clockwise direction. Note: Full summary and video sequence can be seen in Appendix 7 and Appendix 37.

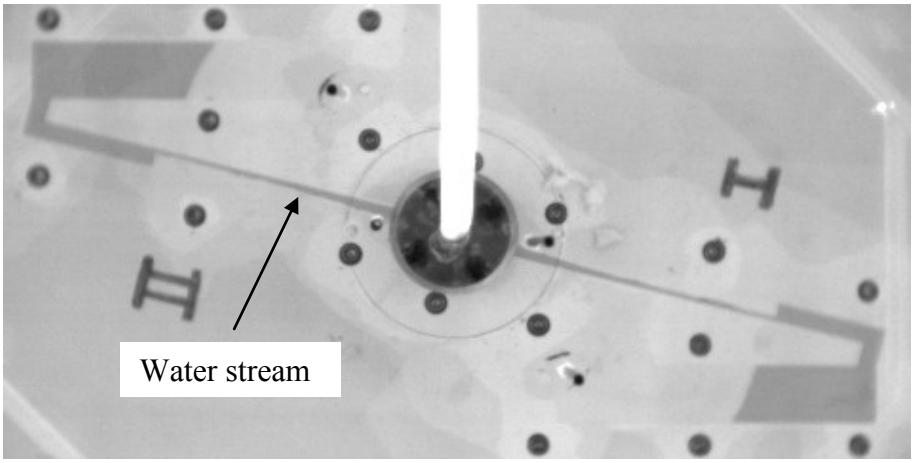

(a) 200 rpm (t = 1.21 s)

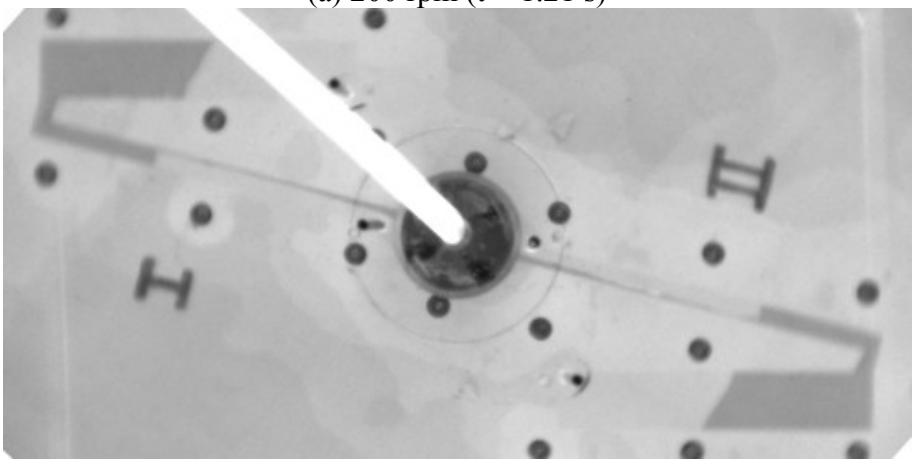

(b) 300 rpm (t = 1.21 s)

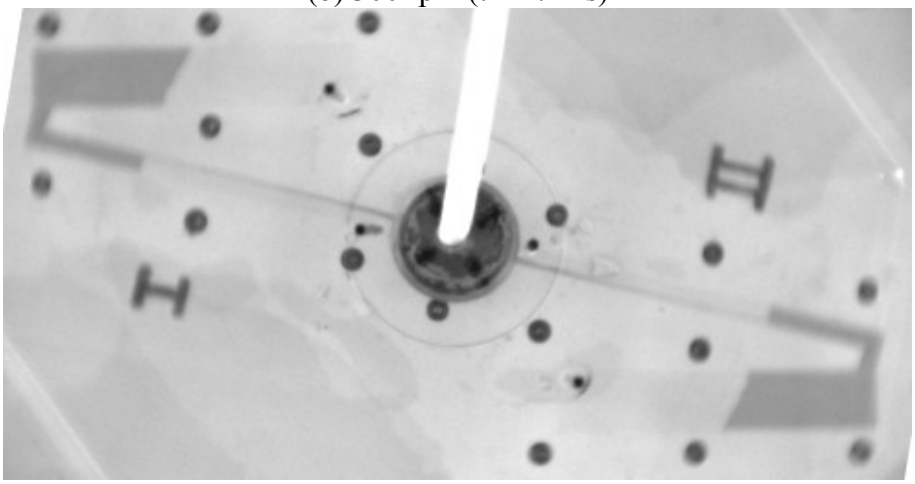

(c) 400 rpm (t = 1.21 s)

Figure 6 - 81. Comparison of the high speed camera snapshots of the indirect gated mould at 200, 300 and 400 rpm in the anti-clockwise direction.

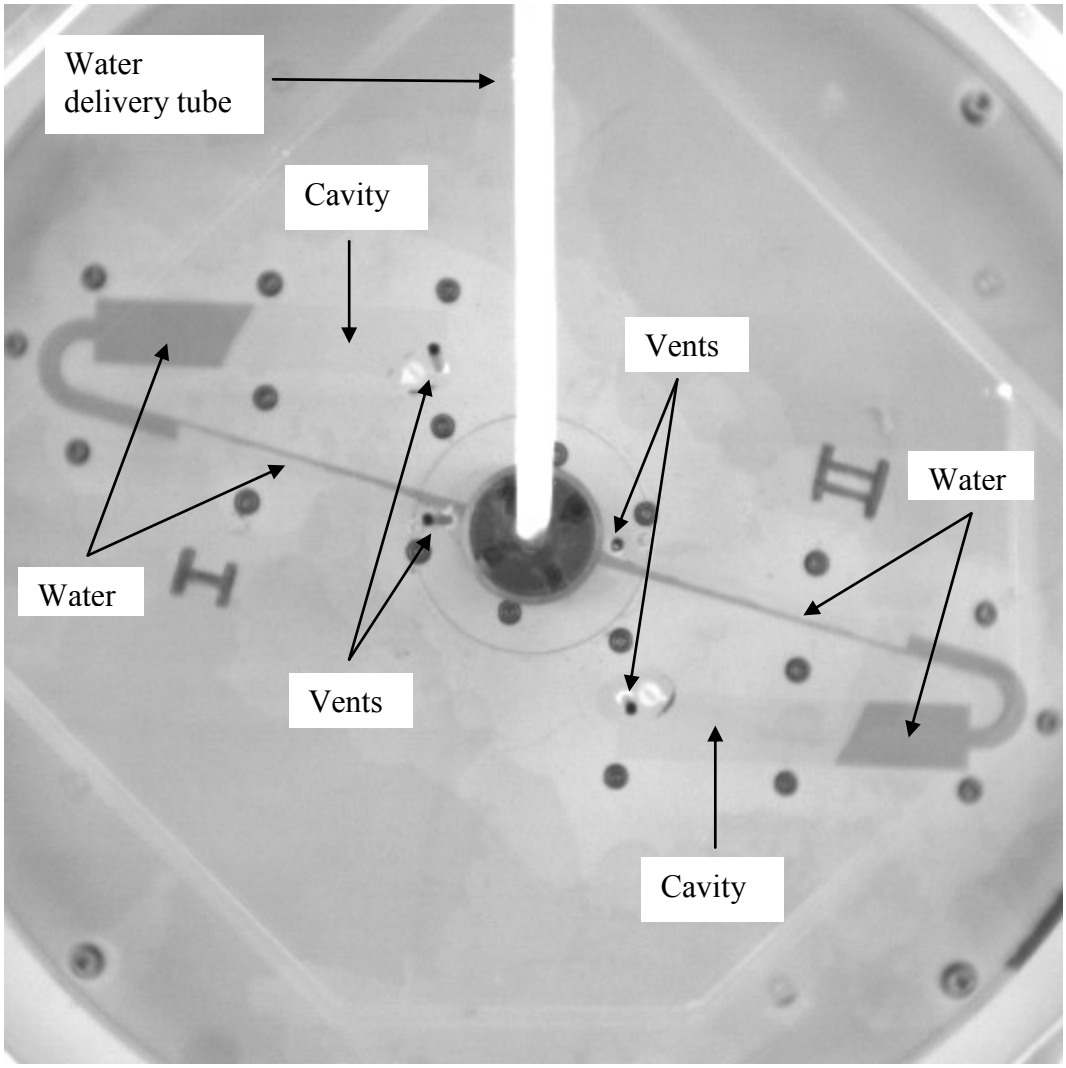

Figure 6 - 82. Snapshot obtained with the high speed camera for the modified indirect gated mould at 1.14 s. The rotational velocity was 200 rpm in the anti-clockwise direction.

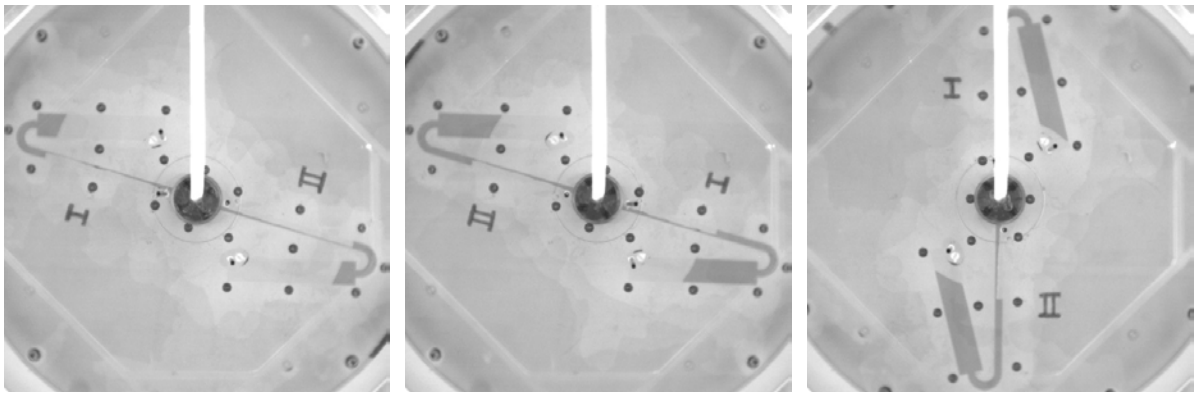

0.84 s 1.29 s 1.68 s

Figure 6 - 83. Summary of the high speed camera results of the modified indirect gated mould filling process. The rotational velocity was 200 rpm in the anti-clockwise direction. Note: Full summary and video sequence can be seen in Appendix 8 and Appendix 38.

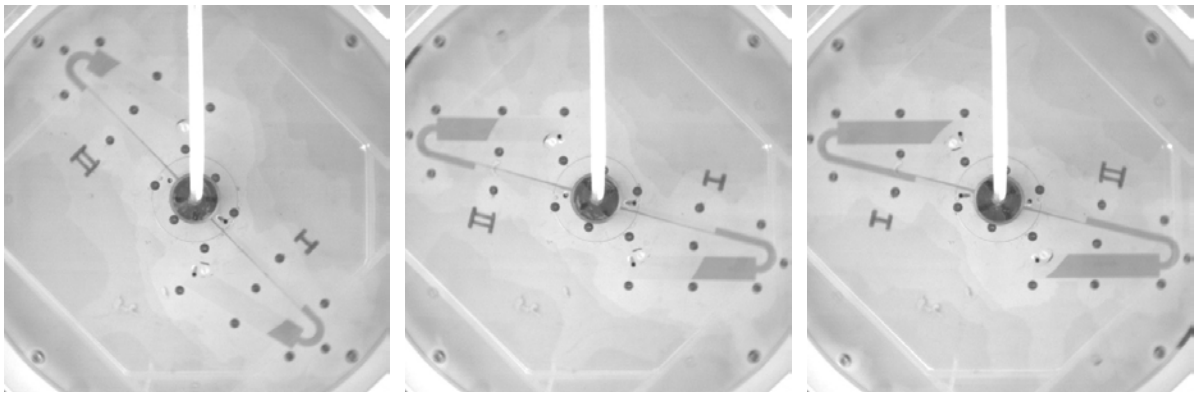

0.85 s 1.27 s 1.77 s

Figure 6 - 84. Summary of the high speed camera results of the modified indirect gated mould filling process. The rotational velocity was 300 rpm in the anti-clockwise direction. Note: Full summary and video sequence can be seen in Appendix 9 and Appendix 39.

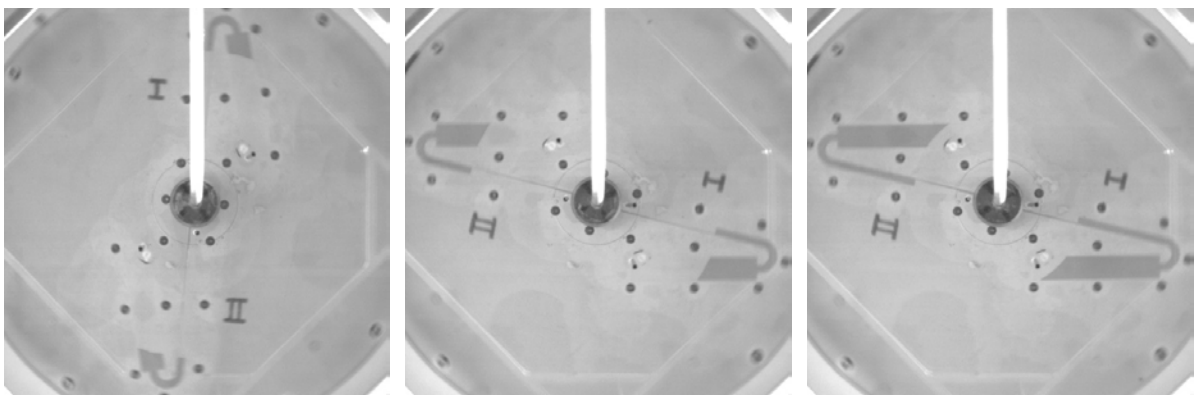

0.82 s 1.23 s 1.83 s

Figure 6 - 85. Summary of the high speed camera results of the modified indirect gated mould filling process. The rotational velocity was 400 rpm in the anti-clockwise direction. Note: Full summary and video sequence can be seen in Appendix 10 and Appendix 40.

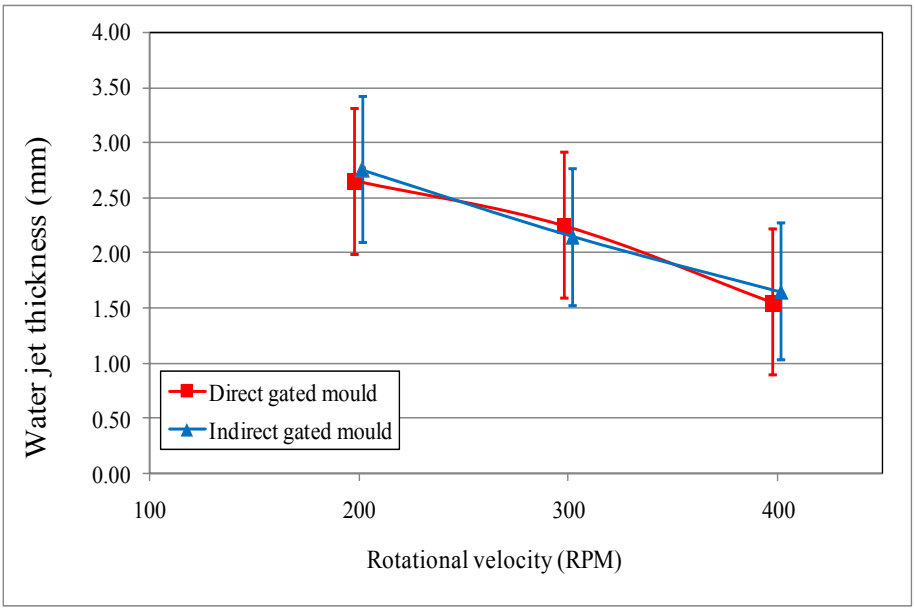

Figure 6 - 86. Experimental results and comparison of the water jet thickness as a function of rotational velocity for the direct and indirect gated moulds.

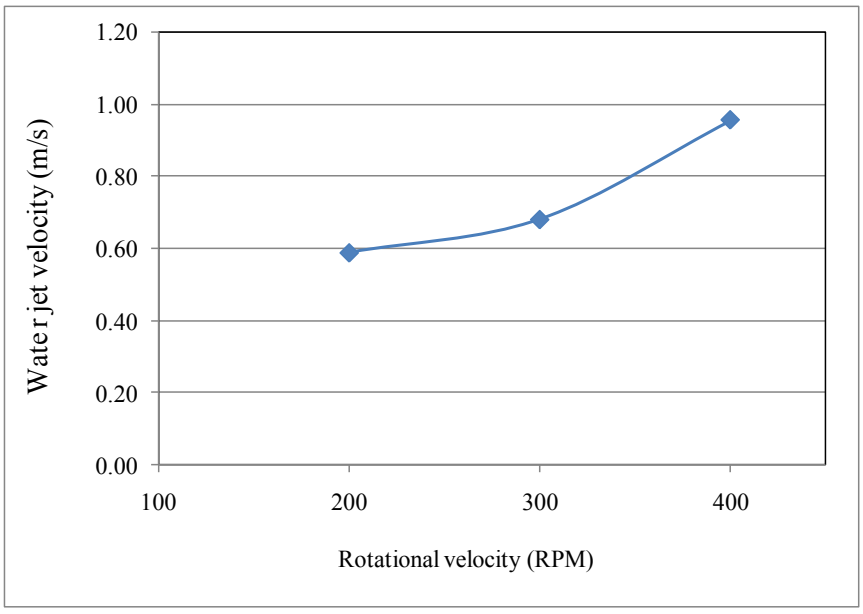

Figure 6 - 87. Experimental results of calculated water jet velocity as a function of rotational velocity for the direct gated mould.

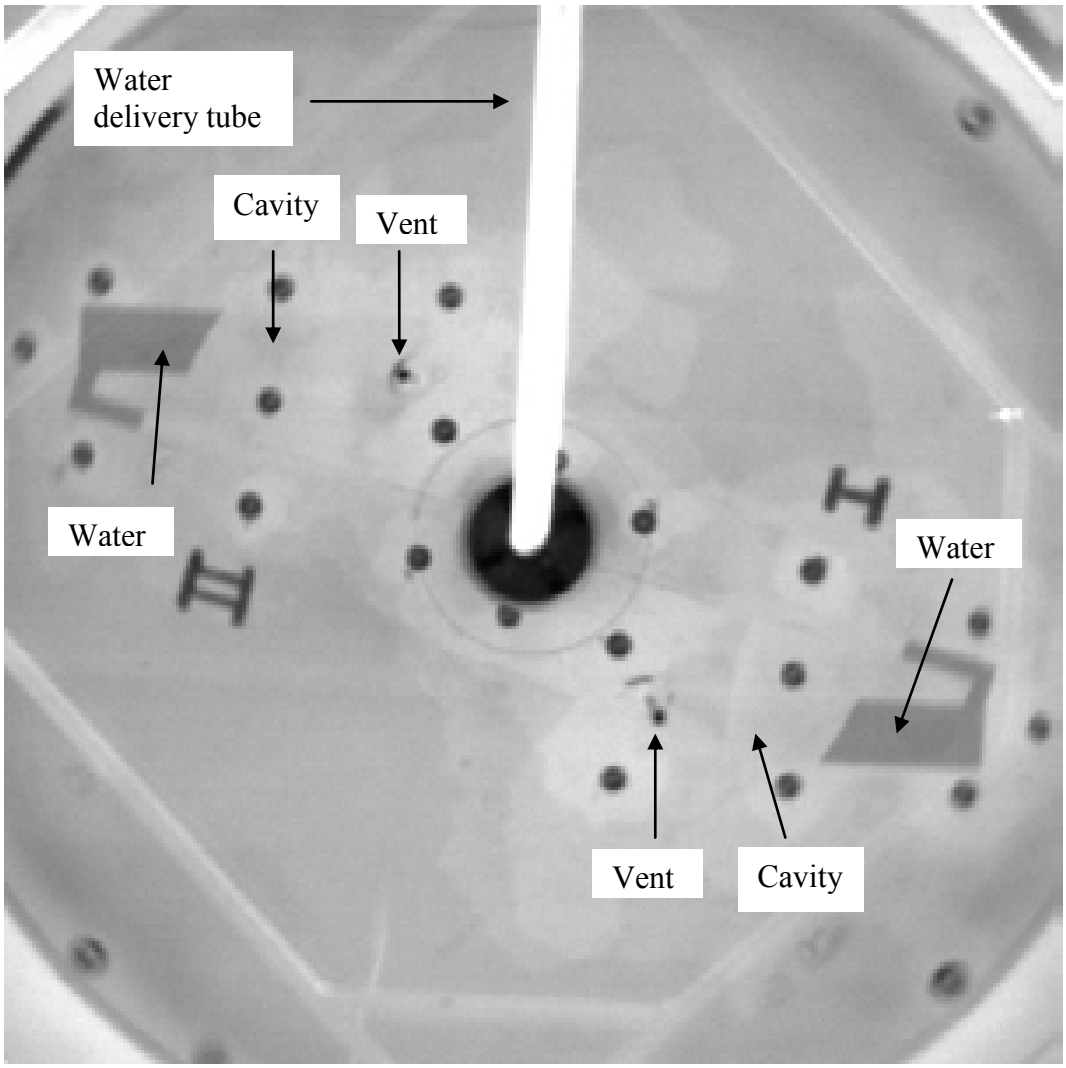

Figure 6 - 88. Snapshot obtained with the high speed camera for the indirect gated mould, which did not include the vents in the runners. The time was 2.60 s and the rotational velocity was 200 rpm in the anti-clockwise direction.

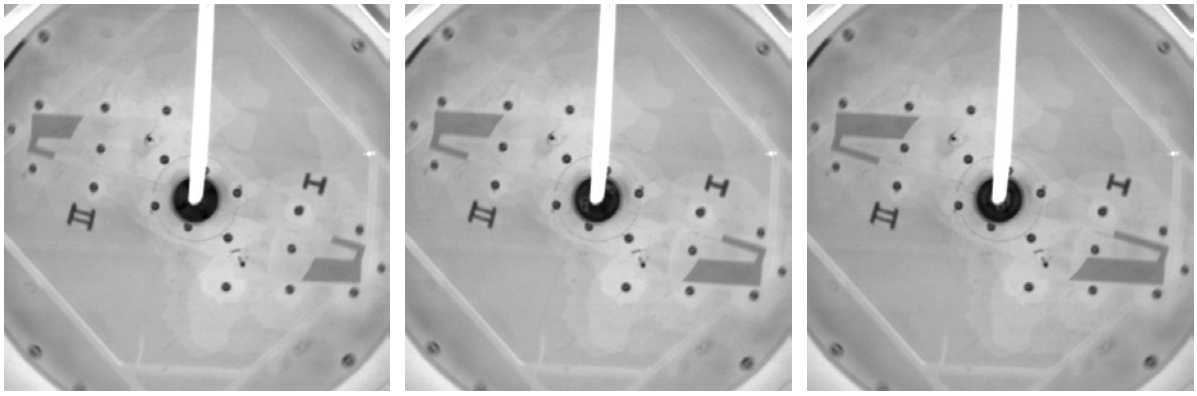

2.60 s 7.99 s 13.39 s

Figure 6 - 89. Summary of the high speed camera results of the indirect gated mould filling process. The Perspex moulds did not include the vents in the runners and the rotational velocity was 200 rpm in the anti-clockwise direction. Note: Full summary can be seen in Appendix 11

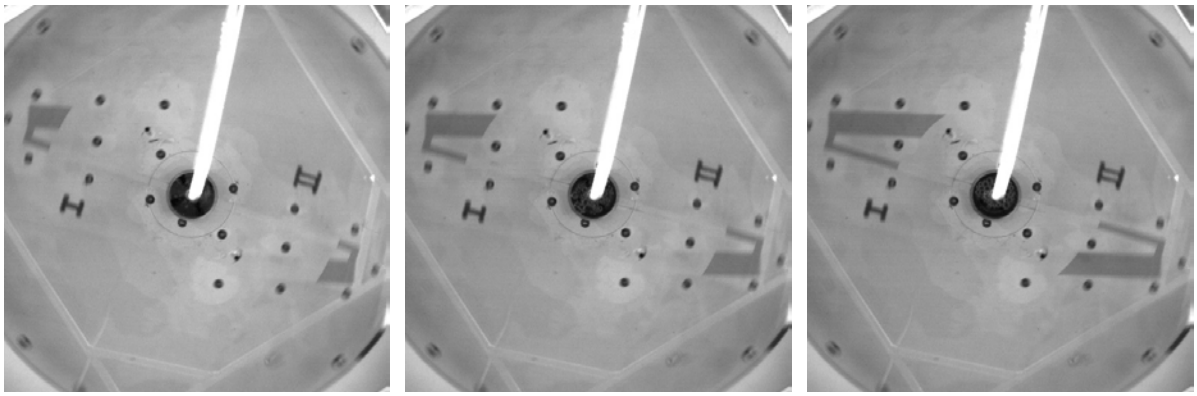

1.90 s 4.10 s 6.50 s

Figure 6 - 90. Summary of the high speed camera results of the indirect gated mould filling process. The Perspex moulds did not include the vents in the runners and the rotational velocity was 300 rpm in the anti-clockwise direction. Note: Full summary can be seen in Appendix 12.

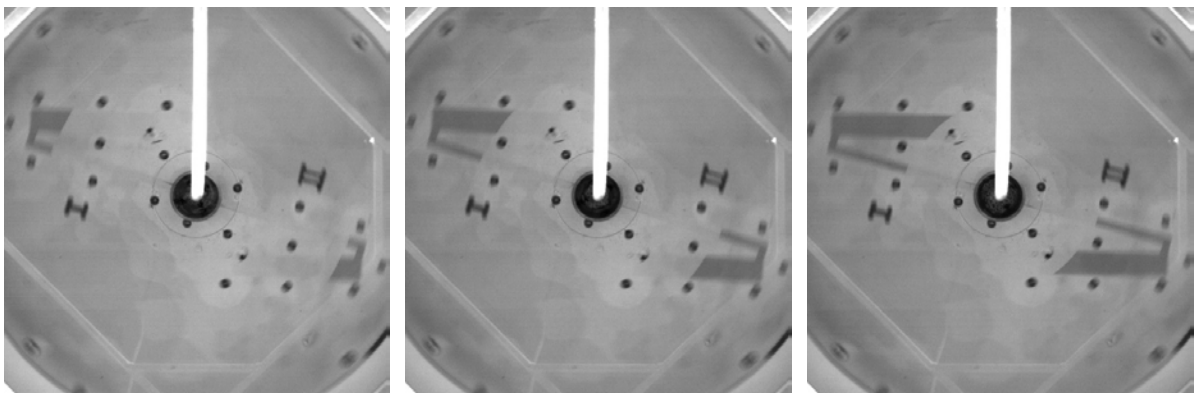

1.87 s 3.67 s 6.07 s

Figure 6 - 91. Summary of the high speed camera results of the indirect gated mould filling process. The Perspex moulds did not include the vents in the runners and the rotational velocity was 400 rpm in the anti-clockwise direction. Note: Full summary can be seen in Appendix 13.

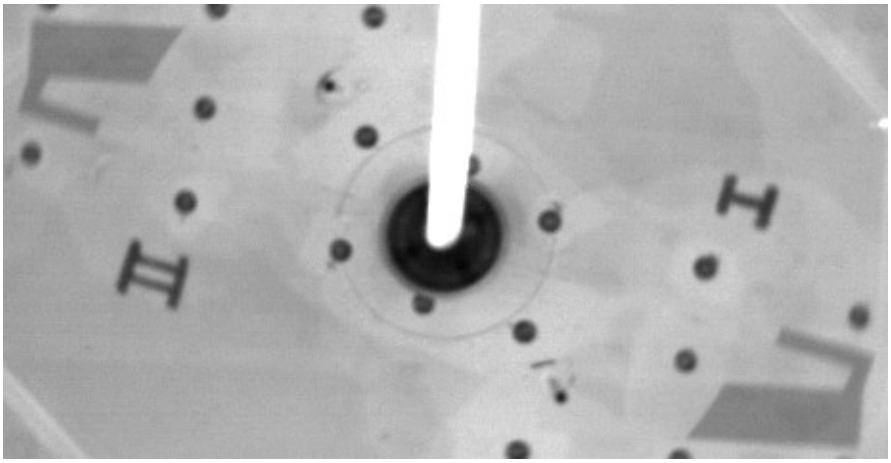

(a) 200 rpm (t = 4.40 s)

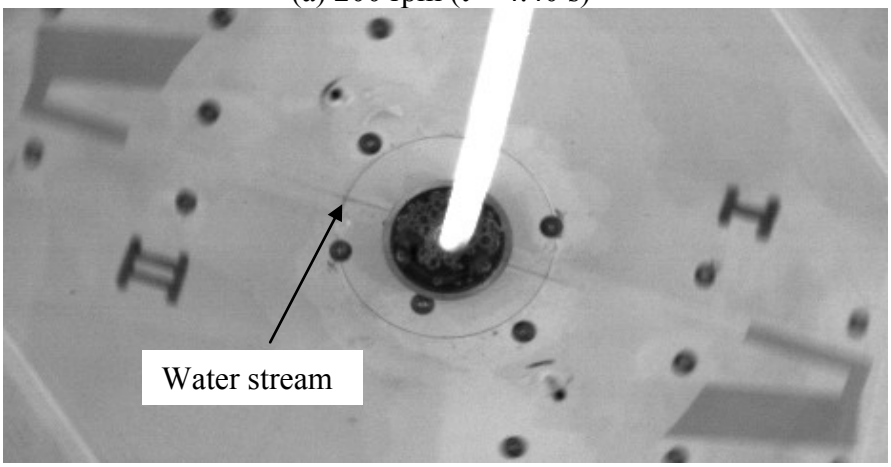

(b) 300 rpm (t = 4.40 s)

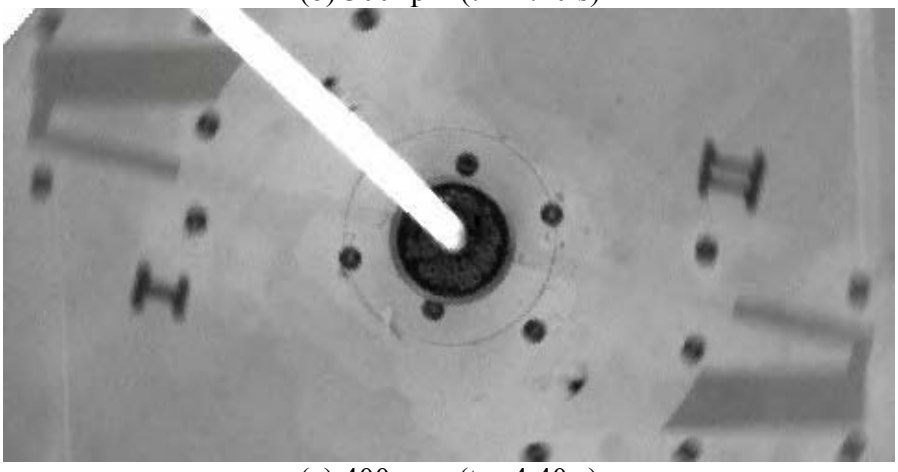

(c) 400 rpm (t = 4.40 s)

Figure 6 - 92. Comparison of the high speed camera snapshots of the indirect gated mould at 200, 300 and 400 rpm in the anti-clockwise direction. The Perspex mould did not include the vents in the runners.

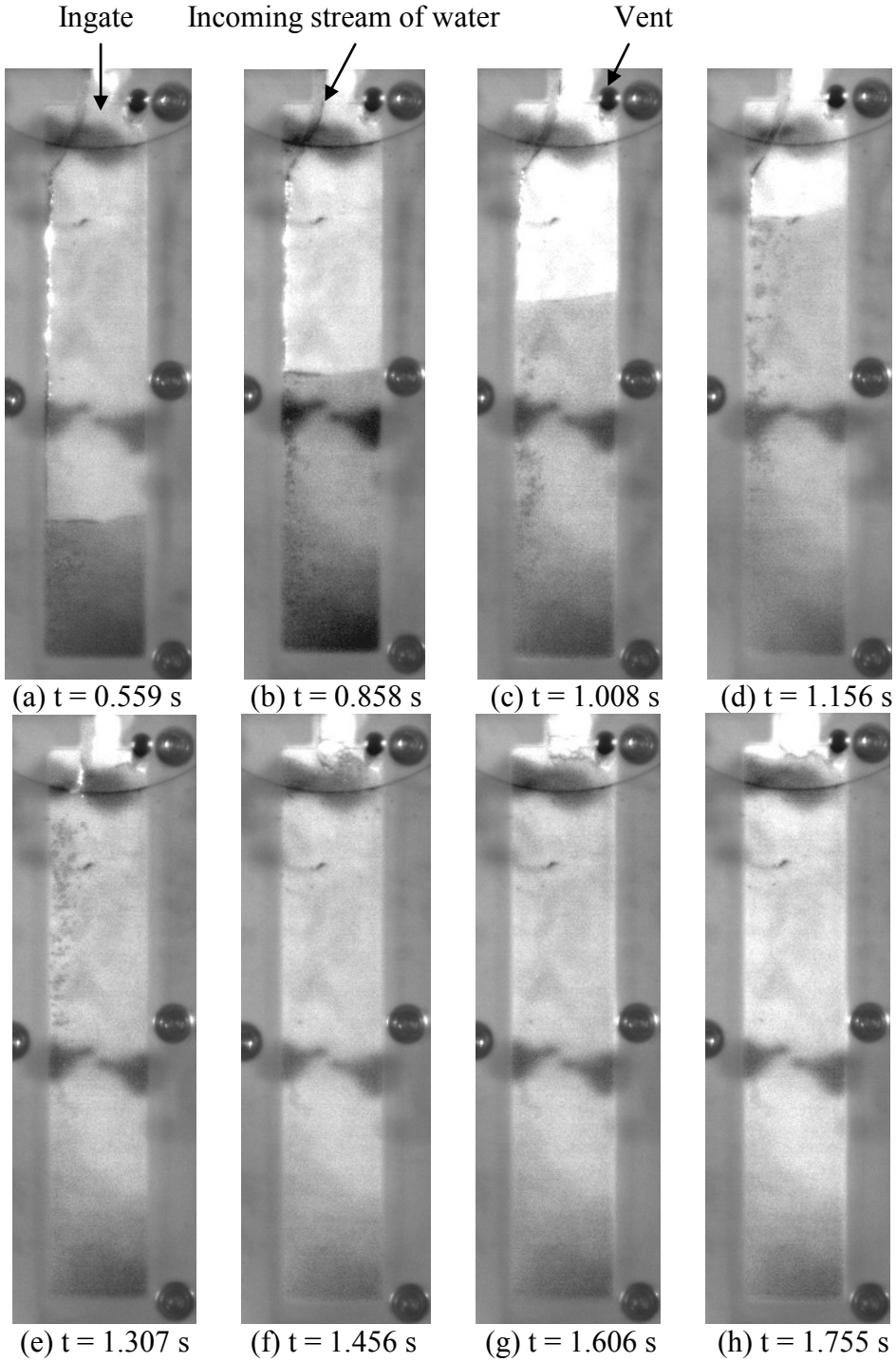

Figure 6 - 93. High speed camera results of the direct gated mould filling process. The thickness of the cavity was 2 mm and the rotational velocity was 400 rpm in the anti-clockwise direction. The snapshots were taken from the test bar I. Note: The areas marked S are shadows from the bolts used to assemble the Perspex moulds to the turntable. Full video sequence can be seen in Appendix 41.

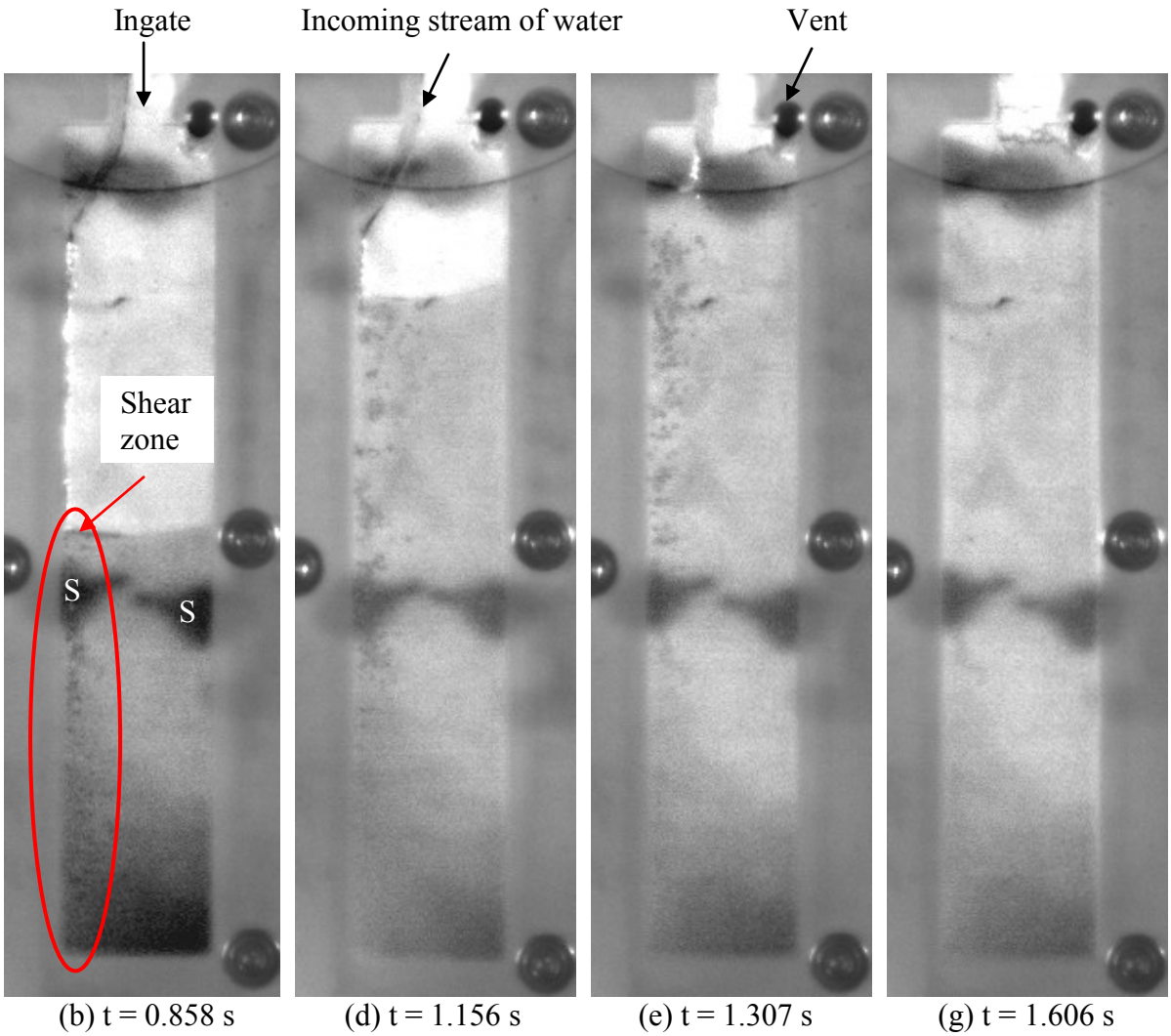

Figure 6 - 94. Close-up of high speed camera results of the direct gated mould filling process. The thickness of the cavity was 2 mm and the rotational velocity was 400 rpm in the anti-clockwise direction. The snapshots were taken from the test bar I. Note: The areas marked S are shadows from the bolts used to assemble the Perspex moulds to the turntable. Full video sequence can be seen in Appendix 41.

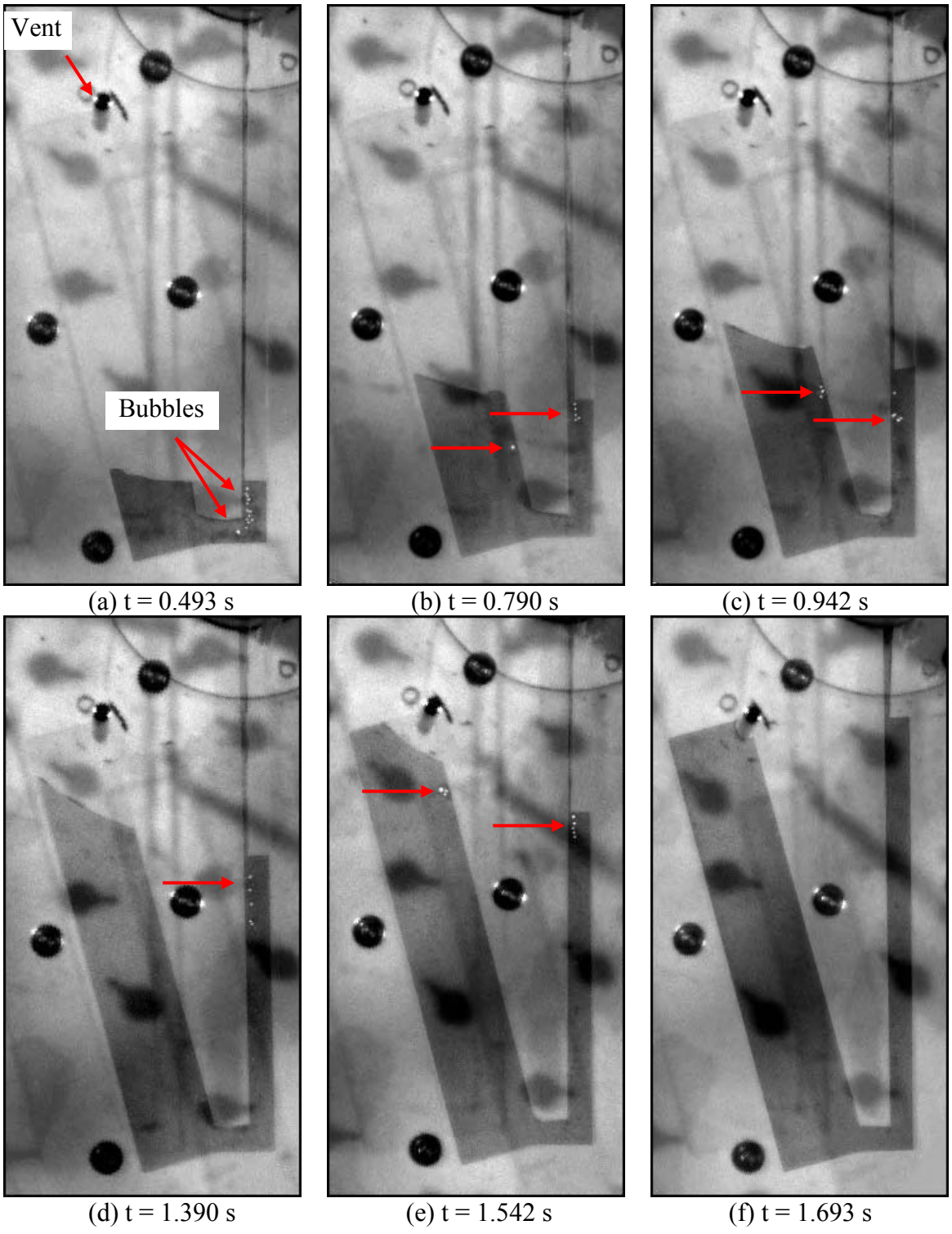

Figure 6 - 95. High speed camera results of the indirect gated mould filling. The thickness of the cavity was 2 mm and the rotational velocity was 400 rpm in the anti-clockwise direction. The snapshots were taken from the test bar I. Note: Full video sequence can be seen in Appendix 42.

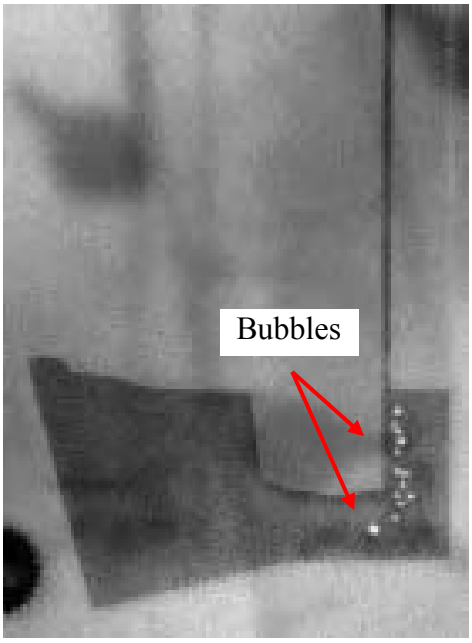

(a) t = 0.493 s

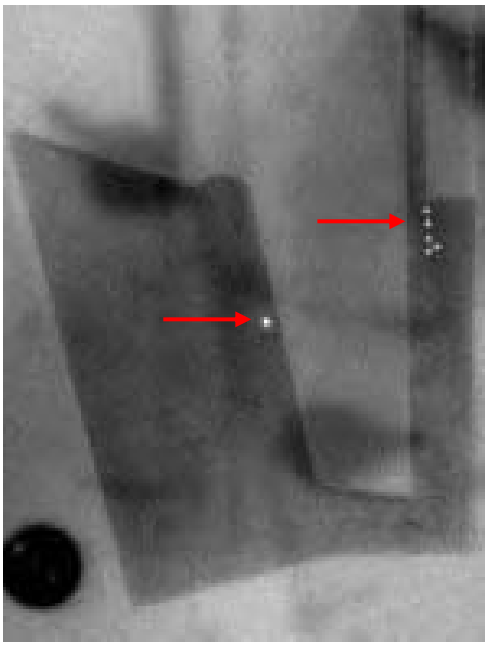

(b) t = 0.790 s

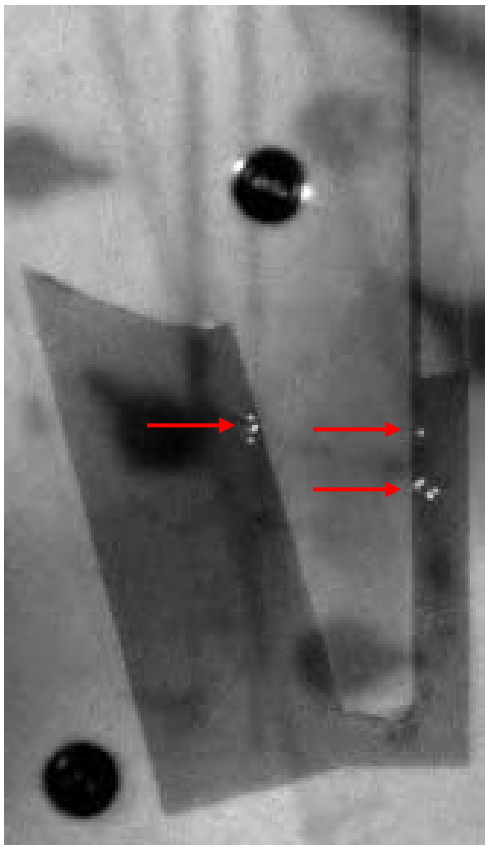

(c) t = 0.942 s

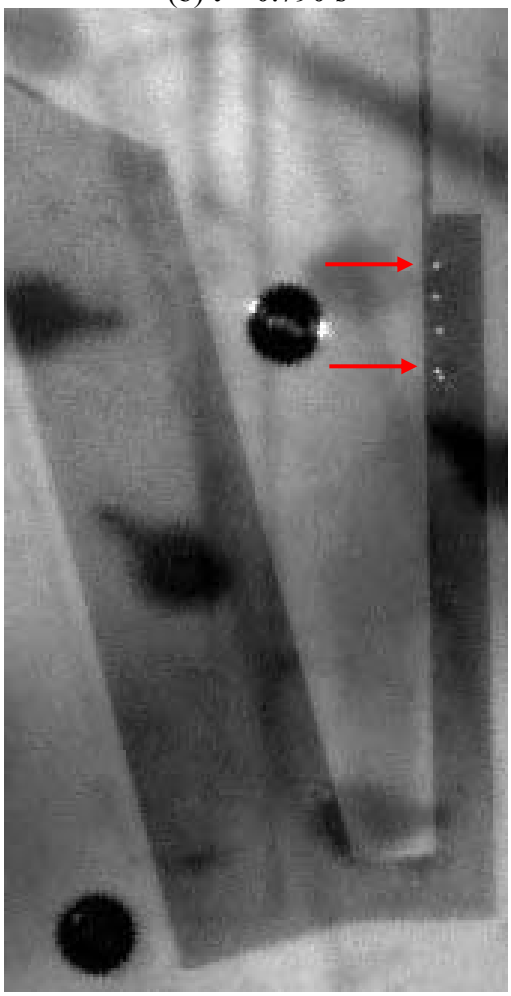

(d) t = 1.390 s

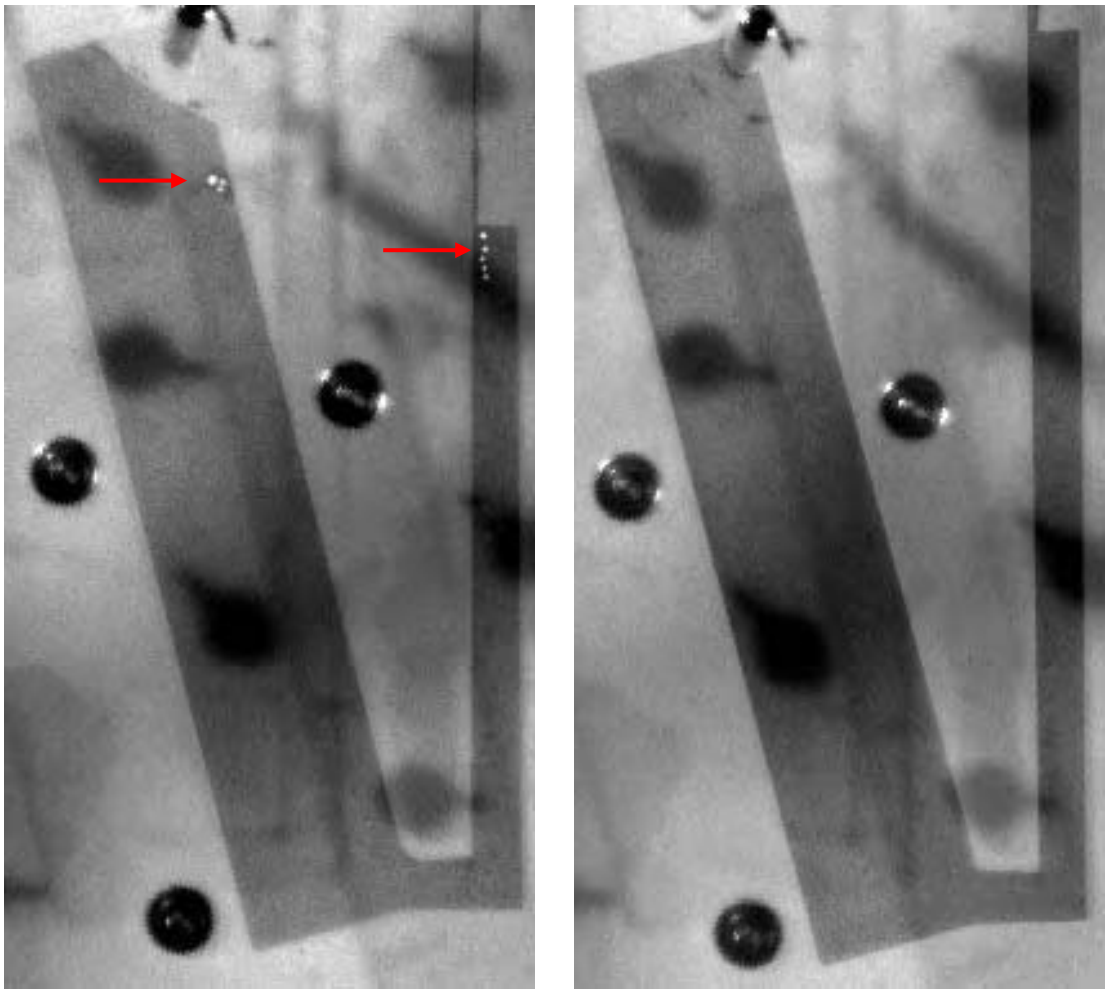

(e) t = 1.542 s (f) t = 1.693 s

Figure 6 - 96. Close-up of high speed camera results of the indirect gated mould filling. The thickness of the cavity was 2 mm and the rotational velocity was 400 rpm in the anti-clockwise direction. The snapshots were taken from the test bar I. Note: Full video sequence can be seen in Appendix 42.

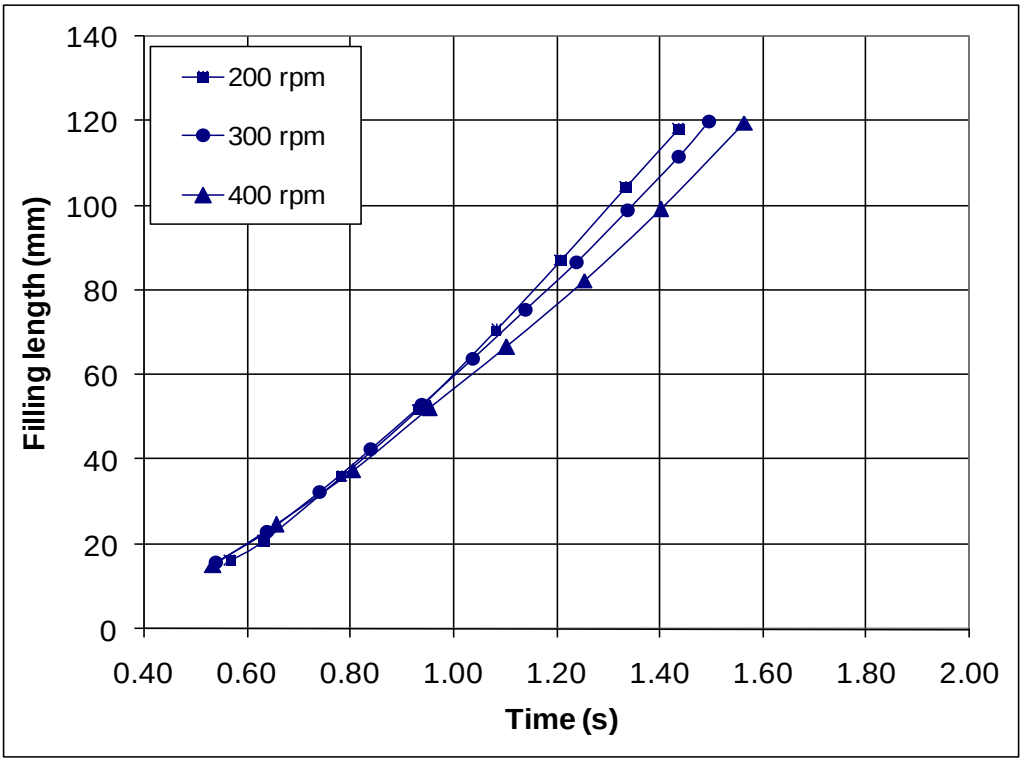

Figure 6 - 97. Experimental water modelling results of filling length measurements for the direct gated mould design showing average results obtained from both test bars.

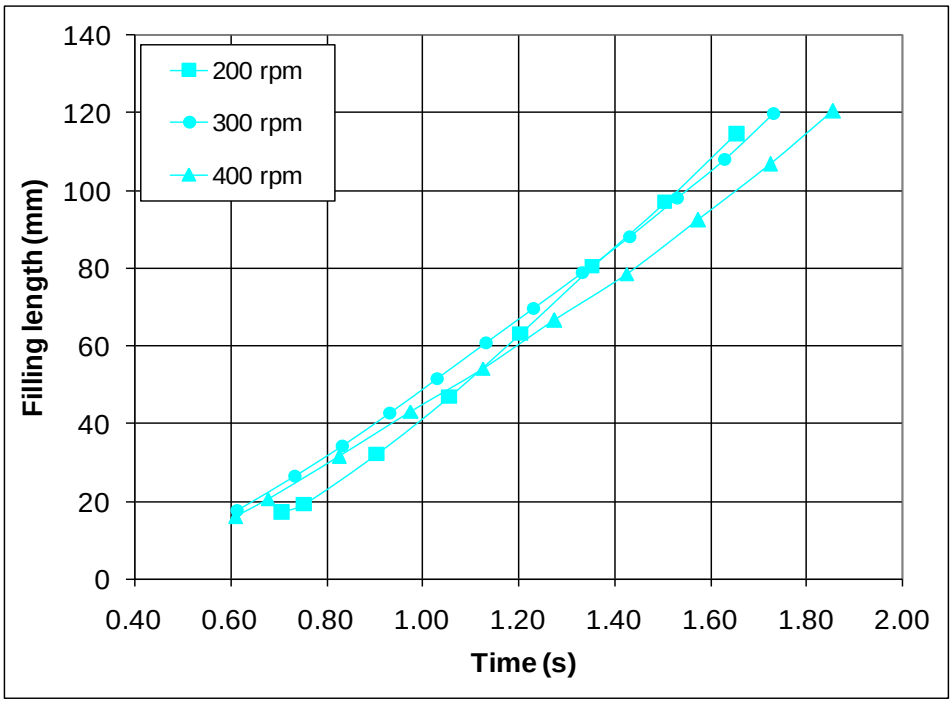

(a)

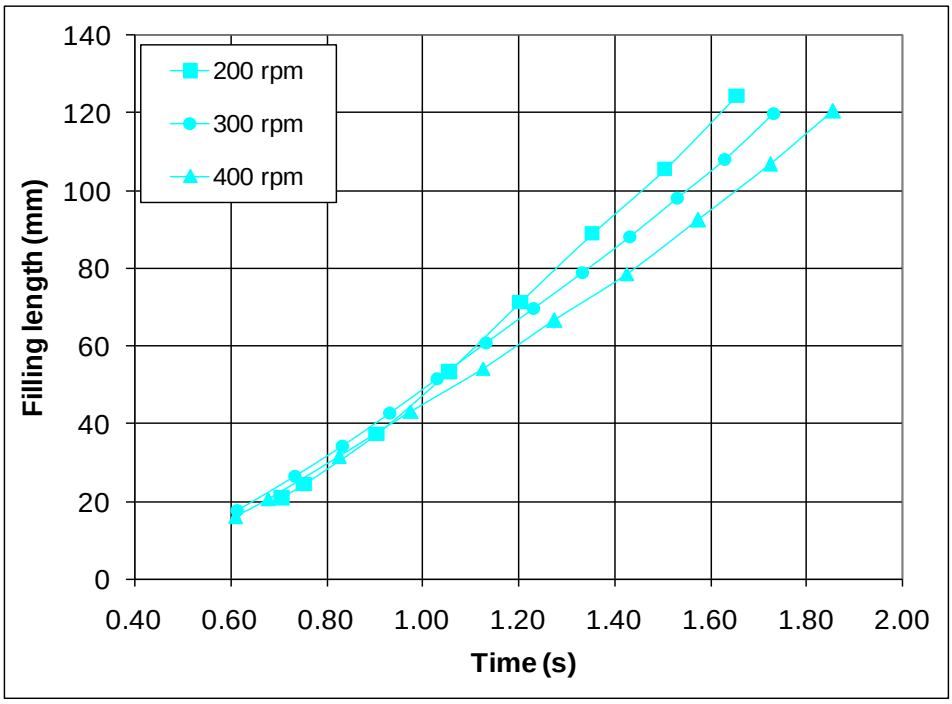

(b)

Figure 6 - 98. Experimental water modelling results of filling length measurements for the indirect gating mould design showing (a) average results obtained from both test bars and (b) average results obtained from both test bars except for rotational velocity of 200 rpm, where results are only from test bar 2.

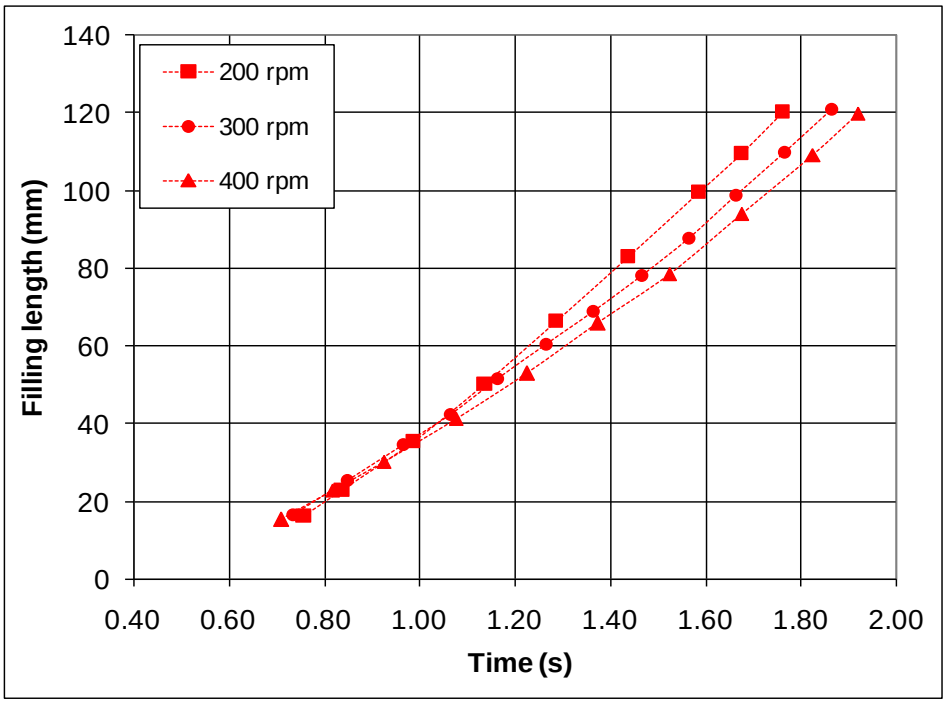

Figure 6 - 99. Experimental water modelling results of filling length measurements for the modified indirect gating mould design showing average results obtained from both test bars.

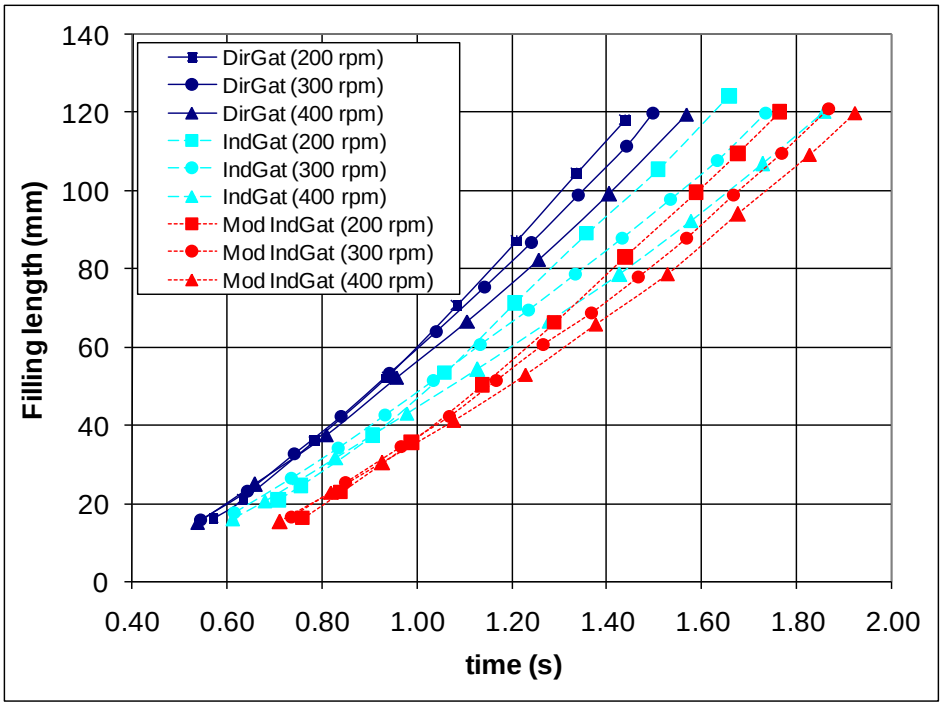

Figure 6 - 100. Comparison of experimental water modelling results of filling length as a function of rotational velocity for the three mould designs.

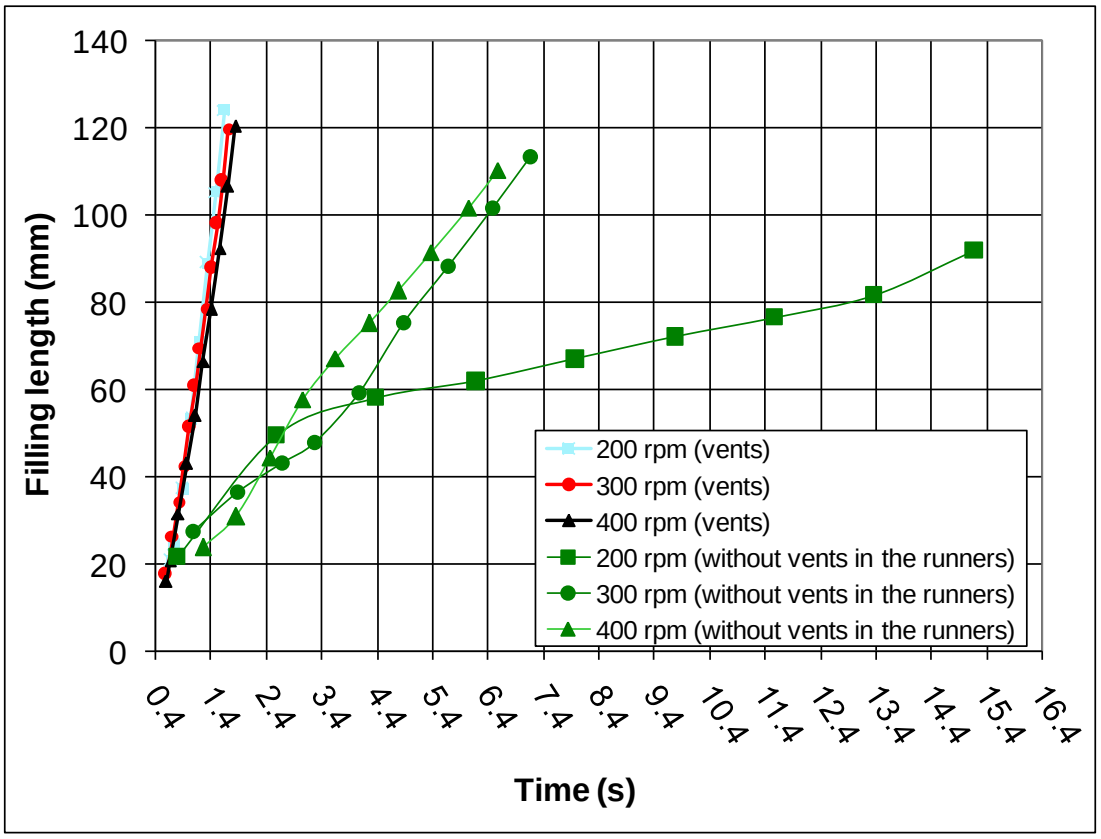

Figure 6 - 101. Comparison of the experimental water modelling results of filling length measurements for the indirect gating mould design with and without vents in the runners.

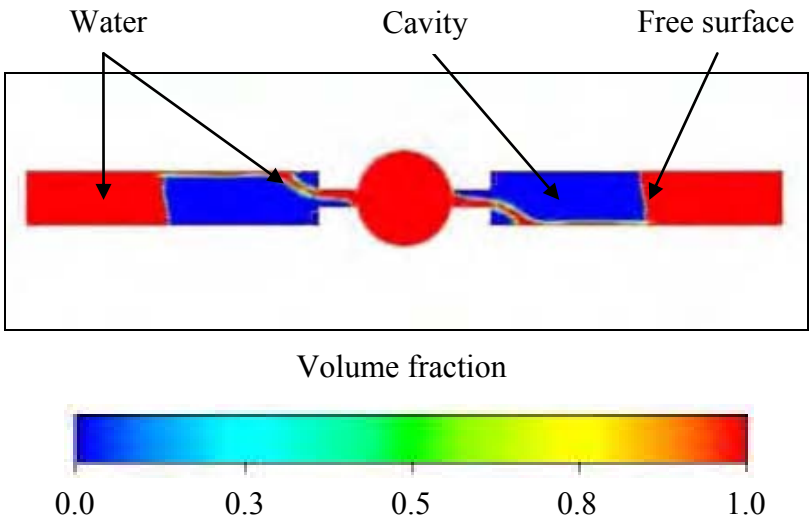

Figure 6 - 102. 2D snapshot obtained with ANSYS CFX for the direct gated water model mould showing plan view at 1.02 s. The rotational velocity was 200 rpm in the anti-clockwise direction and the cut plane was taken 0.5 mm from the base.

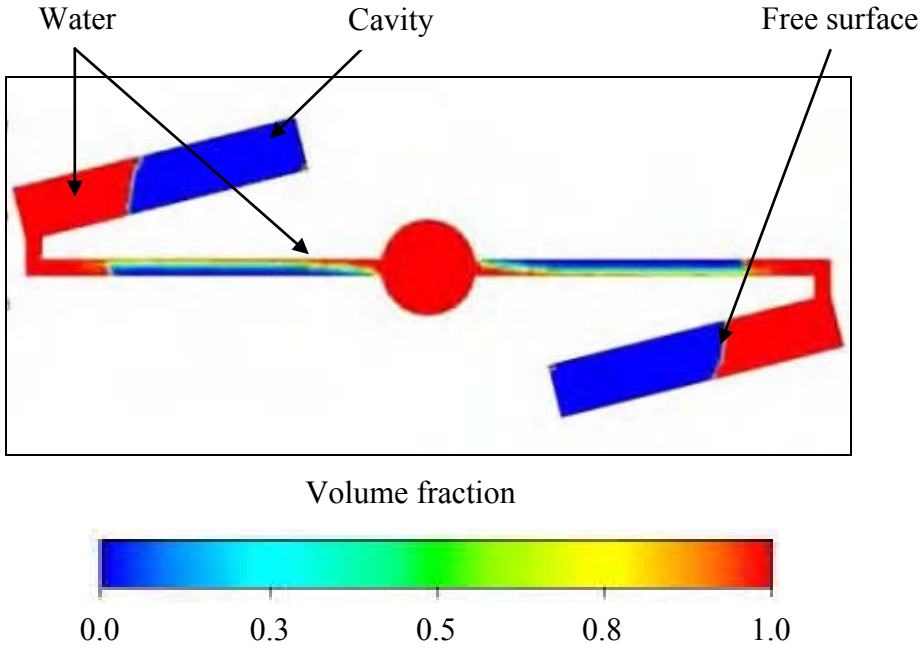

Figure 6 - 103. 2D snapshot obtained with ANSYS CFX for the indirect gated water model mould showing plan view at 1.05 s. The rotational velocity was 200 rpm in the anti-clockwise direction and the cut plane was taken 0.5 mm from the base.

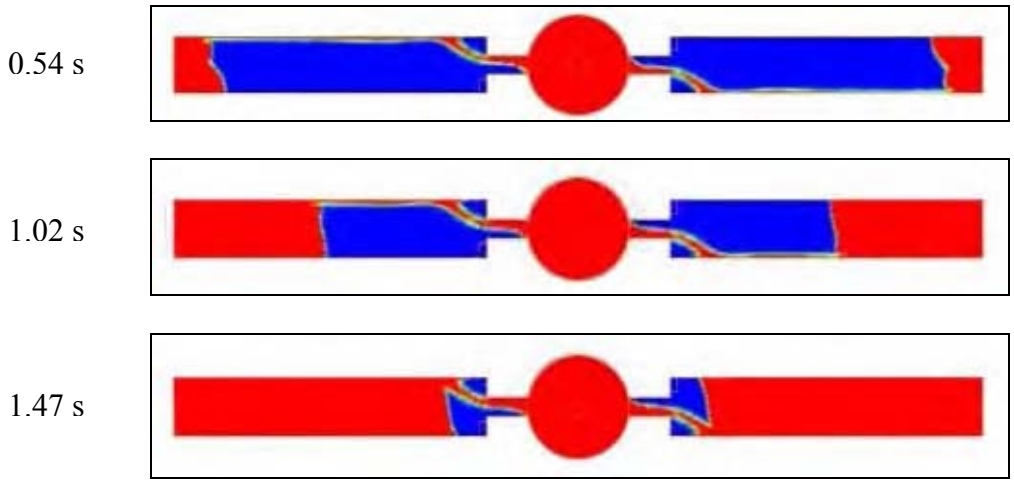

Figure 6 - 104. ANSYS CFX results of the direct gated water model mould showing plan view. The rotational velocity was 200 rpm in the anti-clockwise direction and the cut plane was taken 0.5 mm from the base. Note: Full summary and video sequence can be seen in Appendix 14 and Appendix 43.

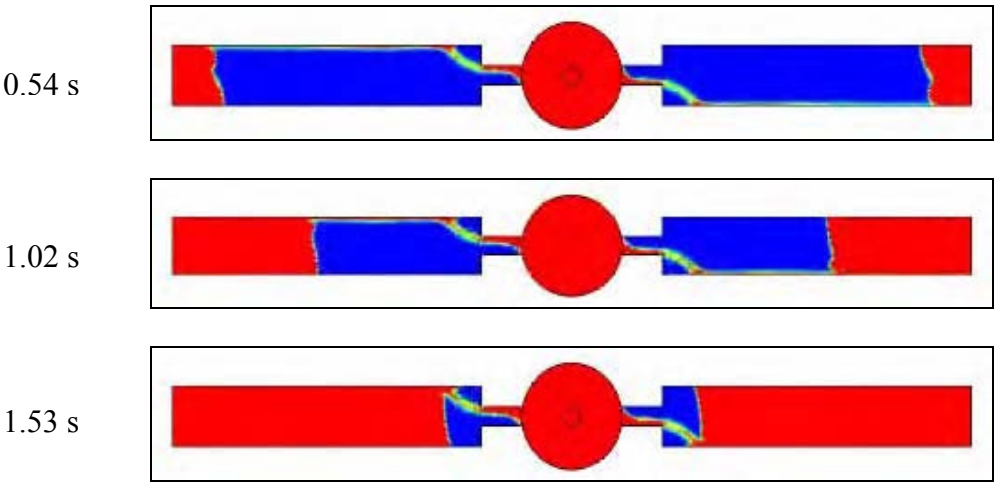

Figure 6 - 105. ANSYS CFX results of the direct gated water model mould showing plan view. The rotational velocity was 300 rpm in the anti-clockwise direction and the cut plane was taken 0.5 mm from the base. Note: Full summary and video sequence can be seen in Appendix 15 and Appendix 44.

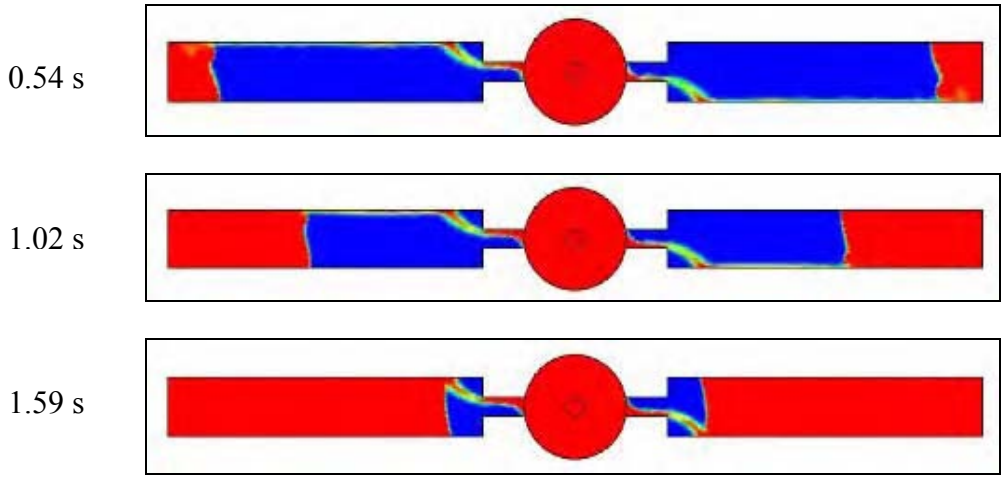

Figure 6 - 106. ANSYS CFX results of the direct gated water model mould showing plan view. The rotational velocity was 400 rpm in the anti-clockwise direction and the cut plane was taken 0.5 mm from the base. Note: Full summary and video sequence can be seen in Appendix 16 and Appendix 45.

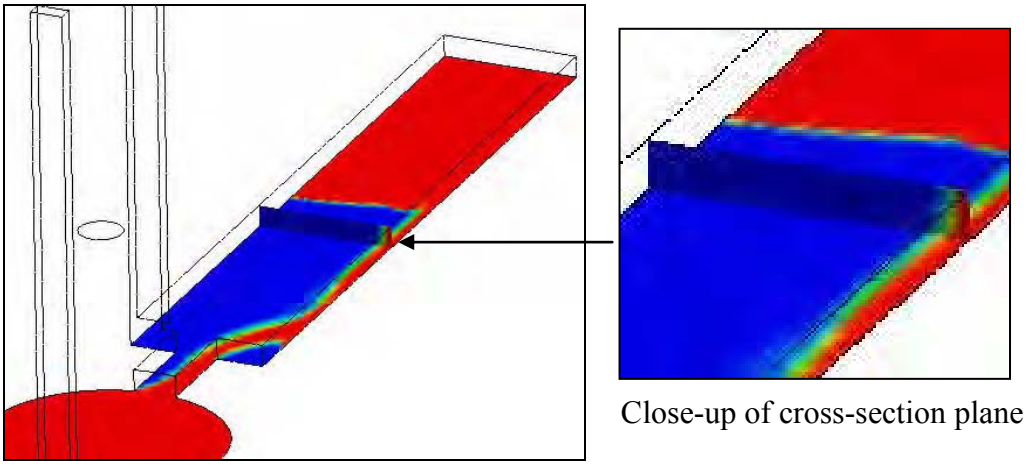

(a) 200 rpm (t = 1.05 s) Mass flow rate = 10.31 g/s

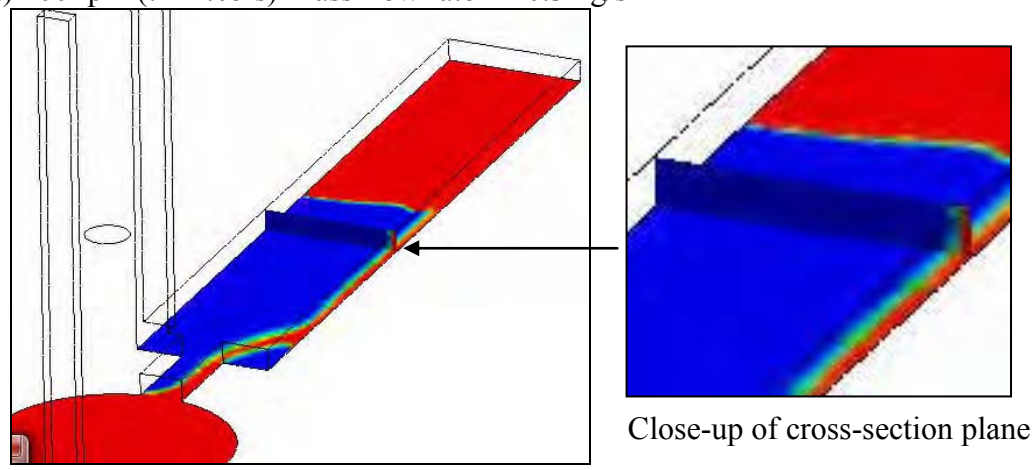

(b) 300 rpm (t = 1.05 s) Mass flow rate = 9.70 g/s

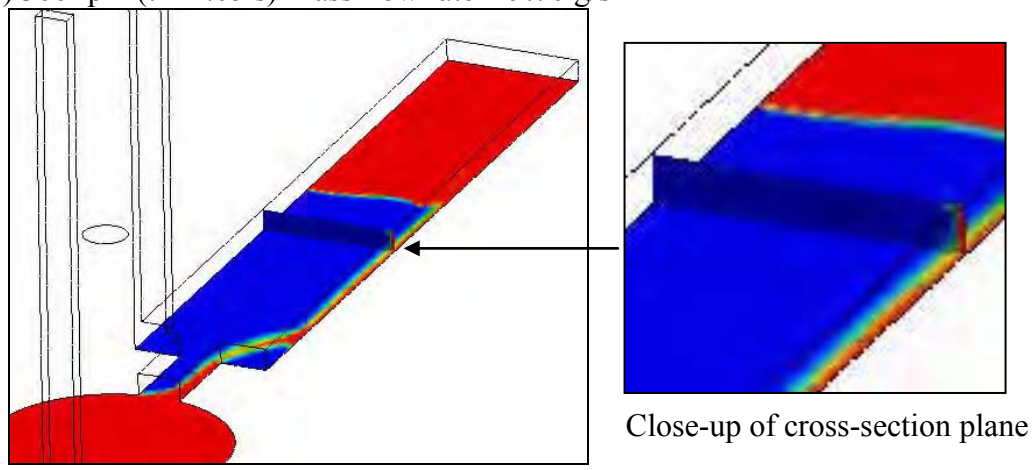

(c) 400 rpm (t = 1.05 s) Mass flow rate = 9.11 g/s

Figure 6 - 107. Comparison of the simulation results of the direct gated mould at (a) 200, (b) 300 and (c) 400 rpm in the anti-clockwise direction. The cut plane was taken close to the test bar base and the cross-section cut plane was taken at a radial distance of 95 mm.

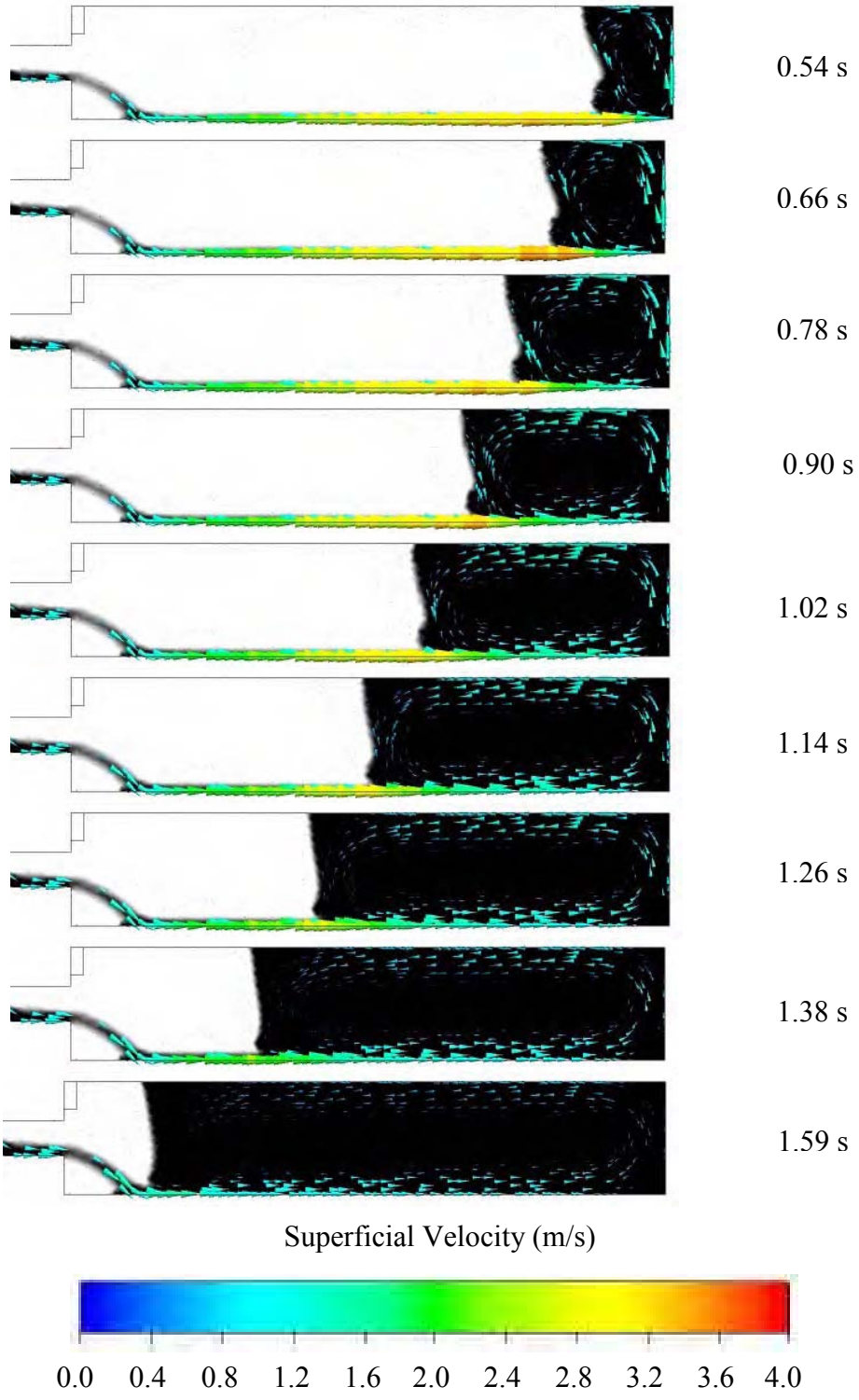

Figure 6 - 108. ANSYS CFX results of the direct gated water model mould showing close-up of the right hand test bar and velocity vectors (see Figure 6 - 106). The rotational velocity was 400 rpm in the anti-clockwise direction and the cut plane was taken 0.5 mm from the base.

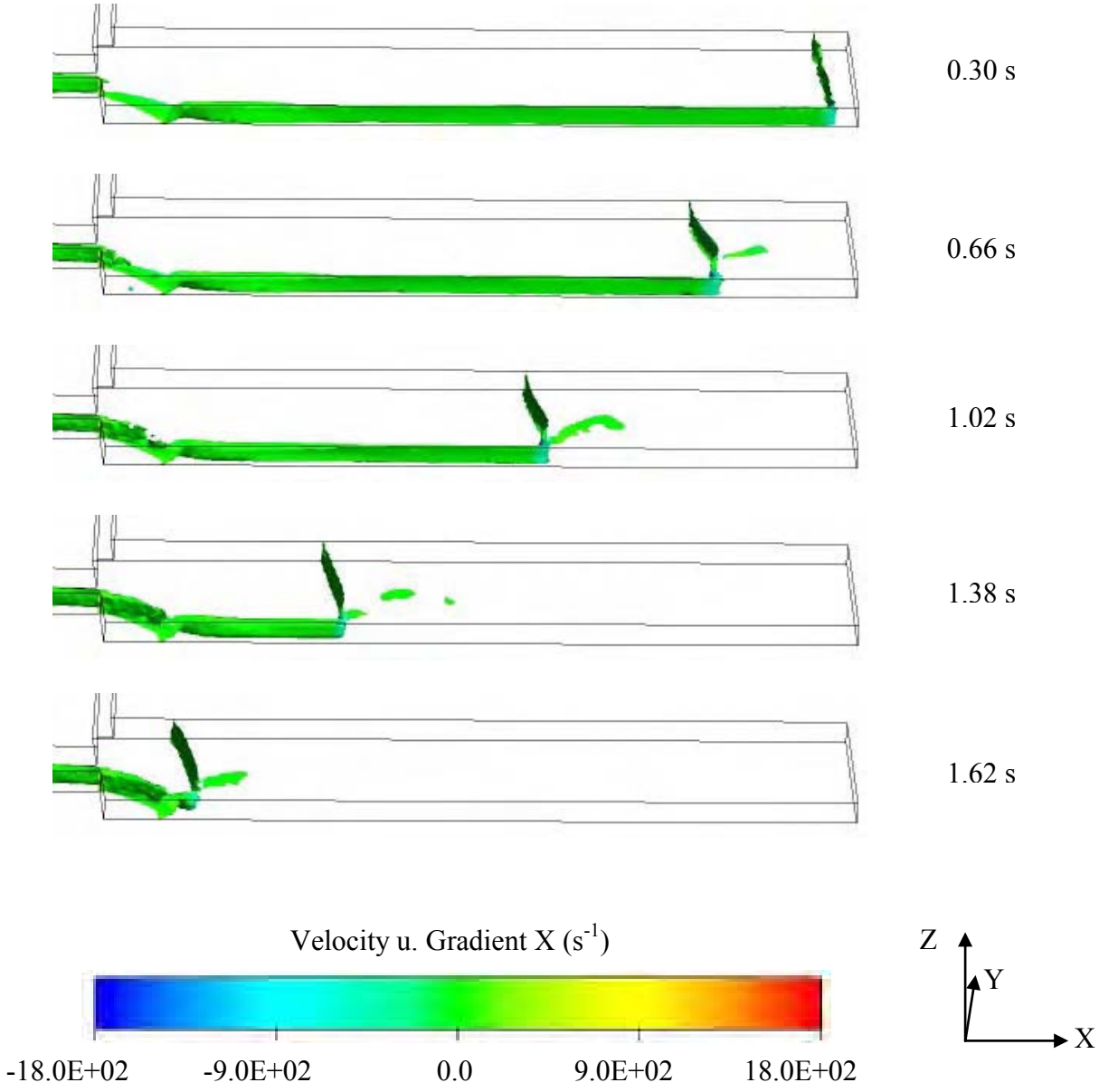

Figure 6 - 109. ANSYS CFX results of the direct gated water model mould showing close-up of the right hand test bar, isosurface (0.5 volume fraction) and velocity gradients in "X" axis (see Figure 6 - 106). The rotational velocity was 400 rpm in the anti-clockwise direction. Note: Full summary can be seen in Appendix 17.

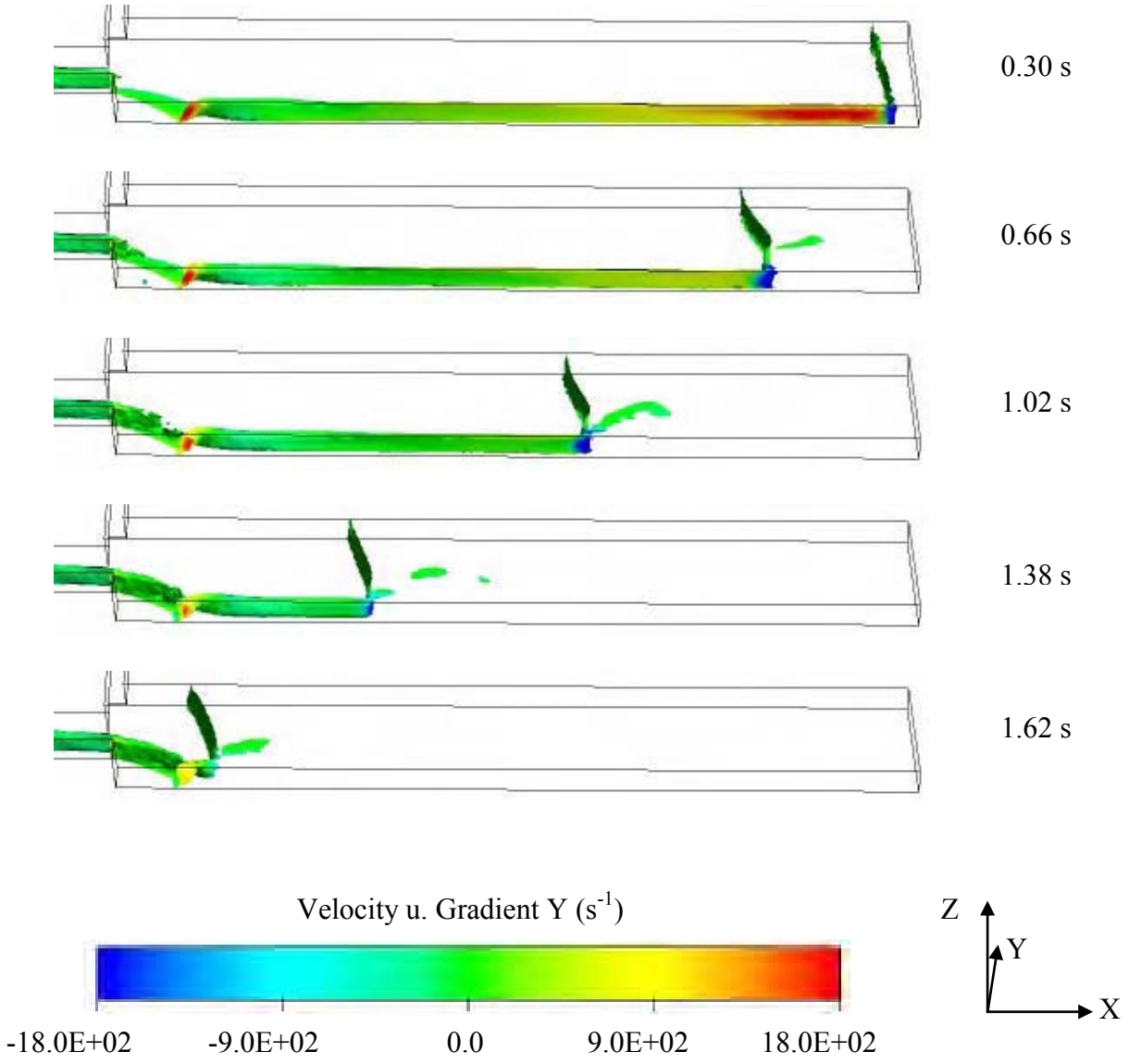

Figure 6 - 110. ANSYS CFX results of the direct gated water model mould showing close-up of the right hand test bar, isosurface (0.5 volume fraction) and velocity gradients in "Y" axis (see Figure 6 - 106). The rotational velocity was 400 rpm in the anti-clockwise direction. Note: Full summary can be seen in Appendix 18.

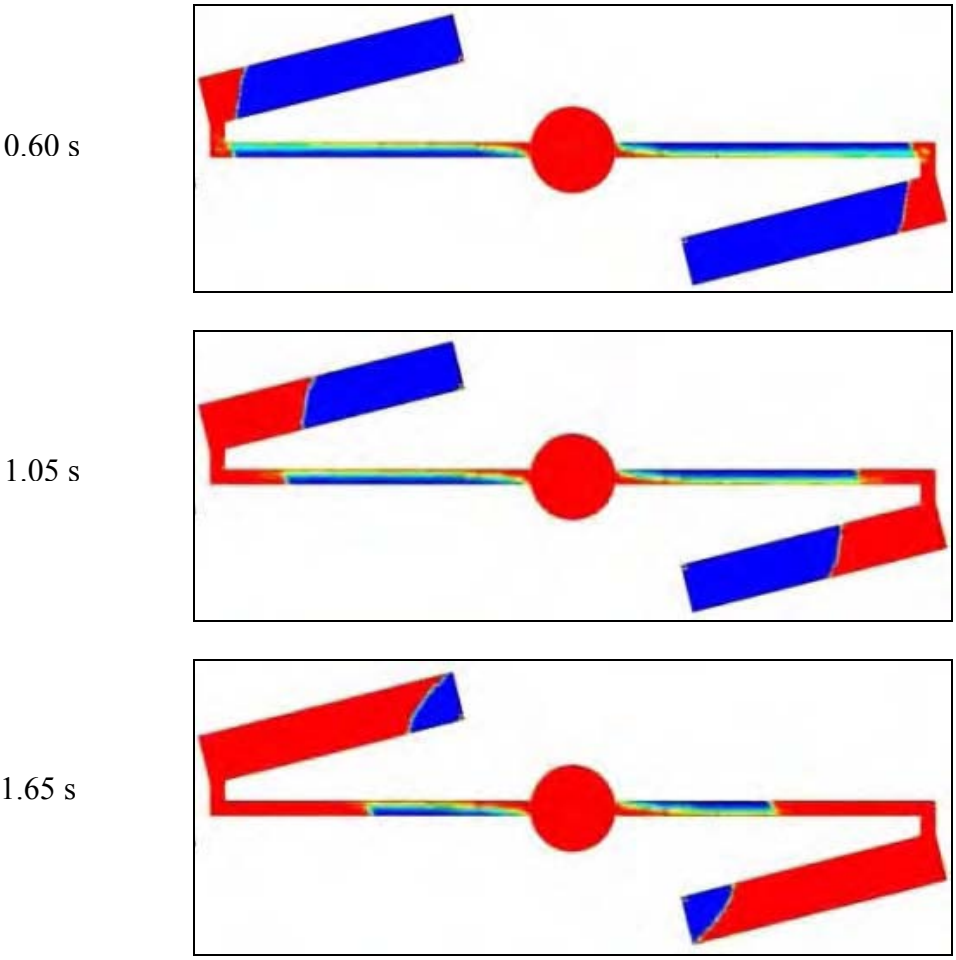

Figure 6 - 111. ANSYS CFX results of the indirect gated water model mould showing 2D plan view. The rotational velocity is 200 rpm in the anti-clockwise direction and the cut plane was taken 0.5 mm from the base. Note: Full summary and video sequence can be seen in Appendix 19 and Appendix 46.

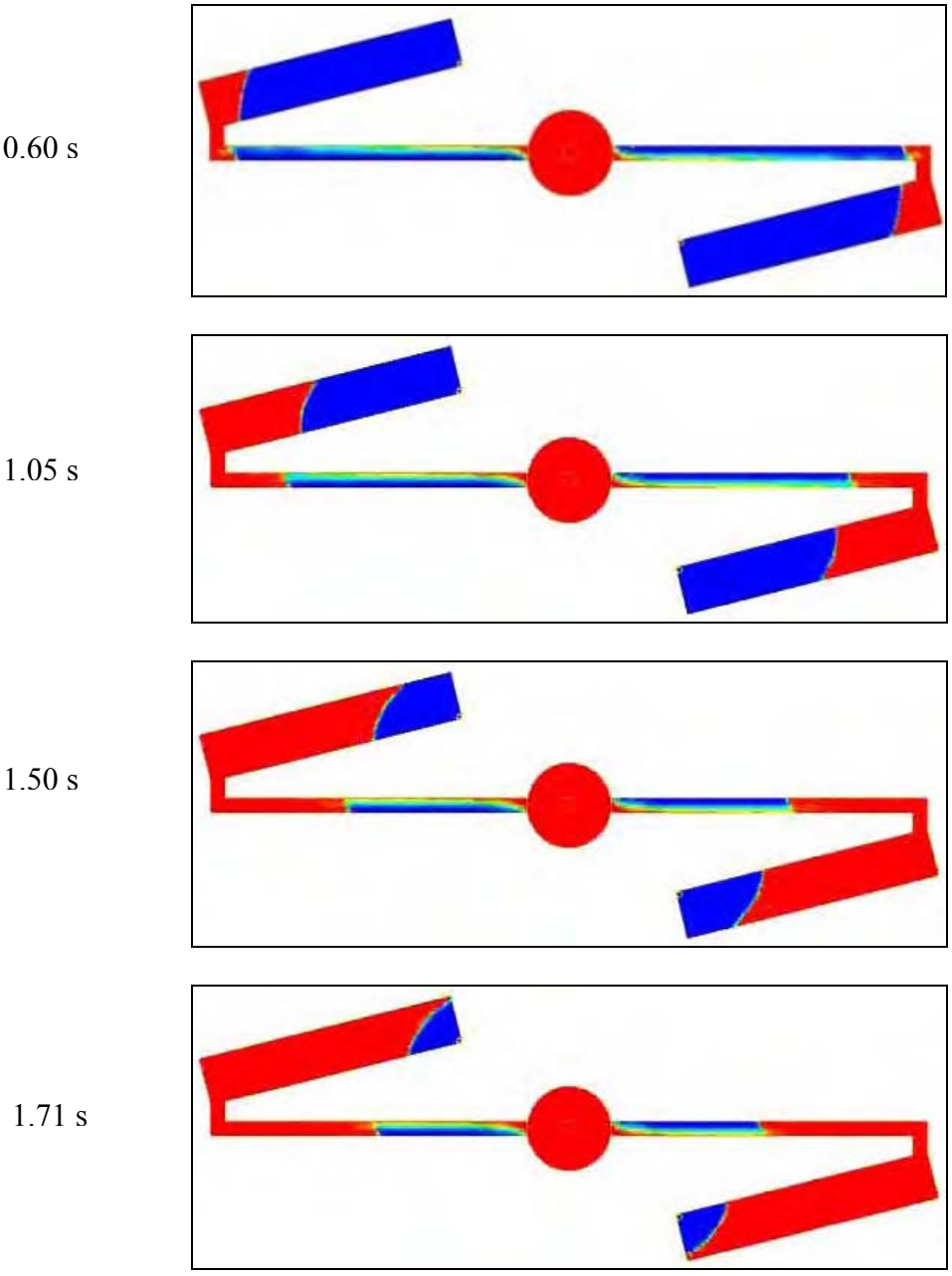

Figure 6 - 112. ANSYS CFX results of the indirect gated water model mould showing 2D plan view. The rotational velocity was 300 rpm in the anti-clockwise direction and the cut plane was taken 0.5 mm from the base. Note: Full summary and video sequence can be seen in Appendix 20 and Appendix 47.

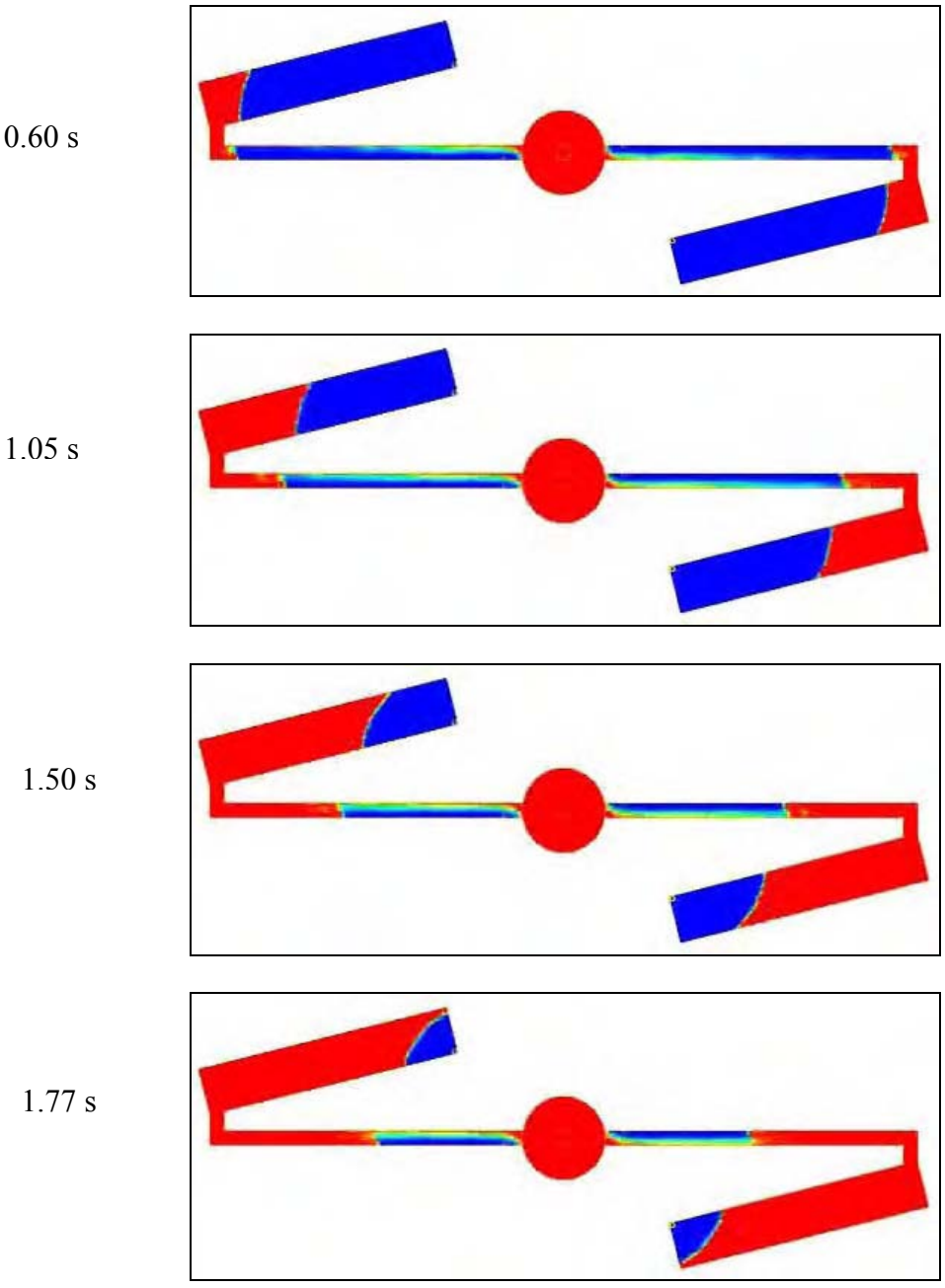

Figure 6 - 113. ANSYS CFX results of the indirect gated water model mould showing 2D plan view. The rotational velocity was 400 rpm in the anti-clockwise direction and the cut plane was taken 0.5 mm from the base. Note: Full summary and video sequence can be seen in Appendix 21 and Appendix 48.

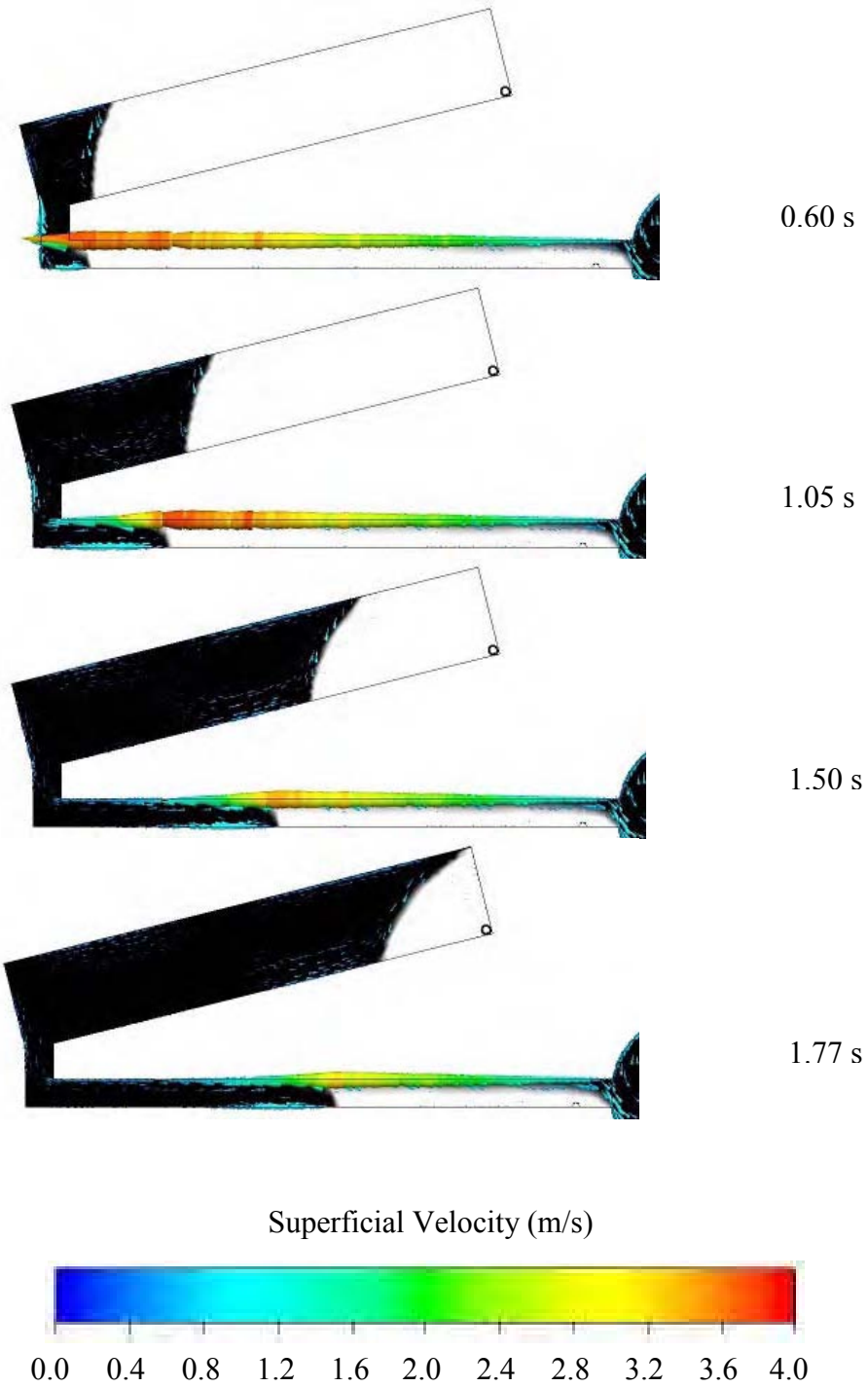

Figure 6 - 114. ANSYS CFX results of the indirect gated water model mould showing close-up of the left hand test bar and velocity vectors (see Figure 6 - 113). The rotational velocity was 400 rpm in the anti-clockwise direction and the cut plane was taken 0.5 mm from the base. Note: Full summary can be seen in Appendix 22.

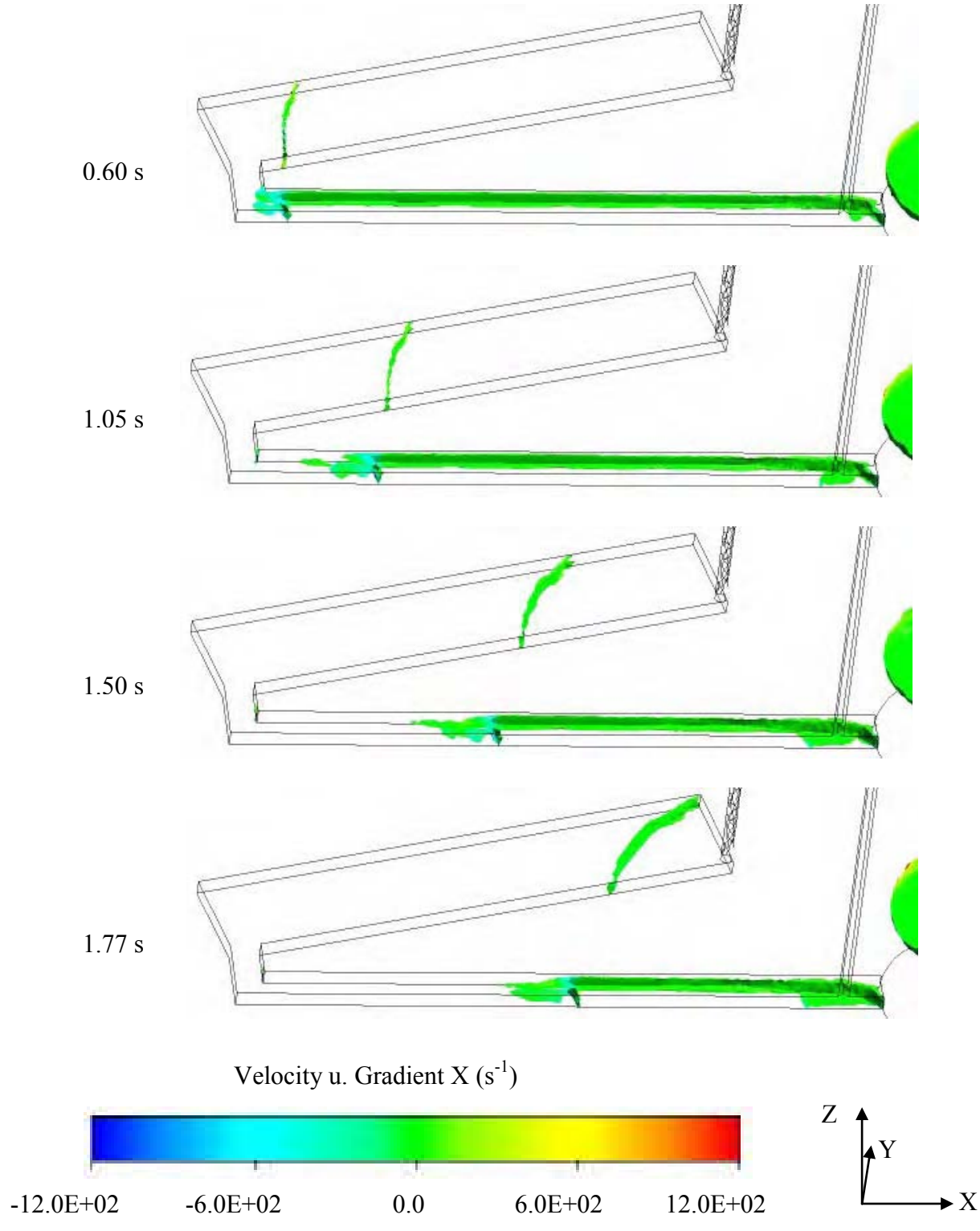

Figure 6 - 115. ANSYS CFX results of the indirect gated water model mould showing close-up of the left hand test bar, isosurface (0.5 volume fraction) and velocity gradients in "X" axis (see Figure 6 - 113). The rotational velocity was 400 rpm in the anti-clockwise direction. Note: Full summary can be seen in Appendix 23.

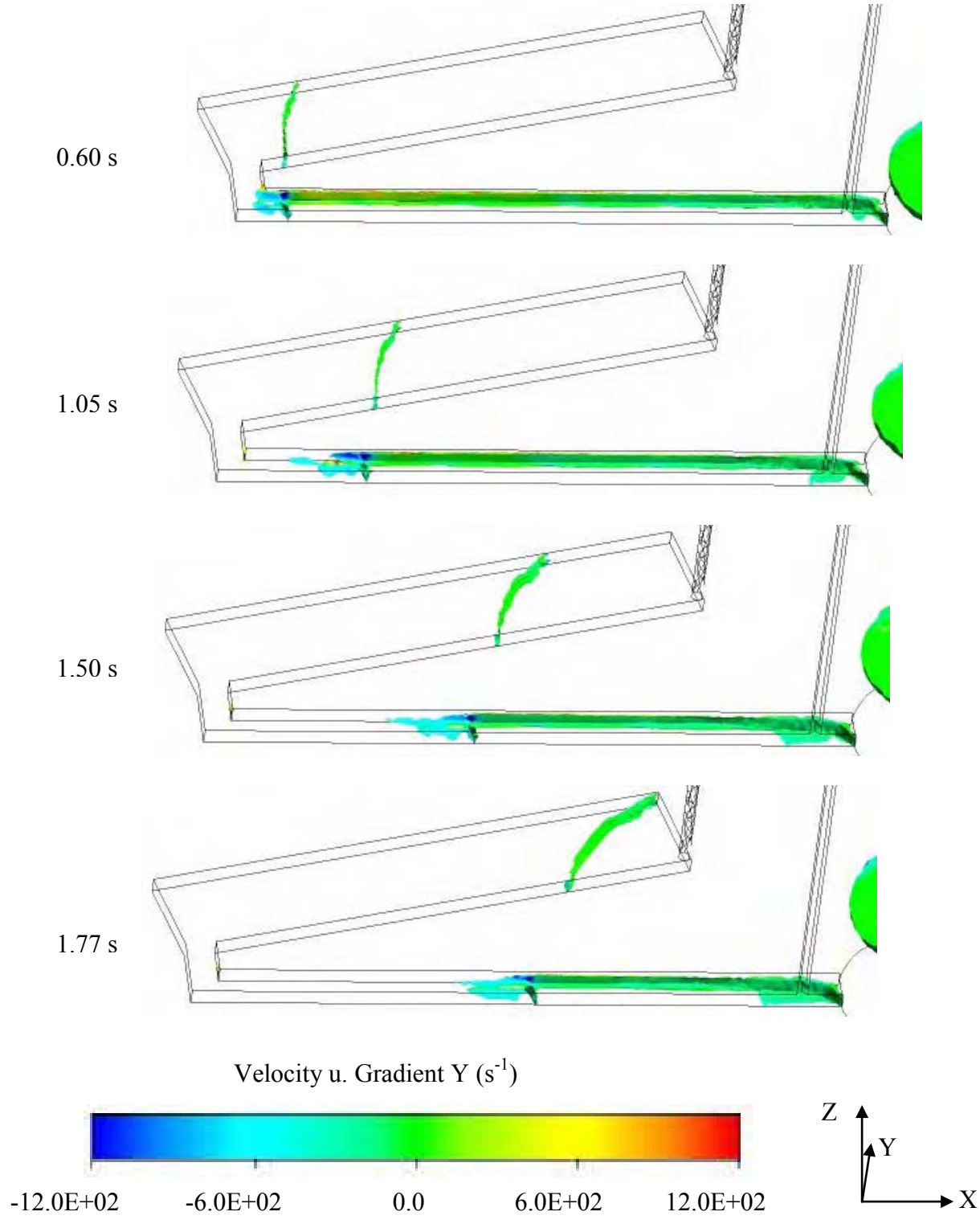

Figure 6 - 116. ANSYS CFX results of the indirect gated water model mould showing close-up of the left hand test bar, isosurface (0.5 volume fraction) and velocity gradients in "Y" axis (see Figure 6 - 113). The rotational velocity was 400 rpm in the anti-clockwise direction. Note: Full summary can be seen in Appendix 24.

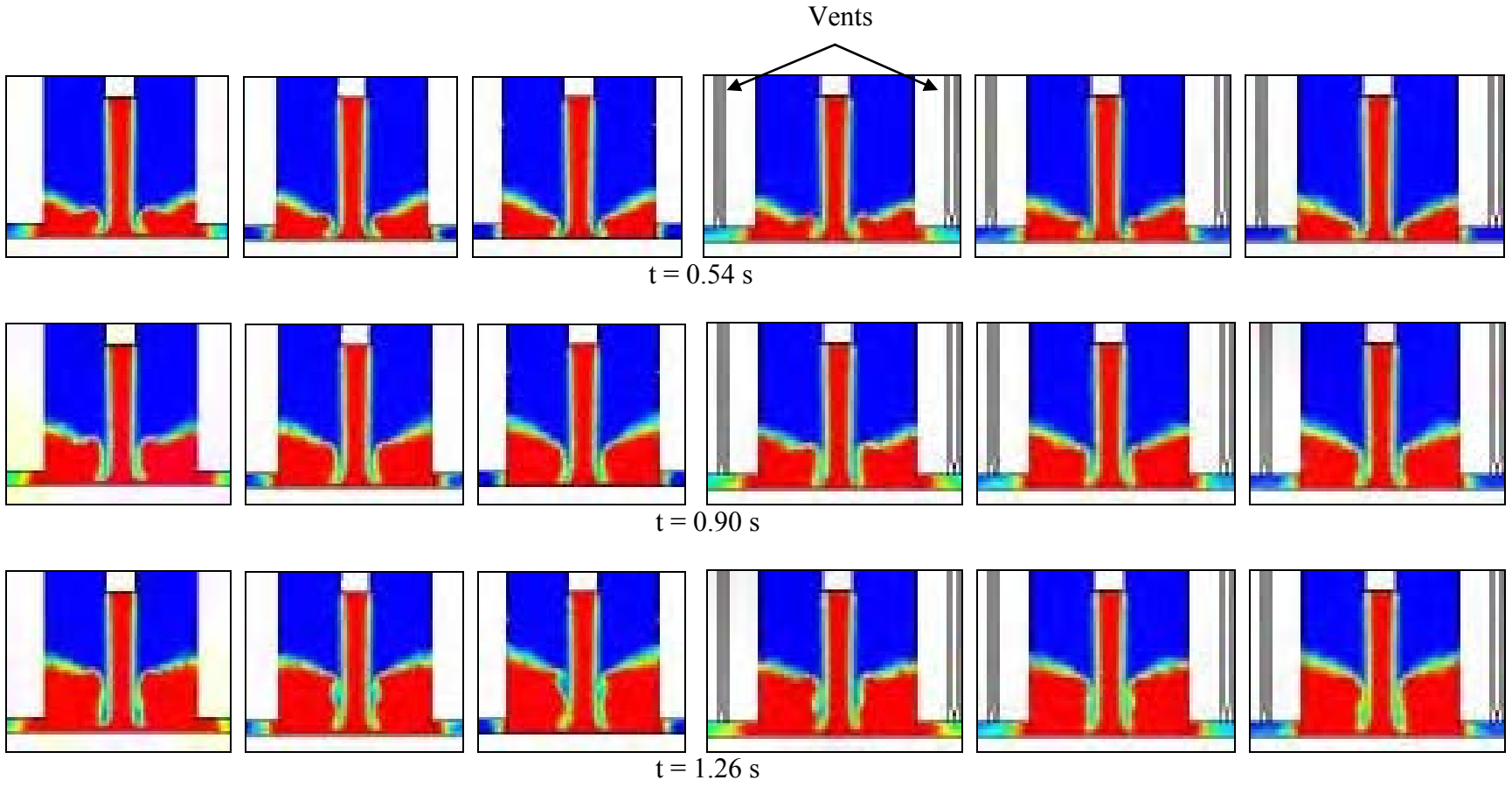

Figure 6 - 117. ANSYS CFX results of the direct and indirect gated moulds showing 2D side view. The rotational velocities were 200, 300 and 400 rpm in the anti-clockwise direction. The cut plane was taken along the sprue diameter.

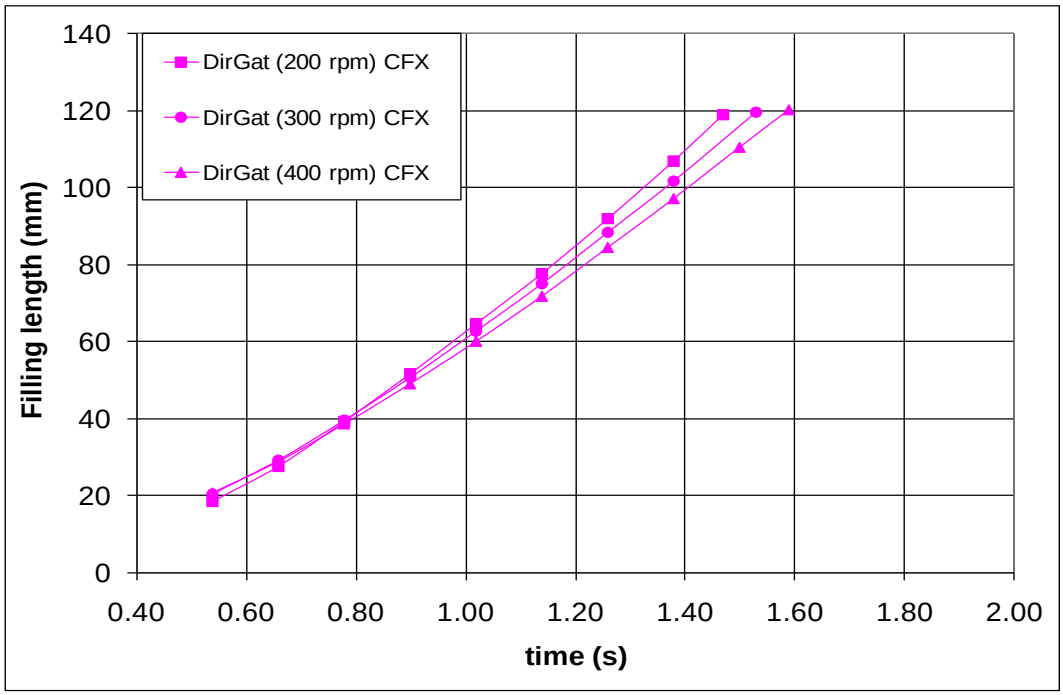

Figure 6 - 118. ANSYS CFX results of filling length measurements for the direct gated water model mould design showing average results obtained from both test bars.

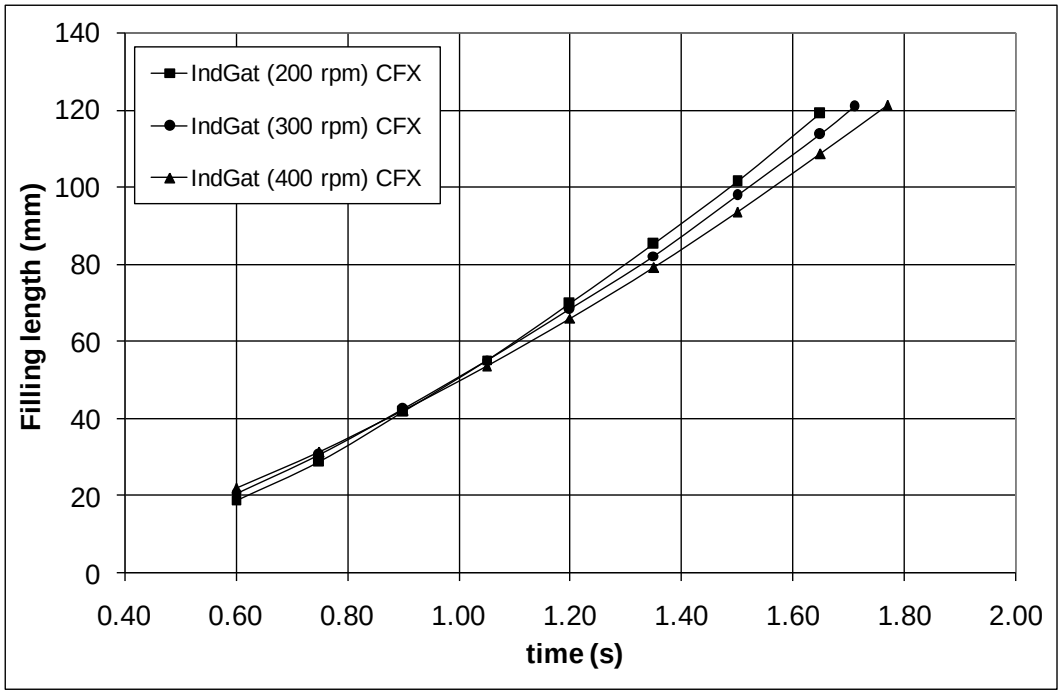

Figure 6 - 119. ANSYS CFX results of filling length measurements for the indirect gated water model mould design showing average results obtained from both test bars.

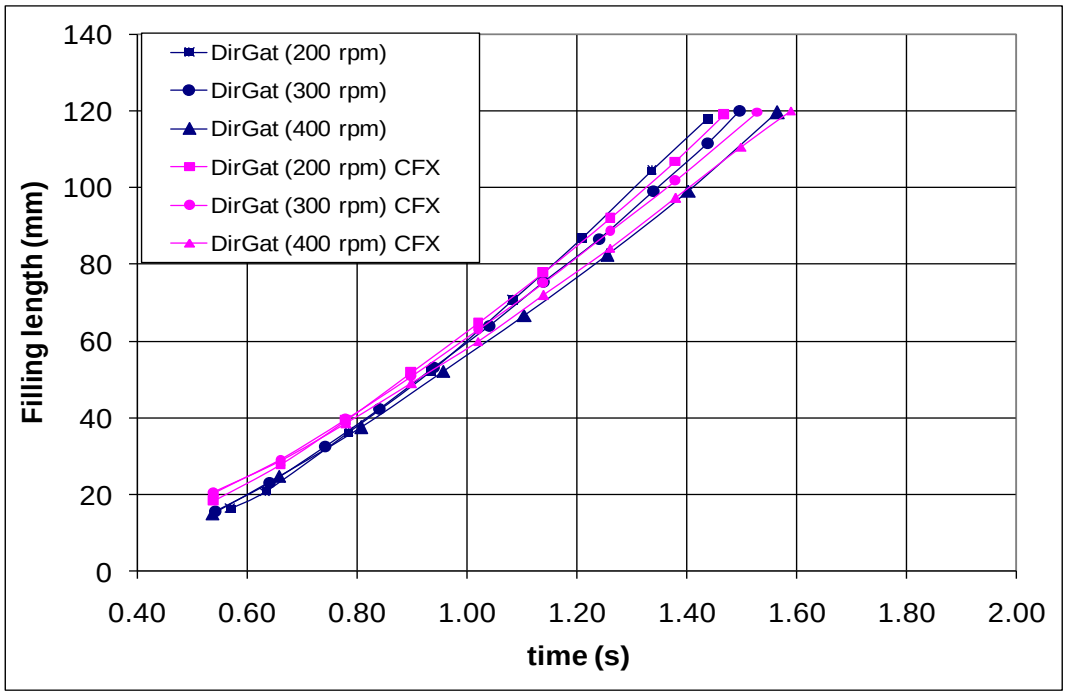

Figure 6 - 120. Comparison of experimental and ANSYS CFX results for the direct gated mould design as a function of the rotational velocity.

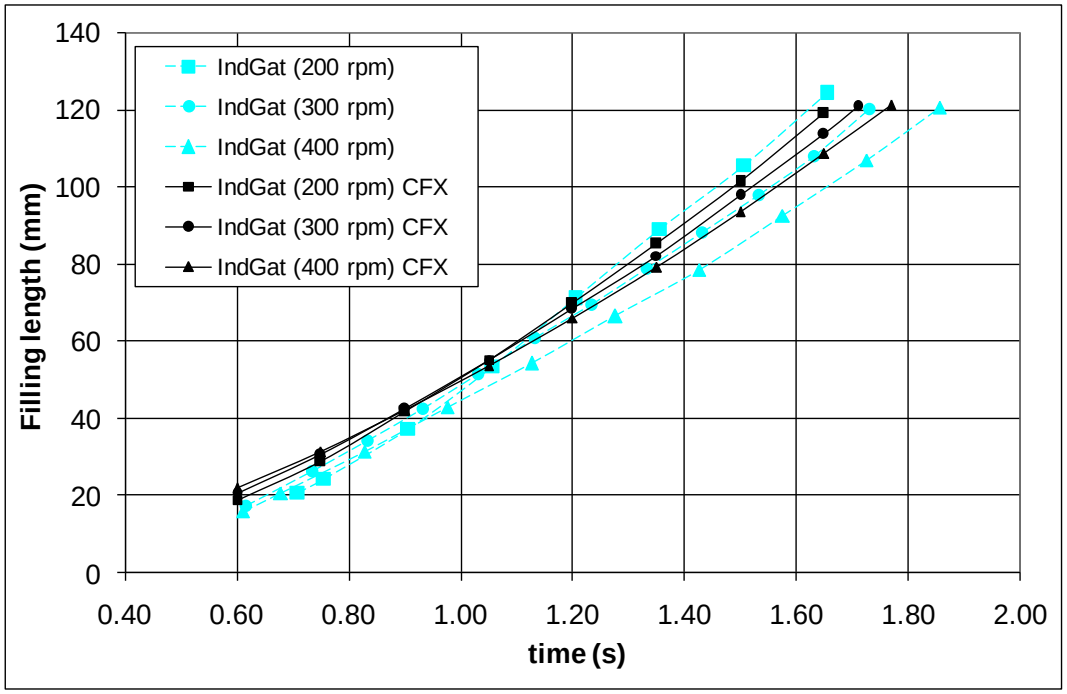

Figure 6 - 121. Comparison of experimental and ANSYS CFX results for the indirect gated mould design as a function of the rotational velocity.

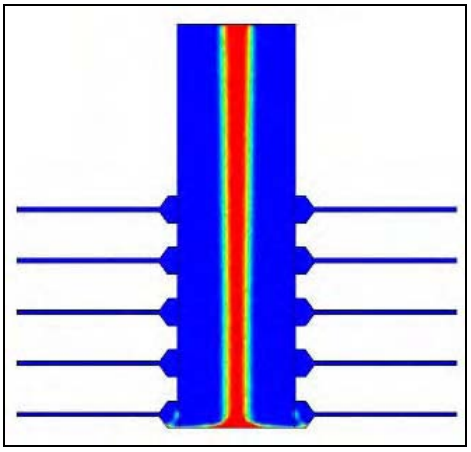

0.18 s

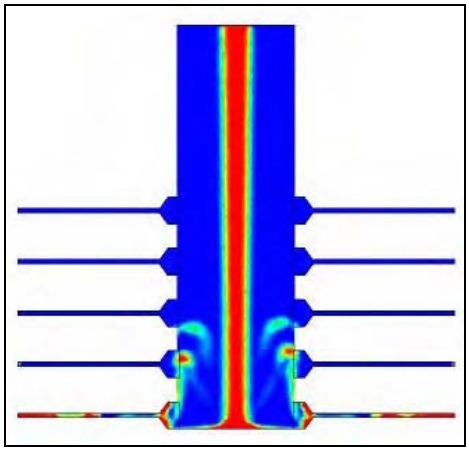

0.33 s

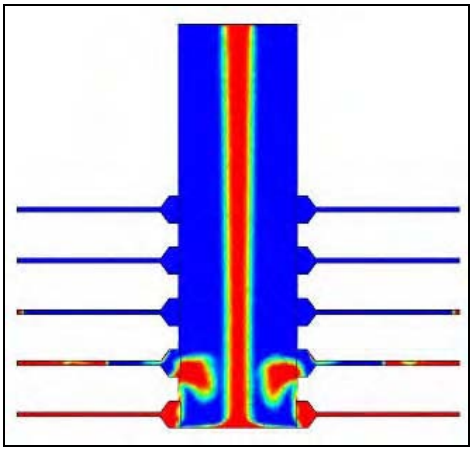

0.51 s

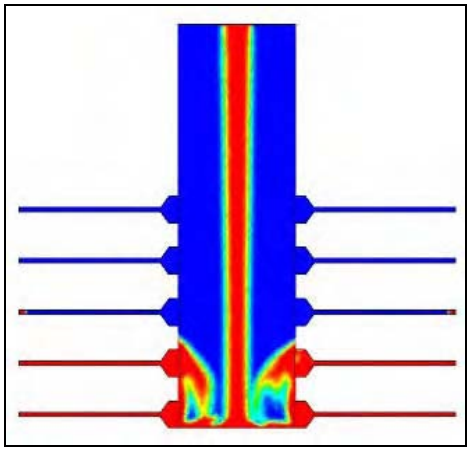

0.69 s

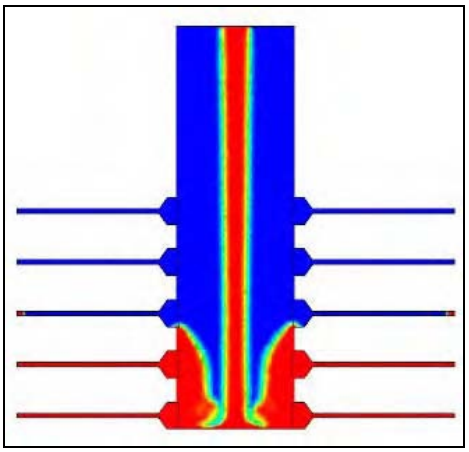

0.87 s

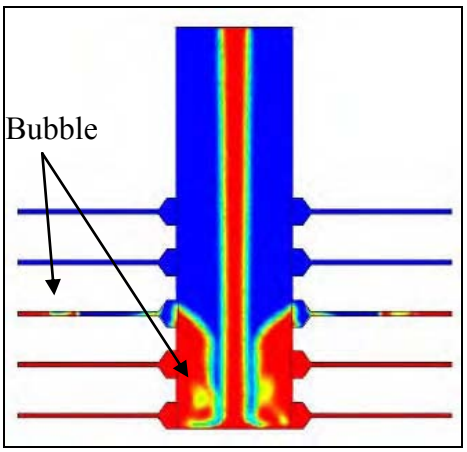

1.05 s

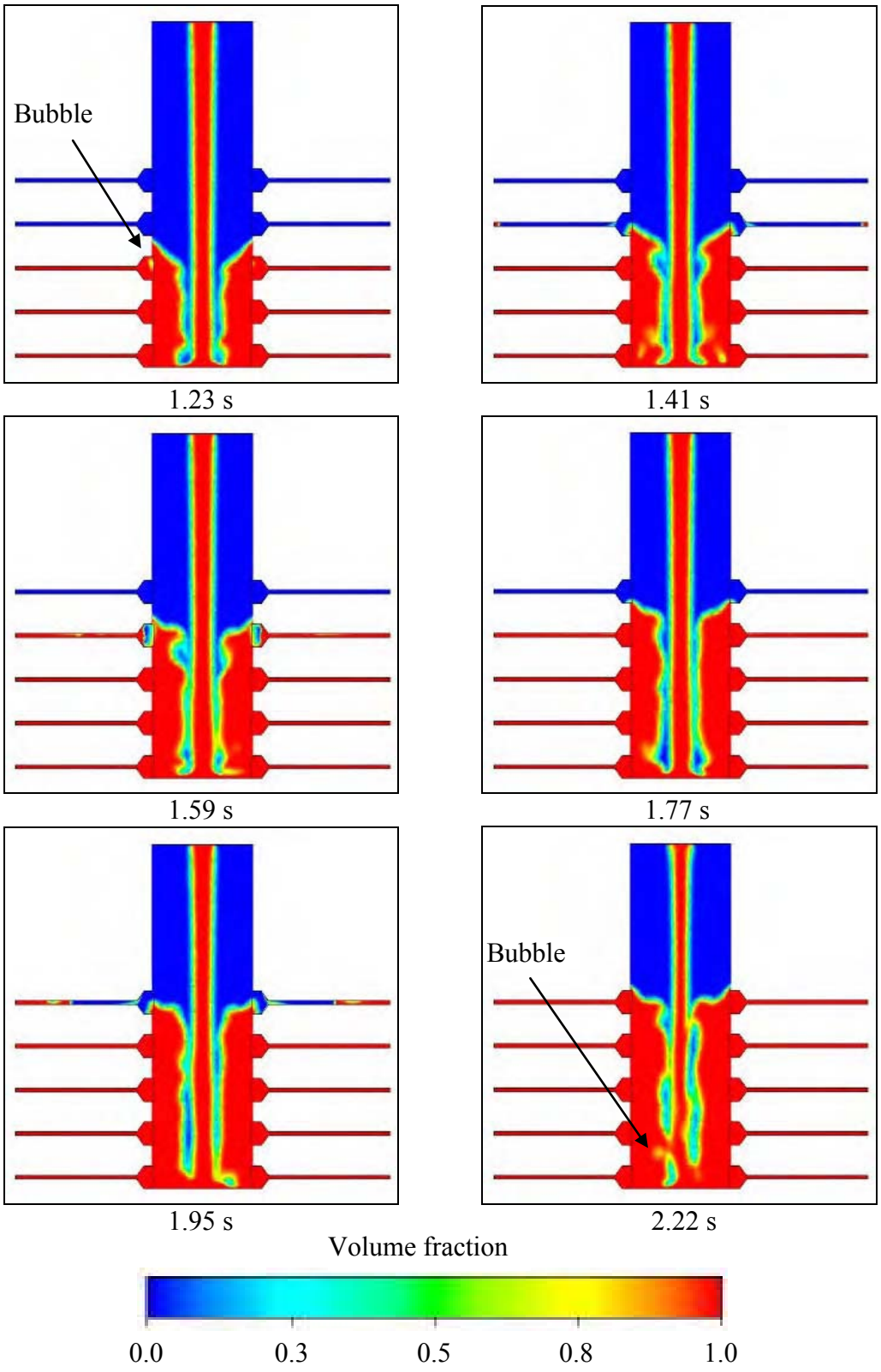

Figure 6 - 122. ANSYS CFX results of the direct gated casting mould showing side view (volume fraction). The cut plane was taken along the sprue diameter. Note: Full video sequence can be seen in Appendix 49.

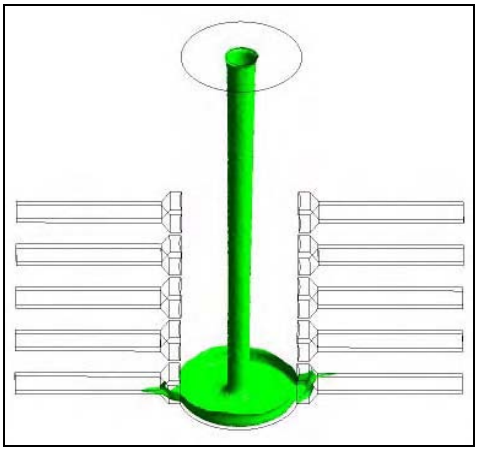

0.18 s

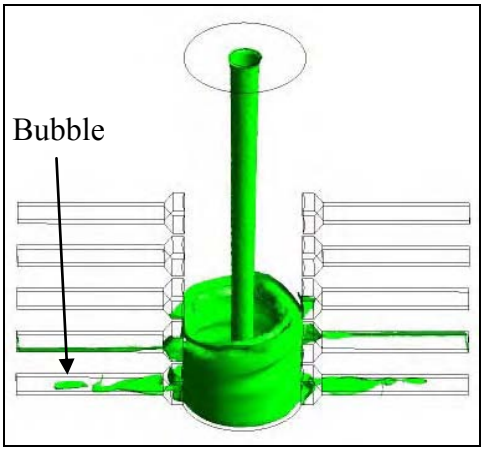

0.33 s

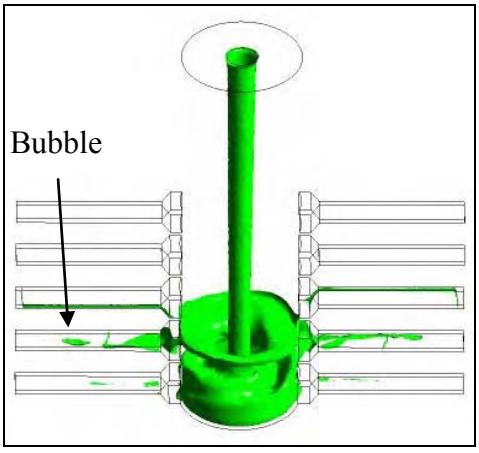

0.51 s

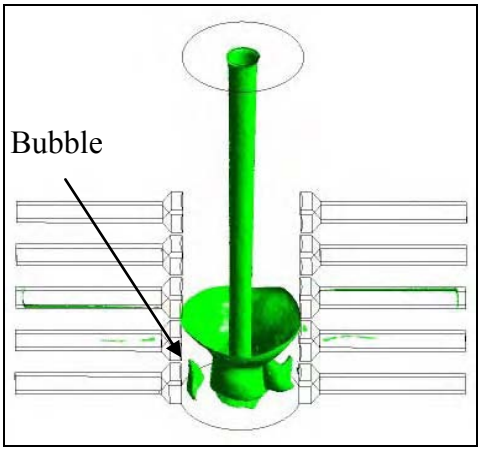

0.69 s

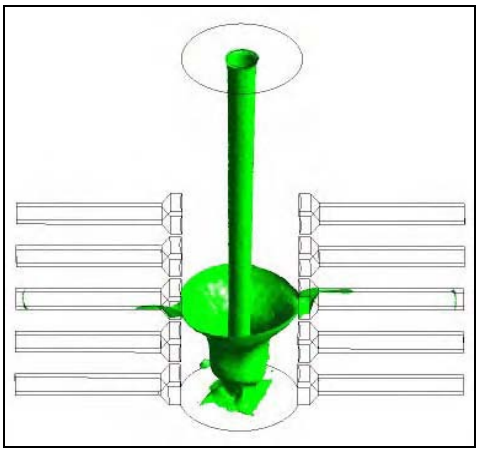

0.87 s

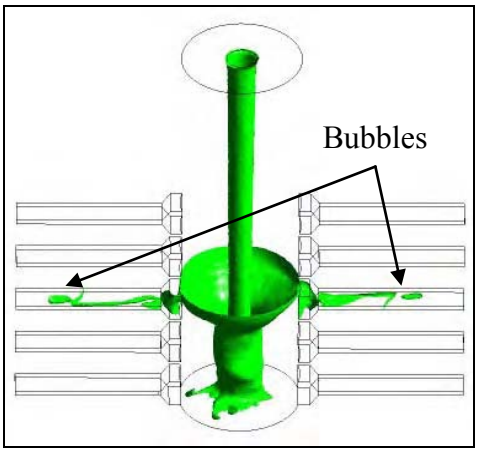

1.05 s

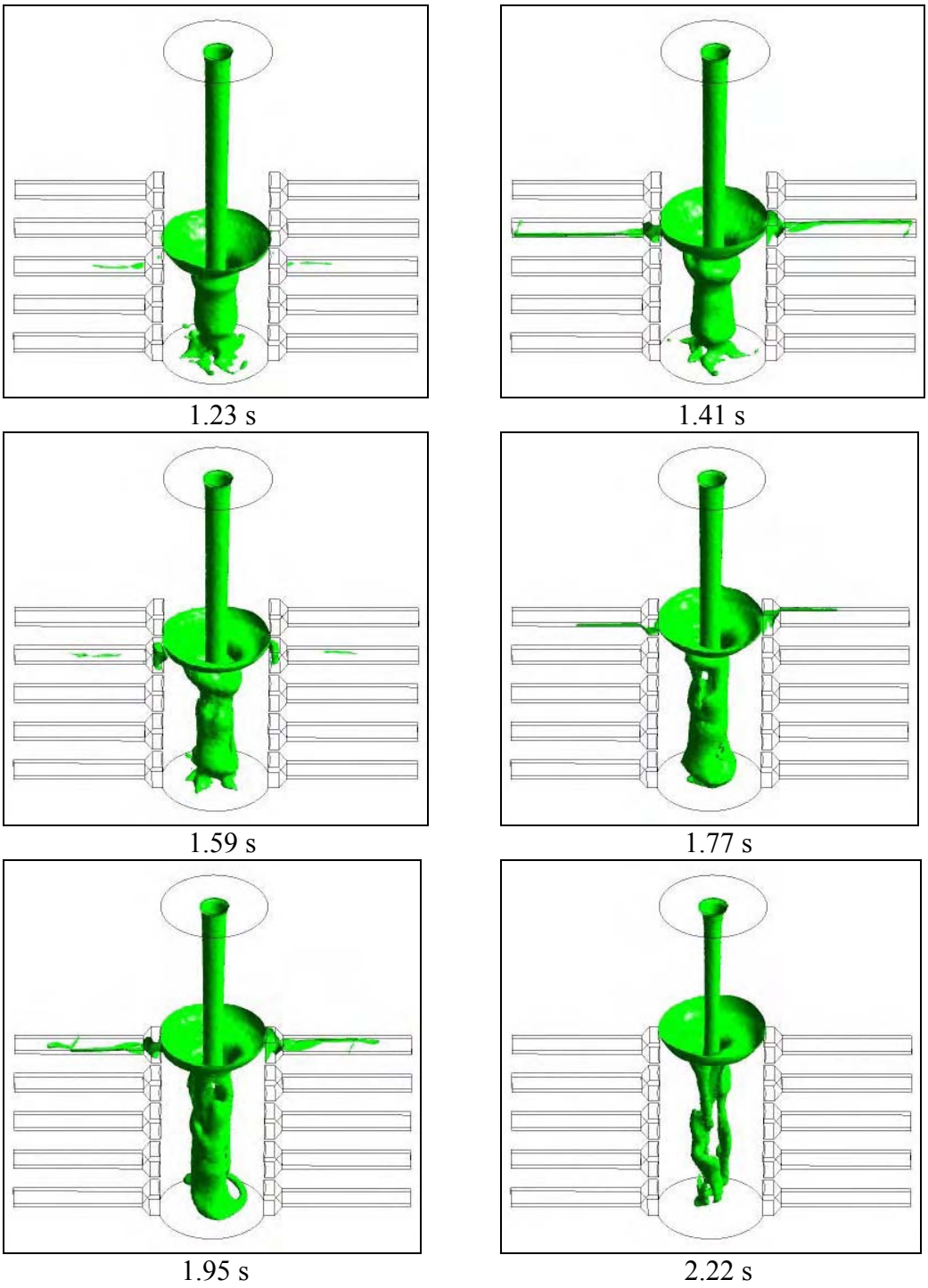

Figure 6 - 123. ANSYS CFX results of the direct gated casting mould filling process showing Isosurface (0.5 volume fraction). Note: Full video sequence can be seen in Appendix 50.

0.39 s

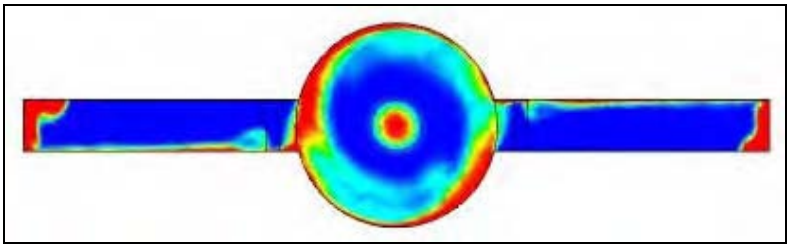

0.42 s

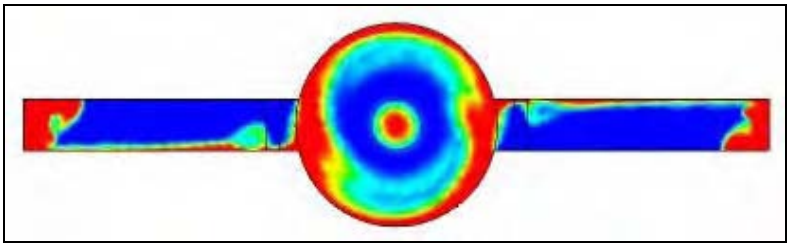

0.45 s

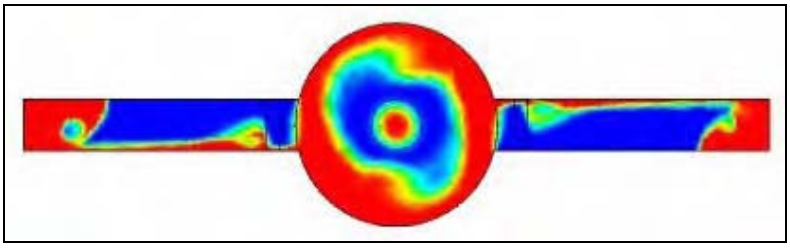

0.48 s

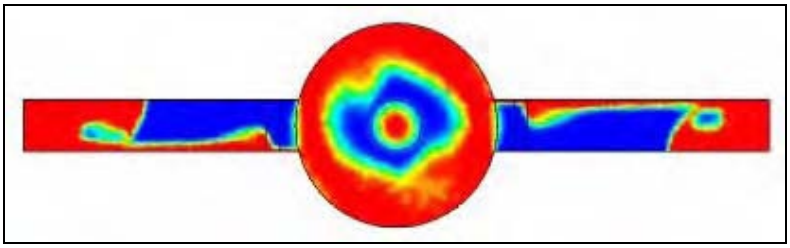

0.51 s

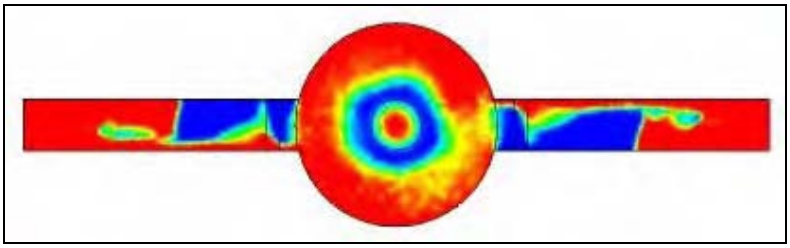

0.54 s

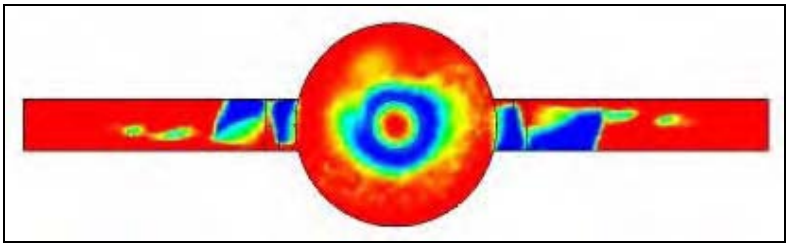

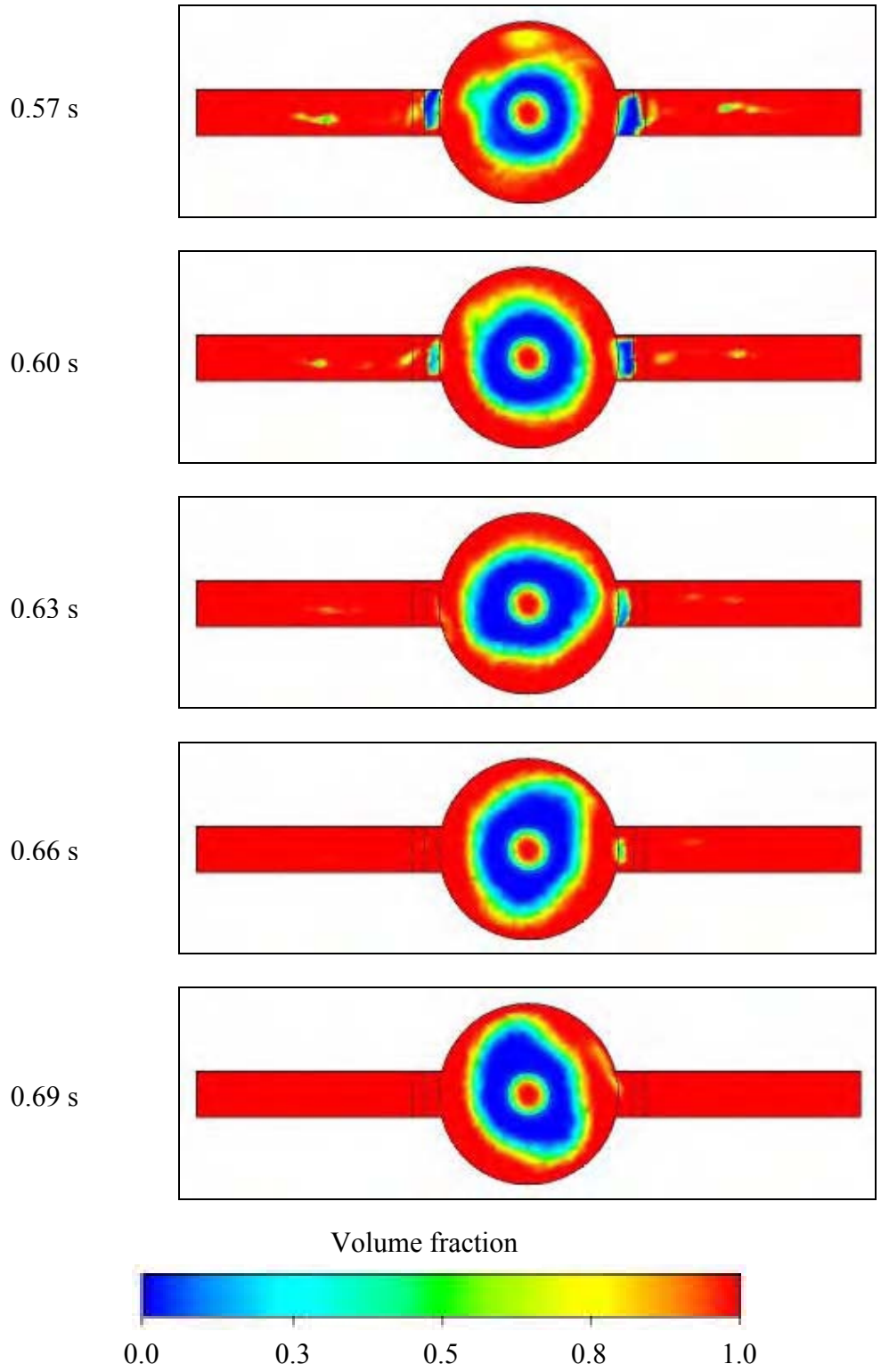

Figure 6 - 124. ANSYS CFX results of the direct gated casting mould showing plan view (volume fraction). The cut plane was taken at mid-thickness of the test bar pair C1L2DG (4) – C1R2DG (7) (see Figure 6 - 1). Note: Full video sequence can be seen in Appendix 51.

0.39 s

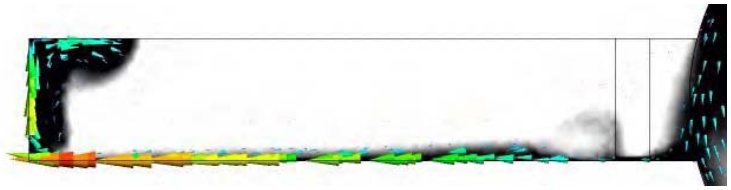

0.42 s

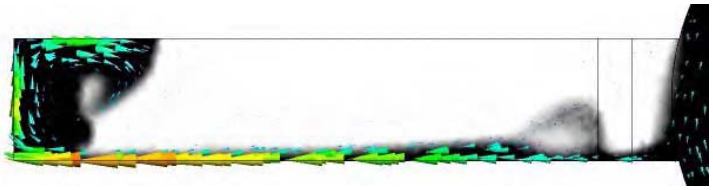

0.45 s

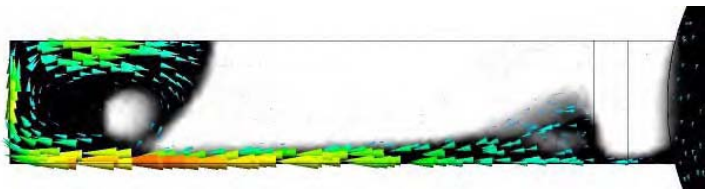

0.48 s

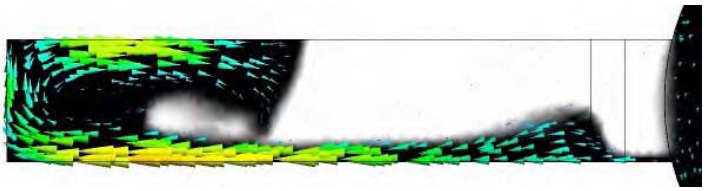

0.51 s

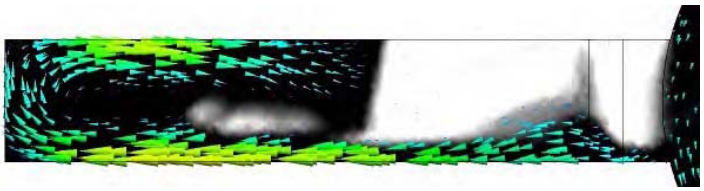

0.54 s

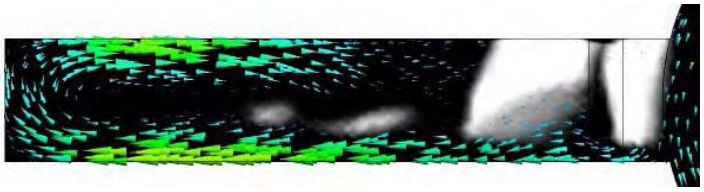

0.57 s

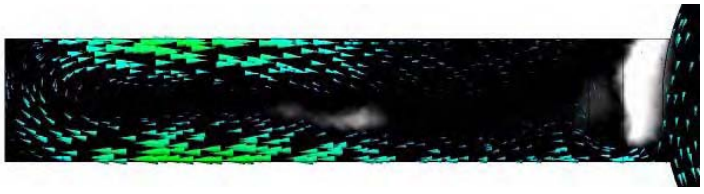

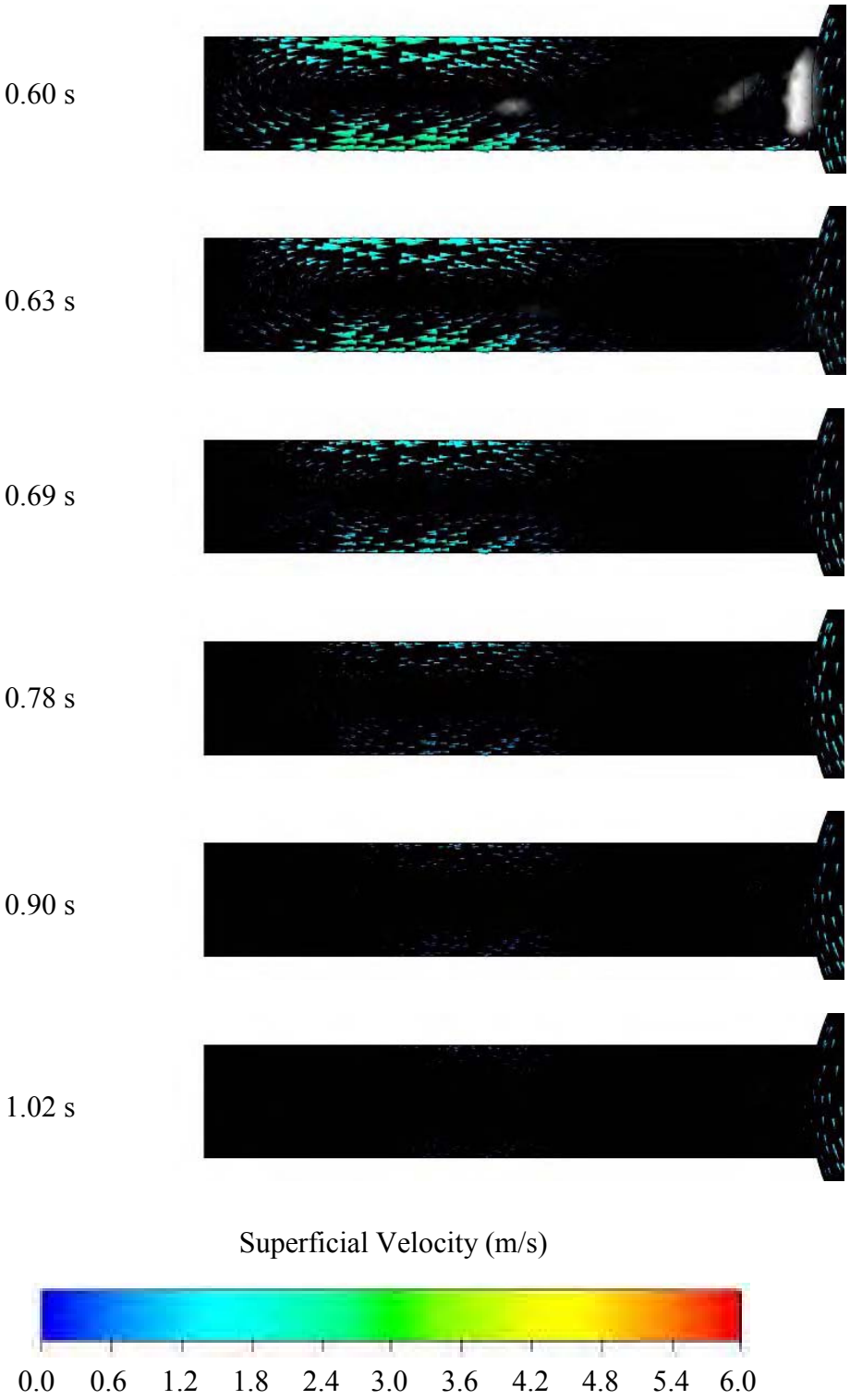

Figure 6 - 125. ANSYS CFX results showing close-up plan view of the left test bar and velocity vectors. The cut plane was taken at mid-thickness of the direct gated test bar C1L2DG (4) (see Figure 6 - 1 and Figure 6 - 124). Note: Full video sequence can be seen in Appendix 52 .

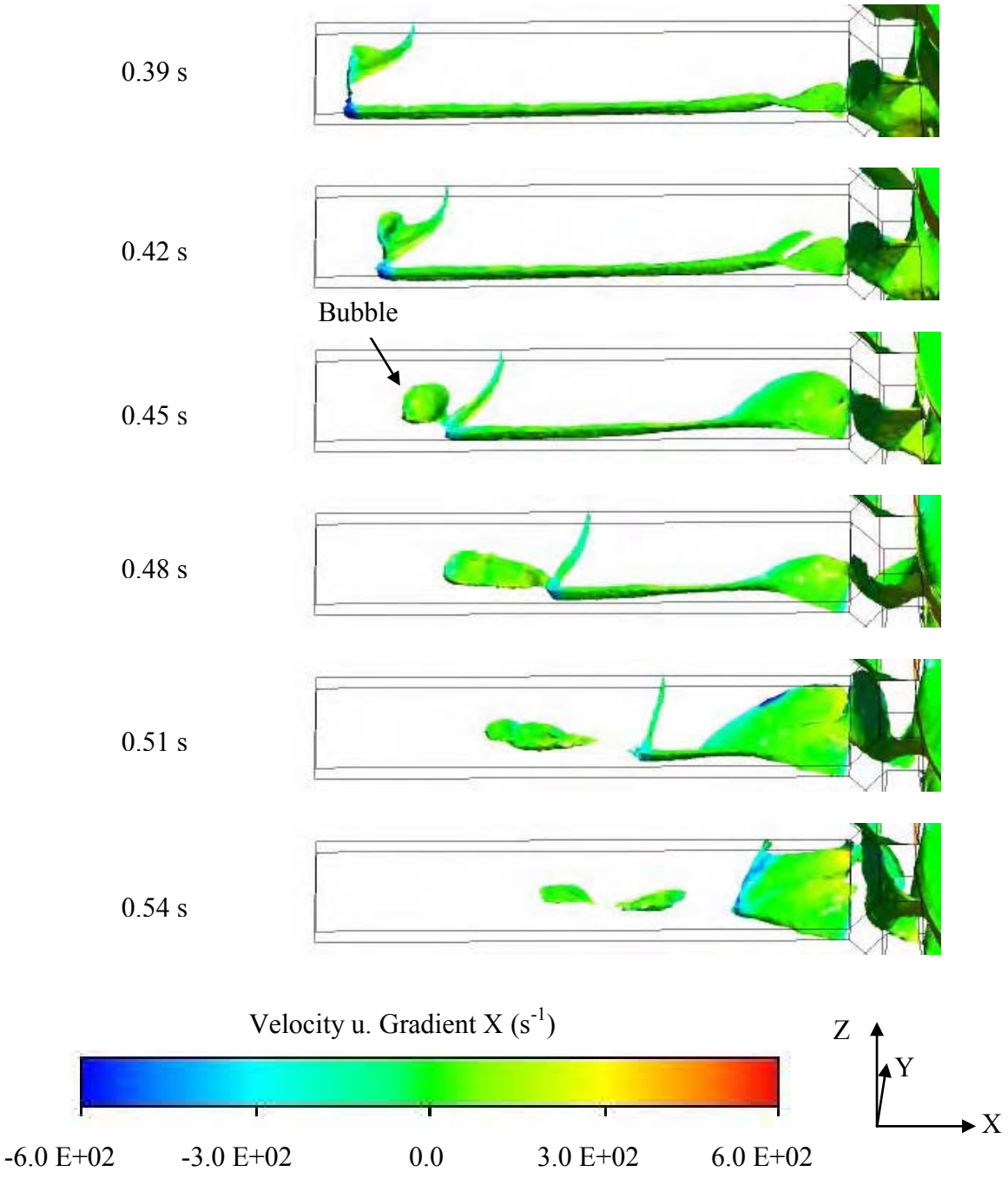

Figure 6 - 126. ANSYS CFX results showing close-up of the left test bar, isosurface (0.5 volume fraction) and velocity gradient in 'X' axis. The direct gated test bar was C1L2DG (4) (see Figure 6 - 1 and Figure 6 - 124).

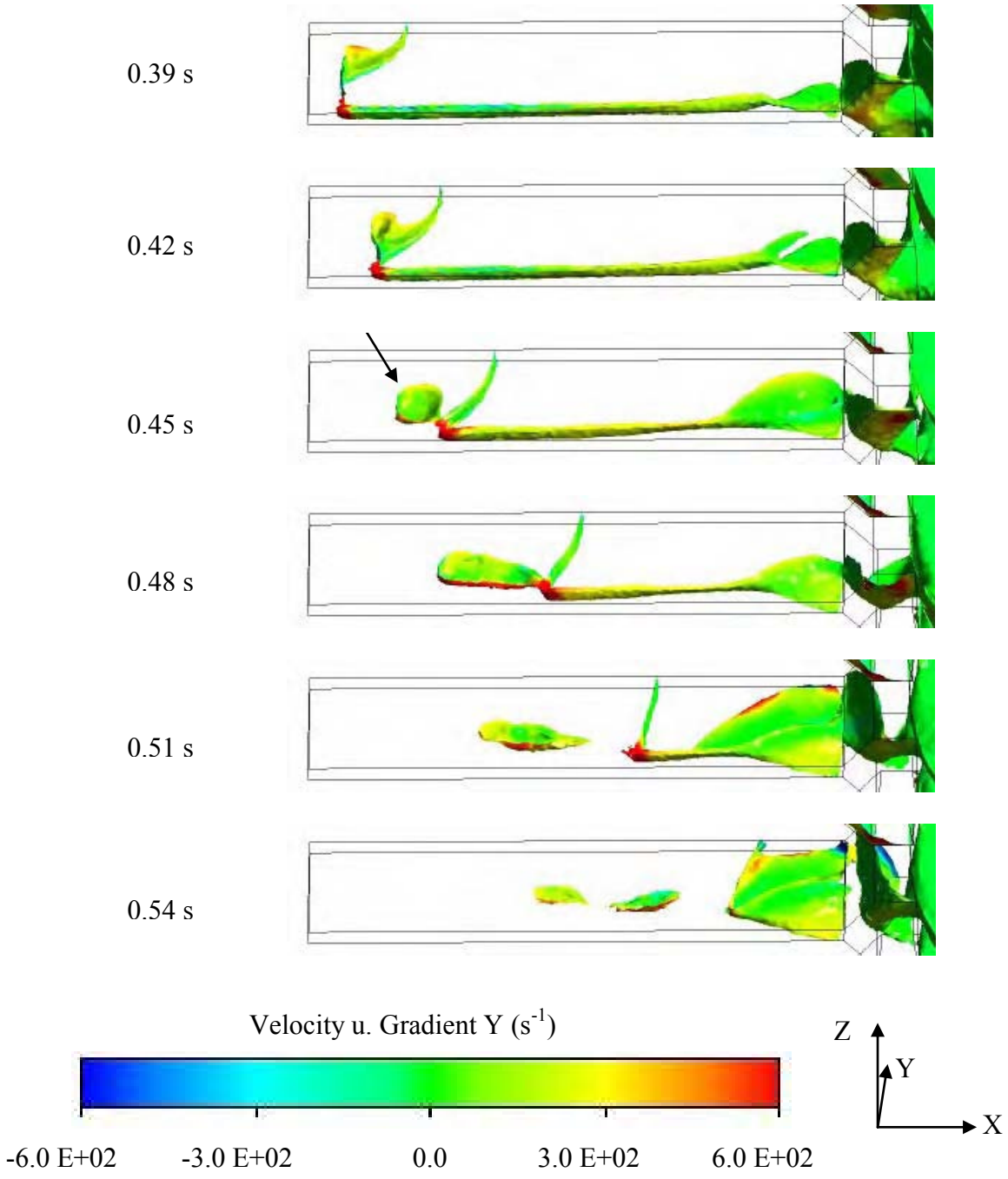

Figure 6 - 127. ANSYS CFX results showing close-up of the left test bar, isosurface (0.5 volume fraction) and velocity gradient in 'Y' axis. The direct gated test bar was C1L2DG (4) (see Figure 6 - 1 and Figure 6 - 124).

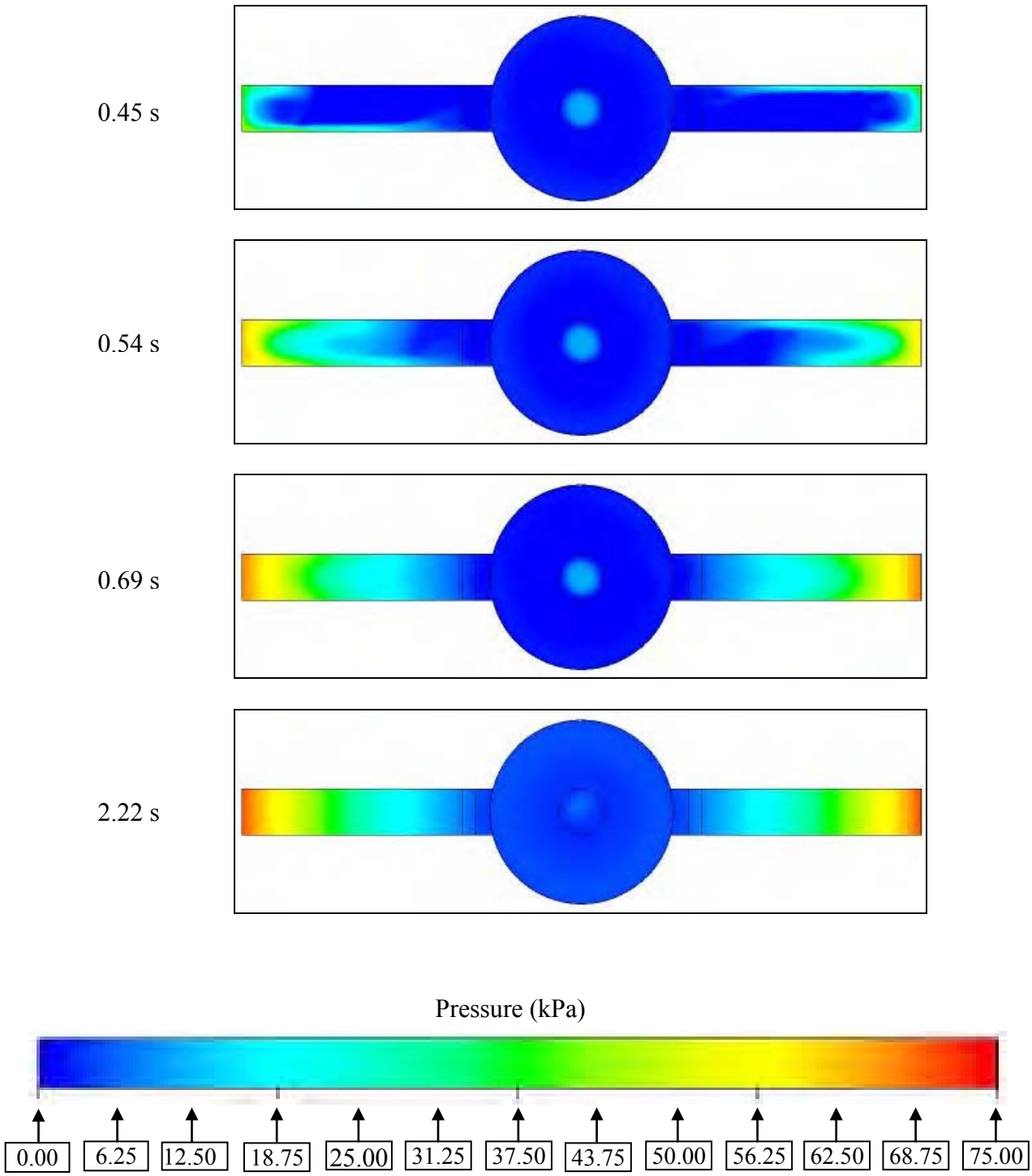

Figure 6 - 128. ANSYS CFX results of the direct gated casting mould showing plan view and pressure. The cut plane was taken at mid-thickness of the test bar pair C1L2DG (4) – C1R2DG (7) (see Figure 6 - 1).

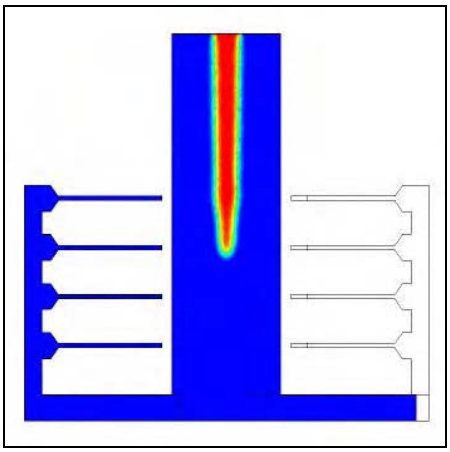

0.09 s

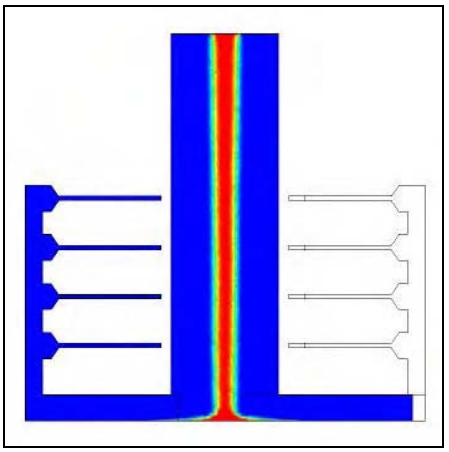

0.18 s

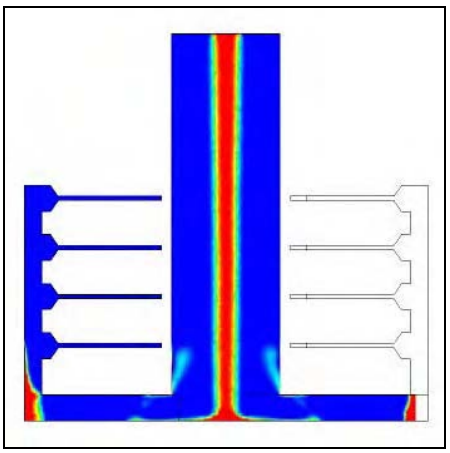

0.27 s

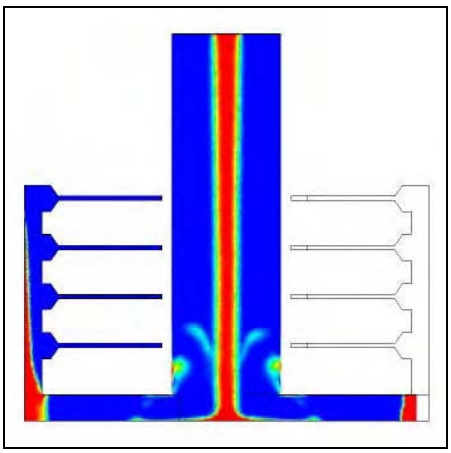

0.36 s

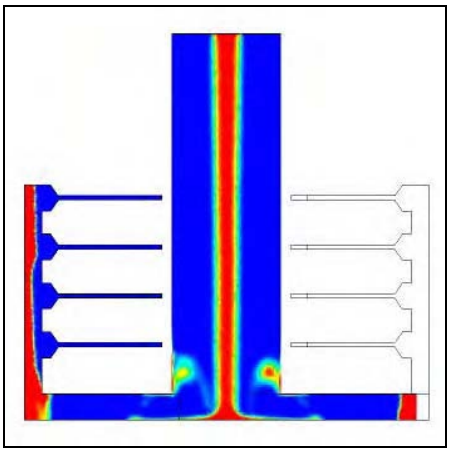

0.45 s

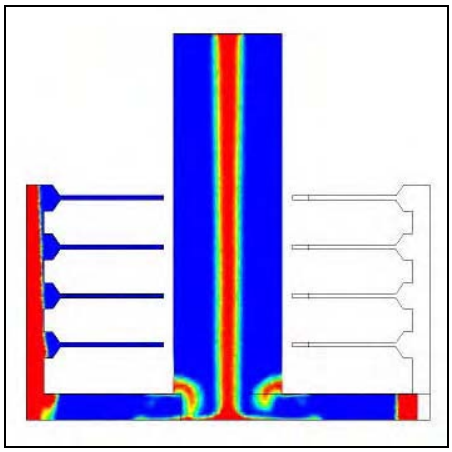

0.54 s

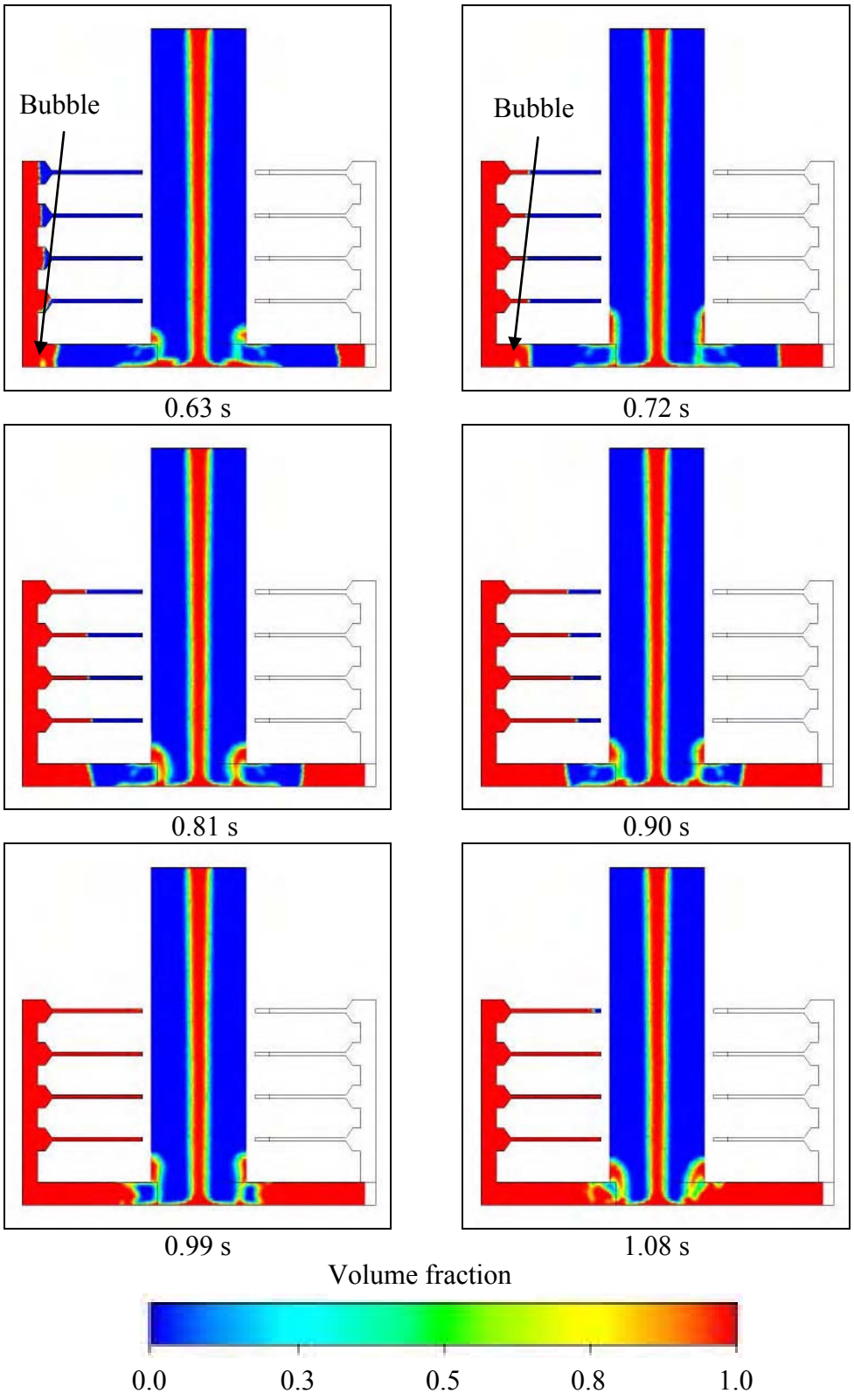

Figure 6 - 129. ANSYS CFX results of the indirect gated casting mould showing left side view (volume fraction). The cut plane was taken 2 mm from the centre line of the mould. Note: Full video sequence can be seen in Appendix 53.

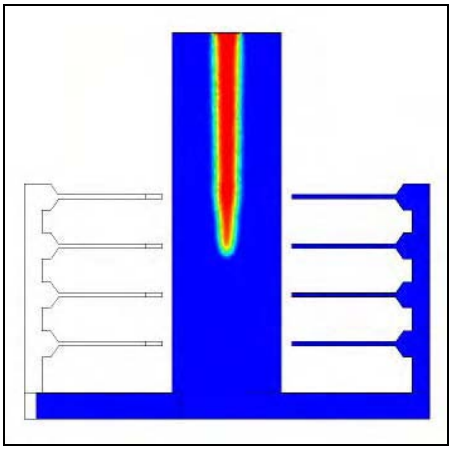

0.09 s

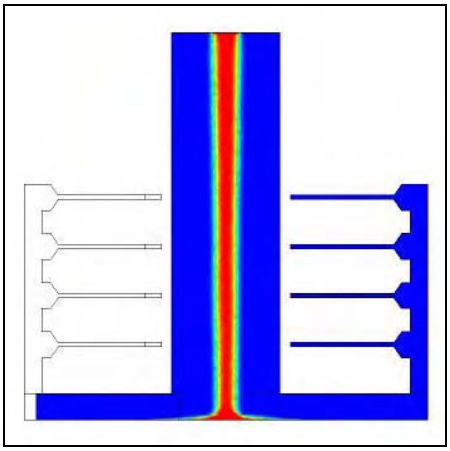

0.18 s

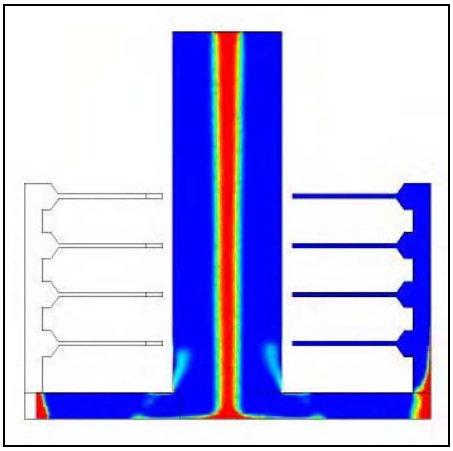

0.27 s

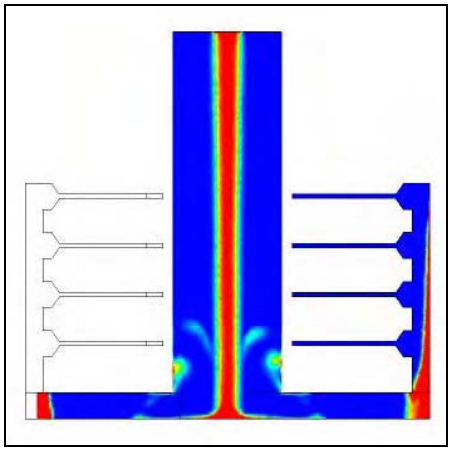

0.36 s

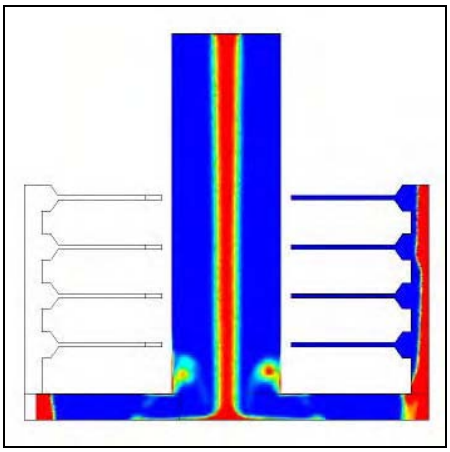

0.45 s

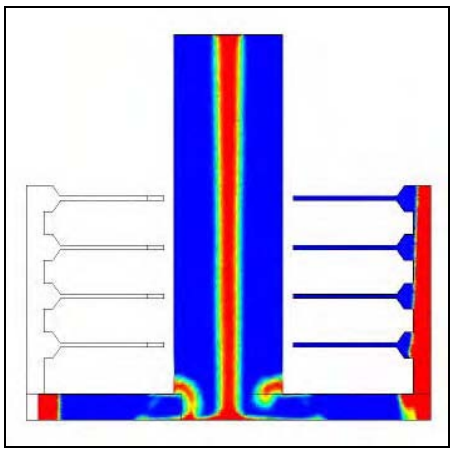

0.54 s

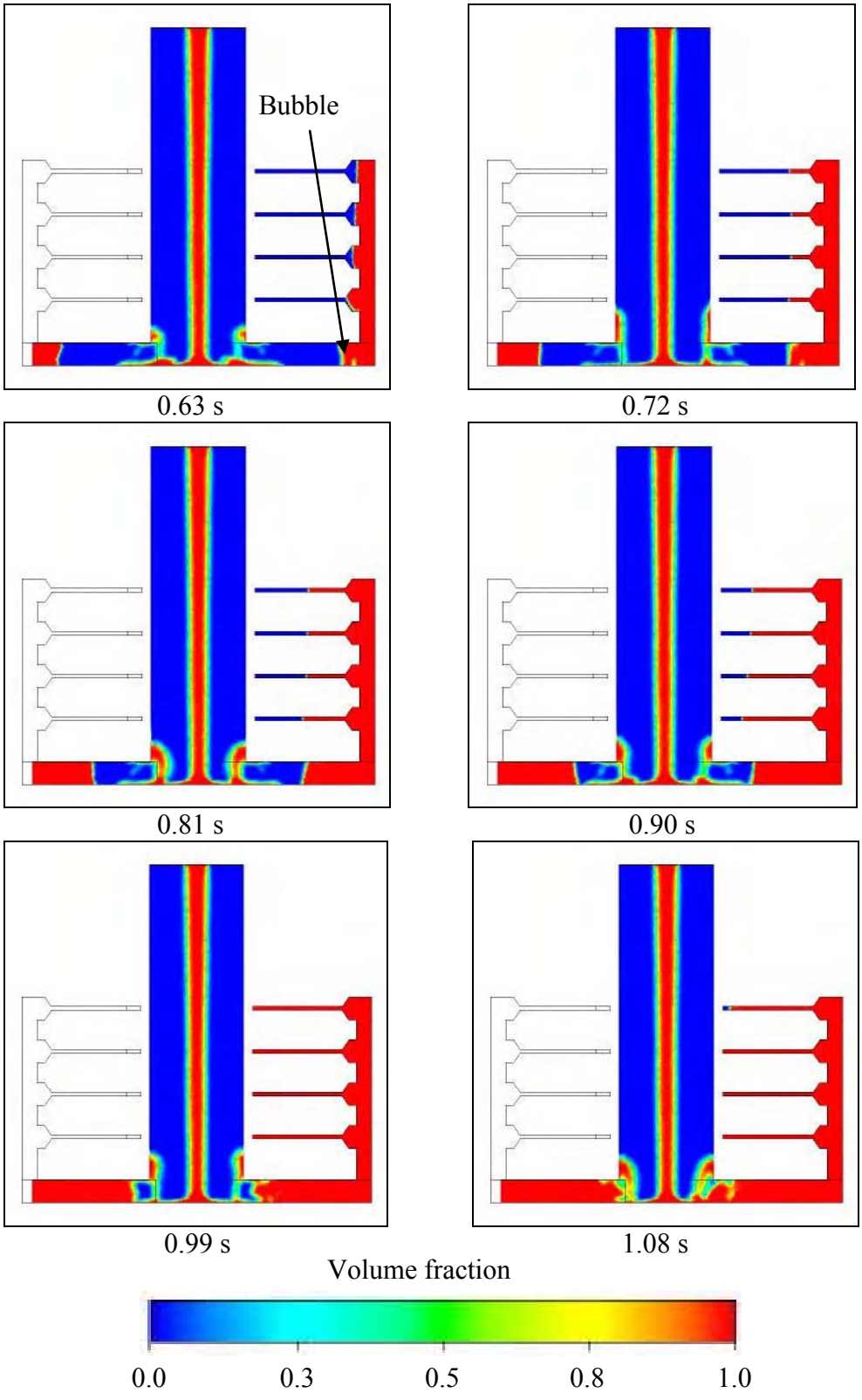

Figure 6 - 130. ANSYS CFX results of the indirect gated casting mould showing right side view (volume fraction). The cut plane was taken 2 mm from the centre line of the mould. Note: Full video sequence can be seen in Appendix 54.

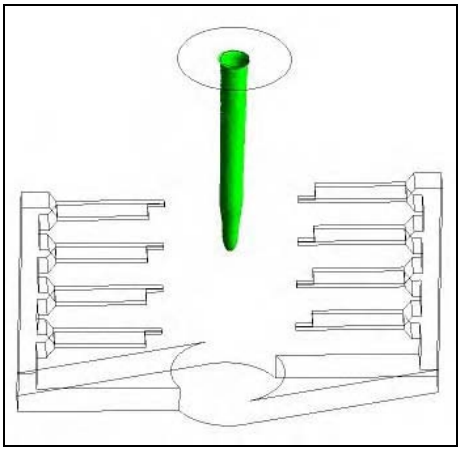

0.09 s

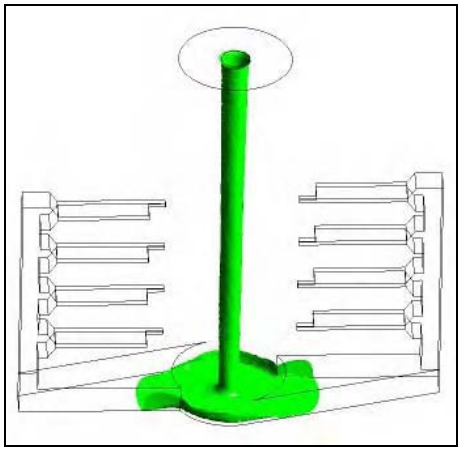

0.18 s

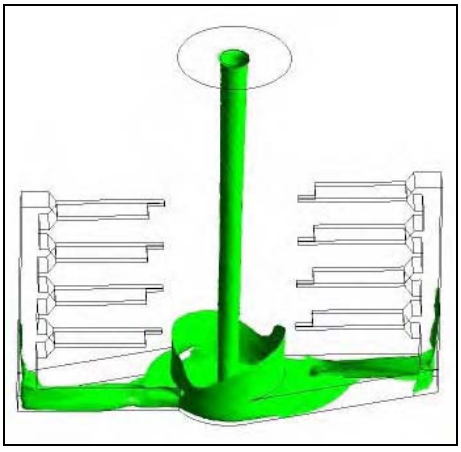

0.27 s

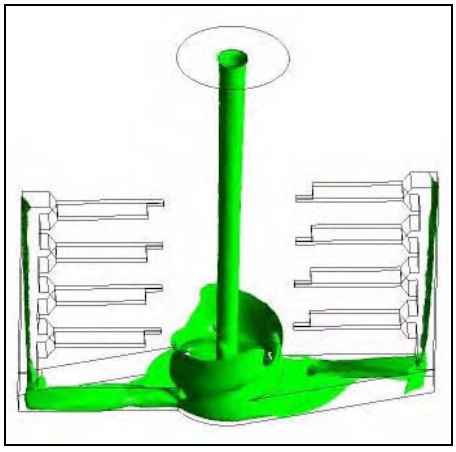

0.36 s

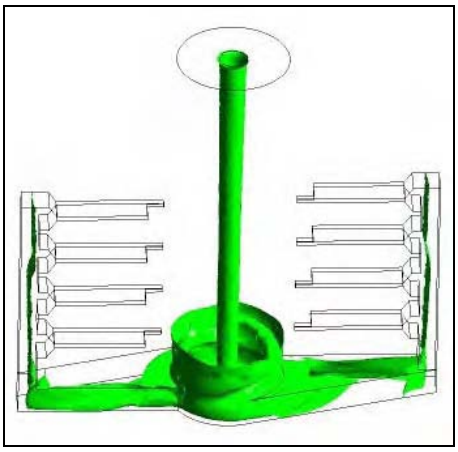

0.45 s

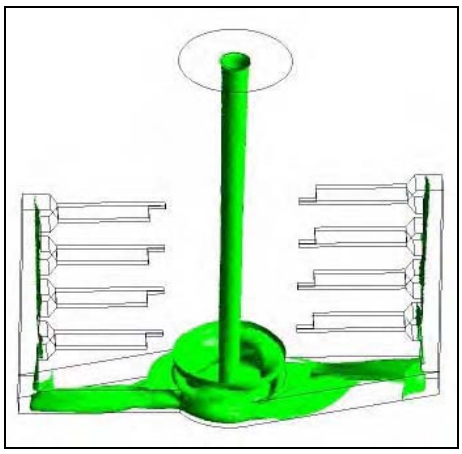

0.54 s

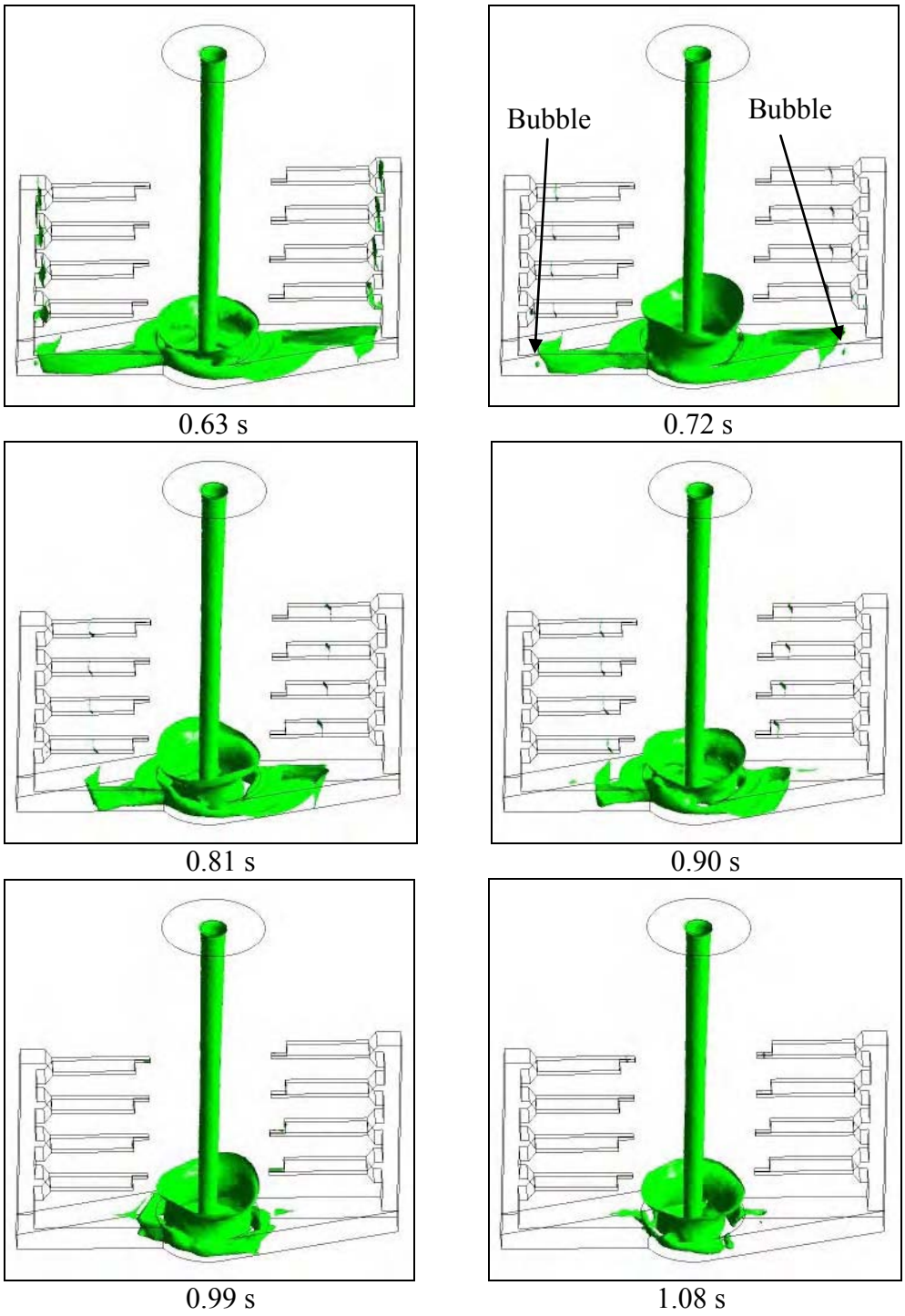

Figure 6 - 131 ANSYS CFX results of the indirect gated casting mould filling process showing isosurface (0.5 volume fraction). Note: Full video sequence can be seen in Appendix 55.

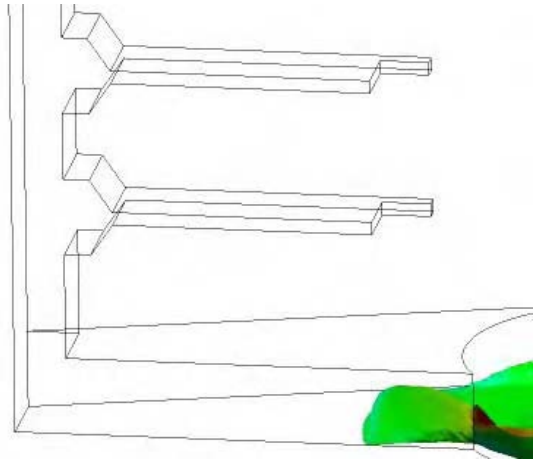

0.18 s

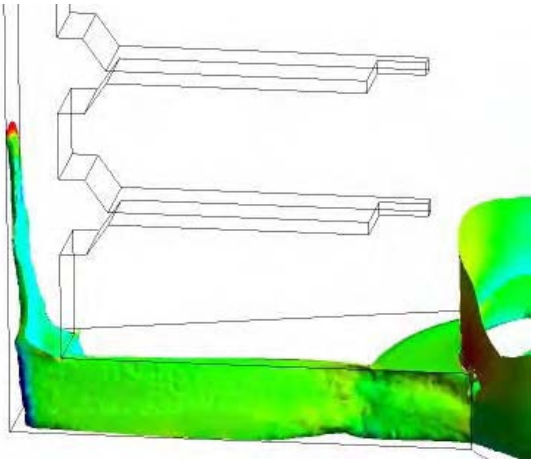

0.27 s

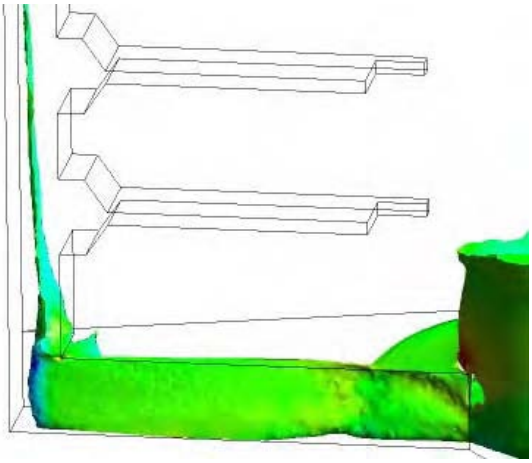

0.36 s

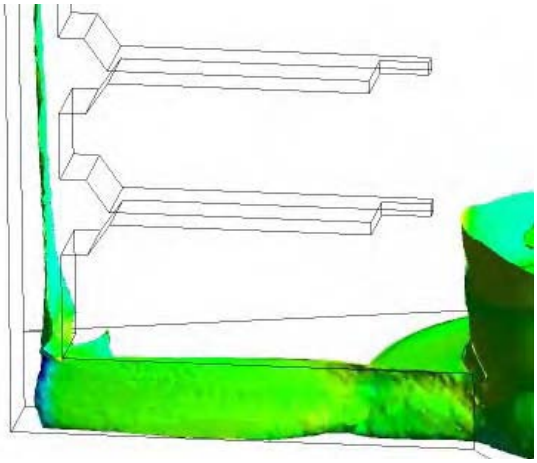

0.45 s

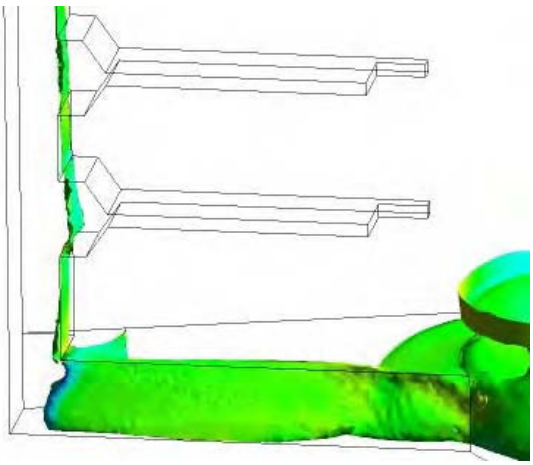

0.54 s

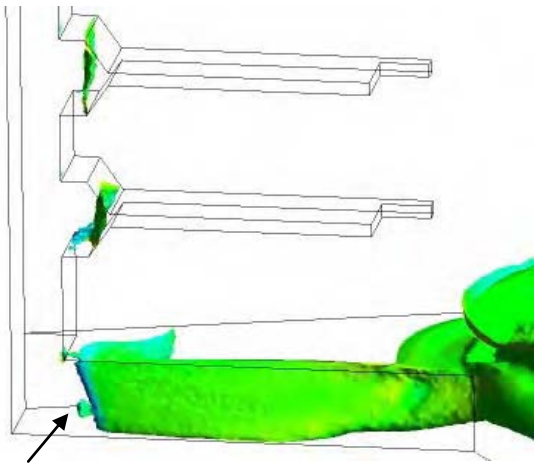

0.63 s

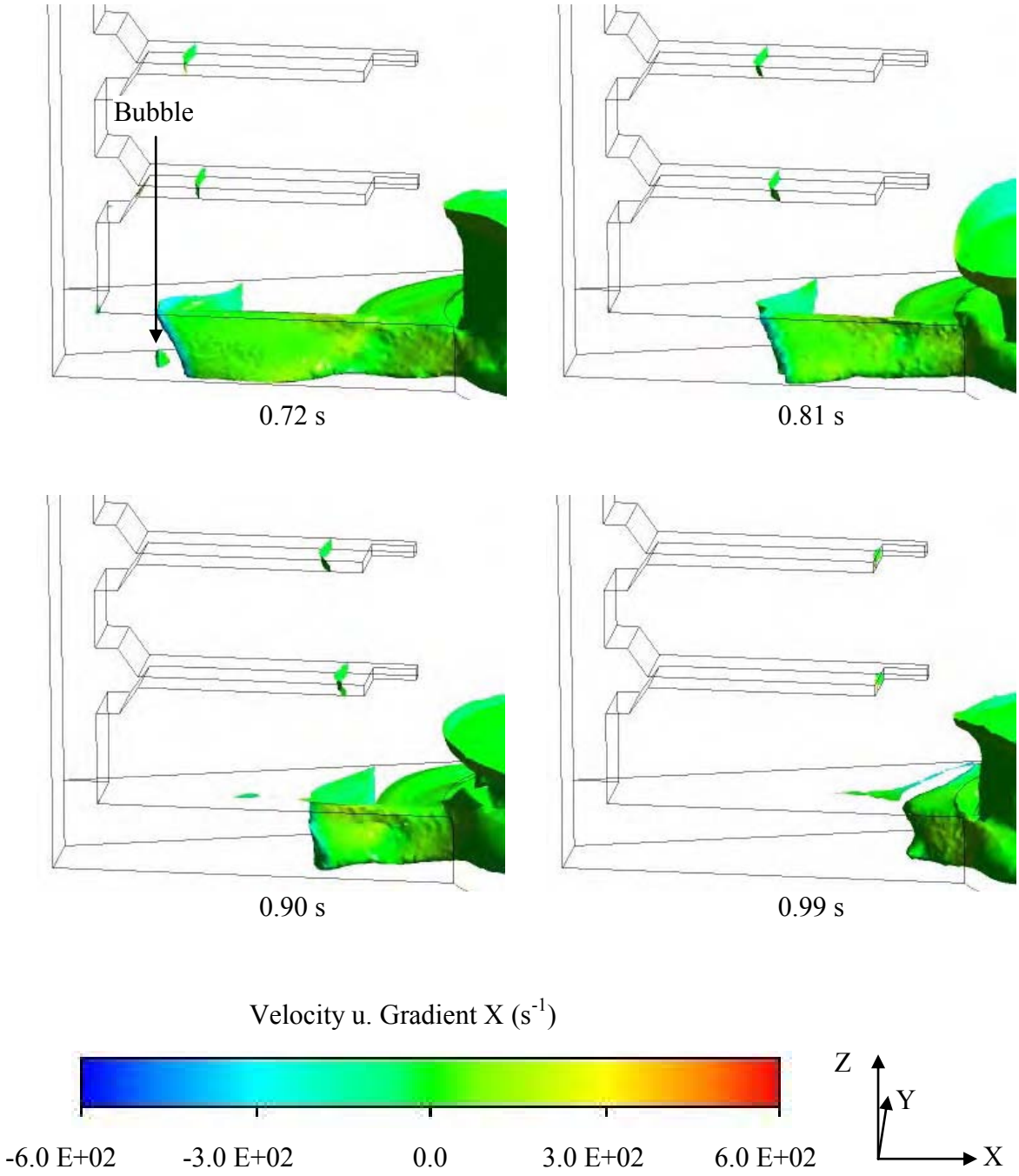

Figure 6 - 132 Close-up of the left horizontal and vertical runner bars of the indirect gated casting mould filling process showing isosurface (0.5 volume fraction) and velocity gradient in 'X' axis.

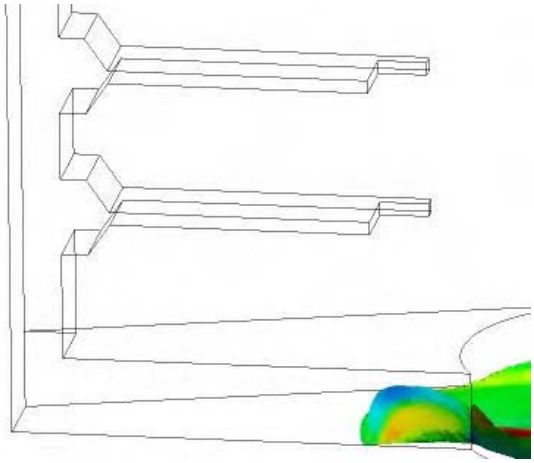

0.18 s

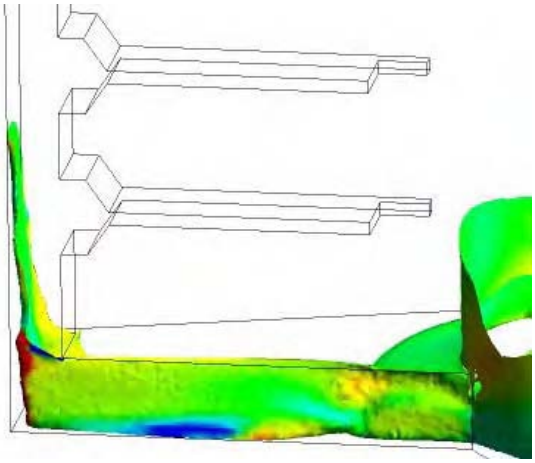

0.27 s

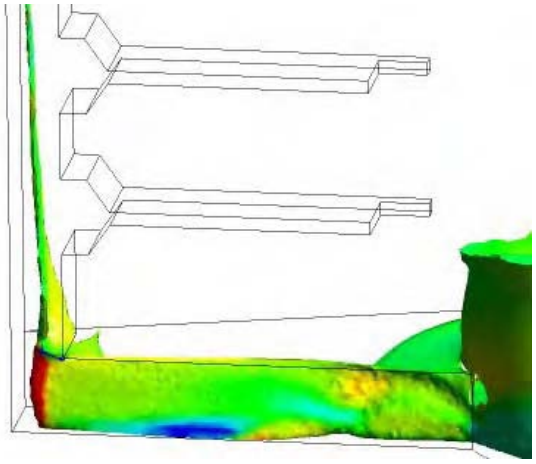

0.36 s

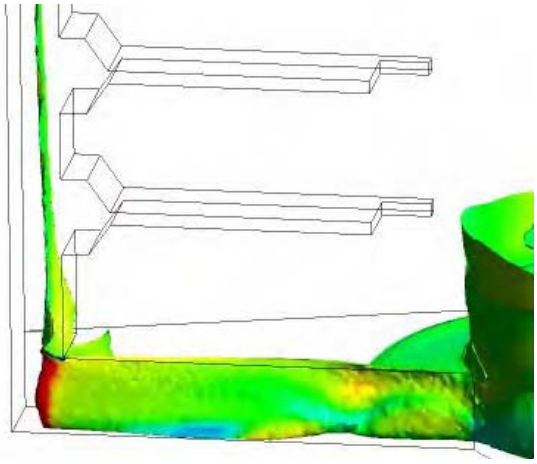

0.45 s

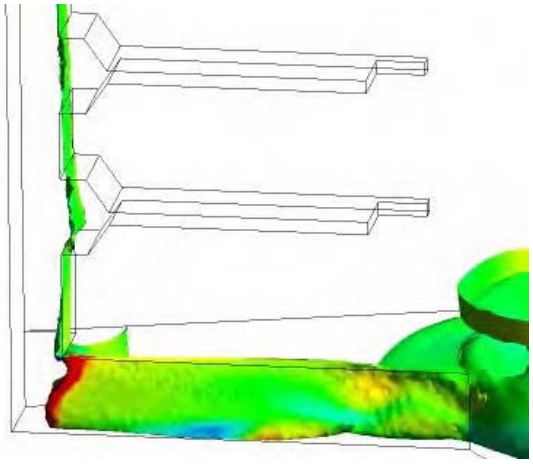

0.54 s

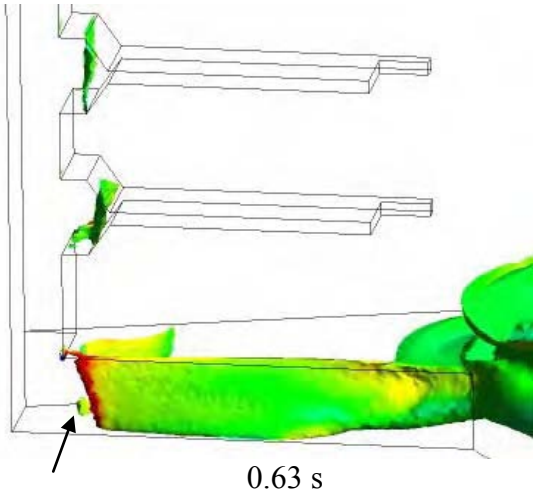

0.63 s

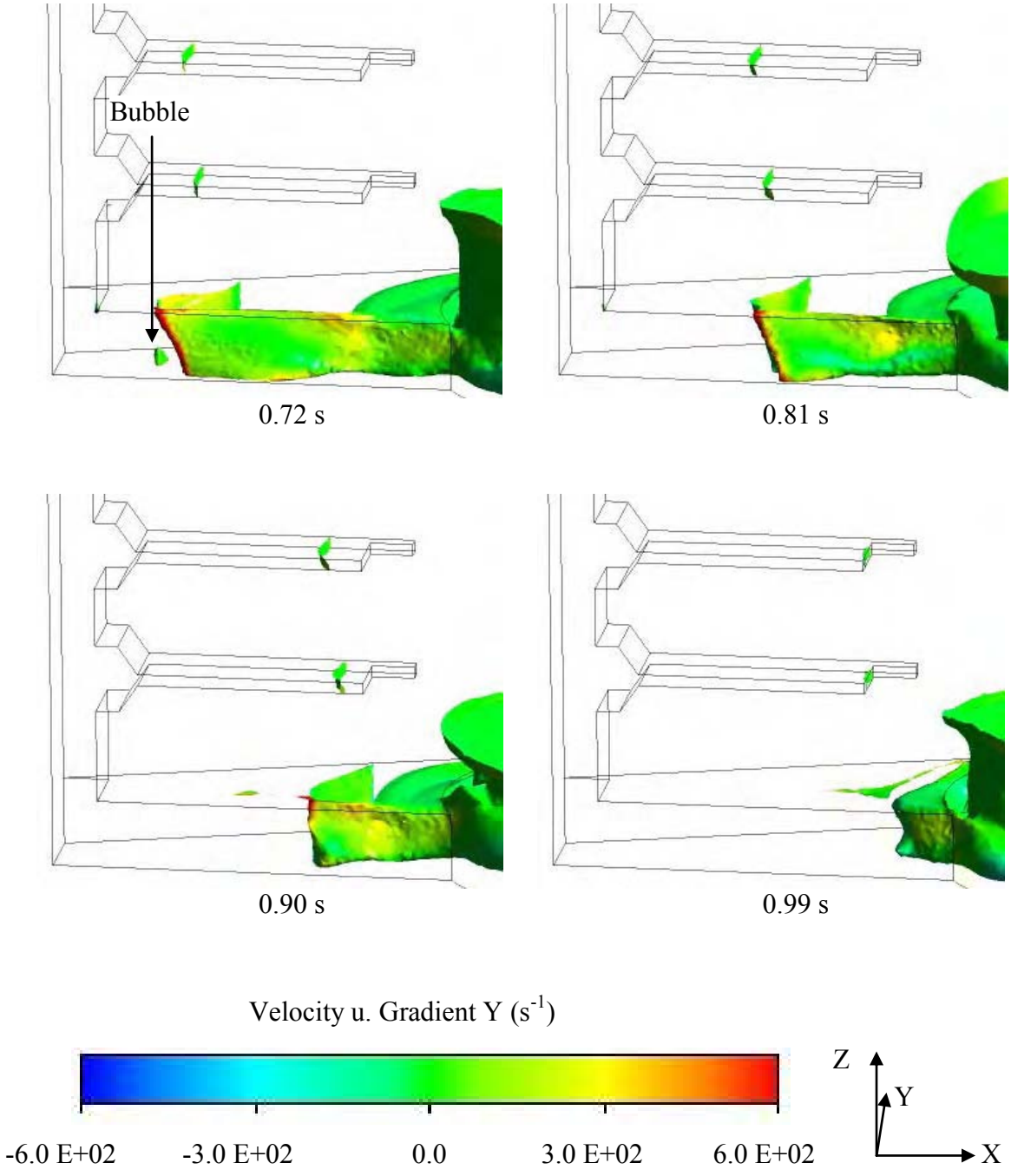

Figure 6 - 133 Close-up of the left horizontal and vertical runner bars of the indirect gated casting mould filling process showing isosurface (0.5 volume fraction) and velocity gradient in 'Y' axis. Note: Full video sequence can be seen in Appendix 56.

0.48 s

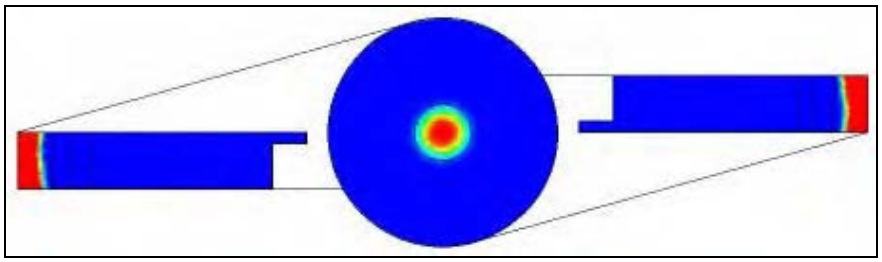

0.54 s

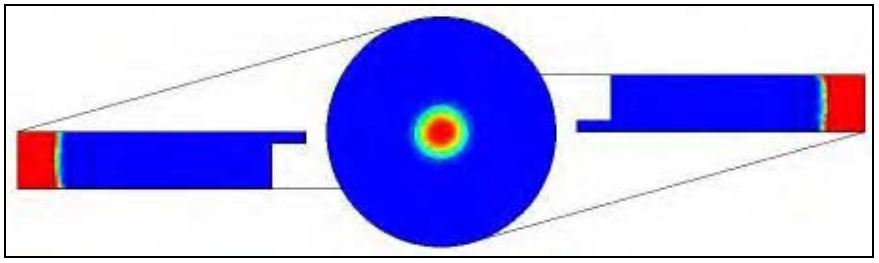

0.60 s

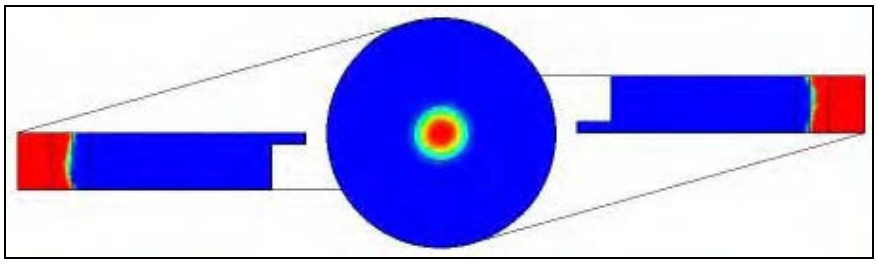

0.66 s

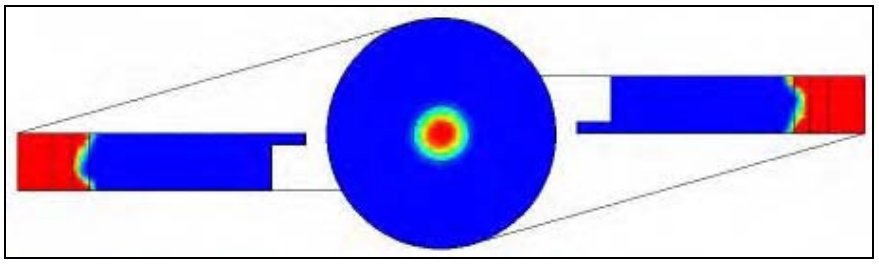

0.72 s

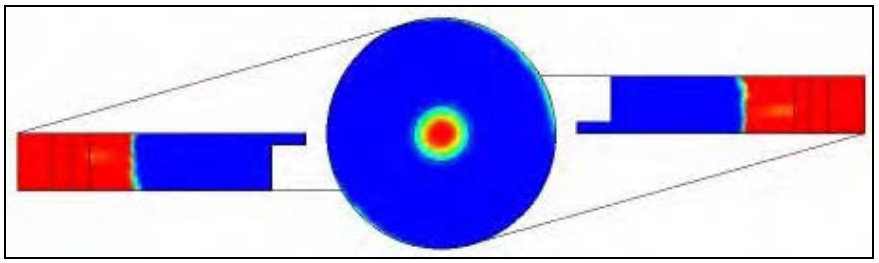

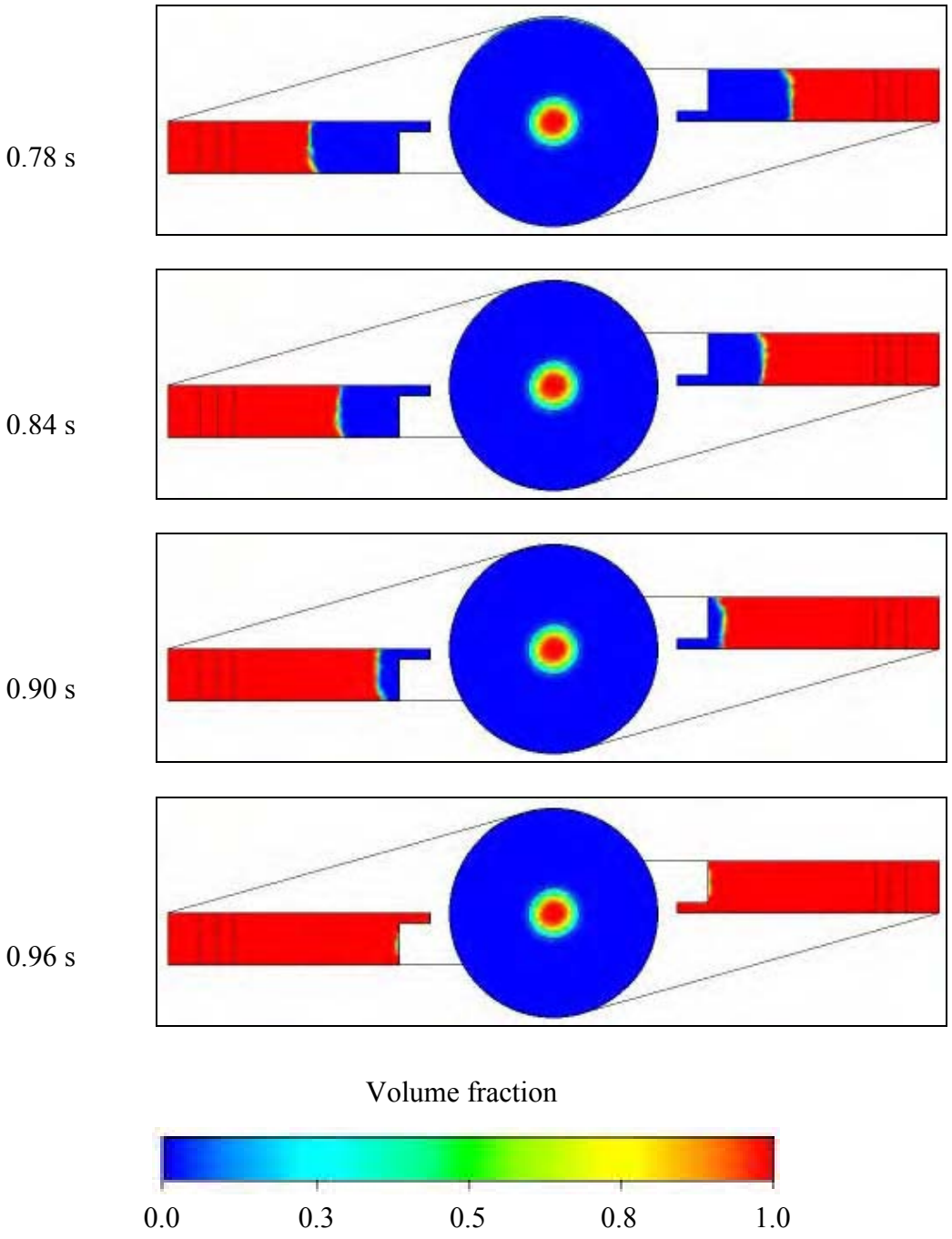

Figure 6 - 134. ANSYS CFX results of the indirect gated casting mould showing plan view (volume fraction). The cut plane was taken at mid-thickness of the test bar pair C1L1IG (4) – C1R1IG (5) (see Figure 6 - 2). Note: Full video sequence can be seen in Appendix 57.

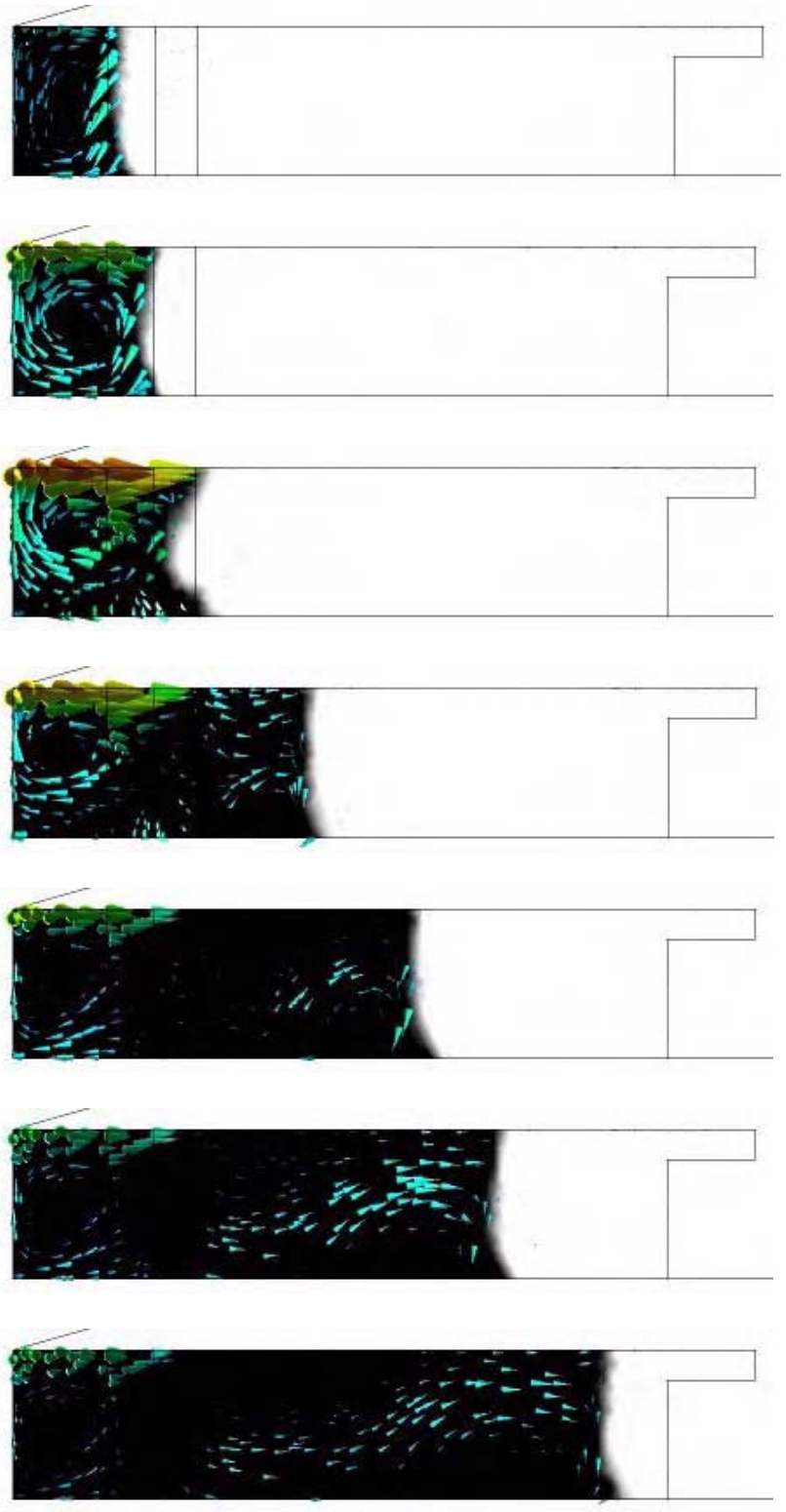
0.54 s
0.60 s
0.66 s
0.72 s
0.78 s
0.84 s
0.90 s

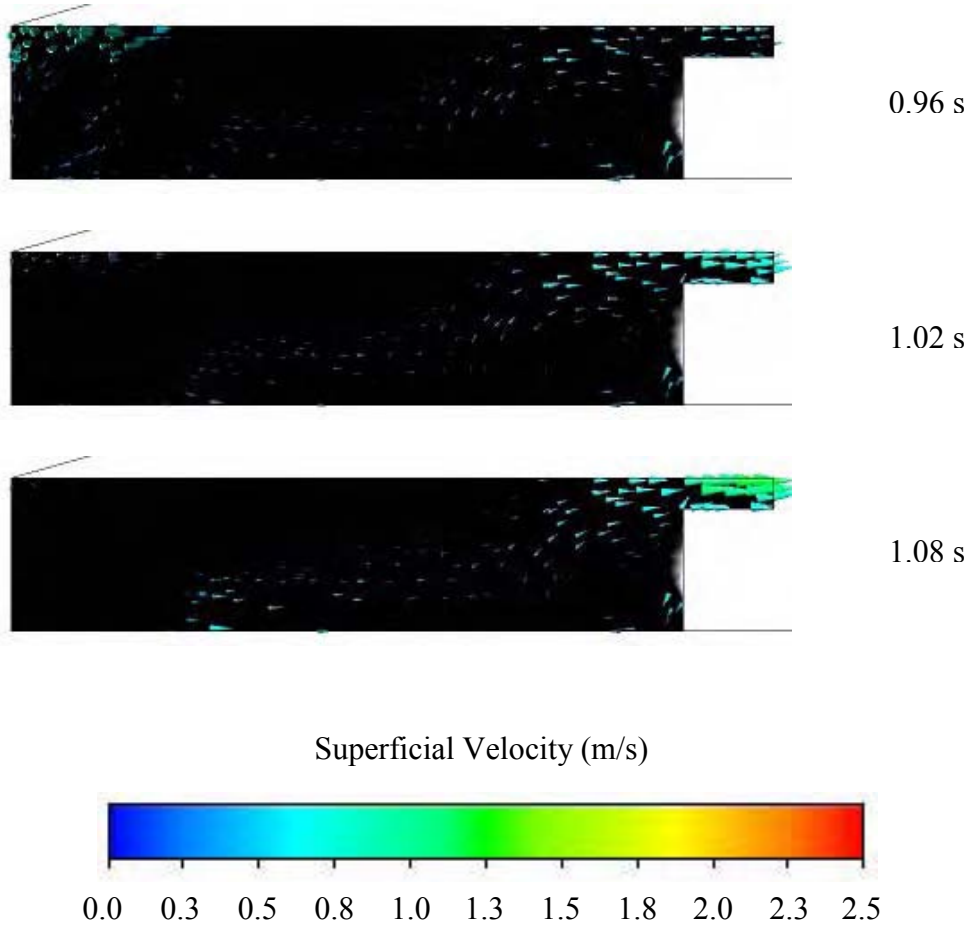

Figure 6 - 135. ANSYS CFX results showing close-up plan view of the left test bar and velocity vectors. The cut plane was taken at mid-thickness of the test bar C1L1IG (4) (see Figure 6 - 2 and Figure 6 - 134). Note: Full video sequence can be seen in Appendix 58.

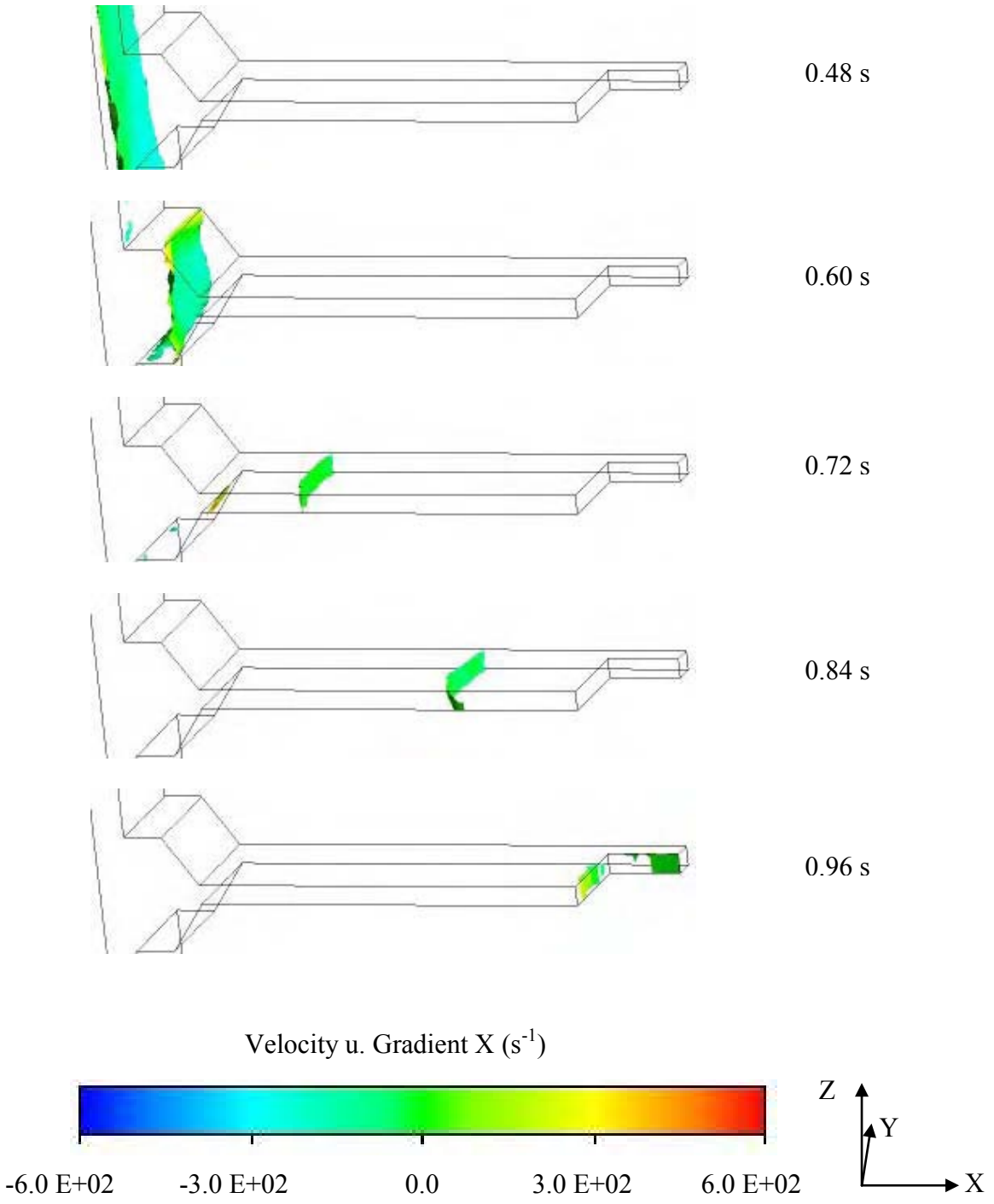

Figure 6 - 136. ANSYS CFX results showing close-up of the left test bar, isosurface (0.5 volume fraction) and velocity gradient in 'X' axis. The indirect gated test bar was C1L1IG (4) (see Figure 6 - 2 and Figure 6 - 134).

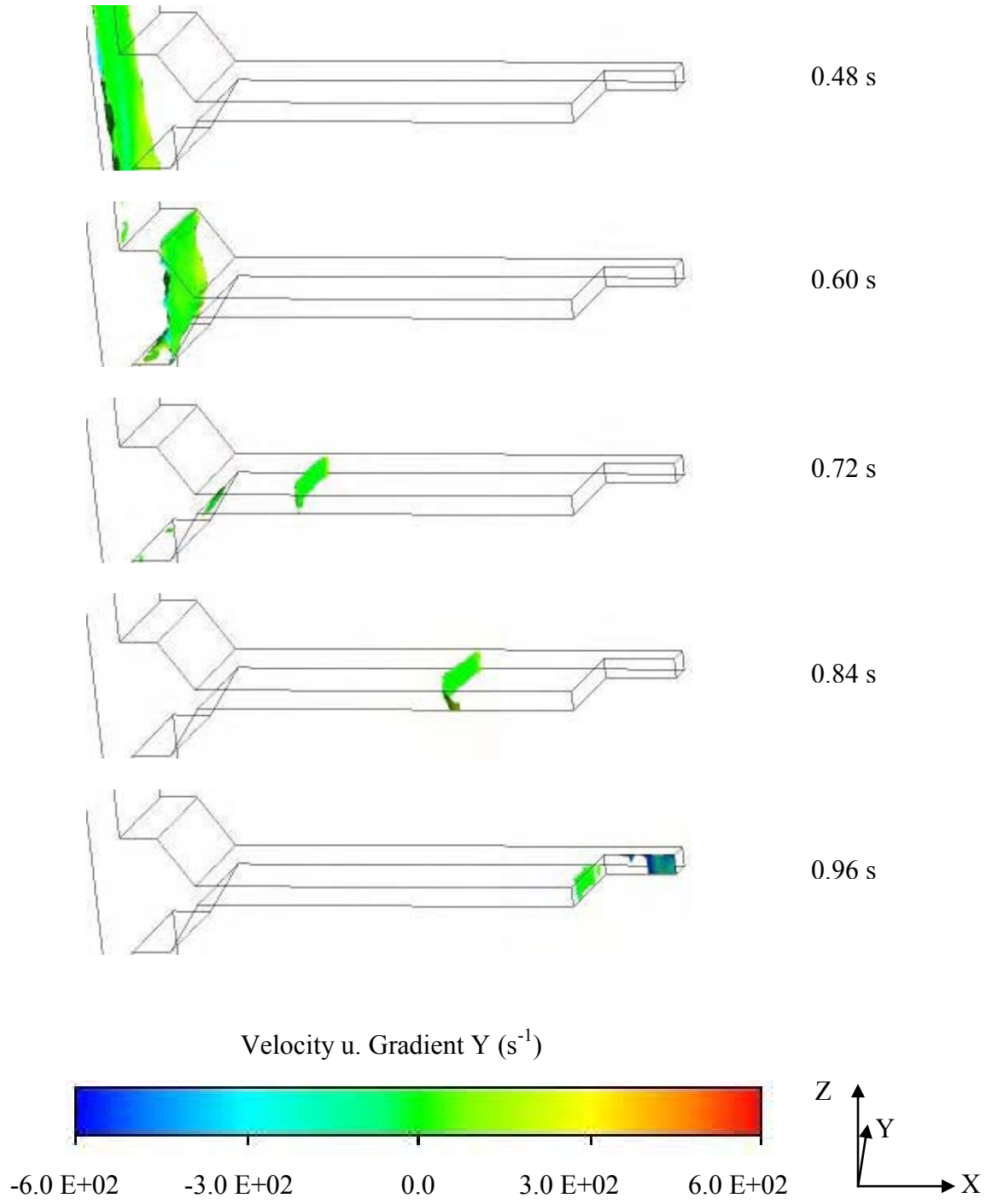

Figure 6 - 137. ANSYS CFX results showing close-up of the left test bar, isosurface (0.5 volume fraction) and velocity gradient in 'Y' axis. The indirect gated test bar was C1L1IG (4) (see Figure 6 - 2 and Figure 6 - 134).

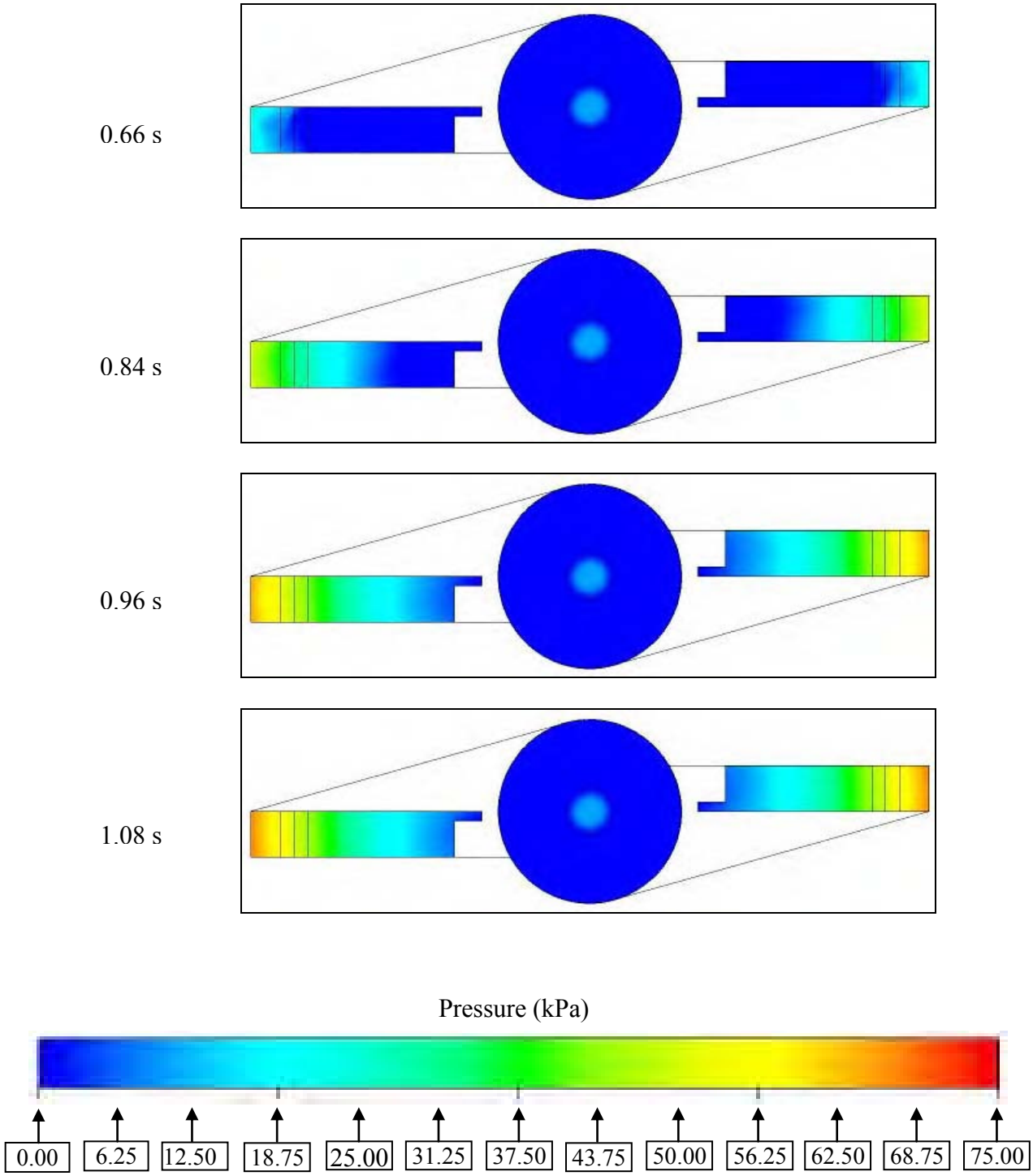

Figure 6 - 138. ANSYS CFX results of the indirect gated casting mould showing plan view and pressure. The cut plane was taken at mid-thickness of the test bar pair C1L1IG (4) – C1R1IG (5) (see Figure 6 - 2).

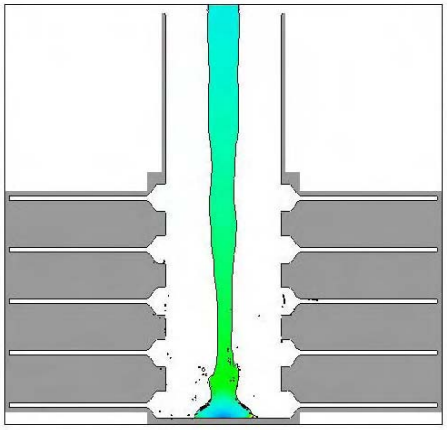

0.18 s

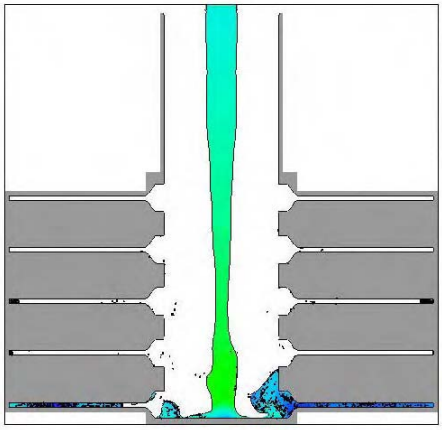

0.33 s

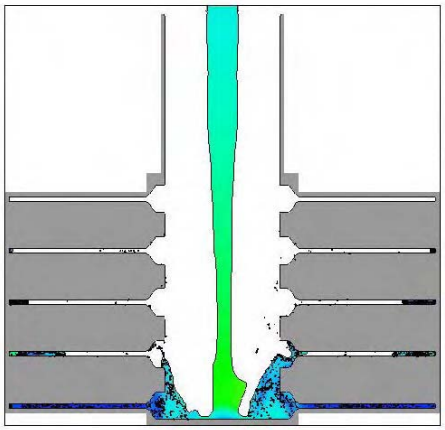

0.52 s

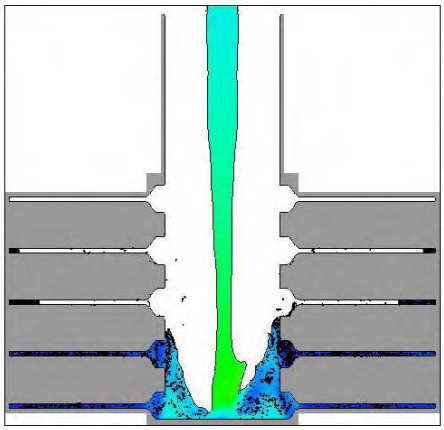

0.70 s

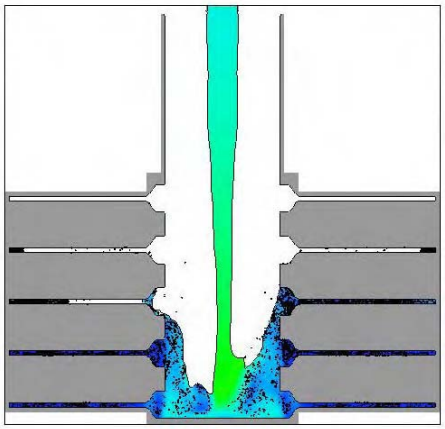

0.88 s

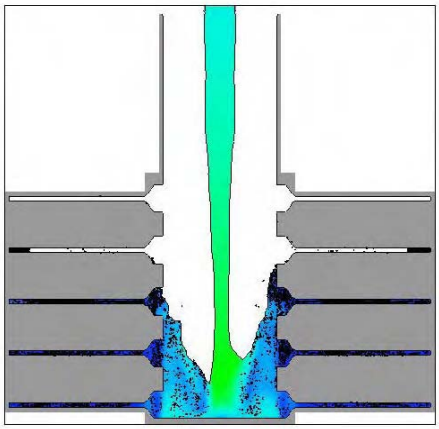

1.05 s

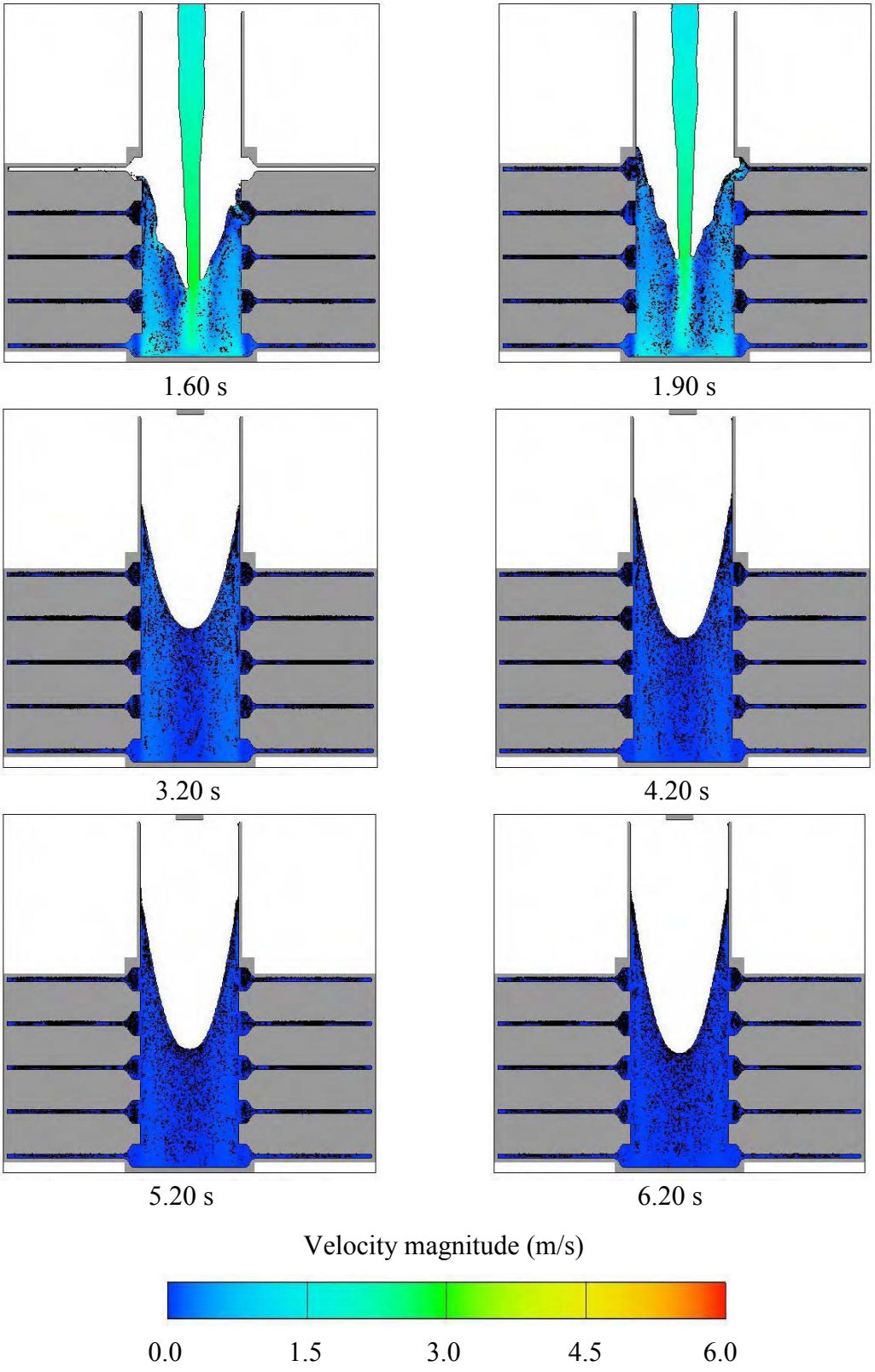

Figure 6 - 139. Flow-3D results of the direct gated casting mould showing 2D side view and particles. The cut plane was taken along the sprue diameter. Note: Full video sequence can be seen in Appendix 59.

0.28 s

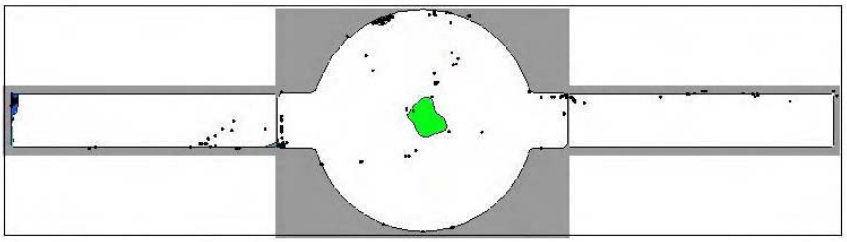

0.42 s

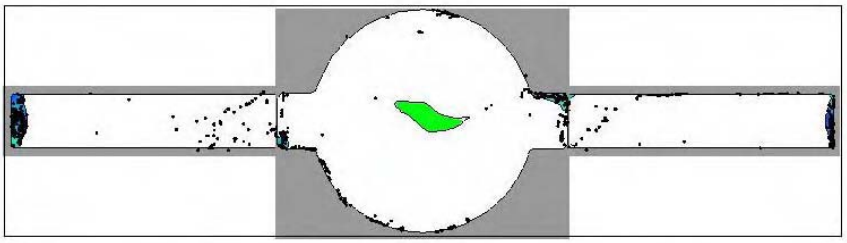

0.48 s

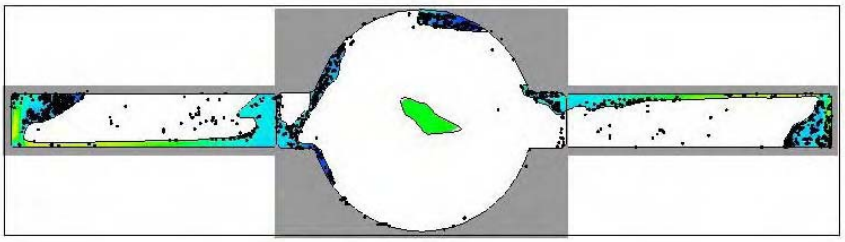

0.50 s

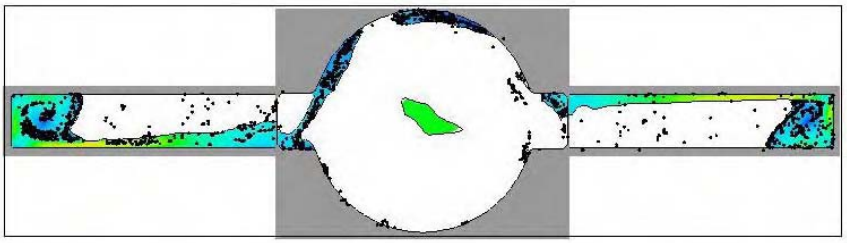

0.58 s

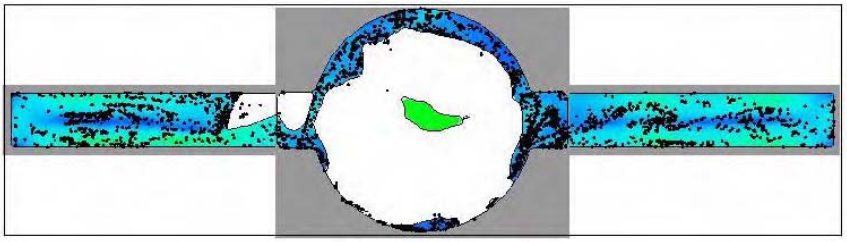

0.60 s

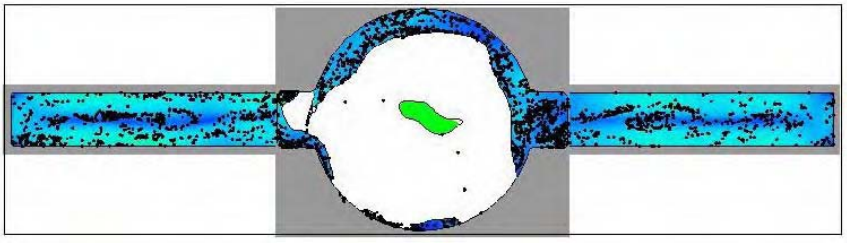

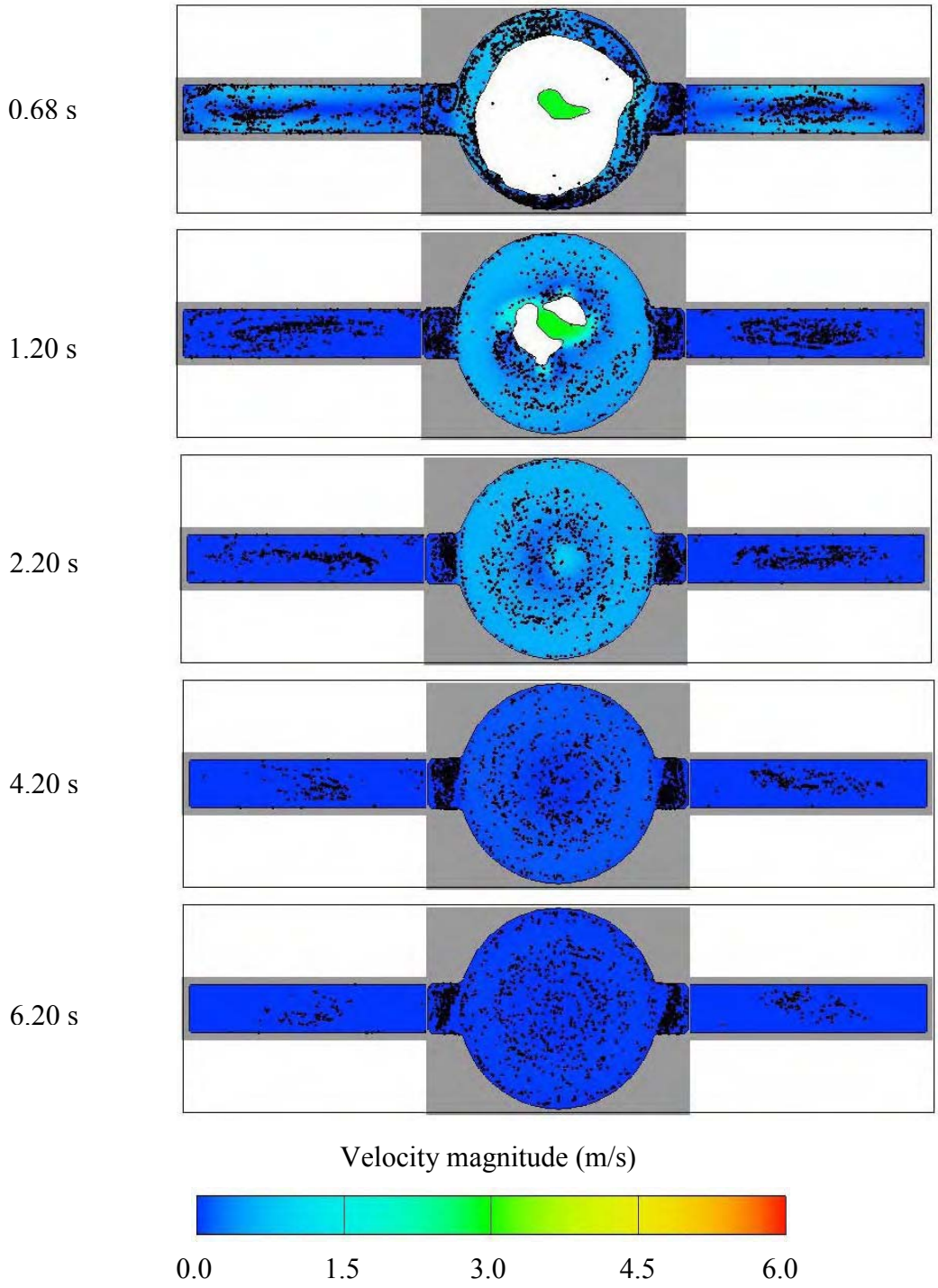

Figure 6 - 140. Flow-3D results of the direct gated casting mould showing plan view and particles. The cut plane was taken at mid-thickness of the test bar pair C1L2DG (4) – C1R2DG (7) (see Figure 6 - 1). Note: Full summary and video sequence can be seen in Appendix 25 and Appendix 60.

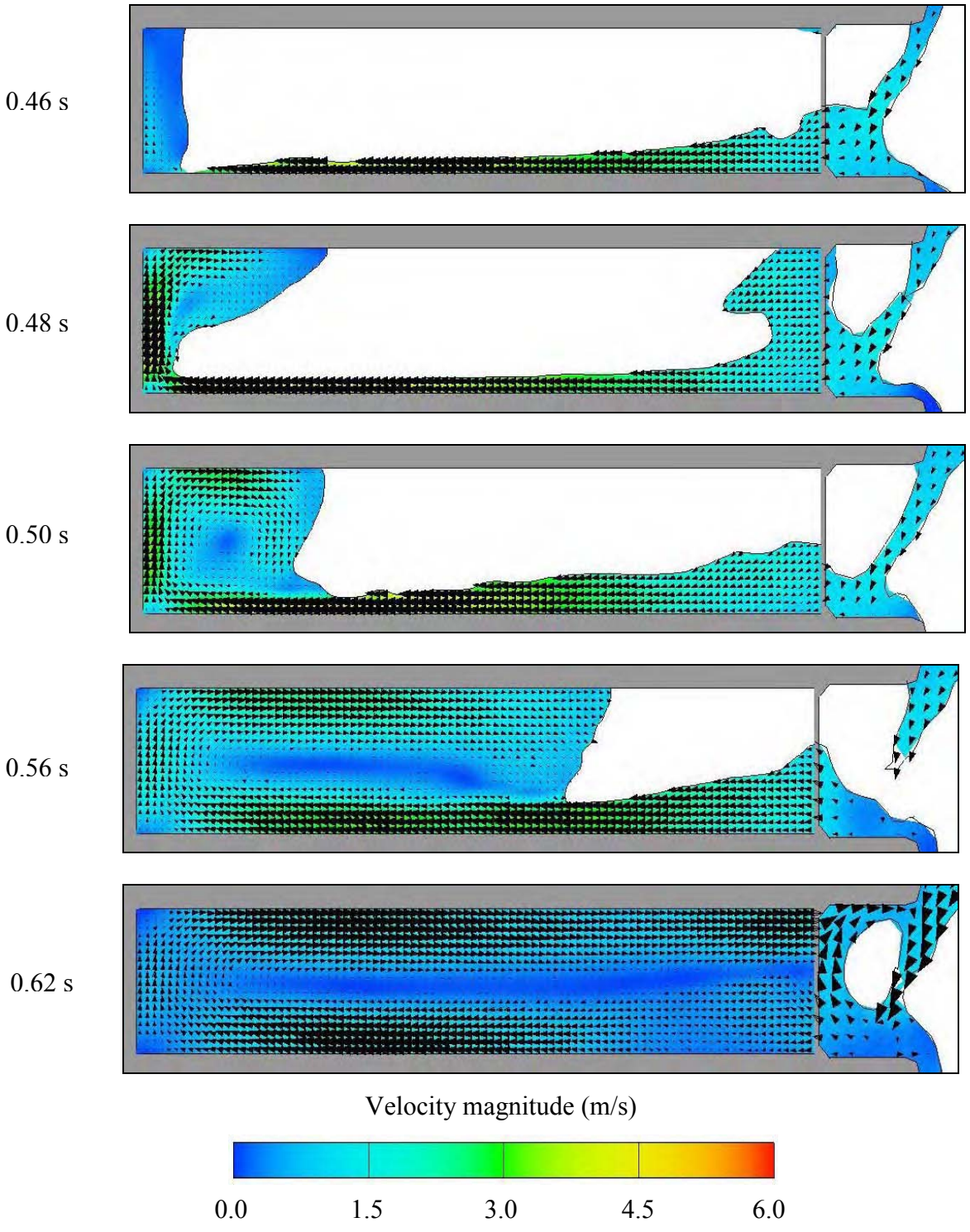

Figure 6 - 141. Flow-3D results showing close-up plan view of the left test bar and velocity vectors. The cut plane was taken at mid-thickness of the test bar C1L2DG (4) (see Figure 6 - 1 and Figure 6 - 140). Note: Full summary can be seen in Appendix 26.

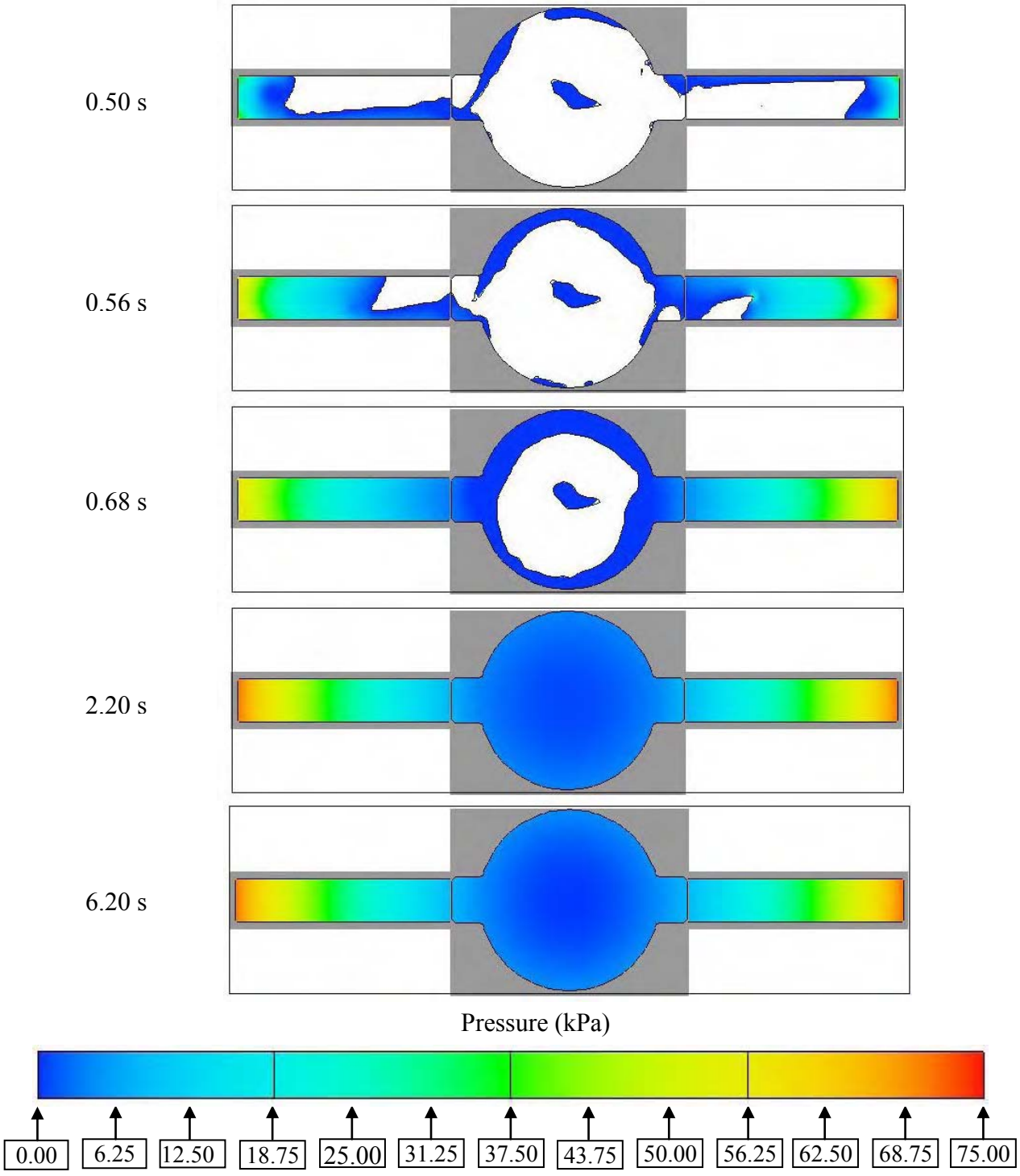

Figure 6 - 142. Flow-3D results of the direct gated casting mould showing plan view and pressure. The cut plane was taken at mid-thickness of the test bar pair C1L2DG (4) – C1R2DG (7) (see Figure 6 - 1).

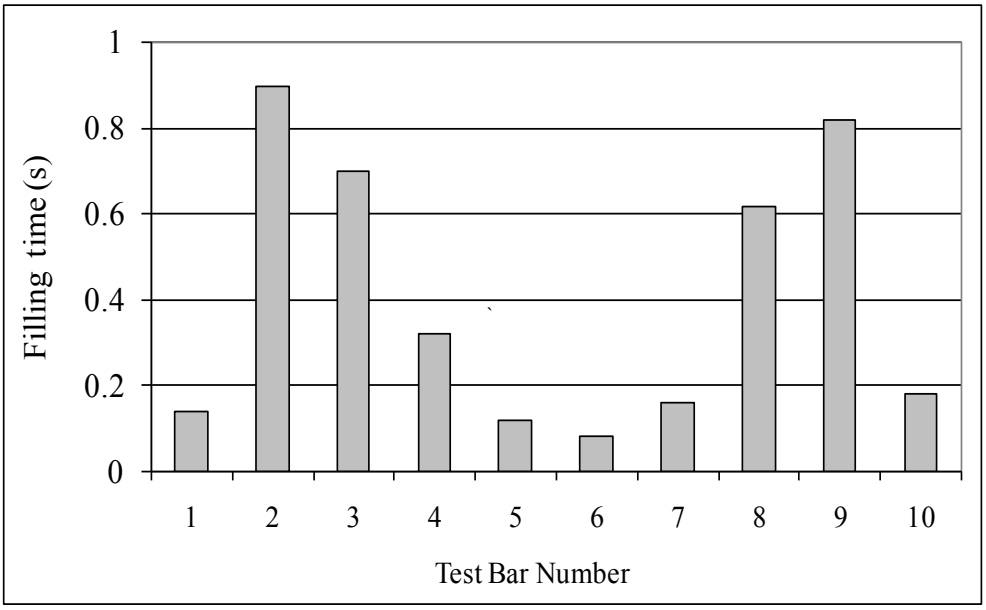

Figure 6 - 143. Filling time as a function of test bar position (see Figure 6 - 1).

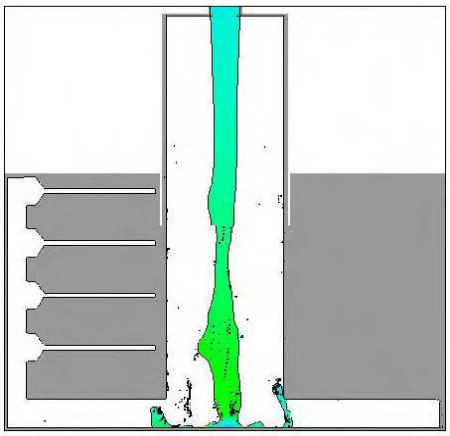

0.24 s

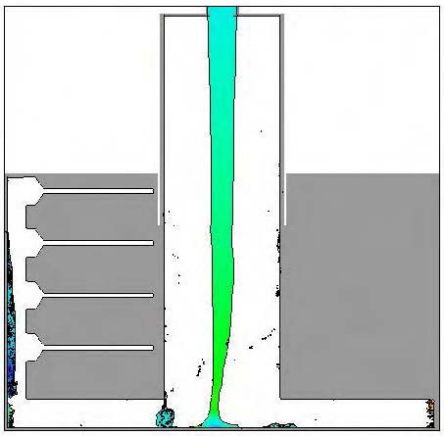

0.38 s

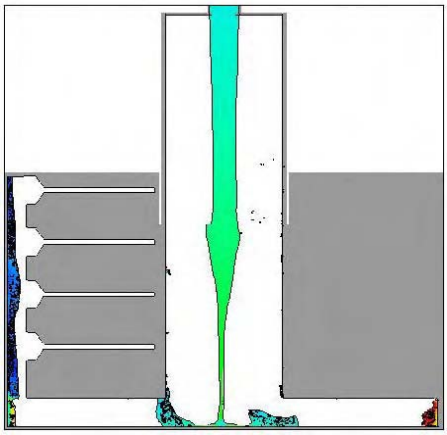

0.52 s

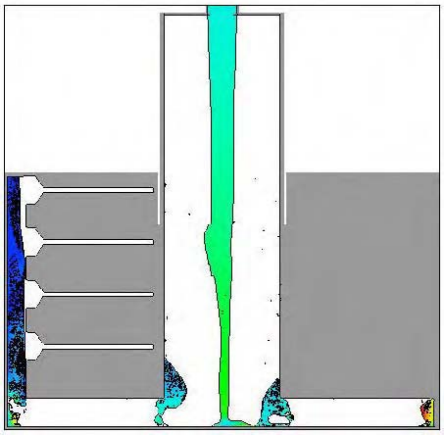

0.66 s

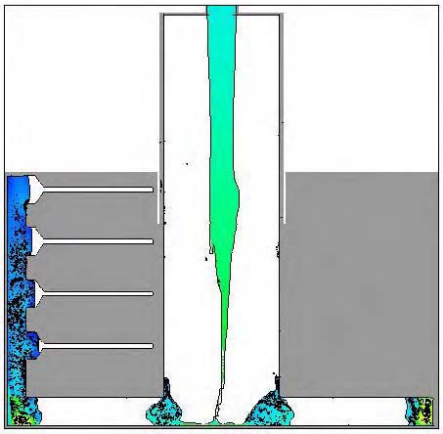

0.80 s

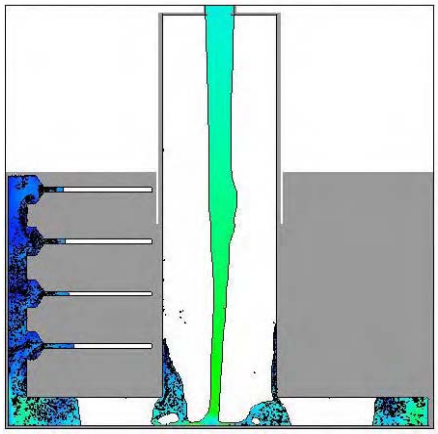

0.94 s

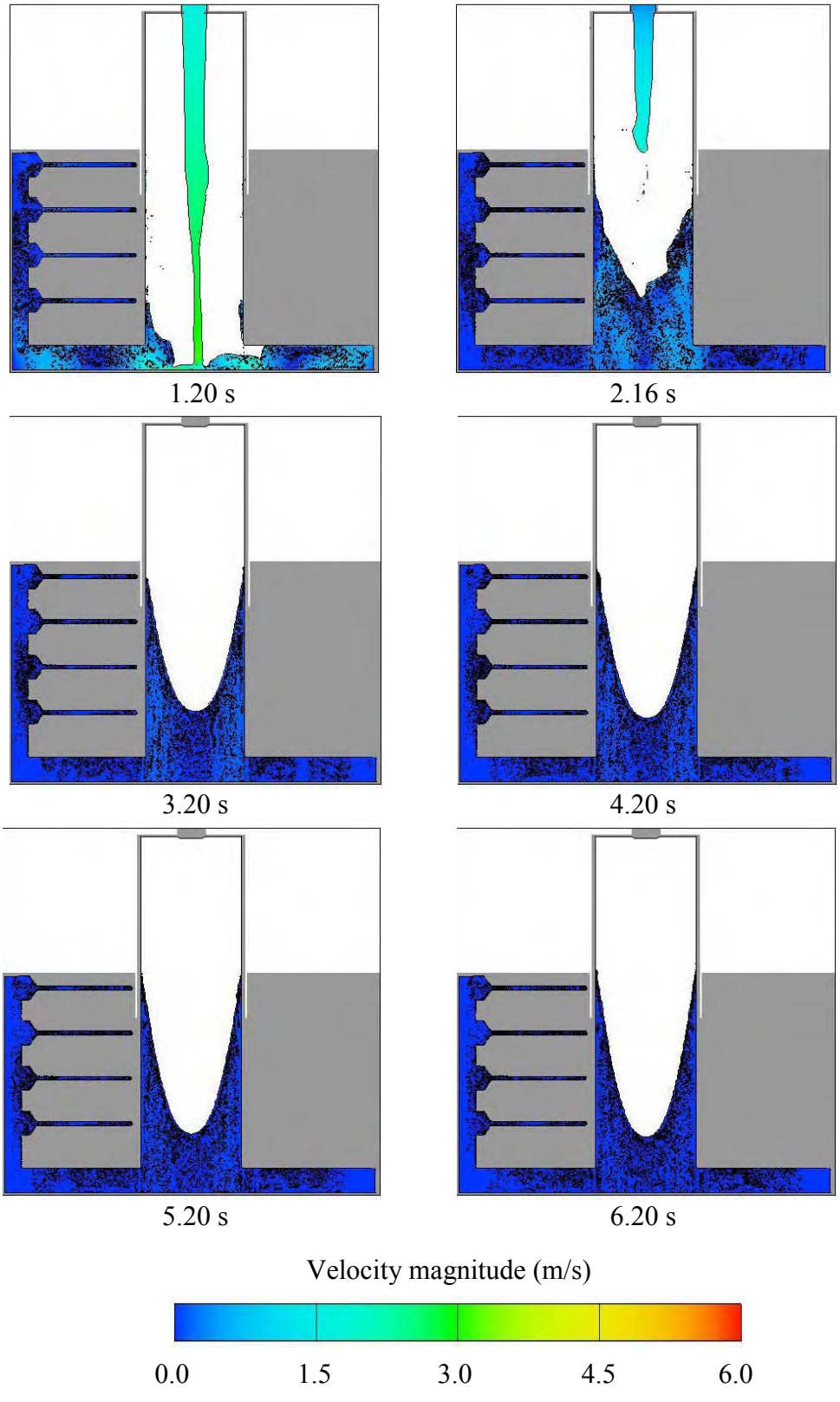

Figure 6 - 144. Flow-3D results of the indirect gated casting mould showing left side view. The cut plane was taken 2 mm from the centre line of the mould. Note: Full video sequence can be seen in Appendix 65.

0.48 s

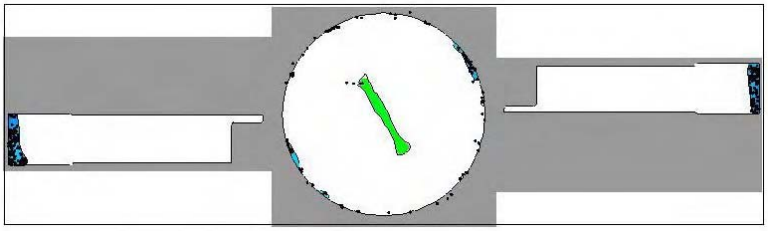

0.66 s

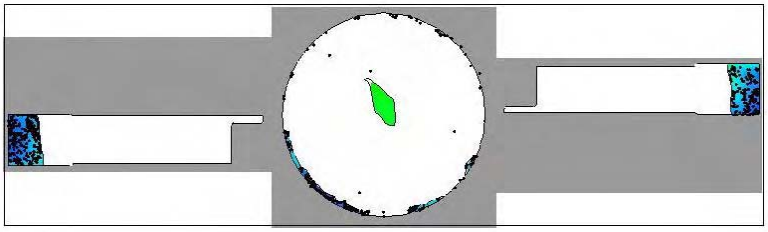

0.84 s

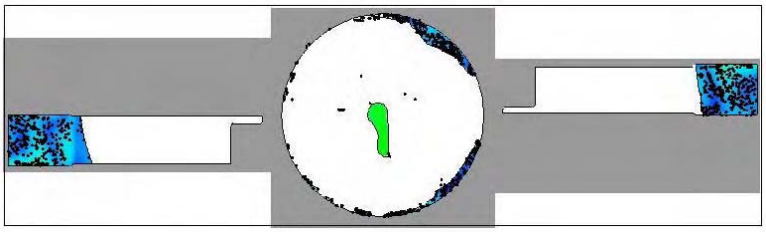

0.90 s

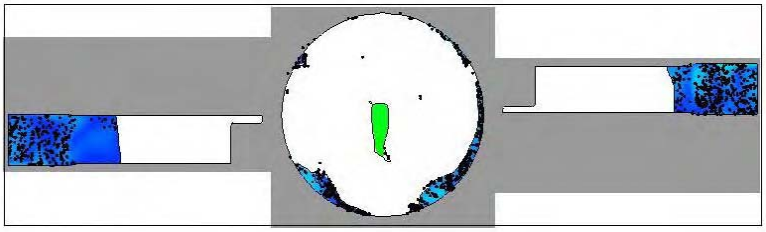

0.96 s

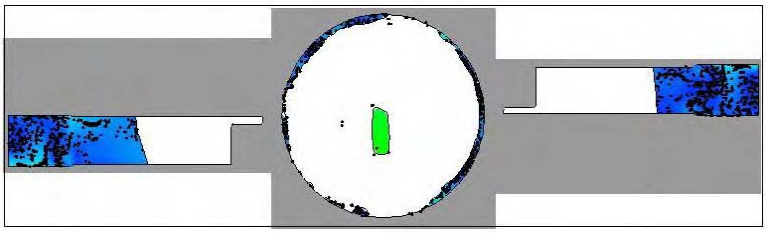

1.02 s

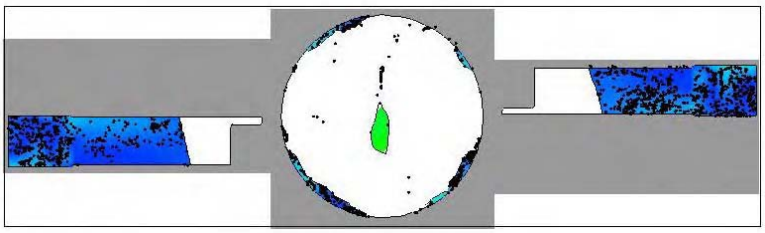

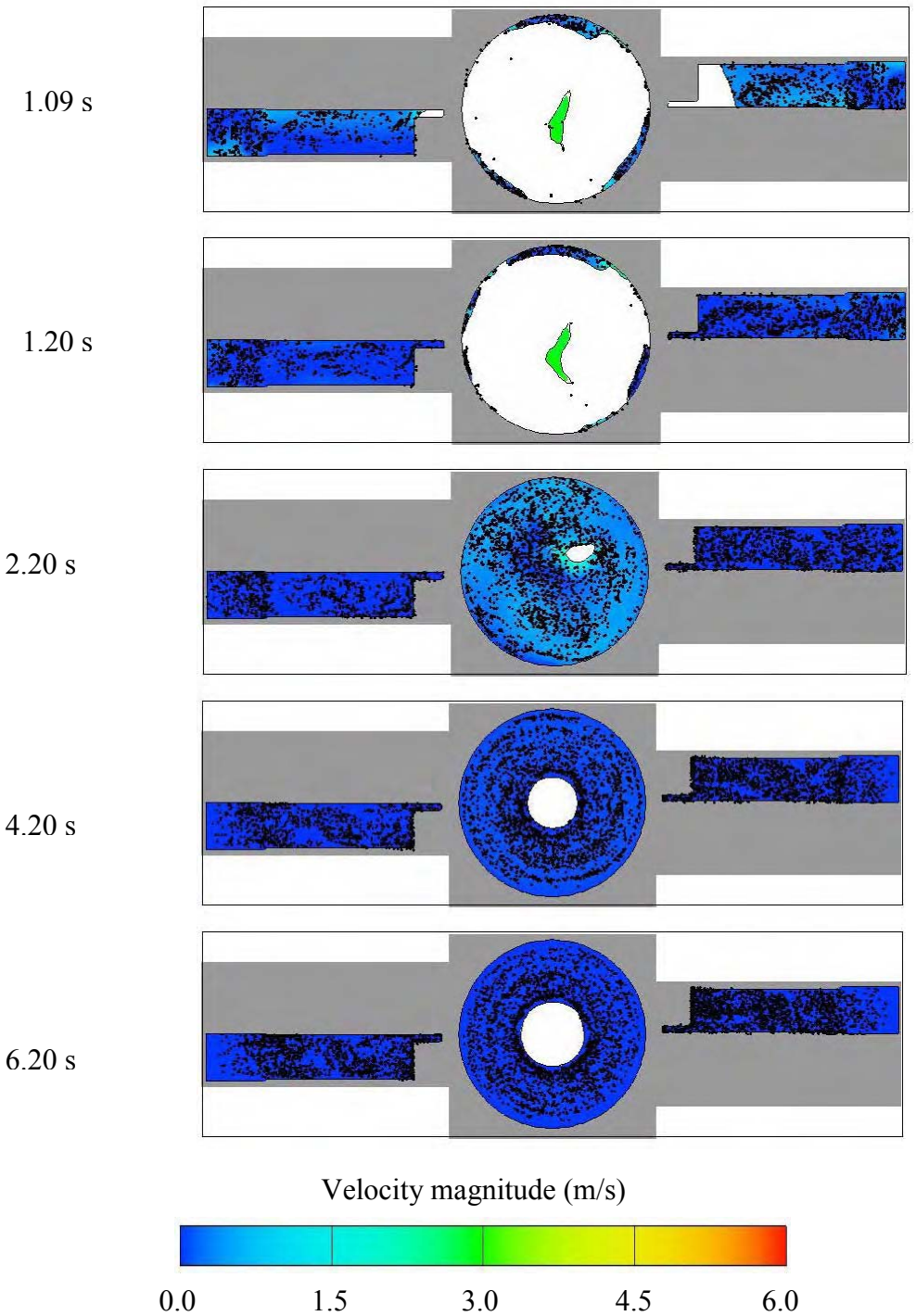

Figure 6 - 145. Flow-3D results of the indirect gated casting mould showing plan view. The cut plane was taken at mid-thickness of the test bar pair C1L1IG (4) – C1R1IG (5) (see Figure 6 - 2). Note: Full summary and video sequence can be seen in Appendix 31 and Appendix 66.

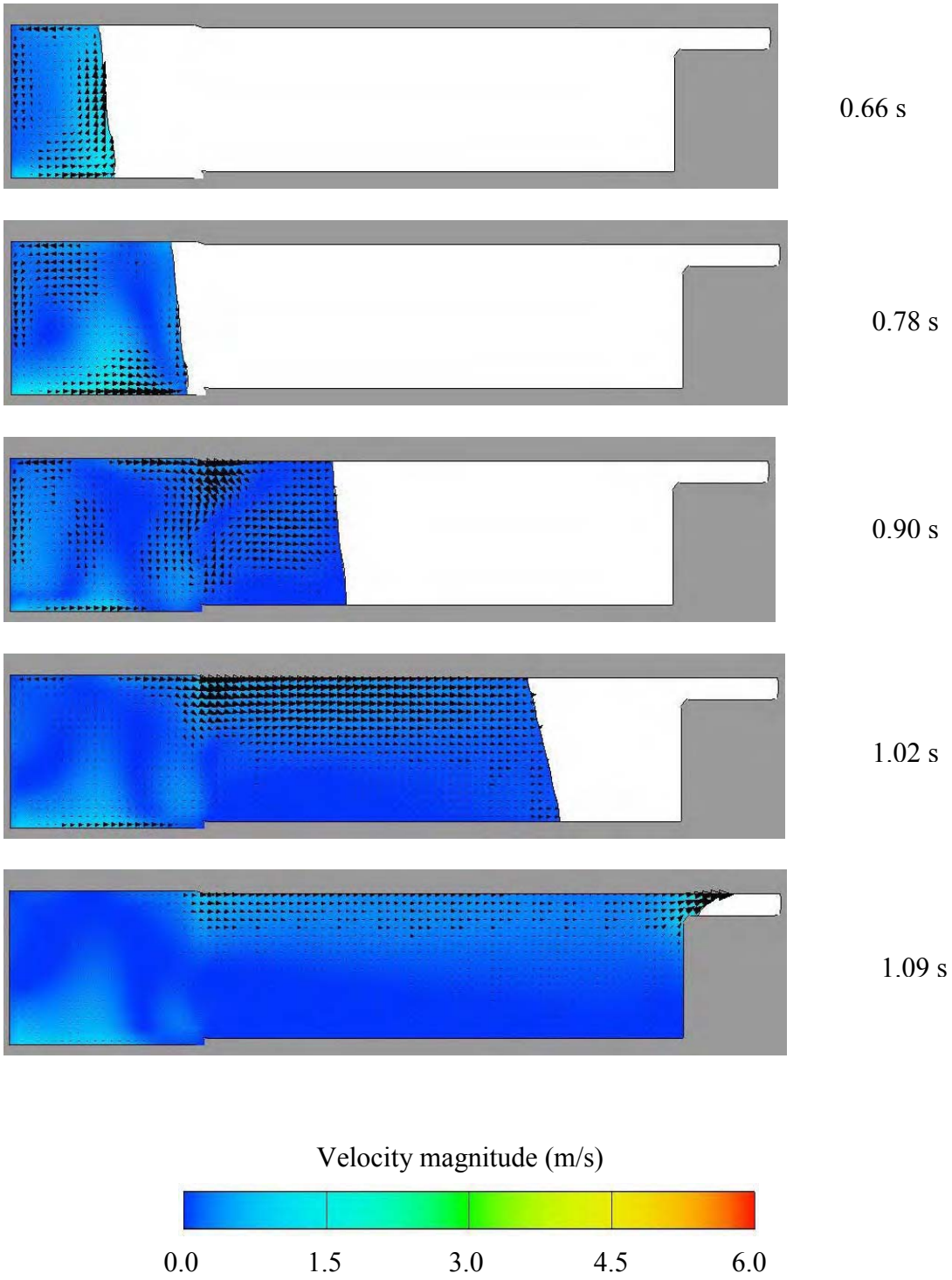

Figure 6 - 146. Flow-3D results showing close-up plan view of the left test bar and velocity vectors. The cut plane was taken at mid-thickness of the test bar C1L1IG (4) (see Figure 6 - 1 and Figure 6 - 145).

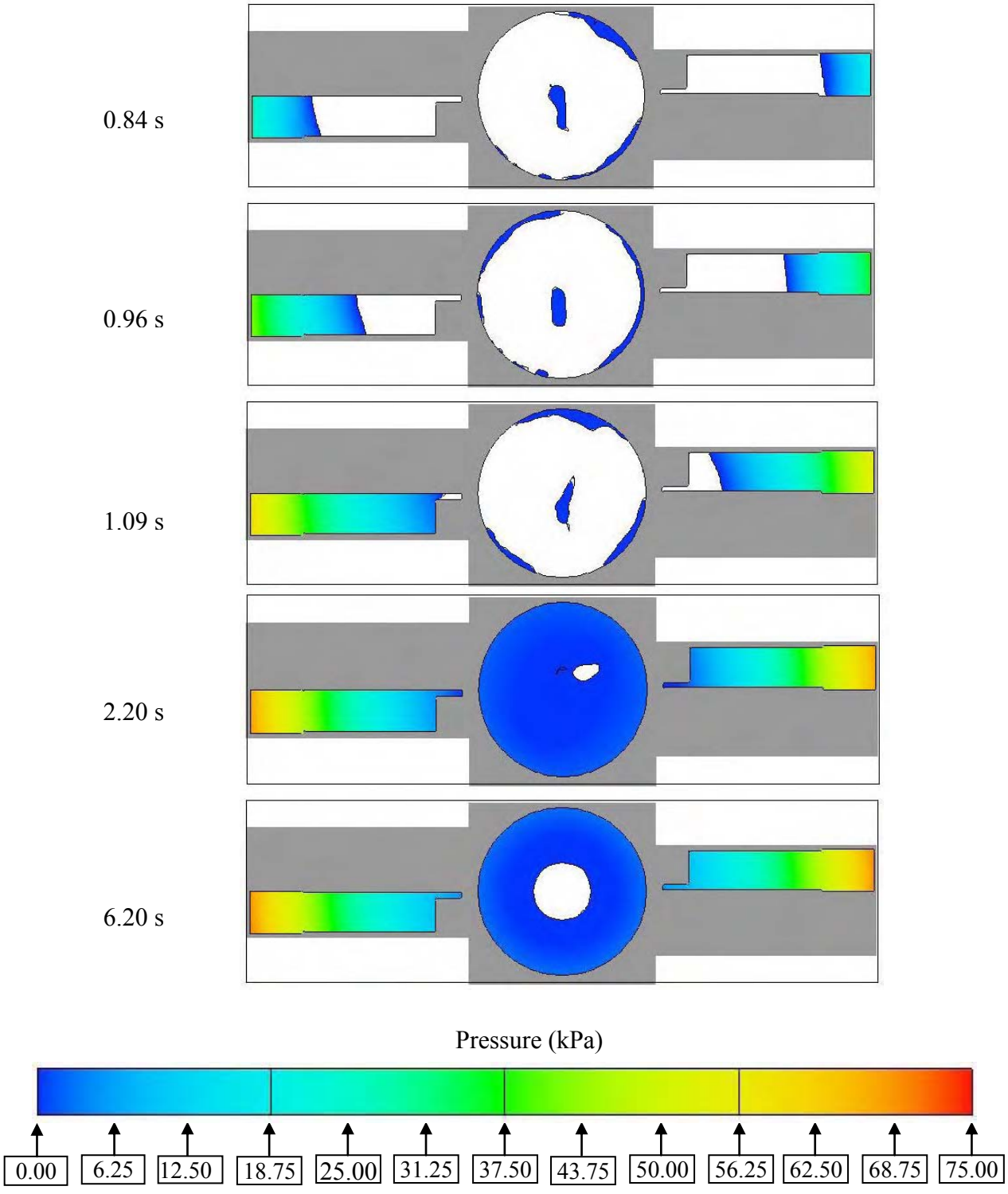

Figure 6 - 147. Flow-3D results of the indirect gated casting mould showing plan view and pressure. The cut plane was taken at mid-thickness of the test bar pair C1L1IG (4) - C1R1IG (5) (see Figure 6 - 2).

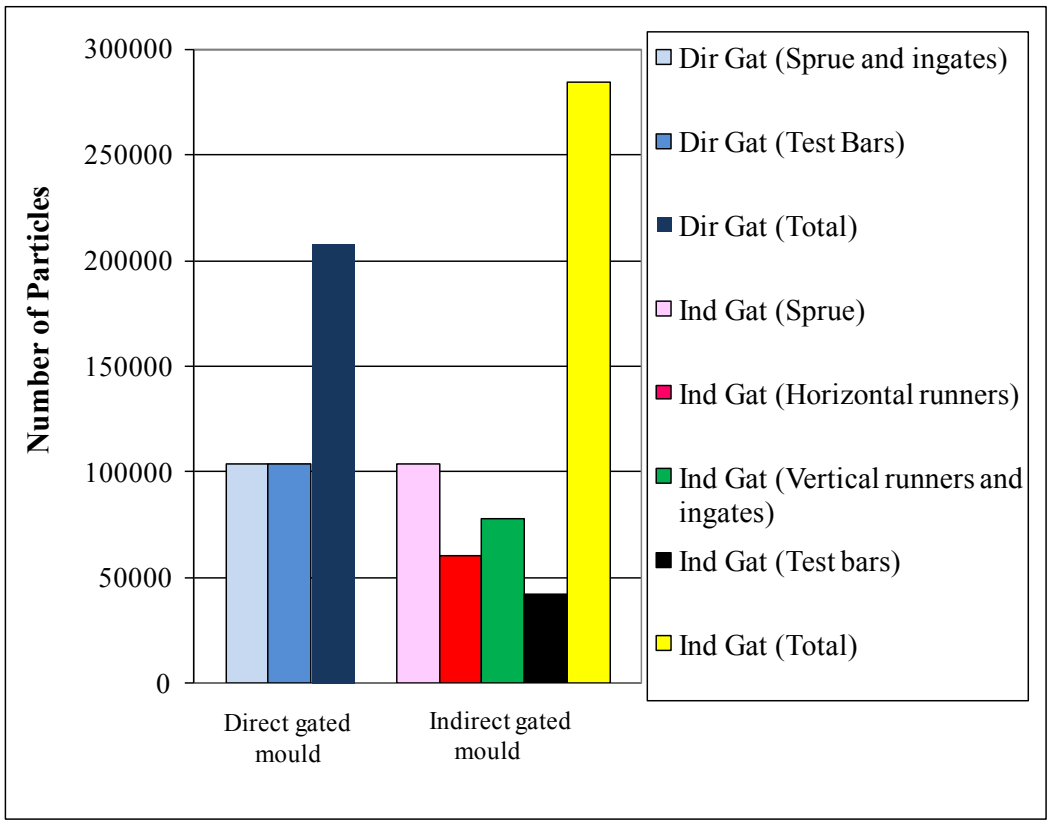

Figure 6 - 148. Comparison of total number of particles placed in direct and indirect gated moulds (see Figure 6 - 1 and Figure 6 - 2).

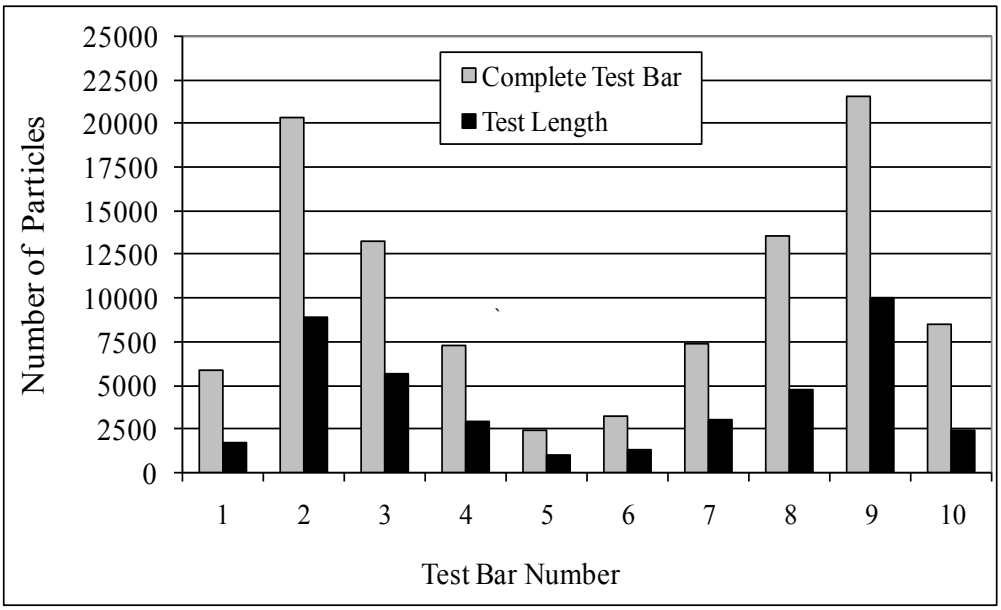

Figure 6 - 149. Number of particles in the complete direct gated test bars and test length (see Figure 6 - 1).

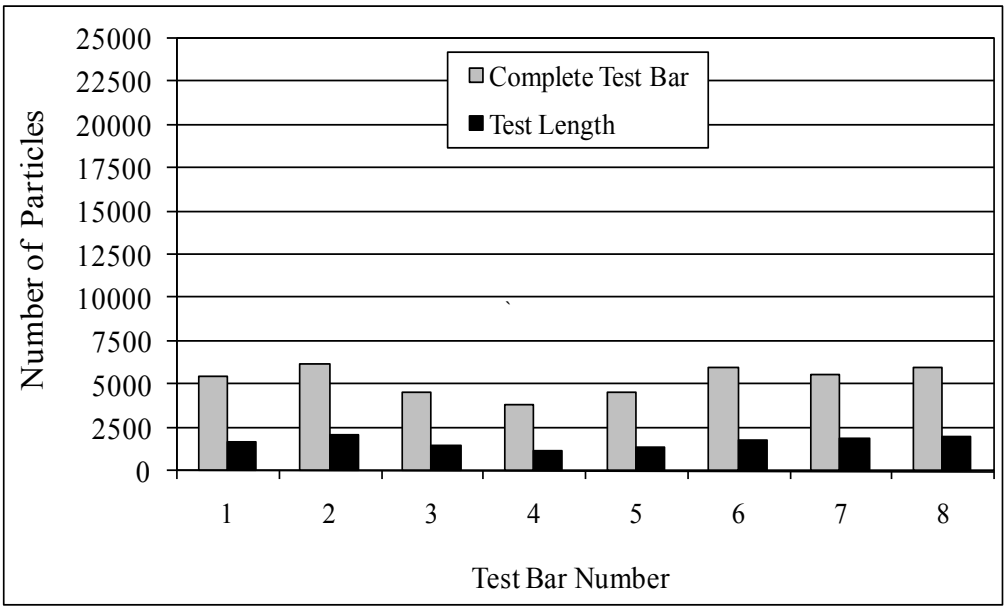

Figure 6 - 150. Number of particles in the complete indirect gated test bars and test length (see Figure 6 - 2).

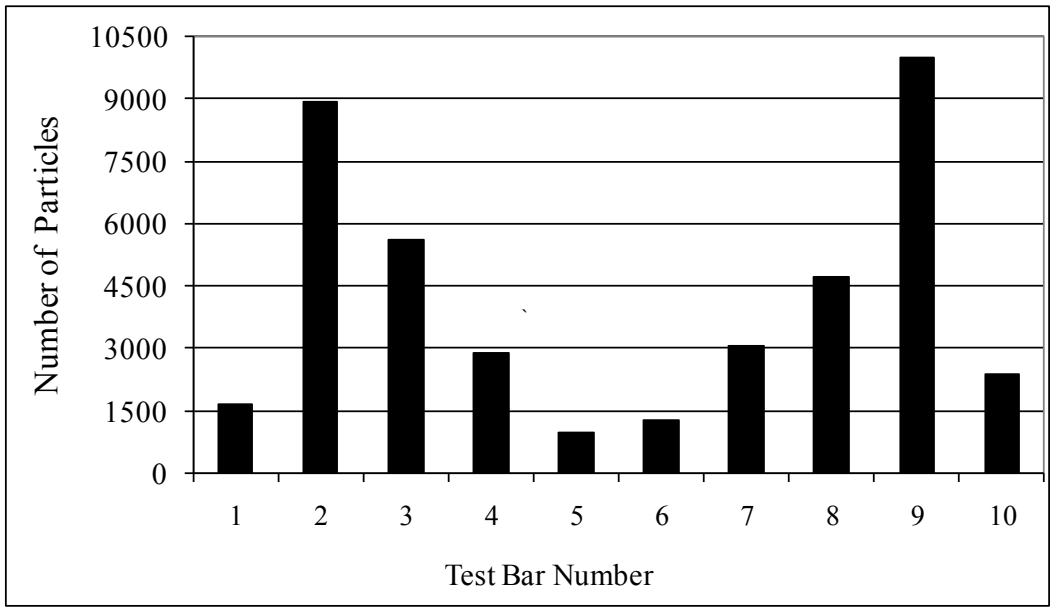

Figure 6 - 151. Number of particles in the test length of the direct gated test bars (see Figure 6 - 1).

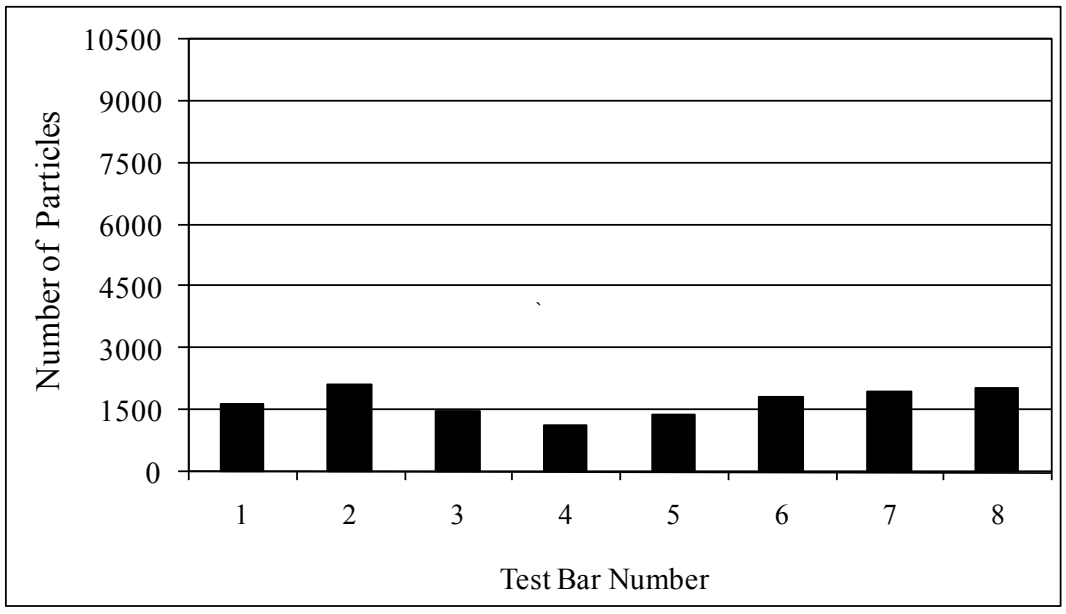

Figure 6 - 152. Number of particles in the test length of the indirect gated test bars (see Figure 6 - 2).

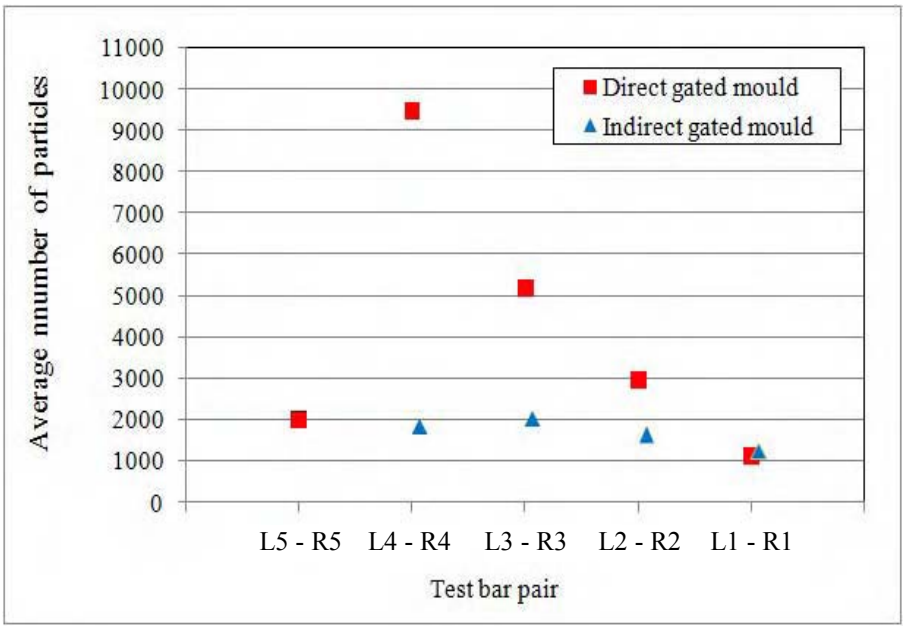

Figure 6 - 153. Average number of particles in the test length as a function of test bar pair and position in the direct and indirect gated moulds. Each point is the average of two test bars.

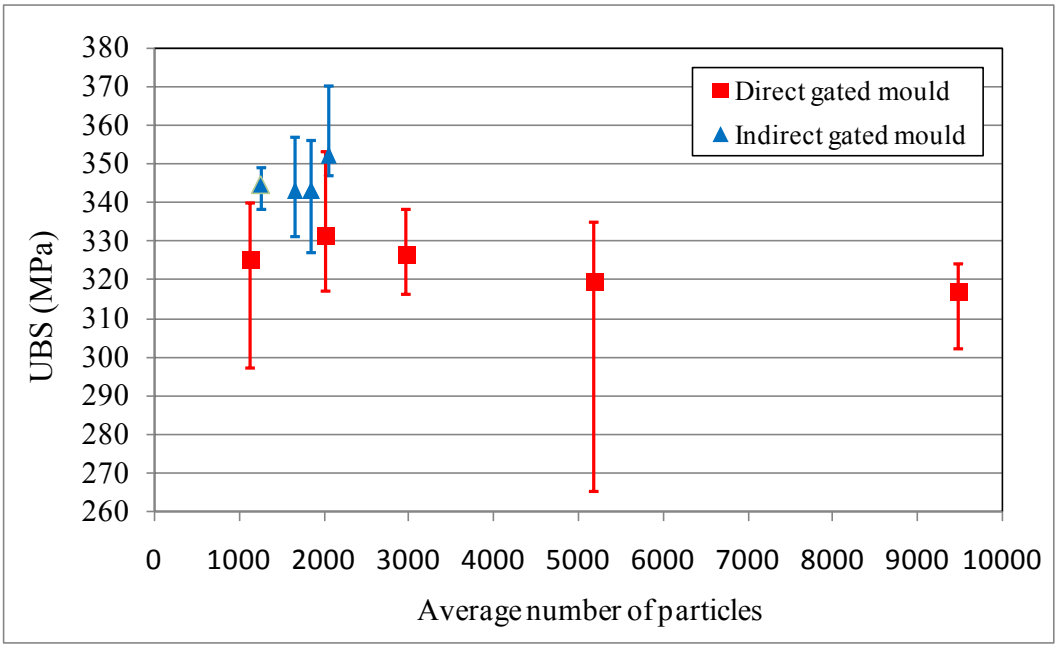

Figure 6 - 154. Average UBS vs. Average number of particles in the test length as a function of test bar position for direct and indirect gated moulds. Note: The UBS values have to be multiplied by a factor of 1.371.

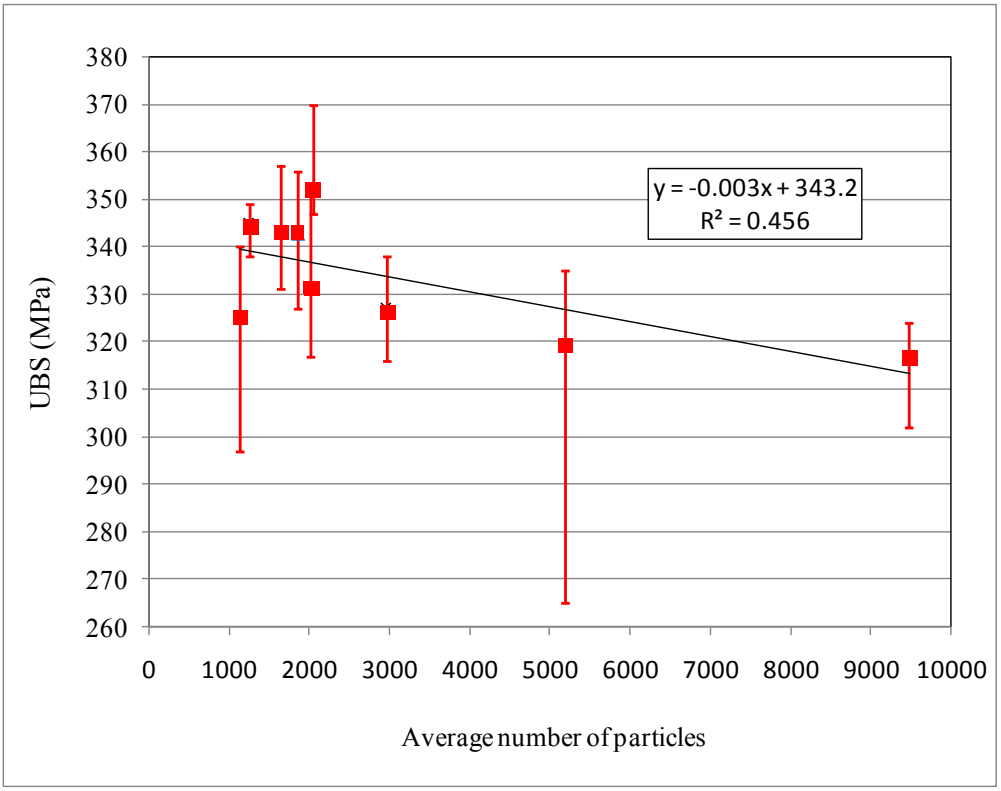

Figure 6 - 155. Average UBS vs. Average number of particles in the test length as a function of test bar position for the combined data of the direct and indirect gated moulds. Note: The UBS values have to be multiplied by a factor of 1.371.

7. DISCUSSION OF RESULTS

7.1 Experimental Centrifugal Castings

7.1.1 Bend Testing Properties and Weibull Modulus

As described in Section 6.1.2, it was found out that the UBS values have to be multiplied by a factor of 1.371 and this change did not affect significantly the calculated values of the Weibull modulus, Figure 6 - 9 and Figure 6 - 10, which will be also discussed in this section.

The results obtained in Table 6 - 11 showed that the average ultimate bend strength (UBS) was improved from a value of 323 MPa (corrected value: 443 MPa) for the direct gating system to 346 MPa (corrected value: 474 MPa) for the indirect gating system, which represented an improvement of approximately 7%. The modulus of elasticity (E) was also improved by approximately 5%, from 53.35 GPa for the direct gated bars to 55.83 GPa for the indirect gated test bars. The standard deviations, which are a measure of how the results are dispersed from the average value, indicated that the UBS and E data for the direct gated test bars had a wider spread compared to the data for indirect gated test bars.

Comparing the modulus of elasticity (E) obtained by tensile test (reported in the literature), Table 6 - 2, with the average E values obtained in this investigation for the direct and indirect gated test bars (53.35 and 55.83 GPa, respectively), it can be seen that the difference is approximately 23 and 19%. This difference could have been attributed to three main factors: (i) the presence of porosity in the cast test bars, which ranged from 1.4 and 6.9% (Table 6 - 25) and reduced the modulus of elasticity in a similar way to Mg alloys (Sumitomo et al., 2002); (ii) the maximum percentage of error of 5% when comparing modulus of elasticity

values obtained from tensile and bend test (Mujika et al., 2006); and (iii) the test rig used for the three-point bend test, which was not specifically designed to carry out precise measurements of modulus of elasticity in bend test (ASTM, 2008) (ASTM, 2010).

Table 6 - 11 and Figure 6 - 9 showed that the Weibull modulus of the UBS was clearly improved by using an indirect gating system. Table 7 - 1 compares these results with the values reported in previous research (Section 2.6.3) for conventional casting processes such as gravity and tilt casting where bend testing was used to evaluate the mechanical properties of flat test bars. The Weibull modulus of 23 obtained in the present work for the direct gated castings is close to the values of 23 and 26 obtained previously for the top gated gravity-filled moulds. Thus, although the centrifugal force helped to fill the mould cavities, the extensive surface turbulence led to the generation of defects such as oxide films and entrapment of bubbles, which reduced the reliability of the castings. However, the Weibull modulus value of 45 obtained in the present work for the indirect gated castings exceeds the value of 38 for an unfiltered bottom filled mould and is approaching the bottom end of the range of 49-54 reported for the optimized design of bottom-gated gravity-filled mould incorporating a filter. The reliability of indirectly gated centrifugal castings appears to lie about midway between the worst and best tilt castings.

Thus, despite the high surface turbulence generated by centrifugal casting during the initial stage of the filling process and even in the absence of a filter, an indirect gated mould design enables the Weibull modulus to be significantly improved to a value similar to those for low turbulence gravity and tilt casting processes.

The Weibull modulus of Young's modulus (E) was also improved from a value of 19 for the direct gating system to 32 for the indirect gating system. However, Weibull modulus values

have not been reported for gravity casting, tilt casting, or any other casting processes where bend testing was used to evaluate the mechanical properties of flat test bars, so it is not possible to compare the Weibull modulus of E obtained in this investigation.

7.1.2 Microstructure

As described in Section 6.3.2, the computer simulations obtained with Flow-3D showed that the filling process of the direct gated test bars involved counter-flow (similar to the phenomenon seen in a returning wave), Figure 6 - 140, which resulted in a continuous generation of oxide films in the shear zone. For the indirect gated mould, although the filling process of the test bars was only unidirectional, Figure 6 - 145, the generation of oxide films occurred mainly during the formation of the vertical and horizontal plunging jets, Figure 6 - 144.

It has been reported by Li et al. (2011) and Kotadia et al. (2010) that for an aluminium alloy AlZnMgCuTi and Al-10.2%Si respectively, when oxide films are present in the liquid metal and dispersed by intensive shearing in the liquid state prior to solidification, these defects can provide effective sites for heterogeneous nucleation and hence provoke a significant grain refinement. This is known as multi-step nucleation mechanism. Likewise, Fan et al. (2009) demonstrated experimentally in an aluminium alloy AZ91D that intense shearing in the liquid state can effectively disperse oxide films and nano-sized skins of MgO particles, which act as potent heterogeneous nucleation sites. This was confirmed by detailed crystallographic analysis and TEM investigation.

As mentioned in Section 4.2.1, the metallographic section selected for microstructural characterization was located close to the fracture and on the tensile surface of the test bar,

Figure 4 - 14. Since the fracture was located at approximately the mid-length of the direct and indirect test bars, this resulted in analysis of samples taken at different distances from the sprue radius, Figure 7 - 1. It can be seen that the pressure at the mid-length of the direct gated test bar was about 37.50 kPa, compared about 25 kPa for the indirect gated test bar. The Flow-3D results confirmed these results with similar pressure values, Figure 7 - 2. Although there were different pressure conditions during the solidification of the direct and indirect cast test bars, the microstructure was a rosette-like morphology, Figure 6 - 13 and Figure 6 - 14, respectively.

Moreover, it has been reported that the heat transfer coefficient increases due to the higher pressure between the mould and liquid metal (Browne and O'Mahoney, 2001). This could have affected the local solidification rate of the solidifying test bar bars.

Therefore, the difference of grain size in the measurement areas between the direct and indirect gated test bars can be attributed to the combination of two mechanisms: the generation, fragmentation and dispersion of oxide films which could have acted as effective sites for heterogeneous nucleation, and the difference of pressure in the measurement areas of the test bars during the solidification. For the measurement area of the direct gated test bars, the mentioned experimental conditions resulted in an average dendrite cell size of 25 μm, an estimated solidification rate of 4.5 °C/s and a grain size of 214 μm, Table 6 - 14 and Table 6 - 16. For the measurement area of the indirect gated cast samples, the mentioned experimental conditions resulted in an average dendrite cell size of 31 μm, an estimated solidification rate of 2.6 °C/s and a bigger grain size of 302 μm, Table 6 - 14 and Table 6 - 16. The estimated solidification rates were calculated using the Equation 2 - 14.

Although the direct gated samples had a smaller dendrite cell size, which is well-known to improve the mechanical properties (Miguelucci, 1985), they had a lower average strength. Therefore, this implies that the ultimate bend strength was mainly affected by the combination of casting defects rather than differences in the dendrite cell size.

7.1.3 X-ray radiography

Comparing the radiograph of the direct gated sample, Figure 6 - 21, with the corresponding sample in the as-polished condition, Figure 6 - 22, it can be seen that it was possible to observe the small scale porosity which was randomly distributed over the whole sample.

Similarly, for the indirect gated test bar, comparing the radiograph, Figure 6 - 23, with the corresponding as-polished sample, Figure 6 - 24, besides the visible small scale porosity, the large fragmented and entrapped bubbles located in the far end were clearly detected. This large scale porosity was also present in all the indirect gated test bars as shown in Figure 6 - 20.

It is important to mention that the radiographs show the integrated distribution of the defects through the whole thickness of the test bars. Furthermore, it is not possible to reveal defects smaller than approximately 40 - 50 μm, since the resolution of the radiographs is not better than 1.2% of the section thickness (4 mm) (Halmshaw, 1995). This is using optimum radiograph viewing conditions and the resolution will be reduced significantly when the film is scanned.

7.1.4 Casting Defects and Stereological Measurements

Since all the centrifugal casting experiments were carried out under the same conditions, which were described in Section 4.1.3, the porosity developed in the cast test bars was only attributed to the mould design. Based on this assumption, the analysis of results is presented in the following paragraphs.

In general, for both the direct and indirect gated cast bars, the number of pores was reduced when the size category increased from 20 to 100 μm, Figure 6 - 38. Likewise, there was a clear distinction between the frequency histograms of the four direct and the four indirect gated test bars. This was more noticeable for size categories smaller than 40 μm and for pores bigger than 100 μm. Therefore, the results suggest that the indirect gated mould design was very effective in decreasing the number of pores in the mid-length, for size categories smaller than 40 μm, where all the values are lower than 9 pores/mm^2 and especially more importantly (due to their effect on the mechanical properties) in decreasing the number of pores bigger than 100 μm, Figure 6 - 38.

The cumulative probability plots of the four direct gated test bars (Figure 6 - 39 and Figure 6 - 40) showed that the UBS was strongly related to the presence of large pores found in the analyzed metallographic sections. As a general tendency, the UBS increased when the size of the largest pores decreased. On the other hand, the group of indirect gated test bars did not present the same tendency and surprisingly the strongest sample with UBS of 357 MPa had the largest pores found in the metallographic section with a maximum Feret diameter of approximately 800 μm, Figure 6 - 41 and Figure 6 - 42. However, the indirect gating system was effective in decreasing the total number of pores bigger than 100 μm found in each metallographic section, which ranged between 56 and 68 (Table 6 - 21 to Table 6 - 24). For

the direct gated test bars, the range was between 70 and 221 pores (Table 6 - 17 to Table 6 - 20).

Although the stereological measurements made on metallographic sections of indirect gated test bars did not produce a similar trend to direct gated test bars, they certainly helped to establish that the large pores had a detrimental effect on the UBS. This was also confirmed by Figure 6 - 68 and Figure 6 - 69, which showed that the fracture paths went preferentially through porosity leading to characteristic transgranular and intergranular fracture.

Figure 6 - 44 and Figure 6 - 46 illustrated that when combining the data of test bars from both gating systems, the effect of porosity area fraction and density of porosity on UBS was clear and showed that UBS increased when the area fraction of porosity and density of porosity decreased. This was also represented by mathematical expressions with a reasonably good correlation coefficient of 0.94 and 0.70, respectively. Similar trends were obtained by Yang et al. (2006), who reported the relation between ultimate bend strength (UBS) and Casting defect density and Casting defect area (%), Figure 2 - 41 and Figure 2 - 42 respectively. Details about the runner systems used to cast the plates and subsequently the test bars used in three-point bend test are described in Section 2.6.1. It is important to note that the number of analyzed samples in this investigation were fewer compared to those obtained by Yang et al. (2006), which affected the correlation coefficients. Therefore, this is merely a sampling effect.

7.1.5 Fractography

The macrofractographs of five selected direct and indirect gated test bars with different values of UBS in Figure 6 - 47 to Figure 6 - 56 showed that UBS was related to the amount of porosity present on the fracture surfaces. In general, the UBS increased when the amount of porosity was reduced. These results show a similar trend to those reported on tensile specimens, where the relation between area fraction of porosity, ultimate tensile strength and elongation were analyzed (Gokhale and Patel, 2005) (Lee et al., 2005).

Likewise, the present results have demonstrated that the indirect gating design significantly reduced the amount and size of pores presented on fracture surfaces, Figure 6 - 52 to Figure 6 - 56. A similar tendency resulted from quantitative analysis obtained from metallographic sections of test bars with different UBS (Section 6.1.6).

As mentioned in Section 4.2.1, in bend testing, the strains and stresses on the tensile surface are maximum at a position in line with the load roller and decrease away from this position towards the centre line (neutral axis) of the samples (Figure 4 - 13) and the other half is subjected to compression stresses. Since failure would be expected to be initiated at casting defects on the tensile side, it would be meaningless to try to measure large defects crossing both the tensile and compression sides on the fracture surface. Therefore, the present work did not include quantitative measurements on fracture surfaces as described by Gokhale and Patel (2005) and Boileau et al. (2001).

In this investigation, no attempt was made to distinguish between young and old oxide films as described by Nyahumwa et al. (1998). It was assumed that the extruded billet used for casting both direct and indirect gating moulds contained a consistent amount of old oxide

films. Furthermore, since the aluminium alloy was air melted, the number of young oxide films undoubtedly increased during the melting process.

The results of Energy Dispersive X-ray analysis carried out on the fracture surfaces of direct and indirect gated test bars confirmed the presence of oxide films resulting from surface turbulence during mould filling. This agrees with the results reported by Nyahumwa et al. (1998) where test bars cast under highly turbulent conditions showed a higher concentration of this defect.

The macrofractographs and secondary electron micrographs suggest that the crack initiation may have preferentially occurred in the most defect-populated section or a section containing the largest defect, especially those located at the tensile side of the test bars. Likewise, the combination of shrinkage, fragmented and large bubbles and oxide films, which jointly created sharp and tortuously-shaped spaces, acted as significant strain concentrators and created a crack linkage that was propagated causing failure, Figure 6 - 59.

7.2 Water Modelling

As mentioned in Section 4.3, the water modelling was carried out in order to validate the computer models of centrifugal casting and not as a direct simulation of the centrifugal casting trials. Table 5 - 1 and Table 5 - 2 show that the dynamic viscosity of water and liquid aluminium alloy is rather similar, 0.001 kg/m s (20 °C) and 0.00105 kg/m s (700 °C), respectively. However, the surface tension of aluminium, 0.864 N/m (700 °C), is one order of magnitude greater than that of water, 0.0728N/m (20 °C), which may lead to different levels of air entrainment in hydraulic structures such as the plunging jet, returning wave and fluid front collision. In this investigation, the difference in the air entrainment between water and

liquid metal was not studied and the information obtained from the water model was only intended to identified and understand the active entrainment mechanisms.

7.2.1 Experimental and Computer Simulations of the Filling Pattern

Figure 6 - 93 and Figure 6 - 94 have shown that, for a direct gated mould with a 2 mm thick cavity filled at 400 rpm, bulk and surface turbulence occurred continuously at the interface between the incoming liquid on the cavity wall and the liquid backfilling the test bar, resulting in a column of bubble entrapment in the shear zone. However, due to the specific gravity difference between the air bubbles and the water, and the continuous centrifugal force, the bubbles were pushed into the test bar ingate, and eventually escaped through it.

The entrainment of bubbles can be explained and related to the liquid velocity gradients generated in the shear zone. The computer modelling results obtained for a direct gated mould with a 4 mm thick cavity filled at 400 rpm, Figure 6 - 109 and Figure 6 - 110, showed that continuous velocity gradients were developed in the shear zone, which led to the continuous air entrainment. These ranged between 0 and -900 s^{-1} in the X direction and between 1800 and -1800 s^{-1} in the Y direction. It was not possible to measure experimentally the velocity of the liquid flowing in the test bar cavities, but it is assumed that the computer simulation results give a reasonable approximation of the velocities developed during the filling process. It is important to note that the experimental results (Section 6.2.2) were obtained using a Perspex mould with a 2 mm thick cavity and due to time limitations it was not possible to carry out water modelling experiments using a 4 mm thick cavity.

The experimental results obtained for the 2 mm thick indirect gated mould showed that, although the filling process in the test bar cavities was unidirectional and only included liquid

flowing radially inwards, in the runner bar, liquid flowed radially outwards on the runner wall (opposite to the rotation direction) and also radially inwards. This also caused a continuous formation of bubbles, which were subsequently forced to flow through the ingate and the test bar cavities during the whole filling process, Figure 6 - 95 and Figure 6 - 96. This demonstrates that the indirect gated mould may not necessarily produce a non-turbulent filling process. However, the centrifugal force helped the entrapped bubbles to be pushed into the far end of the test bar and eventually escape from the cavity, Figure 6 - 96. It is also important to note that the number of generated bubbles in the runner bar were far fewer compared to those generated in the shear zone of the direct gated mould, Figure 6 - 93 and Figure 6 - 94.

The air entrainment can also be related to the velocity gradients in the runner bar predicted by ANSYS CFX, which ranged between 0 and -600 s^{-1} in the X direction and between 0 and -1200 s^{-1} in the Y direction, Figure 6 - 115 and Figure 6 - 116. These were lower than the velocity gradients in the direct gated test bar cavity, which ranged between 0 and -900 s^{-1} in the X direction and between 1800 and -1800 s^{-1} in the Y direction, Figure 6 - 109 and Figure 6 - 110.

In general, the ANSYS CFX simulation results showed only the air entrainment and not the formation of bubbles as those seen in the experimental results, Figure 6 - 94 and Figure 6 - 96. This is related to the Eulerian-Eulerian multiphase model implemented in ANSYS CFX (Section 2.3.8) which has limitations resolving bubbles in free surface flows. This is one of the most difficult tasks since the free surface develops and changes in time. Similar problems with the Eulerian-Eulerian multiphase flow have been reported by Bai and Thomas (2001).

7.2.2 Filling Length vs. Rotational Velocity

The experimental results (Figure 6 - 100) showed that the general tendency for the direct, indirect and modified indirect gated mould designs was that the higher the rotational velocity, the lower the filling length. This was unexpected since it was assumed that when the rotational velocity increased, the volume of the water flowing radially outwards also increased, and therefore the filling process would be quicker.

The water jet thickness flowing on the wall of the cavities and runner bars was thinner when the rotational velocity increased. This was illustrated from the experimental results in Figure 6 - 76, Figure 6 - 81, Table 6 - 27 and Figure 6 - 86 (page 226). The error bars in Figure 6 - 86 showed that these measurements were also affected by the different resolution (1.5 and 1.6 pixels/mm) of the individual snapshots obtained from each experiment. Although there was a higher velocity of the liquid flowing radially outwards when the rotational velocity was increased, Table 6 - 28 and Figure 6 - 87, the flow rate was decreased. This was confirmed by the computer modelling results, Figure 6 - 107 (page 242), which showed the comparison of the water jet and the reduction of mass flow rate when the rotational velocity increased in the direct gated mould. A similar behaviour would be expected in the indirect gated mould.

Comparing the experimental and computer modelling results, Figure 6 - 120 and Figure 6 - 121, it can be seen that there was an excellent correlation. However, the simulation results were more precise for the direct compared to the indirect gated mould. The higher separation between the experimental curves for the indirect gated moulds, compared to the direct gated moulds, can possibly be attributed to a momentary backpressure effect. For the direct gated mould, the entrapped gas was exhausted quickly through the ingate and vents, Figure 4 - 22.

However, for the indirect gated mould, the position of the vents on the runners, Figure 4 - 23, may have resulted in them being initially blocked by the water flowing in the runner and causing a momentary backpressure effect, which delayed the filling process in the test bars.

As presented in Figure 6 - 100, it was illustrated that it took longer to fill the cavities of the indirect and modified indirect gated moulds compared to the direct gated mould. This is due to the longer distance that the water flowed through the runner to reach the ingate and subsequently the cavity. This was approximately 157 and 160 mm for indirect and modified indirect gated moulds respectively (Figure 4 - 21).

7.2.3 Comparison with Results Reported in the Literature

The experimental conditions for water modelling of direct and indirect gated moulds for the present investigation were explained in detail in Section 4.3. Likewise, the experimental conditions used by Li et al. (2006) were summarized in Section 2.3.4. Although the water modelling experiments were carried out under different experimental conditions such as water flow rate, dimensions of the sprue, gating and runner system, it is possible to compare the general effect of rotational velocity on the filling process of the test bar cavities with equal dimensions for both direct and indirect gating mould designs.

Comparing the results obtained in this investigation for the Perspex moulds, which included the vents in the test bar cavities and runners, Figure 6 - 97 to Figure 6 - 100, with those reported by Li et al. (2006), Figure 2 - 20, it can be seen that the effect of rotational velocity on the filling rate was totally opposite. In the present investigation, the filling rate decreased with increasing rotational velocity, whereas Li et al. (2006) showed that the filling rate increased with increasing rotational velocity. Li et al. (2006) attributed their results to the

absence of a proper venting system and so air was trapped in the cavities. In contrast, a better venting system was used in the present investigation, Figure 4 - 22 to Figure 4 - 24, although a small and short-lived backpressure might have been generated during the initial stage of the filling, especially for the indirect gated mould design as discussed previously.

As discussed in Section 2.3.4, Wu et al. (2006) carried out numerical modelling of the same direct and indirect gated moulds used by Li et al. (2006). The results presented in Figure 2 - 21 shows that the experimental and calculated filling lengths increased with increasing rotational velocity for both gating mould designs. It is important to note that the results obtained by using their self-developed casting simulation software closely matched their experimental results. This suggests that their software was able to simulate both phases (liquid and gas) simultaneously and that the effect of the backpressure in the simulations was almost the same as that in the experimental work, both of which seem somewhat unlikely.

The experiments carried out for the indirect gated mould without the vents in the runners showed an opposite tendency to the previous results obtained in this investigation (where the Perspex moulds included the vents in the runners), *i.e.* the filling rate increased with increasing rotational velocity, Figure 6 - 100 and Figure 6 - 101 (pages 237 and 238). Likewise, for the rotational velocity of 200 rpm the water did not completely fill the test bar cavities within the maximum acquisition time of the camera (16.376 s) and the filling time was far longer than expected. Moreover, for the rotational velocities of 300 and 400 rpm, although the water completely filled the test bars cavities, the time was also longer compared to the indirect gated mould, which included the vents in the runners, Figure 6 - 101 (page 238). These results were attributed to the backpressure effect generated in the runner bars. For the three rotational velocities, the air entrapped in the runner bars decreased the water jet

flowing radially outwards, which is illustrated in Figure 6 - 92 (page 229). However, this effect was severer for the rotational velocity of 200 rpm.

It is believed that the higher rotational velocity of 300 and 400 rpm provoked a lower resistance for the water jet to flow radially outwards and a higher force to push the air (entrapped in the runner bars) through the ingates. This air eventually escaped through the test bars vents. However, due to the lower acquisition rate of 500 frames/s and the maximum resolution obtained at this rate (1.5 pixels/mm), it was not possible to show clear evidence of this supposition. In summary, although the general tendency obtained in this investigation for this particular set of experiments, agrees with the results reported by Li et al. (2006) and Wu et al. (2006), the filling time was far longer.

In contrast, when an alternative design was used for the indirect gated mould (stepped gating system), Figure 2 - 22 (page 27) (Changyun et al., 2006), the results showed that for the rotational velocities of 211 and 366 rpm, Figure 2 - 23 (page 28) the general tendency was the same as that seen for the bottom gating design, Figure 2 - 20 (b) (page 25). However, when the rotational velocity was increased to 428 rpm, the filling rate was reduced. This tendency differs from that reported by Li et al. (2006) and Wu et al. (2006) and can be attributed to a lower backpressure effect in the runner bar. However, it could be expected that the curve for 366 rpm would be situated between the curves of 211 and 428 rpm, so there is a consistency of results. Therefore, this suggest that the venting system used by Li et al. (2006), Wu et al. (2006) and Changyun et al. (2006) was inefficient and that there is an inconsistency of results reported by these authors.

7.3 Computational Modelling of Centrifugal Castings

7.3.1 Modelling with ANSYS CFX

For the direct gated moulds, the simulation results showed that the plunging jet in the sprue provoked the continuous generation of bubbles in the liquid metal, Figure 6 - 122 and Figure 6 - 123 (Appendix 49 and Appendix 50). These bubbles were infrequent and large in comparison to reported experimental data (Shevchenko et al., 2009).

Additionally, since the filling process of the test bar cavities involved counter-flow (similar to the phenomenon seen in a returning wave), continuous velocity gradients in the X and Y directions were developed in the shear zone, which also led to the continuous formation of bubbles. For the test bar C1L2DG (4), these ranged between -600 and 0 s^{-1} in the X direction and between 0 and 600 s^{-1} in the Y direction, Figure 6 - 126 and Figure 6 - 127. Although the entrapped bubbles disappeared when the test bar cavities were filled, the results allowed the prediction of the magnitude of the velocity gradients, which were developed and consequently generated the casting defects. The X-ray radiograph obtained from the experimental castings (Figure 6 - 19) confirmed the presence of fragmented and entrapped bubbles, which were scattered randomly throughout the samples, especially for the casting 3.

For the indirect gated bars, since the filling process of the test bars was only unidirectional (radially inwards), velocity gradients were not as developed as those in the direct gated test bars, Figure 6 - 136 and Figure 6 - 137. However, the X-ray radiograph of the experimental castings (Figure 6 - 20) showed that, except for the test bars ‘C3L4’ and ‘C3R4’, a wide range of pores appeared at the end opposite to the ingate.

The simulation results appeared to demonstrate that these bubbles were not generated in the test bar cavities, and the main damage to the liquid was caused by vertical and horizontal plunging jets, Figure 6 - 131 to Figure 6 - 133. Although, the simulation results do not show the transport of bubbles during the filling of the test bar cavities, it can be inferred from the experimental results that these entrapped bubbles were transported in the liquid metal through the horizontal and vertical runner bars and eventually the damaged liquid was forced to flow radially inwards through the ingates and to fill the test bar cavities, Figure 6 - 129 to Figure 6 - 131. This can be confirmed by the X-ray plates from the test bars 'C3L4' and 'C3R4' (Figure 6 - 20), which contained some bubbles, part way through the test bar, which did not reach the opposite end due to onset of solidification.

The apparent disappearance of the entrapped bubbles in the direct gated bars can be attributed to the limitations of the Eulerian-Eulerian multiphase model implemented in ANSYS CFX (Section 2.3.8). This would also explain why the entrapped bubbles were apparently not transported during the filling of the indirect gated moulds. Due to the software limitations and the time required for modelling using ANSYS CFX, no further attempt was made to resolve the transport and formation of smaller bubbles using a finer mesh than that described in Section 5.4.1.

7.3.2 Modelling with Flow-3D and Oxide Film Entrainment Model (OFEM)

For both direct and indirect gated moulds, the liquid was damaged by the plunging jet in the sprue, which led to a persistent large-scale entrainment during the whole filling process, Figure 6 - 139 and Figure 6 - 144 (Appendix 59 and Appendix 65). The final number of particles placed in the liquid contained in the sprue and ingates of the direct gated mould was 104,146. This was rather similar to the particles placed in the sprue of the indirect gated

mould (103,760), Table 6 - 36, Table 6 - 37 and Figure 6 - 148. Likewise, the indirect gated mould generated a higher total number of particles (284,522) compared to the direct gated mould (207,796). This represented an increase of approximately 37%, which is mainly attributed to the particles placed in the horizontal and vertical runner bars, which added 138, 515 particles to the total count, Table 6 - 37. Assuming that all the placed particles had a maximum diameter of 60 μm and specific gravity of 2250 kg/m^3 (Table 5 - 3), the total mass added in the direct and indirect gated moulds were 0.052 g and 0.072 g respectively, which can be considered negligible.

For the direct gated test bars, unlike the experimental results obtained for UBS and E shown in Figure 6 - 3 and Figure 6 - 6, the simulation results showed that there was a systematic variation in the number of particles contained in individual test bars in both the complete test bars and the test lengths, Figure 6 - 149. However, since the purpose of this investigation was to compare the number of particles contained in the test length with the mechanical properties obtained in the experimental test bars of both mould designs, the discussion of the results will be focused on the number of particles contained only in the test length, Figure 6 - 151 and Figure 6 - 152.

For the direct gated test bars, comparing Figure 6 - 143 and Figure 6 - 151, it can be seen that there was a clear correlation between the number of particles entrained in the test lengths and the filling times for each bar. The test bars in positions # 5 and # 6 had the lowest number of particles and filling time, whereas those in positions # 2 and # 9 had the highest number of particles and filling time. Regarding the test bar pair # 1 and # 10, it could have been expected that these would have the longest filling time and the highest number of particles. However, when the falling stream of liquid impacted the sprue bottom and splashed on the sprue wall,

the liquid did not reach the fifth test bar level 'L5-R5', Figure 6 - 139 (Appendix 59). The liquid then filled the test bars levels from L1-R1 to L4-R4 and reached the last level at approximately 1.64 s, (Appendix 30 and Appendix 64). Therefore, the filling time was shorter and consequently the number of particles was lower.

For the indirect gated test bars, most of the particles were entrained in the plunging jet and whilst the liquid flowed through the horizontal and vertical runners, Figure 6 - 144 (Appendix 65) and Figure 6 - 148. These particles were then transported through the ingate and into the test bar cavity. This was clearly illustrated on the left bar at a simulation time between 0.84 and 1.02 s, Figure 6 - 145 (Appendix 66). It can be seen that there is a low number of particles close to the free surface of the advancing front and a much higher density of particles entering the test pieces from the vertical runner bar. This demonstrates that most of the placed particles were not generated in the test bar cavities. Therefore, the results presented in Table 6 - 39 and Figure 6 - 152 showed the number of particles that were mainly generated in different regions of the mould and eventually transported in the liquid metal filling the test bar cavities.

Since the mould was kept rotating at constant speed of 400 rpm after the filling was completed at approximately 1.20 s, Figure 6 - 145, the particles contained in the liquid metal were forced to move inwards under the action of the radial pressure gradient, Figure 7 - 1 and Figure 7 - 2. This phenomenon was clearly illustrated between 2.20 and 6.20 s, Figure 6 - 145 (Appendix 66), and was driven by the difference in the specific gravities of the liquid metal and the solid particles, which were 2400 and 2250 kg/m^3, respectively (Table 5 - 3). Due to the extensive run time and the high computational intensity required to track of all the generated particles in the mould, it was not possible to model a longer time.

Although the Oxide Film Entrainment Model (OFEM) technique modelled only the entrainment of particles and not the entrapment of bubbles, which have much lower specific gravity (Campbell, 2003), the movement induced by the centrifugal force on the entrained particles contained in the liquid metal was demonstrated. Therefore, the tendency of the entrained particles moving radially inwards (observed in the simulation results) correlates well with the X-ray plates obtained from experimental cast test bars, Figure 6 - 20, which show that except for the test bars 'C3L4' and 'C3R4', the defects (porosity and oxides) appeared at the ends opposite to the ingate. Therefore, this buoyancy effect between the liquid metal and casting defects entrained in the liquid, resulted in a cleaning effect in the indirect gated test bars.

As discussed in Sections 7.1.4 and 7.1.5, the indirect gated mould design significantly reduced the amount and size of pores presented in the metallographic sections and fracture surfaces. This led to an improvement of the ultimate bend strength 'UBS' and modulus of elasticity 'E' obtained from the indirect gated test bars. However, the results of EDX analysis confirmed the presence of oxide films on fracture surfaces of indirect gated test bars, Figure 6 - 62 and Figure 6 - 63. Therefore, this suggests that the cleaning effect was mostly effective for large casting defects such as fragmented and entrapped bubbles, whilst the large surface area and marginal density difference between a bifilm defect and the liquid metal results in much slower motion under the action of the centrifugal pressure gradient.

Regarding the direct gated test bars, the simulation results showed that the liquid was damaged by the plunging jet in the sprue and subsequently it was subjected to further damage by the filling of the test bar cavities. In this case, the centrifugal force did not cause the same cleaning effect as that presented in the indirect gated test bars. This can be confirmed by the

rotational movement of the entrained particles placed in the test cavities, Figure 6 - 140 (Appendix 60).

7.3.2.1 Estimation of the Solidification Time for the Cast Test Bars

Since the heat transfer and solidification stages were not modelled due to time limitations, the discussion in the following paragraphs attempts to explain an approximate time figure in which the cleaning effect in the cast test bars took place.

According to the experimental procedure (Section 4.1.3), the mould temperature at the time of pouring was 450 ± 10°C and the metal temperature was 695 ± 10°C. The molten metal was poured from the crucible into the ceramic mould through a funnel, which was preheated in an electric resistance furnace at 500°C to minimise heat loss from the molten metal, Figure 4 - 9 and Figure 4 - 10.

The solidification rate of the cast indirect gated test bars was estimated to be 2.6 °C/s, Table 6 - 14. Likewise, it has been reported that the solidus and liquidus temperature of the aluminium alloy 6082 are 600 and 642 °C respectively (Table 5 - 3) (Mills, 2002). According to the simulation results obtained with ANSYS CFX and Flow-3D, the filling of the indirect gated mould was completed at 1.08 s and 1.20 s, respectively. Assuming that the liquid metal temperature dropped to approximately 655 - 665 °C once the cavities were filled, the further time it took the liquid metal to reach the liquidus temperature (642 °C) was 5.0 - 8.8 s, based on the cooling rate of 2.6 °C/s. This represents the approximate time frame in which the casting defects were pushed into the far end of the test bars.

Similarly, for the direct gated test bars, the solidification rate was estimated to be 4.5 °C/s (Table 6 - 14) and according to the results obtained with ANSYS CFX and Flow-3D, the

filling of the five test bar levels was completed at 2.22 s and 1.90 s, respectively. Assuming that the liquid metal temperature dropped to approximately 645 - 655 °C (because of the larger filling time), the further time it took the liquid metal to reach the liquidus temperature (642 °C) was 0.7 – 2.9 s, based on the cooling rate of 4.5 °C/s. Since there were different filling times depending on the level of the test bars, this time frame was maximum at the base of the mould (L1-R1) and gradually reduced at the highest test bar level (L5-R5). This figure was lower compared to the indirect gated bars and also represented the time frame in which the casting defects were pushed towards the test bar ingate.

However, although solidification started once the liquidus temperature was reached, some separation could have taken place thereafter, although it becomes increasingly more difficult as the solid fraction increases.

7.3.2.2 Oxide Film Entrainment Model (OFEM) and Mechanical Properties

Figure 6 - 153 shows the number of particles in the test length as a function of test bar pair and position for both mould designs, where each point is the average of two test bars. This graph is simply a different way to interpret the results already shown in Figure 6 - 151 and Figure 6 - 152. Similarly, the average values of UBS and E were obtained from up to 6 test bars and were previously presented in Table 6 - 5, Table 6 - 6, Figure 6 - 5, Table 6 - 9, Table 6 - 10 and Figure 6 - 8.

From Figure 6 - 5, it can be seen that the test bar levels L4-R4 and L3-R3 had the lowest average UBS in the direct gated moulds. Considering that the higher the number of particles, the lower the UBS, this behaviour correlates well with the results obtained from the computational simulations for the same levels (L4-R4 and L3-R3), Figure 6 - 153. The

experimental results illustrated in Figure 6 - 8, which were obtained from the average E, only had a similar tendency for the test bar level L3-R3. In contrast, the test bar levels L5-R5, L2-R2 and L1-R1 (Figure 6 - 5) had the highest average UBS. Then, following the same logic, the simulation results (Figure 6 - 153) showed that the same test bar levels (L5-R5, L2-R2 and L1-R1) had the lowest average of particles placed in the test length. The experimental results illustrated in Figure 6 - 8, which were obtained from the average E, only had a similar tendency for the test bar levels L5-R5 and L2-R2.

In general, there seems to be a certain relation between the between the number of particles placed in the test length and the average experimental results of UBS for the five different test bar levels. However, further experimental and computer modelling work are necessary to confirm this first finding.

For the indirect gated bars, the dispersion of the average values of UBS and E was smaller than for the direct gated bars, Figure 6 - 5 and Figure 6 - 8. A similar trend was also found in the simulation results (Figure 6 - 153). This confirms that a less turbulent filling process leads to a smaller dispersion of the mechanical properties.

The above is summarized by Figure 6 - 154, which shows the average UBS as a function of the number of particles placed in the test length for different test bar pairs and positions. For the indirect gated test bar pairs, the four pairs were clustered together and that there was no discernible effect of the number of particles, whereas for the direct gated test bar pairs they were lower and more dispersed. However, when the data from both gating systems were combined, Figure 6 - 155, a correlation was found showing that the average UBS decreased as the number of particles increased.

In general, there seemed to be a correlation between the average UBS and the number of placed particles, which could be attributed to the kind of defects that affect the UBS. In the experimental stage, it was found that the UBS was mainly affected by the combination of large casting defects (refer to Section 7.1.4 and 7.1.5). Likewise, it is important to mention that not all the mechanisms of entrainment are equally damaging and the severity of entrainment due to any mechanism will vary with, for example, absolute velocity. Therefore, some errors in what is predicted are inevitable.

7.4 Relation between Experimental and Computer Modelling Results

The differences in the location of the defects in the direct and indirect gated test bars, as in the radiographs, Figure 6 - 19 and Figure 6 - 20, can be attributed to the combination of two mechanisms: filling and centrifugal separation.

Regarding the first mechanism, in the direct gated test bars, the generation of bubbles operates continuously at the interface between the incoming stream and the metal in the bars, so bubbles will be distributed throughout the test bar cavities, Figure 6 - 124, Figure 6 - 126 and Figure 6 - 127. This will be aided by the circulating flow, Figure 6 - 125. Eventually, the fragmented bubbles and oxide films will be randomly distributed over the samples, Figure 6 - 19 (e) (f).

In the indirect gated test bars, the generation of bubbles occurs mainly during the formation of the plunging jet in the sprue. Then, in the vertical bar before the metal reaches the ingates, some centrifugal separation of air bubbles from the liquid metal may take place. Subsequently, this metal will enter the test bar cavities and the damaged metal will tend to be

pushed towards the far ends of the bars by the metal flow, possibly aided by further centrifugal separation during filling and the less circulating flow within the cavities, Figure 6 - 135. Likewise, as the horizontal runner progressively backfills, there will be progressively less damage, so the metal entering the test bars should be of progressively better quality, Figure 6 - 132 and Figure 6 - 133. As a result, at the end of the filling, the bubbles and oxide films are concentrated towards the far ends of the indirect gated test bars, Figure 6 - 20, Figure 6 - 23 and Figure 6 - 24.

Regarding the centrifugal separation, as demonstrated by the water modelling experiments of direct and indirect gated moulds, Figure 6 - 94 (Appendix 41) and Figure 6 - 96 (Appendix 42), respectively, the generated bubbles will tend to move towards the sprue as a result of their specific gravity difference and the centrifugal force, so this should cause some 'cleaning' of the metal in the centrifugal castings. This was confirmed by the Flow-3D simulations; however, it was more evident for the indirect gated test bars between 2.20 and 6.20 s, Figure 6 - 145 (Appendix 66).

As discussed in Section 7.3.2.1., the dendrite cell size measurements indicated that the indirect gated bars had a lower solidification rate, so the extent of centrifugal cleaning should be greater in these cast bars compared to the direct gated bars. This was confirmed by the radiographs shown in Figure 6 - 20, where except for the test bars ‘C3L4’ and ‘C3R3’, the defects appeared on the end opposite to the ingate. In the direct gated bars, Figure 6 - 19 showed that the centrifugal cleaning was more effective in the castings 1 and 2. Likewise, it is important to notice that in Casting 3, most of the defects were closer to the ingate side, which is more evident in the right test bars. This suggests that the solidification could have been completed in a shorter time.

The information obtained from the water modelling and the computer simulations using ANSYS CFX and Flow-3D, and their correlation to the casting defects and mechanical properties in the direct and indirect gated test bars, has helped to understand the entrainment mechanisms resulting in defect formation during the filling process.

The Eulerian-Eulerian multiphase model implemented in ANSYS CFX showed that for the direct gated casting mould, since the filling process of the test bar cavities involved bidirectional flow (similar to the phenomenon seen in a returning wave), velocity gradients were developed in the shear zone, which resulted in the formation of bubbles. In contrast, for the indirect gated test bars, since the filling of the test bar cavities was unidirectional, velocity gradients were not as developed as those in the direct gated test bars. This technique demonstrated that there is a correlation between the generation of velocity gradients and the entrapment of bubbles. However, there are several serious limitations which should be considered. First, it is not known what minimum velocity gradient is required to cause entrainment. Second, the formation and transport of small bubbles cannot be simulated. Third, the coalescence of small bubbles to form larger bubbles and, conversely, the fragmentation of large bubbles to form smaller ones, cannot be simulated.

Regarding the OFEM technique implemented in Flow-3D, this demonstrated that entrainment mechanisms such as the plunging jet and the returning wave led to a persistent large-scale entrainment. However, this technique places particles in individual cells where entrainment events occur, and these particles are then treated as separate and independent particles. In reality, entrainment generally involves much larger surfaces meeting and forming double oxide films (bi-films) which move through the liquid as an entity. This suggests that a real oxide film could be equivalent to several tens or hundreds of particles which move together in

a coordinated manner, which is quite different to the independent motion of particles implemented in the OFEM. Although the results obtained in this investigation showed some correlation with the experimental results obtained from cast test bars, further development of the OFEM technique and experimental validation are required. This is currently being undertaken by Yue (2011a).

The use of ANSYS CFX and Flow-3D to study the fluid flow in the filling of direct and indirect gated test bars has shown that there are severe limitations for accurately modelling the generation and interaction of bubbles and oxide films. However, the information generated has helped to explain the source of these detrimental casting defects and their effect on the scatter of mechanical properties.

7.5 Tables

Table 7 - 1. Comparison of the Weibull modulus values obtained on investment casting aluminium alloys using different casting techniques. Bend testing was used to evaluate the mechanical properties of flat test bars.

Alloy	Casting Technique	Mould Design	Weibull Modulus	Reference
2L99 (Al-7Si-0.4Mg)	Gravity	Top filled	26	Cox et al. (2003)
			23	Cox and Harding (2007)
		Uncontrolled bottom filled	27	Cox et al. (2003)
		Controlled bottom filled	38	Cox et al. (2003)
		Controlled bottom filled with filter	54	Cox et al. (2003)
			49	Cox and Harding (2007)
	Tilt	Single stage cycles	30	Cox and Harding (2007)
		Single stage cycles	45	Cox and Harding (2007)
		Multi-stage cycles	42	Cox and Harding (2007)
		Multi-stage cycles	55	Cox and Harding (2007)
6082	Centrifugal	Direct Gated	23	Present work
		Indirect Gated	45	Present work

7.6 Figures

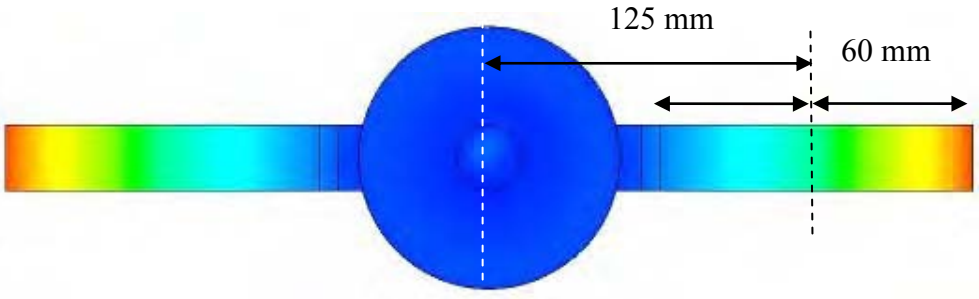

(a) t = 2.22 s

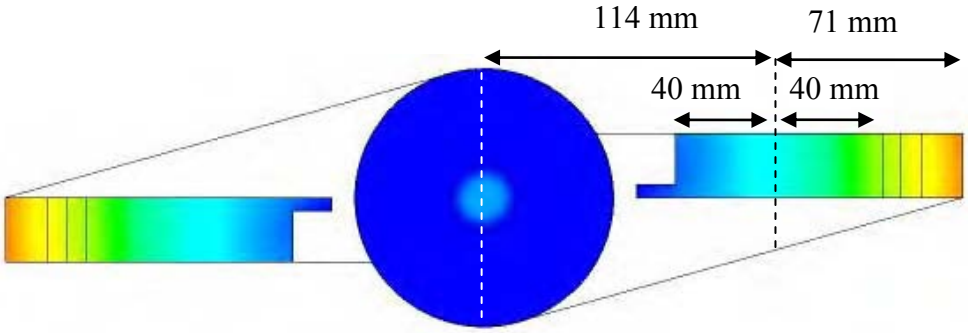

(b) t = 1.08 s

Pressure (kPa)

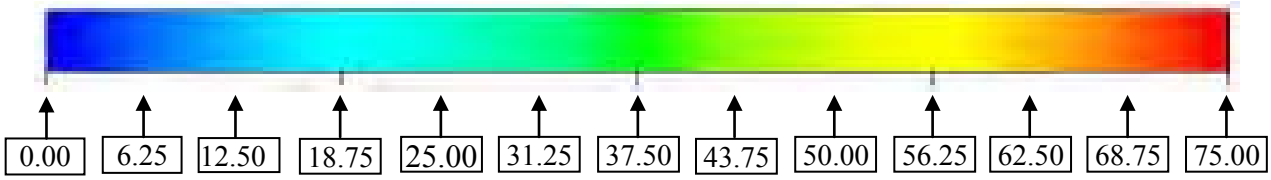

Figure 7 - 1. Comparison of pressure predicted by ANSYS CFX of (a) direct gated test bar; the cut plane was taken at mid-thickness of the test bar pair C1L2DG (4) – C1R2DG (7) and (b) indirect gated test bar; the cut plane was taken at mid-thickness of the test bar pair C1L1IG (4) – C1R1IG (5).

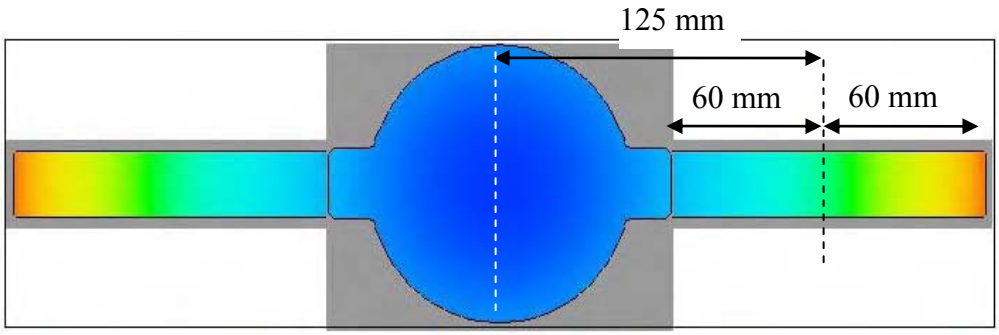

(a) t = 6.20 s

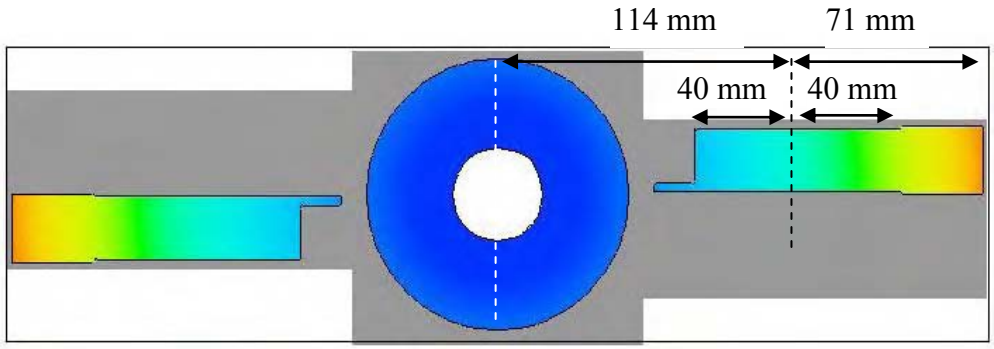

(b) t = 6.20 s

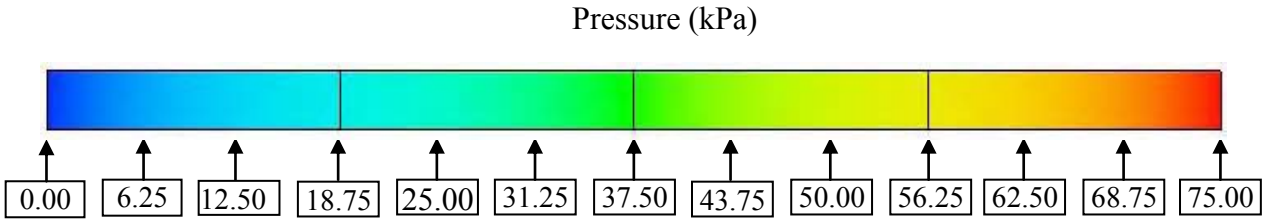

Figure 7 - 2. Comparison of pressure predicted by Flow-3D of (a) direct gated test bar; the cut plane was taken at mid-thickness of the test bar pair C1L2DG (4) – C1R2DG (7) and (b) indirect gated test bar; the cut plane was taken at mid-thickness of the test bar pair C1L1IG (4) – C1R1IG (5).

8. CONCLUSIONS

The present investigation was aimed at increasing the overall understanding of the effect of mould design on the quality of components made using the centrifugal casting process. The experimental and simulation results led to the following conclusions:

- The average ultimate bend strength (UBS) was improved from a value of 323 MPa (corrected value: 443 MPa) for the direct gating system to 346 MPa (corrected value: 474 MPa) for the indirect gating system, which represented an improvement of approximately 7%. The average modulus of elasticity (E) was also improved by approximately 5%, from 53.35 GPa for the direct gated bars to 55.83 GPa for the indirect gated test bars.

- The Weibull modulus of the UBS was significantly improved from 23 for a direct gating system to 45 for an indirect gating system. Likewise, the Weibull modulus of E was improved from 19 for a direct gating system to 32 for an indirect gating system.

- Both direct and indirect gated cast test bars developed a rosette-like morphology and equiaxed grain shape. However, the difference in the filling process and pressure conditions during solidification resulted in differences in the dendrite cell size and grain size. For the direct gated test bars, an average dendrite cell size of 25 μm and a grain size of 214 μm were obtained; whereas for the indirect gated test bars an average dendrite cell size of 31 μm and a larger grain size of 302 μm were obtained. The dendrite cell sizes were used to estimate solidification rates of 4.5 °C/s and 2.6 °C/s in the direct and indirect gated castings respectively.

- The decrease of UBS and E is attributed to the presence of porosity distributed in the test bar volume under analysis. These mechanical properties were more affected by the combination of large casting defects rather than by a high density of small pores.

- The indirect gated mould design was very effective in decreasing the number of pores, for size categories smaller than 40 μm (density of pores lower than 9 pores/mm^2) and especially more important (due to their effect on the mechanical properties) in decreasing the number of pores bigger than 100 μm.

- In general, the indirect gated mould design decreased the area fraction, density and size of porosity.

- The water modelling results, which included an efficient venting system, showed that the general tendency for the direct, indirect and modified indirect gated mould designs was that the higher the rotational velocity, the lower the filling length and consequently the lower the filling rate. Likewise, an excellent correlation was obtained between the filling observed in water models of direct and indirect gated moulds and those predicted by ANSYS CFX.

- Simulation of the mould filling with ANSYS CFX demonstrated that there is a correlation between the development of velocity gradients at and near to the free surface and the formation of bubbles.

- Simulation of the mould filling with the Oxide Film Entrainment Model (OFEM) technique implemented in Flow-3D demonstrated that entrainment mechanisms such as the plunging jet and the returning wave were extremely detrimental to the integrity of the liquid metal.

- Simulation of the indirect gated mould design with the OFEM technique and Flow 3-D demonstrated that the centrifugal force provoked a buoyancy effect between the liquid metal and casting defects entrained in the liquid. This resulted in a cleaning effect in the indirect gated test bars, pushing the casting defects into the far end of the test bars.

- ANSYS CFX and Flow-3D demonstrated that a less turbulent filling process in the test bar cavities leads to a decrease in entrainment defects such as entrapment of bubbles and oxide films.

9. FUTURE WORK

The results obtained in this investigation of an aluminium alloy have highlighted the need for further research. As mentioned earlier, the ultimate goal of this centrifugal casting research is to develop techniques for producing complex thin wall engineering components in TiAl alloys. Therefore, the following are recommendations for future work:

When casting Al alloys, the superheating is not a limitation for completely filling the mould cavities, which was demonstrated in this investigation. However, as mentioned earlier, it is common practice to melt TiAl alloys in a water-cooled copper crucible using energy supplied by an induction coil (ISM), which provides only limited superheat ~ 40 - 60°C. This makes it difficult to fill thin section castings. Therefore, in future research it would be important to consider the filling time when the indirect gated mould design is applied in TiAl alloys.

Likewise, it is also important to reduce the surface turbulence, which is generally obtained by decreasing the liquid velocity during the filling process, in order to reduce the generation of oxide films. As mentioned in Section 2.3.3.3, although the presence of oxide films in TiAl has been found (Mi et al., 2003), the solubility of these defects can be achieved under appropriate time and temperature in the HIP process, which has been reported by Hu and Loretto (Campbell, 2003). Therefore, the presence of oxide films in cast components of TiAl alloys and Al alloys should be considered.

It is also proposed to assess the incorporation of feeders to capture the damaged metal in the components.

10. APPENDIX

10.1 Mesh Sensitivity Results and Summary of Sequences

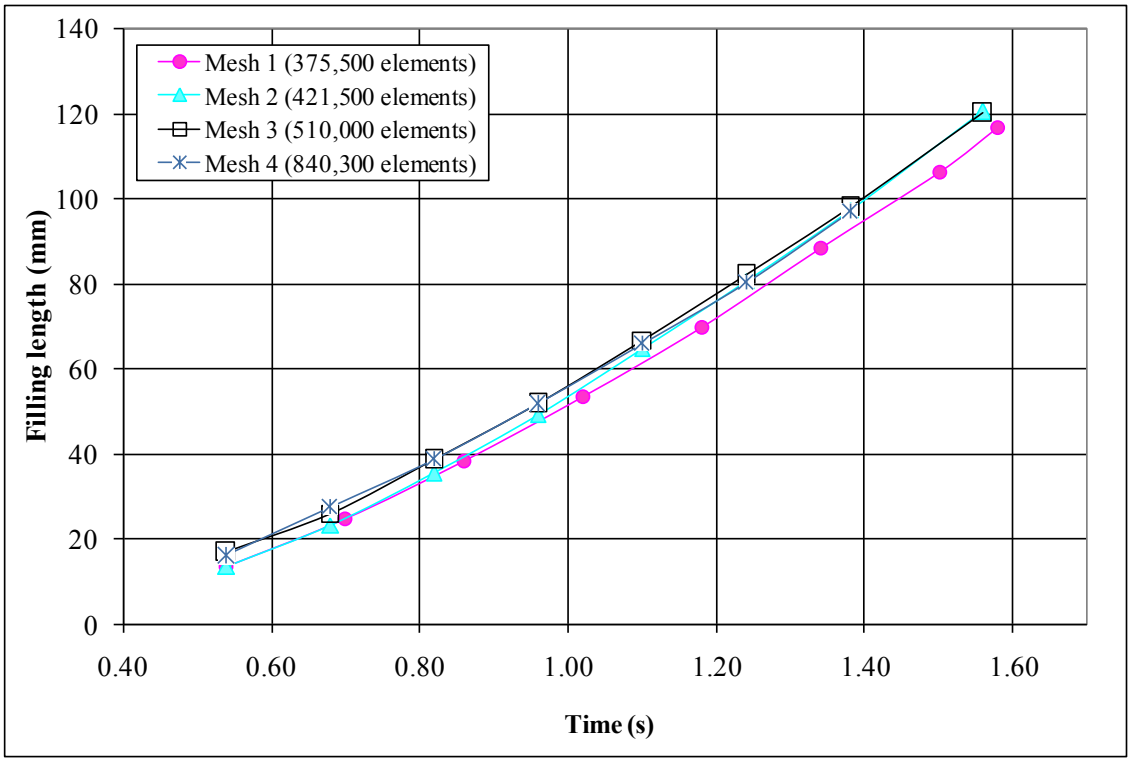

Appendix 1. Mesh sensitivity results for the direct gated mould (see Figure 5 - 2). The rotational velocity was 300 rpm in the anti-clockwise direction.

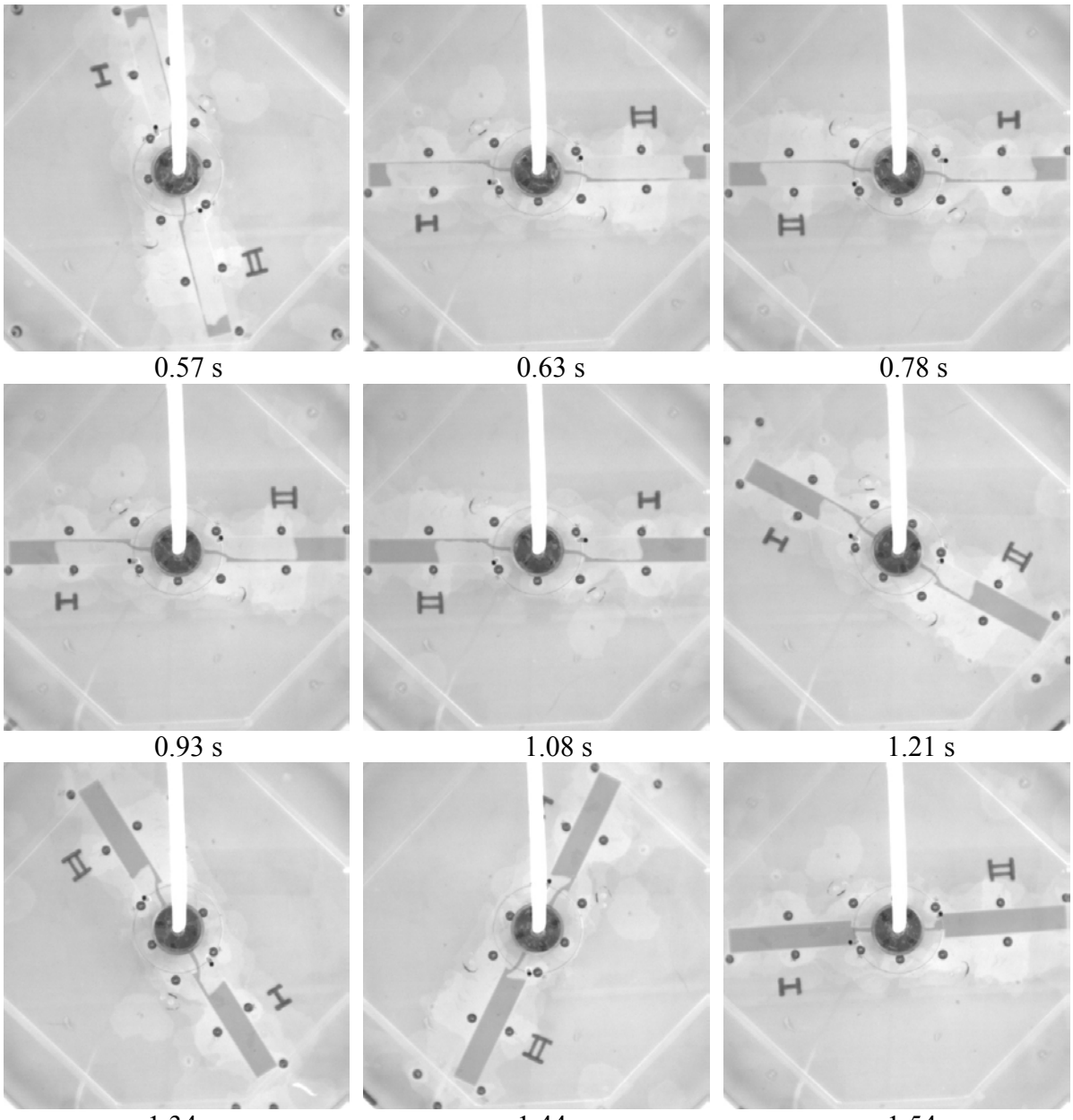

Appendix 2. Summary of the high speed camera results of the direct gated mould filling process. The rotational velocity was 200 rpm in the anti-clockwise direction. Note: Video sequence can be seen in Appendix 32.

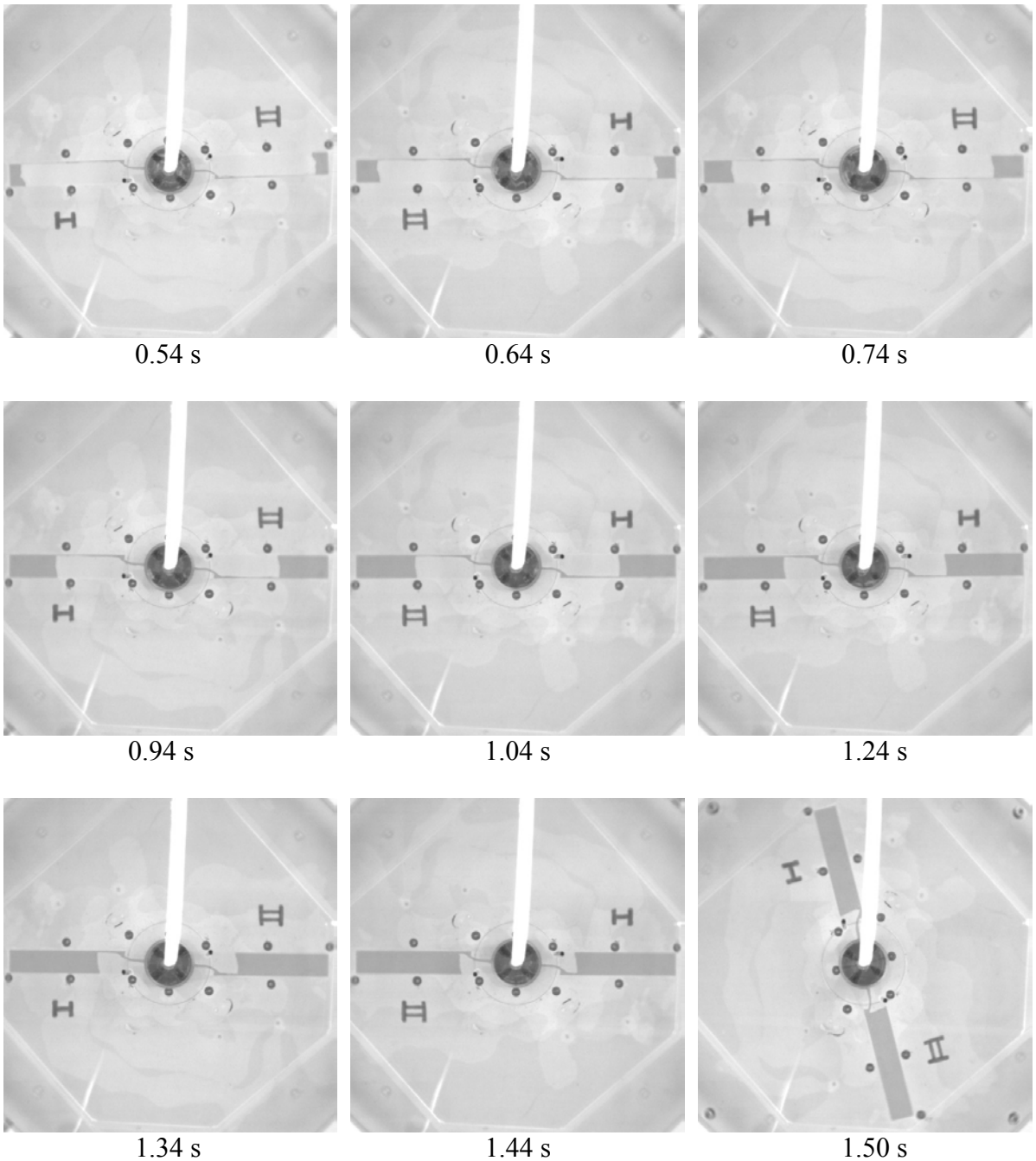

Appendix 3. Summary of the high speed camera results of the direct gated mould filling process. The rotational velocity was 300 rpm in the anti-clockwise direction. Note: Video sequence can be seen in Appendix 33.

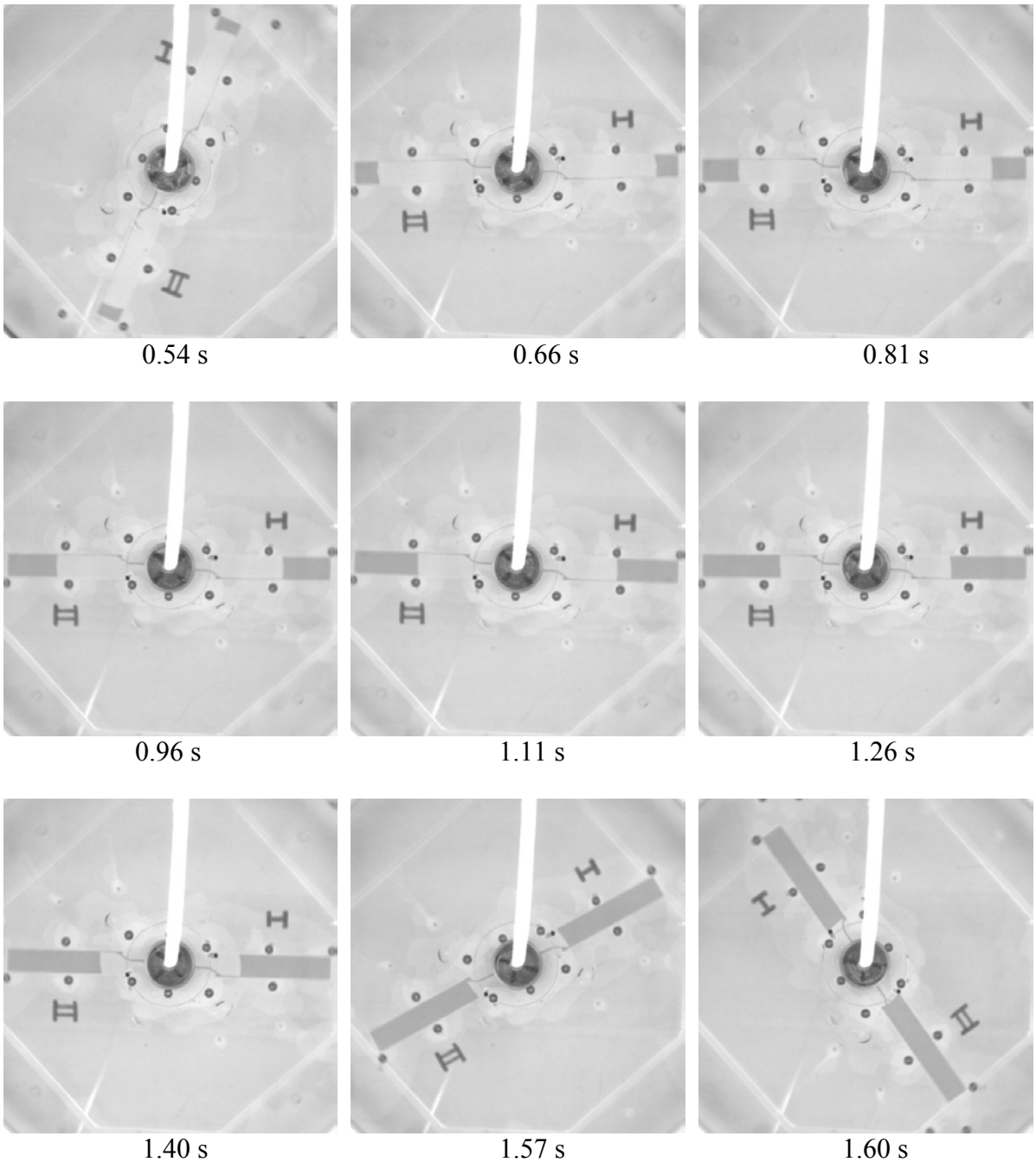

Appendix 4. Summary of the high speed camera results of the direct gated mould filling process. The rotational velocity was 400 rpm in the anti-clockwise direction. Note: Video sequence can be seen in Appendix 34.

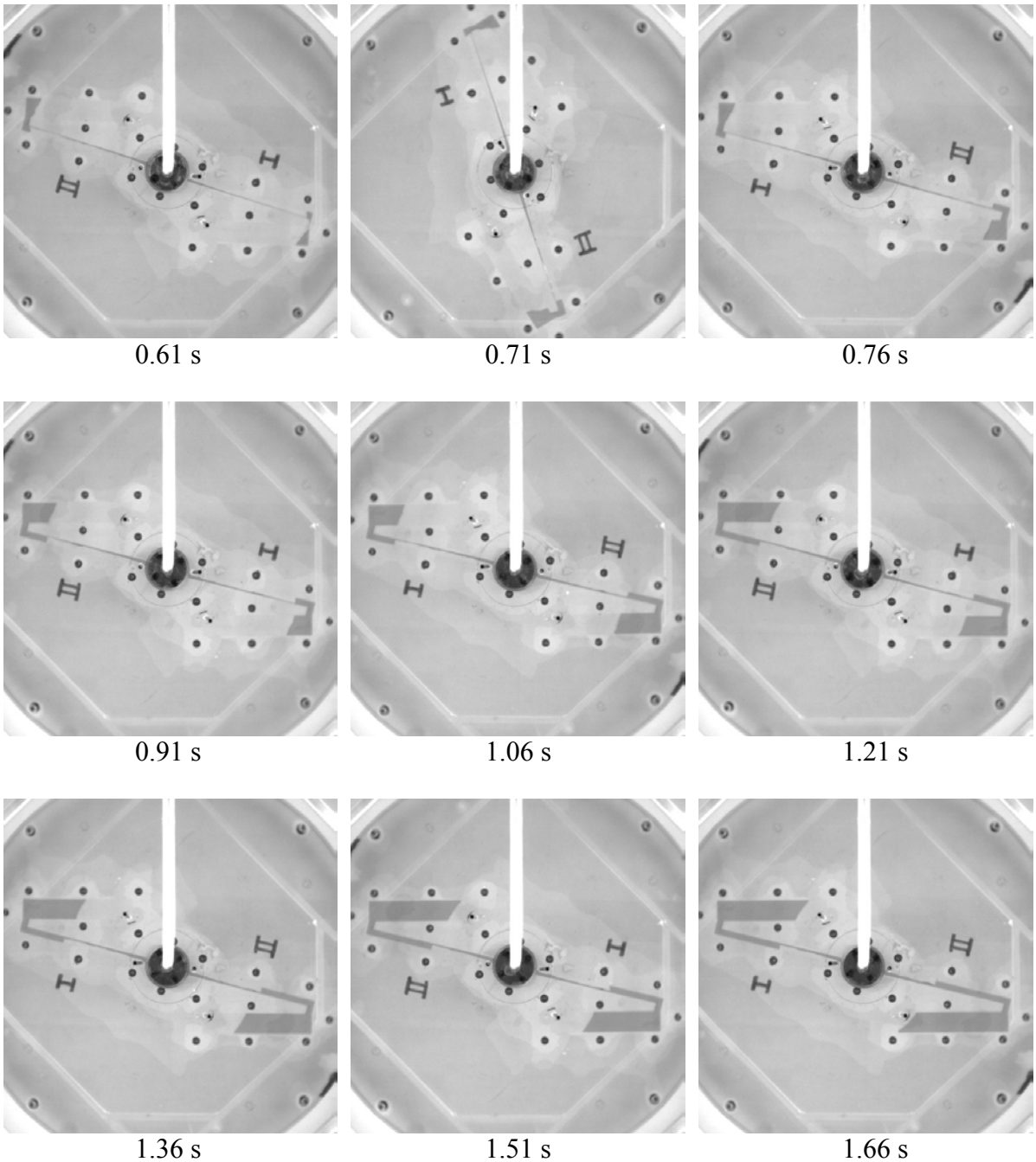

Appendix 5. Summary of the high speed camera results of the indirect gated mould filling process. The rotational velocity was 200 rpm in the anti-clockwise direction. Note: Video sequence can be seen in Appendix 35.

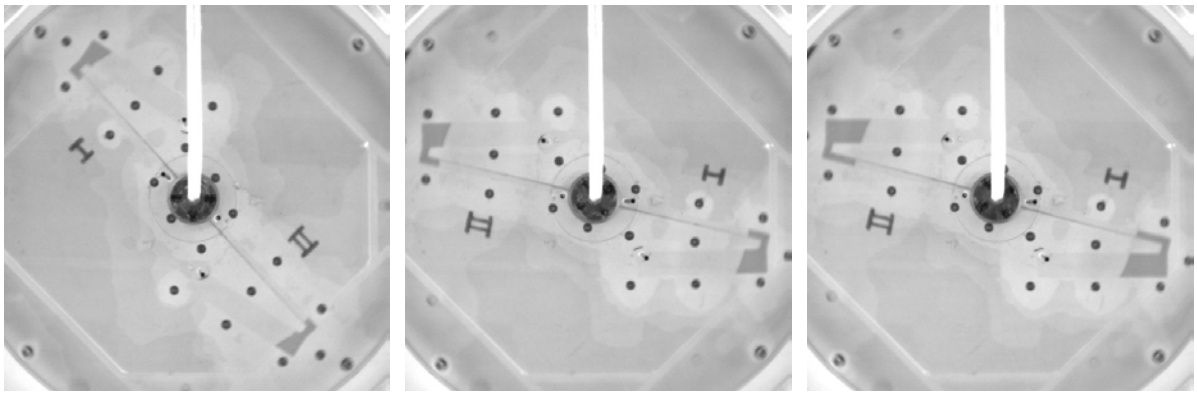

0.62 s 0.73 s 0.93 s

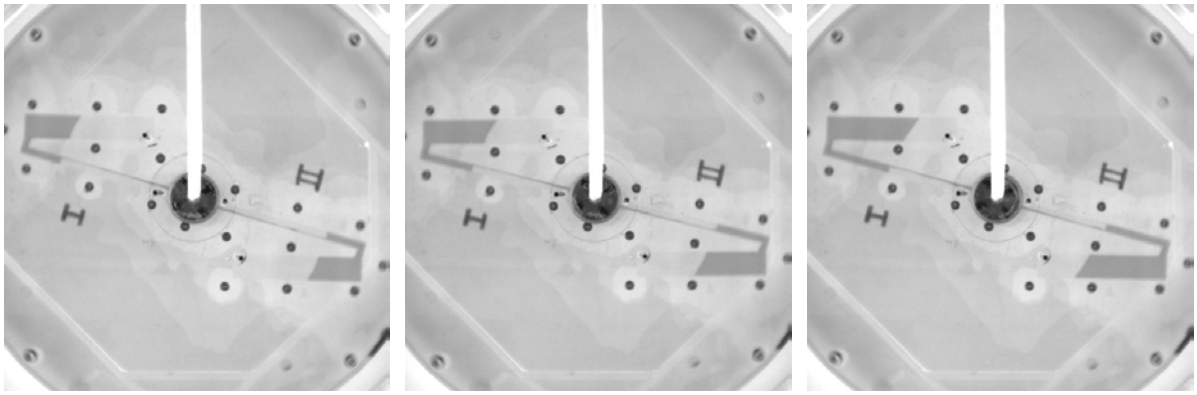

1.03 s 1.23 s 1.43 s

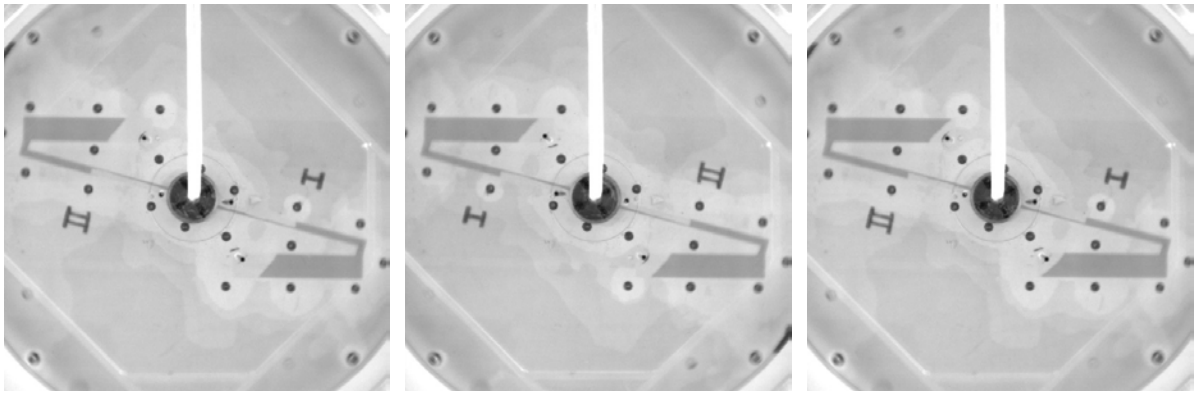

1.53 s 1.63 s 1.73 s

Appendix 6. Summary of the high speed camera results of the indirect gated mould filling process. The rotational velocity was 300 rpm in the anti-clockwise direction. Note: Video sequence can be seen in Appendix 36.

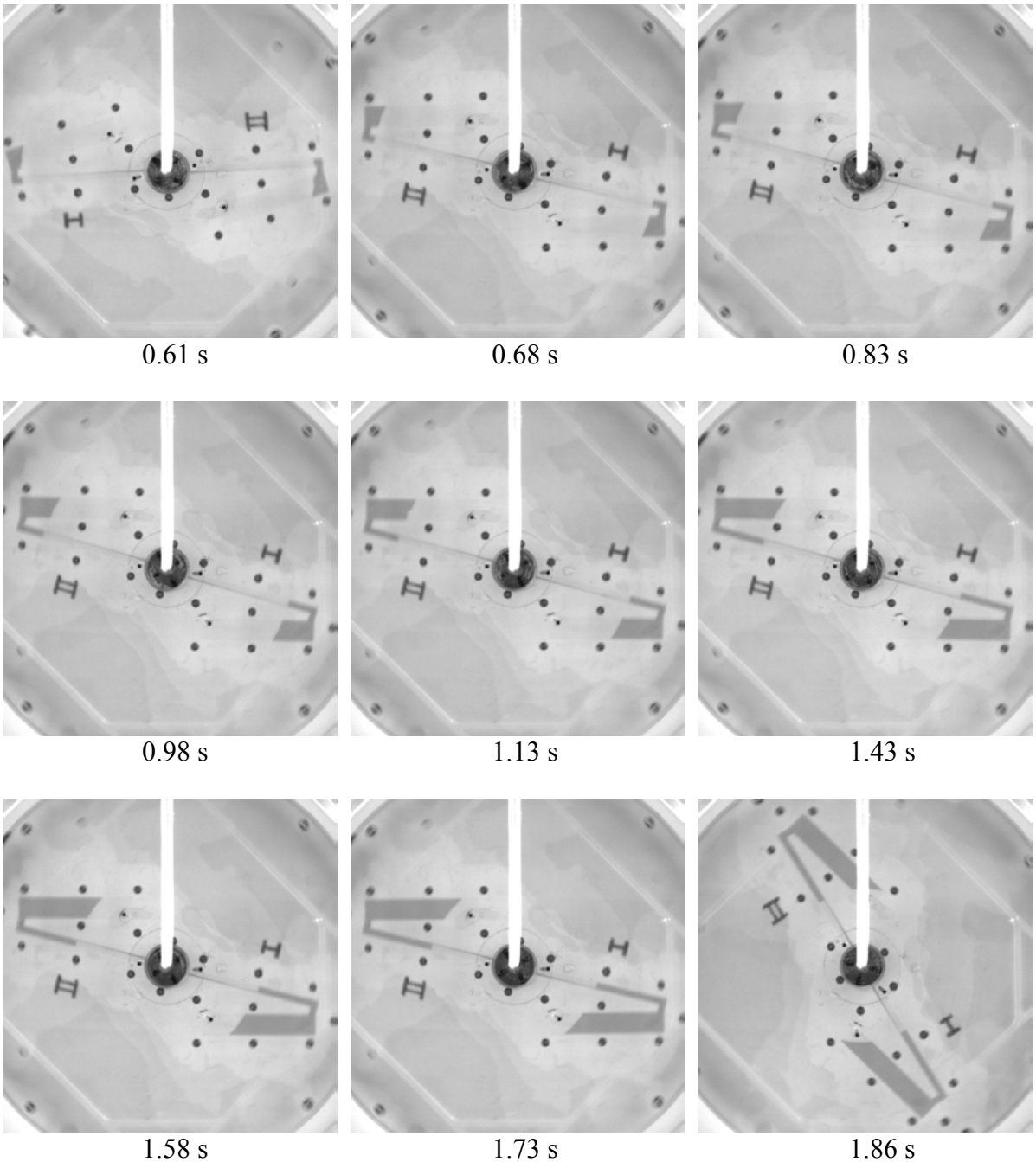

Appendix 7. Summary of the high speed camera results of the indirect gated mould filling process. The rotational velocity was 400 rpm in the anti-clockwise direction. Note: Video sequence can be seen in Appendix 37.

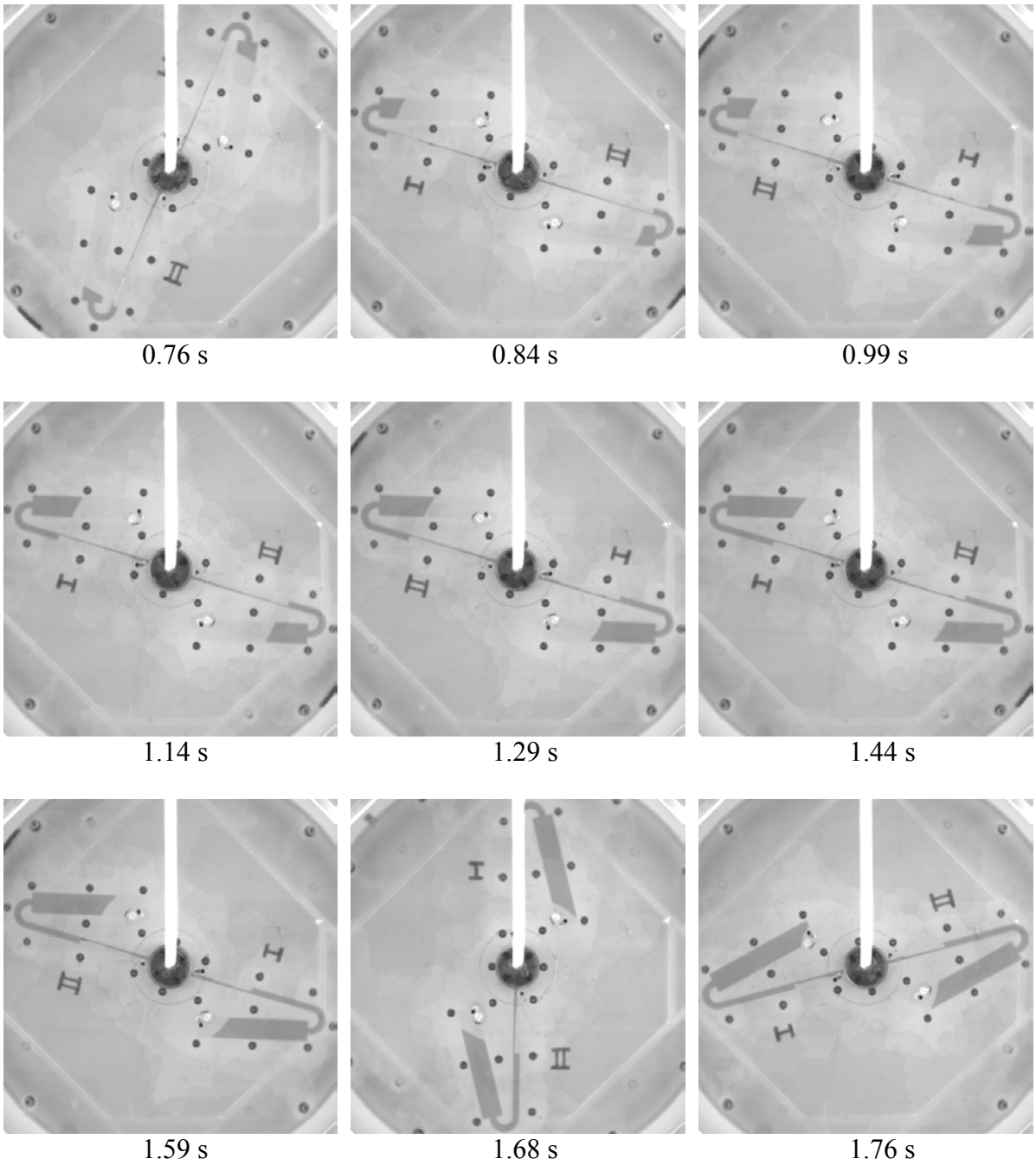

Appendix 8. Summary of the high speed camera results of the modified indirect gated mould filling process. The rotational velocity was 200 rpm in the anti-clockwise direction. Note: Video sequence can be seen in Appendix 38.

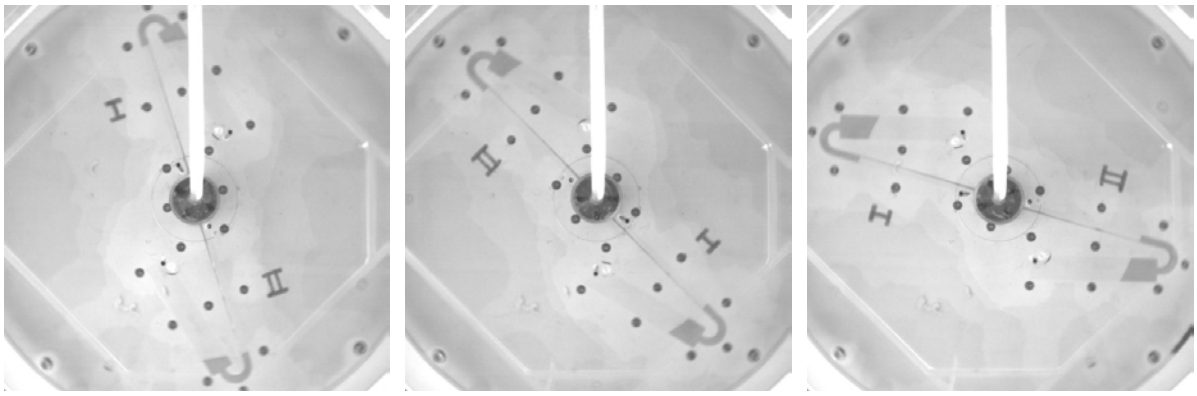

0.74 s 0.85 s 0.97 s

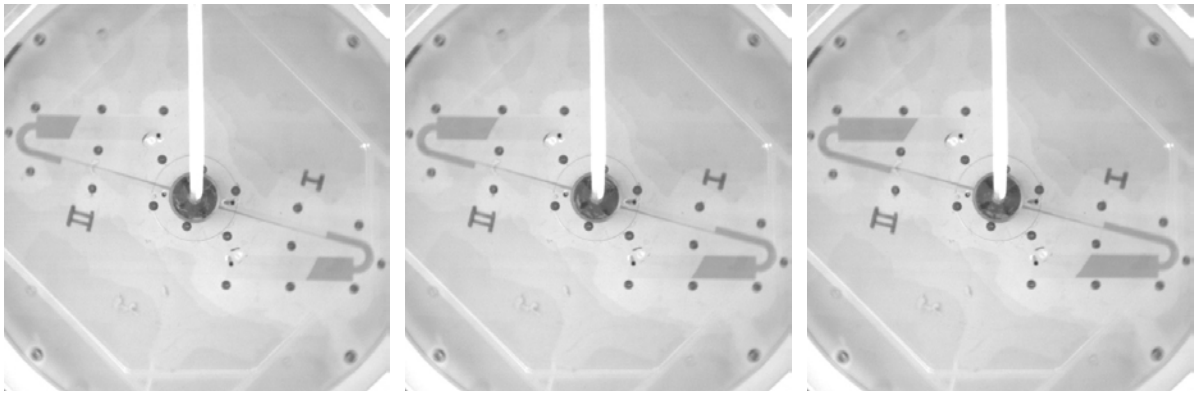

1.07 s 1.27 s 1.47 s

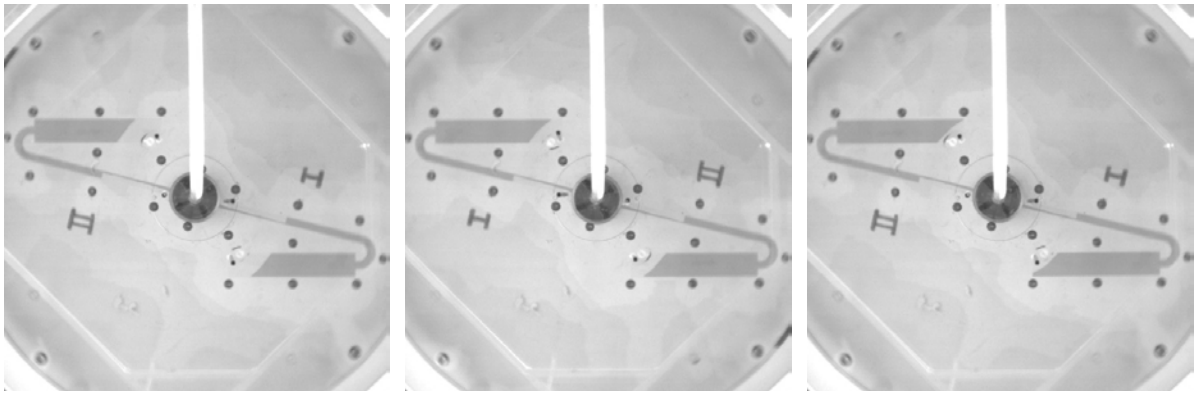

1.67 s 1.77 s 1.87 s

Appendix 9. Summary of the high speed camera results of the modified indirect gated mould filling process. The rotational velocity was 300 rpm in the anti-clockwise direction. Note: Video sequence can be seen in Appendix 39.

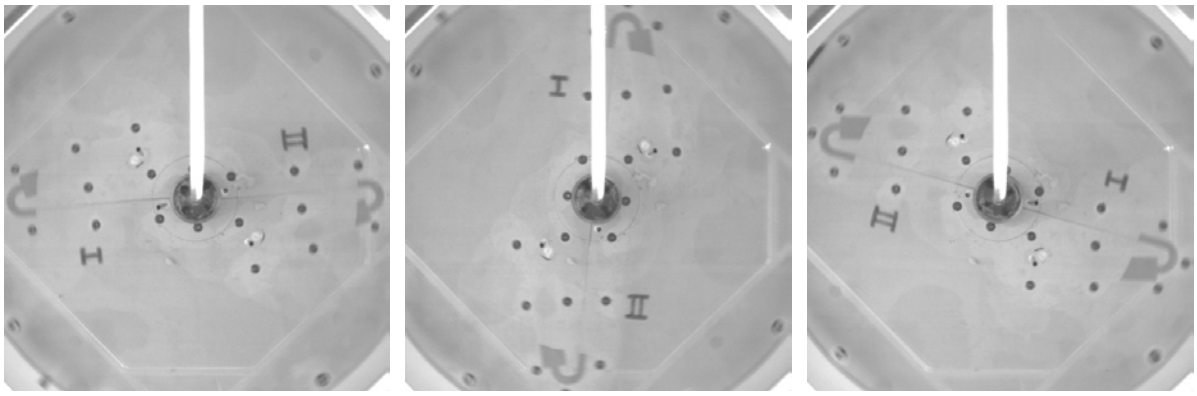

0.71 s 0.82 s 0.93 s

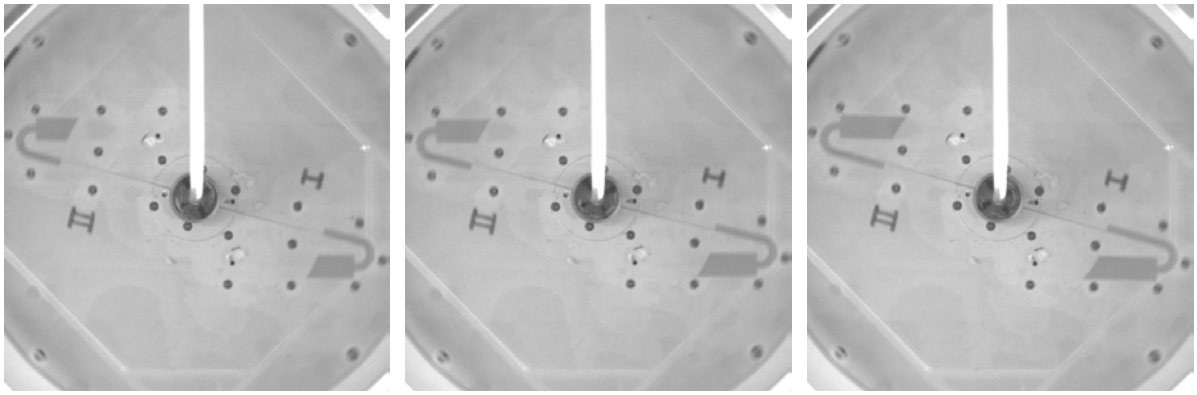

1.08 s 1.23 s 1.38 s

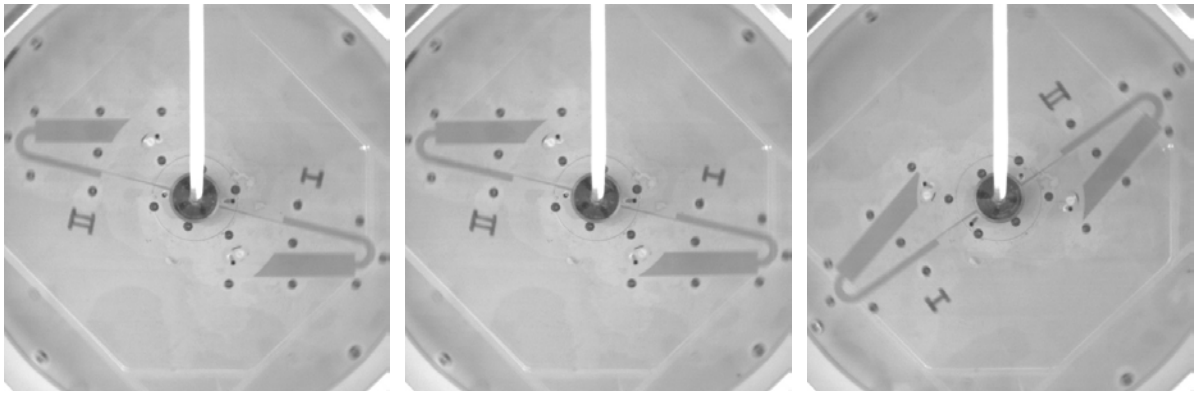

1.68 s 1.83 s 1.92 s

Appendix 10. Summary of the high speed camera results of the modified indirect gated mould filling process. The rotational velocity was 400 rpm in the anti-clockwise direction. Note: Video sequence can be seen in Appendix 40.

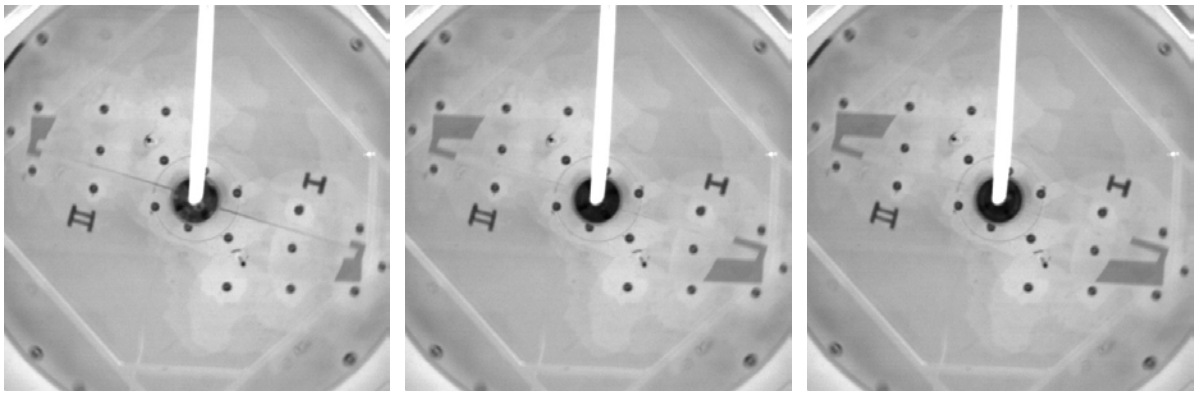

0.81 s 2.60 s 4.40 s

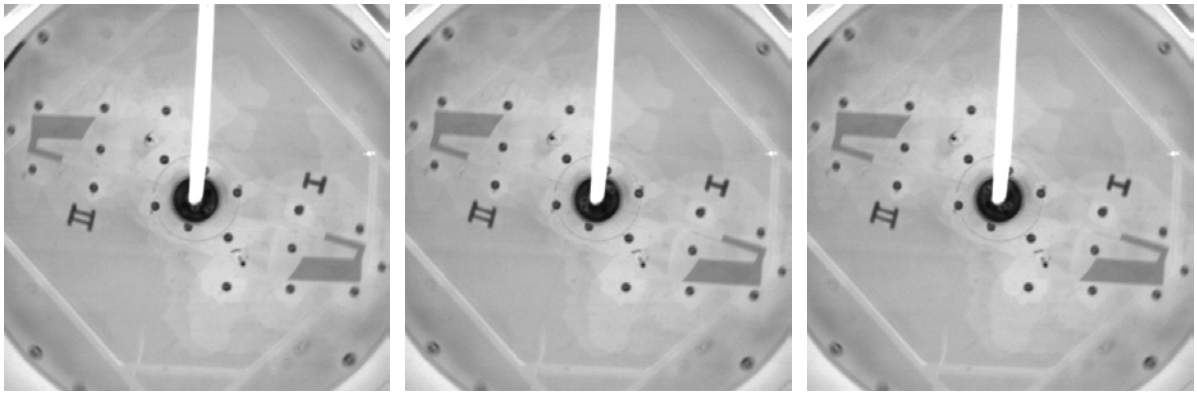

6.20 s 7.99 s 9.79 s

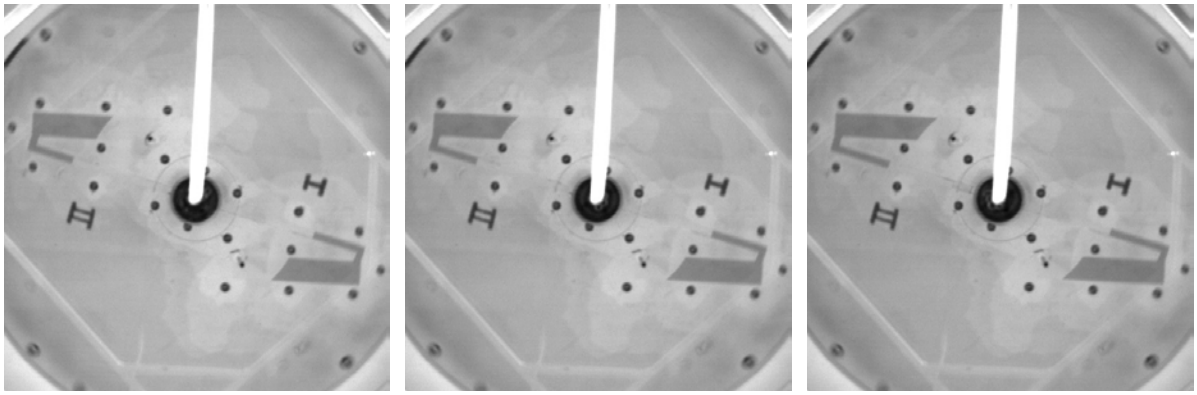

11.59 s 13.39 s 15.19 s

Appendix 11. Summary of the high speed camera results of the indirect gated mould filling process. The Perspex mould did not include the vents in the runners. The rotational velocity was 200 rpm in the anti-clockwise direction.

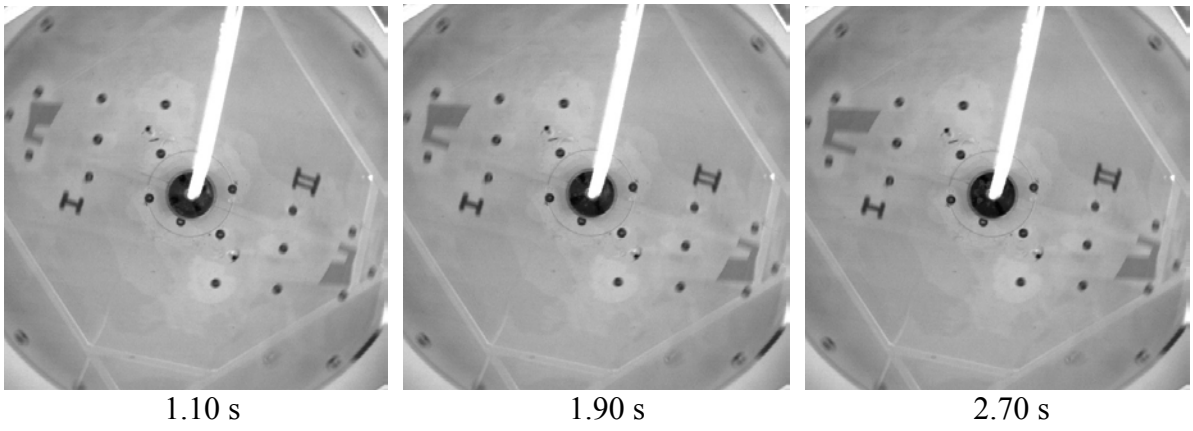

1.10 s 1.90 s 2.70 s

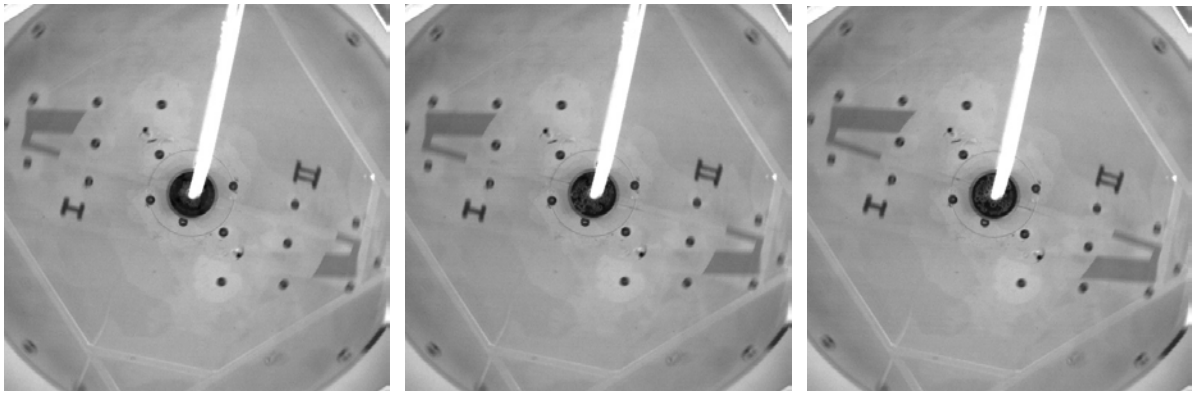

3.30 s 4.10 s 4.90 s

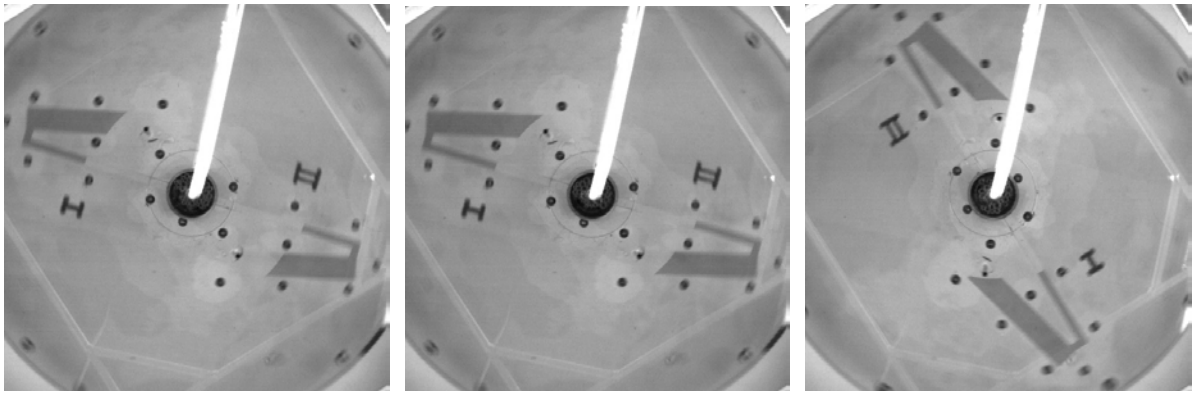

5.70 s 6.50 s 7.18 s

Appendix 12. Summary of the high speed camera results of the indirect gated mould filling process. The Perspex mould did not include the vents in the runners. The rotational velocity was 300 rpm in the anti-clockwise direction.

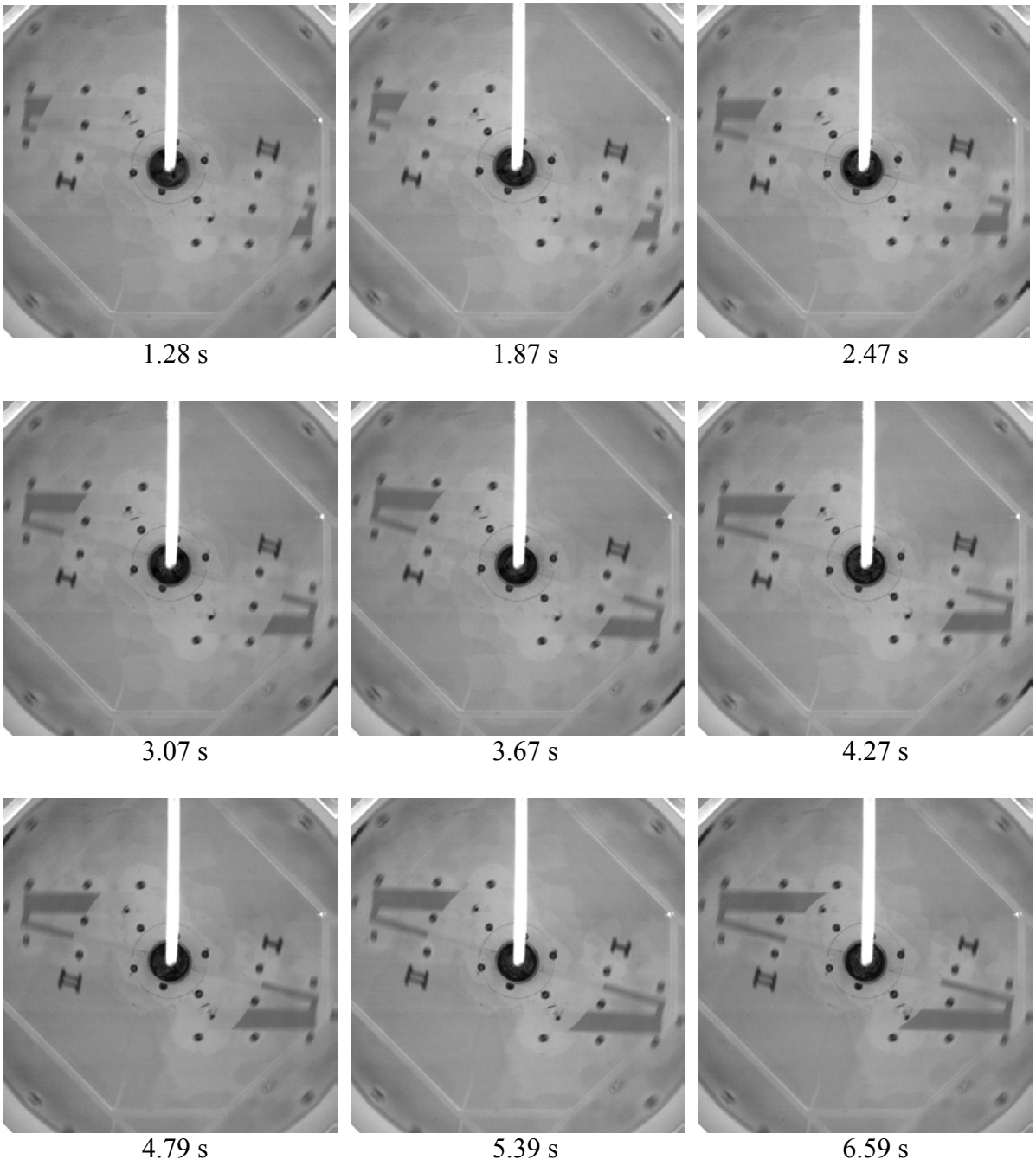

Appendix 13. Summary of the high speed camera results of the indirect gated mould filling process. The Perspex mould did not include the vents in the runners. The rotational velocity was 400 rpm in the anti-clockwise direction.

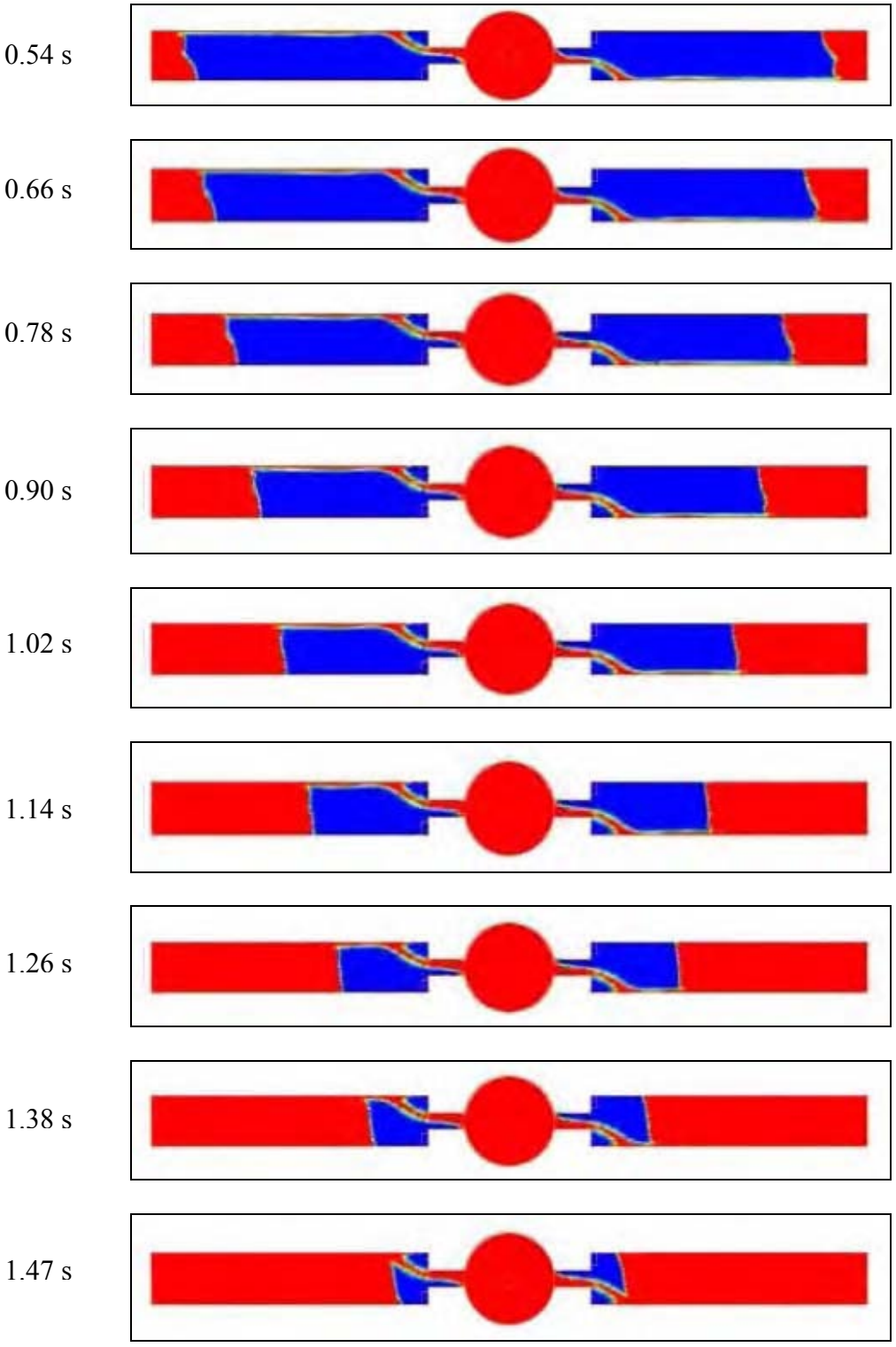

Appendix 14. ANSYS CFX results of the direct gated water model mould showing plan view. The rotational velocity was 200 rpm in the anti-clockwise direction and the cut plane was taken 0.5 mm from the base. Note: Video sequence can be seen in Appendix 43.

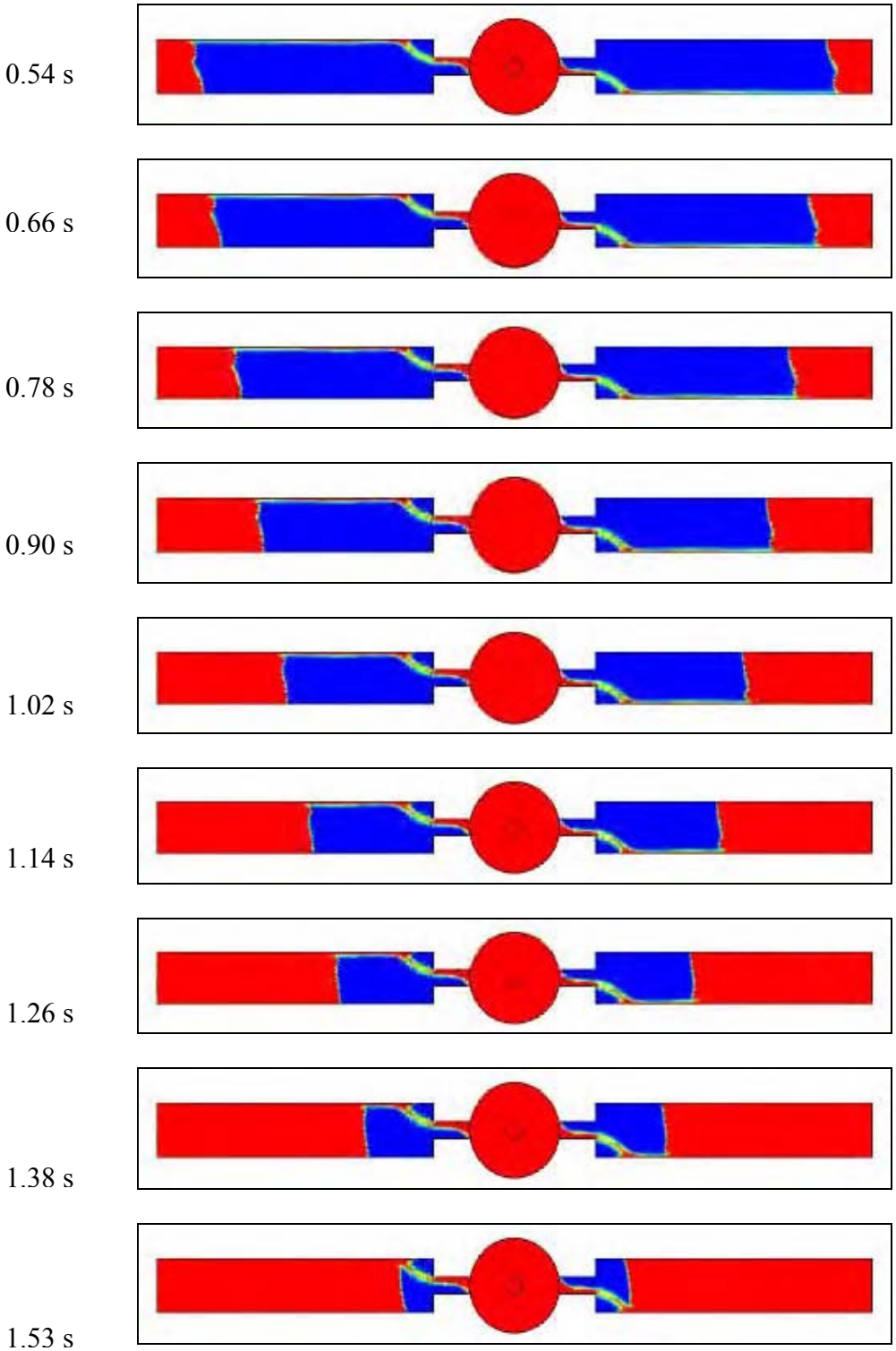

Appendix 15. ANSYS CFX results of the direct gated water model mould showing plan view. The rotational velocity was 300 rpm in the anti-clockwise direction and the cut plane was taken 0.5 mm from the base. Note: Video sequence can be seen in Appendix 44.

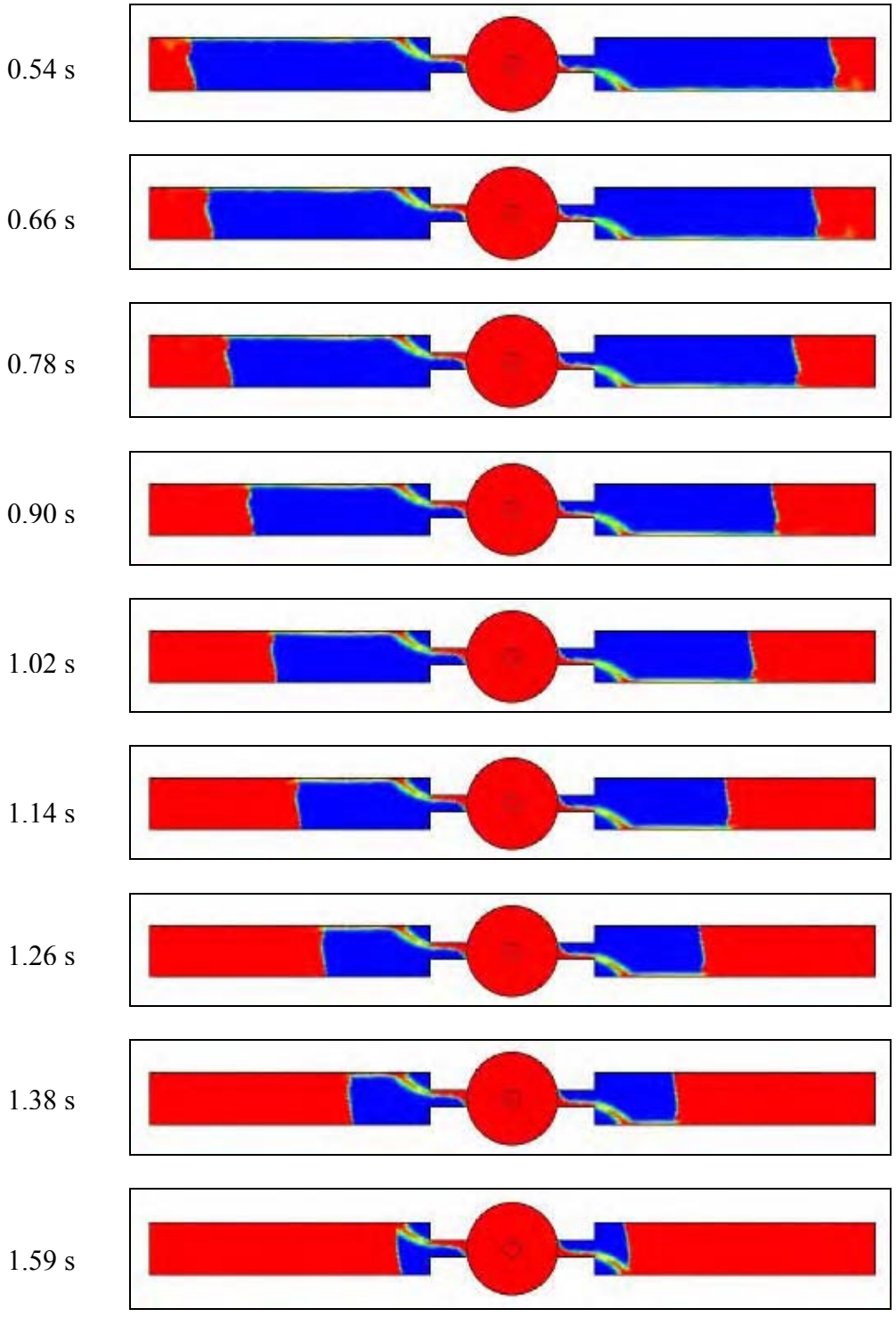

Appendix 16. ANSYS CFX results of the direct gated water model mould showing plan view. The rotational velocity was 400 rpm in the anti-clockwise direction and the cut plane was taken 0.5 mm from the base. Note: Video sequence can be seen in Appendix 45.

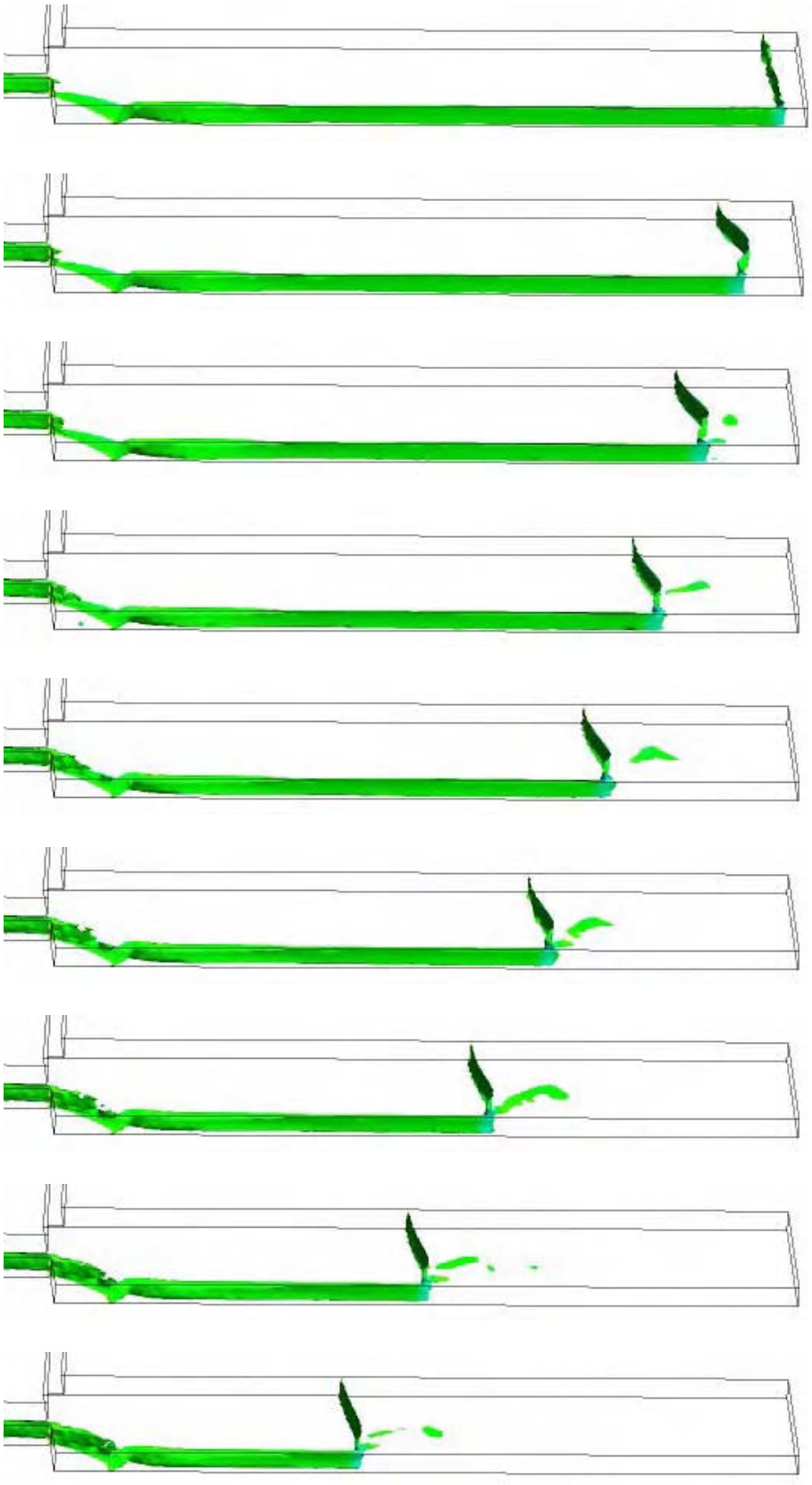
0.30 s
0.42 s
0.54 s
0.66 s
0.78 s
0.90 s
1.02 s
1.14 s
1.26 s

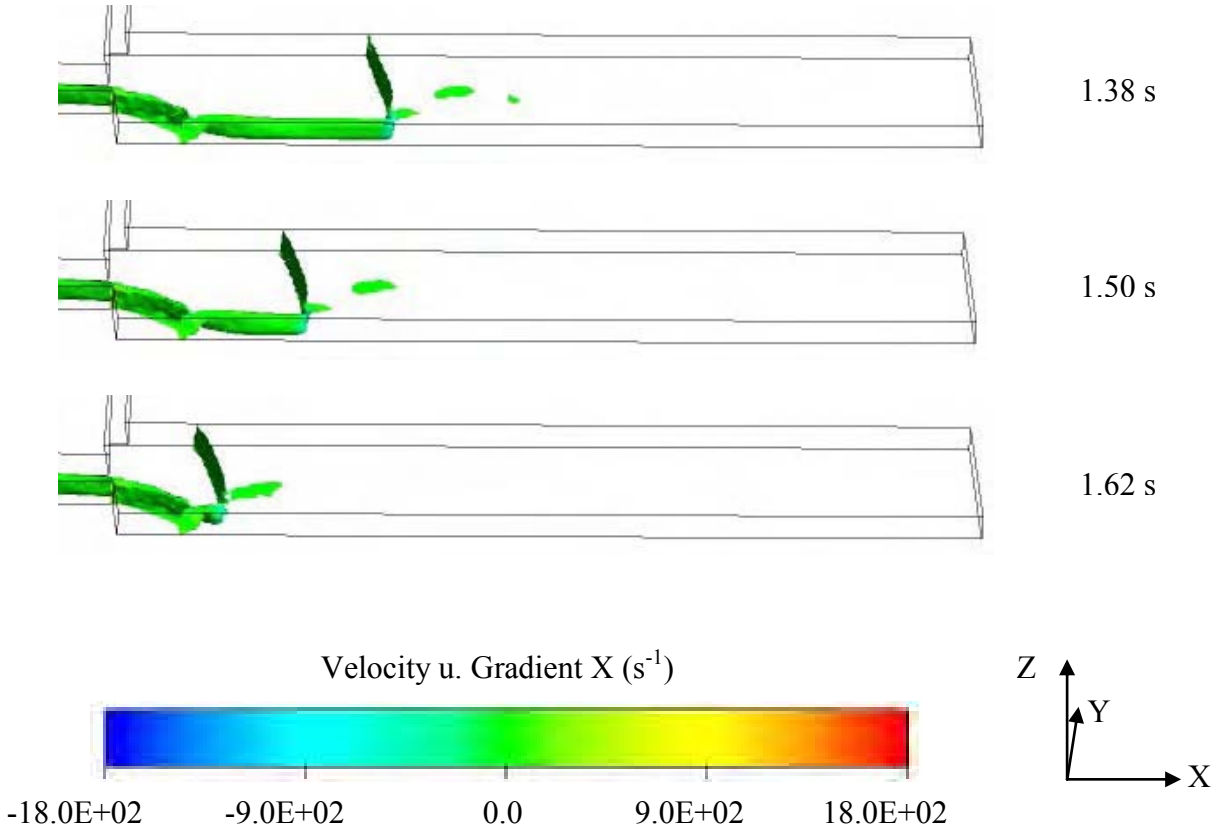

Appendix 17. ANSYS CFX results of the direct gated water model mould showing close-up of the right hand test bar, isosurface (0.5 volume fraction) and velocity gradients in "X" axis (see Figure 6 - 106). The rotational velocity was 400 rpm in the anti-clockwise direction.

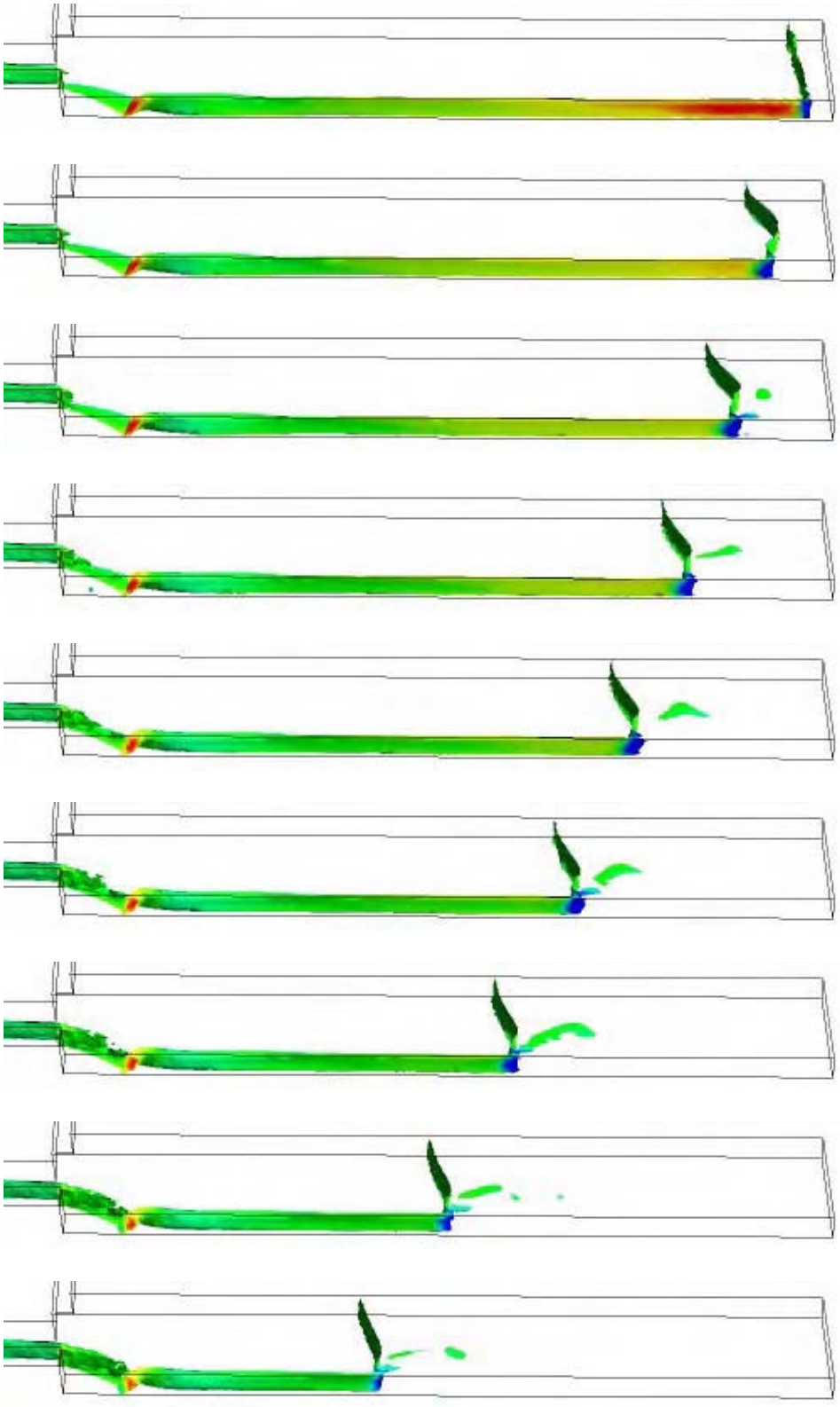
0.30 s
0.42 s
0.54 s
0.66 s
0.78 s
0.90 s
1.02 s
1.14 s
1.26 s

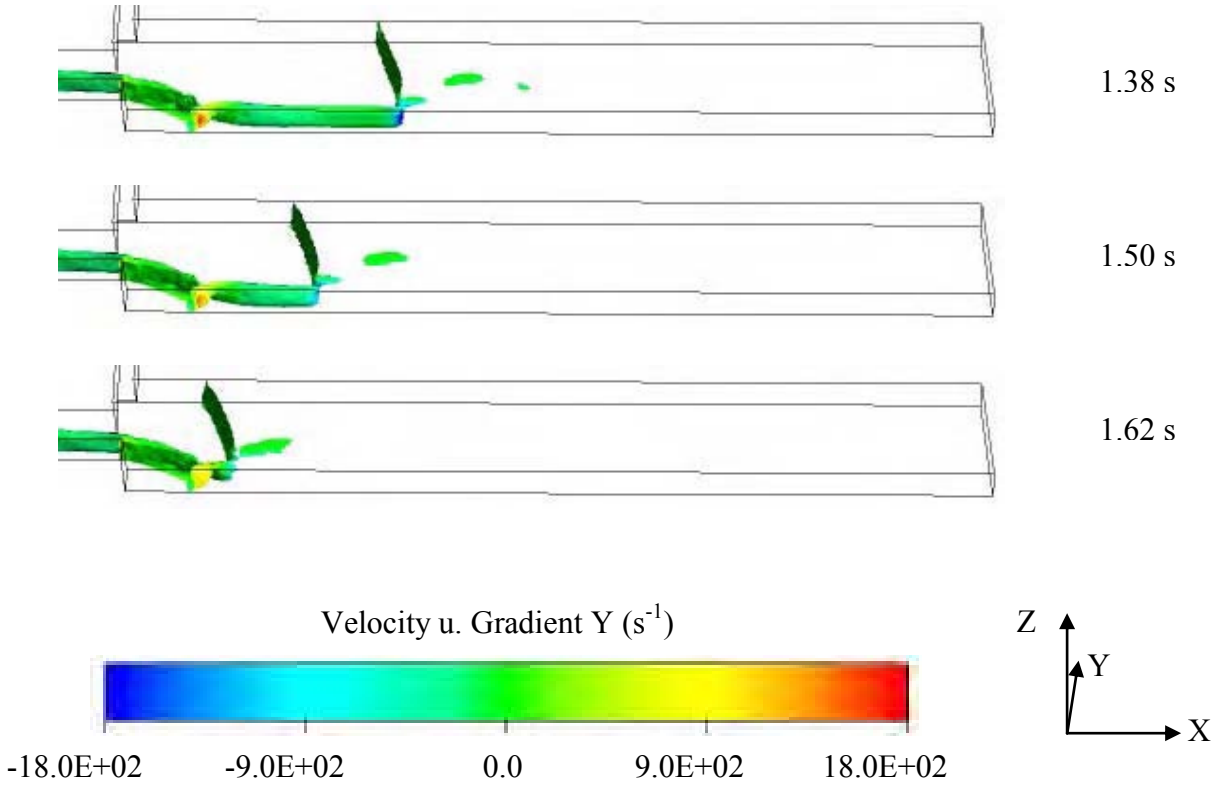

Appendix 18. ANSYS CFX results of the direct gated water model mould showing close-up of the right hand test bar, isosurface (0.5 volume fraction) and velocity gradients in "Y" axis (see Figure 6 - 106). The rotational velocity was 400 rpm in the anti-clockwise direction.

0.60 s

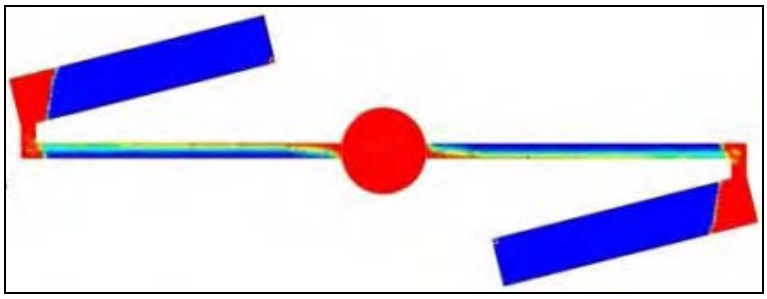

0.75 s

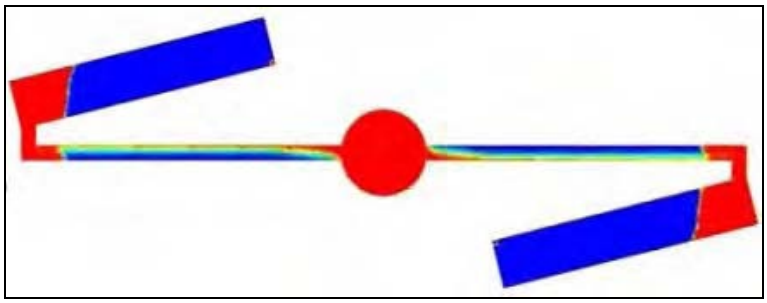

0.90 s

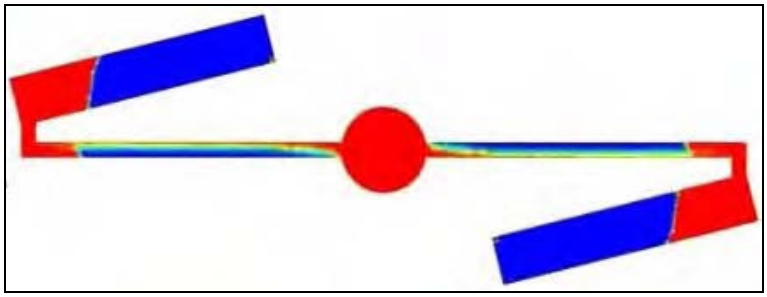

1.05 s

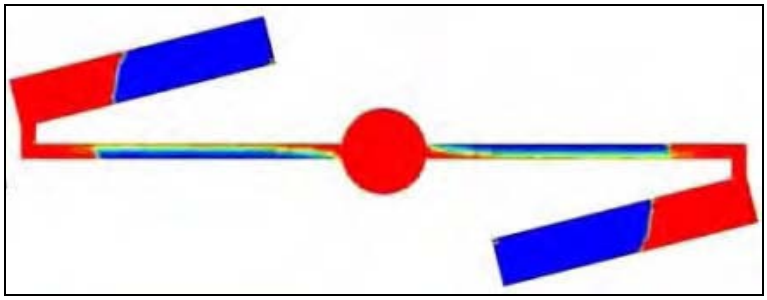

1.20 s

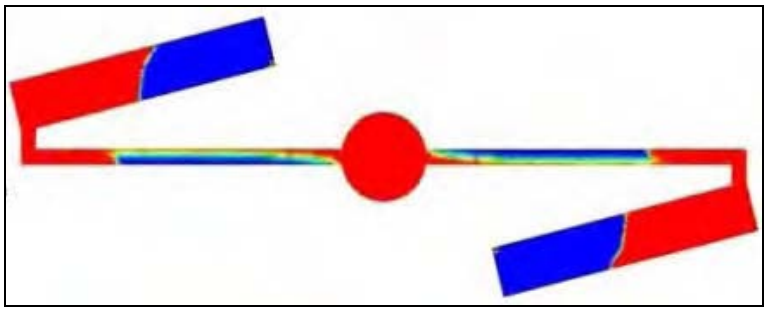

1.35 s

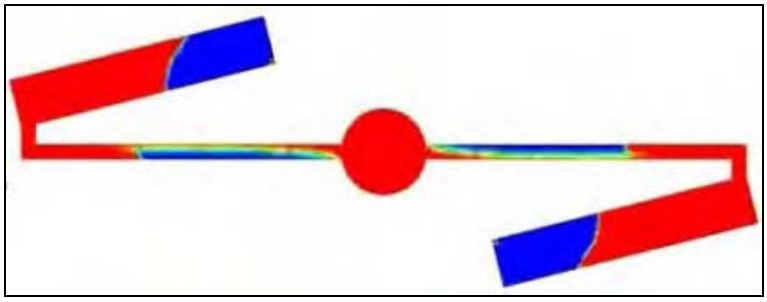

1.50 s

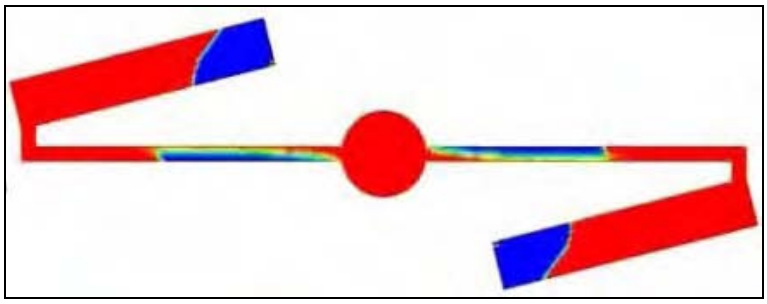

1.65 s

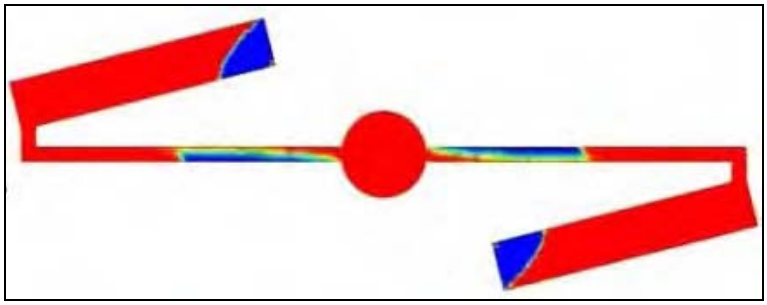

Appendix 19. ANSYS CFX results of the indirect gated water model mould showing plan view. The rotational velocity was 200 rpm in the anti-clockwise direction and the cut plane was taken 0.5 mm from the base. Note: Video sequence can be seen in Appendix 46.

0.60 s

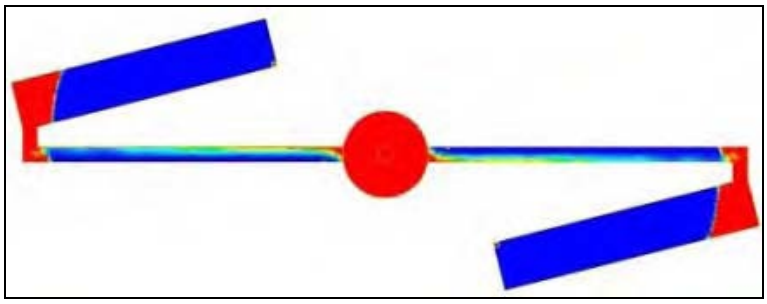

0.75 s

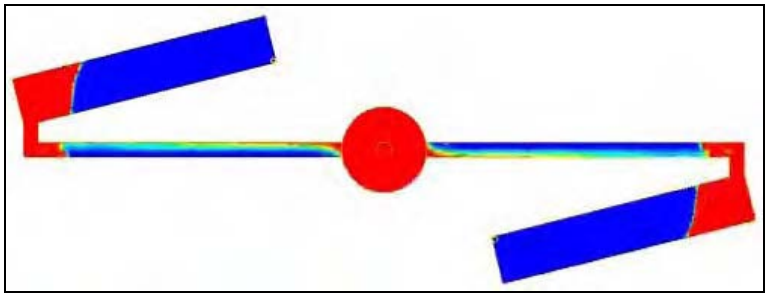

0.90 s

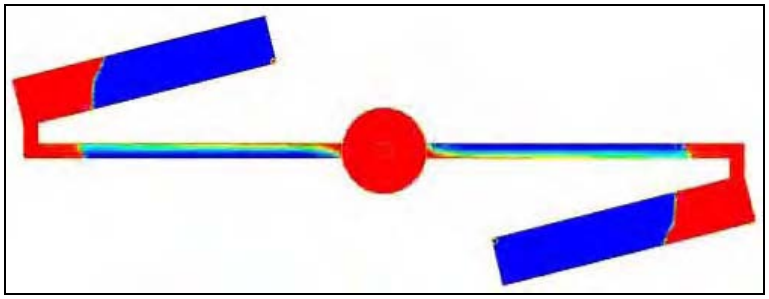

1.05 s

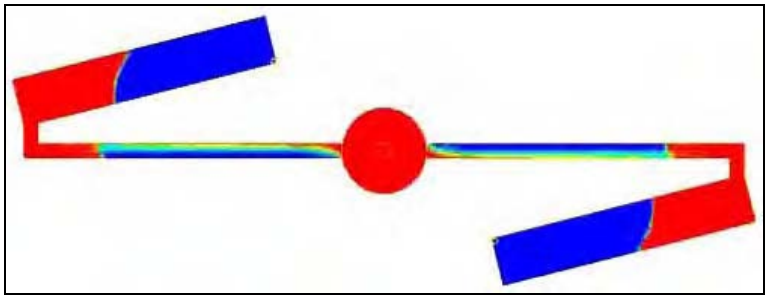

1.20 s

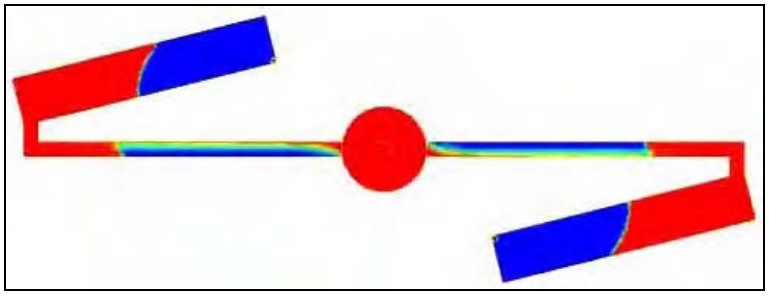

1.35 s

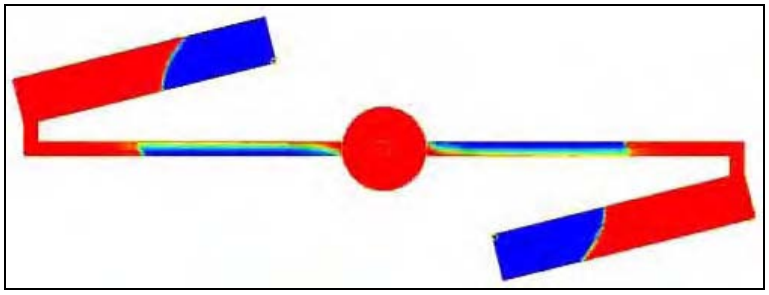

1.50 s

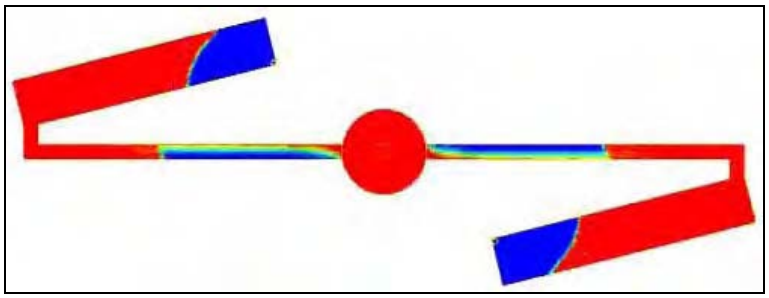

1.65 s

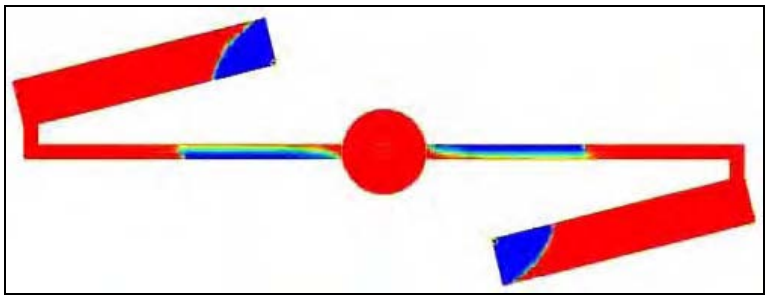

1.71 s

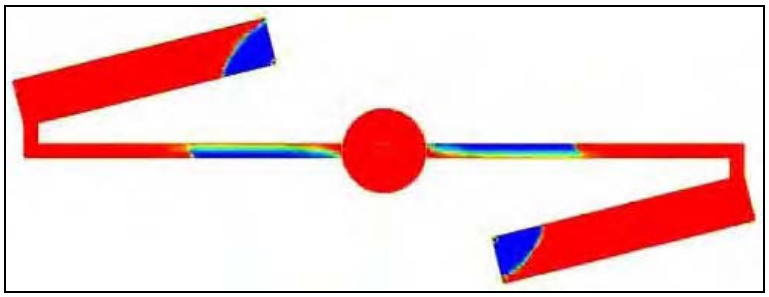

Appendix 20. ANSYS CFX results of the indirect gated water model mould showing plan view. The rotational velocity was 300 rpm in the anti-clockwise direction and the cut plane was taken 0.5 mm from the base. Note: Video sequence can be seen in Appendix 47.

0.60 s

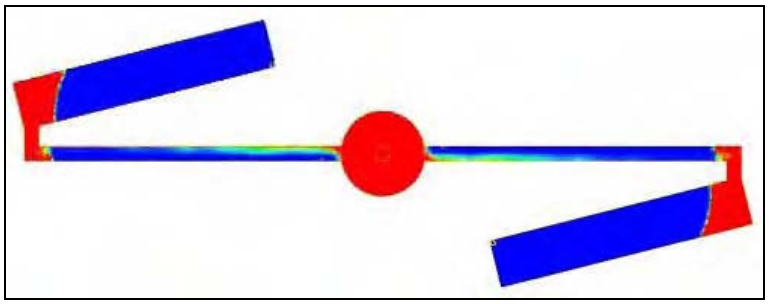

0.75 s

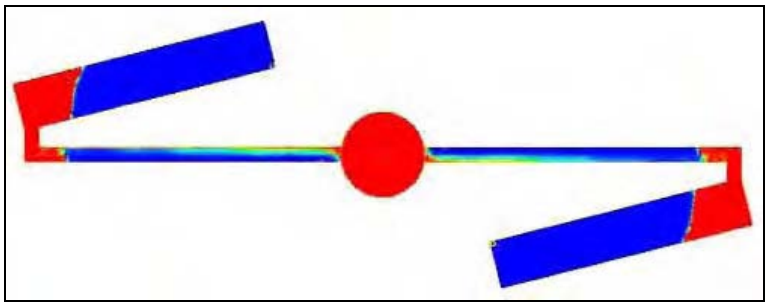

0.90 s

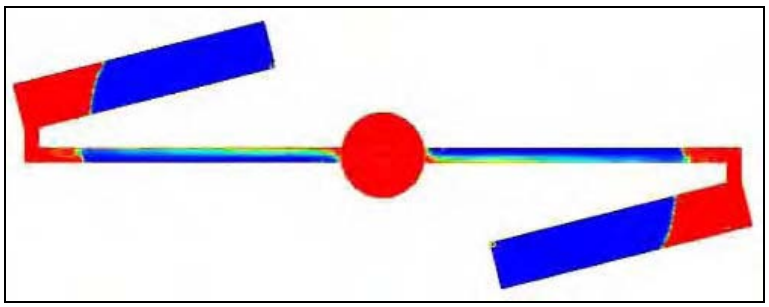

1.05 s

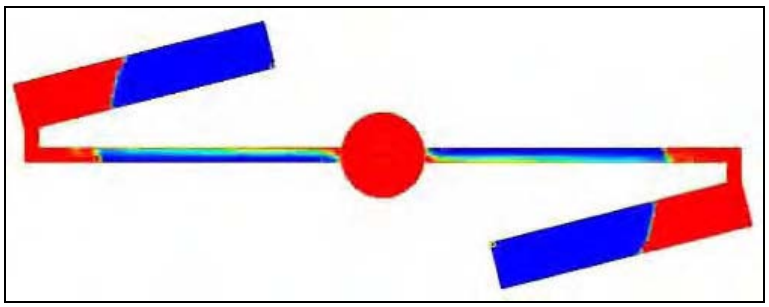

1.20 s

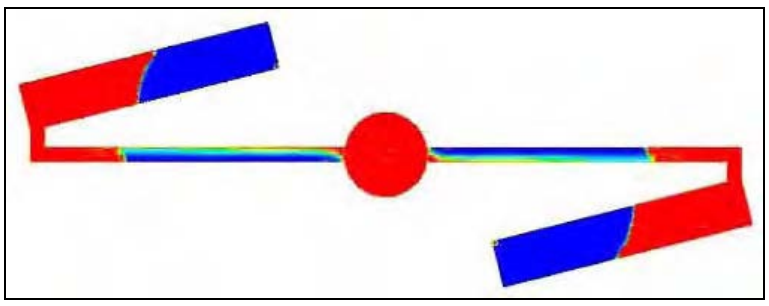

1.35 s

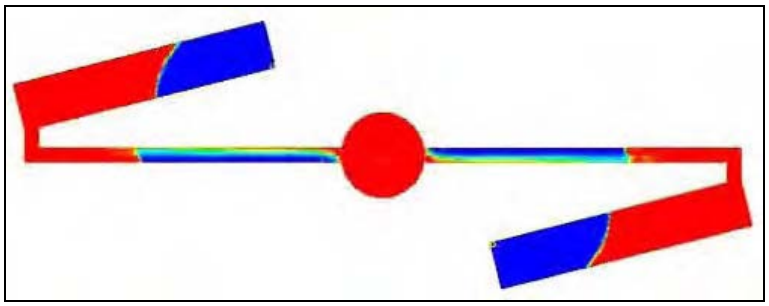

1.50 s

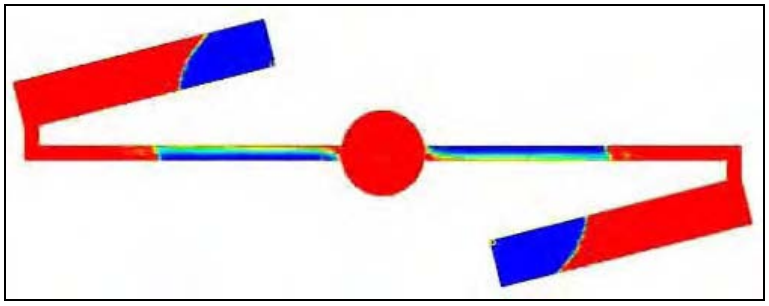

1.65 s

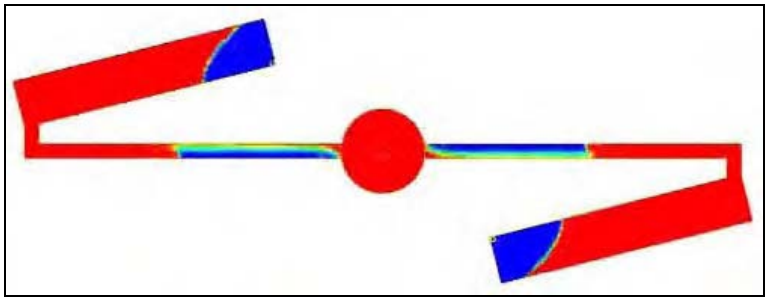

1.77 s

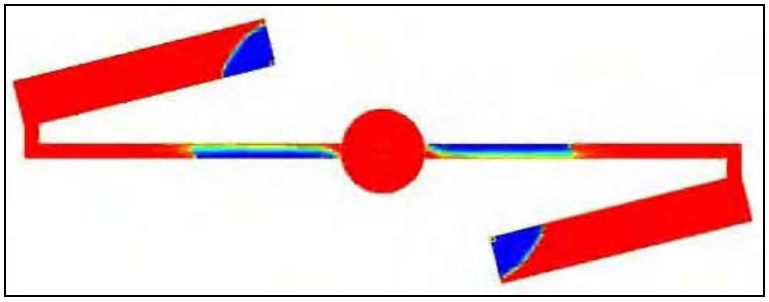

Appendix 21. ANSYS CFX results of the indirect gated water model mould showing plan view. The rotational velocity was 400 rpm in the anti-clockwise direction and the cut plane was taken 0.5 mm from the base. Note: Video sequence can be seen in Appendix 48.

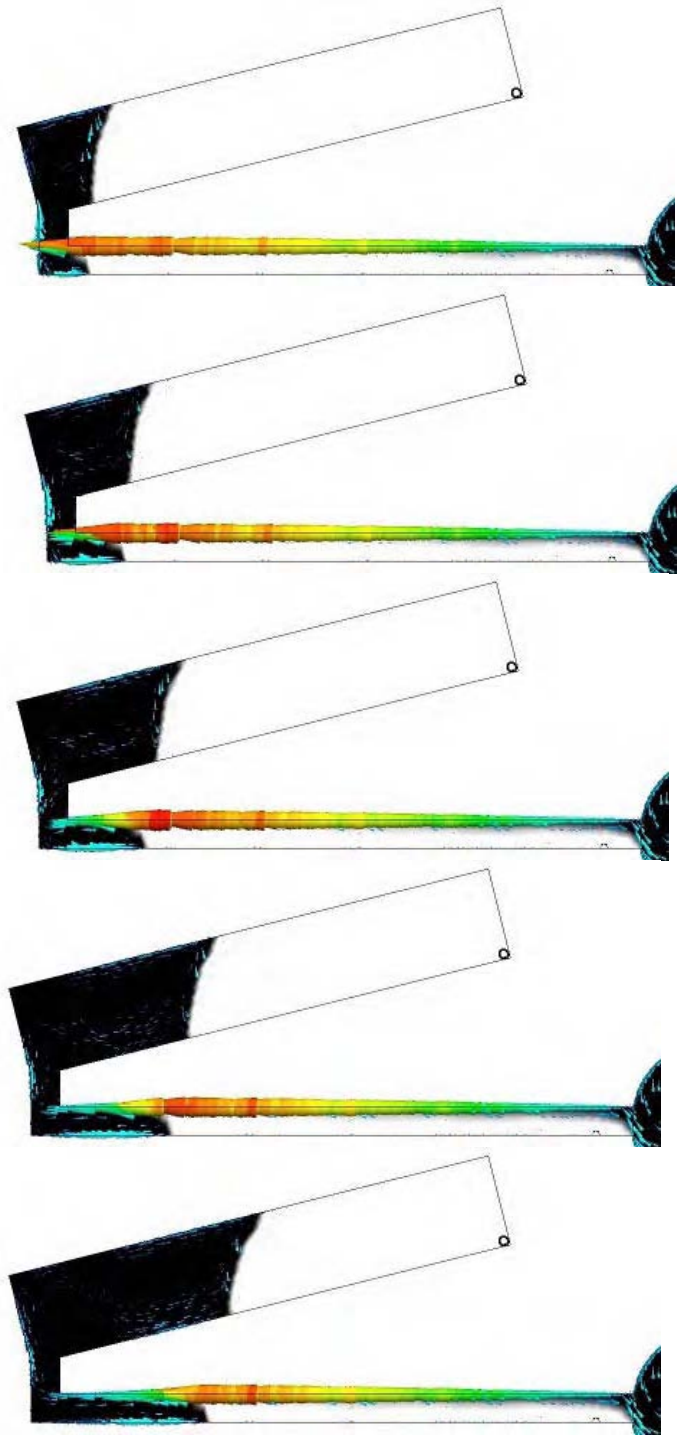
0.60 s
0.75 s
0.90 s
1.05 s
1.20 s

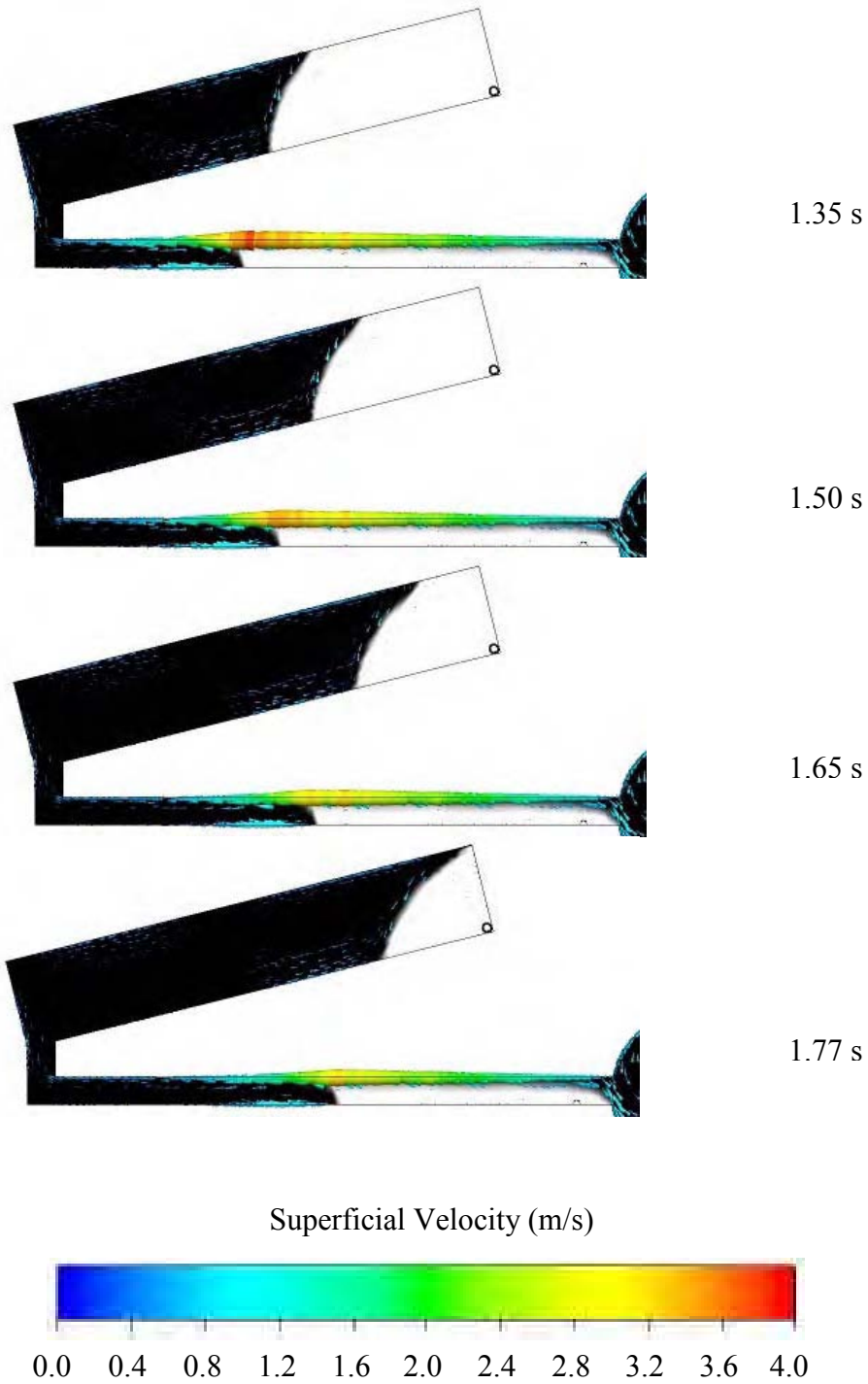

Appendix 22. ANSYS CFX results of the indirect gated water model mould showing close-up of the left hand test bar and velocity vectors (see Figure 6 - 113). The rotational velocity was 400 rpm in the anti-clockwise direction and the cut plane was taken 0.5 mm from the base.

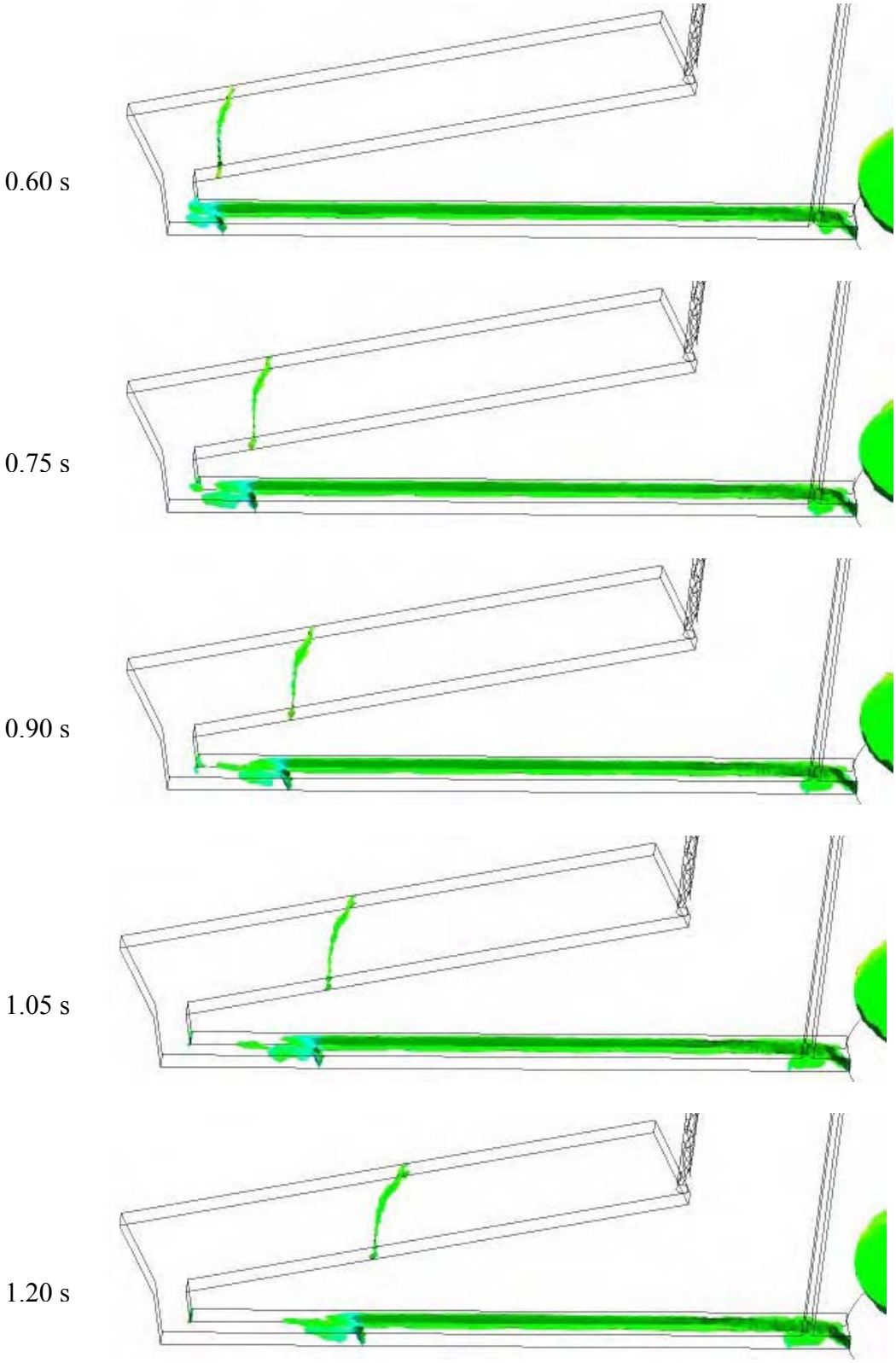
0.60 s
0.75 s
0.90 s
1.05 s
1.20 s

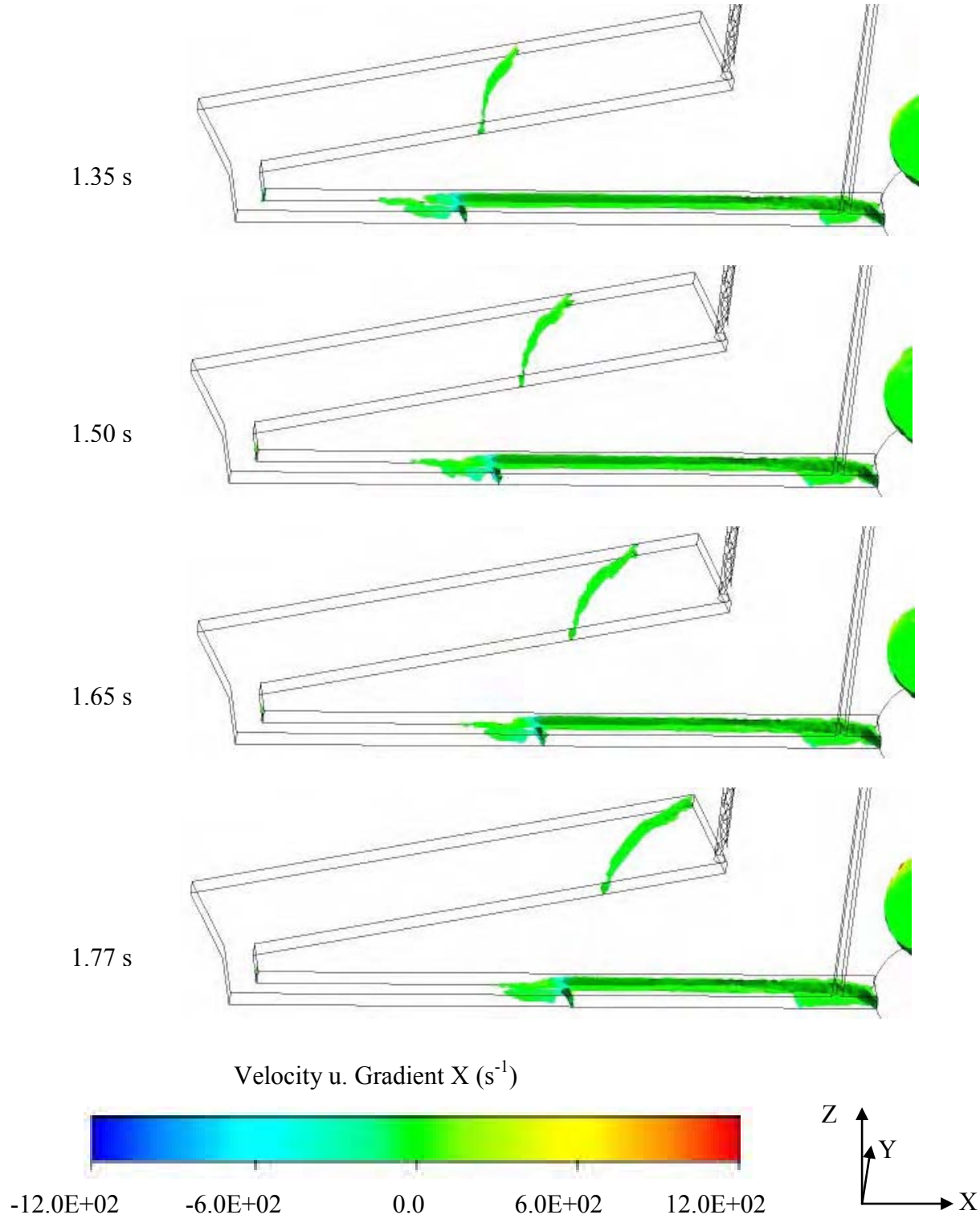

Appendix 23. ANSYS CFX results of the indirect gated water model mould showing close-up of the left hand test bar, isosurface (0.5 volume fraction) and velocity gradients in "X" axis (see Figure 6 - 113). The rotational velocity was 400 rpm in the anti-clockwise direction.

0.60 s

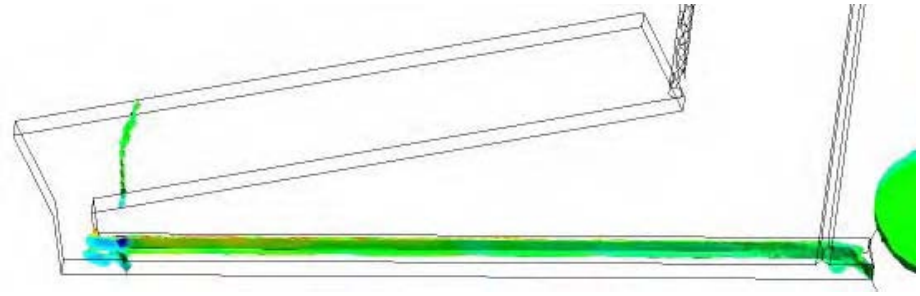

0.75 s

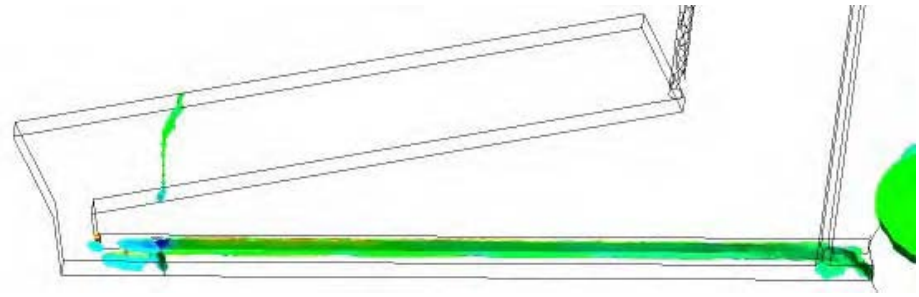

0.90 s

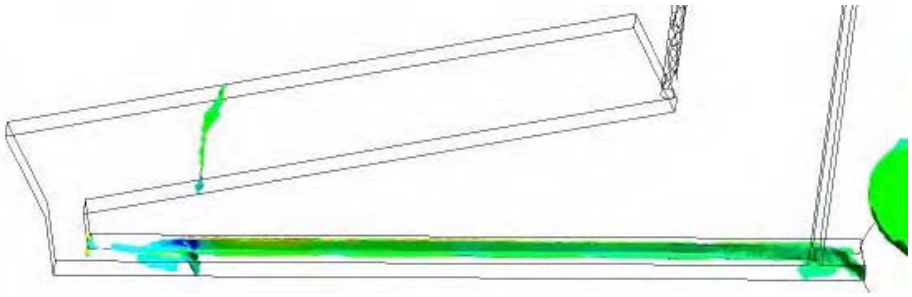

1.05 s

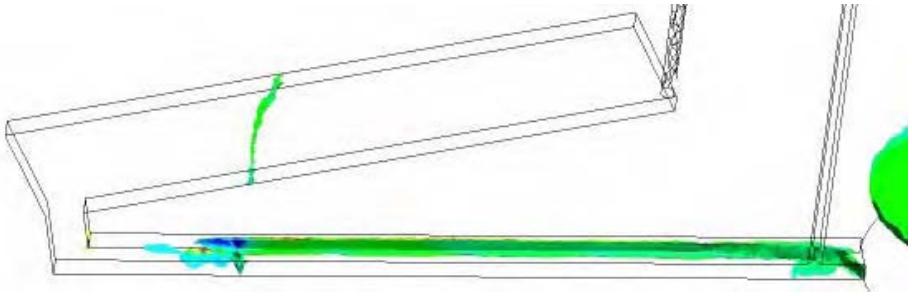

1.20 s

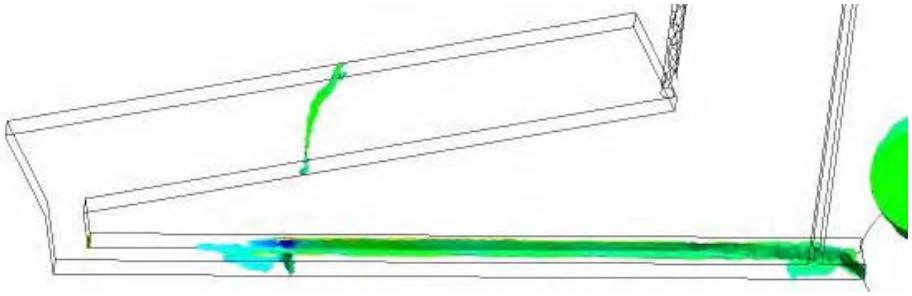

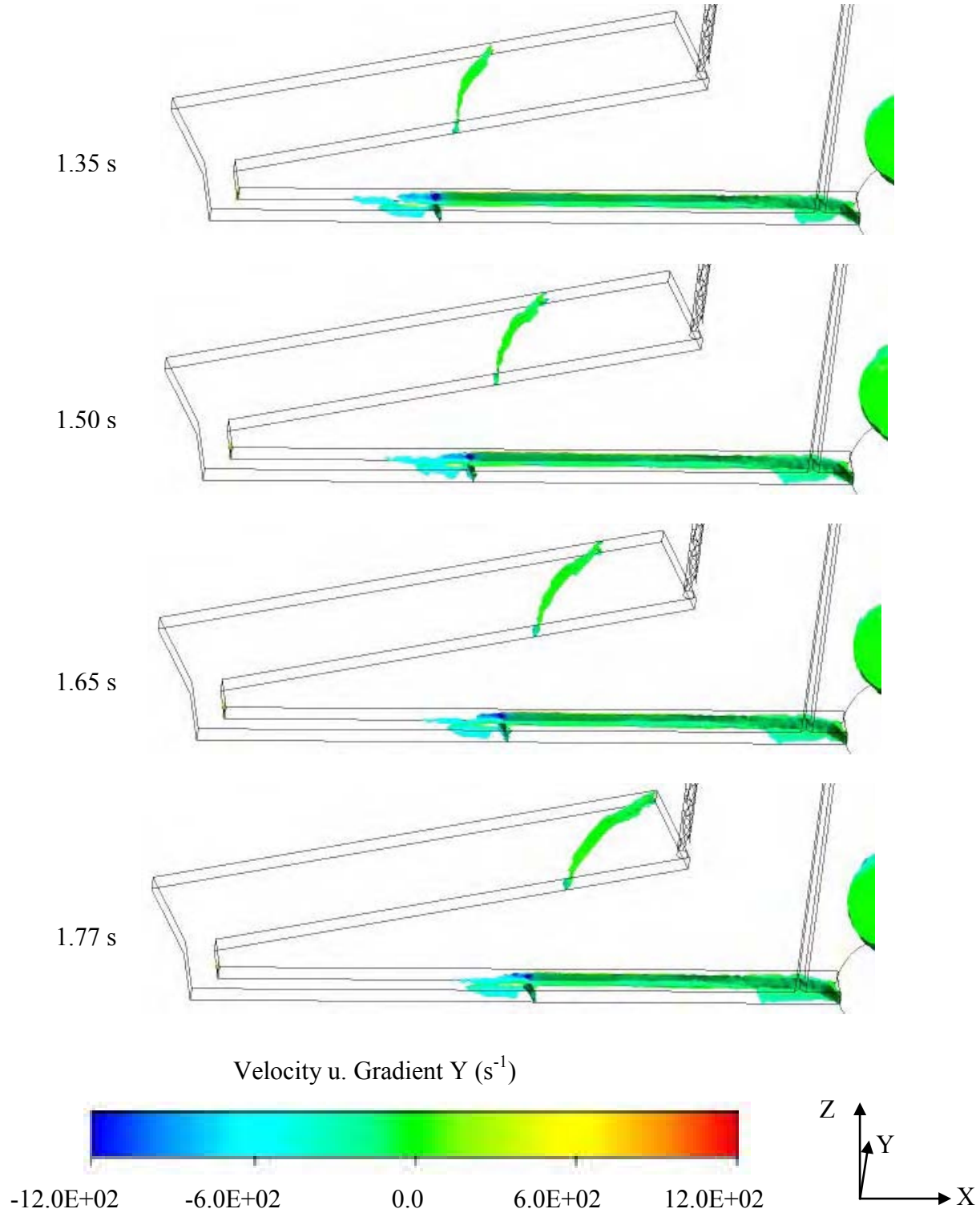

Appendix 24. ANSYS CFX results of the indirect gated water model mould showing close-up of the left hand test bar, isosurface (0.5 volume fraction) and velocity gradients in "Y" axis (see Figure 6 - 113). The rotational velocity was 400 rpm in the anti-clockwise direction.

0.28 s

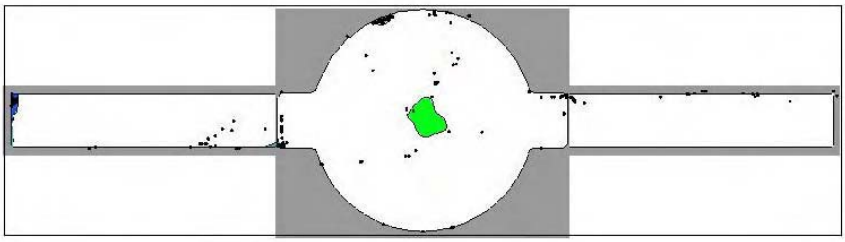

0.42 s

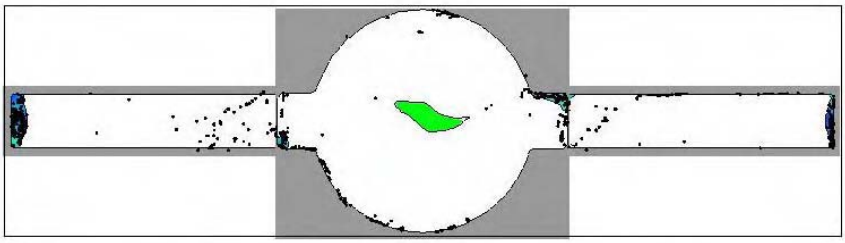

0.48 s

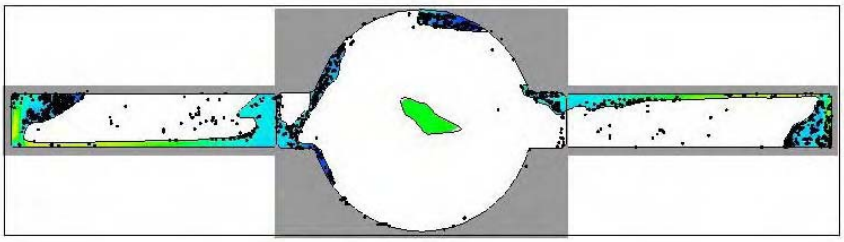

0.50 s

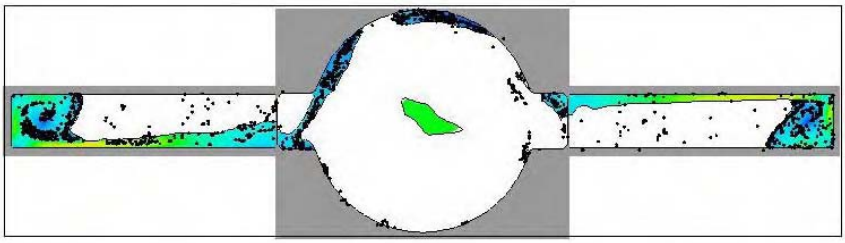

0.52 s

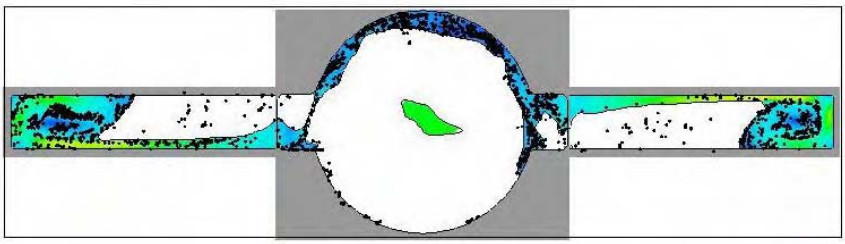

0.54 s

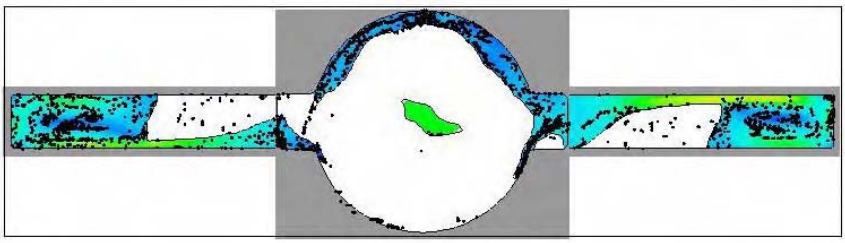

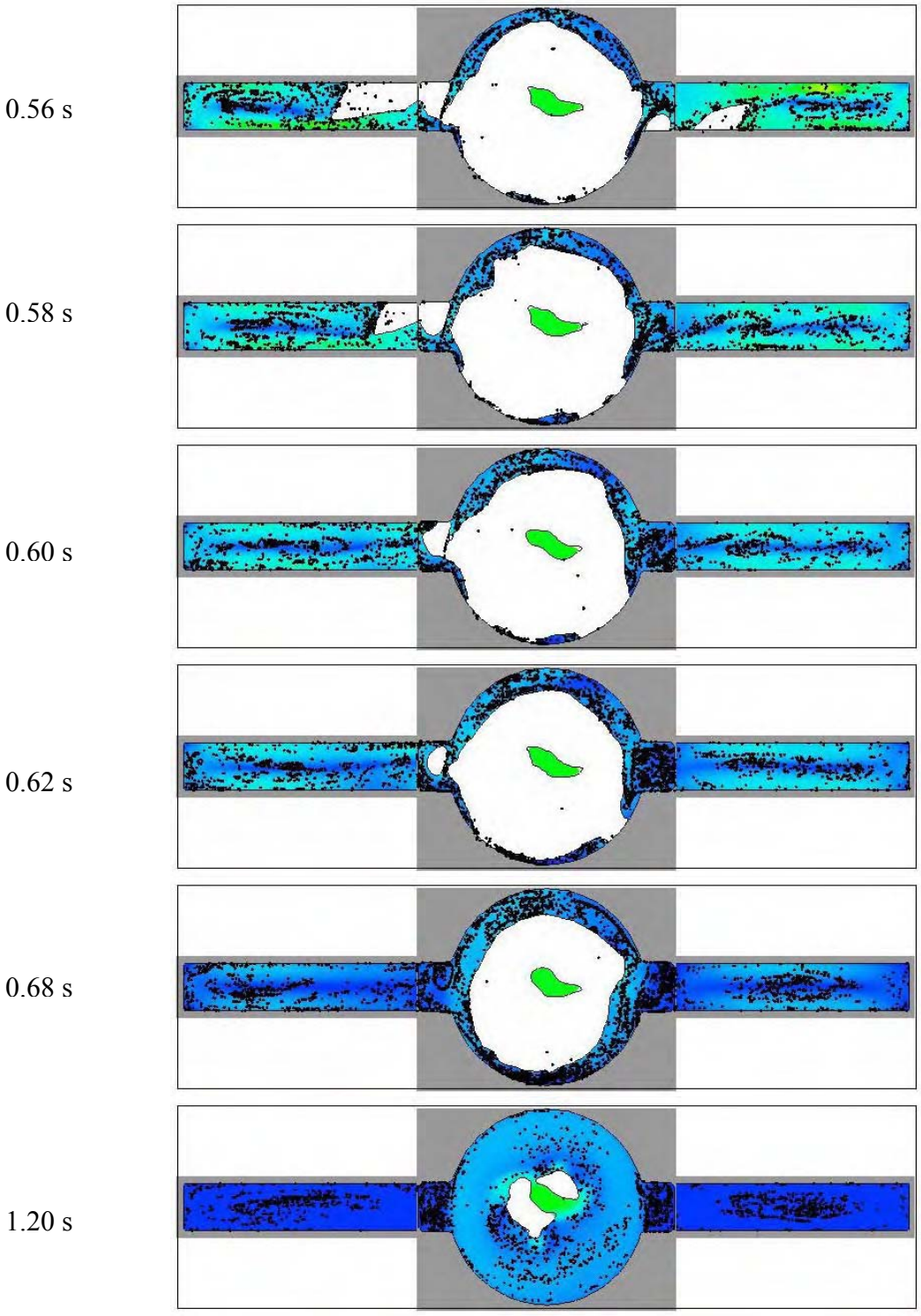
0.56 s
0.58 s
0.60 s
0.62 s
0.68 s
1.20 s

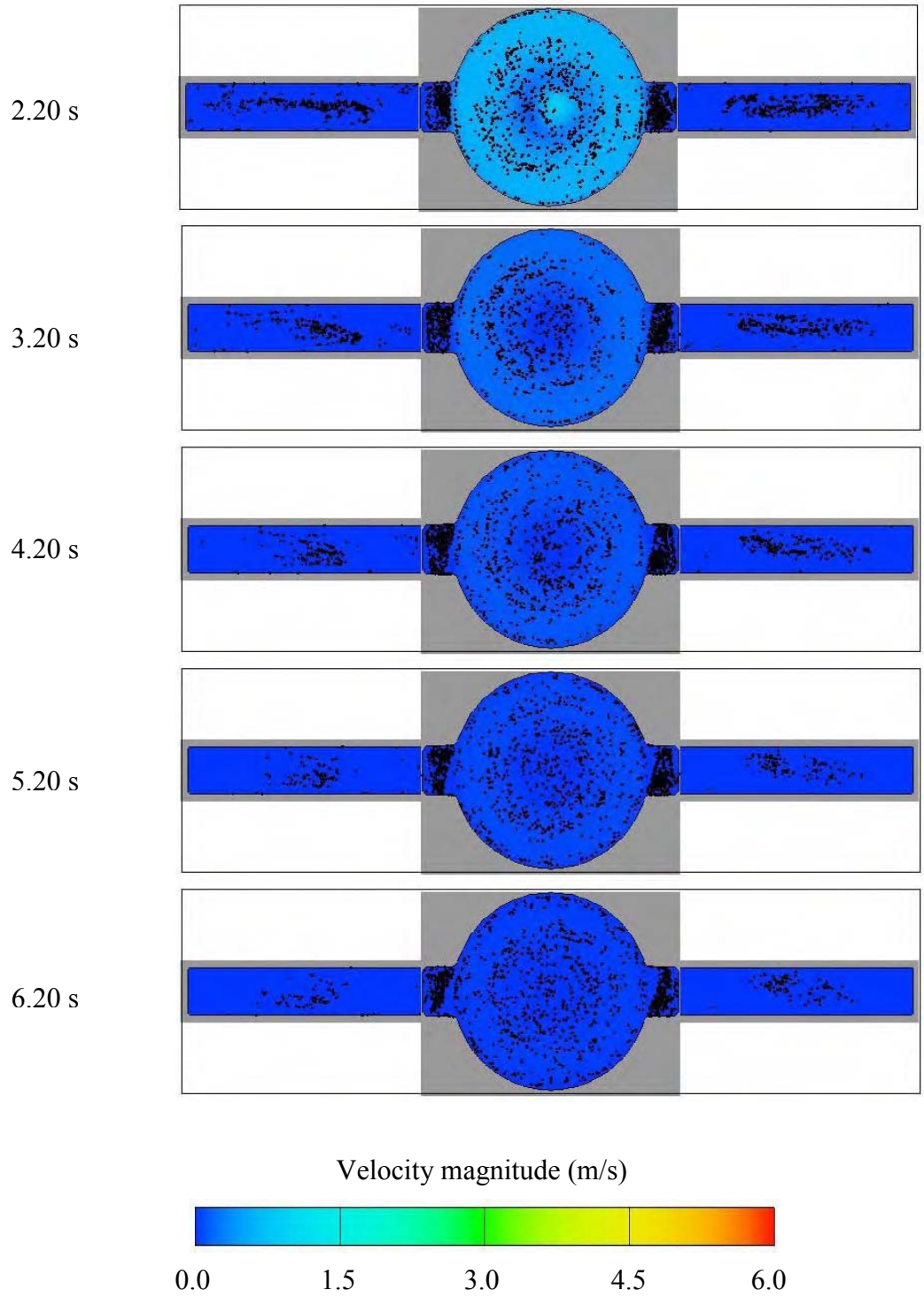

Appendix 25. Flow-3D results of the direct gated casting mould showing plan view and particles. The cut plane was taken at mid-thickness of the test bar pair C1L2DG (4) – C1R2DG (7) (see Figure 6 - 1). Note: Video sequence can be seen in Appendix 60.

0.46 s

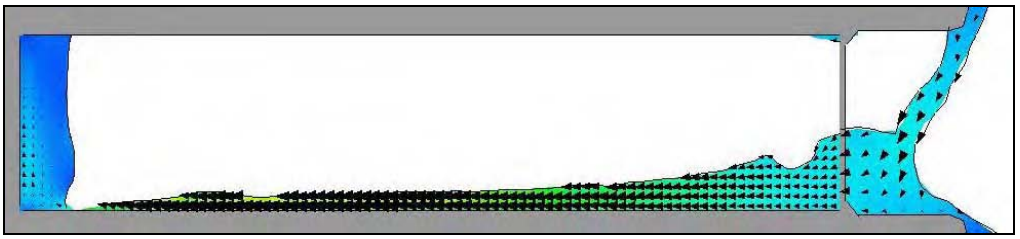

0.48 s

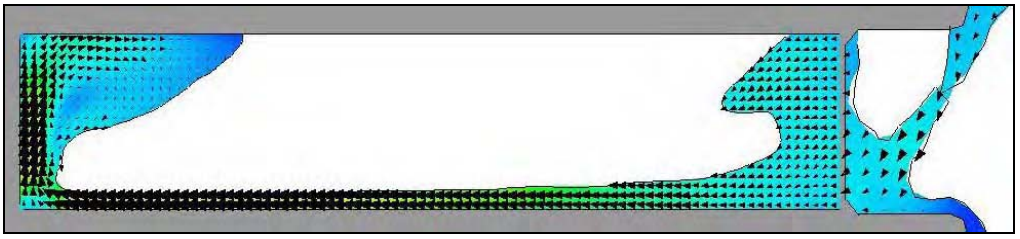

0.50 s

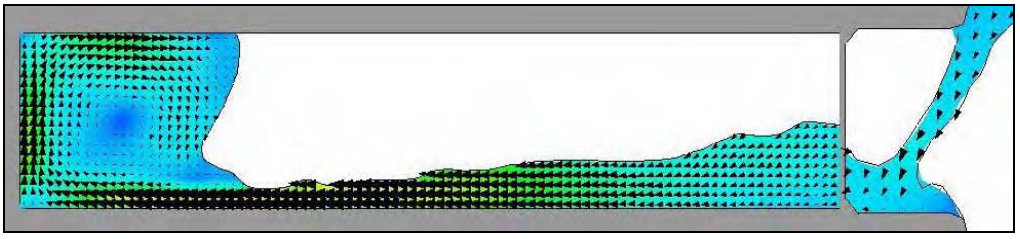

0.52 s

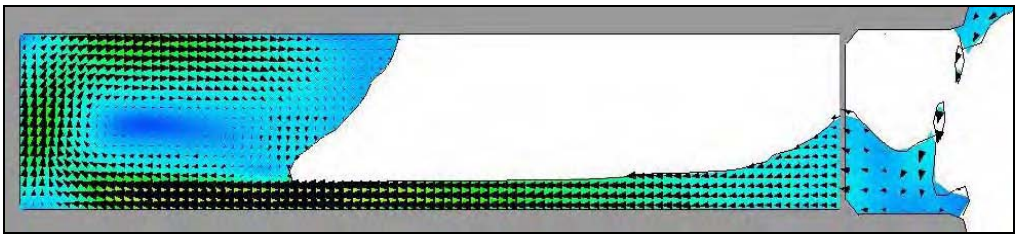

0.54 s

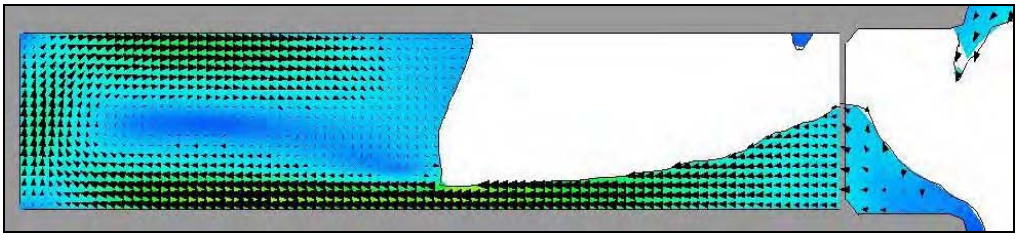

0.56 s

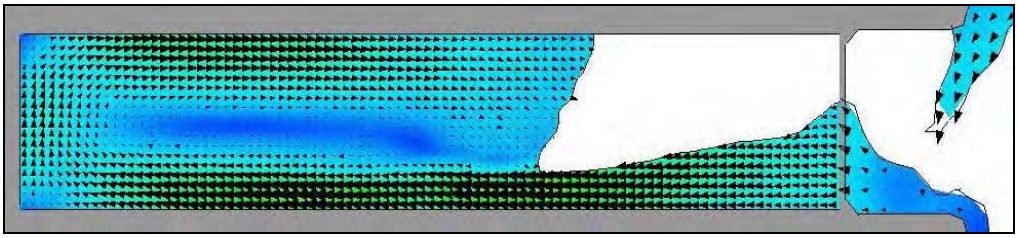

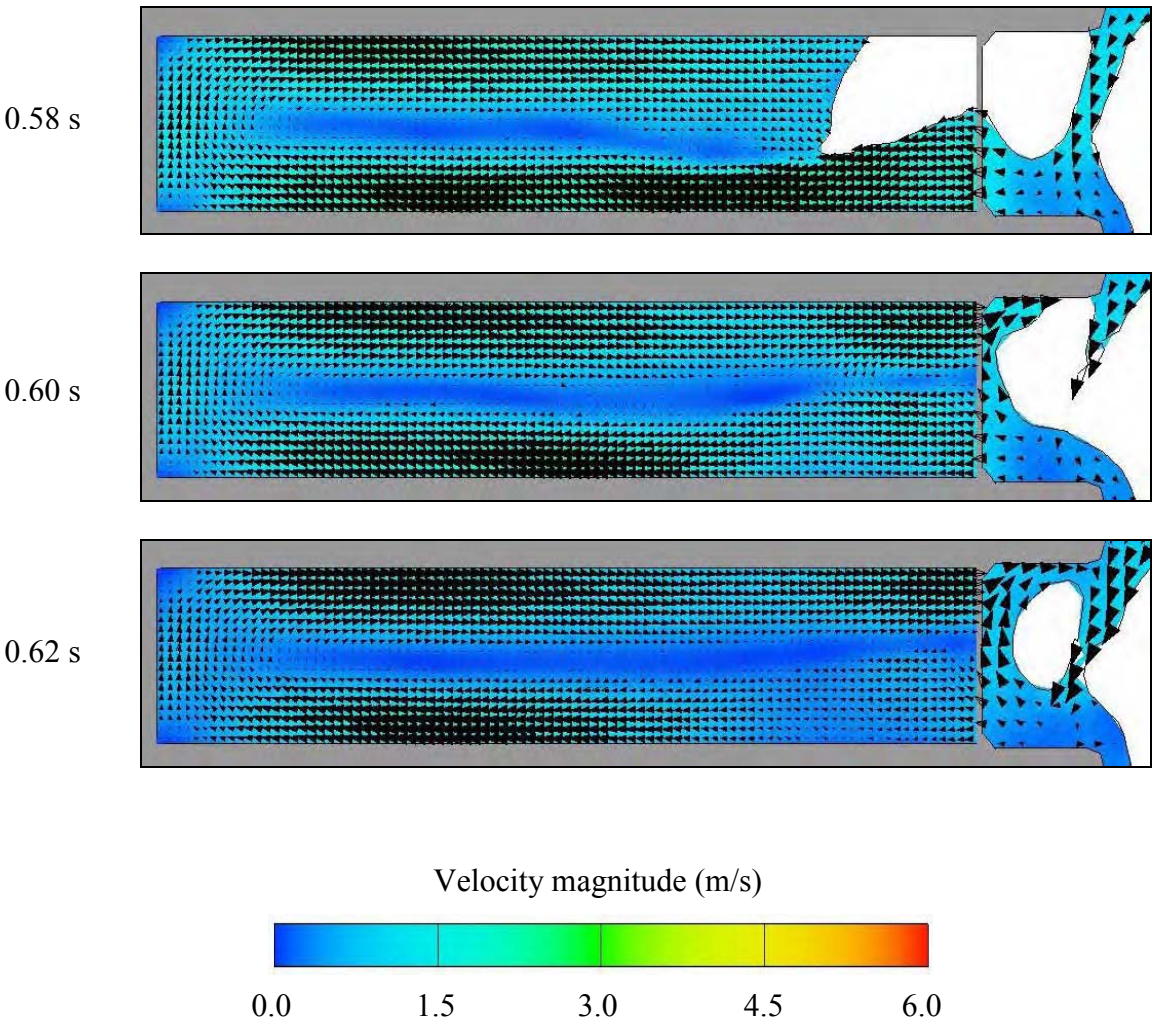

Appendix 26. Flow-3D results showing close-up plan view of the left test bar and velocity vectors. The cut plane was taken at mid-thickness of the test bar C1L2DG (4) (see Figure 6 - 1 and Figure 6 - 140).

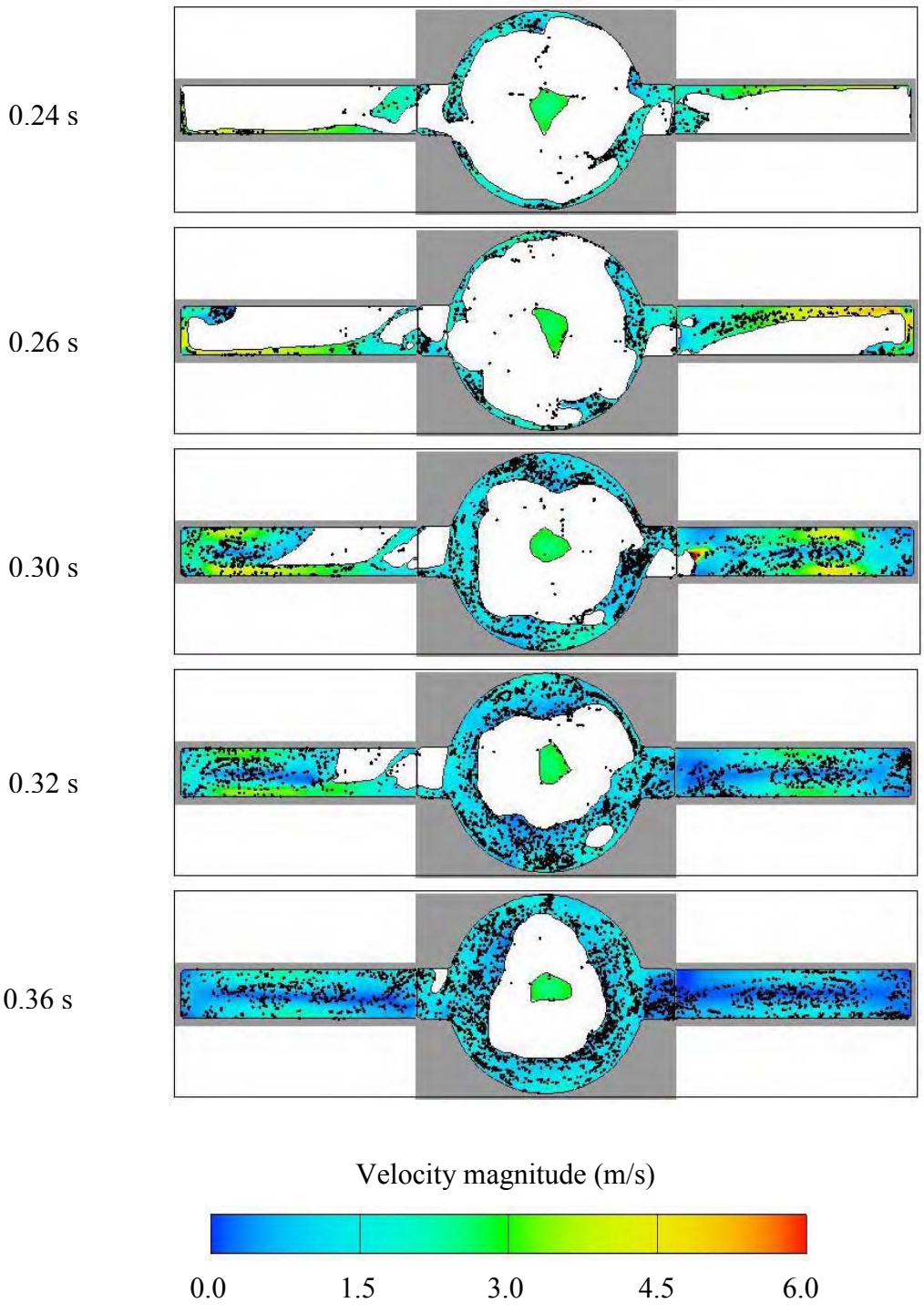

Appendix 27. Flow-3D results of the direct gated casting mould showing plan view. The cut plane was taken at mid-thickness of the test bar pair C1L1DG (5) – C1R1DG (6) (see Figure 6 - 1). Note: Video sequence can be seen in Appendix 61.

0.24 s

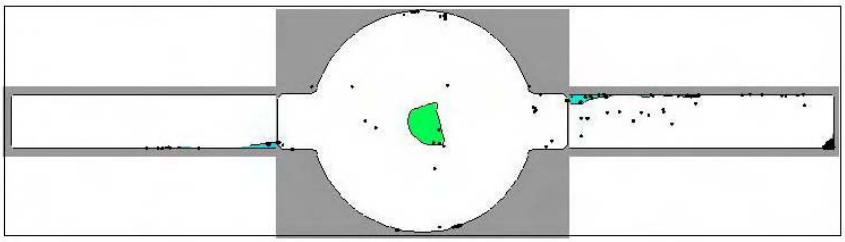

0.28 s

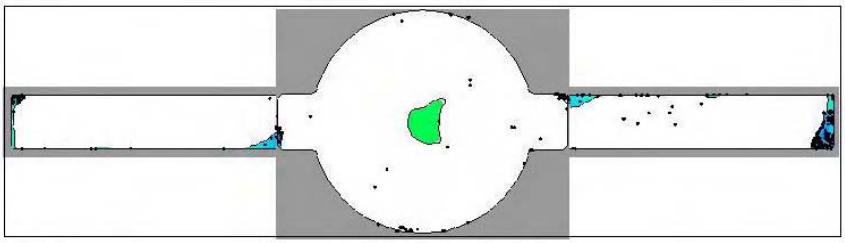

0.50 s

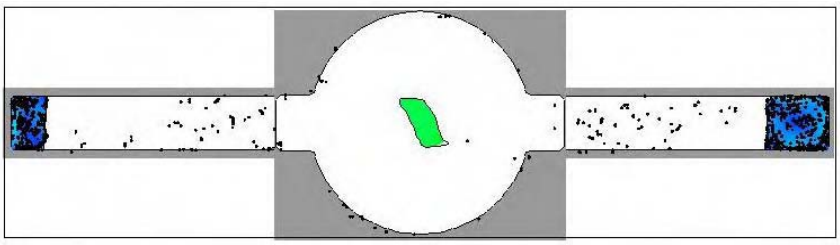

0.60 s

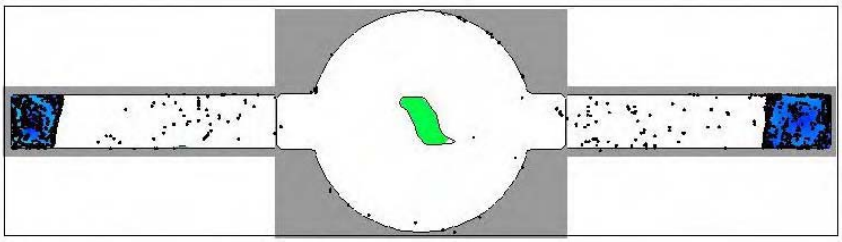

0.70 s

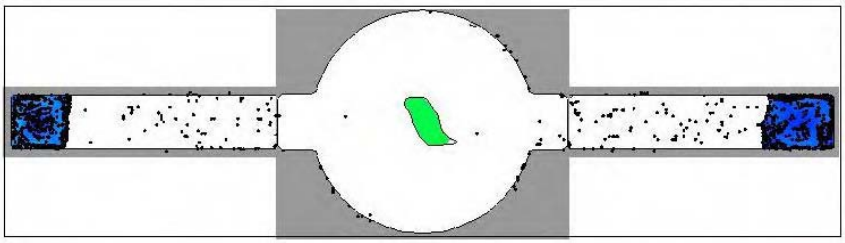

0.76 s

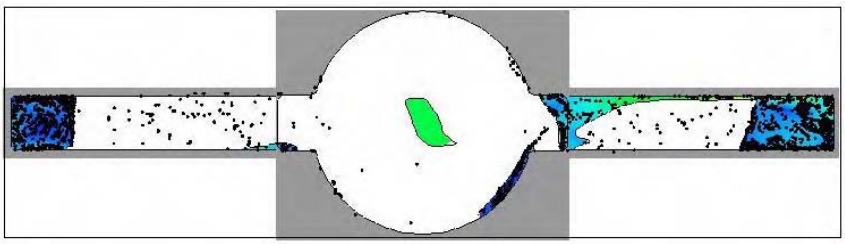

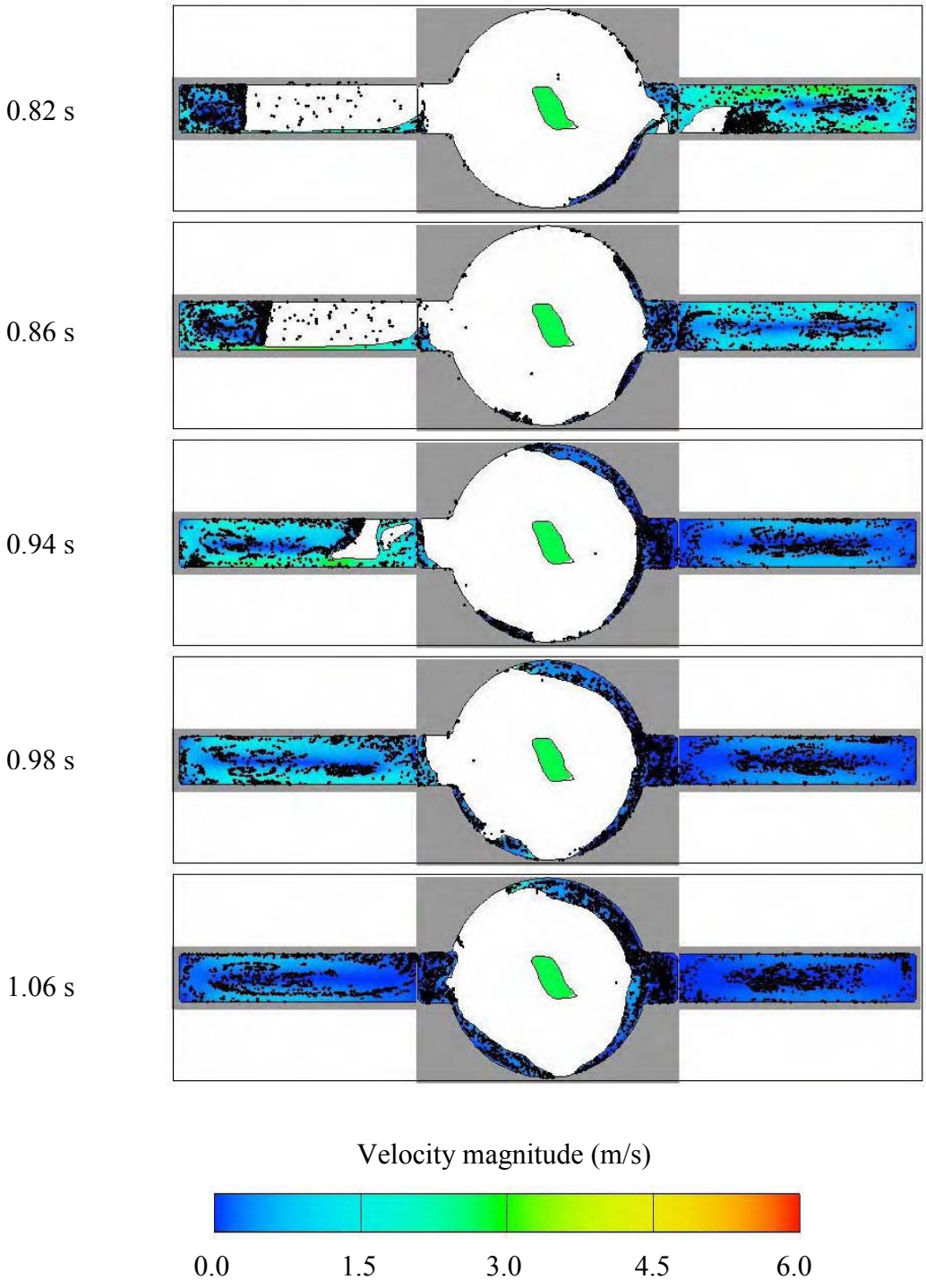

Appendix 28. Flow-3D results of the direct gated casting mould showing plan view. The cut plane was taken at mid-thickness of the test bar pair C1L3DG (3) – C1R3DG (8) (see Figure 6 - 1). Note: Video sequence can be seen in Appendix 62.

0.44 s

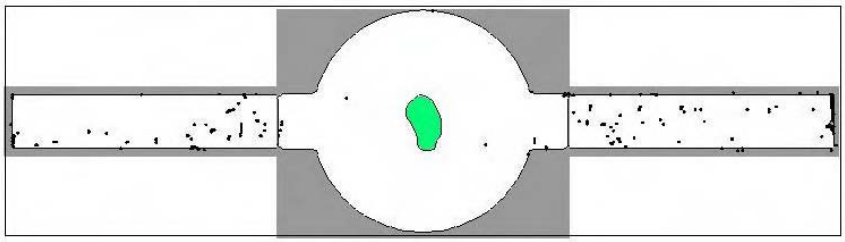

0.48 s

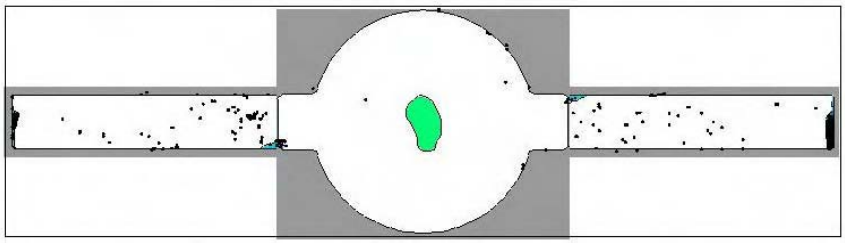

0.80 s

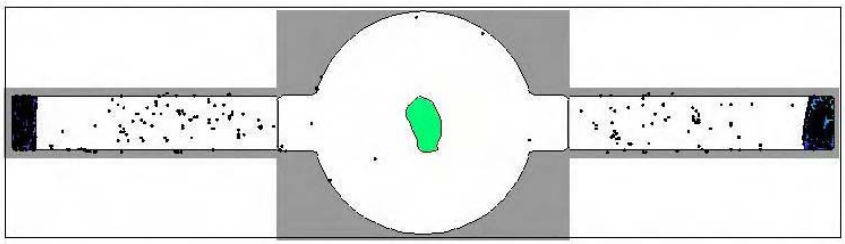

0.90 s

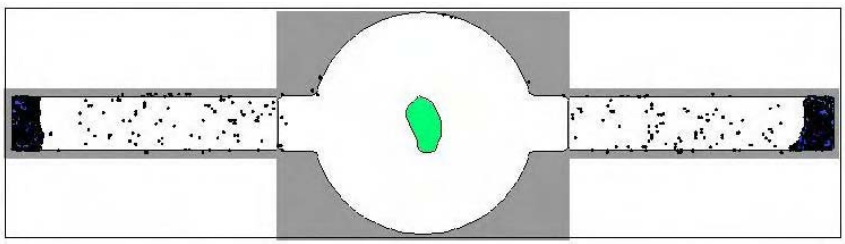

1.00 s

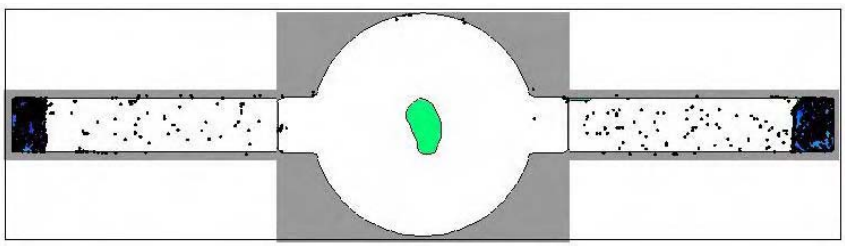

1.10 s

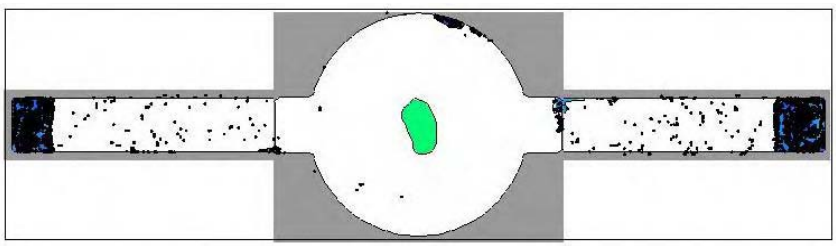

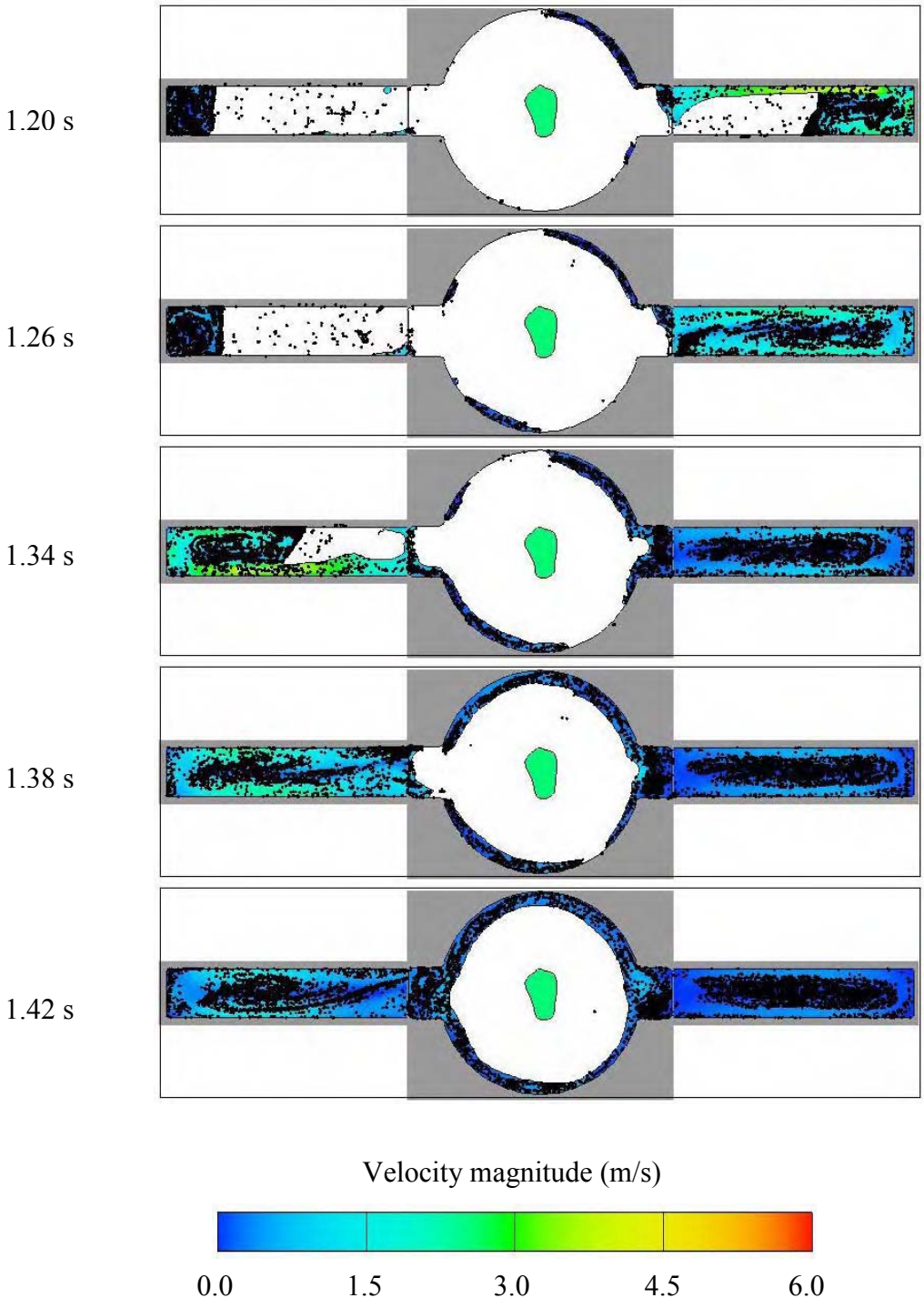

Appendix 29. Flow-3D results of the direct gated casting mould showing plan view. The cut plane was taken at mid-thickness of the test bar pair C1L4DG (2) – C1R4DG (9) (see Figure 6 - 1). Note: Video sequence can be seen in Appendix 63.

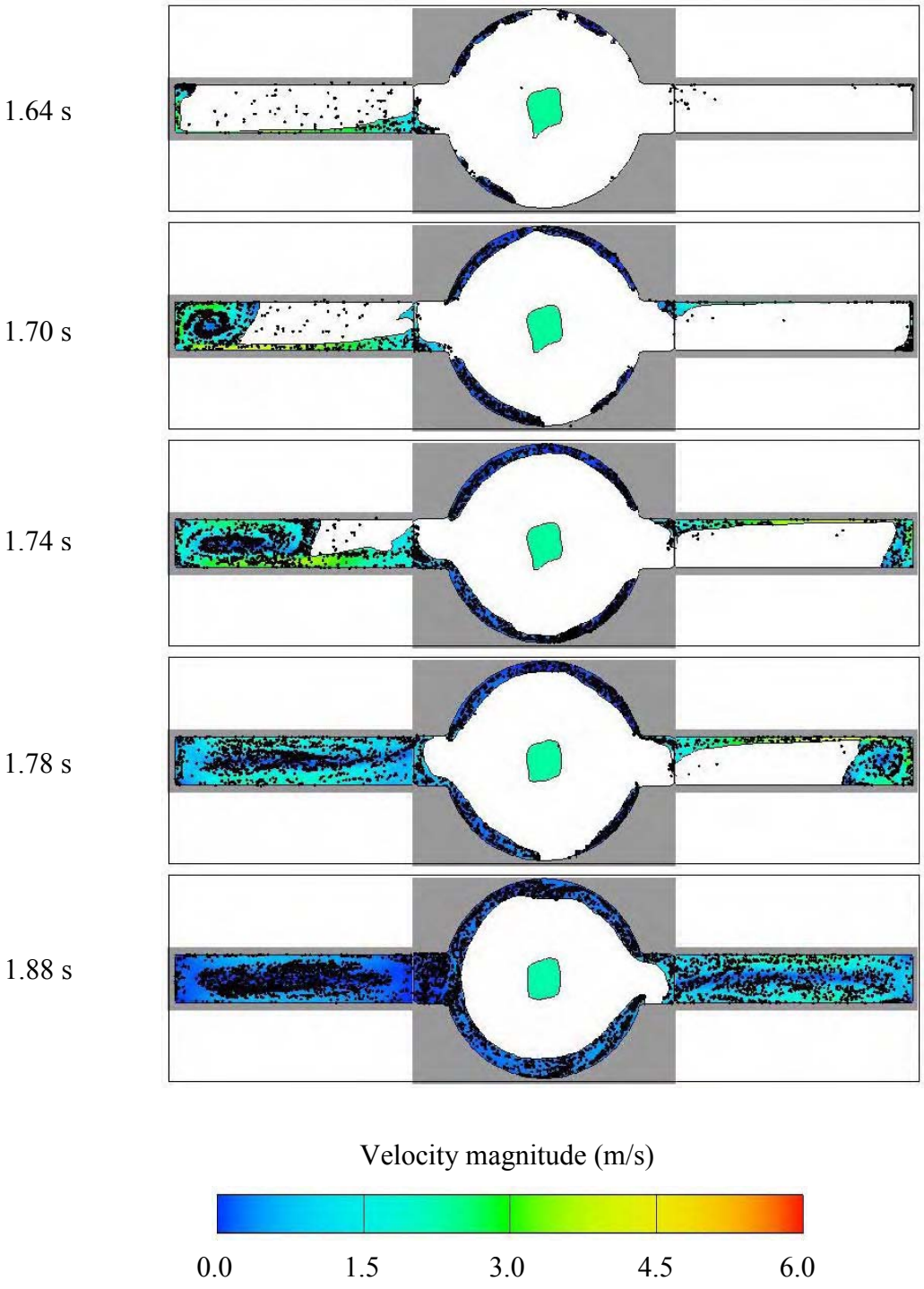

Appendix 30. Flow-3D results of the direct gated casting mould showing plan view. The cut plane was taken at mid-thickness of the test bar pair C1L5DG (1) – C1R5DG (10) (see Figure 6 - 1). Note: Video sequence can be seen in Appendix 64.

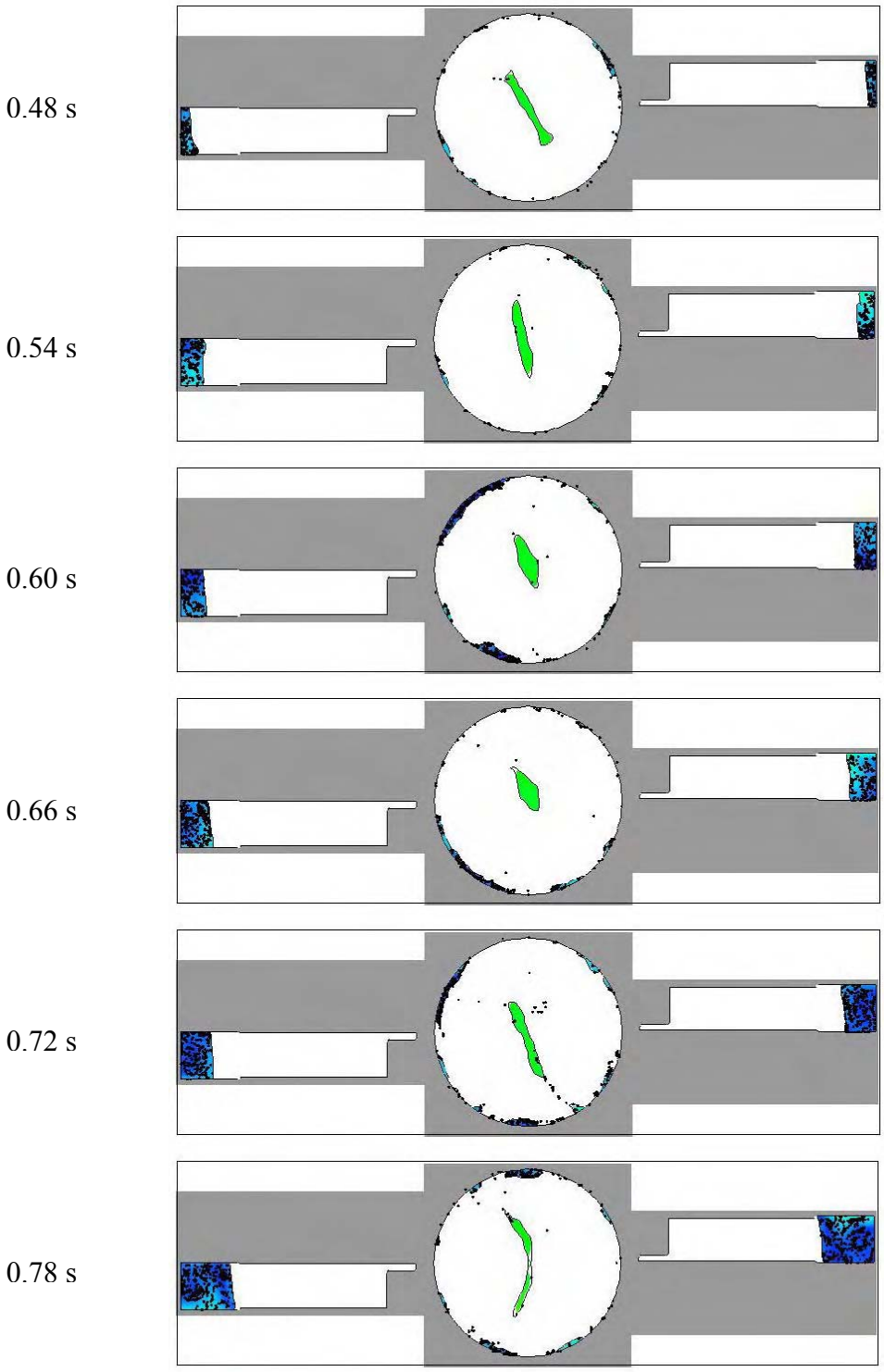
0.48 s
0.54 s
0.60 s
0.66 s
0.72 s
0.78 s

0.84 s

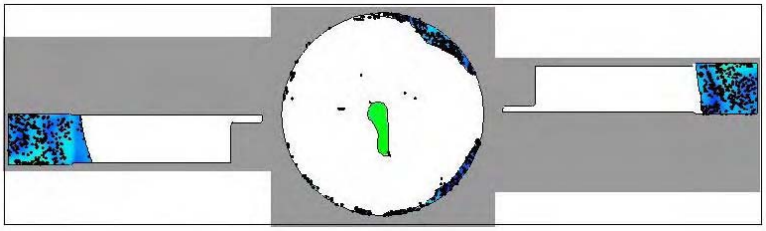

0.90 s

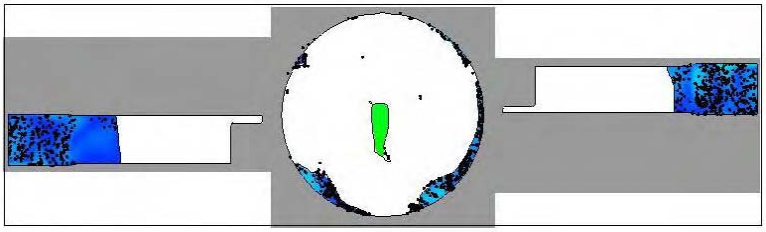

0.96 s

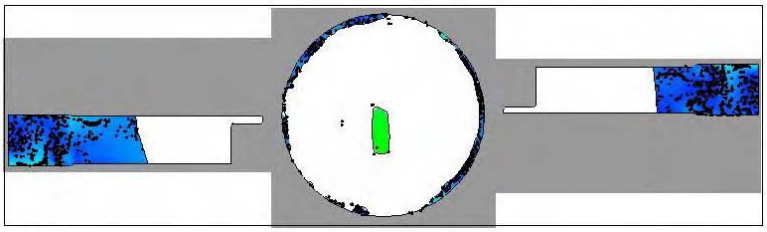

1.02 s

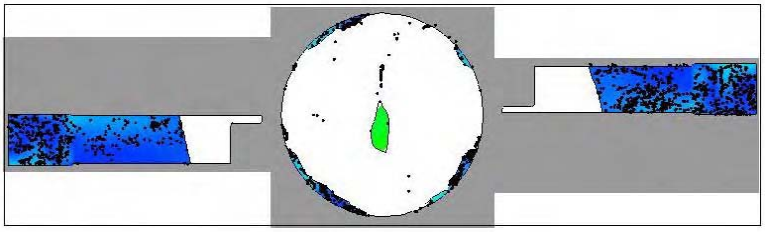

1.09 s

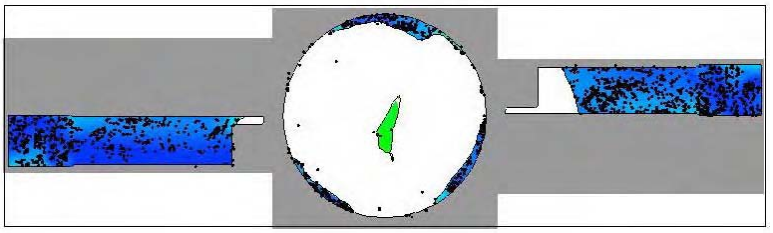

1.20 s

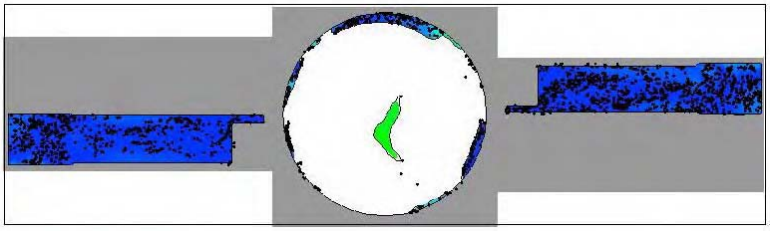

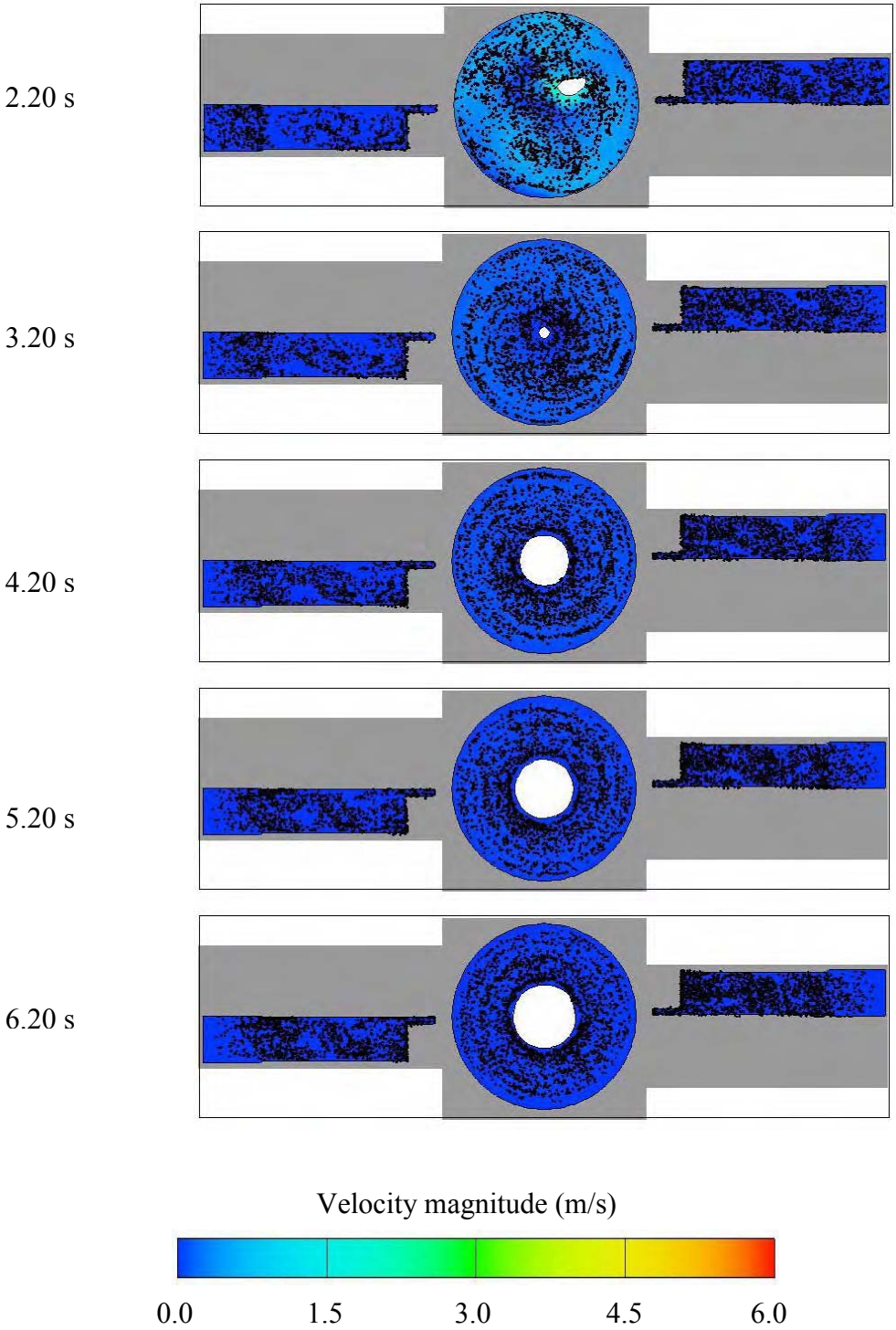

Appendix 31. Flow-3D results of the indirect gated casting mould showing plan view. The cut plane was taken at mid-thickness of the test bar pair C1L1IG (4) – C1R1IG (5) (see Figure 6 - 2). Note: Video sequence can be seen in Appendix 66.

10.2 Video Sequences

These appendices are located in the attached DVD.

As mentioned in Section 4.3.2 the water modelling sequences for the moulds with a cavity thickness of 4 mm were recorded at 1000 frames/s, Appendix 32 to Appendix 40. The close-up of water modelling sequences for the moulds with a cavity thickness of 2 mm were recorded at 2000 frames/s, Appendix 41 and Appendix 42.

Appendix 32. Water modelling of the direct gated mould at 200 rpm.

Appendix 33. Water modelling of the direct gated mould at 300 rpm.

Appendix 34. Water modelling of the direct gated mould at 400 rpm.

Appendix 35. Water modelling of the indirect gated mould at 200 rpm.

Appendix 36. Water modelling of the indirect gated mould at 300 rpm.

Appendix 37. Water modelling of the indirect gated mould at 400 rpm.

Appendix 38. Water modelling of the modified indirect gated mould at 200 rpm.

Appendix 39. Water modelling of the modified indirect gated mould at 300 rpm.

Appendix 40. Water modelling of the modified indirect gated mould at 400 rpm.

Appendix 41. Close-up of water modelling of the direct gated mould at 400 rpm.

Appendix 42. Close-up of water modelling of the indirect gated mould at 400 rpm.

Appendix 43. CFX water modelling results of the direct gated mould at 200 rpm.

Appendix 58. CFX centrifugal casting results of the indirect gated casting mould showing plan view of the left test bar C1L1IG (4) and velocity vectors.

Appendix 59. Flow-3D of the direct gated casting mould showing side view. The velocity magnitude scale is in m/s.

Appendix 60. Flow-3D of the direct gated casting mould showing plan view of the test bar pair C1L2DG (4) - C1R2DG (7). The velocity magnitude scale is in m/s.

Appendix 61. Flow-3D of the direct gated casting mould showing plan view of the test bar pair C1L1DG (5) - C1R1DG (6). The velocity magnitude scale is in m/s.

Appendix 62. Flow-3D of the direct gated casting mould showing plan view of the test bar pair C1L3DG (3) - C1R3DG (8). The velocity magnitude scale is in m/s.

Appendix 63. Flow-3D of the direct gated casting mould showing plan view of the test bar pair C1L4DG (2) - C1R4DG (9). The velocity magnitude scale is in m/s.

Appendix 64. Flow-3D of the direct gated casting mould showing plan view of the test bar pair C1L5DG (1) - C1R5DG (10). The velocity magnitude scale is in m/s.

Appendix 65. Flow-3D of the indirect gated casting mould showing left hand side view. The velocity magnitude scale is in m/s.

Appendix 66. Flow-3D of the indirect gated casting mould showing plan view of the test bar pair C1L1IG (4) – C1R1IG (5). The velocity magnitude scale is in m/s.

11. REFERENCES

ABRAMS, H. 1971. Grain Size Measurement by the Intercept Method. *Metallography,* 4**,** 59-78.

ALCAN. 2011. *http://sales.riotintoaluminium.com/freedom.aspx?pid=526*

ANSYS-CFX. 2011. *http://www.ansys.com/Products/Simulation+Technology/Fluid+Dynamics/ANSYS+CFX*

ASTM 2004. ASTM Standard E112-96 (Reapproved 2004). Standard test methods for determining average grain size. Pennsylvania, USA: ASTM International.

ASTM 2008. ASTM Standard E 855 – 08. Standard Test Methods for Bend Testing of Metallic Flat Materials for Spring Applications Involving Static Loading. Pennsylvania, USA: ASTM International.

ASTM 2009. ASTM Standard E290-09. Standard test methods for bend testing of material for ductility. Pennsylvania, USA: ASTM International.

ASTM 2010. ASTM Standard D790 - 10. Standard Test Methods for Flexural Properties of Unreinforced and Reinforced Plastics and Electrical Insulating Materials. Pennsylvania, USA: ASTM International.

AXIOVISION. 2011. *http://www.zeiss.de/C12567BE0045ACF1/Contents-Frame/668C9FDCBB18C6E2412568C10045A72E*

BAI, H. & THOMAS, B. G. 2001. Turbulent Flow of Liquid Steel and Argon Bubbles in Slide-Gate Tundish Nozzles: Part I. Model Development and Validation. *Metallurgical and Materials Transactions B,* 32B**,** 253-267.

BALASUNDARAM, A. & GOKHALE, A. M. 2001. Quantitative characterization of spatial arrangement of shrinkage and gas (air) pores in cast magnesium alloys. *Materials Characterization,* 46**,** 419-426.

BARDES, B. P. & FLEMINGS, M. C. 1966. Dendrite arm spacing and solidification time in a cast aluminum-copper alloy. *AFS Transactions,* 74**,** 406-412.

BARKHUDAROV, M. 1995. Additions to the particle transport and difussion model for Flow-3D. *Flow Science Inc.,* FSI-95-TN42.

BARKHUDAROV, M. & DITTER, J. L. 1994. Particle transport and difussion. *Flow Science Inc.,* FSI-94-TN39.

BARKHUDAROV, M. R. 2004. Lagrangian VOF advection Method for Flow-3D, http://www.flow3d.com/pdfs/tn/FloSci-TN63R.pdf.

BIDWELL, H. T. 1997. *Investment Casting Handbook,* Dallas, Texas, Investment Casting Institute.

BLUEBEAR. 2011. http://www.bear.bham.ac.uk/bluebear/

BLUM, M., JARCZYK, G., SCHOLZ, H., PLEIER, S., BUSSE, P., LAUDENBERG, H. J., SEGTROP, K. & SIMON, R. 2002. Prototype plant for the economical mass production of TiAl-valves. *Materials Science and Engineering A,* 329-331**,** 616-620.

BOILEAU, J. M., WEBER, S. J., SALZMAN, R. H. & ALLISON, J. E. 2001. The effect of porosity size on the tensile properties of a cast 319-T7 aluminium alloy. *AFS Transactions,* 109**,** 419-432.

BRANDES, E. A. & BROOK, G. B. 1998. *Smithells Light Metals Handbook,* Oxford, Butterworth-Heinemann.

BRITISH-STANDARD 2005. British standard. BS EN ISO 7438:2005. Metallic materials - Bend test.

BROWN, J. R. 1999. *Foseco Non-Ferrous Foundryman's Handbook*, Butterworth-Heinemann.

BROWNE, D. J. & O'MAHONEY, D. 2001. Interface Heat Transfer in Investment Casting of Aluminum Alloys. *Metallurgical and Materials Transactions A,* 32A**,** 3055 - 3063.

BROWNE, D. J. & SAYERS, K. Year. Experimental measurement of investment shell properties and use of the data in casting simulation software. *In:* Modeling of casting, Welding and Advanced Solidification Processes VII, 1995 London, England. The Minerals, Metals & Materials Society, 441-448.

CAMPBELL, J. 2003. *Castings,* Oxford, United Kingdom, Butterworth-Heinemann, Elsevier Science.

CAMPBELL, J. 2004. *Casting Practice. The 10 Rules of Castings,* Oxford, United Kingdom, Butterworth-Heinemann, Elsevier Science.

CASELLAS, D., PEREZ, R. & PRADO, J. M. 2005. Fatigue variability in Al–Si cast alloys. *Materials Science and Engineering A,* 398**,** 171-179.

CHANGYUN, L., SHIPING, W., JINGJIE, G. & HENGZHI, F. 2006. Hydraulic modelling of mould filling behaviour during vertical centrifugal casting processing. *International Journal of Cast Metals Research,* 19**,** 237-240.

CHANSON, H. 1995. Air-water gas transfer at hydraulic jump with partially developed inflow. *Water Research,* 29**,** 2247-2254.

CHANSON, H. 2007. Bubbly flow structure in hydraulic jump. *European Journal of Mechanics B/Fluids,* 26**,** 367-384.

CHOUDHURY, A. & BLUM, M. 1996. Economical production of titanium-aluminide automotive valves using cold wall induction melting and centrifugal casting in a permanent mold. *Vacuum,* 47**,** 829-831.

CLEARY, P., HA, J., ALGUINE, V. & NGUYEN, T. 2002. Flow modelling in casting processes. *Applied Mathematical Modelling,* 26**,** 171-190.

CLEARY, P. W., HA, J., PRAKASH, M. & NGUYEN, T. 2006. 3D SPH flow predictions and validation for high pressure die casting of automotive components. *Applied Mathematical Modelling,* 30**,** 1406-1427.

COCHRAN, C. N., BELITSKUS, D. I. & KINOSZ, D. L. 1977. *Metallurgical and Materials Transactions B,* 8B**,** 323 - 332.

COX, M. & HARDING, R. A. 2007. Influence of tilt filling on Weibull modulus of 2L99 aluminium investment castings *Materials Science and Technology,* 23**,** 214-224.

COX, M., HARDING, R. A. & CAMPBELL, J. 2003. Optimised running system design for bottom filled aluminum alloy 2L99 investment castings. *Materials Science and Technology,* 19**,** 613-625.

COX, M., WICKINS, M., KUANG, J. P., HARDING, R. A. & CAMPBELL, J. 2000. Effect of top and bottom filling on reliability of investment castings in Al, Fe, and Ni based alloys. *Materials Science and Technology,* 16**,** 1445-1452.

CROSS, M., PERICLEOUS, K., CROFT, T. N., MCBRIDE, D., LAWRENCE, J. A. & WILLIAMS, A. J. 2006. Computational Modeling of Mold Filling and Related Free-Surface Flows in Shape Casting: An Overview of the Challenges Involved. *Metallurgical and Materials Transactions B,* 37B**,** 879-885.

DAI, X., YANG, X., CAMPBELL, J. & WOOD, J. 2003. Effects of runner system design on the mechanical strength of Al-7Si-Mg alloy castings. *Materials Science and Engineering A,* A354**,** 315-325.

DAI, X., YANG, X., CAMPBELL, J. & WOOD, J. 2004. Influence of oxide film defects generated in filling on mechanical strength of aluminium alloy castings. *Materials Science and Technology,* 20**,** 505-513.

DAVOUST, L., ACHARD, J. L. & EL HAMMOUMI, M. 2002. Air entrainment by a plunging jet: the dynamical roughness concept and its estimation by a light absorption technique. *International Journal of Multiphase Flow,* 28**,** 1541-1564.

DIVANDARI, M. & CAMPBELL, J. 2001. Mechanisms of bubble trail formation in castings. *AFS Transactions,* 109**,** 433-442.

DIVANDARI, M. & CAMPBELL, J. 2004. Oxide film characteristics of Al–7Si–Mg alloy in dynamic conditions in casting. *International Journal of Cast Metals Research,* 17**,** 182-187.

DIVANDARI, M. & CAMPBELL, J. 2005. Morphology of oxide films of Al–5Mg alloy in dynamic conditions in casting. *International Journal of Cast Metals Research,* 18**,** 187 - 192.

DOUGLAS, J. F., GASIOREK, J. M., SWAFFIELD, J. A. & JACK, L. B. 2005. *Fluid Mechanics,* England, Pearson. Prentice Hall.

DOWLING, N. E. 1999. *Mechanical Behavior of Materials*, Prentice-Hall, Inc.

FAN, Z., WANG, Y., XIA, M. & ARUMUGANATHAR, S. 2009. Enhanced heterogeneous nucleation in AZ91D alloy by intensive melt shearing. *Acta Materialia,* 57**,** 4891 - 4901.

FIJI. 2011. *http://pacific.mpi-cbg.de/wiki/index.php/Auto_Threshold*

FLEMINGS, M. C., KATTAMIS, T. Z. & BARDES, B. P. 1991. Dendrite arm spacing in aluminum alloys. *AFS Transactions,* 99**,** 501-506.

FLOW-3D. 2011. *www.flow3d.com/*

FU, P. X., KANG, X. H., MA, Y. C., LIU, K., LI, D. Z. & LI, Y. Y. 2008. Centrifugal casting of TiAl exhaust valves. *Intermetallics,* 16**,** 130-138.

GOKHALE, A. M. & PATEL, G. R. 2005. Origins of variability in the fracture-related mechanical properties of a tilt-pour-permanent-mold cast Al-alloy. *Scripta Materialia,* 52**,** 237-241.

GREEN, N. R. & CAMPBELL, J. 1993. Statistical distributions of fracture strengths of cast Al-7Si-Mg alloy. *Materials Science and Engineering,* A173**,** 261-266.

GREEN, N. R. & CAMPBELL, J. 1994. Influence of oxide film filling defects on the strength of Al-7Si-Mg alloy castings. *AFS Transactions,* 102**,** 341-347.

GRIFFITHS, W. D., COX, M., CAMPBELL, J. & SCHOLL, G. 2007. Influence of counter gravity mould filling on the reproducibility of mechanical properties of a low alloy steel. *Materials Science and Technology,* 23**,** 137-144.

GUNEWARDANE, D. 2009. The effect of centrifugal casting on the heat transfer coefficient between a solidifying metal and a mould. Metallurgy and Materials. The University of Birmingham, Birmingham.

HALLIDAY, D., RESNICK, R. & WALKER, J. 2001. *Fundamentals of physics,* New York, Wiley.

HALMSHAW, R. 1995. *Industrial Radiology. Theory and Practice,* London, United Kingdom, Chapman & Hall.

HARDING, R. A. 2006. Towards more reliable investment castings. *International Journal of Cast Metals Research,* 19**,** 289-301.

HARDING, R. A. & WICKINS, M. 2003. Temperature measurements during induction skull melting of titanium aluminide. *Materials Science and Technology,* 19**,** 1-12.

HILLIARD, J. 1964. Estimating Grain Size by the Intercept Method. *Metal Progress,* 85.

IMAGEJ. 2011. http://rsb.info.nih.gov/ij/

JAKUMEIT, J., LAQUA, R., HECHT, U., GOODHEART, K. & PERIC, M. Year. Coupled mould filling and solidification simulation applied to centrifugal casting of TiAl parts. *In:* Proceedings of the 5th Decennial International Conference on Solidification Processing, Sheffield, 2007. 292-296.

KATE, R. P., DAS, P. K. & CHAKRABORTY, S. 2008. An investigation on non-circular hydraulic jumps formed due to obliquely impinging circular liquid jets. *Experimental Thermal and Fluid Science,* 32**,** 1429-1439.

KAUFMAN, J. G. & ROOY, E. L. 2004. *Aluminum Alloy Castings. Properties, Processes and Applications,* Materials Park, OH. USA, ASM International.

KENUKE, Y. & FENG, X. 2002. Mechanism of structure formation in circular hydraulic jumps: numerical studies of strongly deformed free-surface shallow flows. *Physica D,* 161**,** 202-219.

KHALILI, A. & KROMP, K. 1991. Statistical properties of Weibull estimators. *Journal of Materials Science,* 26**,** 6741-6752.

KOTADIA, H. R., HARI BABU, N., ZHANG, H. & FAN, Z. 2010. Microstructural refinement of Al–10.2%Si alloy by intensive shearing. *Materials Letters,* 64**,** 671 - 673.

LEE, S. G., GOKHALE, A. M., PATEL, G. R. & EVANS, M. 2006. Effect of process parameters on porosity distributions in high-pressure die-cast AM50 Mg-alloy. *Materials Science and Engineering A,* 427**,** 99-111.

LEE, S. G., PATEL, G. R., GOKHALE, A. M., SREERANGANATHAN, A. & HORSTEMEYER, M. F. 2005. Variability in the tensile ductility of high-pressure die-cast AM50 Mg-alloy. *Scripta Materialia,* 53**,** 851-856.

LEYENS, C. & PETERS, M. 2003. *Titanium and Titanium Alloys,* Koln, Germany, Wiley-VCH V GmbH & Co. KGaA. Weinheim.

LI, C., WU, S., GUO, J., SU, Y., BI, W. & FU, H. 2006. Model experiment of mold filling process in vertical centrifugal casting. *Journal of Materials Processing Technology,* 176**,** 268-272.

LI, H. T., XIA, M., JARRY, P., SCAMANS, G. M. & FAN, Z. 2011. Grain refinement in a AlZnMgCuTi alloy by intensive melt shearing: A multi-step nucleation mechanism. *Journal of Crystal Growth,* 314**,** 285–292.

LIU, K., MA, Y. C., GAO, M., RAO, G. B., LI, Y. Y., WEI, K., WU, X. & LORETTO, M. H. 2005. Single step centrifugal casting TiAl automotive valves. *Intermetallics,* 13**,** 925-928.

MCKEOGH, E. J. & ERVINE, D. A. 1981. Air entrainment rate and diffusion pattern of plunging liquid jets. *Chemical Engineering Science,* 36**,** 1161-1172.

MI, J., HARDING, R. A., WICKINS, M. & CAMPBELL, J. 2003. Entrained oxide films in TiAl castings. *Intermetallics 11,* 11**,** 377 - 385.

MIGUELUCCI, E. W. 1985. The aluminum association cast alloy test program: Interim Report. *AFS Transactions,* 93**,** 913 - 916.

MILLS, K. C. 2002. *Recommended values of thermophysical properties for selected commercial alloys,* Cambridge, Woodhead publishing Ltd.

MROWKA-NOWOTNIK, G., SIENIAWSKI, J. & NOWOTNIK, A. 2006. Intermetallic phase identification on the cast and heat treated 6082 aluminium alloy. *Archives of Metallurgy and Materials,* 51**,** 599-603.

MROWKA-NOWOTNIK, G., SIENIAWSKI, J. & WIERZBINSKA, M. 2007. Intermetallic phase particles in 6082 aluminium alloy. *Archives of Materials Science and Engineering,* 28**,** 69-76.

MUJIKA, F., CARBAJAL, N., ARRESE, A. & MONDRAGON, I. 2006. Determination of tensile and compressive moduli by flexural tests. *Polymer Testing,* 25**,** 766 - 771.

MURAKAMI, Y. & ENDO, M. 1994. Effects of defects, inclusions and inhomogeneities on fatigue strength *International Journal of Fatigue,* 16**,** 163-182.

NGUYEN, T. & CARRIG, J. 1986. Water analogue studies of gravity tilt casting copper alloy components. *AFS Transactions,* 94**,** 519-528.

NYAHUMWA, C., GREEN, N. R. & CAMPBELL, J. 1998. Effect of mold-filling turbulence on fatigue properties of cast aluminum alloys. *AFS Transactions,* 106**,** 215-223.

NYAHUMWA, C., GREEN, N. R. & CAMPBELL, J. 2001. Influence of Casting Technique and Hot Isostatic Pressing on the Fatigue of an Al-7Si-Mg Alloy. *Metallurgical and Materials Transactions A,* 32A**,** 349 - 358.

PACIORNIK, S. & HENRIQUE DE PINHO MAURICIO, M. 2004. *ASM Handbook. Metallography and Microstructures. Digital Imaging,* Materials Park, OH., ASM International.

POLMEAR, I. J. 2006. *Light Alloys. From Traditional Alloys to Nanocristals,* Oxford, United Kingdom, Butterworth-Heinemann.

RANADE, V. V. 2002. *Process Systems Engineering. Volume 5. Computational Flow Modeling for Chemical Reactor Engineering*.

REILLY, C. 2010. *Development of Quantitative Casting Quality Assessment Criteria Using Process Modelling.* PhD, University of Birmingham.

REILLY, C., JOLLY, M. R. & GREEN, N. R. 2009. Investigating surface entrainment events using CFD for the assessment of casting filling methods. *Modeling of Casting, Welding and Advanced Solidification Processes - XII. TMS (The Mineral Metals & Materials Society)***,** 443-450.

REYNOLDS, O. 1883. An experimental investigation of the circumstances which determine whether the motion of water shall be direct or sinuous, and of the law of resistance in parallel channels. *Philosophical Transactions of the Royal Society,* 174**,** 935-982.

ROOY, E. L. 1988. *ASM Handbook. Casting. Aluminum and Aluminum Alloys,* Materials Park, OH., ASM International.

RUSS, J. C. 2007. *The Image Processing Handbook,* Printed in the United States of America, CRC Press. Taylor & Francis Group.

SHAPIRO, E. 2000. *ASM Handbook. Mechanical Testing and Evaluation,* Materials Park, OH., ASM International.

SHEVCHENKO, D. M. 2011. *RE: Personal Communication.*

SHEVCHENKO, D. M., MCBRIDE, D., HUMPHREYS, N. J., CROFT, T. N., WITHEY, P., GREEN, N. R. & CROSS, M. 2009. Centrifugal casting of complex geometries: computational modelling and validation experiments. *Modeling of Casting, Welding and Advanced Solidification Processes - XII. TMS (The Mineral Metals & Materials Society)***,** 77 - 84.

SPEAR, R. E. & GARDNER, G. R. 1963. Dendrite cell size. *AFS Transactions,* 71**,** 209-215.

SUMITOMO, T., CACERES, C. H. & VEIDT, M. 2002. The elastic modulus of cast Mg–Al–Zn alloys. *Journal of Light Metals,* 2**,** 49 - 56.

SUNG, S. Y. & KIM, Y. J. 2007. Modeling of titanium aluminides turbo-charger casting. *Intermetallics,* 15**,** 468-474.

SUTTON, T. L. 2007. *The Basic Principles of Fluid Dynamics Applied to Running Systems of Castings,* England, Institute of Cast Metals Engineers.

THIELE, W. 1962. *Aluminium***,** 707 - 715.

TIRYAKIOGLU, M. 2008a. On the size distribution of fracture-initiating defects in Al- and Mg- alloy castings. *Materials Science and Engineering A,* 476**,** 174–177.

TIRYAKIOGLU, M. 2008b. Statistical distributions for the size of fatigue-initiating defects in Al-7%Si-0.3%Mg alloy castings: A comparative study. *Materials Science and Engineering A,* 497**,** 119-125.

TOTTEN, G. E. & MACKENZIE, D. S. 2003. *Handbook of Aluminum. Physical Metallurgy and Processes. Vol. 1, "Castings",* USA, Marcel Dekker, Inc.

UNDERWOOD, E. E. & COONS, W. C. 1965. *The Role of Quantitative Stereology in Deformation Twinning. Deformation Twinning,* New York.

VERSTEEG, H. K. & MALALASEKERA, W. 2007. *An Introduction to Computational Fluid Dynamics. The Finite Volume Method*, Pearson Education Limited.

WAKEFIELD, G. R. & SHARP, R. M. 1992. *Journal of Science and Technology,* 8**,** 1125 - 1129.

WARMUZEK, M. 2004. *ASM Handbook. Metallography and Microstructures. Metallographic Techniques for Aluminum and its Alloys. ,* Materials Park, OH., ASM International.

WELTY, J. R., WICKS, C. E., WILSON, R. E. & RORRER, G. L. 2008. *Fundamentals of Momentum, Heat and Mass Transfer,* USA, John Wiley & Sons, Inc.

WHITE, F. M. 1999. *Fluid Mechanics,* London, McGraw-Hill

WOJNAR, L. 1999. *Image analysis: Applications in Materials Engineering,* Printed in the United States of America, CRC Press LLC.

WOJNAR, L. & KURZYDLOWSKI, K. J. 2000. *Practical Guide to Image Analysis. Chapter 7: Analysis and Interpretation,* Materials Park, OH., ASM International.

WU, S., LI, C., GUO, J., SU, Y., LEI, X. & FU, H. 2006. Numerical simulation and experimental investigation of two filling methods in vertical centrifugal casting. *Transactions of Nonferrous Metals Society of China,* 16**,** 1035-1040.

WU, X. 2006. Review of alloy and process development of TiAl alloys. *Intermetallics,* 14**,** 1114-1122.

YANG, X., HUANG, X., DAI, X., CAMPBELL, J. & GRANT, R. J. 2006. Quantitative characterisation of correlations between casting defects and mechanical strength of Al–7Si–Mg alloy castings. *Materials Science and Technology,* 22**,** 561-570.

YANG, X., HUANG, X., DAI, X., CAMPBELL, J. & TATLER, J. 2004. Numerical modelling of entrainment of oxide film defects in filling of aluminium alloy castings. *International Journal of Cast Metals Research,* 17**,** 321-331.

YI, J. Z., LEE, P. D., LINDLEY, T. C. & FUKUI, T. 2006. Statistical modeling of microstructure and defect population effects on the fatigue performance of cast A356-T6 automotive components. *Materials Science and Engineering A,* 432**,** 59-68.

YUE, Y. 2011a. *Modelling defect formation during casting.* PhD, University of Birmingham.

YUE, Y. 2011b. *RE: Personal Communication.*

ZHANG, B., LUCK, R. & BERRY, J. T. 2004. Effects of pressure applied during feeding on porosity reduction with reference to fatigue behavior. *AFS Transactions,* 112**,** 237-250.